

CONFERENCE
PROCEEDINGS



9th October 2021
The Institution of Engineers,
Sri Lanka



IESL
YMS

YOUNG MEMBERS'
**TECHNICAL
CONFERENCE
2021**

ORGANIZED BY : YOUNG MEMBERS' SECTION - IESL

IESL YOUNG MEMBERS' TECHNICAL CONFERENCE 2021

Conference Proceedings
9th October 2021



Young Members' Section
The Institution of Engineers, Sri Lanka

© The Institution of Engineers, Sri Lanka 2021.

Young Members Technical Conference 2021 – Conference Proceedings

ISBN 978-624-5810-02-4

First Edition February 2022

This book is published open access.

Open Access. This permits any noncommercial use, duplication, adaptation, distribution and reproduction in any medium or format, as long as you give appropriate credit to the original author(s) and the source.

The articles published here are based on Engineering Research and some are of Professional Interest. All published papers have been refereed in anonymity by at least two subject specialists.

This Institution does not, as a body, hold itself responsible for statements made or opinions expressed either in the papers read or the discussions which have occurred at the meetings.

This book is published by the The Institution of Engineers, Sri Lanka.

120/15, Wijerama Mawatha, Colombo 07. info@iesl.lk, www.iesl.lk

CONTENTS

INTRODUCTION	vi
MESSAGE FROM THE IESL PRESIDENT	vii
MESSAGE FROM THE IESL YMS CHAIRMAN	viii
MESSAGE FROM THE CONFERENCE CHAIR	ix
IESL YMS COMMITTEE 2020/2021.....	x
IESL YMS TECHNICAL CONFERENCE COMMITTEE.....	xi
TECHNICAL PAPERS	

Session 01

A Review on Wind Induced Fatigue Analysis for High-Mast Lighting Towers.....	2
Investigation of Relationship Between Mechanical Properties, Microstructural Features, Heat Treatment Variables and Chemical Compositions of Thermo Mechanically Treated Reinforcement Steel Bars.	7
Numerical Analysis of Carbon Fiber Reinforced Polymer (CFRP) Strengthened Retrofitted Out of Plane Curved Beam Under Flexure	13
Combined Web Crippling & Bending Behaviour of CFS LiteSteel Beams	18
Usage of Mixed Construction and Demolition Waste as Fine Aggregates in Producing Concrete... ..	26
Self-Compacting Concrete Strength Variation Under Wet and Dry Cyclic Process with Different Curing Period.....	31
A Study on Failure Behavior of Concrete Elements.....	38
Predicting External Wind Pressure of a C-Shaped Building Using Explainable Machine Learning (XML)	46
Identification of Natural Frequency and Modal Damping Ratio of Tall Buildings in Sri Lanka ..	54
Economic Feasibility of a Hybrid Energy System for Kalpitiya Peninsula from Selected Technologies.....	62
Path Loss Exponent Estimation for Esp8266 Wireless Sensor Network	70

Development of Mechanical Ventilation Strategy to Achieve Thermal Comfort for Large Occupant Spaces.....	75
Surface Area Measurement of Porous Graphene: A Kinetics Study on Methylene Blue Adsorption Method	82
Precision Dual Axis Tracker for Solar Concentrator.....	87
Performance Analysis of Hierarchical Software Defined Network (SDN) Controller Arrangements in SDNs	92
Design an Ocean Wave Energy Converter for Srilanka	98
Boiler Accidents Reported in Sri Lanka.....	106
The Design Optimization and 3D Printing Technique of Biomimetic Cellular Gyroid Lattice Structure in Fused Deposited Modelling Method	114

Session 02

Assessment of Engineering Properties of Expansive Soils for Subgrade of Pavements.....	122
Validation of HCM model to estimate the delays in minor roads of unsignalized T - junctions in suburban areas under mixed traffic conditions	127
Discrete Choice Modeling Approach for Understanding the Mode Choice Variability.....	132
A Comparative Study of ADT Estimation Models Developed for Sri Lankan Road Network	137
Mix Design and Pavement Analysis of Thin Surfaced Asphalt Pavements for Low Volume Roads..	142
Evaluation of Parking Patterns and the Parking Behavior of the Drivers in Kandy, Sri Lanka.....	150
Colloid Mobilization and Transport in Saturated Porous Media: Laboratory Column Experiments and Numerical Verification	155
Density Effects on Soil Gas Diffusivity in Agricultural Soils	162
A Study on Impact of Three-wheelers in Urban Traffic Congestion.....	168
Pavement Degradation Model for Road Infrastructure in Sri Lanka	175

Session 03

Quality Analysis on Spent Filter Backwash Water of Drinking Water Treatment Plants in Sri Lanka for Reuse.....	182
Comparative Evaluation of the Spatial Distribution of Rainfall for Accurate Runoff Modeling; A Case Study in Upper Kelani River Basin.....	190
Development of Damage Curves for Flood Risk Assessment in Rathnapura.....	198
Water Quality Variation in Cascade Irrigation System; A Case Study in Thirappane Tank Cascade System, Anuradhapura, Sri Lanka	204

Poster Session

Surface Urban Heat Island Effect and Vegetation Cover Analysis of Colombo Metropolitan Area (1997-2020), Sri Lanka, Based on Remote Sensing: A Review	213
Spatial and Temporal Aggregation Analysis of Crash in “A004” Road - Development of Traffic Accident Prediction Model using Traffic & Road Characteristics	222
GPR and LiDAR Synergy: Honeycomb detection in Concrete Structures	230
Assessing the Applicability of Lean Construction Techniques in Sri Lankan Construction Sector	238
Challenges in implementing LED Lighting in Commercial Buildings in Sri Lanka	245
Low cost, Compact Webcam-based System for Biomedical Microscopic Image Analysis	249
AI Based Integrated Autonomous and Mind Controlled UAV	256
Identification of Dengue Mosquito Sound Using Spectral Based Features	265
Comparison of Constitutive Models for Nonlinear Response of Cracked Reinforced Concrete.....	269
Determination of Transverse Thermal Conductivity of Coir Fibres by Analytical Methods	274
Experimental Investigation on Compressive Strength and Porosity in Pervious Concrete with the Effect of Aggregate Size	279

INTRODUCTION

IESL Young Members' Technical Conference 2021 is organized by IESL Young Members' Section along with IESL Annual Sessions, with the objective for all young members of IESL to present their technical papers and discuss engineering related topics with industry professionals and academia.

IESL Young Members' Technical Conference 2021 received 145 submissions in the areas of Aeronautical Engineering, Biomedical Engineering, Chemical Engineering, Civil Engineering, Computer Science Engineering, Electrical, Electronic and Telecommunication Engineering, Marine Engineering, Engineering Management and Mechanical Engineering. YMS has appointed a separate conference sub-committee for organizing the conference this year and after the peer-review process, 31% of the papers were accepted for the presentation with the generous contribution of 91 voluntary reviewers.

This book contains the full papers presented at the IESL Young Members' Technical Conference 2021 held on 9th October 2021 via online platform considering the prevailing situation of the country and the best paper based on the marks given by judges at the presentation will be entitled to the prestigious late Eng. Chandrasena Award.

MESSAGE FROM THE IESL PRESIDENT



As President of the Institution of Engineers, Sri Lanka (IESL) for the session 2020/2021, I write this message for the Young Members' Conference 2021 of the Institution of Engineers, Sri Lanka (IESL). Young Members' Conference is a key academic event held annually by the YMS as part of its activities. Young engineers and engineering undergraduate students can present their experiences and research findings in a prestigious setting at the conference. As a result, this is a fantastic opportunity to gain experience presenting and writing technical papers.

The Young Members' Section continues to pique the interest of Young Engineers, Engineering Undergraduates, and School students in IESL affairs and activities, as well as to groom Young Engineers with opportunities for professional skill development, networking, and inter-disciplinary dialogue, while cultivating future leaders and facilitating succession enhancement of IESL activities. As a result, the YMS serves as a link between young engineers, engineering students, school students, and the IESL. Its role in directing them to the IESL is outstanding.

Despite the current COVID situation, YMS has carried out the Young Members Technical Conference via virtual platforms and ICT technologies. This is a demonstration of not only the capabilities of the digital age but also a message to the community that we should not be discouraged by the prevailing situation and find innovative ways to conduct our regular activities even better than before.

I take this opportunity to congratulate all who got selected to present their papers at the YMS conference 2021, and those who did not get selected should not be discouraged. You should hold on and develop your passion for research and your efforts will be recognized sooner than later.

My special appreciation and gratitude go to the Chairman of the YMS, Organizing Committee of the Conference, Chair of the Conference, reviewers of the research papers, session chairs, and most importantly, the contributors.

Eng. K P I U Dharmapala

President - IESL (2020/2021)

MESSAGE FROM THE IESL YMS CHAIRMAN



It is a great pleasure for me to send this message to the Young Members Technical Conference 2021 of the Institution of Engineers, Sri Lanka. As the Chairman of YMS, I am so happy to have this kind of grand event as a one of key events of the YMS annual calendar. This is the second time YMS organize this event under a separate sub-committee of YMS.

I strongly believe this as a very good opportunity for young engineers and engineering undergraduates to present their research findings and experiences in a recognized arena. This would be a very good starting point for them. We observed high interest among young engineers and engineering undergraduates to present their papers in the conference.

The conference became a reality as a result of more than 6 months of hard work. Dr. Samal Dharmarathna as the conference chair and the organizing committee consist of engineering undergraduates put a tireless effort to bring the conference a success. Many academics and industry experts helped for reviewing the abstracts and full papers while some academics contributed to the judging panels, session chairs and co-chairs. This would be a dream without their excellent support.

I would like to thank the President and the Council of IESL, Editorial Board of IESL, Technical program committee, YMS Executive Committee, YMS Conference Sub-committee, IESL Secretariat and each and every person who directly and indirectly supported to make this event in success. I specially thank to the authors those who presented their technical papers to YMS technical conference.

Finally, We, YMS trust that young engineers and engineering undergraduates will take this opportunity to showcase their talents in future as well.

Eng. Damith Disanayaka

Chairman - IESL YMS (2020/2021)

MESSAGE FROM THE CONFERENCE CHAIR



It is a great pleasure and honour to pen this message as the Conference Chair of the IESL Young Members' Section Technical Conference 2021.

Even though the challenges we faced during the last one and a half years due to the COVID-19 pandemic were hard, they taught us to find innovative paths that eventually led to great research findings. Our conference provides good evidence of such findings and I take this opportunity to congratulate all the young authors, co-authors, and their supervisors who published their research findings in this conference.

Having supervised both undergraduate and postgraduate research, I know the potential of our younger generation, and this conference has proved once more to be a great platform for them to showcase their talents and the skills.

This year, the conference received 145 abstracts from various engineering disciplines such as biomedical, chemical, civil, computer, electrical & electronic, management, manufacturing, and mechanical. Each abstract was reviewed by a minimum of two reviewers under the double-blind process, and altogether, 91 reviewers were involved in this process. Review comments were highly constructive and were appreciated by the authors. Fifty-nine full papers were received for the final stage and among them 32 were accepted for oral presentations whereas 13 were accepted for poster presentations. Here also, the review process was double-blind and 68 experts were involved in the reviewing process. I understand that reviewing abstracts and full papers was quite challenging given the busy schedules of our esteemed reviewers and thus, I take this opportunity to appreciate the contribution and the commitment of all our reviewers.

IESL Young Members' Section Technical Conference 2021 was held online due to the COVID-19 pandemic with the participation of young engineers and engineering undergraduates. Session chairs, co-chairs, and judges ensured that all the sessions were held successfully. All processes were supported by our conference technical program committee which comprised of academic experts from local as well as foreign universities and their contribution was invaluable for the successful completion of this conference.

I should state that the Chairman of IESL Young Members' Section 2021 Eng. Damith Dissanayake was the main pillar of strength and I am grateful for his generous contribution. Last but not least, together with the entire organizing team comprising of engineering undergraduates and young engineers, I would like to thank the Institution of Engineers Sri Lanka for providing us with this golden opportunity. I hope that all those who helped me in numerous ways to make the conference a success will continue to support during the next conference as well.

Finally, let me congratulate the presenters once again. I hope you found the content enriching, were able to renew old fellowships and form new fellowships, and had great deliberation that would stimulate more innovative research in future.

Eng. (Dr.) W. R. Samal Sanjeewa Dharmarathna

PhD (Tokyo), MPhil (Peradeniya), BScEng (Hons) (Peradeniya), AMIE(SL), CMILT(SL)

Conference Chair – 2021

IESL YMS Executive COMMITTEE 2020/2021

Chairman

Eng. Damith Dissanayaka

Secretary

Eng. Randitha Rajapaksha

Immediate Past Chairman

Eng. Navodana Kankanamge

Deputy Chairmen

Eng. Ramjee Kuberalingam

Eng. Manjula Palihawadana

Assistant Secretaries

Eng. Zahra Marzook

Eng. Nadeera Sugandi

Eng. H.A.S. Adhikari

Eng. Pasindu Perera

Media Secretary

Eng. Kasun wijesundara

Treasurer

Eng. Mohan Wijesinghe

Editor

Eng. Nalin Ekanayaka

Web Editor

Eng. Arunalu Weerasooriya

IESL YMS TECHNICAL CONFERENCE 2021

Conference Chair

Eng. (Dr.) W. R. Samal Sanjeeva Dharmarathna, Faculty of Engineering, University of Peradeniya.

Conference Secretary

Eng. P.M.G. Dhanushka Madusanka Herath

Organizing Committee

Editors

Mr. Achala Ishanka Tharamasinghe

Mr. Lahiru N. Dissanayake

Session Coordinators

Mr. H.A.M.M.H.G.U.I.S Bandara

Mr. N.H.P.Mihiran

Mr. Sasindu Harshana Mendis Gunawardhane

Mr. R.P. Shathish Dileepa Sandaruwan Malgahamuduna

Mr. John Keshanth. J

Mr. T.N.H. Senanayake

Mr. M.G.G.S.T. Mahanama

Miss. D.W.V.M. Perera

Mr. Adith Missaka Pindenya

Mr. U.A.P.R.H.R. Bandara

Mr. T.M.Lakshan Prasad Bandara Thelasinghe

Miss. W.V.Malsha Pramodi Jayadari

Mr. R.A. Nadun Priyasanka Rupasinghe

Mr. Premarathnage Chirantha Kasun Premarathna

Mr. A.K.C.M. Amarasingha

Mr. Sinharage Dinuka Madushan

Mr. Matheesha Pahankara

Mr. Yasas Wickramasuriya

Miss. Ganesha Nanayakkara

PANEL OF REVIEWERS

Prof. J.M.J.W. Jayasinghe

Prof. Piyal Ekanayake

Dr. Surangika Ranathunga

Dr. A.G.H.J. Edirisinghe

Dr. A.M.R.G. Athapaththu

Dr. Achala Pallegedara

Dr. Balachandran Ketheesan

Dr. Brian Perera

Dr. Buddhika Karunarathne

Dr. C. J. Gamlath

Dr. C.M. Abeysinghe

Dr. C.M. Gunasekara

Dr. C.S. Bandara

Dr. Chamil Jayasundara

Dr. Chanakya Pannila

Dr. Chandana Jayawardana

Dr. Chandana Siriwardana

Dr. Charith Chitraranjan

Dr. Charitha Dias

Dr. D.T.K. Chamindu

Dr. Damayanthi Herath

Dr. Dammika Abeykoon

Dr. Dilan Rathnayaka

Dr. Dulani Meedeniya

Dr. G.N. Paranavithana

Dr. Ganga Samarasekara

Dr. H.D. Yapa

Dr. Himal A. Suraweera

Dr. I.S.K. Wijayawardane

Dr. Isuru Herath

Dr. J.A.S.C. Jayasinghe

Dr. Jayani Amarathunga

Dr. K.D. Wimalasena

Dr. K.J.C. Kumara

Dr. K.K. Wijesundara

Dr. L K T Srimal

Dr. Laksiri Pradeep

Dr. Loshaka Perera

Dr. M. C. M. Nasvi

Dr. M. Danthurebandara

Dr. M.A.C. Niroshinie

Dr. M.A.S. Preethika

Dr. M.B. Dissanayake

Dr. M.M.G.T. De Silva

Dr. M.P.A.P. Wijayasiri

Dr. M.R. Liyanaarachchi

Dr. Mohan Amarasiri

Dr. N. M. Adassooriya

Dr. N.C. Tennakoon

Dr. N.S. Miguntanna

Dr. Nisansa de Silva

Dr. P.A.K. Karunananda

Dr. P.B.G. Dissanayake

Dr. P.J. Binduhewa

Dr. P.M. Senadeera

Dr. Panduka Neluwala

Dr. Pramila Gamage

Dr. Pubudu Jayathilaka

Dr. S. Amila Silva

Dr. S.K. Abeygunawardane

Dr. Samantha Seneviratne

Dr. Samith Buddika

Dr. Sapumal Ahangama

Dr. Sithumini Ekanayake

Dr. Sulochana Sooriyaarachchi

Dr. Sunimal Rathnayake

Dr. Thanuja Ambegoda

Dr. U. Farook

Dr. U.A. Higgoda

Dr. U.S.S. Dharmapriya

Dr. Upaka Rathnayake

Dr. Upul Jayasinghe

Dr. Uthayasanker Thayasivam
Dr. W.A.S Wijesinghe
Dr. W.C.T.K. Gunawardana
Dr. W.M.M.T.S. Weerakoon
Dr. W.M.N.R. Weerakoon
Dr. W.M.V.S.K. Wickramasinghe
Dr. W.R.S.S. Dharmarathna
Dr. Windhya Rankothge
Dr. Melaka Senadeera
Dr. T.W.K.I.M. Dias
Eng (Dr) de Silva C. R.
Eng. Gayanath Rathnayaka
Eng. K.R. Withanage
Eng. N.U. Akwatta
Eng. Pravinth Balthazar
Eng. R.M. Wijesinghe
Eng. Ramesha Soysa
Eng. Sajith Udayanga
Eng. Udari Basnayaka
Eng. W.A. Chanaka Prabhath
Eng. W.A.D.G.I. Wanasinghe
Eng. W.A.M.L. Wasala
Mr. A.D. Peter
Mr. D.D. Dias
Mr. Darshana Priyasad
Mr. Hansika Weerasena
Mr. M. A. K. M. Dharmasiri
Mr. Manesh Jayawardhana
Mr. R A S K Jayasena
Mr. Sachin Mibashara Kahawala

Mr. W. E. P. S. Ediriweera
Ms. Akila Pemasiri
Ms. Shanika Arachchi
Ms. T. Ariyaratna
Ms. Thilini Ranasinghe
Ms. W. Menike

PANEL OF JUDGES

Assoc. Prof. Upaka Rathnayake
Dr. Achala Pallegedara
Dr. Ajith Thamboo
Dr. Amila Silva
Dr. B. Ketheesan
Dr. Champika Ellawala
Dr. Ganga Samarasekara
Dr. Isuru Wijayawardane
Dr. Kamal Karunananda
Dr. Nilan Weerakoon
Dr. Panduka Neluwala
Dr. Rasara Samarasinghe
Dr. Ruwan Appuhami
Dr. Saranga Abeygunawardane
Dr. Shiran Jayakody
Dr. Srimali Preethika
Dr. Vidura Jayasooriya
Dr. WMKRTW Bandara
Mr. Chanaka Prabhath
Mr. Lasitha Weerakoon

TECHNICAL PAPERS

Session 1

A Review on Wind Induced Fatigue Analysis for High-Mast Lighting Towers

K. Jeyamohan
 Dept. of Engineering Technology
 Faculty of Technology
 University of Jaffna
 Kilinochchi, Sri Lanka
 Jeya@tech.jfn.ac.lk

C. S. Bandara
 Dept. of Civil Engineering
 Faculty of Engineering
 University of Peradeniya
 Kandy, Sri Lanka
 csbandara@eng.pdn.ac.lk

J. A. S. C. Jayasinghe
 Dept. of Civil Engineering
 Faculty of Engineering
 University of Peradeniya
 Kandy, Sri Lanka
 supunj@eng.pdn.ac.lk

Abstract— Recent developments on high-mast arm structures have increased awareness of the fatigue behavior associated with these structures. Mast arm structures that are subjected to cyclic loading conditions tend to fail due to fatigue failure. Size and thickness of base plate, geometry and thickness of mast arm, welding thickness and numbers of anchor bolts are highly influencing on the fatigue performance of a high-mast lighting tower system. It was found that, dynamic characteristics and damping ratio of the mast arm also has the most significant effect on the hotspot stress of the mast arm wall system. Palmgren Miner theory of cumulative damage method, Weibull wind distribution and S-N Curves are widely used to estimate the fatigue life of the structures. Since, there are no redundancy built into this high-mast arm structures, failure of these structures would be very hazardous. Generally, failures are observed around the man access hole, base connection and anchor bolt location due to high stress concentration at these locations. Furthermore, lock-in conditions in the second mode must be investigated as this mode is more critical for bending response. So, fatigue study of high-mast arm structures should be performed against excessive stress developed due to resonant vibration of periodic or random oscillation depending upon the flow regime.

Keywords—Hotspot, high-mast arm, damage, fatigue

I. INTRODUCTION

High-mast arm structures are widely used to illuminate the lights for the sports complex, highway interchanges, airports and some industrial yards. There is significant effect on the mast-arm structures from two types of wind action, these are; (1) Along-wind action: -buffeting by atmospheric turbulence, (2) Cross-wind action: - mainly due to vortex shedding action, which acts perpendicular to along wind direction as shown in Fig. 1.

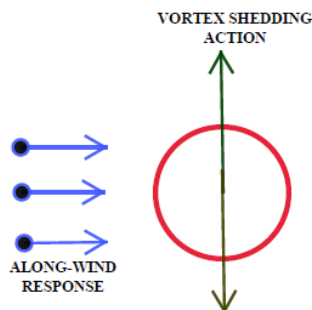


Fig. 1. Vortex shedding action over the cylinder

Spectral method (Hansen method) and vortex resonance method are widely used to estimate the vortex shedding induced forces on slender steel structures [1]. These methods are based on the assumption that, the vortex shedding creates

sinusoidal forces of harmonic nature that are perpendicular to along wind direction. Geometry of mast arm, man access hole, base connection and free-standing length of the pole are important parameters, because these are highly influencing on the fatigue performance of the mast arm structures under cyclic wind action [2]. Wind forces acting on these wind sensitive structures are mainly depending on basic wind speed, terrain category and dynamic response [3]. Generally, vortex shedding concept generates sinusoidal excitation model on circular cylindrical mast arm and negative aerodynamic damping is developed due to this excitation forces. Nominal stress approach and hotspot stress approach are widely used to estimate the fatigue life of mast arm structures under stress cycles which are developed by wind action. Equivalent structural stress method also is one of the best techniques available to estimate the fatigue life with advantage of mesh insensitive quality and capability of unifying different S-N Curves [4]. S-N curves are used to estimate the number of load cycles under hotspot stress with reference value of two million load cycles as shown in Fig. 2.

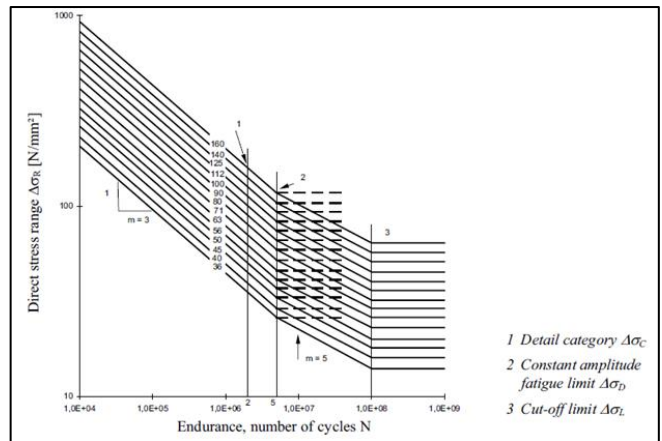


Fig. 2. S-N Curves with suitable category [14]

In mast arm structures, most of the fatigue failures are occurring due to large number of stress cycles which are generated due to large vibration with lock in condition [5]. There are many variables are involved in the hotspot stress variation of mast-arm structures. The major variables are; mean wind profile, damping, mode shapes, natural frequency at each mode, flow characteristics, Reynolds number, surface toughness and mass distribution of structures [6]. Finite element model is used to estimate the hotspot stress due to along and vortex shedding wind action and fatigue life could be estimated by accumulating the fatigue damage with consideration of dynamic response [7]. Wind induced fatigue damage can be mitigated by following methods;

- (1) By altering the geometry of mast arm structures before and after installation.
- (2) By reducing the movement of mast arm by adding aerodynamics devices to disturb the vortex streets.
- (3) By adding mechanical devices to reduce the vibration.

The aim of the study of the mast arm structure is to identify the factors are influencing on the fatigue performance of the system under wind action.

II. THEORETICAL STUDY

The vortex shedding induced forces are mainly depends on Reynolds number Re at the critical wind velocity (V_{crit}) as given in Eq. (1).

$$Re = D * V_{crit} / \nu \quad (1)$$

Where; D is frontal width / diameter of mast arm wall and ν is kinematic viscosity of air ($15 * 10^{-6} m^2/s$). The calculation of vortex shedding induced force, presented in EN 1991-1-4:2005 [8] is directly correlated with deflection ($y_{F,max}$) of mast arm structures as given in Eq. (2).

$$y_{F,max}/b = (1/St^2) * (1/Sc) * K * K_w * Clat \quad (2)$$

where; St is Strouhal number (0.18), Sc is Scruton number, $Clat$ is the lateral force coefficient, L_j is the effective correlation length, K is the mode shape factor and K_w is the effective correlation length factor. Ruscheweyh has modified the basic sinusoidal model by the use of "effective correlation length". This term allows to apply the vortex shedding induced forces over a height range less than total height of mast-arm structures [6]. The assumed vortex shedding induced forces on the high-mast lighting tower system (F_w) can be calculated using Eq. (3), which is given in EN 1991-1-4:2005.

$$F_w = m(s) * (2\pi n_{i,y})^2 \Phi_{i,y}(s) y_{F,max} \quad (3)$$

where; $m(s)$ is the vibrating mass of the structure per unit length (kg/m), $\Phi_{i,y}$ is the mode shape of the structures normalized to 1, y_{max} is the maximum displacement over time of the point with $\phi_{i,y}(s)$ equal to 1 and $n_{i,y}$ is the natural frequency of the system. Modal analysis should be performed to obtain the natural frequency of mast arm structures at 1st and 2nd modes as shown in Fig. 3.

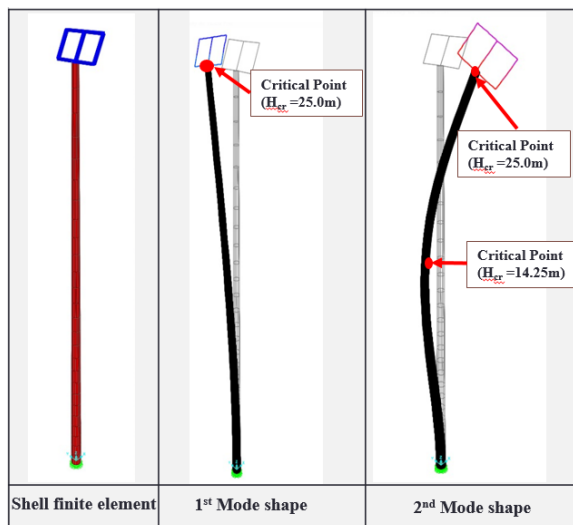


Fig. 3. Modal analysis output for 1st and 2nd mode

Cumulative fatigue damage is generally estimated using Palmgren -Miner rule as shown in Eq. (4).

$$D = \sum \{n_i(\Delta\sigma)/N_i(\Delta\sigma)\} \quad (4)$$

where; $n_i(\Delta\sigma)$ is the number of cycles of stress load for a specified stress range for which $N_i(\Delta\sigma)$ is the cycles of load which is expected before the structure suffers damage [9]. Number of cycles for the particular stress is obtained using S-N curves with consideration of suitable detail category for each structural element. Generally, following detail category should be used for each structural element of mast arm structures [3].

- (1) Category 140 is used for the mast arm wall.
- (2) Category 80 is used for the base connection with fillet weld.
- (3) Category 71 is used for the base connection with butt welds.

Number of Load cycles caused by vortex excitation can be calculated using the mean and critical wind velocity profile and the natural frequency of the cross-wind mode as given in EN1991-1-4:2005 (E10). Also, natural frequency of high-mast arm structures at each mode should be obtained using modal analysis. It is generally assumed that, critical location of vortex shedding induced forces is at antinodes point of mast arm structures as shown in Fig. 4.

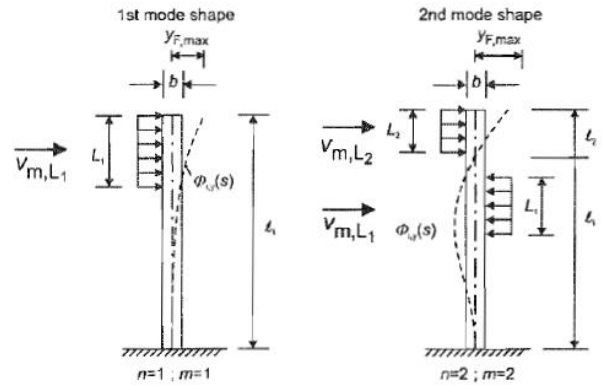


Fig. 4. Effective correlation length for 1st and 2nd mode

III. FACTORS AFFECTING THE FATIGUE PERFORMANCE OF MAST ARM STRUCTURES.

A. Geometry of mast arm and base connection

The variation of stress concentration factor (SCF) with base plate thicknesses from three different research study clearly shows that, base plate thicknesses are highly influencing on the fatigue performances of the high-mast lighting tower system as shown in Fig. 5. SCF is decreased with increasing of the base plate thickness of the mast arm structures. Therefore, it can be concluded that, the base plate thickness of the high mast lighting tower system is an important parameter and special concerns should be given at the time fatigue design of high-mast lighting tower system [2],[10], [11].

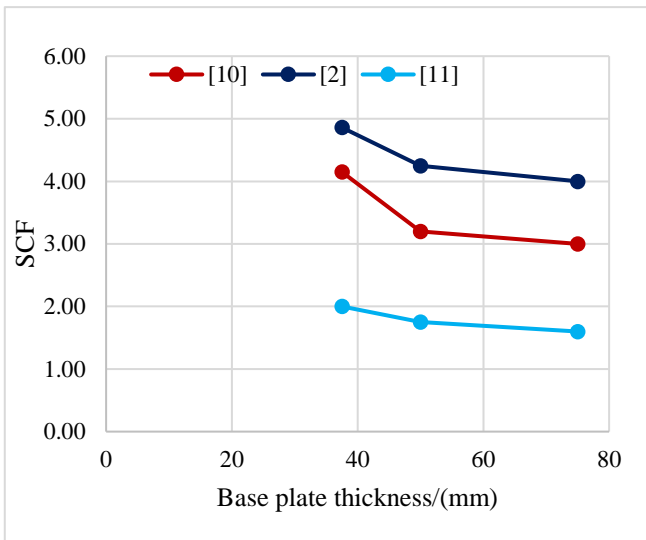


Fig. 5. Variation of SCF with base plate thickness

Increasing the base plate thickness from 37.5mm to 50.0mm for the unstiffened base model of the mast-arm structure, decreases the interface of mast arm wall and base plate SCF by 35%. Therefore, interface of the mast arm wall and the base plate connection was identified as a high stress concentration area and first crack was identified on this particular location of unstiffened base connection, as shown in Fig. 6. Therefore, in order to improve the fatigue life of the high-mast lighting tower system, connection between the base plate and mast arm wall should be designed to withstand the high fatigue loads due to along wind and vortex shedding induced loads [10].

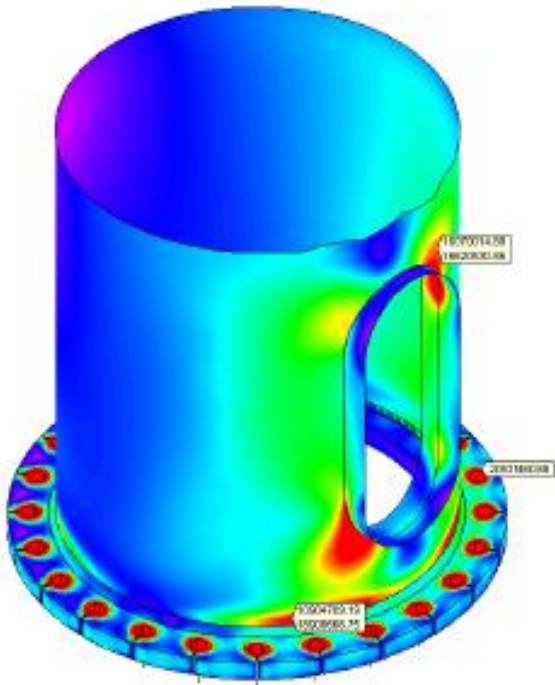


Fig. 6. Location of Fatigue crack [10]

Increasing the base plate thickness provides significant improvement to the fatigue life of the towers by reducing the maximum stress at the base plate to tube wall connection as shown Fig. 7. Therefore, base plate flexibility has a considerable influence on the stress behaviour in the tube wall

adjacent to the unstiffened connection of the high mast lighting tower system [2].

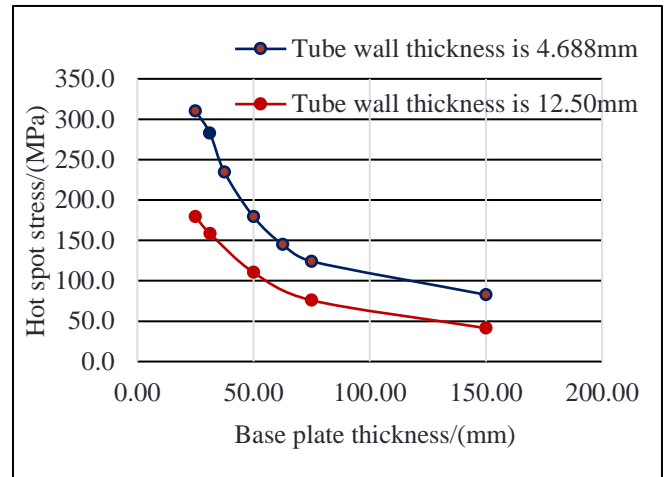


Fig. 7. Variation of hotspot stress with base plate thickness [2].

B. Numbers of Anchor bolts

In this Fig. 8, the normalized hotspot stress decreases as the number of anchor rods are increased. Also, it shows that, increasing the base plate thickness does not have any adverse impact on the hotspot stress variation of the high-mast lighting towers. It is found that, four anchor rods or eight anchor rods configurations are adequate and there is no need to use greater number of anchor rods [2].

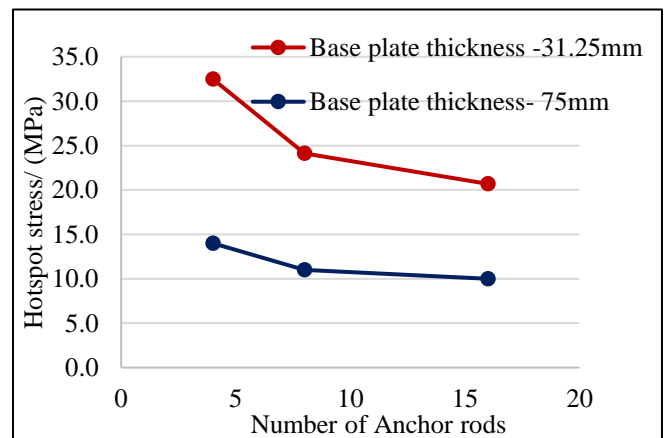


Fig. 8. Variation of hotspot stress with number of Anchor bolts (Mast arm wall thickness -4.68mm) [2].

C. Geometry of Stiffeners

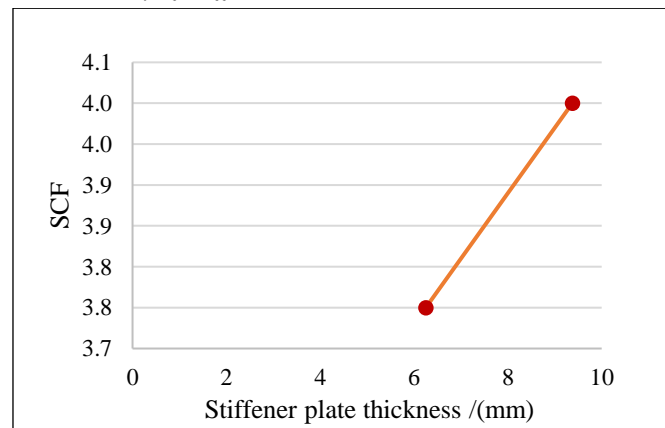


Fig. 9. Variation of SCF with stiffener plate thickness [10]

As shown in Fig. 9, there are no significant effect on SCF at socket weld location due to changing the thickness of the stiffener wall. The stiffener SCF is only increased by 7% when increasing the thickness of the stiffener plate by 50%. Also, it is found that, socket weld SCF for the unstiffened model is greater than the SCF for the stiffened model [10]. It can be concluded that, thicknesses of mast-arm wall and base plate are highly influencing on the SCF and hotspot stress of the mast arm structures compare to number of anchor bolts and geometry of stiffener wall.

IV. FATIGUE STUDY

There are several factors playing an important role to influence the accuracy of estimation of the fatigue life. These are [2];

- (1) Errors in numerical model.
- (2) Errors in estimation of wind forces.
- (3) Approximations on stress estimation using S-N Curves.

S-N curve is used for the fatigue assessment with particular detail category for the each structural elements of the structural system. The detail category takes into consideration the local stress concentrations at the detail, the shape and size of the maximum acceptable discontinuity, the loading condition, metallurgical effects, residual stresses, welding and any post weld improvement [3]. Weibull distribution method is used to estimate the number of cycles of stress load for a specified stress range as shown in Fig. 10. Fatigue damage for the narrow-band vibration for the all-mean wind speed can be obtained by using Weibull distribution and Rayleigh distribution. Total damage caused by along wind action is generally could be ignored, but fatigue damage from vortex shedding action will be significant [12].

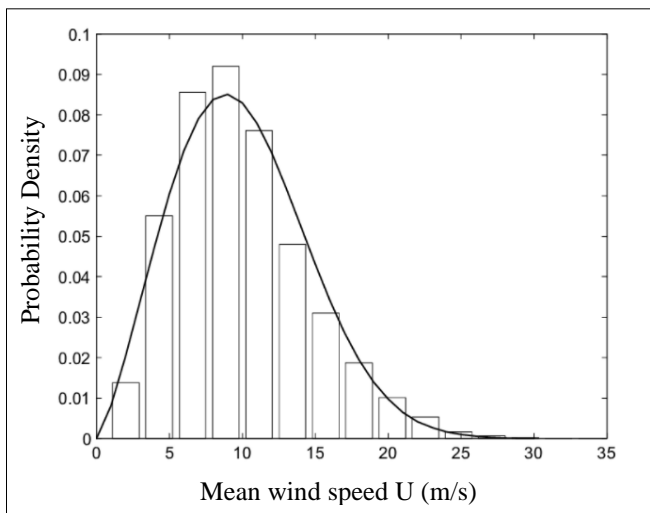


Fig. 10. Weibull wind distribution

It is found that, fatigue life calculated by equivalent structural stress method is 15% higher than that calculated by hotspot stress method as shown in Fig. 11. Also, it can be concluded that, estimation of fatigue damage and fatigue life using equivalent stress method is more conservative and safer than hotspot stress method. But nominal stress method is widely used in the field of civil engineering.

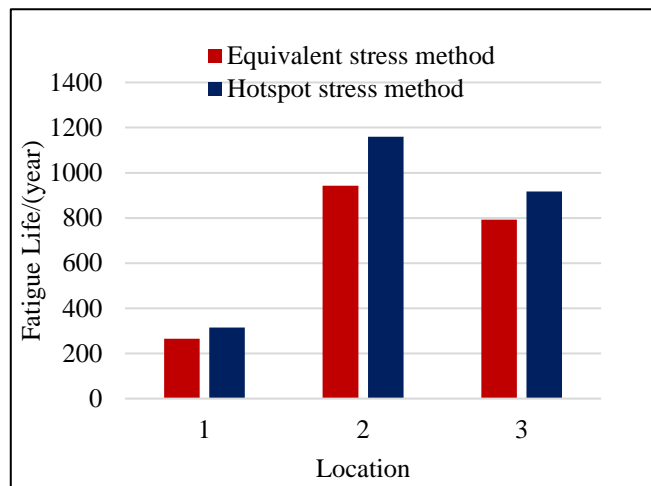


Fig.11. Estimation of fatigue life using equivalent stress method and hotspot stress method.

Cumulative damage variation along with mast arm height helps to identify the critical location due to wind action. Based on literature, fatigue damage is relatively high on base connection area and middle antinode point of mast arm structures compare to other part of mast arm wall as tabulated in Table. I [1]. Cumulative damage is high at 29.5m height due to additional 2nd mode antinode point and also, resultant bending stress at base is lesser, compare to 29.5m height.

TABLE I. DAMAGE VARIATION WITH MAST ARM LENGTH

Z/ (m)	Damage
29.5	0.989
19.22	0.008
9.3	0.000
0	0.584

It is found that, nominal stress method is recommended to be used in the estimation of fatigue life of large scale complex structures and suitable due to consideration of critical components regarding fatigue failures of structures [13]. Generally speaking, fatigue damage estimation of mast arm structures are mainly depending on geometry of whole structural system, base connection and assessment method.

Due to lack of detailed research study on the pole connection, future research study should address detailed study for the pole connection with consideration of all factors which are influencing on the fatigue performance of the system [16].

V. CONCLUSION

Fatigue assessment for the free-standing steel structures is important, due to possibility of sudden failures when the vortices are in lock-in condition. Also, number of factors are influencing in the fatigue performance of the mast-arm structures and also these factors are depending on the assessment method of fatigue damage.

From the review of literatures, following conclusions can be made.

- Maximum hotspot stress at the base of the high-mast lighting tower decreases with increasing of base plate thicknesses.

- Maximum SCF decreases with increasing of base plate thicknesses of the high-mast arm structures.
- Assessment of fatigue damage using equivalent stress method is better than the hotspot stress method. But nominal stress method is widely used in design stage of civil engineering applications.
- Fatigue life of high-mast arm structures increases with increasing of mast arm wall thickness, base plate thickness and number of anchor rods.
- Maximum hotspot stress is identified around the man access hole, welding location and anchor bolt location of mast-arm structures.

Addition to that, detailed finite element analysis and estimation of vortex shedding induced forces are highly recommended to obtain a more accurate fatigue life of mast arm structures.

REFERENCES

- [1] Marina Rakocevic and Svetislav Popovic, "Calculation procedure for determining wind action from vortex-induced vibration with verification of fatigue strength of steel structures," *GRADEVINAR* 70(2018), Page 793-809.
- [2] Margaret K. Warpinski, "The effect of base connection geometry on the fatigue performance of welded socket connections in multi-sided high mast lighting towers," *Theses and Dissertations*, paper 940, 2006.
- [3] Priyan Mendis, Shiromal Fernando, John Holmes, Tharaka Gunawardena, Yousef AbuZidan and Priyan Dias, "Wind Induced analysis of Lotus Tower Mast," *Nineteenth Australian Wind Engineering Society Workshop. Fatigue*, 2018.
- [4] Zhao fang, Aiqun Li, Wanrun Li, and Sheng shen, "Wind-induced fatigue analysis of high-rise steel structures using equivalent stress method" *Article of Applied Sciences*, January 2017.
- [5] I.Giosan, P.Eng., "Vortex Shedding Induced Loads on Free Standing Structures" 2005.
- [6] John D.Holmes, "Response of Cylindrical structures to vortex shedding in the natural wind," *13th Australian fluid mechanics conference*, 1998.
- [7] Li-wei Tsai, Alice Alipour, "Assessment of fatigue life and reliability of high-mast luminaire structures," *Journal of constructional steel research* 170, 2020.
- [8] EN 1991-1-4:2005, "Action on structures (Part 1-4: General Actions – Wind actions)".
- [9] Johan Maljaars, Mladen Lukic and Frans Soetens, "Comparison between the Eurocode for fatigue of steel structures, EN 1993-1-9, and the Eurocode for fatigue of Aluminium structures EN1993-1," *5TH Fatigue Design Conference*, 2013.
- [10] Mark T.Koenigs, Tamer A. Botros, Dylan Freytag and Karl H.Frank., "Fatigue strength of signal mast arm connections," *Research report (9/99-8/01)*, 2003.
- [11] Andrew Stam, Nicholas Richman, Charles Pool, Craig Rios, Thomas Anderson and Karl Frank, "Fatigue Life Steel Base plate to Pole connection for Traffic Structures," *Technical report – 9-1526*, 2011.
- [12] Byungik chang, Brent M. Phares, Partha P. Sarkar, and Terry J. Wipf, "Development of a procedure for fatigue design of slender structures subjected to wind-induced vibration," *Journal of the transportation research board*, pp 22-33, 2009.
- [13] Rayn J. Serman and Robert J. Conner, "Development of a fatigue design load for high-mast lighting towers," *J.Struct Eng*, 2019.
- [14] EN 1993-1-9:2005, "Design of steel structures (Part 1-9: Fatigue)".
- [15] Jay Puckett, Rebecca Johnson and Michael Barker, "Study of the effects of wind power and vortex induced vibrations to establish the fatigue design criteria for High-mast poles," *Civil and Architectural Engineering*, University of Wyoming, 2011.
- [16] Christopher M. Foley, Baolin Wan, Mathew Weglarz, Matthew Hellenthal, Jordan Komp, Andrew Smith and Joseph P. Schmidt, "Fatigue risks in the connections of Sign Support Structures – Phase 1," *Department of Civil & Environmental Engineering*, Marquette University, 2008.
- [17] Karl H. Halse, "On Vortex Shedding and Prediction of Vortex – Induced Vibrations of Circular cylinders," *Department of Marine structures*, Norweign University of Science and Technology, 1997.
- [18] Mustafa Aygul, "Fatigue analysis for the welded structures using the finite element method," *Department of Civil and Environmental Engineering*, Chalmers University of Technology, 2012.

Investigation of Relationship Between Mechanical Properties, Microstructural Features, Heat Treatment Variables and Chemical Compositions of Thermo Mechanically Treated Reinforcement Steel Bars

Eng. Thilina Chathuranga Mathotaarachchi
Melwire Rolling (Pvt.) Ltd.
Colombo, Sri Lanka
thilinaeng@gmail.com

Abstract- Manufacturing of reinforcement steel bars using mild steel is a critical and sensitive process associated with multiple parameters throughout the hot rolling and strengthening stages. Quenching is the subsequent heat treatment technique which strengthens the material after hot rolling of steel. This heat treatment creates tempered martensite outer layer to step up the strength of the material. This study mainly focuses on mechanical property variations with microstructural changes, process variables and chemical compositions in reinforcement steel bars. The grade of steel depends on microstructural changes and process variables. The paper makes an effort to find a relationship and finalizes a safe range of microstructural variables and process variables to have a standardised product.

Key words: Martensite, Quenching, Tempering, Thermo Mechanically Treated (TMT) Steel

I. INTRODUCTION

Reinforcement steel is one of the main components among construction materials. Not only as an engineering material for engineering designs but also it is considered as a major cost component in budgeting processes. Reinforcement steels are used in concrete structures and concrete castings to improve the tensile strength due to poor tensile properties of cement and concrete works. Different diameters of reinforcement bars are used in civil engineering designs as per the load bearing requirements. In Sri Lanka, this, reinforcement steel bar scope is covered by SLS 375 standard.

Reinforcement steel bars commonly known as thermo mechanically treated (TMT) bars are manufactured using a hot rolling process. Basically, heated billets are processed using hot rolling to

reduce its cross-section and get the required diameter with correct rib geometry. Then the rolled material is subjected to a heat treatment which is known as quenching and tempering. Here, crescent shape grade RB 500 reinforcement steel bars were used for this research and it is B500B grade steel as per the BS 4449 standard.

II. LITERATURE REVIEW

Several steel phases are associated with reinforcement bars. Thermo mechanically treated reinforcement steel bars consists of different steel phases such as ferrite, martensite and pearlite [1]. It consists of hard tempered martensite outer ring and ductile ferrite-pearlite core as micro-structural features. These micro structural features are affected by parameters of heat treatment in the manufacturing process. Strength and ductility are important properties of reinforcement steel bars and it is lead by micro-structural features of the bar [2]. Heated raw material should be subjected to rapid cooling rate during the heat treatment when manufacturing thermo mechanically treated bars [1]. When heating raw material up to 1100 C^0 , the resultant phase is austenite and the phase is changed from austenite to martensite as an outer periphery under high cooling rate [2]. The phase of the core is changed from austenite to ferrite-pearlite under a slow cooling rate.

Excessively high strength leads to poor ductility in reinforcement steel bars [3]. It is one of the main reasons for unwanted brittle fractures. Therefore tensile properties should be optimised to get both strength and ductility without brittleness. Self tempering is a one part of the heat treatment

process. When quenched bar is allowed to cool down under normal air, remaining heat in the core transfer to martensite periphery and it is heated again to a temperature below lower critical temperature [3]. This temperature doesn't pass critical temperatures and therefore a phase change is not occurred. This type of heating of the martensite layer and after normal air cooling is known as tempering process. Tempering reduces stresses without disturbing to the phase. Therefore brittleness of martensite is reduced and ductility is improved.

Strength and hardness depend on the cooling rate in a heat treatment process [2]. Cooling rate leads to property variations. Ultimate tensile strength to yield strength ratio and elongation is used to measure ductility properties of reinforcement steel bars [4]. Both strength and ductility are important for a reinforcement bar. There are strength measuring parameters and ductility measuring parameters separately. Those are considered in standards of reinforcement bars. Thermo mechanically treated reinforcement bars are characterised by its soft core and hardened outer layer [4]. It is manufactured using thermo mechanical treatment process.

III. METHODOLOGY

Two sets of samples were selected. One sample set consists of 40 numbers of samples covering all the standard profiles to observe diameter independent properties and other set consisted with only 16 mm profile samples to observe diameter dependant properties.

Forty samples which has more than 620 mm length were randomly selected covering all the profiles from 10 mm to 40 mm. Ten millimetre out of 620 mm of a sample was separated for chemical analysis, another 10 mm out of 620 mm was separated for microstructural analysis and remaining 600 mm part was used for the tensile test. One sample was removed due to a machine error while carrying the tensile test, hence total number of test specimen is 39. Ultimate tensile load, yield load, ultimate tensile strength to yield strength ratio were considered as mechanical properties of a specimen. All the chemical element percentages required to calculate carbon equivalent including carbon and manganese were considered for chemical composition analysis. All the formed steel phases of a specimen were considered under micro structural analysis. Cooling time in the heat treatment cycle was considered as main operation parameter. Samples for micro structural analysis were prepared using nital etching. These variables with a key process variable were analysed using Microsoft Excel software.

Second sample set of sixteen numbers of 16 mm diameter samples were prepared and analysed same as the other set. In addition to that micro hardness was measured for all the profiles.

IV. RESULTS AND DISCUSSION

Sample set of 16 numbers of 16 mm diameter

Here in Fig. 1 shows the appearance of a Nital etched 16 mm sample which is to be analysed

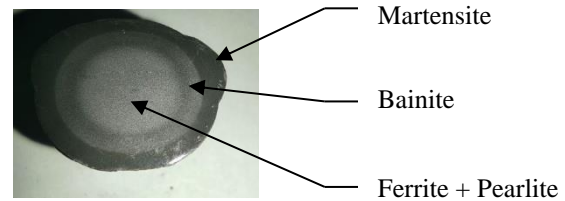


Fig. 1. Etched specimen number 03

There are three phases which are martensite outer periphery, ferrite + pearlite core and bainite intermediate layer in a cross section of a reinforcement steel bars [1]. Those phases of sample number 03 were observed using optical microscope and micro structures of those phases are shown in Fig. 2.

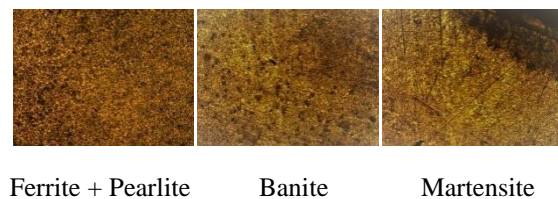


Fig. 2. Microstructure of ferrite + pearlite, bainite and martensite

Fig. 3 describes hardness profile of 16 mm specimen which is sample number 03 and it was carried out through the radius of the cross-section.

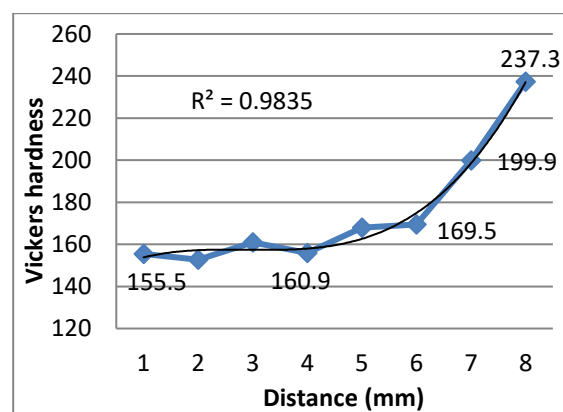


Fig. 3. Hardness (VH) of profile number 03

Highest hardness value shown in Fig. 3 is 237.3 which is martensite phase at 8 mm distance from the center, then it is decreased towards center following bainite phase at 6mm to 7mm from the center and ferrite + pearlite from 5mm distance to the center. Hardness of the bainite phase is lesser than martensite. Ferrite + pearlite core is less hard than other two phases. When core is considered from center point to 5 mm distance, hardness is increased from the center point to 5 mm point even though the phase is same as ferrite + pearlite. Strength and hardness is determined by the cooling rate during the heat treatment [2]. Here, applied cooling rate is relatively high at 5 mm and grain sizes are relatively smaller than center due to less grain growth time [5]. Therefore hardness is increased. Cooling rate is further reduced step by step towards center and hardness is reduced step by step due to increase of grain sizes [6]. Remaining heat energy of the core makes less cooling rate at the core areas. Hardness profiles for all the samples were measured and plotted in a same chart to identify trends. Those 16 numbers of profiles are shown in Fig. 4.

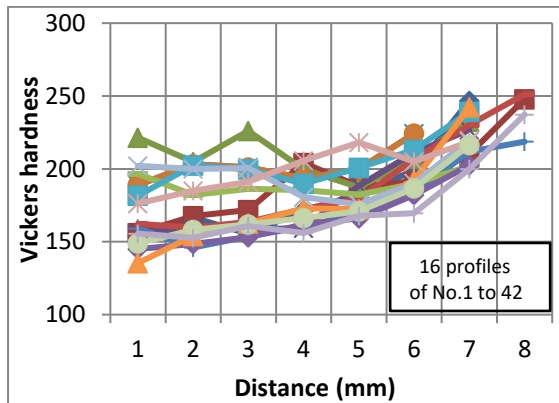


Fig. 4. Micro hardness profiles of specimen

It was observed that hardness values are almost same value when it is taken at the point 08. Hard martensite periphery is formed [1]. It is martensite at the point 8. Martensite formation is started somewhere between 7mm to 8mm from the center of the reinforcement bar. Therefore all the hardness values are narrowed down to a certain value when it comes to martensite at phase such as point 7. Thickness of the martensite outer ring was measured for sixteen samples and it was around 1.5 mm. When consider point 01 readings of all the graphs, there are different hardness values even though the steel phase and process variables are same. The possible reasons can be relatively hard cementite percentage/pearlite percentages and grain size [6]. It seems that there may be a possibility of different hardness values in the core to lead mechanical properties. Hence, core hardness was selected as a one possible

parameter for the mechanical property analysis. Average of the first three readings of each sample was taken as hardness of ferrite + pearlite core for further analysis.

Here, the chemical compositions of 16 mm sample set were studied considering all the elements required for carbon equivalent calculation and it was observed that span of the most influencing elements such as carbon, manganese, carbon equivalent is less. Therefore effect of the chemical elements was not considerably shown on the mechanical property results and micro-structural features of the selected sample set. Basically there coefficient of correlation is 0.67 for carbon - yield strength relationship and 0.70 for carbon equivalent - yield strength relationship. Even though the relationship is not strong enough, carbon equivalent has a significant effect on yield strength than carbon as per the relatively high correlation coefficient.

Single regression analysis was done to find the relationship between yield strength and other variables. None of the relationship was strong enough to have greater correlation coefficient of 0.8. Highest strength was shown by carbon equivalent-yield strength relationship (Correlation coefficient of 0.7) and core hardness-yield strength relationship (Correlation coefficient of 0.64). Hence, these two variables were selected for the multiple regression analysis.

“LINEST” function of Microsoft Excel was used to do multiple regression analysis and all results are given in Table I.

TABLE I. MULTIPLE REGRESSION ANALYSIS

Sample Number	Core H	CE Cal	YS
40	149	0.2653	527
41	195	0.2741	547
36	184	0.2766	569
32	151	0.2775	532
5	188	0.2848	560
13	162	0.2883	540
42	153	0.2912	558
24	165	0.2936	551
1	158	0.3010	551
26	159	0.3027	551
27	201	0.3075	583
4	156	0.3140	577
3	156	0.3193	548
16	198	0.3221	573
7	173	0.3289	579
17	217	0.3378	580
Multiple Regression Analysis	446.332	0.36454	361.403
	141.517	0.14116	40.6799
	0.664	10.885	#N/A
	12.8686	13	#N/A
	3049.46	1540.29	#N/A

As per the results of multiple regression analysis, yield strength is lead by core hardness and

carbon equivalent with a coefficient of determination of 0.664 (Coefficient of correlation 0.815). Therefore, correlation is satisfactory and there is a strong relationship with correlation coefficient greater than 0.8 and coefficient of determination greater than 0.64. Correlation coefficient between core hardness and carbon equivalent (r) is 0.358 ($r^2 = 0.128$). Hence, yield strength is the dependent variable and core hardness and carbon equivalents are independent variables.

As per the analysis, the model of the relationship between dependant variable yield strength vs. independent variables core hardness and carbon equivalent is;

$$\text{Yield Strength} = (446.332 * \text{Carbon Equivalent}) + (0.3645 * \text{Core Hardness}) + 361.403$$

Sample set of 39 numbers including all diameters from 10 mm to 40 mm

Characteristic loads were analysed against martensite layer thickness. Here, ultimate tensile load and yield load were considered against martensite layer thickness. The resultant graph is shown in Fig. 5.

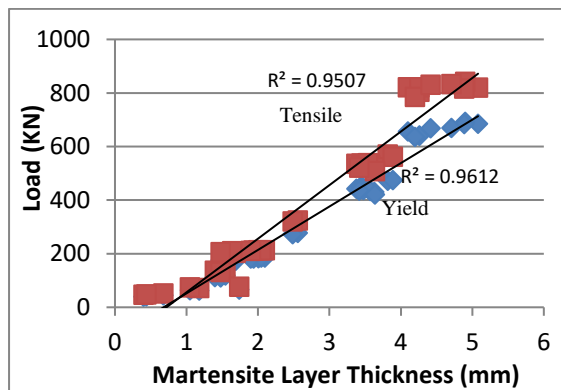


Fig. 5. Characteristic load vs. martensite layer thickness

Both graphs show linear relationships against martensite layer thickness and more than 0.64 coefficient of determination. Yield load against martensite layer thickness was separately considered in Fig. 6.

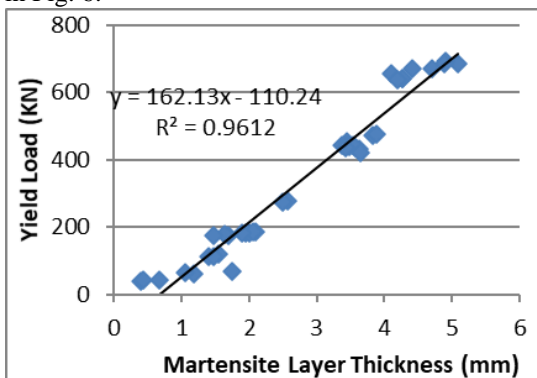


Fig. 6. Yield load vs. Martensite layer thickness

When Martensite layer thicknesses are increased, yield loads and tensile loads are increased. When it comes to yield load, these yield loads have linear relationships (0.961 coefficient of determination) against martensite layer thickness as per the Fig. 6. Maximum martensite layer thickness appears on 40mm diameter reinforcement steel bar which is the largest profile in the market at the yield strength of 650 MPa which is the highest characteristic yield strength as per the national and international product standards. Minimum martensite layer thickness appears in 8mm reinforcement steel bar which is the smallest profile in the market at 500 MPa yield strength which is the minimum accepted yield strength.

As per the Sri Lankan and British standards on reinforcement steel bars, accepted yield strength range is 500-650 MPa. Therefore minimum and maximum acceptable martensite layer thicknesses were calculated and shown in Table II.

TABLE II. MIN. AND MAX. MARTENSITE LAYER THICKNESSES FOR 500-650 MPA STRENGTH RANGE

Nominal Dia.(mm)	Min. Yield Load (KN)	Max. Yield Load (KN)	Min. Martensite Thickness (mm)	Max. Martensite Thickness (mm)
8	25.15	32.695	0.8350	0.8815
10	39.25	51.025	0.9220	0.9946
12	56.5	73.45	1.0284	1.1329
16	100.5	130.65	1.2998	1.4858
20	157	204.1	1.6484	1.9389
25	245.5	319.15	2.1943	2.6487
32	402	522.6	3.1598	3.9038
40	628.5	817.05	4.5571	5.7202

Highest Martensite thickness is required for 40 mm diameter and it is varied between 4.56 mm to 5.72 mm when yield strength is varied 500 MPa to 650 MPa. Smallest thickness is observed for 8 mm from 0.835 mm to 0.882 mm between pre considered strength range. All other profiles have their own specific martensite thickness range to give required yield strength properties of 500 to 650 MPa.

If the yield strength is high, there is a possibility to reduce the ductility. Ductility property is measured using elongation at maximum force and elongation after fracture. Elongation is not considered for this study. Therefore, applicable maximum martensite thicknesses of each diameter may be decreased due to less ductility as per the standard requirements.

Main parameter of the heat treatment process is cooling time period. It was measured and analysed

with other property parameters. Here, yield load and cooling time periods are analysed in Fig. 7.

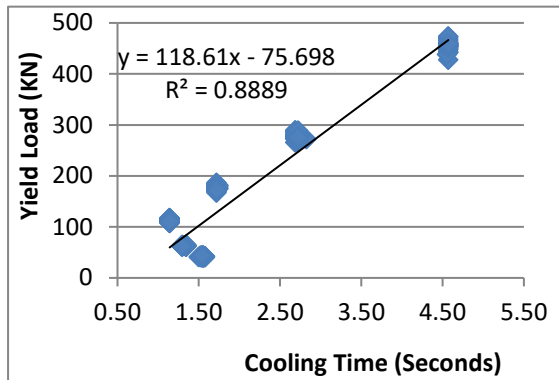


Fig. 7. Yield load vs. cooling time

When cooling time increases, yield load increases. It has a strong linear relationship with 0.888 coefficient of determination. Hence, cooling time periods for each profile to manufacture reinforcement steel bars within accepted characteristic yield strength range of 500-650 MPa were calculated and given in Table III.

TABLE III. REQUIRED COOLING TIME

Nominal Diameter (mm)	Min. Yield Load (KN)	Max. Yield Load (KN)	Min. Cooling Time (s)	Max. Cooling Time (s)
8	25.15	32.695	0.8503	0.9139
10	39.25	51.025	0.9691	1.0684
12	56.5	73.45	1.1146	1.2575
16	100.5	130.65	1.4856	1.7398
20	157	204.1	1.9620	2.3591
25	245.5	319.15	2.7082	3.3292
32	402	522.6	4.0277	5.0446
40	628.5	817.05	5.9375	7.5273

Base on the analysis, required cooling time is from 0.8503 second to 7.5273 second considering all the profiles. Maximum cooling time (heat treatment time) requires for 40 mm reinforcement steel bars and minimum cooling time requires for 8 mm bars. There are separate cooling time periods for each profile to get the characteristic yield strength properties as per the standards. Maximum cooling

time for each profile can be decreased due to less ductility as per the standard requirements.

Tensile load has a linear relationship against yield load according to the results observed and it is shown in Fig. 8.

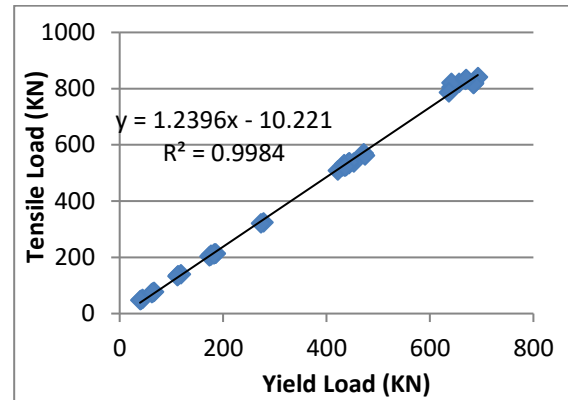


Fig. 8. Tensile load vs. yield load

V. CONCLUSION

This research observed that yield load and tensile load of a reinforcement steel bar are linearly related against formed martensite layer thickness. The author has finalized specific martensite layer thicknesses for each standard nominal diameter size of reinforcement steel bars to achieve accepted yield strength range (500- 650 MPa). Therefore this specific martensite layer thickness range for each profile can be used as a secondary mechanical property verification method in case of dispute.

It is observed that there is a strong linear relationship between yield load and cooling time. Therefore it can be concluded that yield load is lead by martensite layer thickness and martensite layer thickness is lead by cooling time period during the heat treatment. The author has finalized specific cooling time periods which should be followed for each standard profile during the heat treatment to achieve 500-650 MPa characteristic yield strength. The cooling time periods for each profile ensure mechanical properties of finished product as per the standards.

There is a potential for future researches to continue this research to develop a model to predict final product properties using process variables before conduct a destructive test. The author has finalized a model equation for yield strength based on core hardness and carbon equivalent.

ACKNOWLEDGMENT

I would like to thank my supervisor C.Eng. (Mrs.) Sumana Witharana for all the guidance, supports and encouragement given me to conduct and publish this research paper.

REFERENCES

- [1] S. O. Nair, and R. G. Pillai, "TM Ring Test' A quality control test for TMT steel reinforcement bars used in reinforcement concrete systems," ICI Journal, pp. 1-9, April 2017.
- [2] J. Haeju, M. Kang, G. W. Park, B. J. Kim, "Effect of cooling rate on quenching and tempering conditions on microstructures and mechanical properties of carbon steel flange," Materials, Vol. 13, 2020.
- [3] I. R. Kabir, and M. A. Islam, "Hardened case properties and tensile behaviours of TMT steel bars," American Journal of Mechanical Engineering, Vol. 2, pp. 8-14, 2014.
- [4] U. O. Uzodimma, O. V. Odinaka, and O. Osarenkhoe, "Variability of mechanical properties and reliability of thermo mechanically treated reinforcements in Nigeria," Journal of Science and Technology Research, Vol. 2, pp. 1-12, 2020.
- [5] M. Umemoto, Z. H. Guo, and I. Tamura, "Effect of cooling rate on grain size of ferrite in carbon steel," Materials Science and Technology, Vol. 3, pp. 249-256, 1987.
- [6] B. Smoljan, L. Stic, and K. Hajdek, "Prediction of microstructure constituents' hardness after the isothermal decomposition of austenite," Metals, pp. 1-14, 2021.
- [7] P. D. Sudersanan, N. Kori, S. Aprameyan, and U. N. Kempaiah, "The effect of carbon content in martensite on the strength of dual phase steel," Bonfring International Journal of Industrial Engineering and Management Science, Vol. 2, 2012.

Numerical Analysis of Carbon Fibre Reinforced Polymer (CFRP) Strengthened Retrofitted Out of Plane Curved Beam Under Flexure

K.Thushanthan
Department of Civil Engineering
University of Moratuwa
Sri Lanka
kthushanthan@yahoo.com

V.Dilakshan
Department of Civil Engineering
University of Moratuwa
Sri Lanka
dilakshanvigneswaran@gmail.com

Prof.(Mrs) J.C.P.H. gamage
Department of Civil Engineering
University of Moratuwa
Sri Lanka
kgamage@uom.lk

Abstract—Curved concrete structures retrofitted with CFRP application have become increased in recent years because of economic benefit. In this paper finite element analysis was conducted on six cracked curved beams retrofitted with CFRP plates. All beams had the same cross section but different radius of curvature. Linear elastic isotropic model was used to model the behavior of CFRP. Concrete damaged plasticity model was used to model the behavior of concrete. Crack location and width were identified in the beams and modelled by creating gap between continuum elements. Beams were loaded under four-point bending. The analysis results show good argument with experimental data with respect to load-displacement response and failure load

Keywords—Carbon Fibre Reinforced polymer (CFRP), Curved beam, Finite element analysis, Strengthening, Concrete damage plasticity model (CDP)

I. INTRODUCTION

Reinforced concrete curved beams are widely used in the construction industry for the construction of rounded corners of buildings, circular structures, etc. A beam that has a curved neutral axis rather than a straight axis in the unloading condition or if the beam is initially curved is regarded as curved beams [1]. If the load direction is normal to plane of curvature, the load can induce combined action of flexure, torsion, and shear in the beam. This combined action results in complexity in the analytical analysis of such members. Non-homogeneous nature of concrete makes the analysis even more complex.

Using FRP to increase the load-carrying capacity of a concrete structure is becoming famous in the modern construction industry. Recent trend in construction industry focuses much on aesthetic appearance of buildings so that usage of curved sections are increasing. But when comparing to straight beams strengthened with CFRP fewer researches are done on curved beams strengthened with CFRP.

To simulate the correct behavior of concrete in finite element software elastic and inelastic behavior of concrete including strain softening region when subjected to compression, tension softening, tension stiffening and bond behavior of concrete when subjected to tension need to be identified [2]. Many researchers have proposed several models to represent the behavior of reinforced concrete but some of these models cannot be directly applicable to finite element program. Slight modification needed to avoid the early termination of the analysis.

In this paper finite element method was used to model the behavior of retrofitted curved beam strengthened with Near Surface Mounted (NSM) CFRP. The study was carried out using six beams retrofitted with CFRP plates, which were initially tested for flexural behavior and reported by Kahandawa Arachchi, Gamage & Chandrathilake (2019) [3].

II. EXPERIMENTAL PROGRAM

Beam geometry and reinforcement property details were obtained from an experimental study done by Kahandawa Arachchi, Gamage & Chandrathilake (2019) [3]. Five out of plane curved reinforced concrete beams with 2000 mm and 4000 mm radius which has been strengthened with CFRP by NSM method were tested for flexural performance. Among the tested beams two 4000 mm radius curved control beams, two 4000 mm NSM CFRP strengthened beams and one 2000 mm NSM CFRP strengthened beams were retrofitted using adhesive and NSM CFRP in order to study the flexural performance of the retrofitted curved beams. Beam details are provided in TABLE I Behaviors of these retrofitted curved beams were analyzed using finite element program ABAQUS.

All beams were 200 mm high and 200 mm wide. The reinforcement arrangement of these beams is shown in Fig. 1. Shear reinforcement for all beams consists of ϕ 6 mm c/c 75mm and 25mm nominal cover was maintained. 15mm deep and 2.5mm wide 3 grooves were cut on the soffit of the beams to embed CFRP plates. Grooves were cut in equal spacing of 50mm.

The Span length of all six curved beams was 1800mm. Span length was measured in the middle axis of the curved beams.

Out of plane loading was provided in four-point loading condition. The distance between the loading points was 600mm along the middle-curved axis.

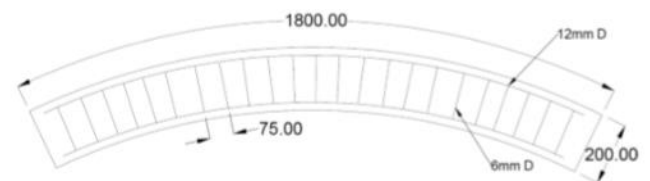


Fig. 1. Geometry and reinforcement arrangement of the beam

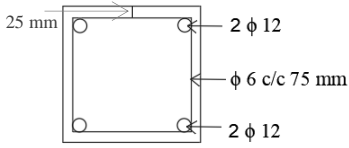


Fig. 2. Vertical cross section of beam

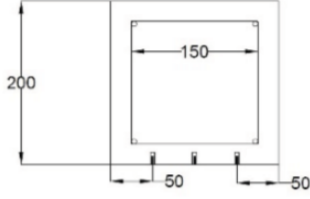


Fig. 3. Groove arrangement in the soffit of the beam

TABLE I. BEAM DETAILS

Radius of curvature	Beam	Initial condition
4000mm	B1	CB
	B2	CB
	B3	NSM CFRP
	B4	NSM CFRP
2000mm	B5	NSM CFRP

CB- Control beam

NSM CFEP- Near Surface Mounted CFRP strengthened beam

III. FINITE ELEMENT MODELING

Nonlinear behavior of the beam was modeled using FEM package Abaqus/standard.

A. Material properties

1) Concrete

Concrete damaged plasticity model (CDP) was selected to represent the behavior of concrete in tension and compression. According to the CDP model, two failure modes are tensile cracking and compressive cracking. When concrete subjected to uniaxial tension stress-strain relationship is linear up to fail stress and after reaching failure stress stress-strain curve shows a softening response due to micro cracking [4]. Elastic modulus of concrete E_c , maximum compressive strength f'_c , tensile strength f_{ct} are needed to establish the concrete damaged plasticity model. The measured average compressive strength was 35MPa during the testing phase [3]. E_c and f_{ct} were calculated by [5]:

$$E_c = 4730\sqrt{f'_c} = 27983 \text{ MPa} \quad (1)$$

$$f_{ct} = 0.33\sqrt{f'_c} = 1.95 \text{ MPa} \quad (2)$$

Where f'_c is given in MPa.

The stress-strain relationship developed by Saenz (1964) [6] was used to represent the compressive behavior of concrete.

$$\sigma_c = \frac{E_c \epsilon_c}{1 + (R + R_E - 2) \left(\frac{\epsilon_c}{\epsilon_0} \right) - (2R - 1) \left(\frac{\epsilon_c}{\epsilon_0} \right)^2 + R \left(\frac{\epsilon_c}{\epsilon_0} \right)^3} \quad (3)$$

Where

$$R = \frac{R_E(R_\sigma - 1)}{(R_E - 1)^2} - \frac{1}{R_E} \quad (4)$$

$$R_E = \frac{E_c}{E_0}, E_0 = \frac{f'_c}{\epsilon_0} \quad (5)$$

and $\epsilon_0 = 0.0025$, $R_\epsilon = 4$, $R_\sigma = 4$ [7].

The stress-strain relationship developed by Nayal & Rasheed (2006) [8] was used to represent the tension behavior of concrete. In order to eliminate the run time error due to a sudden drop at fail stress modified stress-strain curve proposed by Wahalathanri et al. (2011) [2] was used.

The stress-strain relationship of concrete in tension is represented in Fig. 4.

The Stress-strain relationship of concrete in compression is represented in Fig. 5.

0.2 was assumed for Poisson's ratio for concrete

2) Steel reinforcement

Steel reinforcement was considered as elastic perfectly plastic material. Properties of the steel reinforcements were obtained from a study conducted by Tamura and Murata (2010) [9]. Properties of steel reinforcement are listed in the TABLE II

3) CFRP

The behavior of CFRP was assumed as linear elastic isotropic until failure. The elastic modulus of taken as 165 GPa and Poisson's ratio was taken as 0.3. Other properties are listed in the TABLE III

4) Epoxy resin for cracks

TamRaz 220TG epoxy was injected into the cracks. The mechanical properties of the epoxy are in TABLE IV

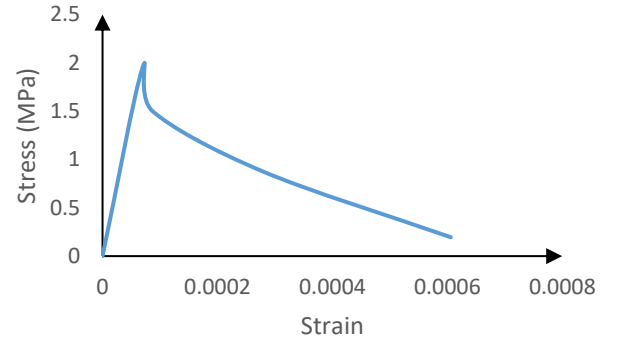


Fig. 4. Stress-strain relationship of concrete under uni-axial tension

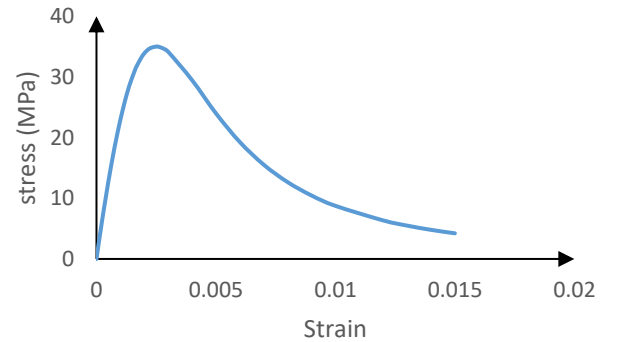


Fig. 5. Stress-strain relationship of concrete under uni-axial compression

TABLE II. STEEL REINFORCEMENT PROPERTY DETAILS

Type of reinforcement	Bar diameter(mm)	Tensile strength (MPa)
Tension/compression	12	500
Shear links	6	250

5) Epoxy for CFRP plate

Mechanical properties of thixotropic adhesive paste are tabulated in TABLE V

TABLE III. CFRP PROPERTY DETAILS

Density	1600 kg/m ³
Elastic Modulus	165 GPa
Tensile strength	2800 N/mm ²
Poisson's ratio	0.3

TABLE IV. EPOXY RESIN PROPERTY DETAILS

Density	1050 kg/m ³
Elastic modulus	1250 MPa
Tensile strength	25 N/mm ²
Shear bond strength	15 N/mm ²
Poisson's ratio	0.3

TABLE V. EPOXY FOR CFRP PROPERTY DETAILS

Density	1630 kg/m ³
Elastic modulus	10 GPa
Tensile strength	20 N/mm ²

B. Numerical analysis

8-node 3 dimensional hexahedral elements were used for the reinforced concrete and epoxy. Reinforcement steel was modeled by 2-node 3-dimensional truss elements. S4R element type was used to model CFRP plates.

Steel bars were embedded into curved beams as shown in Fig. 6, in order to provide the concrete-steel interaction. Nodes of concrete were selected as host and nodes of steel bars were selected as slave. CFRP plate elements were embedded into Epoxy resin elements. The bond between the epoxy resin and concrete elements was taken as a perfect bond.

Crack location and width were identified in the beams. Cracks were modeled in the identified location in the curved beams by making a suitable gap between the continuum elements. Adhesive elements were placed inside these gaps.

1) Boundary condition and loading

The Boundary condition in the experiment was similar to the boundary condition used in the experiment done by Kahandawa Arachchi, Gamage & Chandrathilake (2019) [3]. Both ends of the beams were pinned except for torsion, it was restrained to avoid the beam rotation when loading at the ends and four-point loading was applied, two rotations UR1, UR2 and one displacement UR1 was restrained to obtain the partially fixed boundary condition [10]. The boundary conditions are illustrated in Fig. 7. Midspan deflections were plotted against loading.

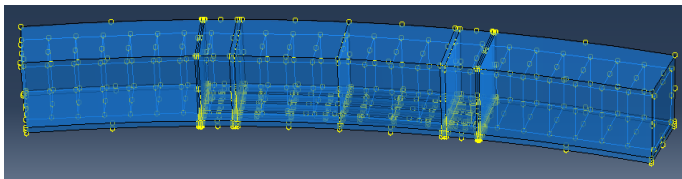


Fig. 6. Connection between steel bars and concrete in B1

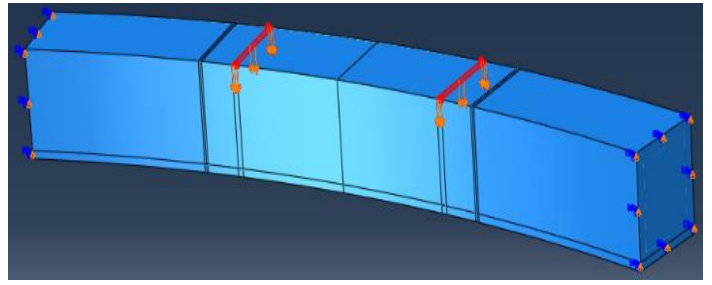


Fig. 7. Loading and boundary condition

IV. RESULTS

Load displacement curve obtained for retrofitted beams from experiment and finite element modeling are discussed below

A. B1 and B2

Experimental results of B1 and B2 show good argument with the FEM results. B2 had a maximum crack width of 3mm and B1 had a maximum crack width of 1.5mm. Other cracks in the range of 0.2mm-1mm were approximately same with respect to location. Failure load of B2 was slightly higher than B1. Fig 8 and Fig 9 shows the load vs deflection behavior of B1 and B2 respectively.

B. B3 and B4

Experimental failure loads of B3 and B4 show a good argument with FEM failure load. Load-deflection curves were almost similar in both experimental and FEM see Fig. 10 and Fig. 11, but FEM predict the behavior of B4 as more stiff than actual beam, see Fig 11. B4 had an initial crack near the end of CFRP plate. The crack might be much deeper than measured crack depth. This might cause the FEM to predict a stiffer behavior for B4.

C. B5

Experimental results show a good argument with FEM results. The deviation in failure load occurred might be because of actual crack depth was higher than the measured crack width. So that FEM predicted the behavior of beam stiffer than actual case, see Fig. 12.

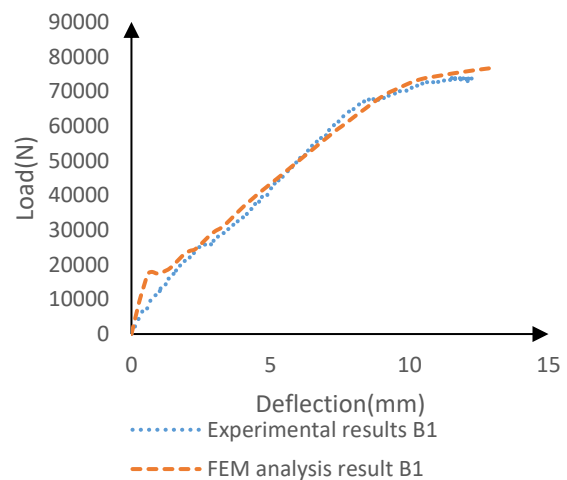


Fig. 8. load-deflection curve of B1

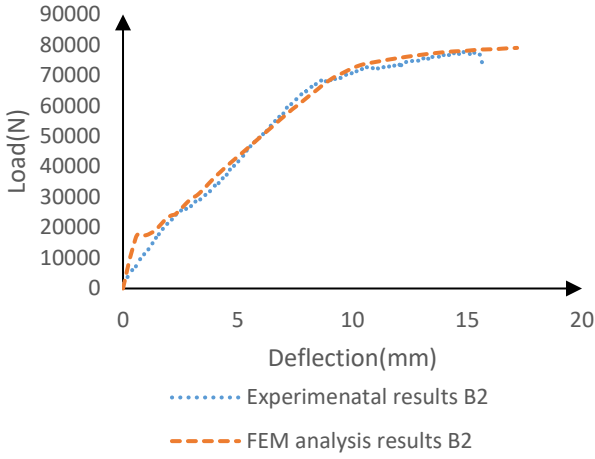


Fig. 9. load-deflection curve of B2

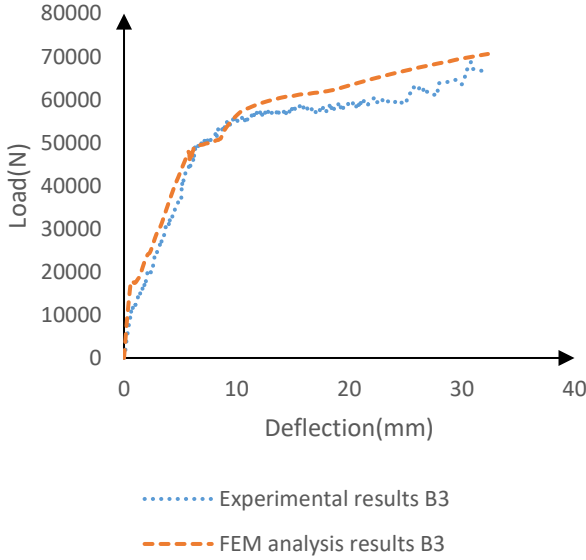


Fig. 10. load-deflection curve of B3

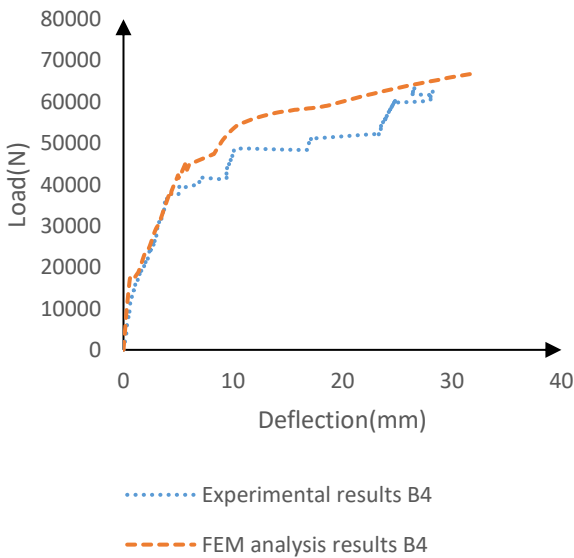


Fig. 11. load-deflection curve of B4

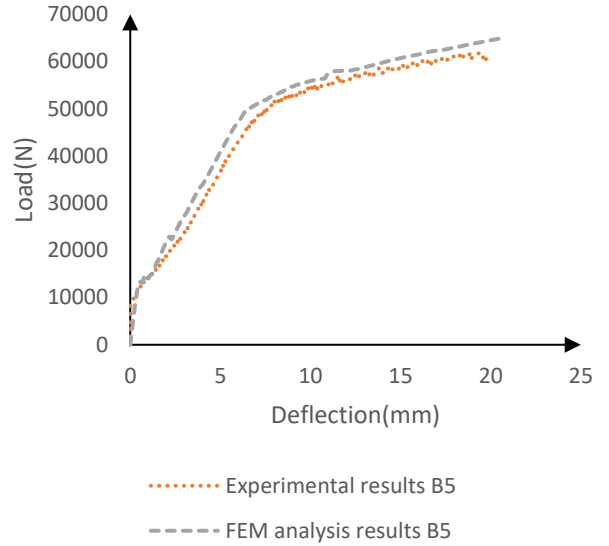


Fig. 12. load-deflection curve of B5

Failure loads obtained from experiment and failure loads from FEM are compared and percentage differences are calculated in TABLE VI.

TABLE VI. EXPERIMENTAL FAILURE LOAD AND FEM FAILURE LOAD

Beam	Failure load-Experiment(kN)	Failure load-FEM(kN)	percentage difference
B1	73	76	3.9%
B2	77	79	2.5%
B3	68.7	70.6	2.6%
B4	63	67	5.9%
B5	62	65	4.6%

V. CONCLUSIONS

This paper presented a nonlinear FEM developed to predict the flexural performance of retrofitted RC curved beams. FEM results show a good argument with experimental results with a percentage difference of less than 6%.

- The bond between the concrete and adhesive can be modeled as a perfect bond but this causes a slight increase in the failure load.
- Modeling a crack as a gap between continuum elements does not affect the behavior of the beam significant.
- FEM predicted the behavior of the beams slightly stiffer than actual beam this might be because of in the modeling perfect bond was created between adhesive and concrete interface but in actual case the bond is not perfect there might be bond slip can occur and actual crack depth might be higher than measured crack width.

VI. ACKNOWLEDGEMENT

The authors would like to express their sincere gratitude to all technical staff in building materials laboratory and Structural testing laboratory. The financial support provided by Senate Research Committee (Grant SRC/LT/2019/21) is greatly appreciated.

VII. REFERENCES

- [1] D. K. Kayathri and C. D. R. Balaji, "Experiemntal and Analytical Study on Flexural Behavior of Curved Beams," *International Journal of Science and Engineering Application*, vol. 4, no. 3, pp. 146-152, 2015.
- [2] B. L. Whalathantri, D. P. Thambiratnam, T. H. T. Chan, and S. Fawzia, "A Material Model for Flexural Crack Simulation in Reinforced Concrete Elements Using ABAQUS," in *First International Conference on Engineering, Designing and Developing the Built Environment for Sustainable Wellbeing*, pp. 260-264, 2011.
- [3] K. A. D. Y. T. Kahandawa Arachchi, J. C. P. H. Gamage, and E. R. K. Chandrathilake, "Bond Performance of Carbon Fiber Reinforced Polymer (CFRP) Strengthened Reinforced Concrete Curved Beams," in *International Conference on Civil Engineering and Applications*, p. 1-6, 2019.
- [4] Abaqus 6.14-1, "Analysis user manual," Dassault Systems Simula Corp., Providence, Rhode, 2014.
- [5] ACI Committee 318. *Building code requirements for structural concrete and commentary (ACI 318-99)*. Detroit (MI): American Concrete Institute; 1999.
- [6] L. P. Saenz, "Equation for the stress-strain curve of concrete," *ACI Journal*, 61:1229-35, 1964.
- [7] Hu H-T, and W. C. Schnobrich, "Constitutive modelling of concrete by using nonassociated plasticity," *Journal of Materials in Civil Engineering (ASCE)*, no. 61, pp. 199-216, 1989.
- [8] R. Nayal and H. A. Rasheed, "Tension Stiffening Model for Concrete Beams Reinforced with Steel and FRP Bars." *Journal of Materials in Civil Engineering*, 18(6), pp. 831-841, 2006.
- [9] T. Tamura and H. Murata, "Experimental Study on the Ultimate Strength of R/C Curved beams," *Fracture Mechanics of Concrete and Concrete structures – High Performance, Fiber reinforced Concrete, Special Loading and Structural Applications*, pp. 1783-1788, 2010.
- [10] S. Aaruga, E. R. K. Chandrathilaka and J. C. P. H. Gamage, "Finite Element Modelling on Flexural Performance of CFRP Strengthened Reinforced Concrete Curved Beams," in *Moratuwa Engineering Research Conference (MERCon)*, pp. 662-667, 2019.

Combined Web Crippling & Bending Behaviour of CFS LiteSteel Beams

Dushadhi Athapaththu
Department of Civil Engineering
Faculty of Engineering, University of Jaffna
Kilinochchi, Sri Lanka
athapaththu@eng.jfn.ac.lk

R. Kajanana
Department of Civil Engineering
Faculty of Engineering, University of Jaffna
Kilinochchi, Sri Lanka
2015e015@eng.jfn.ac.lk

Thilini Yasarathna
Department of Civil Engineering
Faculty of Engineering, University of Jaffna
Kilinochchi, Sri Lanka
2015e026@eng.jfn.ac.lk

Balasubramaniam Janarathanan
Department of Civil Engineering
Faculty of Engineering, University of Jaffna
Kilinochchi, Sri Lanka
jana151188@eng.jfn.ac.lk

Abstract— It is widely accepted that cold-formed steel sections replace the conventional hot-rolled steel members due to their high strength to thickness ratio. Generally, in the construction industry, cold-formed steel lipped channel, unlipped channels and Zee-sections are widely used. However, these open sections are susceptible to lateral-torsional buckling, and hence flexural capacity reduces. To fix this shortcoming and improve flexural capacity, rectangular hollow flange channel sections, also commercially known as LiteSteel beam, were introduced. However, these sections are vulnerable to web crippling failure due to their slender webs under concentrated loads and support reaction. These sections are critical under combined web crippling and bending when the specimen length increases. However, the behaviour of these LSB sections under combined web crippling and bending is unknown. Hence its has been investigated in this study using finite element analysis. Three different finite element models were developed, such as pure web crippling, pure bending, and combined web crippling and bending using ABAQUS software and validated using existing experimental data. Through the validation of FE models, common boundary conditions were determined for each bending and web crippling behaviour. A later parametric study was carried out using 350 FE models of LSBs. The observed results were extensively studied with the current design guidelines, and the effect of each parameter on the combined web crippling and bending capacity also studied. Final results indicate that the existing all three design equations are conservative for the combined web crippling and bending actions of LSBs subjected to concentrated loading via bearing lengths of 50, 60 and 75 mm.

Keywords— *lite steel beam, web crippling, bending, combined actions, finite element validation*

I. INTRODUCTION

Cold-formed steel replaces hot-rolled steel in many applications in construction industry, mainly due to its high strength to its weight ratio. The cold-formed steel sections are available in many shapes, commonly channel and z-sections. These sections are mostly used as joists and bearers in a steel floor system, hence subjected to bending actions. These traditional opened sections suffer due to torsional and distortional buckling modes with increasing specimen lengths, hence flexural capacity reduces. Rectangular hollow flange channel beams as shown in Fig. 1 also commercially known as LiteSteel beams (LSBs), has been introduced to the construction industry to replace the traditional CFS sections with the claim of reduced torsional and distortional buckling

modes [1]. As shown in Fig.1, LSB sections are made of two hollow flanges and a slender web, which is connecting those two flanges. These LSB sections are vulnerable to web crippling due to their slender webs at the concentrated loading and support reactions. Web crippling failure is distinguished in to four types such as (i) End-Two-Flange (ETF), (ii) Interior-Two-Flange (ITF), (iii) End-One-Flange (EOF) and (iv) Interior-One-Flange (IOF) based on failure location and distance between load and support reaction as shown in Fig. 2 [2]. Among the considered four failure types, the specimens are subjected to combined web crippling and bending actions for Interior-One-Flange loading with increased specimen length.



Fig. 1. LiteSteel Beam section profile

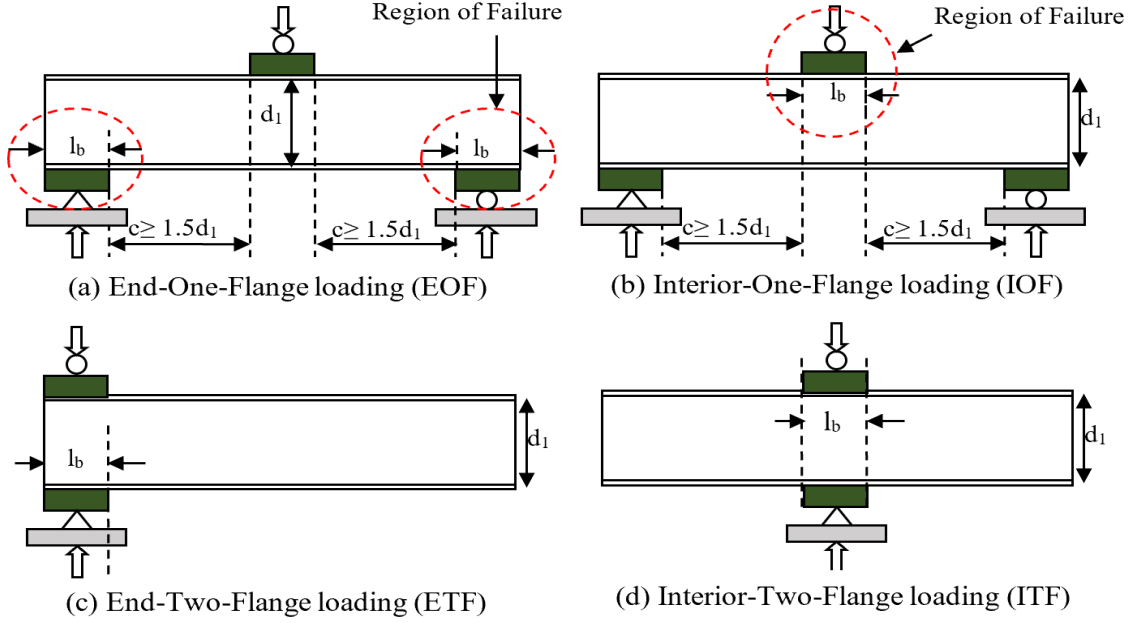


Fig. 2. Web rippling failure load cases [2, 3]

Cold-formed steel specifications such as North American Specification (AISI S100) [3], Australian/ New Zealand standard (AS/NZS 4600) [4] and Eurocode 3 [5] uses different equations to determine the safety of the sections under combined web crippling and bending. All three equations are given below (1, 2 & 4). In the Equations, Australian/ New Zealand standard and North American Specification uses same equation to determine the web crippling (3) and bending capacity while using slightly different equation for combined web crippling and bending.

For Australian/ New Zealand specification

$$1.07 \left(\frac{P}{P_n} \right) + \left(\frac{M}{M_n} \right) \leq 1.42 \quad (1)$$

North American specification

$$0.91 \left(\frac{P}{P_n} \right) + \left(\frac{M}{M_n} \right) \leq 1.33 \quad (2)$$

Web crippling equation of AISI S100 & AS/NZS 4600

$$R_b = Ct^2 f_y \sin \theta \left(1 - C_w \sqrt{\frac{d_1}{t}} \right) \left(1 - C_r \sqrt{\frac{r_i}{t}} \right) \left(1 + C_l \sqrt{\frac{l_b}{t}} \right) \quad (3)$$

where d_1 - clear web height of channel section. l_b - bearing length, r_i - inside corner radius, t - section thickness, f_y - material yield strength, C , C_r , C_l and C_w - web crippling coefficients, P - Design concentrated load or reaction in the presence of bending moment, P_n or R_b - Nominal capacity for concentrated load or reaction, M - Design bending moment at, or immediately adjacent to, the point of application of the design concentrated load (P) or reaction (R^*) and M_n - Nominal section moment capacity. The set of equations used by Eurocode is different from AS/NZS 4600 and AISI S100.

$$\frac{P}{P_n} + \frac{M}{M_n} \leq 1.25 \quad (4)$$

Web crippling equation in Eurocode

For $l_b/t \leq 60$

$$P_n = \frac{k_3 k_4 k_5 \left[14.7 - \frac{h_w/t}{49.5} \right] \left[1 + 0.007 \frac{l_b}{t} \right] t^2 f_y}{\gamma_{M1}} \quad (5)$$

For $l_b/t > 60$

$$P_n = \frac{k_3 k_4 k_5 \left[14.7 - \frac{h_w/t}{49.5} \right] \left[0.75 + 0.011 \frac{l_b}{t} \right] t^2 f_y}{\gamma_{M1}} \quad (6)$$

where h_w is the web height between the midlines of the flanges, γ_{M1} is the material safety factor, and k_3 , k_4 and k_5 are the coefficients for flange-web angle, material yield strength and inside corner radius to thickness ratio.

Also these equations are developed for channel sections with thickness less than 3 mm. The applicability of these three equations for thick channel sections was reevaluated by [6]. LiteSteel beams [LSBs] sections are recently introduced and their behaviour and applicability these three interaction equations under combined web crippling and bending should be checked. Therefore, this study investigated the behaviour of cold-formed steel LiteSteel beams under combined web crippling and bending using finite element analysis software ABAQUS CAE. About 350 FE models were generated in ABAQUS CAE after proper validation of web crippling and bending models.

II. LITERTURE REVIEW

The web crippling capacity reduction was first observed for corrugated sheeting by Baehre [7] in 1975 when author did the experimental study for long specimens. In this study, 151 tests were performed and the web crippling-bending interaction equation was proposed based on concentrated load, bending moment generated due to the concentrated load and web crippling and bending capacities of the section. Later that

same year, Ratliff [8] investigated the combined web crippling and combined behaviour of channel sections made of three thicknesses and two depth values and proposed two web crippling-bending interaction equations, one is for channel sections without web stiffeners and other is for channel sections with web stiffeners. Hetrakul and Yu [9] investigated the combined web crippling and bending behaviour of channel sections using thirty-eight tests and proposed new equation. The specimen arrangement used by [9] and [8] is different, which may also affect the accuracy of developed equations. Also, the developed equations are empirical, and their applicability is limited to certain conditions. The equations developed from above two studies are limited to section thicknesses less than 3 mm.

Cold-formed steel sections are currently available in greater thicknesses and higher strengths. Due to this, Young and Hancock [10] investigated the combined behaviour of web crippling and bending for thick unlippped channels. They have performed web crippling, bending and combined web crippling and bending experimental studies and based on that the applicability of the current combined web crippling and bending design equation was revalidated. In this study, the specimen supports were considered as unfastened, which is not common. Recently, Janarthanan and Mahendran [6] investigated the combined web crippling and bending behaviour of unlippped channel sections but with fastened supports using finite element studies. They have reported that currently existing all three combined action design equations are conservative for thick unlippped channels with fastened supports. Also, they have proposed new design equation.

Rectangular hollow flange channel sections also known as LiteSteel beams (LSBs) is recently introduced to construction industry. The shear and web crippling behaviour of this LSB sections are thoroughly investigated until now. However, combined web crippling and bending behaviour has not investigated. Hence, this study investigated the combined web crippling and bending behaviour of LSBs using finite element analysis and report here.

III. METHODOLOGY

This study is purely based on finite element analysis hence fe validation plays a crucial role. There are three types of finite element models developed in this study such as web crippling FE models of LSB sections, FE models of combined web crippling-bending of unlippped channels and pure bending FE models of unlippped channels. Young and Hancock [10] test data was used for the validation of bending and combined web crippling and bending models while Keerthan and Mahendran [11] test data was used to validate web crippling models of LSBs under IOF load case. Abaqus/CAE software was employed to model the problems. The suitable FE model was chosen based on the validation and then that model is used to investigate the web crippling-bending behaviour of LiteSteel beams.

A. Pure web crippling test

Web crippling test results of LiteSteel beams under IOF load condition performed by Keerthan and Mahendran [11] was considered for the validation of web crippling FE models.

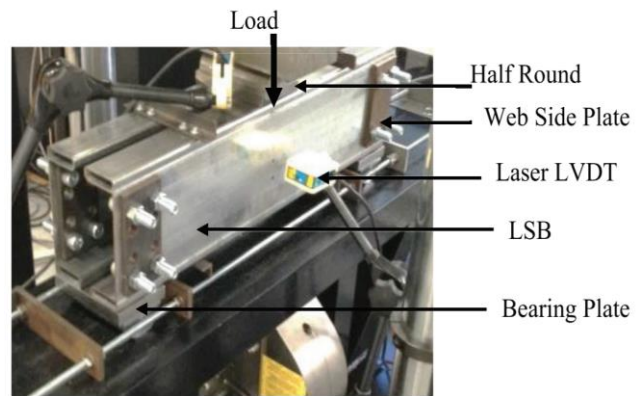


Fig. 3. Web crippling IOF test set-up [11]

In their tests, specimen depth varied from 150 to 200 mm, thickness varied from 1.5 to 2.5 mm and flange width varied from 45 to 60 mm. Altogether eleven test values were used for the validation purpose. Test specimen arrangement was made of two LiteSteel beams while the specimen length is equal to three times overall depth plus three times bearing length. The used test set-up is shown in Fig. 3. FE models includes number of contacts to simulate the actual test set-up hence creating two specimen test set-up in FE software is computationally expensive. However due to symmetry, only one beam can be simulated in FE modelling in order to reduce the computational expenses. As shown in Fig. 3, it is three-point loading arrangement where two pinned supports at the end of the specimen which is simulated using half rounds and the load was applied at the mid-span using displacement control method. The webs at the end of specimens were stiffened by steel plates to prevent web crippling failure at the end supports. Similar test set-up but using one test specimen was developed in ABAQUS/CAE with suitable boundary conditions.

B. Pure bending test

Pure bending experimental study of thick unlippped channel sections performed by Young and Hancock [10] is used to validate pure bending FE models. As shown in Fig. 4, four point loading test set-up was used in pure bending experimental study, where two hinge supports were established at the end of specimens using two half rounds while equal loads were applied at the mid-span with certain distance between them. Similar to experimental study, finite element model will be developed and should be validated using the experimental values.



Fig. 4. Bending test set-up [10]

C. Combined web crippling and bending

Same as test set-up shown in Fig. 3, but with increased specimen length was used by Young and Hancock [10]. The specimen length was equal to $2a+90$ mm, where a is given by the below equation.

$$a = \frac{4kM_{EXP}}{P_{EXP}} \quad (7)$$

In (7), “ k ” is an interaction factor which determines the interaction between moment and concentrated load as per past research studies. M_{EXP} and P_{EXP} are the pure bending and web crippling capacities of the sections. After validation, all developed finite element models with same boundary conditions will be applied to LiteSteel beam sections. Based on the observed data, combined web crippling and bending behaviour of LSB sections will be investigated.

IV. FINITE ELEMENT ANALYSIS

Finite element simulation was performed in ABAQUS/CAE software. There are mainly two parts in FE modelling such as tested specimen and the loading plates. The tested specimens were created in the software using centerline dimensions which were determined based on measured values, then created section was extruded to the measured specimen length. The accuracy of the finite element model depends on several factors such as material properties, boundary conditions, mesh sizes and element types. There are lots of element types are available in ABAQUS library. Here the specimens were modelled using shell elements due to their negligible thickness compared to their other dimensions. Among shell elements, S4R is commonly used due to its higher prediction accuracy and less time consumption compared to other shell element types such as S4 and S4R5. Mesh size plays an important role in analysis time as well as accuracy of the model. Here based on initial analysis [01], mesh size was chosen. According to the sensitive analysis, $5 \text{ mm} \times 5 \text{ mm}$ mesh size was chosen for deformable shell elements while $10 \text{ mm} \times 10 \text{ mm}$ mesh size is chosen for rigid support and loading plates. Material properties can be derived as perfect plastic or multilinear material models with strain hardening effects. Janarthanan et al. [12] showed that the effect of strain hardening on the web crippling failure is negligible hence perfect plastic material property can be used. During the material definition, Young modulus with the value of 200,000 MPa and measured yield strength values were inputted to ABAQUS/CAE software. Boundary conditions play an important role in the prediction behaviour of finite element models. Figs. 5 and 6 shows the finite element boundary conditions of web crippling and bending models, respectively. As shown in Fig.5, for support plates, translations about x and y axes were fixed while rotation about axis x was allowed to simulate the half-rounds used in the test. Similarly translations about x and z axes were fixed while allowing the rotation about x axis at loading plate. Also initial displacement was setted as -40 mm and amplitude value of one was given to generate displacement control method in finite element models.

Similar to web crippling FE model, FE model was developed to determine pure bending capacities. The boundary conditions of pure bending model is shown in Fig. 6. As seen in Fig. 6, two supports of the beam are pinned while equal loading is applied at the mid-span.

Translations about x and $y = -40$
Rotations about y and z are fixed

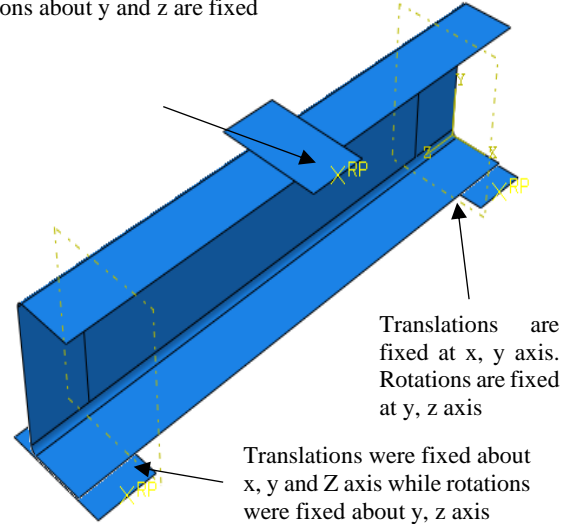


Fig. 5. Web crippling FE model

Roller support (Translations were fixed in x, y directions and Rotations were restricted about y and z directions)

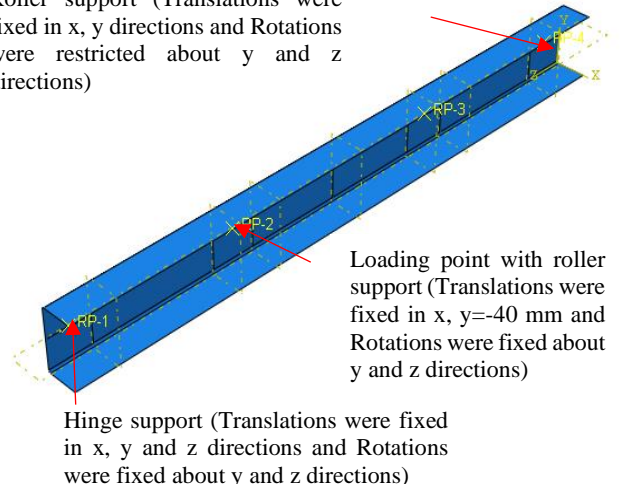


Fig. 6. Bending FE model

V. VALIDATION

Table 1 shows the comparison of finite element model prediction with web crippling test values of LiteSteel beams. As seen in Table 1, mean value of test to FEA value is 0.98 while COV is 0.05. Hence it can be concluded that developed FE model predicted the web crippling behaviour of LiteSteel beams accurately. Table 2 shows the comparison of pure bending test values and predictions of finite element models. As seen in Table 2, mean of test to FE is 0.99 while COV is 0.05. This showed that the developed FE models predicted the bending behaviour of unlippped channels well and hence this particular FE modal with boundary conditions can be used to predict the bending capacity of LSB sections as well. Then parametric study was performed using validated FE models. Fig 7 shows the failure mode of pure bending FE model which matches well with experimental study. Same as web crippling models, combined web crippling and bending models also developed and validated using Young and Hancock's [10] data. Table 3 shows the comparison of tests and FE predictions.

TABLE I. WEB CRIPPLING CAPACITIES OF LSB SECTIONS UNDER IOF LOAD CASE

Specimen	Bearing length	Test (kN)	Test/ FEA
150× 45× 1.6	50	33.00	0.98
150× 45× 2.0	50	54.14	0.96
200× 45× 1.6	50	32.47	0.93
200× 60× 2.5	50	75.16	0.97
150× 45× 1.6	100	34.08	0.91
150× 45× 2.0	100	62.74	1.07
200× 45× 1.6	100	34.75	1.02
200× 60× 2.5	100	101.65	1.13
150× 45× 1.6	150	42.80	1.02
150× 45× 2.0	150	66.10	0.93
200× 45× 1.6	150	33.56	1.02
Mean			1.00
COV			0.06

^a. Note: 200× 45× 1.6 → overall depth × flange width × thickness

TABLE II. COMPARISON OF BENDING CAPACITIES OF UNLIPPED CHANNEL SECTIONS WITH FEA VALUES

Specimen	d (mm)	b _r (mm)	t (mm)	Test (kN)	Test/ FEA
75× 40× 4.0	74.4	40.3	3.85	6.44	1.03
100× 50× 4.0	99.2	50.3	3.83	11.64	1.09
125× 65× 4.0	124.9	65.5	3.84	16.20	1.02
200× 75× 5.0	198.8	75.9	4.70	40.48	0.98
250× 90× 6.0	249.5	90.0	6.00	79.90	0.90
300× 90× 6.0	298.8	91.2	6.00	92.89	0.93
Mean					0.99
COV					0.07

^b. Note: d- overall depth, b_r- flange width, t- thickness

TABLE III. COMPARISON OF COMBINED WEB CRIPPLING-BENDING TEST CAPACITY VALUES WITH FE PREDICTIONS

No	l _b (mm)	d (mm)	b _r (mm)	t (mm)	r (mm)	F _{EXP} / F _{FE}
1	50.0	99.40	50.4	3.83	4.1	0.99
2	50.0	99.40	50.4	3.82	4.1	1.01
3	50.0	99.30	50.5	3.83	4.1	1.07
4	25.0	99.40	50.5	3.83	4.1	1.04
5	25.0	99.40	50.4	3.83	4.1	1.05
6	25.0	99.40	50.4	3.84	4.1	1.05
7	75.0	198.40	75.9	4.72	4.2	0.80
8	75.0	198.80	75.8	4.71	4.2	1.03
9	75.0	198.70	75.9	4.72	4.2	0.92
12	37.5	198.60	75.7	4.73	4.2	0.92
13	90.0	298.50	91.2	6.00	8.4	0.93
14	90.0	298.40	91.1	6.01	8.4	0.98
15	45.0	298.00	91.5	6.00	8.4	1.00
16	45.0	298.10	91.2	6.00	8.4	0.96
Mean						0.98
COV						0.07

^a. Note: d- overall depth, b_r- flange width, t- thickness, r- Corner radius, l_b- bearing length

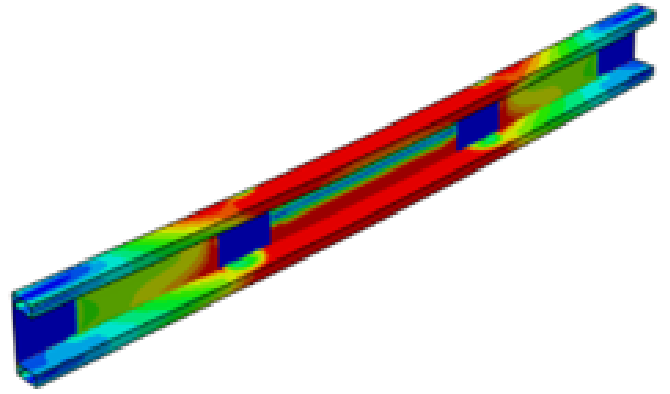


Fig. 7. Observed failure mode – Bending FE model

As shown in Table 3, the developed combined web crippling and bending models predicted the capacity accurately with the mean value of 0.98 while COV value of 0.07. This shows developed all FE models are accurate and able to predict the failure behaviours.

VI. PARAMETRIC STUDY

Basically the parameters affecting to the combined bending and web crippling behavior such as bearing length, section thickness, flange width, depth of the section as well as material yield strength values were decided as shown in the Table 4. Young and Hancock [10] defined an interaction factor to overcome the interaction between bending and web crippling behavior. In this study, interaction factors are selected as 0.50, 0.75 and 1.25 (Table 4) based on the past research studies.

Then python scripts were developed by ABAQUS journal files since, the easiness of the creating models. Based on that, 352 models were created and extensive parametric study was conducted for 350 FE models such as 48 models in terms of pure web crippling, 16 models in terms of pure bending as well as 288 models in terms of combined bending and web crippling. Table 5 shows the observed pure web crippling capacities while Table 6 shows the pure bending capacities of the LSBs. Furthermore, Table 7 briefs the combined bending and web crippling capacities for the 50 mm bearing length specimen set with 250 MPa yield strength while Table 8 shows the 450 MPa yield strength values. Table 9 shows the combined bending and web crippling capacities for 60 mm bearing length, Table 10 shows the 75 mm bearing length with 250 MPa yield strength while Table 11 shows 450 MPa yield strength

TABLE IV. SELECTED PARAMETERS FOR THE PARAMETRIC STUDY

Parameter	Selected values
Bearing length	50, 60 & 75 mm
Thickness	1,2 & 3 mm
flange width	45,60 & 75 mm
Section depth	100, 150 & 200 mm
Interaction factor	0.5, 0.75 & 1.25
Yield strength	250 & 450 Mpa

TABLE V. WEB CRIPPLING CAPACITIES OF LSBs (kN) FROM PARAMETRIC STUDY

Section	lb = 50mm		lb = 60mm		lb = 75mm	
	250 MPa	450 MPa	250 MPa	450 MPa	250 MPa	450 MPa
	(k)	(k)	(k)	(k)	(k)	(k)
100x45x1	11.2	16.6	13.0	13.4	15.4	20.3
100x45x2	32.9	55.6	37.9	64.01	43.7	72.3
100x45x3	59.8	100.8	64.9	110.3	69.9	119.6
150x60x1	10.6	12.7	11.5	13.8	12.8	15.2
150x60x2	32.4	55.4	37.6	62.7	45.3	68.3
150x60x3	61.0	100.2	68.7	114.5	77.7	131.7
200x75x1	8.8	11.2	9.3	11.7	10.2	12.4
200x75x2	32.4	54.0	37.7	57.6	44.0	61.8
200x75x3	59.4	98.3	67.4	112.5	79.5	127.8

TABLE VI. SECTION MOMENT CAPACITIES (kNm) OF LSBs FROM PARAMETRIC STUDY

Section	Moment capacity (kNm)	
	Fy = 250 MPa	Fy = 450 MPa
	(kNm)	(kNm)
100x45x1	2.72	6.47
100X45X2	5.33	9.48
100X45X3	7.79	13.88
150X60X1	5.30	7.52
150X60X2	11.28	20.08
150X60X3	16.58	22.31
200X75X1	29.59	34.86
200X75X2	18.40	29.05
200X75X3	28.05	49.45

TABLE VII. COMBINED BENDING AND WEB CRIPPLING CAPACITIES FOR 50MM BEARING LENGTH

Section	Yield strength Fy=250 MPa					
	Concentrated load (kN)			Bending Moment (kNm)		
	0.5 (k)	0.75 (k)	1.25 (k)	0.5 (k)	0.75 (k)	1.25 (k)
100X45X1	11.5	10.0	7.3	1.5	2.1	2.4
100X45X2	36.9	34.4	24.5	3.9	5.0	5.6
100X45X3	70.3	64.1	46.7	6.3	7.9	8.8
150X60X1	10.5	8.7	6.6	2.9	3.5	4.3
150X60X2	35.0	32.2	22.9	7.0	9.2	10.6
150X60X3	69.7	63.3	45.1	11.2	14.5	16.4
200X75X2	32.1	30.6	22.6	9.9	13.8	16.6
200X75X3	68.7	58.8	43.5	17.9	22.3	26.8

TABLE VIII. COMBINED BENDING AND WEB CRIPPLING CAPACITIES FOR 50MM BEARING LENGTH

Section	Yield strength Fy=450 MPa					
	Concentrated load (kN)			Bending Moment (kNm)		
	0.5 (k)	0.75 (k)	1.25 (k)	0.5 (k)	0.75 (k)	1.25 (k)
100X45X1	22.5	19.6	15.8	5.7	6.8	7.5
100X45X2	61.5	56.4	40.4	6.8	8.6	9.6
100X45X3	116.5	106.9	77.1	10.9	13.7	15.2
150X60X1	15.2	12.3	8.8	4.9	5.8	6.8
150X60X2	58.4	51.9	37.2	12.1	15.4	17.8
150X60X3	79.4	82.2	51.1	19.6	24.2	20.1
200X75X2	55.8	50.0	38.4	16.4	21.4	26.7
200X75X3	110.1	96.9	70.8	30.5	39.0	46.3

TABLE IX. COMBINED BENDING AND WEB CRIPPLING CAPACITIES FOR BEARING LENGTH OF 60 MM

Section	Yield strength Fy=250 MPa					
	Concentrated load (kN)			Bending Moment (kNm)		
	k=0.5	0.75	1.25	k=0.5	0.75	1.25
100X45X1	11.9	11.6	8.7	1.5	2.1	2.5
100X45X2	42.2	40.0	29.2	4.0	5.2	5.9
100X45X3	76.6	71.4	52.9	6.5	8.2	9.3
150X60X1	11.7	9.9	7.5	3.0	3.7	4.5
150X60X2	40.2	37.6	27.1	7.0	9.4	10.8
150X60X3	76.0	71.8	51.9	11.1	14.8	17.0
200X75X2	39.2	35.3	26.6	10.6	13.8	16.9
200X75X3	75.1	67.2	49.9	17.5	22.6	27.2

TABLE X. COMBINED BENDING AND WEB CRIPPLING CAPACITIES FOR BEARING LENGTH OF 75 MM

Section	Yield strength Fy=250 MPa					
	Concentrated load (kN)			Bending Moment (kNm)		
	0.5	0.75	1.25	0.5	0.75	1.25
100X45X1	9.1	13.9	10.4	1.0	2.2	2.5
100X45X2	49.9	47.8	35.8	4.3	5.6	6.4
100X45X3	86.1	81.8	61.2	6.9	8.9	10.1
150X60X1	13.4	11.6	8.5	3.1	3.9	4.6
150X60X2	47.9	45.4	33.8	7.2	11.4	11.4
150X60X3	85.5	81.7	61.4	11.3	15.1	17.9
200X75X2	46.4	42.1	32.2	10.9	14.2	17.6
200X75X3	85.1	79.8	60.3	17.1	23.1	28.1

TABLE XI. COMBINED BENDING AND WEB CRIPPLING CAPACITIES FOR BEARING LENGTH OF 75 MM

Section	Yield strength $F_y=450$ MPa					
	Concentrated load (kN)			Bending Moment (kNm)		
	0.5 (k)	0.75 (k)	1.25 (k)	0.5 (k)	0.75 (k)	1.25 (k)
100X45X1	19.1	26.9	4.6	8.9	14.3	13.7
100X45X2	83.9	79.5	57.3	7.6	9.8	10.8
100X45X3	146.8	118	102.1	12.2	13.2	17.4
150X60X1	18.9	15.9	10.9	5.2	7.1	7.1
150X60X2	75.7	67.7	49.2	13	16.6	19.3
150X60X3	100.6	103.8	94.6	26.9	27.5	36.1
200X75X2	68.1	62.1	47.6	17.7	23.5	29.2
200X75X3	140.9	129.6	96.5	30.8	40.8	49.1

^b. Observed results for the pure bending, pure web crippling and combined bending and web crippling capacities, were used to defined (P/P_n) and (M/M_n) values to compare with the (2) & (1)

After obtained results, all these observed results were plotted against ratio of bending to bending capacity vs ratio of concentrated load to web crippling capacity as shown in Figs. 8 to 11. As seen in all figures, it can be seen that both Australian and New Zealand standard and Eurocode are conservative for LSB sections under combined web crippling and bending action.

VII. RESULTS AND DISCUSSION

This study has investigated the behaviour of the LSB sections under combined web crippling and bending using Finite element analysis. FE models of Pure web crippling, pure bending, combined web crippling and bending have developed and validated using existing experimental data. The standard test length for the web crippling under IOF load case is $3d_1 + l_b$ and that length is used for this study. Also this study targeted web crippling and bending. Thus, it does not investigate global buckling of beams which occurs rarely.

In the validation, FEA results were compared with the experimental results in terms of mean and coefficient of variance. In finite element model prediction with web crippling test, the mean value of test to FEA values is 0.98 while COV is presenting 0.05. Predicted finite element models with pure bending tests present the mean of the test to FE is 0.99 and COV is 0.05. Moreover, developed combined web crippling and bending models show the mean of the tests is 0.98 while COV is 0.07. Thus, it can be concluded that, all predicted models are accurate. Therefore, common boundary conditions were developing for each web crippling and bending failures.

Web crippling, bending capacities and the failure load and bending moment was observed from the parametric study and values were substitute to the (1) as well as (2). It shows that the equations of Australian/ New Zealand standard and Eurocode are predicting conservative results for LSBs. Hence the both codes interaction equations can be used for LSB sections made of 250 and 450 MPa material strengths.

Furthermore, the observed results were plotted as (P/P_n) Vs. (M/M_n) as shown in the Figure 8 and 9 against the Eurocode Equation (Equation 2.0) . It shows a similar pattern of the data with three bearing length values. Meanwhile Figure 10 and 11 shows the same variation against the AS/NZS equation.

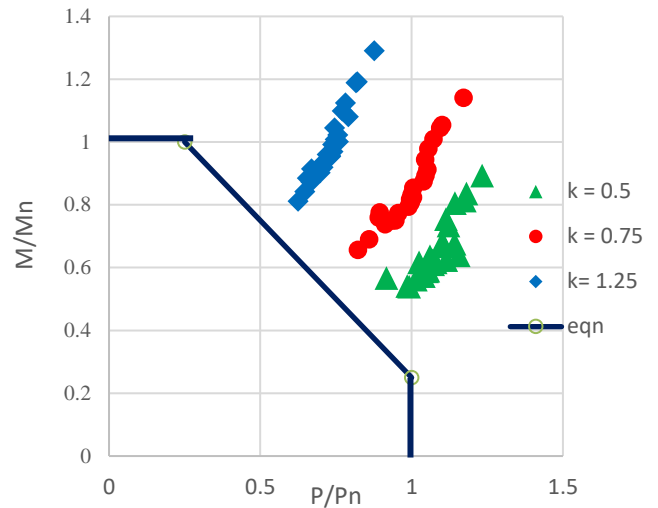


Fig. 8. P/P_n Vs M/M_n variation for 250 MPa (Compared to Eurocode Equation)

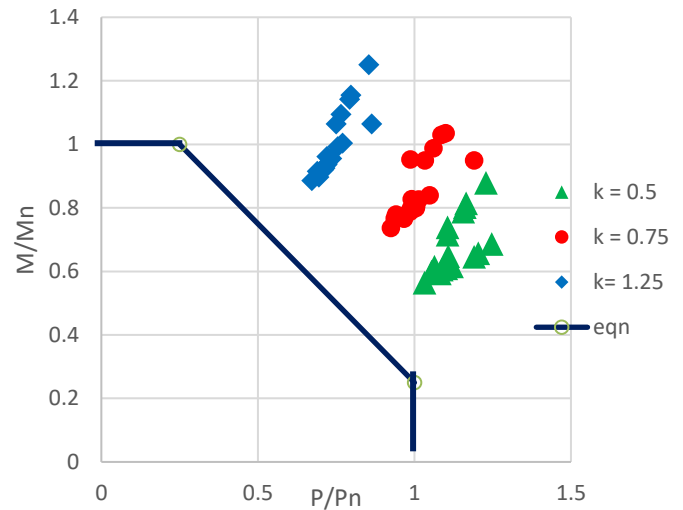


Fig. 9. P/P_n Vs M/M_n variation for 450 MPa (Compared to Eurocode Equation)

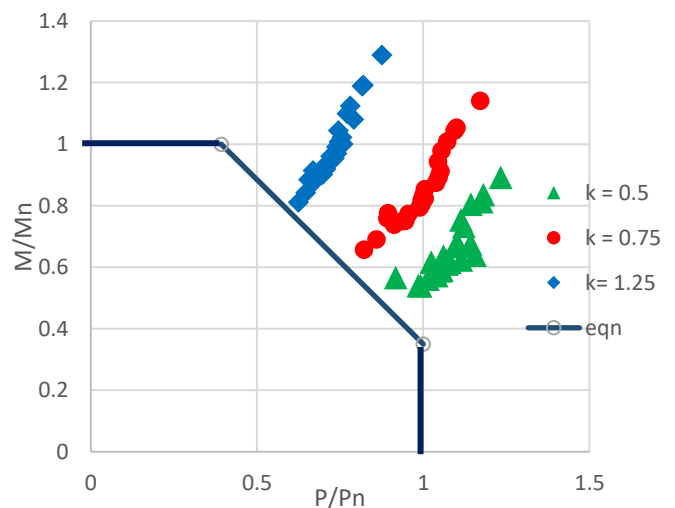


Fig. 10. P/P_n Vs M/M_n variation for 250 MPa (Compared to AS/NZS Equation)

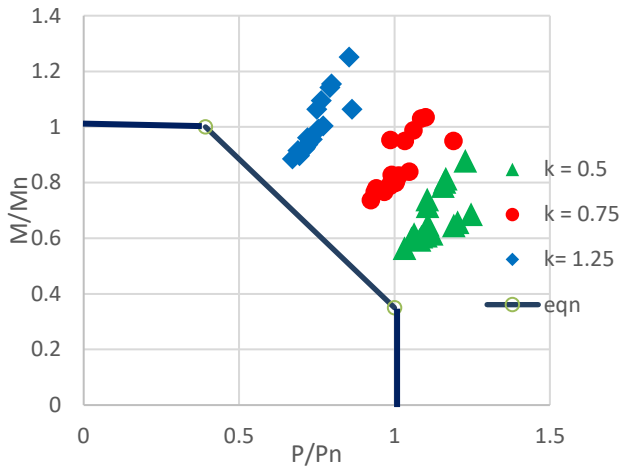


Fig. 11. P/Pn Vs. M/Mn variation for 250 MPa (Compared to AS/NZS Equation)

VIII. CONCLUSION

This research is an effort towards to presenting the behaviour of the LSB sections under combined web crippling and bending using Finite element analysis. In Three different finite element models, mean value of test to FEA value was around 1.00 and the coefficient of variance was around 0.05. thus, all developed FE models are accurate and able to predict the failure behaviours. Based on the parametric study results, it is found that the AS/NZS 4600 and Eurocode predicting conservative results for the combined behavior of LSBs with the bearing lengths of 50, 60 and 75 mm.

ACKNOWLEDGMENT

The authors gratefully acknowledge the support given by the Department of Civil Engineering, University of Jaffna.

REFERENCES

- [1] K. Elilarasi and B. Janarthanan, "Effect of web holes on the web crippling capacity of cold-formed litedeel beams under end-two-flange load case" Structures, vol. 25, 2020, pp. 411–425, <http://dx.doi.org/10.1016/j.istruc.2020.03.022>.
- [2] Standard Test Method for Determining the Web Crippling Strength of Cold Formed Steel Beams, AISI S909, American Iron and Steel Institute, Washington DC, USA, 2017.
- [3] Specifications for the Cold-Formed Steel Structural Members, Cold-Formed Steel Design Manual, AISI S100, American Iron and Steel Institute (AISI), Washington DC, USA, 2012
- [4] Australia/New Zealand Standard AS/NZS 4600 Cold-Formed Steel Structures, Standards Australia/Standards New Zealand (SA), Sydney, Australia, 2018
- [5] Eurocode 3 Part 1.3 (ECS), Design of Steel Structures: Part 1.3: General Rules Supplementary Rules for Cold-Formed Thin Gauge Members and Sheeting, European Committee for Standardization, Brussels, Belgium, 2006.
- [6] B. Janarthanan and M. Mahendran, "Numerical study of cold-formed steel channel sections under combined web crippling and bending action", Thin-Walled Structure, vol. 152, 2020, <http://dx.doi.org/10.1016/j.tws.2020.106766>.
- [7] R. Baehre, Sheet metal panels for use in building construction – Recent research projects in Sweden, Proceeding of the third international specialty conference on cold-formed steel structures, University of Missouri-Rolla, Rolla, Missouri, USA, 1975.
- [8] G.D. Ratliff, Interaction of concentrated loads and bending in C-shaped beams, Proceedings of the third specialty conference on cold-formed steel structures, University of Missouri-Rolla, Rolla, Missouri, USA, 1975.
- [9] N. Hetrakul and W.W. Yu, "Structural behaviour of beam webs subjected to web crippling and a combination of web crippling and bending", Final report, Civil Engineering Study 78-4, University of Missouri-Rolla, Rolla, Missouri, USA, 1978
- [10] B. Young and G. Hancoc, "Tests of channels to combined bending and web crippling", *Journal of Structural Engineering*, Vol. 128, 2002, pp. 300-308.
- [11] P. Keerthan and M. Mahendran, "Experimental study on web crippling strength of hollow flange channels under end-one-flange and interior-one-flange load cases", *Advances in Structural Engineering*, Vol. 19, 2016, pp. 966-981.
- [12] B. Janarthanan, M. Mahendran and S. Gunalan, "Numerical modelling of web crippling failures in cold-formed steel unlippped channel sections", *Journal of Conctructional Steel Research*, Vol. 158, 2019, pp. 486-501.

Usage of Mixed Construction and Demolition Waste as Fine Aggregates in Producing Concrete

R. N. Udarika

Department of Civil Engineering
University of Peradeniya
Peradeniya, Sri Lanka
nipuni.ranasinghe@yahoo.com

C.K. Pathirana

Department of Civil Engineering
University of Peradeniya
Peradeniya, Sri Lanka
chin@civil.pdn.ac.lk

Finding an alternative to the use of natural sand in the construction industry has often been a major topic of development. Sri Lanka needs to think seriously about producing eco-friendly varieties of sand so that its dependence on river sand mining can be minimized. In contrast, reuse and recycling have become a major concern in waste management as construction and demolition (C&D) waste poses critical challenges to environmental, social, economic, and human health. Therefore, this study seeks to utilize recycled fine aggregates (RFA) from mixed C&D waste as an alternative to fine aggregates in concrete.

Physical properties of RFA were tested and compared favorably with those of natural sand. The RFA was soaked in water for 24 hrs, removed, and air-dried in the laboratory for 48 hrs to bring approximately saturated surface dry (SSD) condition. The sand was replaced by weight at intervals of 10% up to 60%, while 0% represents the control. M30 concrete was produced with maintaining Constant Slump and additional water requirement was recorded. The properties of wet concrete and hardened concrete were evaluated.

The study revealed that, however, the compressive strength is declined with higher RFA percentages, flexural and splitting tensile strength are not significantly affected with RFA replacement for natural sand. By considering the design compressive strength, the optimum percentage of replacement is 30 % for the RFA. Thus, it is concluded that RFA can be used as supplementary fine aggregates material in concrete.

Keywords— Construction and demolition waste, recycled fine aggregates, recycling

I. INTRODUCTION

Construction and demolition waste has become a major challenge worldwide due to activities of renovation and demolition in the maintenance and modernization of buildings and civil structures. According to the researches, 40% of global waste is generated by construction and demolition (C&D) of buildings [1]. Construction activities generate approximately 50% of waste deposits in the UK [2], 20-30% in Australia, and one-third of landfills in the US [3]. C&D waste generation is assessed to be 180 million tons per year, even excluding the earth and some other waste and considering the population of approximately 370 million, the per capita annual waste generation is about 480 kg [4].

Sri Lanka is also struggling with waste management because of C&D waste mostly from Tsunami and terrorist activities [5]. Sri Lanka generates 7000 MT of solid waste per day, with the Western Province accounting for 60% of that statistic [6]. This rate varies depending on the income levels of individuals and households as well as on the degree of urbanization of settlements.

For decades, landfills have provided a convenient solution to C&D waste, but it's no longer affordable, due to the lack of

landfill sites for waste disposal and causes problems with environmental pollution, serious health hazards and wastage of natural resources [1].

As solid waste has become a serious problem in all over the world, more remedial actions and management processes implemented. One of the ways of achieving the solution related to construction practice is by reuse and recycling of building materials [7], mainly C&D wastes. Reuse and recycling bring back waste into the material cycle while reprocessing of material into new products through recycling and increasing the number of usages of the same material through reusing [8].

Aggregate consumption of the construction industry in the world in 2010 was recorded as 37.4 billion metric tons and it was forecasted to reach 48.0 billion metric tons in 2015 [6]. World demand for construction aggregates is rising 5.2 percent annually to 51.7 billion metric tons in 2019 [7]. According to the latest Input-Output table (2000) for Sri Lanka [8], Construction is the largest buyer in the Mining and quarrying sector and it is recorded as 76.45% [9]. It is estimated that the total annual sand requirement is at 21 million cubic meters [10]. Further, the sustainable annual supply of river sand will be around 10 million cubic meters (MCM). As such at least eight MCM should be met from washed and sieved sea sand and balance two MCM from manufactured sand [11].

Almost all of the sand requirement is manually or mechanically harvested from river beds. Mechanized sand mining has caused irreparable damage to the ecology of the affected areas [10]. The high demand for aggregates in the construction industry is gradually expanding as the economy grows. However, the supply of aggregates will be a massive struggle in the future because of limitations in natural resources.

Tiles, brick, blocks, concrete and asphalt, the large portion of C&D waste, are reprocessed and used in large building and construction projects for sub-base and concrete aggregates [12]. Especially in the USA, 14% of the aggregate requirements for construction are fulfilled with recycled aggregates [6]. Recycled aggregates are produced from the reprocessing of mineral waste materials, with the largest source being C&D waste.

As aggregates usually occupy approximately 60 to 70% of the volume of concrete and mortar, researchers have become more interested in replacing natural aggregates with recycled aggregates [13]. Several researches were made to identify the possibility and extent of replacing the natural sand with RFA [14], [15]. Further pretreatment processes and quality enhancement methods were added to increase the RFA replacement volume [16]. However, so far there has been a gap in research into the use of a C&D waste mixed form.

II. OBJECTIVES

The aim of this research is to find out the ability to utilize recycled aggregates of mixed C&D waste as fine aggregates in concrete while maintaining the required quality. Also, compare the properties of recycled fine aggregates with natural sand when it is used in concrete without compromising the quality. Ultimately identify the optimum proportion of recycled fine aggregates that can be successfully used in concrete.

III. EXPERIMENTAL WORK

A. Materials

Natural quarry stones, maximum size 20mm and river sand, maximum size 5mm were used as the crushed coarse aggregate and uncrushed fine aggregates respectively together with Ordinary Portland cement to make concrete of Grade 30. The fine recycled particles produced from mixed C&D waste were used as well to find the possibility of replacing natural sand by RFA. Fig. 1 shows the materials used for the experiments.

Crushed particles from C&D waste were sieved through a 5mm sieve to produce recycled fine aggregate. The sample was soaked in water for 24 hours inside the laboratory, removed and air-dried for 48 hours to get the approximately saturated surface dry (SSD) condition before the experiments. Potable drinking water which was deemed fit for human consumption was used for mixing.

B. Fine Aggregate Characterisation

All acceptable material properties including sieve analysis (BS812-103.1: 1985), specific gravity and water absorption (ASTM C128-84), bulk density (BS812: Part2: 1995) and field settling silt content of these recycled fine aggregates and natural sand were tested. The main properties of natural and recycled fine aggregate are shown in Table 1.

RFA has low bulk density and specific gravity and greater silt content than natural sand. Water absorption with RFA is also high, suggesting that higher porosity may result in higher water absorption with increasing replacement rate with RFA.



Fig. 1. Materials used for the Experiments

TABLE I. EXPERIMENTAL RESULTS OF PHYSICAL PROPERTIES FOR NATURAL AND RECYCLED FINE AGGREGATE

Properties	RFA	Natural sand
Specific gravity	1.67	3.15
Apparent Specific gravity	1.95	3.25
Silt content	12.74	6.42
Loose bulk density (kg/m ³)	1234	1567
Compacted bulk density (kg/m ³)	2300	2620
Water absorption (%)	12.2	1.1
Porosity (%)	3.2	2.8

According to previous researches, the major reason that affects the quality of recycled aggregate is a large amount of cement mortar remains in aggregates [14] and other non-stone contaminants such as brick, tile, glass, ceramics, slag, mineral waste, gypsum and other impurities [17]. It is resulting in higher porosity, water absorption rates and thus a weaker interfacial zone between new cement mortar and aggregates, which weakens the strength and mechanical performance of recycled concrete.

Particle size distributions of natural fine aggregate (NFA) and recycled fine aggregates were also tested according to the BS812-103.1: 1985 and the results are presented in Fig. 2. As the percentages of RFA material passing through each sieve are within the acceptable limits given in BS 882, natural sand can be replaced by RFA without further treatments.

C. Concrete Mix and Specimen Preparation

The Site mixed concrete was used for casting concrete cubes, cylinders and beams. These test samples were used to test the compressive strength, splitting tensile strength, and flexural strength. Grade 30 concrete is prepared according to the mix design under the weight adapting DOE mix design methodology and maintains a constant slump for each category by changing with the addition of water.

IV. RESULTS AND DISCUSSION

A. Workability

The experimental procedure was conducted on the basis of the constant slump method. However expected slump values are obtained for the conventional concrete mixtures (control mix), i.e. concrete with no substitution of recycled aggregates, slumps values were decreased with the increase of percentage replacement of recycled fine aggregates.

Therefore, by adding water in addition to the mix, the slump of all concrete mixes were maintained in the range of 75 ± 10 mm. The final water-cement ratios for the concrete mixtures were also calculated. The graphical variation of slump values versus effective w/c ratio for the different RFA replacement percentages is represented in Fig. 3.

It shows that all mixes met the target workability with modified w/c ratios which are higher than the conventional value derived from concrete mix design. Therefore, it shows that with the increase in RFA, an additional volume of water is required.

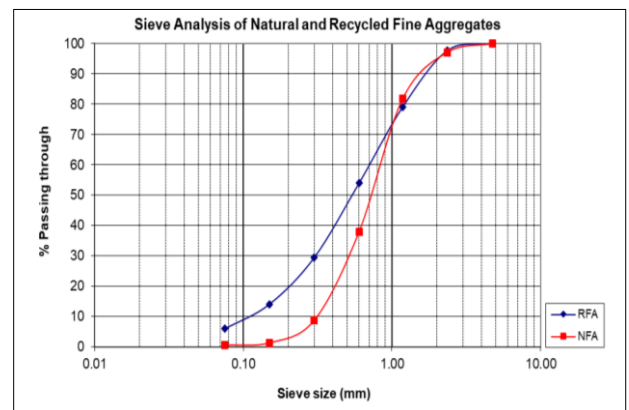


Fig. 2. Sieve Analysis of NFA and RFA

Fig. 4 shows the relationship of the effective water/cement ratios between concrete mixes with the replacement of fine natural aggregate by RFA. The results show that the water / cement ratios increase with the increase in the percentage of fine aggregates total replacement. This is because the higher water absorption capacity inherent in the recycled fine aggregate collection requires more water demand to be able to operate within the desired range of workability.

B. Wet Density of Concrete

The results presented in Fig. 5, show that the incorporation of RFA, which has lower particle density than NFA, leads to a decrease in the concrete's density. The decreases in wet densities are quite small and follow the same reduction pattern up to 40% replacement of NFA with RFA in concrete mixes. However, the replacement beyond the 40% of RFA, shows the sudden drop in wet density variation.

As the density of concrete is the function of aggregate pore space, the low density can be related to the high porosity of RFA which contributes to the overall porosity of concrete. The low bulk densities and specific gravity inherent with RFA lead to a decline in the wet density of concrete with higher RFA replacement percentages.

C. Compressive Strength

The average compressive strength (f_{cu}), measured at 28 and 7 days for all RFA incorporation ratios are presented in Fig. 6 and Fig. 7.

It shows that the compressive strength decreases with an increase in the content of RFA replacement for natural sand. This is because the aggregates are a mix of aggregates and old mortar that increases the new concrete porosity. In addition, this porosity increases mainly in the transition zone between aggregates and the new mortar, which decreases the mechanical performance of concrete.

It was observed that mixes containing 10% recycled aggregates attained a slightly higher value than conventional concrete in RFA incorporation. This was a 6% increase over the conventional mix and a 20% increase over the limit of 30 MPa. Furthermore, the RFA 20% replacement was also improving strength by about 13% from the limit. This is due to the contamination of the non-reactive cement content of the RFA, which acts as an additional binder in the concrete itself.

The compressive strength values have decreased beyond the limit of 30 MPa at the percentage replacement greater than 30%.

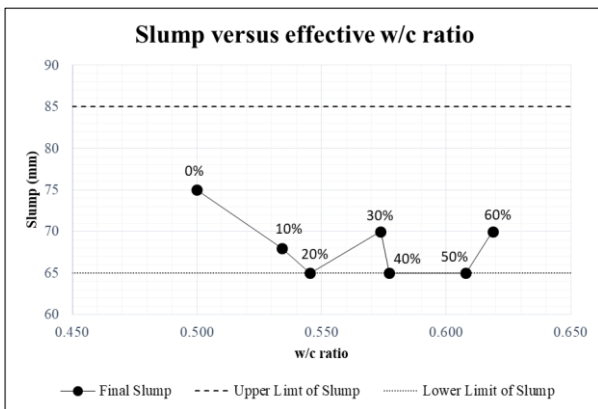


Fig. 3. Slump versus effective water/cement ratio for all NFA/RFA replacement percentage

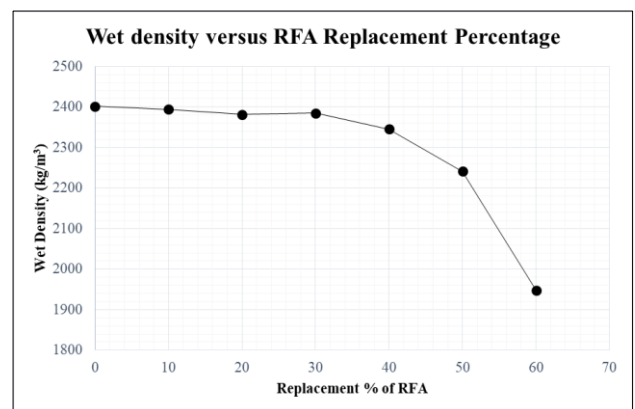


Fig. 5. Wet density of concrete versus FNA/RFA replacement percentage

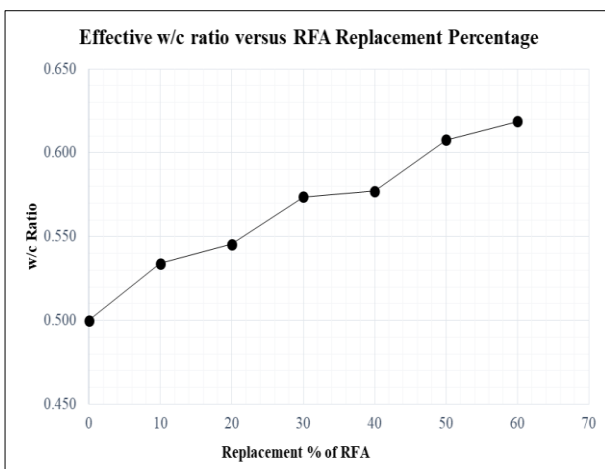


Fig. 4. Effective water/cement ratio versus NFA/RFA replacement percentage

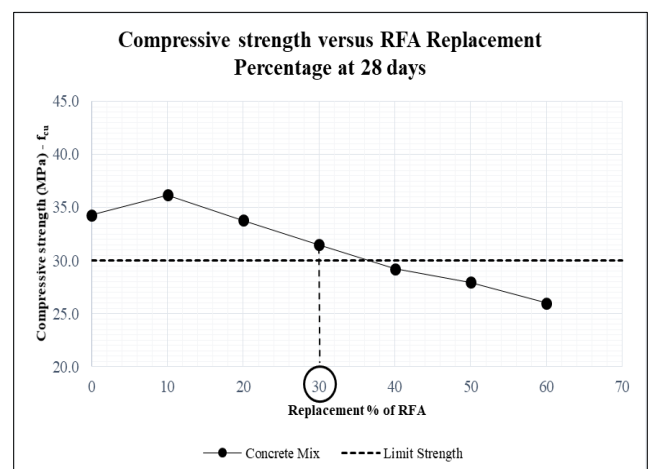


Fig. 6. Compressive strength versus RFA Replacement Percentage at 28 days

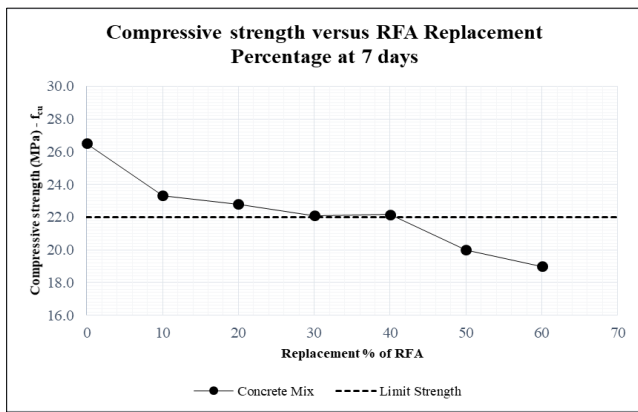


Fig. 7. Compressive strength versus RFA Replacement Percentage at 7 days

The results for the incorporation of RFA are in agreement with previous studies, and this performance may be explained by the higher un-hydrated cement content in the mix providing additional hydraulicity, the interfacial zone between the RFA and the cement paste may have benefited from the porosity of RFA having decreased locally, with the w/c ratio allowing more effective filling in by the hydrated products and filler effects linked to the RFA.

Apart from the replacement ratio, it is reported that the extent of compressive strength reduction is also related to the several parameters such as type of C&D waste used for making the recycled, water/cement ratio and the moisture content of the recycled aggregates.

According to the literature, the Compressive strength at 7 days is approximately equal to the 65 - 75% of 28 days strengths. Assuming the 21 MPa, the limit of 7 days strengths, the optimum percentage replacements were again proved with the results concluded with 28 days compressive strength.

Concluding the results, the advanced value for percentage replacement of RFA was 30% without compromising the required compressive strength and optimizing the natural sand replacement.

D. Splitting Tensile Strength

One of the important properties of concrete is “tensile strength” as structural loads make concrete vulnerable to tensile cracking. The splitting tensile strength up to 28 days of hydrations for various percentages of natural sand replacement with crushed C&D wastes is presented in Fig. 8.

The small variations of the tensile strength can be seen. According to the results obtained from the experiment, the splitting tensile strengths of concrete mixtures are increased with an increasing proportion of aggregate replacement up to 10%. It shows a sudden decline of between 10-20% and the gradual decline continues. For higher replacement levels, the splitting tensile strength of concrete decreases almost linearly as the RFA content increases.

The splitting tensile strength of concrete is reduced by 20% when 30% RFA is incorporated as a sand substitute. However, the splitting tensile strength at 30% substitution for RFA was an acceptable value for M30 concrete.

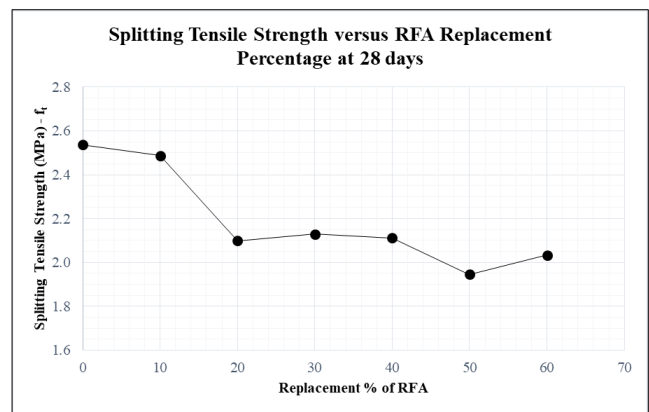


Fig. 8. Splitting Tensile Strength versus RFA Replacement Percentage

E. Flexural Strength

Flexural strength is one measure of the tensile strength of concrete. It is a measure of an unreinforced concrete beam to resist failure in bending.

The flexural strength variation at 28 days hydration periods of different concrete mixes with different percentage replacement of sand with crushed C&D waste is illustrated in Fig. 9. The variation in flexural strength is not much significant when increasing the percentage replacement of sand with RFA.

According to the previous studies, flexural strength is about 10 to 20 percent of compressive strength depending on the type, size and volume of coarse aggregates used. At 30% replacement of RFA, the flexural strength is 6 MPa, which is about 20% of the compressive strength of concrete. Therefore, 30% of the optimal substitution of RFA can be further justified with flexural strength properties.

SUMMARY AND CONCLUSION

An experimental programme was conducted to study the cumulative use of fine-grained recycled aggregates produced from mixed form of C&D waste to partially replace natural fine aggregates in the production of structural concrete. The experimental results indicates that it is viable to produce concrete with fine recycled aggregates suitable for structural concrete, considering that;

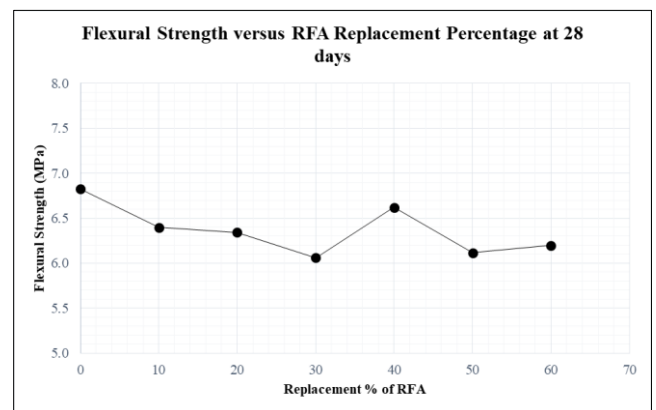


Fig. 9. Flexural Strength versus RFA Replacement Percentage at 28 days

1. The compressive strength does not seem to be affected by the fine aggregates replacement percentage, at least for up to 30% replacement ratio and the strength levels considered in this study.
2. On days 7 and 28, the compressive strength clearly shows the only correlation with the RFA replacement percentages, so that the compressive strength gained over time remains acceptable for each RFA replacement ratio.
3. As the replacement percentage increases, the flexural strength and the splitting tensile strength do not decrease significantly; However, the values obtained for both properties are still acceptable, especially a reasonable level of replacement ratio (30%).
4. Since the constant slump method was used for the experiments, the workability of the concrete is within an acceptable range.

Considering all the properties and results, it can be concluded that the optimum percentage of RFA replacement is limited to 30 % for crushed C&D waste. Thus, it is concluded that RFA can be used as supplementary fine aggregate materials.

It should be noted that the RFA used were obtained from the mixed form of C&D waste without any qualitative control in the collection and crushing process. It is expected that RFA obtained from different field conditions would like to have particles from different qualities that might alter their performance.

ACKNOWLEDGMENT

This research was supported by the Faculty of Engineering, University of Peradeniya, Sri Lanka. I thank our academic staff, who provided insight and expertise that greatly assisted the research, and laboratory staff of the material lab of the Civil Engineering Department, mainly with Mr. A.H.E. Parakrama, laboratory assistant who provided valuable support in relation to complete the experiments.

REFERENCES

- [1] J. Opeyemi, O. Kolapo O., A. Lekan M. and O. Ignatius O., "RECYCLING FINE SANDCRETE BLOCK WASTE (FSBW) AS FINE AGGREGATE IN THE PRODUCTION OF SANDCRETE BLOCK," *IJRRAS*, vol. 15, no. 3, June 2013.
- [2] R. Islam, T. H. Nazifa, A. Yuniarto, A. S. Uddin, S. Salmiati and S. Shahid, "An empirical study of construction and demolition waste generation and implication of recycling," *Waste Management*, no. 95, pp. 10-21, 26 May 2019.
- [3] L. Evangelista and J. d. Brito, "Concrete with fine recycled aggregates: a review," *Environmental and Civil Engineering*, vol. 18, no. 2, pp. 129 - 172, 30 September 2013.
- [4] A. Rao, K. N. Jha and S. Misra, "Use of aggregates from recycled construction and demolition waste in concrete," *Resources, Conservation and Recycling*, no. 50, pp. 71 - 81, 2007.
- [5] Raufdeen and Rameezdeen, "Construction Waste Management, Current status and Challengers in Sri Lanka," COWAM, 2009.
- [6] Z. Dawoodbhoy, "ENVIRONMENT & WILDLIFE," 2019. [Online]. Available: [https://roar.media/english/life/environment-](https://roar.media/english/life/environment-wildlife/counteracting-srilankas-waste-problem/)

- wildlife/counteracting-srilankas-waste-problem/. [Accessed 3 April 2019].
- [7] H. Ranjan, G. Karunasena and U. Rathnayake, "Construction and Demolition Waste Management Gaps in Construction Industry," 2014.
- [8] L. T. Gunaruwan and N. W. Gunasekara, "Management of Municipal Solid Waste in Sri Lanka: A Comparative Appraisal of the Economics of Composting," *NSBM Journal of Management*, vol. 2, no. 1, pp. 27 - 45, June 2016.
- [9] ELAW, *National Policy on Sand as a Resource for the Construction Industry (DRAFT)*, Colombo, Sri Lanka: News Paper - "Daily News", 2005.
- [10] C. Jayatileke, *A river sand substitute*, Colombo, Sri Lanka: News paper - "Daily News", 2020.
- [11] S. Hannan, *Impending sand shortage: Consider alternatives to river sand, urges Env. Ministry*, Colombo, Sri Lanka: News paper - "The Sunday Morning", 2021.
- [12] D. Pawar and R. Sawant, "Construction & Demolition Waste Recycling Market by Source (Construction, Renovation, and Demolition), Service (Collection and Disposal), and Material (Concrete, Bricks, Metal, Wood, and Others): Global Opportunity Analysis and Industry Forecast, 2020–202," Allied Market Research, Aug 2020.
- [13] F. Rodrigues, M. T. Carvalho, L. Evangelista and J. d. Brito, "Physical-chemical and mineralogical characterization of fine aggregates from construction and demolition waste recycling plants," *Cleaner Production*, vol. 52, pp. 438-445, 2013.
- [14] A. Katz, "Properties of concrete made with recycled aggregate from partially hydrated old concrete," *Cement and Concrete Research*, vol. 33, p. 703–711, 2003.
- [15] M. Solyman, "Classification of recycled sand and their applications as fine aggregates for concrete and bituminous mixtures (Unpublished PhD thesis)," Fachbereich Bauingenieurwesender University, Kessel, Germany, 2005.
- [16] I. H. Song and J. S. Ryou, "Hybrid techniques for quality improvement of recycled fine aggregate," *Construction and Building Materials*, no. 72, pp. 56-64, 2014.
- [17] H.-L. Ho, R. Huang, W.-T. Lin and A. Cheng, "Pore-structures and durability of concrete containing pre-coated fine recycled mixed aggregates using pozzolan and polyvinyl alcohol materials," *Construction and Building Materials*, no. 160, pp. 278-292, 2018.
- [18] A. A. Umoh, "RECYCLING DEMOLITION WASTE SANDCRETE BLOCKS AS FINE AGGREGATE IN CONCRETE," *ARPN Journal of Engineering and Applied Sciences*, vol. 7, pp. 1111-1118, SEPTEMBER 2012.
- [19] Freedonia, "World Construction Aggregates - Demand and Sales Forecasts, Market Share, Market Size, Market Leaders," Freedonia, 2016.
- [20] S. Levy and P. Helène, "Durability of concrete mixed with fine recycled aggregates," vol. 5, pp. 25-34, 2007.
- [21] B. Vinay Kumar, H. Ananthan and K. Balaji, "Experimental studies on utilization of recycled coarse and fine aggregates in high performance concrete mixes," *Alexandria Engineering Journal*, 2017.
- [22] M. Quattrone, B. Cazacliu and S. C. Angulo, "Measuring the water absorption of recycled aggregates, what is the best practice for concrete production," *Construction and Building Materials*, vol. 123, no. 123, pp. 690-703, 2016.
- [23] C.-C. Fan, R. Huang, H. Hwang and S.-J. Chao, "Properties of concrete incorporating fine recycled aggregates from crushed concrete wastes," *Construction and Building Materials*, no. 112, pp. 708-715, 2016.
- [24] International ASTM, ASTM C127-08: Standard test method Density, Relative Density (Specific Gravity) and Absorption of Fine Aggregates, Annual Book of ASTM Standards, 2008.

Self-Compacting Concrete Strength Variation Under Wet and Dry Cyclic Process with Different Curing Period

S. Hareindirarma
Department of Civil Engineering
Faculty of Engineering, University of
Jaffna
Kilinochchi, Sri Lanka
hareindirarma@gmail.com

S.Jatheesan
Department of Civil Engineering
Faculty of Engineering, University of
Jaffna
Kilinochchi, Sri Lanka
psjathe@gmail.com

C.Pirakash
Department of Civil Engineering
Faculty of Engineering, University of
Jaffna
Kilinochchi, Sri Lanka
pirakashc94@gmail.com

B.Janarthanan*
Department of Civil Engineering
Faculty of Engineering, University of
Jaffna
Kilinochchi, Sri Lanka
jana151188@eng.jfn.ac.lk

Abstract— In contemporary society, increasing environmental and economic issues have been considered as a significant factor due to the high amount of concrete production; thus, the several techniques have been proposed for the sustainability of concrete production; inclusion of waste products as a cementitious material such as rice husk ash (RHA), fly ash etc. Although the durability performance of concrete has a serious consideration in the field of the concrete industry, there are still gaps regarding the durability performance of self-compacting concrete (SCC) with the inclusion of RHA is still unknown. Buildings in the coastal area interact with chlorides present in moisture which can also change the durability properties of SCC having RHA. Therefore, this research study looks forward to finding the effect in the self-compacting concrete due to wet and dry cyclic processes, including rice husk ash. The research study was carried out based on different variables such as partial replacement of cement with RHA (0%, 5%, 10% and 15%) and cyclic wet and dry conditions (10, 14, 28 and 36 days). Furthermore, slump flow, V-funnel, J-ring, and U-box tests have been performed to ensure the self-compacting concrete fresh property status as per the EFNARC guidelines. Comparing the compressive strength of concrete cubes between cubes with normal curing days and cubes with the continuous cyclic process has been investigated. Based on the results, a 5% RHA-SCC replacement results in a 3.2% increase in compressive strength than 0% of RHA-SCC due to the presence of highly reactive amorphous silica.

Keywords— Self-compacting concrete (SCC), Rice husk ash (RHA), Wet and dry cyclic process, Compressive strength

I. INTRODUCTION

The development of concrete type, quality and ingredients are gradually changing with time, whereas one of the major industries under constant change these days is the concrete industry [1]. The most significant evolution of this industry in this decade is the development of self-compacting concrete (SCC) [1]; SCC is defined as concrete that can flow and compact under its own weight and fill formwork through reinforcement, ducts, etc. whilst maintaining homogeneity. SCC was initially developed in Japan in the late 1980s due to the lack of skilled workers to place the concrete in the way

that satisfies the requirement, and this issue has caused a decrease in durability and overall quality of the concrete [1].

The uniqueness of SCC is a self-compacting property without any need for external compaction. However, to obtain the desired flow properties, the SCC has a more delicate material than conventional concrete, reducing aggregate volume. The effect of aggregate volume on the hardened state of SCC in strength, stiffness and stability is protected by the addition of fly ash and colloidal Nano silica [2], so the total aggregate volume does not pose a threat. The addition of additives to the concrete will play a significant role in decreasing the heat of hydration and cost of concrete while increasing the cohesion and segregation properties of concrete. Rice husk ash is one such mineral with high silica content [3,4], hence it shows a high pozzolan reaction. Varying RHA percentage shows varying compressive strength values with time comparing to the no- RHA added SCC [3]. Thus, researches are being undertaken to find the relationship between compressive strength and RHA percentages.

Since constructions undergo different weather conditions, appropriate specimen shape and wet-dry cyclic test conditions need to be developed to resemble practical effects in buildings. In SCC, cement is replaced by RHA to reduce production costs. More than that, the buildings in a coastal area interact with chlorides present in moisture which can also change the durability properties of SCC having RHA. Thus the concentration of chloride present in the air needs to be designed for laboratory modelling. Nevertheless, the production ways of RHA also have a significant effect on its compression strength value. Hence an optimum production way should be formulated such that it is easy for mass production and has better results. Further, different percentages of RHA addition also change the durability. Therefore, the compressive strength of SCC with RHA under wet-dry cyclic loading should be investigated.

Therefore, this research study aims to determine the variation of compressive strength of RHA-SCC for wet-dry conditions and variation in curing patterns. Thus, based on the experimental investigations, the detailed results of

compressive strength variation of RHA-SCC with different percentages (0%, 5%, 10% and 15%) under wet-dry cyclic processes have been reported in this paper.

II. LITERATURE REVIEW

Self-compacting concrete can be made with several types of materials to optimise with the proper selection of materials. Thus, compared to normal concrete SCC, it has a sensitive change with the material properties. Rob and Noel [5] stated that self-compacting concrete flows and passes through reinforcement and fill formwork due to its own weight and is more beneficial compared to traditional concrete. Rob and Noel [5] listed some of those beneficial factors such as less construction time, labour cost reduction, improved working environment, and improved surface quality. The main drawback of SCC is its cost of production more than that due to the production of one ton of cement; it is estimated that one ton of CO₂ will be released, which contributes to global warming and demand for concrete is increasing by 1m³ per year per person [6]. Therefore, reducing the consumption of cement becomes a significant concern without reduction in strength and according to Salas et al. [3] by having fly-ash, metakaolin, rice husk ash (RHA), Ground granulated blast furnace slag or silica fume as a cement replacement to a certain percentage the cost could be reduced along with a slight increase in strength.

It was found later that thermal cracks formation due to the heat of hydration and less cohesion and segregation resistance in the fresh concrete are the main reasons for the decrease in compressive strength of both conventional and self-compacting concrete [1]. The uniqueness of SCC is a self-compacting property without any need for external compaction; however, to obtain the desired flow properties, the SCC has more fine material compared to conventional concrete, which reduces the total amount of aggregate volume.

One of the primary supplementary cementing materials is RHA. As mentioned by Chopra et al. [7], rice husk, obtained from rice processing mills when burnt adequately at a temperature lower than 700°C, generates rice husk ash containing reactive amorphous silica content is most suited for use as a pozzolan to improve the microstructure of the interface between cement paste and aggregate in SCC. Moreover, using RHA as supplementary cementing material is considered a sustainable environmental solution since it reduces the need for cement, reducing the CO₂ emission percentage. As studied by several researcher's pre-treatment of rice husk will produce high reactive pozzolan. Salas et al. [3] formulated two methods to producing high reactive pozzolan through rice husk. Initially, samples are to be washed and dried then separated to produce different types of ashes. The conventional type of RHA is produced by burning the rice husk in a programmable furnace for 600°C for three hours at a rate of 10°C/ min. The ash produced in this manner is called the conventional type of RHA. The second method of RHA preparation is by having the rice husk washed with hydrochloric acid having a concentration of 1 mol/dm³ for 24 hours. After separating the rice husk, the liquid remains carefully removed, and the rice husk is washed in normal water thoroughly until its pH is neutralized. Then the chemically treated rice husk is produced by burning the rice husk in a programmable furnace for 600°C for three hours at a rate of 10°C/ min. These two methods were compared to those of a reference concrete with silica fume. Compressive

strength was determined at 28, 56, 90 and 180 days. The modulus of elasticity and flexural strength was found on the 56th day. The resistance to chloride-ion penetration was found according to ASTM C1202 [8] standard. This research concludes that the chemical-thermal process has increased compressive strength and flexural strength compared to other processes.

Zain et al. [9] stated production is by the combustion of rice husk with fire duration of 30 min, 60 mins of air supply and cooled down for two days. This method produces white RHA having a carbon content of 3.21%, and then grinding of burnt ash using a combination of steel rods expedited the grinding process. Although grinding for 30 min produced a good result, grinding for 60 min or more is recommended for achieving the standard fineness of RHA. This research states that this type of RHA production has created good quality ash with only 3.21% carbon content, but it is not tested for compressive strength.

Unfortunately, as RHA being an organic compound, its durability in SCC until the design period becomes a threat. So many researchers have performed different types of durability tests to ensure the RHA added SCC everlasting characteristic. These are some of the most important tests: rapid chloride permeability testing, water absorption and porosity testing, electrical resistivity testing, acid resistance testing, the freeze and thaw test, and the wet-dry cyclic loading test [4]. Increased permeability values were observed when RHA is used as a partial replacement for cement; nevertheless, these values remain lower than the control mix until RHA is used at a percentage of 20% of the total cement [10]. As per Sandhu and Siddique [4] research study, the permeability of SCC decreases with the addition of RHA because the high particle packing characteristic makes SCC denser as a result of the addition of RHA. These occurrences are generated by the reaction of silica-rich RHA with calcium hydroxide, which results in the formation of extra C-S-H gel, which stabilises the microstructure of SCC and increases its endurance. Even though good quality concrete should have water absorption less than 5 percent, according to Kosmatka et al. [11], reducing water absorption leads to an increase in the quality of the concrete. Therefore, in order to reduce water absorption, either the density of the concrete or the pore size of the concrete should be increased. When RHA was added to SCC, Safiuddin et al [12] found that water absorption was reduced, and that small absorption was gained for 30% RHA inclusion for a 0.35 w/b ratio, which results in 35% less water-absorbing than for 0% RHA added SCC. According to the findings, the total porosity decreased with an increase in RHA content, and a reduction in 5% - 35% of total porosity was found for different RHA contents [12].

Omrane et al. [13] investigated the performance and long-term durability of SCC constructed with recycled aggregates and natural pozzolan, respectively. All the fresh property tests were performed for SCC, and compressive strength was determined at various ages. However, in this test, chloride ion diffusion was examined using Fick's second law, and the loss in mass following immersion in sulfuric acid was also investigated. The results show that it is possible to use recycled aggregates up to 50% of the time, and that the inclusion of pozzolan at concentrations of 10% and 15% reduces the penetration depth of chloride ions by 50% and the mass loss under sulfuric acid. Kannan and Ganesan [14] investigated corrosion behaviour using self-combusted RHA

(SCRHA) and metakaolin (MK) and found that both substances were effective. Different mix proportions were created by substituting SCRHA and MK for cement in varying quantities (ranging from 0 percent to 30 percent). In order to determine the blending properties of the new concrete, slum flow, V-funnel, and l-box tests were carried out on it. The ASTM C 1202 [8] standard was used to evaluate the material's strength properties (compressive strength) and durability properties during the fast chloride penetration test. According to the findings of this investigation, 15% SCRHA, 10% MK, and 10% SCRHA +10% MK demonstrated excellent efficacy in both fresh and hardened SCC samples.

III. METHODOLOGY

A. Materials

The following properties of materials were used in this research study: fine aggregate, which is washed river sand with a fineness modulus of 2.78, specific gravity of 2.53, and water absorption of 21.3 percent; coarse aggregate, which has a maximum nominal size of 12 mm and water absorption, void ratio, and specific gravity of 0.6%, 38.4%, and 2.77%, respectively. Fine aggregate has a fineness modulus of 2.78, specific gravity of 2.53, and The gradation curves for fine and coarse aggregates, as determined by sieve analysis following BS 882:1992 [15]. Typical commercial Type I Portland cement provided by Nippon cement manufactured by Tokyo Cement Co. (Lanka) PLC was used. The required rice husk ash was collected from a rice mill in Kilinochchi, Sri Lanka.

This project requires a huge RHA quantity, so open-air burned RHA was selected for the project as cement substitution, which will be drawn from the rice mill in Kilinochchi. Closed air burned RHA found in the same mill was taken for usage; this particular RHA burns at a temperature of 700°C- 800°C. As shown in Fig.1(a), this RHA was primarily white in color, which means it contains high silica content than the other RHA shown in Fig. 1(b). In



Fig. 1. Types of RHA (a) Long burned (b) short burned

a study [16], it was determined that the RHA was preferred for partial replenishment of cement after passing through a filter with an opening of 75 microns. The superplasticizer was provided by CHRYSO Lanka Pvt Ltd, which conforms to ASTM C 494 Type A, F and G [17] and BS EN 934-2[18]. In this product, polycarboxylate and modified phosphonate are combined to make a new generation superplasticizer with a specific gravity of 1.07, which is meant to deliver the maximum possible performance in water reduction. For the mixing process, ordinary drinking water was used.

B. Experimental study

Three criteria were considered to determine the best mix design for SCC, including RHA: partial substitution of cement with RHA percent, aggregate size, and the water to binder ratio, among others. Several different mix designs have been explored to attain favourable fresh concrete qualities, and the fresh concrete properties have been evaluated using standardised [19] tests, as indicated in Table I.

The SCC elements were divided into batches based on the proportions of the combination. The SCC mixture was made in three processes. In the beginning, the aggregates, sand and cement were mixed for one minute in dry form to ensure proper mixing. Second, two-thirds of the water containing the total superplasticizer solution was added and mixed for ten minutes. The remainder of the water was then added to the mixture, and everything was thoroughly mixed for another ten minutes. SCC slump flow, V-funnel and U-box experiments were carried out immediately after the 20-minute mixing period to determine the fresh properties of the SCC. The tests were carried out in a clean, stabled, and levelled base plate without the use of any external compacting action such as rodding or vibration.

Slump Flow test: Immediately after the mixing for 20 minutes slump flow test was performed in a clean, stabled and levelled base plate by filling upright mold without any external compacting action such as rodding or vibrating. The spread diameters were determined by measuring the largest diameter of the flow spread and the one perpendicular to it, using the ruler and averaging the measurements. The slump flow experiment is shown in Fig. 2(a).

V-Funnel Test: The segregation resistance and filling ability were tested using the V-Funnel test. This test is performed in a wet interior of the funnel by filling the funnel with SCC without applying any compaction or rodding. The V-Funnel flow times were determined by the difference in the stopwatch time from the moment of the gate opening until the clear space is visible through the funnel's opening. Picture of V-Funnel experiment is shown in Fig. 2(b).

U-Box Test: The passing ability was tested using the U-Box test. This test is performed by sliding gate and partition plate with an obstacle into the U-shaped or Box-shaped container and continuously placing the concrete without rodding, tamping or tapping. The difference in U-Box is determined by measuring the height difference between concrete surfaces. The test apparatus of the U-Box is shown in Fig. 2(c).

TABLE I. ACCEPTANCE CRITERIA FOR SELF-COMPACTING CONCRETE [19]

Method	Unit	The typical range of values	
		Minimum	Maximum
Slump flow	mm	650	800
V-funnel	Sec	6	12
U-box	mm	0	30

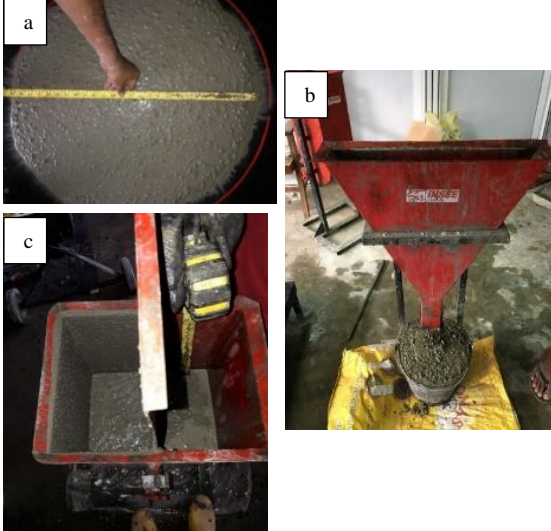


Fig. 2. Fresh property tests (a) Slump flow test (b) V-funnel test (c) U-box test

Immediately following completion of the fresh concrete tests, the SCC was poured into the 150 mm cube molds, and after 24 hours, the specimens were removed from the mold

and allowed to cure in a water tank until the age of testing was reached.

Set1: compressive strength gain with no of curing days, which means strength variation was determined in 7, 14, 28 and 49 days with the mean value obtained from three specimens for each category (RHA-SCC: 0%, 5%, 10% and 15%).

Set2: compressive strength variation with no of the wet-dry cycle (one day wet & one day dry): Specimen (RHA-SCC: 0%, 5%, 10% and 15%) were introduced to 3, 7 12 and 18 continuous cyclic process and compressive strength of respective categories were taken.

Quality control is a procedure to ensure that all the casted specimens will show the same results with the same mix design, procedure, and environmental conditions. Therefore, similar properties of aggregates, cement, water source, and admixture were used throughout the research project. Thus, aggregate properties tests were done before using aggregate samples, such as the Aggregate Impact Value and Particle Size Distribution analyses. Before starting the experiment, mixing procedures and initially, some cubes were cast to ensure proper mixing by considering the variation of results.

IV. RESULTS

A. Fresh concrete properties

In the self-compacting concrete, fresh properties possess the key properties including flow ability, filling ability and passing ability. However, the water-cement ratio, aggregate cement ratio, rice husk ash percentage, and admixture percentage highly influence the SCC properties. Slump flow, v-funnel and u-box test were done to identify whether SCC has fulfilled all the EFNARC [19] standard guidelines in plastic conditions. The findings showed that v-funnel time

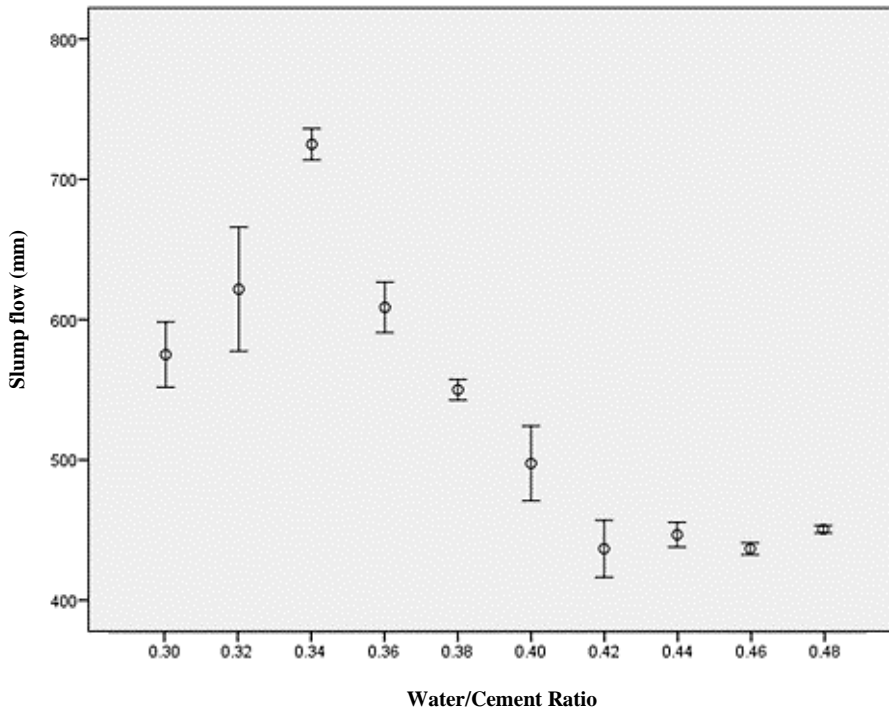


Fig. 3. Slump flow variation with water-cement ratio

was between 6-9 seconds and U-box height difference was between 0-30 mm.

The results are shown in Fig. 3, in terms of slump flow versus water-cement ratio based on the control cube experiment data. The more water was added leads for the more deformability and flow of SCC increased. Nevertheless, the slump flow value achieved an optimum value of 720 mm at the stage of 0.34 water-cement ratio (W/C) (Based on 40 control cube mix designs), then it shows the reduction in the slump flow reaches a minimum slump flow value of 430 mm. Furthermore, 0.34 W/C ratio resulted in a small amount of error variation compared to other W/C ratios. In addition, visual observation indicated that most of the mixes deformed and flow homogeneously which the flow spread was approximately circular shape; also, coarse aggregate did not remain or stick together in the centre of slump flow after removal of slump cone. If the W/C ratio is higher than 0.34, that leads to the segregation effect (It was identified from visual observation) due to that the slump value was reduced.

B. Compressive strength performance

Fig. 4 shows the relationship between compressive strength and the curing days of SCC until forty nine days. This was performed for all four categories of RHA-SCC; 0%, 5%, 10% and 15%. It can be seen that 5% RHA-SCC has higher strength compared to all other percentages. The highest compressive strength was obtained for SCC, which contained 5% RHA from the beginning; even in 7 days, it has shown a higher value. Replacements of 5% RHA causes the compressive strength to increase 3.2%, and by replacing 10% and 15% RHA, compressive strength decreases by 3.9% and 14.4%, respectively, compared to the control cubes. Also, 10% RHA added SCC is showing more strength than 15%. From the above figure, it can be seen SCC graph pattern is also similar to that of the conventional concrete strength vs age graph. The reason for 5% RHA-SCC showing more value than control specimens, 10% and 15% RHA-SCC is due to the hydrated RHA creating C-S-H gel, which is the reason for the strength of concrete and reactive amorphous silica. However, 10 and 15% RHA addition has shown poor performance. This phenomenon is because of the abundance of RHA or, in other words, the presence of untreated RHA,

which contains lower reactive amorphous silica. It is clear that increasing the RHA replacement ratio, due to the densification of the microstructure of the RHA based SCC leads to more brittle failure occurs.

C. Wet-Dry cyclic process

Fig. 5 illustrates the compressive strength variation under wet and dry cyclic process with different RHA percentages. An approximate steady increase in compressive strength throughout the whole test was observed, as shown in Fig. 5(a). However, cubes that underwent a wet/dry cyclic process showed a lower compressive strength value than the cubes that underwent drying. This pattern shows that the wet/dry cyclic process affects the durability with 0% RHA in the SCC. Fig. 5(b) shows a pattern like Fig. 4(a) but shows the difference between the compressive strength deviation among wet/dry cyclic processed cubes and dry-processed cubes have almost the same value compared to 0% RHA-SCC. Fig. 5(c) shows the same behavioural pattern as Fig. 5(a) and Fig. 5(b), but it has shown a lower variation in strength. 10% RHA addition has created only 1.3 average deviations, and other RHA percentages have created more deviation concerning 10%. The results indicate that the brittleness of SCC increases with an increase in the RHA replacement ratio. However, 15% RHA-SCC has shown higher deviation, this might be because of higher water consumption needed for obtaining correct workability of SCC, but it might have created more micropores, which has increased the ratio of shrinkage crack in the concrete.

w/d stands for the total number of days of wet and dry cycles applied for the specimens. According to the bar chart shown in Fig. 6, it can be seen that 5% RHA-SCC has shown noticeable improvement in compressive strength comparing to all other specimens, even under wet/dry cyclic process also. Higher compressive strength might be because of the presence of hydrated RHA, and the reason for better performance in the wet-dry cyclic process is the presence of dense microstructure.

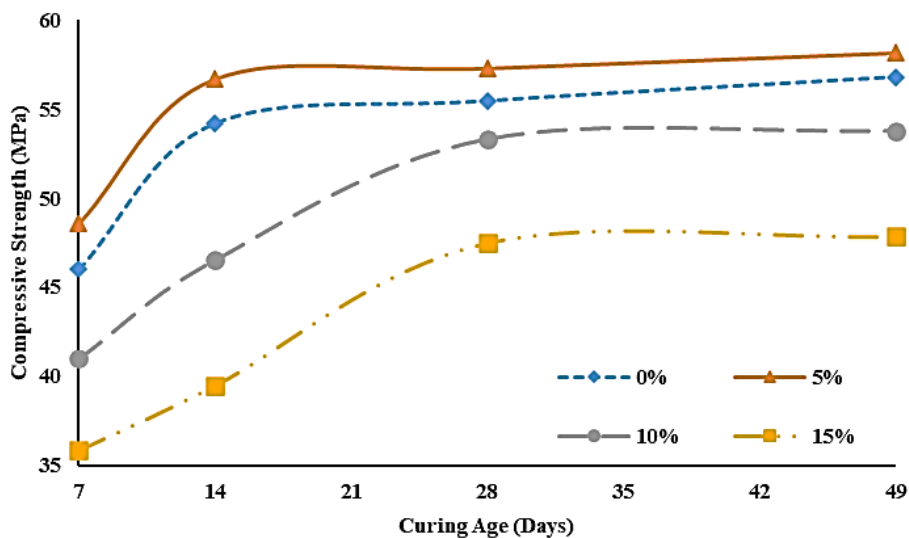


Fig. 4. Compressive strength variation with curing days for different RHA percentages

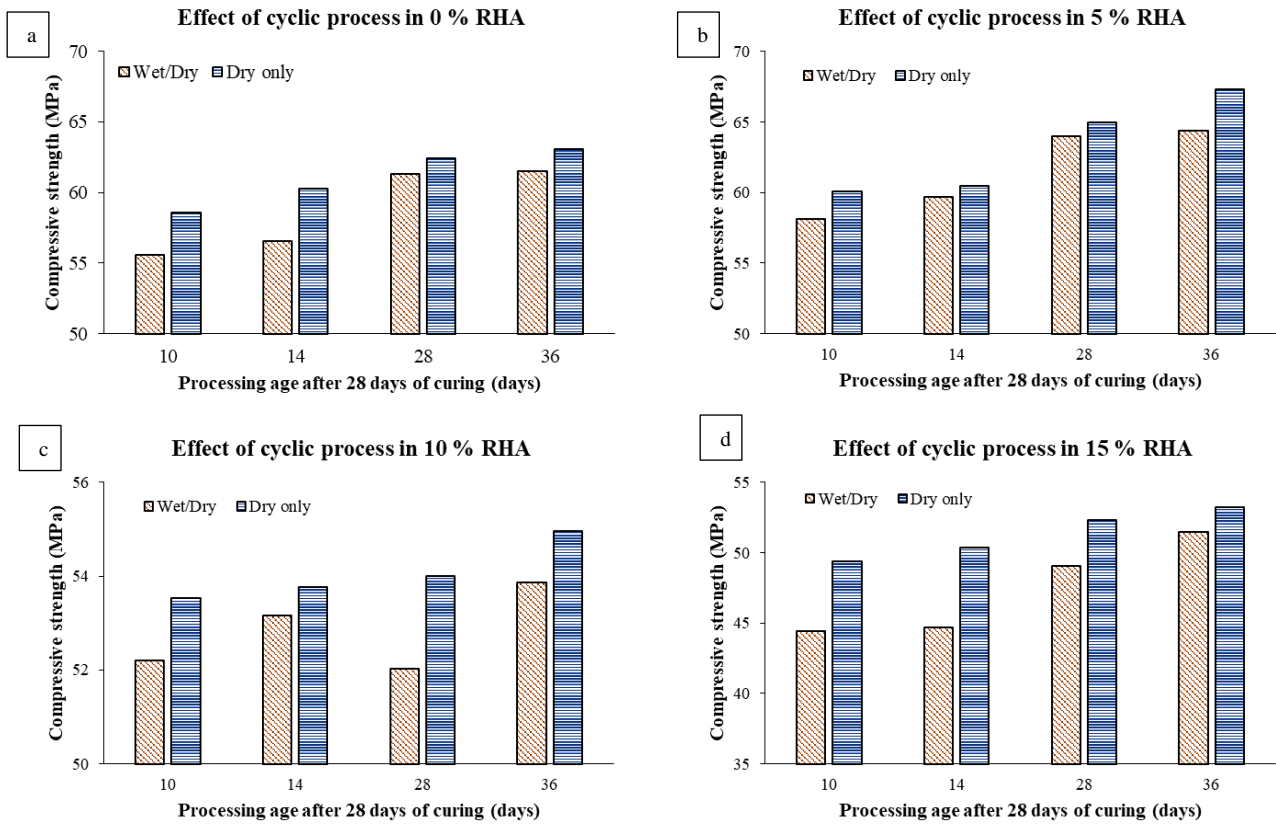


Fig. 5. Effect of Wet/Dry cyclic process in the SCC

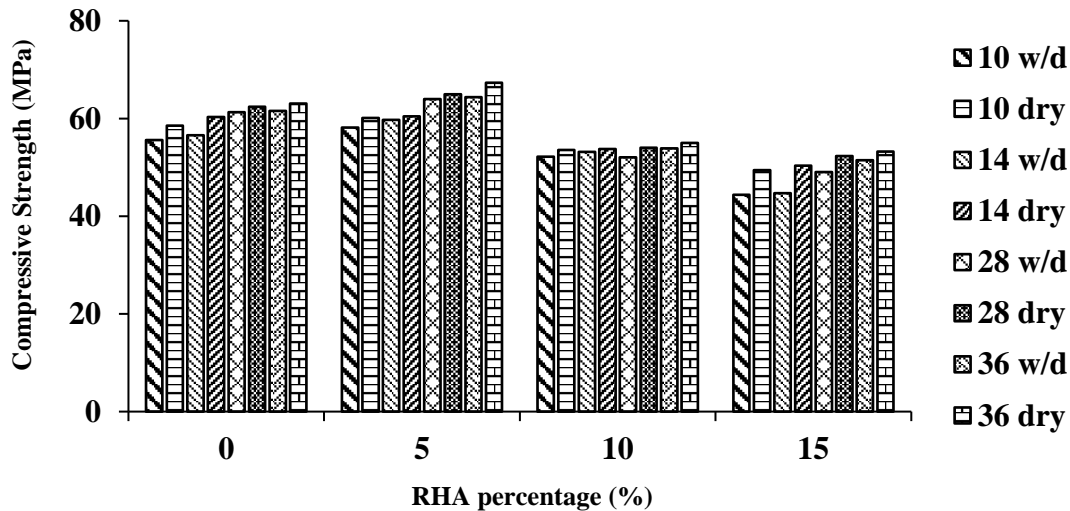


Fig. 6. Variation of compressive strength with Wet/Dry cyclic processes for different RHA percentages

V. CONCLUSION

Based on this research study, a 5% RHA replacement results in a 3.2% increase in compressive strength of self-compacting concrete. Moreover, the increase in compressive strength is attributed to the pozzolanic activity of RHA as well as its micro filling ability. RHA combines with a calcium hydroxide byproduct of cement hydration to form additional calcium silicate hydrates (C-S-H). The inclusion of C-S-H reduces the porosity of concrete, resulting in an improvement in the microstructure of the concrete and an increase in compressive strength.

It was observed that more water is needed to bring the same fresh concrete properties of SCC when RHA is added.

0.32, 0.40, 0.47 and 0.50 W/C was needed for 0, 5, 10 and 15% RHA respectively. An increase in the amount of RHA in the binder improves the surface area and volume fraction of the binder and its ability to absorb more water. The drop in compressive strength observed in the 10% and 15% specimens is most likely due to the presence of a high concentration of accessible silica in the hydrated cement, which reacts with all of the calcium hydroxide formed in the mixture.

All specimens subjected to the wet/dry cycle process demonstrated lower values than those subjected to the dry process alone due to the difference in temperature between the core and the surface of the SCC's surface. As soon as the SCC is wetted after a full day of drying, the surface attempts

to shrink but is unable to do so, resulting in the surface becoming immediately under strain. In addition, by preventing shrinkage, the core is compressed and becomes more compact.

As a result of some minute scratch or imperfection in the surface, a crack begins to form, expanding and spreading until the stress has been suitably eased. As a result, it can be stated that the wet/dry condition causes shrinkage fractures within SCC, which may result in poor durability performance. The ten percent RHA-SCC specimen has demonstrated more excellent resistance to the wet-dry cycle process than the other specimens tested. This effect is caused by the presence of dense microstructure in the SCC due to the addition of RHA to the solution.

ACKNOWLEDGMENT

The authors would like to express their gratitude to the Department of Civil Engineering at the University of Jaffna and the laboratory staff for their assistance.

REFERENCES

- [1] A. Ghadban, N. Wehbe, and T. Pauly, "Seismic performance of self-consolidating concrete bridge columns," *Engineering Structures*, vol. 160, pp. 461-472, 2018.
- [2] M. Durgun, and H. Atahan, "Strength, elastic and microstructural properties of SCCs' with colloidal nano silica addition," *Construction and Building Materials*, vol. 158, pp. 295-307, 2018.
- [3] A. Salas, S. Delvasto, R. de Gutierrez, and D. Lange, "Comparison of two processes for treating rice husk ash for use in high performance concrete," *Cement and Concrete Research*, vol. 39(9), pp.773-778, 2009. Available from: doi:10.1016/j.cemconres.2009.05.006.
- [4] R. K. Sandhu, R. Siddique, "Influence of rice husk ash (RHA) on the properties of self-compacting concrete," *Construction and Building Materials*, vol. 153, pp. 751-764, 2017. Available from: doi: 10.1016/j.conbuildmat.2017.07.165.
- [5] G. Rob, D. Noel, "Self-Compacting Concrete," *Advanced Concrete Technology*, vol. 4, pp.1-23, 2003. Available from: doi:10.1016/B978-075065686-3/50295-0.
- [6] J. Alex, J. Dhanalakshmi, and B. Ambedkar, "Experimental investigation on rice husk ash as cement replacement on concrete production," *Construction and Building Materials*, vol. 127, pp. 353-362, 2016.
- [7] D. Chopra, R. Siddique, and Kunal, "Strength, permeability and microstructure of self-compacting concrete containing rice husk ash," *Biosystems Engineering*, vol. 130, pp. 72-80, 2015.
- [8] ASTM C 1202, "Electrical Indication of Concrete's Ability to Resist Chloride Ion Penetration," vol.4.02,Annual Book of American Society for Testing Materials, Philadelphia, 2000
- [9] M. Zain, M. Islam, F. Mahmud, and M. Jamil, "Production of rice husk ash for use in concrete as a supplementary cementitious material," *Construction and Building Materials*, vol. 25(2), pp. 798-805, 2011.
- [10] M. Zhang, R. Lastra, and V. Malhotra, "Rice-husk ash paste and concrete: Some aspects of hydration and the microstructure of the interfacial zone between the aggregate and paste," *Cement and Concrete Research*, vol. 26(6), pp. 963-977, 1996.
- [11] Kosmatka, H. Steven, B. Kerkhoff, and W. C. Panarese, "Design and control of concrete mixtures," IL: Portland Cement Association, Skokie, vol. 5420, 2002.
- [12] M. Safiuddin, J. West, and K. Soudki, "Hardened properties of self-consolidating high performance concrete including rice husk ash," *Cement and Concrete Composites*, vol. 32(9), pp. 708-717, 2010.
- [13] M. Omrane, S. Kenai, E.-H. Kadri, and A. Ait-Mokhtar, "Performance and durability of self compacting concrete using recycled concrete aggregates and natural pozzolan," *Journal of Cleaner Production*, vol. 165, pp. 415-430, 2017.
- [14] V. Kannan, and K. Ganesan, "Chloride and chemical resistance of self compacting concrete containing rice husk ash and metakaolin," *Construction and Building Materials*, vol. 51, pp. 225-234, 2014.
- [15] BS EN 882 (1992), Specification for aggregates from natural sources for concrete, British standards institution.
- [16] R. Madandoust, and R. Ghavidel, "Mechanical properties of concrete containing waste glass powder and rice husk ash," *Biosystems Engineering*, vol. 116(2), pp.113-119, 2013.
- [17] ASTM C494 / C494M-19, Standard Specification for Chemical Admixtures for Concrete, ASTM International, West Conshohocken, PA, 2019, www.astm.org.
- [18] BS EN 934 (2001), Admixtures for concrete, mortar and grout, Concrete admixtures —Definitions, requirements, conformity, marking and labelling, British standards institution, Part 2.
- [19] EFNARC, Specifications and Guidelines for Self-Compacting Concrete, English ed., European Federation for Specialist Construction Chemicals & Concrete Systems, May 2005

A Study on Failure Behavior of Concrete Elements

Tharsika Premakanthan
Faculty of Engineering,
University of Peradeniya
Kandy, Sri Lanka
tharsikaprem@gmail.com

Abirami Thuraisingam
Faculty of Engineering,
University of Peradeniya
Kandy, Sri Lanka
thuraisingamabirami@gmail.com

Chaminda S. Bandara
Faculty of Engineering
University of Peradeniya
Kandy, Sri Lanka
csbandara@eng.pdn.ac.lk

Abstract—Concrete is the most important constituent in many civil engineering structures. It is a known fact that concrete is easily susceptible to failure due to cyclic loading such as earthquakes and wind wave effects. Therefore, cyclic performance of concrete has attracted great attention. The main focus of this study is to model simple plain concrete elements numerically to obtain cyclic failure behavior. In this study, a literature review was conducted to look into the experimental, analytical and numerical techniques available to find the cyclic performance of medium grade concrete (Grade 37.5). 3D numerical models of plain concrete cylinder and cuboid were developed using ABAQUS software based on the findings of past experimental and analytical studies. To represent the complex nonlinear behavior, concrete damage plasticity model was adopted. Then, the models were first validated for linear, nonlinear behavior under monotonic loading. Hourglass behavior of stress distribution is observed in both models that causes shear failure. In the next step, further validation of the model was done for the cyclic behavior using past experimental results. Then, comparison study between cylindrical model & cuboid model under monotonic loading and comparison study between monotonic loading and cyclic loading were done. It is observed that there is a good agreement between monotonic stress strain curve and backbone curve of cyclic stress strain curve. These models will be used to further investigate the low cyclic loading behavior, fatigue performance, failure patterns and modes.

Keywords—Plain concrete, Concrete damage plasticity, Numerical model, Low cycle fatigue, Failure behavior

I. INTRODUCTION

Concrete is one of the most common materials in many civil engineering structures and its behavior is nonlinear. Cyclic performance of concrete is very important as the structures are subjected to cyclic loadings such as seismic loading, wind load and water wave effects. Cyclic failure is the failure of materials under the action of repeated stresses and strains. This cyclic loads cause the concrete structures to fail before reaching its maximum strength. Therefore, fatigue behaviors of the construction materials have fascinated great considerations in recent decades by most of the researchers. Furthermore, concrete exhibit a nonlinear response under low cycle fatigue with high stress level. On the other hand, it shows a linear response under high cycle fatigue with low stress level. However, this study was mainly focused on low frequency cyclic loading with high stress level for normal strength concrete ranging from grade 20 - 40.

Experimental programs in laboratories give real results for studying the behavior of plain concrete under both monotonic and cyclic loading. But they are limited to particular dimensions, sizes, shapes, loading patterns and boundary conditions. One of the first experimental research to identify the behavior of plain concrete under cyclic loading was conducted by Sinha [1]. Also, there are some available experimental, analytical and numerical studies in past years [2, 3, 4, and 5]. Most refer only to the cyclic compressive behavior of concrete and only a few consider about the cyclic tensile behavior.

Even though concrete is commonly used, when it comes to numerical simulation, precise description of its behavior is challenging. The ability of software is important for the accurate material modelling of concrete. Some of such software are ABAQUS, ANSYS, LS-DYNA and ADINA. In this study ABAQUS finite element software was employed to model simple plain concrete elements such as concrete cylinder and concrete cube. In these models, two main failure mechanisms were assumed; compressive crushing and tensile cracking [6]. The ABAQUS software has the ability of analyzing concrete elements both in the linear and nonlinear regions due to its powerful engineering simulation. Geometry, material properties, boundary conditions and the loading are to be modeled correctly. Combining the plasticity and damage properties are the important technique to predict the stress strain behavior of concrete. Here, isotropic behavior of the concrete was used to describe the plasticity of concrete even though many concrete failures are not isotropic [7]. This study used concrete damage plasticity model in ABAQUS program which is suitable for simulating the concrete material properties.

As mentioned earlier due to the limitations in experimental study, there is a lack of experimental data to use as ABAQUS input parameters. Several numerical models have been developed until today by researchers to overcome this difficulty with a main common target of simulating the concrete behavior as same as it is possible under various load conditions. One of such models was created by Labibzadeh in 2017. However, it is difficult to prepare an accurate model which would adequately capture the response of real elements. Hence, it is required to validate the numerical model using available experimental data and analytical equations with minimum error percentage. Analytical equations are available to predict the stress – strain behavior and damage behavior of plain concrete [8].

Generally, most failure modes in cylinders are shear crack, concrete spalling and crushing etc. Concrete specimen subjected to monotonic loading lead to macroscopic persistent cracks or sample splitting [4]. A German engineer Hubert Rüschi conducted studies about slenderness and determined that the value of 2 was the most appropriate relationship between the height and diameter of cylindrical specimen [9]. Thereby, in this study cylindrical specimen with the height of 300mm and diameter of 150mm and cuboid specimen with 200mm length, 200mm height and 50mm width were selected.

A. Research Significance

When considering previous work related to this study, even though many experimental results are available for failure behavior of plain concrete, there is a lack of numerical simulations for failure behavior. The scope of this research work is to model simple plain concrete elements (cylindrical and cuboid models) numerically to observe failure behavior of normal concrete under monotonic and cyclic loadings. In future, structural concrete elements can be modelled to assess the failure behavior under different types of loadings.

II. LITERATURE REVIEW

A. Experimental Study

Over the past few decades' lots of experiments have been carried out to investigate the behavior of concrete using cylindrical and prismatic specimens. One of the earlier experimental investigations about the performance of plain concrete under cyclic loading was conducted by Sinha [1]. They did an experiment which involved a series of 48 tests on concrete cylinders with compressive strengths ranging from 20 to 28 MPa and subjected to cyclic axial compressive loading in order to decide the main factors leading the cyclic response of concrete. To examine the effects of load history, cyclic loads were applied in two different methods, containing complete loading and partial unloading [10]. Unloading and reloading response of concrete depends on the previous load history [3].

To gain the behavior of plain concrete under various cyclic compressive loading histories, Karsan and Jirsa [11] did an experimental study using 46 short rectangular concrete columns where the cylinder compressive strengths of concrete ranging from 24-35 MPa. Here, four different types of loading were applied on the testing specimens. They are monotonic increasing loading to failure, cycles to envelope curve, cycles to envelope curve adding a specified strain increment during each cycle and cycles between maximum and minimum stress levels. They showed that unloading and reloading curves are nonspecific but depend on the preceding load history [11].

Bahn and Hsu [3] conducted an experimental study to investigate the behavior of concrete under cyclic compressive uniaxial loading [3]. Tests of 76 mm by 152 mm concrete cylinders were conducted under four different loading regimes: monotonic loading; cycles to envelope curve; cycles to common point; and cycles with random loading. Cycles with random loading was involved with the combination of all possible loading patterns. There are full unloading and full reloading, full unloading and partial reloading, partial unloading and full reloading, and partial unloading and partial reloading. Fig. 1 suggested that envelope curve for a concrete subjected to cyclic axial compression loads may be considered to coincide with stress-strain curve under monotonic load [3].

A generally accepted behavior for plain concrete under cyclic loading is that of an envelope curve also called backbone curve, which provides a bound between the upper limit and lower limit for the stress-strain curve. It can be reached under different loading paths. The existence of an envelope curve for a concrete can be studied by comparing the experiment results of cycles to envelope curve with the corresponding results of monotonic loading [3].



Fig. 1. Cyclic envelope curve and monotonic stress-strain curve of Bahn and Hsu (1998)

Cyclic performance of low-strength plain concrete (LSPC) between 5MPa and 10MPa was investigated by Ozcelik R (2015). In their study, they showed cyclic behavior of LSPC significantly depends on aggregate used during preparation on concrete. In 2016, Bezerra et al. conducted experimental test on standard cylindrical specimen to observe the failure behavior of concrete. They found that most failure modes in cylinders under monotonic loadings were shear mode of failure as per Fig. 2 and column-like failure as shown in Fig. 3. In addition, they showed the hourglass shape forces the concrete to break at a certain angle ($\approx 46^\circ$) at which the shear occurs [9].

Song et al.[4] presented the failure patterns of concrete under monotonic and cyclic compressive loading. They showed that the size and the type of cracks is directly related to the loading methods. It was found that under monotonic loading, almost all grains on the failure surface are highly cracked and failure pattern is brittle. Under cyclic loading, most of the grains are cracked-free and failure develops mainly along grain boundaries [4]. Experimental investigation on 150mm x 150mm x 150mm cube concrete specimen indicated that the extent of cracking throughout the specimen is denser in cube than in the cylinders [12]. Hour glass shape of failure was observed in cube specimen as shown in Fig. 4. [12].



Fig. 2. Shear plane mode of failure in plain concrete (Bezerra et al. 2016)



Fig. 3. Column-like mode of failure in plain concrete (Bezerra et al. 2016)



Fig. 4. Hour glass crack pattern of cube (Tripura, D., and Singh, K.D, 2017)

Soleimani, et al. [21] examined fatigue due to low-cycle tensile loading in plain concrete under different conditions using the pressure-tension apparatus. A total of 22 wet or dry standard concrete cylinders were tested. They showed that the concrete samples subjected to low-cycle tensile loading will fail after a relatively low number of cycles of loading and at a lower magnitude of stress compared to the maximum value applied during cyclic loading. The samples with greater water content fail at a greater tensile resistance as compared to dry specimens. The failure mode in pressure tension testing varies from a single crack to a volumetric failure at a lesser applied tensile stress for dry samples [21].

B. Analytical Study

1) Stress strain relationship for monotonic compression

Stress-strain relationships for uniaxial compressive behavior of concrete subjected to monotonic loading were developed by many researchers in the past years. Carreira and Chu [13] proposed general form of the serpentine curve which represents the uniaxial strain-stress relationship for unconfined concrete is given in (1) and (2) for $\beta \geq 1.0$ and $\varepsilon \leq \varepsilon_u$.

$$\frac{f_c}{f'_c} = \frac{\beta \left(\frac{\varepsilon}{\varepsilon'_c}\right)}{\beta - 1 + \left(\frac{\varepsilon}{\varepsilon'_c}\right)^\beta} \quad (1)$$

$$\beta = \frac{1}{1 - \frac{f'_c}{\varepsilon' E_{it}}} \quad (2)$$

where, f'_c is the maximum stress which denotes the concrete strength and it can be determined according to ASTM C 39, Standard Test Method for Compressive Strength of Cylindrical Specimens, ε'_c is the corresponding strain for the maximum stress f'_c , E_{it} is the slope at the origin of stress strain curve or initial tangent modulus, usually β is one of the material parameters which depends on the shape of the stress-strain curve. When $\beta \rightarrow \infty$, (1) and (2) had the limits of perfectly elastic material and when $\beta = 1.0$, it showed the perfectly plastic material limits. Thus, (1) and (2) deliver a nonlinear transition for those two extreme cases. In addition, (3) can be used for the estimation of ε'_c .

$$\varepsilon'_c = (4.88 f'_c + 168) \times 10^{-5} \quad (3)$$

where, f'_c is in ksi. Generally, ε'_c is considered as 0.002 for the design purposes [8].

2) Stress strain relationship for monotonic tension

Generally, the tensile strength of concrete is evaluated as ten to fifteen percent of compressive strength. If experimental data is not available, the tensile strength of concrete can be calculated as in (4).

$$f_{ctsp} = 1.38 (f'_c)^{0.69} \text{ psi} \quad (4)$$

Here, f_c is uniaxial compressive strength of concrete which can be easily obtained from laboratory experiments. Tensile stress-strain relationship of concrete was assumed to be behave linearly up to the uniaxial tensile strength and then determined using the exponential function as in (5) [22].

$$\sigma = f_t (\varepsilon_t / \varepsilon)^{(0.7 + 1000\varepsilon)} \quad (5)$$

3) Stress strain relationship for cyclic compression

Simple empirical formula to simulate general stress strain behavior of normal concrete under cyclic loading were derived by Bahn and Hsu in 1988 [3]. Relation between unloading strain and plastic strain is given in (6).

$$S_{pu} = C_p (S_{eu})^{n_p} \quad (6)$$

where, S_{pu} is the unloading plastic strain ratio, S_{eu} is the unloading strain ratio on the backbone curve, C_p is a coefficient of plastic strain which is suggested as 0.30 and n_p is an optimum order of proposed equation type in the concentrated test data. Relation between reloading strain and unloading strain is given in (7).

$$S_{er} = S_{eu} + \delta S_{er} \quad (7)$$

where, S_{er} is reloading strain on the backbone curve, δS_{er} is the difference between unloading and reloading strain on the backbone curve for full unloading and reloading cycles. Unloading curve is given in (8).

$$U_{unlo} = c_u U_{eu} \left(\frac{S - S_p}{S_{eu} - S_p} \right)^{n_u} \quad (8)$$

where, U_{unlo} is a nonlinear function of unloading curve, U_{eu} is an envelope unloading stress ratio at the corresponding strain ratio on the envelope curve, S is located at any location of assumed straight line for unloading, S_p is the plastic strain ratio, c_u is the coefficient of unloading curve and n_u is expressed as function of plastic strain.

Reloading curve is given in (9).

$$U_{relo} = c_r U_{er} \left(\frac{S - S_p}{S_{er} - S_p} \right) \quad (9)$$

where, U_{relo} is a linear function of reloading curve, U_{er} is an envelope reloading stress ratio at the corresponding reloading strain ratio on the envelope curve, S_{er} is a reloading strain on the envelope curve and c_r is the coefficient of reloading curve.

For the type of partial unloading and partial reloading, (9) can be written as in (10).

$$U_{relo} = U_{ppu} + c_r (U_{erpu} - U_{ppu}) \left(\frac{S - S_{ppu}}{S_{erpu} - S_{ppu}} \right)^{n_r} \quad (10)$$

where, U_{erpu} is the envelope reloading stress ratio at the corresponding reloading strain ratio. S_{erpu} and U_{ppu} is the partial unloading stress ratio at the corresponding strain ratio. U_{ppu} is equal to zero when full unloading previously occurs [3]. To represent the concrete response analytically, a polynomial relationship was adopted for the envelop curve (Palermo, 2002).

A simple uniaxial stress strain model based on the geometric properties of the loading history curves in the uniaxial stress-strain plane was proposed by Yankelevsky and Reinhardt [5]. They modeled the entire unloading-reloading cycle by a set of pieced linear curves determined by a set of six geometrical loci in the stress-strain plane.

C. Numerical Study

Numerical simulations are often used by the researchers in present days to investigate the behavior of concrete. Because, the development of computer based methods for designing and simulation have also increased the urge for the exact solutions of the problems. The achievements of the

researchers are well cited and presented in various literatures and technical papers but still there are much more things to be considered and researched [7]. ABAQUS numerical model for standard plain concrete cylinder and cube were modelled by Labibzadeh et al [8]. Their literature showed a new method to find concrete damage plasticity model input parameter identification for ABAQUS software with minimum error percentage.

The elastic behavior of concrete was modelled using simple linear elasticity with Young's modulus and Poisson's ratio. However, for plastic states where deformations become irreversible, different type of models are available to represent the failure envelope [14]. There are four main modelling techniques available in ABAQUS Finite Element Modeling (FEM) package. They are; Smeared crack model, Concrete damage plasticity model, Brittle crack model and Mohr-Coulomb failure criterion model.

In smeared crack concrete model, the commencement of cracking process at any location occurs when the concrete stresses achieve one of the failure surfaces such as biaxial tension region or combined tension and compression region. Cracking is taken as the most common failure feature of the concrete and the representation of cracking and post-cracking anisotropic behavior governs the modeling. This model can be used for plain concrete structures, although it is planned primarily for the analysis of reinforced concrete structures. It is designed for the practices in which the concrete is exposed to monotonic straining at low confining pressures [7]. Brittle crack model has the capability of modeling concrete in all type of structures. But, it only considers the elastic behavior.

Mohr-Coulomb failure criterion model is a pressure dependent model, highly used for brittle material like concrete. It is based on the fact that the material becomes stronger as the pressure increases [14].

Concrete Damage Plasticity (CDP) model in ABAQUS program is suitable for concrete, quasi-brittle materials, which can simulate the tensile cracking and compressive crushing of concrete materials, considering the isotropic elastic damage and plastic behavior of materials. CDP model is assumed that the damage of concrete material is mainly caused by compressive crushing and tensile cracking. When the ABAQUS CDP model is used for analysis, the compression, tensile stress and the corresponding non-elastic strain and damage factor of the material are required [15].

There are mainly two types of the stress strain relationship assigned for the finite element model. They are compressive stress-strain relationship and tension stiffening relationship. The compressive stress-strain relationship of the unconfined concrete is shown in Fig. 5 [16].

Some equations used for uniaxial compressive behavior in concrete damage plasticity model were provided by Hafezolgborani, et al [6] as follows.

Compressive strain ε_c is given in (11)

$$\varepsilon_c = \varepsilon_c^{pl,h} + \varepsilon_c^{el} \quad (11)$$

where, $\varepsilon_c^{pl,h}$ is compressive plastic hardening strain and ε_c^{el} is elastic compression strain.

Stress-strain relation under uniaxial compression is given in (12).

$$\sigma_c = (1 - d_c) \cdot E_0 \cdot (\varepsilon_c - \varepsilon_c^{pl}) \quad (12)$$

where, ε_c^{pl} is compressive plastic strain, σ_c is uniaxial compressive stress, E_0 is initial elastic stiffness of the material (undamaged) and d_c is compressive damage.

The size of the yield or failure surface is determined by effective cohesion stresses. Effective compressive cohesion stresses $\bar{\sigma}_c$ can be defined as in (13) and (14).

$$\bar{\sigma}_c = \frac{\sigma_c}{1 - d_c} \quad (13)$$

$$\varepsilon_c^{\sim pl} = \varepsilon_c^{\sim in} - \frac{d_c}{1 - d_c} \frac{\sigma_c}{E_0} \quad (14)$$

Some equations used for uniaxial tensile behavior in concrete damage plasticity model were provided by Hafezolgborani, et al [17]. Fig. 6 shows the tension stiffening relationship of the concrete [16].

When considering loading pattern, mainly there are two types of loadings. They are static loading and dynamic loading. In literature, for static loading, three-point bending test of a pre-notched beam was considered for testing the precision of the obtained CDP model in simulating the behavior of the unreinforced concrete structures [8]. In dynamic loading impact vibration was given for the analysis [14].

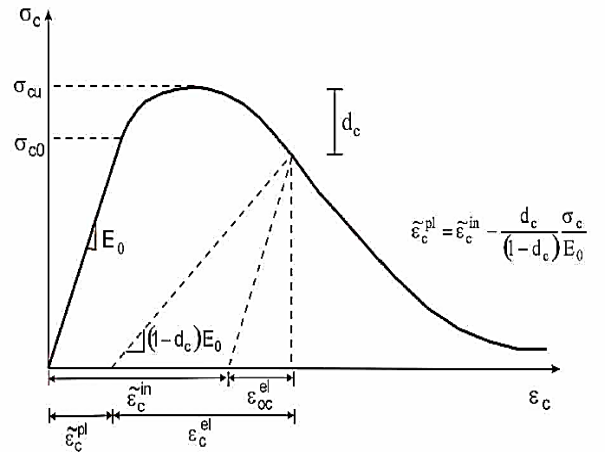


Fig. 5. Compressive stress-strain relationship of concrete (Abaqus User Manual, 2008)

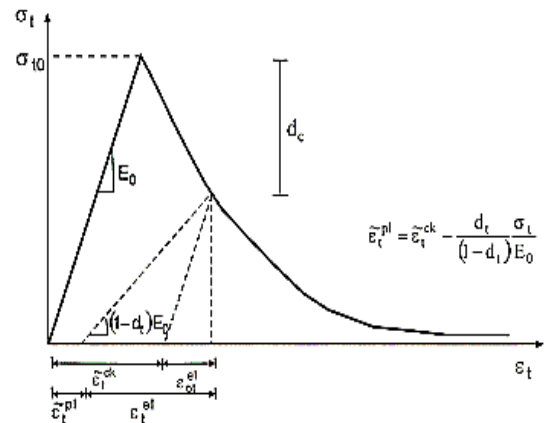


Fig. 6. Tension stiffening relationship of concrete (Abaqus User Manual, 2008)

III. METHODOLOGY

The methodology for this research study can be described into several steps. Initially, basic study on analytical, experimental and numerical work was done. Secondly, identifying experimental / analytical / numerical models and important parameters for models (Material properties, Element type) was carried out. After that, FEM models such as cylinder and cuboid model for monotonic and cyclic loading were modelled using ABAQUS explicit/dynamic finite element software. Thereafter, Validations of FEM for monotonic and cyclic loading were done. Finally, the failure behavior was observed in numerical model and results were compared with existing experimental data to reach conclusions.

A. Finite Element Modelling

A plain concrete cylindrical model of size 150mm x 300mm and a cuboid model of size of 200mm x 200mm x 50mm were modelled as 3D deformable solid using CDP model. For modelling, both the linear and nonlinear regions were considered. Material properties of concrete and some input parameters for ABAQUS software are given in Table. 1. Other input parameters such as yield strength and inelastic strain for compressive and tensile behavior, compression and tension damage were same for both models [8].

Since the test simulations in the ABAQUS were made by the explicit module of the software, the viscosity parameter was automatically set to zero by the package [8]. However, very small non-zero viscosity parameter can be used to improve the convergence of the model [14]. Two discrete rigid plates were assembled at the top and bottom of the models to distribute applied loading uniformly over the surface. The interaction between platens and specimen were defined using tie constraint. Cylinder and cuboid models were meshed using C3D8R elements. Plates were meshed using R3D4 elements. Boundary conditions for bottom ends of models were assigned as pinned and for top end only axial translational movements were allowed. Fig. 7 shows the cylindrical model with assigned boundary conditions. The appropriate mesh size was determined after a mesh convergence test. This test optimizes the number of elements and reduces the computational time. Here the maximum stresses at the top and middle part of the cylinders were plotted against number of elements as shown in Fig. 8. In this study, approximately 9000 elements with 9mm mesh size was considered for cylindrical model. However, for cuboid model mesh size of 10mm was directly taken from the literature [18]. Cuboid model with proper meshing is shown in Fig. 9.

TABLE I. TABULATION OF MATERIAL PROPERTIES

Concrete Properties	Values
Compressive Strength (f'_{co})	37.5 MPa
Corresponding Strain to f'_{co} (ϵ_{co})	0.002
Young's modulus (E)	33000 MPa
Poisson's ratio (ν)	0.18
Mass Density	1E-5
Dilation angle	35°
f_{bo}/f_{co} ratio	1.12
K factor	0.67
Eccentricity	0.1
Viscosity Parameter	0.0001

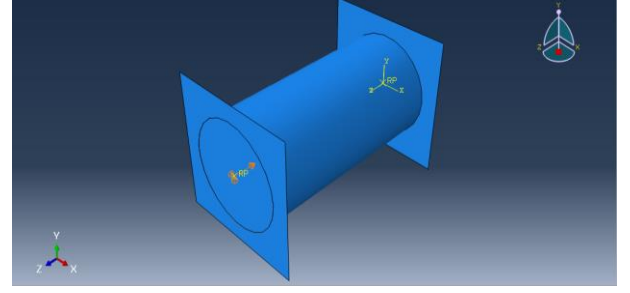


Fig. 7. Plain concrete cylinder model with rigid plates

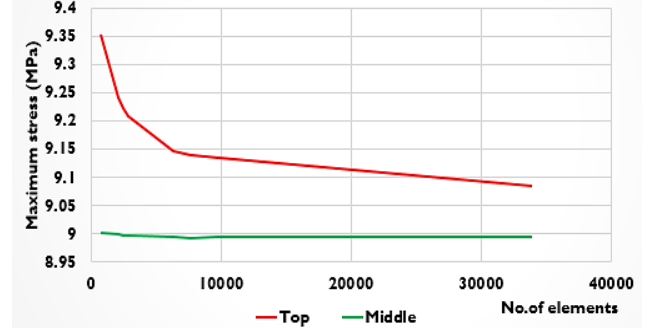


Fig. 8. Convergence test

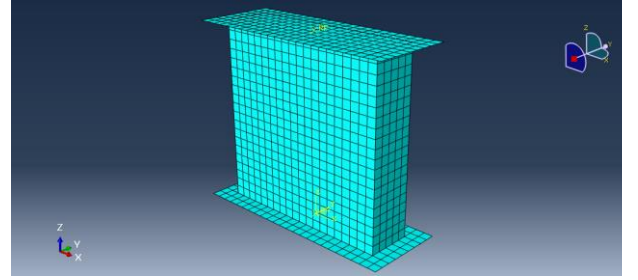


Fig. 9. Plain concrete cuboid model with appropriate meshing

B. Uniaxial monotonic loading

Uniaxial monotonic compressive loading was applied on both cylindrical and cuboid models. After creating the model, required material properties were inputted into the model. Then, boundary condition was assigned using displacement control method. A distance of 3mm was applied as ultimate axial compressive displacement using smooth step amplitude at a reference point defined in the top rigid plate. Step time was taken as one second. Reaction force and displacement were taken as output from the model at reference points in top and bottom rigid plates. Stress was calculated by dividing reaction force at the bottom reference point by the surface area and the strain was calculated by dividing displacement at the top reference point by the initial length of the model.

C. Uniaxial Cyclic compressive loading

Uniaxial cyclic compressive loading was applied on the validated monotonic loading cylindrical model. Input parameters for this model were same as the parameters used for monotonic compressive behavior model. Compressive and tensile damages were inputted into CDP model only for this test. After initial step, three steps were defined in the step module. For each step, proper boundary conditions were assigned using displacement control method. Sine amplitude was assigned and the step time was taken as 6.3s. The finite element mesh specifications of this model were same as the models of monotonic loading. Reaction force and

displacement were taken as output from the model at the reference points in the top and bottom rigid plates. Stress and strain were calculated in the same way as for monotonic loading.

IV. RESULTS AND DISCUSSION

A. Validation of the monotonic stress-strain curve of cylinder and cuboid models

1) Uniaxial monotonic compressive loading

The stress-strain variation obtained from the cylinder model under uniaxial monotonic compressive loading was compared with the empirical stress-strain curve [8]. A precise agreement between both stress-strain behavior was not observed as shown in Fig. 10.

This is understandable because the empirical models contain number of factors that are not general for all the concrete mixes.

The stress-strain variation obtained from the cuboid model was compared with the existing experimental stress-strain variations under uniaxial monotonic compressive loading [13, 18]. A good agreement between experimental and numerical stress-strain behavior was observed as shown in Fig 11. The error percentage between the numerical and experimental results was calculated by using Mean Absolute Percentage Error method (MAPE). It was less than 5%.

2) Uniaxial monotonic tensile loading

The stress-strain variation obtained from the cylinder model was compared with the existing experimental stress-strain variation under uniaxial monotonic tensile loading [8]. A good correlation between the experimental and numerical stress-strain behavior was not observed as shown in Fig 12.

For monotonic direct tensile loading cylinder and cuboid models, displacement was applied in the opposite direction of the compressive loading model. This is the only difference between the monotonic compressive and tensile loading. Direct tensile test of concrete does not give accurate results in the experiment because of the brittleness of concrete. Hence, a good agreement between experimental and numerical results could not be expected. However, splitting tensile test on the model (only for cylinder model) may give good validation with experimental data.

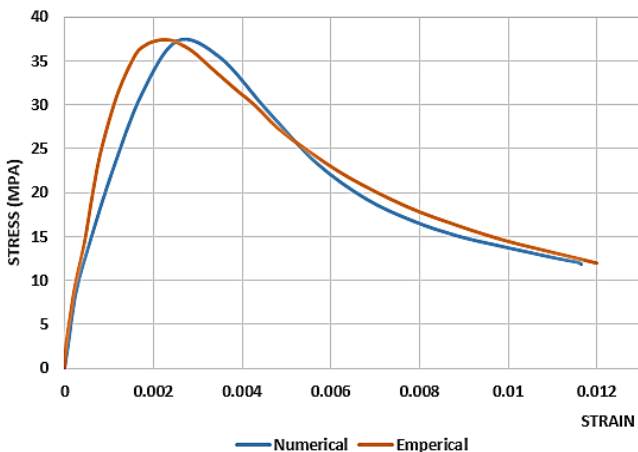


Fig. 10. Stress vs strain – Comparison of empirical and numerical data under monotonic compressive loading in cylinder

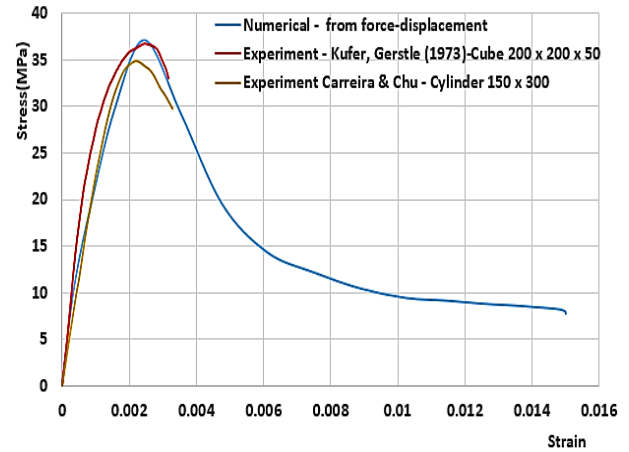


Fig. 11. Stress vs strain – Comparison of experimental and numerical data under monotonic compressive loading in cuboid

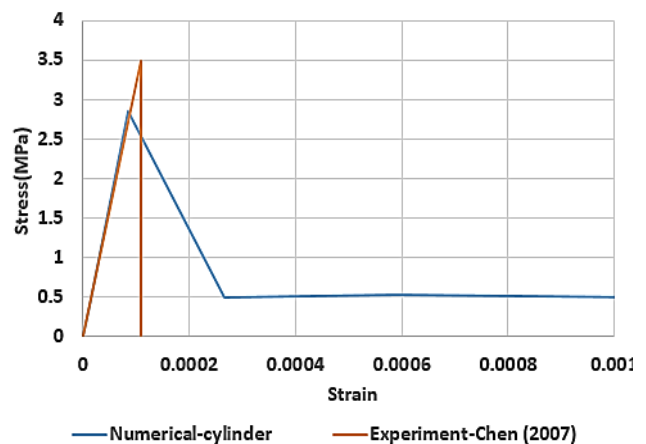


Fig. 12. Stress vs strain – Comparison of experimental and numerical data under monotonic tensile loading in cylinder

B. Comparison of the failure behavior of cylinder and cuboid under uniaxial monotonic loading

One of the main objectives in this study is to study the failure behavior of cylinder and cuboid under uniaxial loading. Common failure modes are crushing in compression and cracking in tension as mentioned above. Results are presented in this section.

1) Uniaxial monotonic compressive loading

The stress variation observed in cylinder model under uniaxial monotonic compressive loading was hour glass stress variation as shown in Fig. 13 and the observed failure pattern was shear failure. The stress variation observed in cuboid under uniaxial monotonic compressive loading was also hour glass stress variation as shown in Fig. 14. Both cylinder and cuboid were shown similarity in stress variation. Here it is important to note that, hourglass effect may occur in the finite element analysis when the C3D8R elements are used in the models [19].

The failure mode of cuboid was associated with the shearing as in a cube as shown in Fig. 15. This is very similar to the experimental failure pattern where hour glass crack pattern was observed [9].

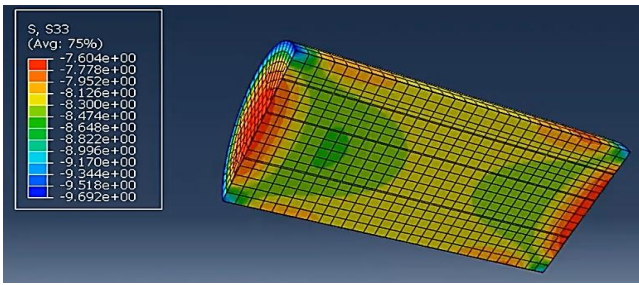


Fig. 13. Hour glass shape stress variation in cylinder model

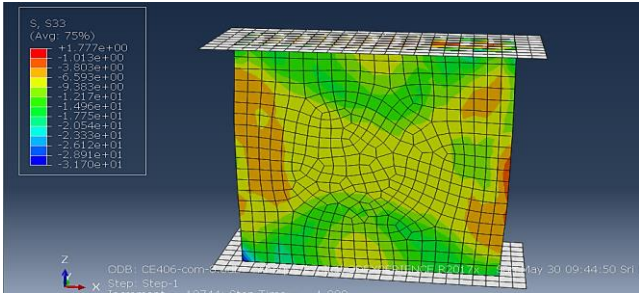


Fig. 14. Hour glass shape stress variation in cuboid model

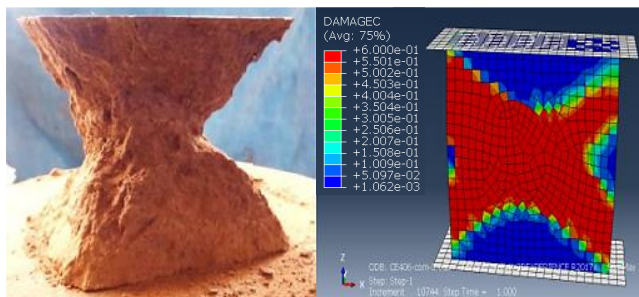


Fig. 15. Comparison of experimental cube failure and numerical cuboid failure

The failure behavior of concrete cylinder model also encountered with shear failure as shown in Fig. 16. This is very similar to the experimental shear failure behavior observed by L. Polus and M. Szumigala in 2019 [19]. Their concrete cylinder sample subjected to uniaxial monotonic compression is shown in Fig. 17.

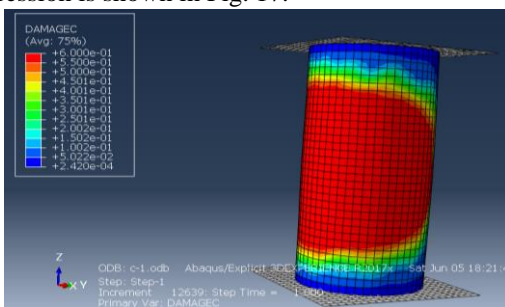


Fig. 16. Damage behavior in cylinder model due to shear failure



Fig. 17. Concrete cylinder specimen subjected to monotonic compression

2) Uniaxial monotonic tensile loading

The concrete elements such as cylinder and cuboid were failed due to cracking orthogonal to the maximum principle tensile stress under uniaxial monotonic tensile loading. Both cylinder and cuboid had similarity in failure pattern. Fig. 18 compares numerical failure of the cylinder with existing experimental failure pattern [20]. A good correlation between numerical and experimental failure patterns was observed.

C. Comparison of monotonic stress-strain curve and cyclic envelope curve under uniaxial compressive loading in cylinder

Numerical cyclic compressive stress-strain variation was compared with the existing experimental cyclic compressive stress-strain variation [3]. A fairly good correlation was observed between them. Envelope curve provides a bound between the upper limit and the lower limit for the stress-strain curve. The numerical uniaxial cyclic compressive envelope curve (backbone curve) coincides with the numerical monotonic stress-strain curve as shown in Fig. 19. Monotonic stress-strain curve can be taken as cyclic envelope curve. Failure behavior of numerical cylinder model under cyclic compressive loading is shown in Fig. 20.

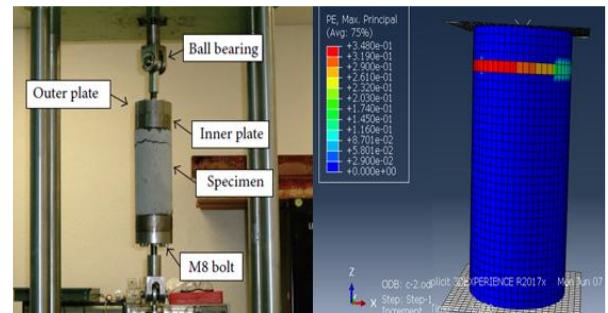


Fig. 18. Comparison of experimental and numerical direct tension test failure behavior in cylinder

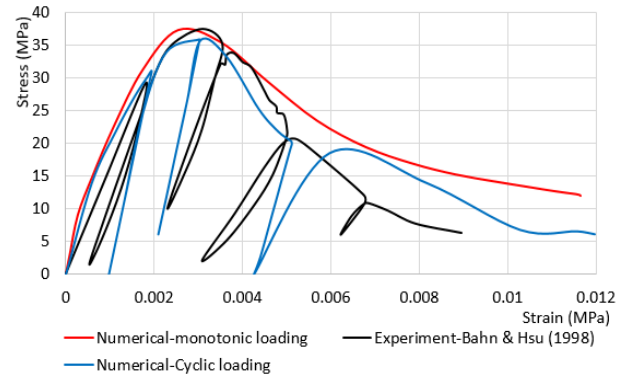


Fig. 19. Comparison of experimental cyclic stress-strain graph and numerical monotonic and cyclic stress-strain graphs

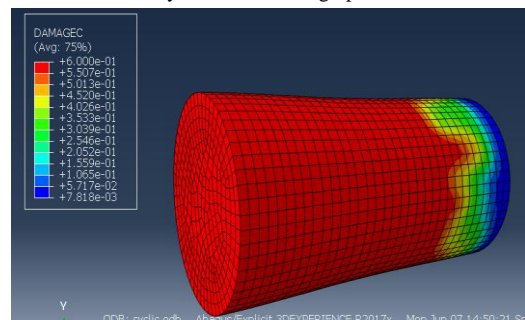


Fig. 20. Failure behavior of cylinder model under low cyclic compressive loading

V. CONCLUSION

In this paper, ABAQUS Concrete Damage Plasticity model was used to investigate the uniaxial tensile and uniaxial compressive failure behavior of concrete. The failure mechanisms obtained from the Finite Element Analysis were compared with the existing experimental results of concrete cylinder and cuboid. The present study allows the following conclusions:

1) *In concrete elements, hour glass stress variation causes shear mode failure under uniaxial monotonic compressive loading. This behavior was observed in the cylinder, cube and cuboid model studies. Experimental failure patterns had a good agreement with the numerical failure patterns under uniaxial loading.*

2) *Experimental stress vs strain curve had a reasonable agreement with the numerical stress vs strain curve under uniaxial loading. This was observed in the cylinder model and the cuboid model.*

3) *Monotonic stress-strain curve can be used as cyclic envelope curve under uniaxial compressive loading. This was clearly observed for the cylinder model.*

These results can be used for further studies of cyclic failure behavior of concrete. It can be used to model a real world problem which is subjected to cyclic loading such as circular bridge piers with reinforcement.

ACKNOWLEDGMENT

Valuable comments given by Dr. J. A. S. C. Jayasinghe and Dr. Dammika Abeykoon, Senior Lecturers in the Department of civil engineering, Faculty of Engineering, University of Peradeniya are gratefully acknowledged.

REFERENCES

- [1] B. P. Sinha, K. H. Gerstle, and L. G. Tulin, "Stress-strain relations for concrete under cyclic loading," *ACI Structural Journal*, vol. 61, no. 2, pp. 195-211, 1964.
- [2] J. F. Sima, P. Roca, and C. Molins, "Cyclic constitutive model for concrete," *Journal of Engineering Structures*, vol. 30, no. 3, pp. 695-706, 2007.
- [3] B. Y. Bahn, and T. T. C. Hsu, "Stress-strain behavior of concrete under cyclic loading," *ACI Material Journal*, vol. 95, no. 2, pp. 178-193, 1998.
- [4] Z. Song, T. Frhwirt, and H. Konietzky, "Inhomogeneous mechanical behaviour of concrete subjected to monotonic and cyclic loading," *International Journal of Fatigue*, vol. 132, 2020.
- [5] D. Z. Yankelevsky, and H. W. Reinhardt, "Model for cyclic compressive behaviour of concrete," *Journal of Structural Engineering*, vol. 113, no. 2, pp. 228-240, 1987.
- [6] B. L. Wahalathanthi, D. P. Thambiratnam, T. H. T. Chan, and S. Pawzia, "A Material model for flexural crack simulation in Reinforced concrete elements using ABAQUS," *Proceedings of the First International conference on Engineering*, pp. 260-264, 2011.
- [7] S. V. Chaudhari, and M. A. Chakrabarti, "Modeling of concrete for nonlinear analysis Using Finite Element Code ABAQUS," *International Journal of Computer Applications*, vol. 44, no. 7, pp. 14-18, 2012.
- [8] M. Labibzadeh, M. Zakeri, and A. A. Shoaib, "A new method for CDP input parameter identification of the ABAQUS software guaranteeing uniqueness and precision," *International Journal of Structural Integrity*, vol. 8, no. 2, pp. 264-284, 2017.
- [9] U. T. Bezerra, S. M. S. Alves, N. P. Barbosa, and S. M. Torres, "Hourglass-shaped specimen: compressive strength of concrete and mortar," *IBRACON Structures and Materials Journal*, vol. 9, no. 4, pp. 510-524, 2016.
- [10] F. Aslani, and R. Jowkarmeimandi, "Stress-strain model for concrete under cyclic loading," *Magazine of Concrete Research*, vol. 64, no. 8, pp. 673-685, 2012.
- [11] I. D. Karsan, and J. O. Jirsa, "Behavior of concrete under compressive loadings," *ASCE Journal of Structural Engineering*, vol. 95, no. 12, pp. 2543-2563, 1969.
- [12] J. J. Kim, and M. R. Taha, "Experimental and Numerical Evaluation of Direct Tension Test for Cylindrical Concrete Specimens," *Advances in Civil Engineering*, vol. 2014, pp. 1-8, 2014.
- [13] D. J. Carreira, and K. H. Chu, "Stress-strain relationship for plain concrete in compression," *ACI Journal*, vol. 82, no. 6, pp. 797-804, 1985.
- [14] M. Jenothan, V. Yuvahini, C. S. Bandara, and J. A. S. C. Jayasinghe, "Experimental and Numerical Study on Force - Displacement & Moment - Curvature Behaviour of a Reinforced Concrete Beam," *IESL Journal*, 2020, in press.
- [15] W. Demin, and H. Fukang, "Investigation for plastic damage constitutive models of the concrete material," *Procedia Engineering*, vol. 210, pp. 71-78, 2017.
- [16] T. Jankowiak, and T. Lodygowski, "Identification of parameters of concrete damage plasticity constitutive model," *Foundations of civil and environmental engineering*, vol. 6, pp. 53-69, 2005.
- [17] M. Hafezolzghorani, F. Hejazi, R. Vaghei, and M. S. B. Jaafar, "Simplified Damage Plasticity Model for Concrete," *Structural Engineering International*, vol. 27, no. 1, pp. 68-78, 2017.
- [18] M. Labibzadeh, and R. Hamidi, "Effect of stress path, size and shape on the optimum parameters of a brittle-ductile concrete model," *Engineering Structures And Technologies*, vol. 9, no. 4, pp. 196-206, 2017.
- [19] L. Polus, and M. Szumigala, "Laboratory test vs. FE Analysis of Concrete Cylinders Subjected to Compression," *AIP Conference proceedings*, vol. 2078, no. 1, pp. 1-11, 2019.
- [20] D. D. Tripura, and S. Das, "Shape and Size Effects on the Compressive Strength of Cement Stabilised Rammed Earth," *Architectural Engineering Institute Conference*, pp. 336-348, 2017.
- [21] S. M. Soleimani, A. J. Boyd, A. J. K. Komar, and S. S. Roudsari, "Fatigue in Concrete under Low-Cycle Tensile Loading Using a Pressure-Tension Apparatus," *Applied Sciences*, vol. 9, no. 16, 2019.
- [22] Y. Dere, and M. A. Koroglu, "Nonlinear FE Modeling of Reinforced Concrete," *International Journal of Structural and Civil Engineering Research*, vol. 6, no. 1, pp. 71-74, 2017.

Predicting External Wind Pressure of a C-Shaped Building Using Explainable Machine Learning (XML)

D. P. P. Meddage
Department of Civil Engineering,
University of Moratuwa
Moratuwa, Sri Lanka
meddagedpp.20@uom.lk

Imesh Udara Ekanayake
Department of Computer Engineering
University of Peradeniya
Peradeniya, Sri Lanka
imeshuek@eng.pdn.ac.lk

A. U. Weerasuriya
Department of Mechanical Engineering
University of Hong Kong
Hong Kong
asiriuw@hku.hk

C. S. Lewangamage
Department of Civil Engineering
University of Moratuwa
Moratuwa, Sri Lanka
sujeewal@uom.lk

Abstract—External wind pressure of buildings is imperative for many applications in wind engineering despite it requires great efforts, time, and money for acquiring pressure data via physical and numerical modeling. An emerging technique of machine learning (ML) provides a suitable alternative for predicting external wind pressure of buildings. This study investigated the potential of six ML models based on linear kernel ridge regression (LKRR), support vector machine (SVM), artificial neural networks (ANN), decision tree (DT), Random Forest (RF), and Extreme-Gradient Boosting (XGBoost) techniques to predict area average external wind pressure ($C_{p,avg}$) on a C-shaped building. The results revealed simple ML models such as LKRR and DT did not accurately estimate the non-linear variation in $C_{p,avg}$. Advanced ML models such as RF, ANN, and XGBoost had better prediction accuracies but their inner workings were incomprehensible to end-users. The explainable ML techniques (XML) such as SHAP (SHapley Additive exPlanations) disclosed the inner working of these models as well as the impacts of inputs on the predictions. The global explanation of SHAP revealed wind incidence angle (θ) as the most influential input overall but its influence greatly varies for different building configurations as shown by the local SHAP explanations. The findings of this study demonstrated the advantages of XML techniques to increase the confidence of end-users to use ML models by improving the understanding of the inner working of black-box type, complex ML models, identifying the influential parameters, and estimating prediction accuracies.

Keywords— explainable machine learning, external wind pressure, regression models, SHAP

I. INTRODUCTION

Wind pressure on buildings' external walls is imperative for estimating wind loads, calculating natural ventilation rates, and reconstructing wind fields near buildings. However, measuring external wind pressure is a strenuous task as it is greatly modified by wind speed, turbulence intensity, building geometry, and the surrounding. Therefore, wind pressure measurements are typically obtained by using advanced modeling techniques such as wind tunnel tests and Computational Fluid Dynamics (CFD) simulation. Despite their credibility, wind tunnel tests and CFD simulations are resource-intensive, time-consuming, and require special facilities and expert knowledge. These difficulties urge researchers to invent an economical, faster, less resource-

dependent, and easy-to-use method for estimating the external wind pressure of buildings. As a result, several analytical models have been developed by researchers [1], [2]. Some of the models are based on linear-regression techniques, thus cannot handle complex, non-linear relationships between wind pressure, and building geometries. Analytical models based on non-linear regression perform better than the linear models, but they too limit to predicting wind pressure of buildings with a few simple configurations such as buildings with square or rectangular shapes.

The recent advancement of computational power, interactive computer languages, and availability of wind pressure data presents a new opportunity to develop an alternative method based on machine learning (ML). ML can develop complex, non-linear relationships between inputs and outputs based on the data available for training, testing, and validation. Arguably, Artificial Neural Network (ANN) is the most popular ML model for predicting external wind pressure on buildings ([3]–[13]). In addition, tree-based regressors and clustering techniques emerge as competitive ML models for estimating wind pressure of non-square-shaped objects such as circular cylinders [14], and buildings ([15], [16]).

Despite their promising performance, ML models often encounter difficulties in balancing accuracy, explainability, and interpretability. Accuracy describes the prediction precision of models. Explainability illustrates how a model utilizes inputs to approximate outputs, and interpretability elucidates how inputs affect predictions. Generally, simple ML models such as linear regressors are easy to explain and interpret (i. e., high explainability) but have low prediction accuracy. In contrast, advanced ML models such as ANN have high prediction accuracy but act as Blackbox models, which do not disclose their inner workings to end-users. The details of the inner working of ML models are of interest to data scientists, business owners, model risk analysts, regulators, and consumers to know the models' correctness, robustness, bias, improvements, transferability, and human comprehensibility.

Explainable machine learning (XML) caters to this need by elucidating models' inner workings such as how outputs depend on inputs or what inputs influence most model predictions. XML can be engineered by using simple ML

models or using post-hoc explainability approaches [17]. The latter is preferable because it can be applied after made predictions (post-hoc), available as model-specific or model agnostic techniques, provide explanations in forms of text, visual, simplified models and statements, and feature relevance at local, and global levels. Given the importance of XML in high-stake decision making, several post-hoc explainability approaches such as permutation feature importance, Partial Dependence Plots (PDPs), Individual Conditional Expectation (ICE) plots, global surrogate models, Local Interpretable Model-agnostic Explanations (LIME) [18], and Shapley Additive Explanations (SHAP) are currently in practice.

According to the authors' best knowledge, for the first time in literature, the current study employed XML to elucidate how building geometrical parameters and wind conditions globally and locally affect ML predictions of external wind pressure. Most importantly, this study tested several ML models for predictions to chose the best model before applying XML. To explore prediction capacity of ML models, this study employs wind pressure data of a building with a C-shaped plan (Section 2) and six ML models developed based on various techniques (Section 3). The comparison of ML prediction with the wind tunnel data reveals the advantages and disadvantages of each model (Section 4). The models' inner working is elucidated by using the SHAP values - an XML technique - to highlight feature importance and how inputs globally and locally affect the model's predictions (Section 5). Conclusion (Section 6) provides insights into how to utilize XML as a technique to predict external wind pressure of buildings.

II. C-SHAPED BUILDING MODEL

Fig. 1. shows the C-shaped building model, for which external wind pressure data were obtained from a wind tunnel test [5]. The building's unconventional shape can be described by curvature ratio (R/D), side ratio without curvature (d/b), overall side ratio (D/B), and aspect ratio (D/H).

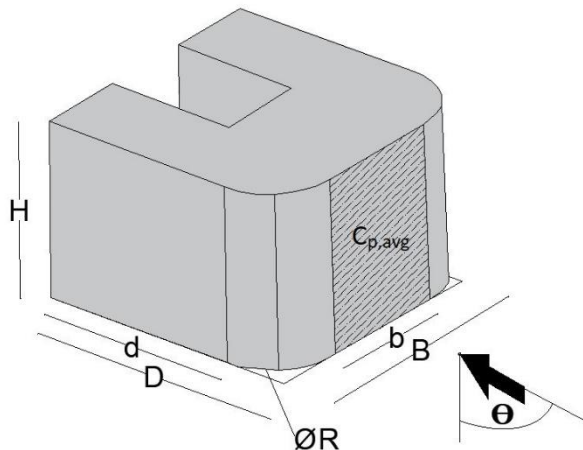


Fig. 1. Perspective view of the C-Shaped building.

The pressure data were recorded for 13 building configurations with various magnitudes of the design parameters tested at several wind incidence angles (θ) in a range of 0° to 180° . Wind pressure on the shaded area of the building is expressed as a normalized area-averaged pressure,

$C_{p,avg}$. [5]. The same data set was used previously to develop ML models based on the group method of data handling neural network (GMDH-NN) and gene expression programming (GEP) to predict $C_{p,avg}$. The comparison between the prediction of $C_{p,avg}$ by the two ML models and two classic analytics models equations proposed by Swami and Chandra [1] and Muehleisen and Patrizi [2] revealed the superior performance of the ML models with higher prediction accuracy.

III. MACHINE LEARNING ALGORITHMS

Unlike many previous studies, the current study employs multiple machine learning algorithms instead of one to predict $C_{p,avg}$. Six ML models selected for the study are based on linear regression, support vector machines, tree-based regression, and ANN. The linear regression is followed the ridge regression and is combined with a linear kernel function to develop the simplest ML model (LKRR) of this study. The simple structure of the LKRR allows end-users to understand its innerworking and present itself as the most transparent ML model. In contrast, the inner working of the ANN model is completely obscure from the end-users thus it is the opaquest model selected for this study. Three tree-based algorithms: Decision Tree (DT), Random Forest (RF), and XGBoost represent the simplest, ensemble trees with the bagging technique, and ensemble trees with the boosting technique, respectively. Support vector machines (SVM) differs from the rest of ML models as it projects low-dimensional data to high-dimensional space to establish relationships between inputs and outputs. A brief introduction to each algorithm selected for this study is shown in the following subsections.

A. Linear-Kernel Ridge Regression (LKRR)

LKRR establishes relationships between inputs and outputs using the least-square error method with the L2 regulation – ridge regression – with a linear kernel function [19]. The LKRR model has non-sparse, closed-form and typically fast performance for medium-sized data sets.

B. Tree-Based Regression

Tree-based algorithms are common in supervised machine learning. The simplest form of tree-based regressor is a single Decision Tree (DT), which can be primarily developed based on logical postulations following a moderately deterministic process. However, a single DT often has low bias and high variance – two adverse qualities that deteriorate prediction accuracy. On the other hand, ensemble tree-regressors have many DT as weak learners to balance bias and variance. They enhance operational efficiency and accuracy via boosting and bagging techniques. The selected tree-based regressors for this study are as follows:

1) *Decision Tree (DT)*: Decision Tree (DT) predicts outputs by learning simple decision rules inferred from the training data sets. Because the DT's technique is similar to the piecewise constant approximation, its flexibility strongly depends on tree structure such as tree depth and the number of leaves ([20]–[22]). The current study employs a DT with a depth of 4 and 20 minimum sample splits. The tree was formed on the Mean Squared Error (MSE) criterion.

2) *Random Forest (RF)*: RF minimizes the issue of low bias and high variance of DTs by parallel assembling many DTs as weak learners ([23], [24]). Each DT is trained by using a subset of the training dataset by following the bootstrap technique. To avoid tree correlation – formation of trees with a similar structure – RF uses randomized feature selection for the split in each node [25]. For this study, 80 trees with a depth of 4 and 10 minimum sample splits were selected for the RF model.

3) *XGBoost*: XGBoost, an acronym for extreme gradient boosting, is a recently developed ensemble tree-regression method with high efficiency and flexibility. The boosting method creates new weak learners sequentially while minimizing the squared error loss function using a gradient descent algorithm for each new tree ([26], [27]). The contribution of each tree is limited by a learning rate that is a scale factor considerably less than 1. XGBoost also uses L1 and L2 regularization to penalize the overfitting of complex models [28]. In addition, XGBoost employs a sparsity-aware split finding algorithm to find sparsity patterns in the training data and a distributed weighted quantile sketch algorithm to handle weighted data. A block structure is embedded to XGBoost to avoid repeating calculation in subsequent iterations, and its out-of-core computing optimizes the disk storage and limited capacity of computer memory. The XGBoost model in current study has hyperparameters: gamma (minimum loss reduction) = 0.00013, number of estimators (number of boosting stages) = 40, maximum tree depth = 4, alpha (L1 regularization term) = 0.0001, random state (Controls the random seed given to each Tree estimator at each boosting iteration) = 154, and learning rate = 0.21 were obtained through a gridsearch.

C. Support Vector Machine (SVM)

SVM forms non-linear relationships between inputs and outputs in a high dimensional space with the aid of special kernel functions ([29], [30]). The radial bias function kernel was used for the SVM regression model. The regularization term was set as 1.0, which was inversely proportional to the strength of regularization. The objective of the SVM is to find the hyper-plane that fits a maximum number of data points, assuming the points are within the decision boundary line.

D. Artificial Neural Network (ANN)

Despite its black box nature, ANN is a powerful tool that can approximate any function using a neural network architecture of the human brain that contains several layers of input, output, and hidden layers with many neurons [31], [32]. The most suitable number of hidden layers and neurons are chosen by trial-and-error to minimize the loss function. Generally, an optimization algorithm is employed to minimize the loss function by updating weights and biases after every epoch until the loss function reached the global optimum. The employed ANN network in this study consisted five hidden layers with 25, 100, 50, 25, and 5 neurons. The activation function was set as ‘relu’ for the hidden layers. Further, the random state, maximum iterations, and learning rate were optimized as 289, 250, and 0.001.

IV. ML MODELS’ PREDICTIONS

A. Correlations Between Inputs

Fig. 2. depicts pairwise correlations between five inputs and the output. Most of the inputs (e.g., θ and D/B; D/H and R/D) show no correlation with other inputs or with the output $C_{p,avg}$. However, d/b and D/B weakly correlate with each other as all four geometrical parameters are plan dimensions. The outright absence of strong correlations between inputs and outputs confirms the uncompetitiveness of simple linear relationships to predict $C_{p,avg}$ using the five inputs.

B. Performance Evaluation of ML Models

Fig. 3 compares the prediction of $C_{p,avg}$ by the six ML models: LKRR, SVM, ANN, DT, RF, and XGBoost with the data from the wind tunnel test. The comparison shows not only the prediction accuracy of each ML model but also any identifiable trends in predictions. For example, the LKRR model has poor prediction accuracy as its predictions deviate more than 20% from the data of the wind tunnel test. Moreover, negative predictions of the LKRR model are scattered indicating no obvious under- or over-estimation with respect to the wind tunnel test data. In contrast, the LKRR model noticeably underestimates positive $C_{p,avg}$ compared to the wind tunnel test data. Most of $C_{p,avg}$ predicted by SVM and DT are in the error range of $\pm 20\%$, despite their predictions vary in a wide range with respect to the same wind tunnel data. Such invariant predictions by the ML models are a result of the piecewise constant approximation for non-linear variations of the output. In contrast, the RF model shows high variation in predicted $C_{p,avg}$ indicating the effectiveness of the bagging technique to capture non-linear variations of the output. The predictions of ANN have a variation similar to that of RF, where most of the predictions are within the $\pm 20\%$ error margin. Among all models, the XGBoost model has the highest prediction accuracy and the lowest error range of $\pm 10\%$. Moreover, its predictions have no apparent under- or over-estimation confirming the superior performance of XGBoost as reported by many previous studies ([33]–[38]).

Performance of ML models is further assessed by using four performance evaluation indices: coefficient of determination (R^2), Pearson correlation coefficient (R), mean absolute error (MAE), and root means square error (RMSE), and Akaike Information Criteria (AIC). R^2 and R estimate how well the predictions match with actual data, and RMSE and MAE estimate the residual of the predictions. AIC estimates the quality of ML models by calculating data loss in predictions. The desirable performance of the ML models is indicated by lower RMSE, MAE, and AIC and large R and R^2 .

Table 1 shows the evaluation metrics calculated for the six ML models. As indicated by Fig. 2, the LKRR model has the lowest R and R^2 and highest MAE and RMSE values indicating substandard performance of the model. In contrast, XGBoost has the highest R and R^2 (0.996 and 0.993) and lowest MAE and RMSE confirming its superior prediction accuracy. Similar values of R, R^2 , MAE, and RMSE of DT, SVM, and ANN suggest the comparable performance of the three models. RT has higher R and R^2 and smaller MAE and MSE values than DT. The corresponding R and R^2 values are lower and MAE and MSE are higher than that of

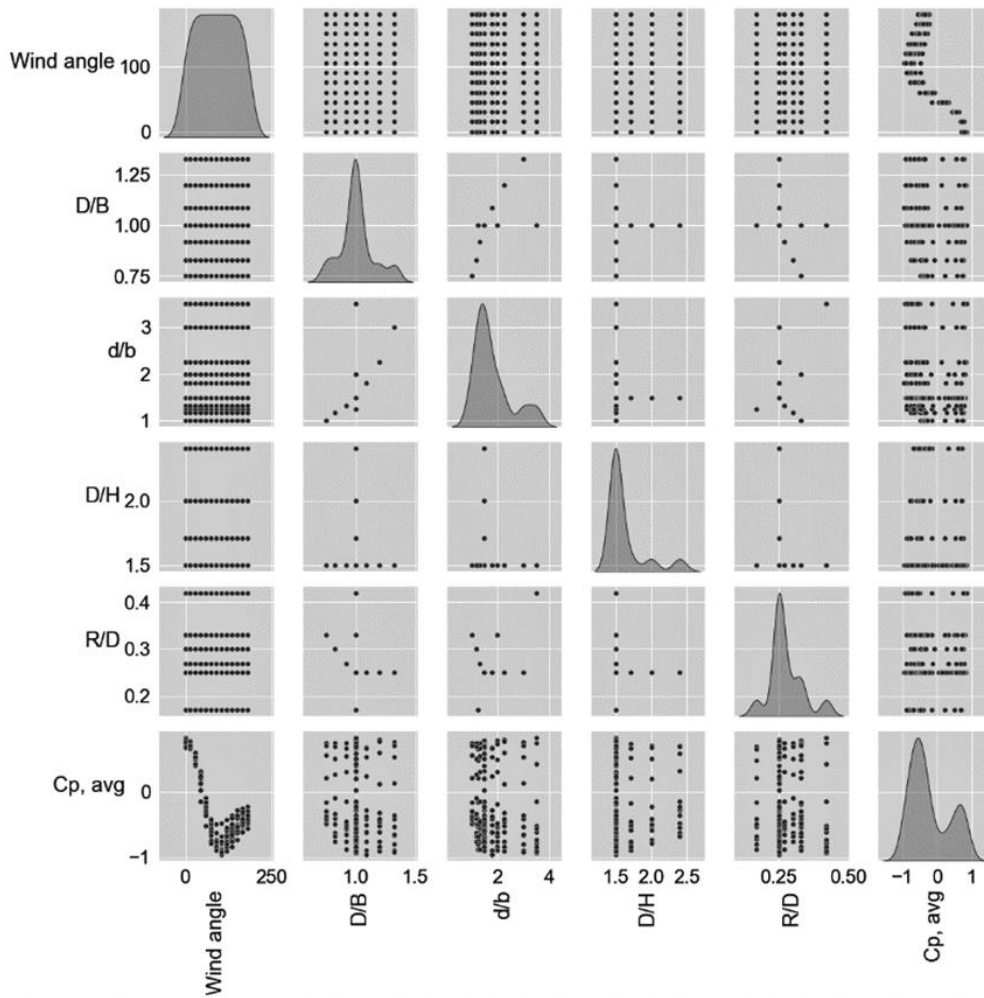


Fig. 2. Pairwise correlation between the five inputs and the output

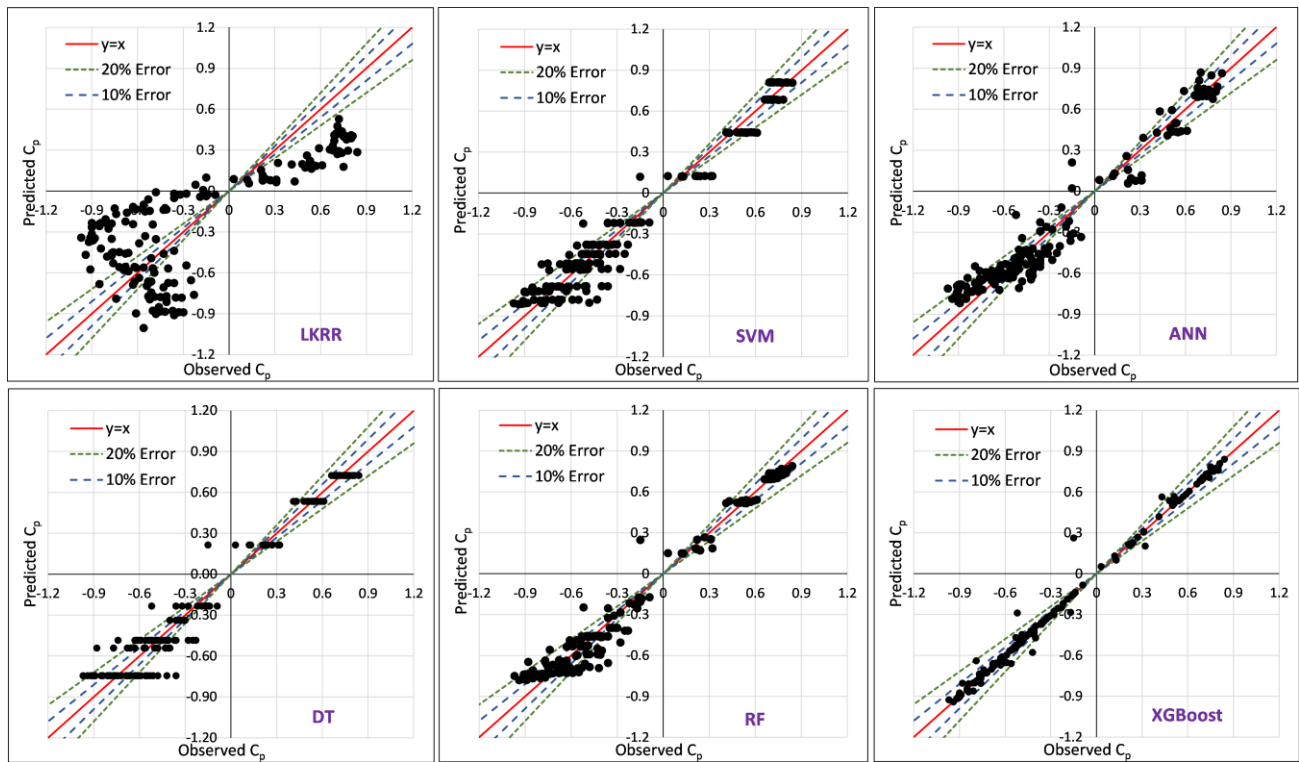


Fig. 3. Comparison of $C_{p,avg}$ between the predictions by the six ML models and the data from the wind tunnel test.

XGBoost. This reaffirms the superior performance of the ensemble technique bagging than a single decision tree. However its performance is inferior compared to the extreme gradient boosting method. AIC has the lowest value (highest negative value) for the XGBoost verifying the minimum data loss in the model predictions. The highest data loss thus the poorest model performance is with LKRR, and the other three ML models have similar data loss according to AIC.

V. EXPLAINABLE MACHINE LEARNING (XML)

A. SHAP Values

The current study chooses SHAP (SHapley Additive exPlanations) as the XML technique to explain and interpret the inner working of the XGBoost model of this study. SHAP is based on the game theory to explain the contribution of inputs to the output. Lundberg and Lee [39] have proposed SHAP as a unified approach for model interpretability. SHAP discloses contributions of each input for a prediction of an instance (i.e., local interpretability), and the collective SHAP values show either positive or negative predictions' contributions to the output. Although Lundberg and Lee [39] proposed several model-specific versions of SHAP, this study uses model agnostic Kernel SHAP. The following subsections present explanations for the predictions of the XGBoost model.

B. Global SHAP Explanations

Fig. 4. shows the SHAP values for the importance of model inputs estimated across the training data sets. The inputs are ranked according to the descending order of their importance such that wind incidence angle (θ) and R/D are the features with highest and lowest importance. Their SHAP values indicate whether the inputs are associated with high or low model outputs (i.e., $C_{p,avg}$). The color of an input - blue or red - expresses its feature value as either high or low at an instance. The combination of feature values with SHAP values explains the correlation between inputs and outputs. For example, small values of θ (i.e., low feature value) result in high model outputs indicating a negative correlation between θ and $C_{p,avg}$. On the other hand, the magnitude of $C_{p,avg}$ decreases with the D/H ratio pointing out a positive correlation between them. However, such definite correlations cannot be inferred for some inputs such as d/b or R/D as their high and low values resulted in mixed positive and negative $C_{p,avg}$.

C. Local SHAP Explanations

Fig. 5. shows the local SHAP explanation on how each of five inputs positively or negatively affect the output $C_{p,avg}$ in four different configurations of the C-shaped building. The base value ($=0.2381$) of each plot is the mean $C_{p,avg}$ of the training dataset, and $f(x)$ is the predicted $C_{p,avg}$ of each case. Red and blue arrow bars show positive and negative impacts

TABLE I PERFORMANCE EVALUATION OF THE SIX ML MODELS

ML model	R	R ²	MAE	RMSE	AIC
LKRR	0.761	0.578	0.324	0.363	-142.617
DT	0.978	0.957	0.086	0.116	-310.356
XGBoost	0.996	0.993	0.019	0.048	-441.180
SVM	0.978	0.957	0.091	0.116	-310.278
ANN	0.978	0.956	0.093	0.118	-308.157
RF	0.984	0.969	0.072	0.098	-334.621

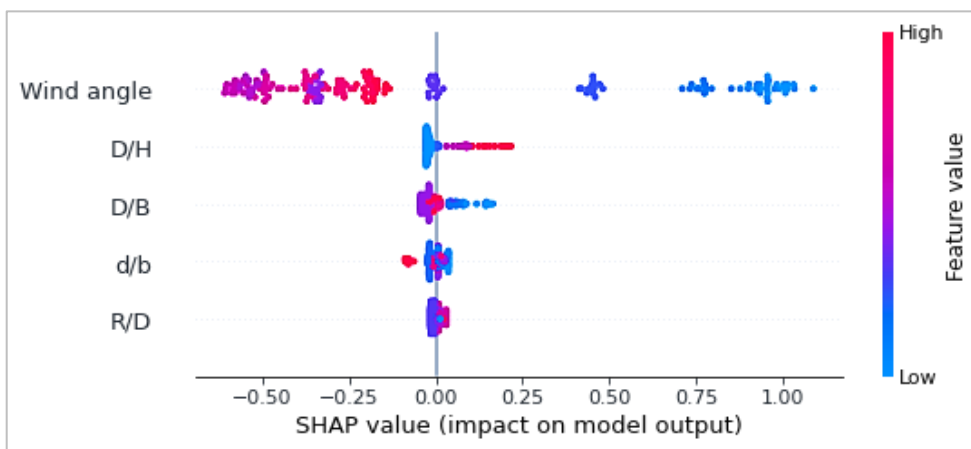


Fig. 4. The SHAP feature importance plot

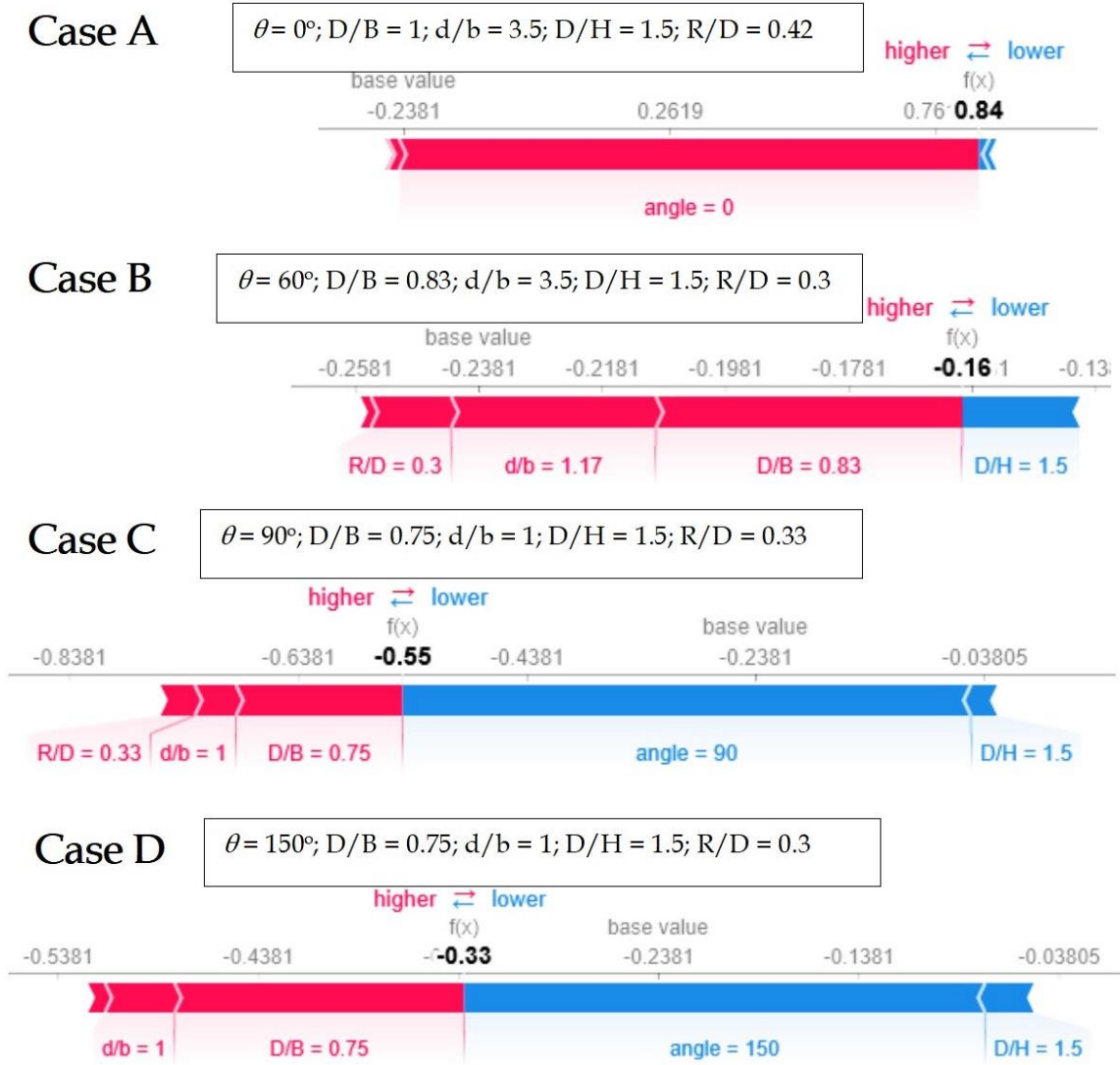


Fig. 5. Individual SHAP value plots for four configurations of C-shaped building

on $C_{p,avg}$, respectively. For instance, the $C_{p,avg}$ of Case A is governed by the positive impact of $\theta = 0^\circ$, which increases $C_{p,avg}$ from the base value of -0.2381 to 0.84. In this particular case, other inputs induce both positive and negative impacts, but their magnitudes are negligible. In Case B with $\theta = 60^\circ$, the inputs: R/D, d/b, and D/B have increased $C_{p,avg}$, while D/H = 1.5 tends to decrease the magnitude of the output. However, this combination cannot produce a positive $C_{p,avg}$, and results in a smaller value $C_{p,avg}$ of -0.16. The magnitude of negative $C_{p,avg}$ is further increased to -0.55 in Case C mainly due to the negative impact of $\theta = 90^\circ$. However, the negative impact of θ is decreased and the positive influences of D/B = 0.75 and d/b=1 increases at $\theta = 150^\circ$ to produce moderately high negative $C_{p,avg}$ of -0.33.

VI. CONCLUSION

This study used an emerging technique of machine learning to predict area-averaged external wind pressure ($C_{p,avg}$) on a building with an unconventional configuration. Six ML models LKRR, SVM, ANN, DT, RF, and XGBoost to evaluate their prediction accuracies techniques. The results revealed ML models based on linear functions (e.g., LKRR)

or simple piecewise constant approximations (DT) cannot accurately estimate non-linear variations of $C_{p,avg}$. As the complexity of the inner working of the ML model increases, their predictions attain high accuracy (e.g., RF \rightarrow ANN \rightarrow XGBoost). However, the fact that how the models make predictions becomes obscure from end-users as ML models transformed from simple models to black-box type, complex models.

The inner working of these complex models can be disclosed by using explainable ML such as SHAP values. The global explanation of SHAP revealed wind incidence angle (θ) as the most influential parameter following by - in the descending order of feature importance - D/H, D/B, d/b, and R/D. However, local explanations of SHAP indicate geometry parameters such as D/B and d/b can induce greater impacts on predictions than θ does for some cases. Explainable ML techniques such as SHAP offer confidence for end-users to understand how black-box type, complex ML models work, identify the influential parameters, and estimate their prediction accuracy.

ACKNOWLEDGMENT

The authors are grateful for the insights and encouragements given by the two anonymous reviewers of this manuscript.

REFERENCES

- [1] M. V. Swami and S. Chandra, "Procedures for Calculating Natural Ventilation Airflow Rates in Buildings," ASHRAE Research Project, 1987.
- [2] R. T. Muehleisen and S. Patrizi, "A new parametric equation for the wind pressure coefficient for low-rise buildings," *Energy Build.*, vol. 57, pp. 245–249, 2013.
- [3] Y. Chen, G. A. Kopp, and D. Surry, "Prediction of pressure coefficients on roofs of low buildings using artificial neural networks," *J. Wind Eng. Ind. Aerodyn.*, vol. 91, no. 3, pp. 423–441, Feb. 2003, doi: 10.1016/S0167-6105(02)00381-1.
- [4] F. Bre, J. M. Gimenez, and V. D. Fachinotti, "Prediction of wind pressure coefficients on building surfaces using Artificial Neural Networks," *Energy Build.*, 2017, doi: 10.1016/j.enbuild.2017.11.045.
- [5] M. Mallick, A. Mohanta, A. Kumar, and K. C. Patra, "Prediction of Wind-Induced Mean Pressure Coefficients Using GMDH Neural Network," *J. Aerosp. Eng.*, vol. 33, no. 1, 2020, doi: 10.1061/(ASCE)AS.1943-5525.0001101.
- [6] J. Y. Fu, S. G. Liang, and Q. S. Li, "Prediction of wind-induced pressures on a large gymnasium roof using artificial neural networks," *Comput. Struct.*, vol. 85, no. 3, pp. 179–192, Feb. 2007, doi: 10.1016/j.compstruc.2006.08.070.
- [7] N. Kwatra, P. N. Godbole, and P. Krishna, "Application of artificial neural network for determination of wind induced pressures on gable roof," *Wind Struct.*, vol. 5, no. 1, pp. 1–14, 2002, doi: 10.12989/was.2002.5.1.001.
- [8] Y. Chen, G. A. Kopp, and D. Surry, "Interpolation of wind-induced pressure time series with an artificial neural network," *J. Wind Eng. Ind. Aerodyn.*, vol. 90, no. 6, pp. 589–615, Jun. 2002, doi: 10.1016/S0167-6105(02)00155-1.
- [9] X. Gavalda, J. Ferrer-Gener, G. A. Kopp, and F. Giralt, "Interpolation of pressure coefficients for low-rise buildings of different plan dimensions and roof slopes using artificial neural networks," *J. Wind Eng. Ind. Aerodyn.*, vol. 99, no. 5, pp. 658–664, May 2011, doi: 10.1016/j.jweia.2011.02.008.
- [10] H. Dongmei, H. Shiqing, H. Xuhui, and Z. Xue, "Prediction of wind loads on high-rise building using a BP neural network combined with POD," *J. Wind Eng. Ind. Aerodyn.*, vol. 170, pp. 1–17, Nov. 2017, doi: 10.1016/j.jweia.2017.07.021.
- [11] J. Sang, X. Pan, T. Lin, W. Liang, and G. R. Liu, "A data-driven artificial neural network model for predicting wind load of buildings using GSM-CFD solver," *Eur. J. Mech. - B/Fluids*, vol. 87, pp. 24–36, May 2021, doi: 10.1016/j.euromechflu.2021.01.007.
- [12] S. Kalogirou, M. Eftekhari, and L. Marjanovic, "Predicting the pressure coefficients in a naturally ventilated test room using artificial neural networks," *Build. Environ.*, vol. 38, no. 3, pp. 399–407, 2003.
- [13] J. Y. Fu, Q. S. Li, and Z. N. Xie, "Prediction of wind loads on a large flat roof using fuzzy neural networks," *Eng. Struct.*, vol. 28, no. 1, pp. 153–161, Jan. 2006, doi: 10.1016/j.engstruct.2005.08.006.
- [14] G. Hu and K. C. S. Kwok, "Predicting wind pressures around circular cylinders using machine learning techniques," *J. Wind Eng. Ind. Aerodyn.*, vol. 198, p. 104099, Mar. 2020, doi: 10.1016/j.jweia.2020.104099.
- [15] B. Kim, N. Yuvaraj, K. T. Tse, D.-E. Lee, and G. Hu, "Pressure pattern recognition in buildings using an unsupervised machine-learning algorithm," *J. Wind Eng. Ind. Aerodyn.*, vol. 214, p. 104629, Jul. 2021, doi: 10.1016/j.jweia.2021.104629.
- [16] G. Hu, L. Liu, D. Tao, J. Song, and K. C. S. Kwok, "Investigation of wind pressures on tall building under interference effects using machine learning techniques," *ArXiv190807307 Cs Eess Stat*, Aug. 2019, Accessed: Aug. 08, 2021. [Online]. Available: <http://arxiv.org/abs/1908.07307>
- [17] Y. Liang, S. Li, C. Yan, M. Li, and C. Jiang, "Explaining the black-box model: A survey of local interpretation methods for deep neural networks," *Neurocomputing*, vol. 419, pp. 168–182, Jan. 2021, doi: 10.1016/j.neucom.2020.08.011.
- [18] Y. Zhang, K. Song, Y. Sun, S. Tan, and M. Udell, "Why Should You Trust My Explanation? Understanding Uncertainty in LIME Explanations," presented at the International Conference on Machine Learning AI for Social Good Workshop, 2019.
- [19] A. Mannodi-Kanakkithodi, G. Pilania, and R. Ramprasad, "Critical assessment of regression-based machine learning methods for polymer dielectrics," *Comput. Mater. Sci.*, vol. 125, pp. 123–135, Dec. 2016, doi: 10.1016/j.commatsci.2016.08.039.
- [20] M. Xu, P. Watanachaturaporn, P. K. Varshney, and M. K. Arora, "Decision tree regression for soft classification of remote sensing data," *Remote Sens. Environ.*, vol. 97, no. 3, pp. 322–336, Aug. 2005, doi: 10.1016/j.rse.2005.05.008.
- [21] V. Rodriguez-Galiano, M. Sanchez-Castillo, M. Chica-Olmo, and M. Chica-Rivas, "Machine learning predictive models for mineral prospectivity: An evaluation of neural networks, random forest, regression trees and support vector machines," *Ore Geol. Rev.*, vol. 71, pp. 804–818, Dec. 2015, doi: 10.1016/j.oregeorev.2015.01.001.
- [22] L. Breiman, J. Friedman, R. Olshen, and C. J. Stone, "Classification and Regression Trees," 1983. doi: 10.2307/2530946.
- [23] L. Breiman, "Random Forests," *Mach. Learn.*, vol. 45, no. 1, pp. 5–32, Oct. 2001, doi: 10.1023/A:1010933404324.
- [24] W. Sullivan [Unknown, Machine Learning For Beginners: Algorithms, Decision Tree & Random Forest Introduction. 2017. Accessed: Aug. 08, 2021. [Online]. Available: <http://gen.lib.rus.ec/book/index.php?md5=264defc31d023c866fe9061533516819>
- [25] A. Cutler, D. R. Cutler, and J. R. Stevens, "Random Forests," in *Machine Learning*, 2011.
- [26] T. Chen and C. Guestrin, "XGBoost: A Scalable Tree Boosting System," in *Proceedings of the 22nd ACM SIGKDD International Conference on Knowledge Discovery and Data Mining*, New York, NY, USA, Aug. 2016, pp. 785–794. doi: 10.1145/2939672.2939785.
- [27] B. Quinto, *Next-Generation Machine Learning with Spark: Covers XGBoost, LightGBM, Spark NLP, Distributed Deep Learning with Keras, and More*, 1st ed. Apress, 2020. Accessed: Aug. 08, 2021. [Online]. Available: <http://gen.lib.rus.ec/book/index.php?md5=9E5654403C64D7FDBAF3CC1578C620DD>
- [28] C. Xu et al., "A study of predicting irradiation-induced transition temperature shift for RPV steels with XGBoost modeling," *Nucl. Eng. Technol.*, Feb. 2021, doi: 10.1016/j.net.2021.02.015.
- [29] V. Kecman (auth.) and P. L. Wang (eds.), *Support Vector Machines: Theory and Applications*, 1st ed. Springer-Verlag Berlin Heidelberg, 2005. Accessed: Aug. 08, 2021. [Online]. Available: <http://gen.lib.rus.ec/book/index.php?md5=b03ea619ee290254313a74993ecaff6f>
- [30] A. Christmann and I. Steinwart (auth.), *Support Vector Machines*, 1st ed. Springer-Verlag New York, 2008. Accessed: Aug. 08, 2021. [Online]. Available: <http://gen.lib.rus.ec/book/index.php?md5=798dde496d8aacdd2650d3358373cfe7>
- [31] S. Chakraverty and S. K. Jeswal, *Applied Artificial Neural Network Methods for Engineers and Scientists: Solving Algebraic Equations. WSPC*, 2021. Accessed: Aug. 08, 2021. [Online]. Available: <http://gen.lib.rus.ec/book/index.php?md5=71C9260081D765A8CE7B4B242C9C5A57>
- [32] S. Shanmuganathan and S. Samarasinghe (eds.), *Artificial Neural Network Modelling*, 1st ed. Springer International Publishing, 2016. Accessed: Aug. 08, 2021. [Online]. Available: <http://gen.lib.rus.ec/book/index.php?md5=f37c0913e72b28ed1cda388981079bb3>
- [33] Z. Zhang, Y. Huang, R. Qin, W. Ren, and G. Wen, "XGBoost-based on-line prediction of seam tensile strength for Al-Li alloy in laser welding: Experiment study and modelling," *J. Manuf. Process.*, vol. 64, pp. 30–44, Apr. 2021, doi: 10.1016/j.jmapro.2020.12.004.
- [34] J. Luo, Z. Zhang, Y. Fu, and F. Rao, "Time series prediction of COVID-19 transmission in America using LSTM and XGBoost algorithms," *Results Phys.*, vol. 27, p. 104462, Aug. 2021, doi: 10.1016/j.rinp.2021.104462.
- [35] M. Ma et al., "XGBoost-based method for flash flood risk assessment," *J. Hydrol.*, vol. 598, p. 126382, Jul. 2021, doi: 10.1016/j.jhydrol.2021.126382.
- [36] C. Yang, M. Chen, and Q. Yuan, "The application of XGBoost and SHAP to examining the factors in freight truck-related crashes: An exploratory analysis," *Accid. Anal. Prev.*, vol. 158, p. 106153, Aug. 2021, doi: 10.1016/j.aap.2021.106153.

- [37] P. Trizoglou, X. Liu, and Z. Lin, "Fault detection by an ensemble framework of Extreme Gradient Boosting (XGBoost) in the operation of offshore wind turbines," *Renew. Energy*, vol. 179, pp. 945–962, Dec. 2021, doi: 10.1016/j.renene.2021.07.085.
- [38] H. Hu, A. J. van der Westhuysen, P. Chu, and A. Fujisaki-Manome, "Predicting Lake Erie wave heights and periods using XGBoost and LSTM," *Ocean Model.*, vol. 164, p. 101832, Aug. 2021, doi: 10.1016/j.ocemod.2021.101832.
- [39] S. M. Lundberg and S.-I. Lee, "A unified approach to interpreting model predictions," in *Proceedings of the 31st International Conference on Neural Information Processing Systems*, Red Hook, NY, USA, Dec. 2017, pp. 4768–4777.

Identification of Natural Frequency and Modal Damping Ratio of Tall Buildings in Sri Lanka

D.G.I.S. Deegoda

Department of Civil Engineering
Faculty of Engineering
University of Peradeniya
Kandy, Sri Lanka
isurudeegoda@gmail.com

D.M.H.B. Dissanayake

Department of Civil Engineering
Faculty of Engineering
University of Peradeniya
Kandy, Sri Lanka
hasidissa1234@gmail.com

H.A.D. Samith Buddika

Department of Civil Engineering
Faculty of Engineering
University of Peradeniya
Kandy, Sri Lanka
samithbuddika@eng.pdn.ac.lk

Abstract— The wind factor becomes a major concern in designing high-rise buildings in Sri Lanka due to its vibration effect. To design a tall building in the habitability region, it is essential to calculate dynamic parameters such as the damping ratio and natural frequency of the building. However, there is not a specific method to identify the damping ratio and natural frequency of the buildings in Sri Lanka. Hence, this study was designed to collect identified damping ratio and natural frequency of tall buildings in Sri Lanka to propose an empirical equation. Three tall buildings in Colombo, Sri Lanka which are greater than 150 m in height were selected and Ambient vibration due to wind on those buildings was measured. Random Decrement Technique (RDT) was used to obtain the Impulse response function from ambient vibration data. Subsequently, it was analysed using both Continuous Wavelet Transformation (CWT) and Fast Fourier Transformation (FFT) to identify Natural frequency and Damping ratio. Results were compared with the values that were based on design codes. It reflects that the results are comparable with each other. Further identification of dynamic parameters of tall buildings is recommended to propose empirical equations for the Natural frequency and Damping ratio of tall buildings in Sri Lanka.

Keywords— *Continuous Wavelet Transformation, Damping ratio, Natural frequency, tall buildings*

I. INTRODUCTION

During the design of tall buildings, the wind has become a dominant consideration. When designing a tall building for wind vibration dynamic responses such as acceleration, velocity, and displacement of the building should be in habitability and safety region. To estimate this dynamic response of a structure, identification of dynamic characteristics such as natural frequency and modal damping ratio is important. Damping indicates how a system dissipates the vibration energy through various mechanisms such as thermal energy, or it radiates outside the boundary of the system. Recommended values and empirical methods to estimate the natural frequency and modal damping ratio have been proposed by several codes and authors.

Values for damping of general buildings varies from 0.3% to 5% for steel buildings and from 0.5% to 5% for RC buildings, showing a significant deviation of design damping values [1]. Smith and Willford [2] were found that damping ratios commonly assumed in designs are inappropriate and not conservative. In Sri Lanka, damping ratios are commonly assumed based on the literature. It may result in excessive sways and ineffective bracing during the high wind period.

Identification of Natural frequencies is almost established. However, the identification of modal damping ratios cannot be evaluated accurately. Arakawa and Yamamoto [3] were illustrated based on measurement data in actual buildings,

estimation of damping ratios is widely dispersed according to amplitude levels, structural materials, foundation types, and number of non-structural members.

Several methods were proposed to identify the modal damping ratio in past decades. Among these methods, Output-Only Modal Analysis (OMA) is used for either single or multi modes under the unknown vibration such as ambient wind excitation. Random Decrement Technique (RDT) is applicable to obtain Impulse Response Function (IRF) in the time domain. Using IRF and measured data Continuous wavelet is applicable to identify model parameters. Continuous Wavelet Transform (CWT) gained popularity as an effective method of signal processing to identify model properties of a structure. In general, complex morlet wavelet is used as the mother wavelet.

Wavelet Transformation is used in many fields as a signal processing tool. Wavelet Transformation is mainly divided into two as Discrete Wavelet Transformation (DWT) and Continuous Wavelet Transformation (CWT). The main advantage of CWT is the ability to analyze a signal at arbitrary scales and locations. The continuous wavelet transform has been widely used for frequency identification. Unlike the discrete wavelet transform, the continuous wavelet transform can change the location and dilation of the mother wavelet in a smooth rather than dyadic manner. This enables the extraction of redundant but rich information from the signal of interest, which makes it well suited for frequency identification.

Continuous Wavelet Transformation (CWT) has the ability to overcome many limitations in analysis using Fast Fourier Transformation (FFT). When performing data analysis by FFT, the information along the time series is lost. It cannot study the nature of the time series in the time-frequency domain. However, analysis of continuous wavelet transform pave the path to study time series in the time-frequency domain. It is shown that CWT has more ability to identify dynamic parameters than FFT (Kankanamge *et al.* [4]).

Continuous Wavelet Transformation (CWT) has been used successfully to estimate the Modal parameters from full-scale ambient vibration measurements of a 5-story steel structure. Le and Tamura [5]. Also, CWT has been widely used in SHM for large-scale bridge structures (Kankanamge *et al.* [4]). In that research this method is used in two case studies: a single-span steel girder bridge in Holland, Michigan, and a cable-stayed bridge in mainland China. It is shown that CWT has the ability to identify the natural frequency and damping ratios accurately.

Moreover, as the mother wavelet Complex Morlet wavelet has been widely used to identify the characteristic features on the structure of the analyzed signals [6][7][8].

This study was designed to collect identified damping ratio and natural frequency of tall buildings in Sri Lanka to propose an empirical equation. Three tall buildings in Colombo, Sri Lanka which are greater than 150 m in height were selected and Ambient vibration due to wind on those buildings was measured. In this paper, Identification of natural frequency and modal damping ratio of The Vertical Tower of Altair building in Colombo, Sri Lanka using Continuous Wavelet Transformation is included.

II. EMPIRICAL METHODS TO ESTIMATE NATURAL FREQUENCY AND DAMPING RATIO

In this section, a summary of reviewed empirical methods to estimate Natural frequency and Damping Ratio is described. Those methods were proposed based on several numerical model analyses or Laboratory tests or Real test results. In this study, variation of results and values from the following methods were illustrated.

A. Methods to estimate Natural Frequency

The natural frequency of a tall building is depending on its height, tip acceleration, and type of building. That value can be obtained by using empirical equations proposed in many designing guidelines. Calculation of Natural frequency is related to the height of the building as well as the structural type according to the literature. According to the methods, the natural frequency of a tall building is below 1 Hz. The summary of reviewed empirical methods to calculate the natural period is shown in Table I.

TABLE I. SUMMARY OF REVIEWED EMPIRICAL METHODS TO CALCULATE THE NATURAL PERIOD

Code	Structural Type	Natural Period
KBC 2009	RC moment frame	$0.073 H^{0.75}$
ASCE 7-10	RC moment frame	$0.067 H^{0.9}$
Eurocode 1	RC	$H/46$
Lagomarsino	RC	$H/55$
Yoon and Joo	RC	$H/52$
(AS/NZS 1170) and Hong Kong design code	Steel and RC	$H/46$
Tamura	Steel	$H/50$ Habitability regime
		$H/42$ Safety regime
Tamura	RC	$H/67$ Habitability regime
		$H/56$ Safety regime

KBC 2009 and ASCE 7-10 give an empirical method for an estimate the Natural frequency of the RC moment frame. Eurocode, Australia and New Zealand standards, and Hong Kong design code illustrate the same estimation method. Based on the Japanese Damping Database Tamura [1] proposed fundamental natural frequencies for the low amplitude habitability design level and the large amplitude safety design level for both RC and Steel structures.

B. Methods to estimate Damping ratio

Damping is an indicator of how a system dissipates the vibration energy through various mechanisms. Damping can be divided into three parts such as under-damp, over-damp, and critical damp. Under damp can be divided into two parts such as negative damping and positive damping. In general, positive under-damp conditions are focused upon.

During the damping phenomena, vibration energy is converted into thermal energy or radiation to the outside of the boundary to get quiescent conditions. Damping in tall buildings is occurred due to Structural Material Damping, Structural Connection Damping, Foundation Damping, Non-structural Damping, Aerodynamic Damping, or Hysteresis of Yielding Components [2].

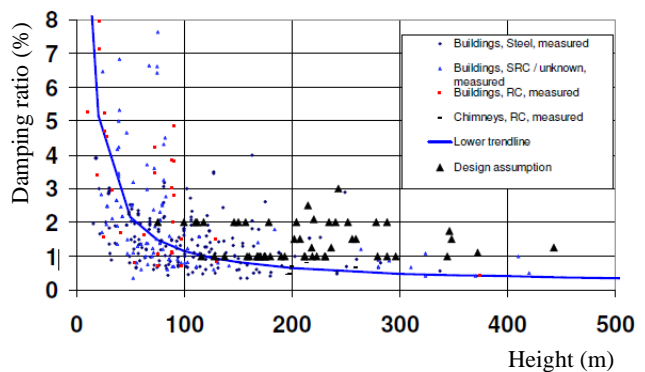


Fig. 1. Damping Ratio variation with building height [2]

TABLE II. SUMMARY OF REVIEWED METHODS FOR ESTIMATE DAMPING RATIO

Method	Code	Structural damping ratio (%)
Single value damping ratio	Eurocode 1	1.57
	AS/NZS 1170	0.5 – 1.0
	ASCE 7-10	2.0
Frequency and amplitude dependent damping ratio	ISO 4354	1.2 – 2.0 (height dependent)
	AIJ 2000	$0.014f_i + 470(X/H) - 0.0018$ (RC)
	AIJ 2000	$0.013f_i + 400(X/H) - 0.0029$ (Steel)
	ESDU 83009	$0.0076f_i + 150(X/H) + 0.003$
	Yoon	$0.0059f_i + 310(X/H) + 0.0039$

Wind load is more dominant when the height of the building increases. The ability of energy dissipation is going down with their height increase. That is shown in Fig. 1. Assumed values for damping of different height buildings from AS/NZS-1170 (1.0%), ASCE 7-10(2.0%) and ISO 4354(1.2-2.0%) are shown in Fig. 1 as design assumptions. Except ISO 4354 other methods are not depend on the building height. However, distinct damping values in this graph implies that the building height is a major factor in damping behavior.

According to Fig. 1, the damping ratio of the building is below 3% when its height is greater than 100m. And also, building above 250m has below 1% of damping ratio. The main reason for this result is due to the less contribution of the Non-Structural damping and more dominant effect from the primary structure.

Damping predictions can be divided into frequency and amplitude-dependent damping ratio and single value damping ratio. The single value damping ratio depends on the type of the structure, building height, and natural frequency. According to the Eurocode, the damping ratio has three parts such as structural damping, aerodynamic damping, and tuned mass dampers and this code categorize with the structural type as well such as RC, Steel, and SRC. Summary of reviewed methods for estimate damping ratio is shown in Table II.

Eurocode suggests this method is a logarithmic decrement damping without considering the height or tip drift of the building. The Australia and New Zealand Standard (AS/NZS 1170) is also using the same approach as Eurocode.

However, this code suggests the damping ratio under two limit states such as serviceability limit state and ultimate limit state. In the ultimate limit state, structures are categorized into three types such as RC structures, bolted steel structures, and welded steel structures. In the serviceability limit state, structures are categorized into two types such as steel structures and RC structures.

Moreover, based on the Japanese Damping Database Tamura [1] proposed damping predictors as empirical regression equations for both RC buildings and Steel Buildings which are dependent on natural frequency and tip drift ratio X/H . Similarly, ISO 4354, ESDU 83009, and Yoon proposed empirical equations for frequency and amplitude-dependent Damping ratio [9].

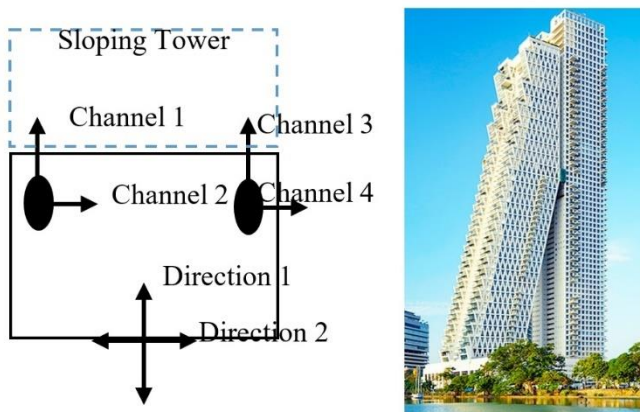


Fig. 2. Arrangement of two Accelerometers on Vertical Tower Altair Building Colombo

III. METHODOLOGY

In this study, the identification of the Natural frequency and Modal damping ratio of tall buildings in Sri Lanka was done. Altair Building in Colombo, Sri Lanka is one of the selected tall buildings for this study. Accelerometers are placed at the top floor of the Selected tall building which has more than 150m in height. Ambient vibration data were extracted using Accelerometers at several periods for various wind speeds. Tip acceleration is used to capture the dynamic response of the RC structure. A high wind period was considered to mitigate the un relevant useless noises. The impulse response function is obtained using the modal identification method Random Decrement Technique. Subsequently, the Natural frequency and Damping ratio of the building were calculated by analyzing the data using Fast Fourier Transformation and Continuous Wavelet Transformation. Morlet wavelet is used as the mother wavelet for CWT analysis. The results were compared with the values obtained using empirical equations that are already available.

A. Ambient Vibration measurement

Altair Building consists of two towers, a Vertical tower, and a Sloping tower as shown in Fig. 2. Response due to ambient wind vibration of the Vertical Tower of the Altair building was measured. It is a rectangular shape Reinforced Concrete structure and it is connected with Slopping Tower at level 39 and level 41. Vertical Tower Altair Buildings consist of 69 levels and it is 240m in height.

The floor vibration on the top floor of the building was measured. Two accelerometers were used to obtain a response in two directions each. Accelerometers were placed at the corners of the floor. Response due to ambient vibration was recorded at a sampling rate of 500 Hz. The arrangement of two Accelerometers on the Altair Building is shown in Fig. 2.

Acceleration data was recorded in the time domain in two-hour intervals. Data for four channels from two accelerometers were recorded at the same time. The obtained signal was filtered using the Butterworth filter. An example of a filtered signal in the time domain is shown in Fig. 3.

B. Random Decrement Technique

Random Decrement Technique (RDT) is used for failure detection and damping measurement of structures in single-mode response and single degree of freedom cases. The basic concept of RDT is based on the random responses of the structure. The random input is composed of two parts as the deterministic part and the random part [10].

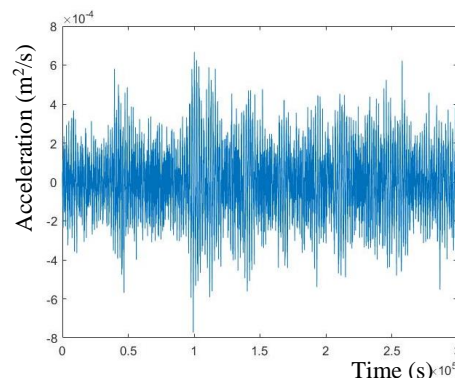


Fig. 3. Bandpass filtered signal in the time domain

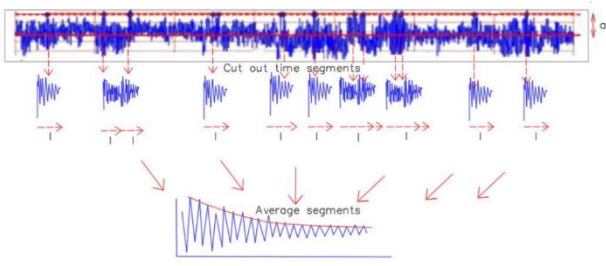


Fig. 4. Principle of Random Decrement Technique

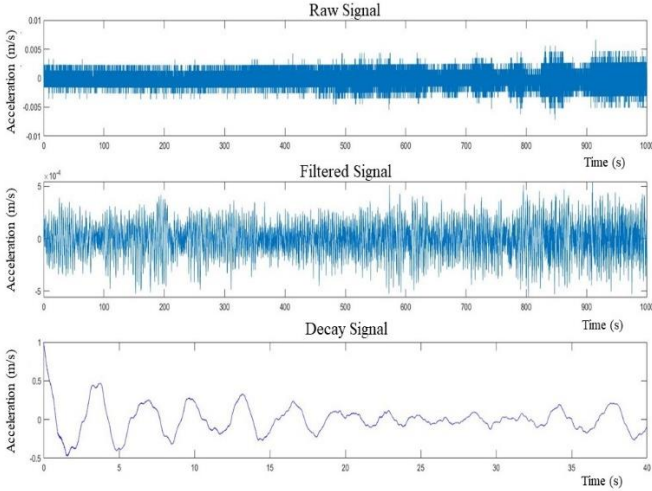


Fig. 5. Time vs Acceleration in channel 1

Application of the random decrement signature technique to multiple signals changes the time correlation between the individual signals. If the resulting responses are to be used to identify several modes of a structure, the random decrement signature technique must be modified to keep the time correlation between signals unchanged.

The vibration response of a randomly excited system consists of three parts. They are, responding to an initial displacement, the response to an initial velocity, and the response to random input loads. Moreover, the two essential parameters of RDT are the length of the time segments and the trigger conditions.

In Random Decrement Technique, Impulse response functions in the time domain are extracted from ambient vibration measurements of structures. It is useful to determine the damping parameters accurately [11]. The random decrement technique has been used successfully for the identification of dynamic parameters of structures in single-mode response cases.

The idea of this technique is, extracting a large number of time segments from the signal starting with the same initial value. Then averaging over those signals, the random part of the response will tend to disappear from the system and solely the responses to the initial conditions will remain [12]. From this technique, the resulting function will be named the Random Decrement function. It has the same damping coefficients and frequencies similar to the free decay function of the structure. The principle of the Random Decrement Technique is shown in Fig. 4.

The Raw signal is filtered using the Butterworth bandpass filter. Subsequently, the Filtered signal is divided into time

segments to create a decay signal according to the RDT. The Raw acceleration signal, filtered signal, and Decay signal in channel 1 are shown in Fig. 5

C. Natural Frequency using CWT

Continuous wavelet is a significant signal processing tool that has the ability to identify modal parameters. CWT is used to identify the natural frequency of the structure.

The general CWT formula used to decompose a function $x(t)$ into a frequency-time domain is given by the following equation.

$$CWT\{x(t)\} = W_x(\tau, s) = \frac{1}{\sqrt{s}} \int_{-\infty}^{+\infty} x(t) \psi^* \left(\frac{t-\tau}{s} \right) dt \quad (1)$$

Where ψ^* is the complex conjugate of mother wavelet (t), t is time, and $W(\tau, s)$ measures the similitude between the function $x(t)$, and the translation (τ) and the scale (s). Low-frequency information is illustrated using long-time intervals. Hence, low frequencies can be captured using high scales. The wavelet amplitude map is constructed using amplitude of wavelet coefficient, $|W(\tau, s)|$. It shows the amplitude of the features in the original signal.

D. Damping Ratio using CWT

The general CWT formula is used to decompose a function $x(t)$ into the frequency-time domain. Wavelet amplitude map is constructed using decompose function. The local maxima of the wavelet amplitude map indicate the natural frequencies of the system. Wavelet envelop is extracted from amplitude map using the parallel slide window on natural frequency. Wavelet amplitude map and wavelet envelop on the selected natural frequency are shown in Fig. 6 and Fig. 7 respectively.

The equation (3) and (4) for Logarithmic decrement ∂_i and damping ratio ζ_i are used to obtain the damping ratio.

$$T_i = \frac{2\pi}{\omega_{di}} \quad (2)$$

T_i is the natural period of the i^{th} mode of the structure.

$$\partial_i = \frac{1}{m} \ln \frac{|W_{xi}(t, \omega_{di})|}{|W_{xi}(t+mT_i, \omega_{di})|} \quad (3)$$

m is any positive integer.

$$\zeta_i = \frac{\partial_i}{\sqrt{4\pi^2 + \partial_i^2}} \quad (4)$$

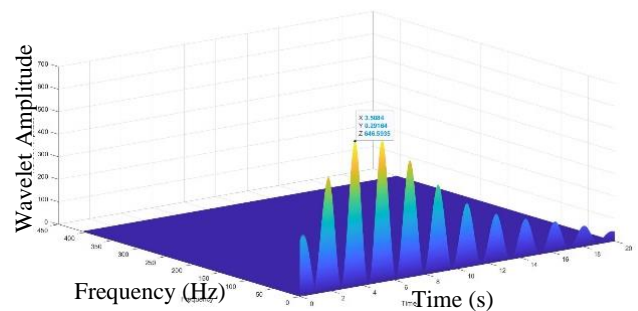


Fig. 6. Example wavelet amplitude map obtain in the present study

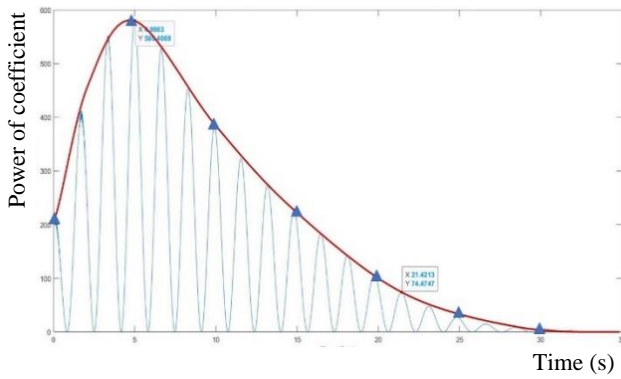


Fig. 7. Wavelet envelop on the selected natural frequency

IV. RESULTS AND DISCUSSION

Fast Fourier Transformation and Continuous Wavelet Transformation are used to obtain the Natural frequency and Damping ratio of the Altair Building in Colombo, Sri Lanka. Results were obtained under two directions. Channel 1 and Channel 3 are used for Direction 1 and Channel 2 and Channel 4 are used for Direction 2. Moreover, variations of results and values from empirical methods were illustrated.

A. The natural frequency of the building

Estimated Natural frequency values of the two directions of the building using Fast Fourier Transformation and Continuous Wavelet Transformation are shown in Table III.

The average Natural frequency for FFT analysis in Direction 1 is 0.2156 Hz and Direction 2 is 0.2157 Hz.

Similarly, the average Natural frequency for CWT analysis in Direction 1 is 0.2217 Hz and Direction 2 is 0.2232 Hz. Those results are in good agreement.

Calculated Natural frequency values according to the empirical methods that available in the literature are compared with the results in Table IV. Considering the values in Table IV, the estimated Natural frequency using ASCE 7-10 highly varies with the measured values. Also, values from Eurocode 1, AS/NZS, and Hong Kong design code are slightly different from the results.

However, estimated values from other methods are comparable with the measured value.

TABLE III. ESTIMATED NATURAL FREQUENCY VALUES OF THE BUILDING USING FFT AND CWT

	Natural Frequency (Hz)	
	Using FFT	Using CWT
Direction 1	0.2156	0.2217
Direction 2	0.2157	0.2232

Identification of Natural frequency for channel 1 in direction 1 and channel 2 in direction 2 using CWT and FFT are shown in Fig. 8. Those results for the same data set shows fair agreement.

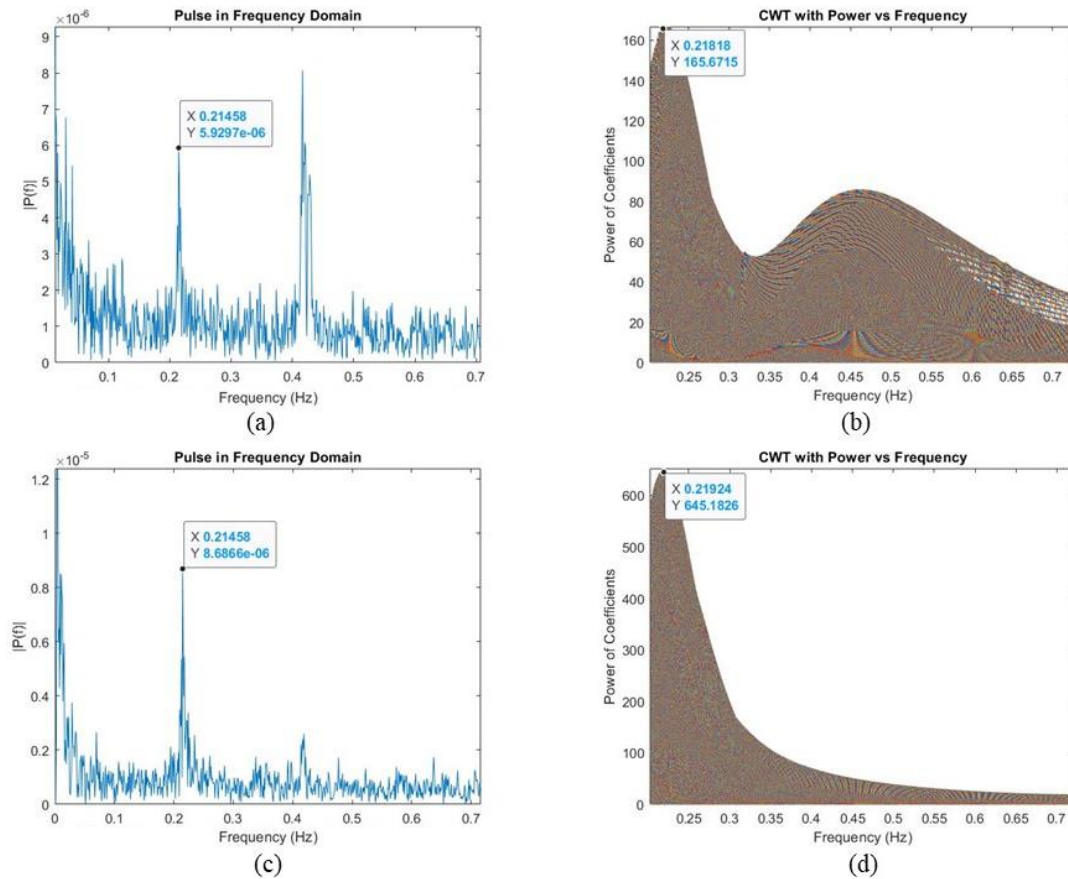


Fig. 8. Identification of Natural Frequency for channel 1 in direction 1 using (a) FFT and (b) CWT, for channel 2 in direction 2 using (c) FFT and (d) CWT

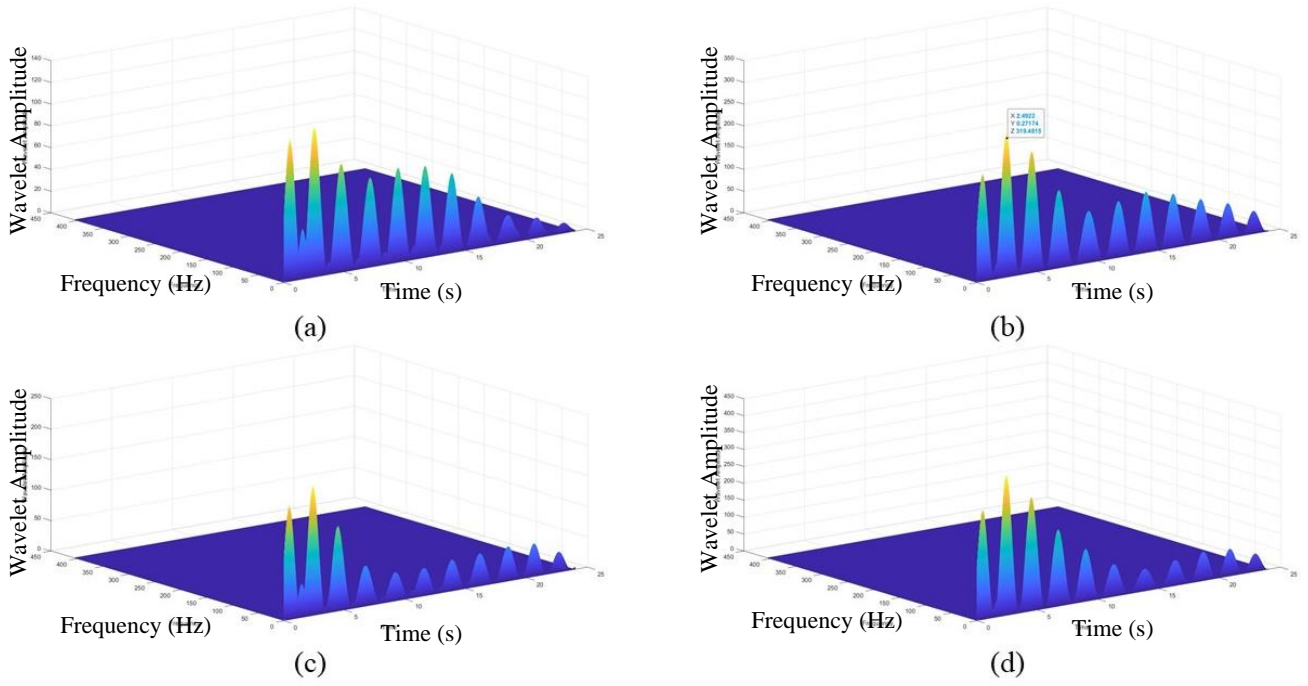


Fig. 9. Wavelet amplitude maps of (a) channel 1 in direction 1 (b) channel 2 in direction 2 (c) channel 3 in direction 1 and (d) channel 4 in direction 2

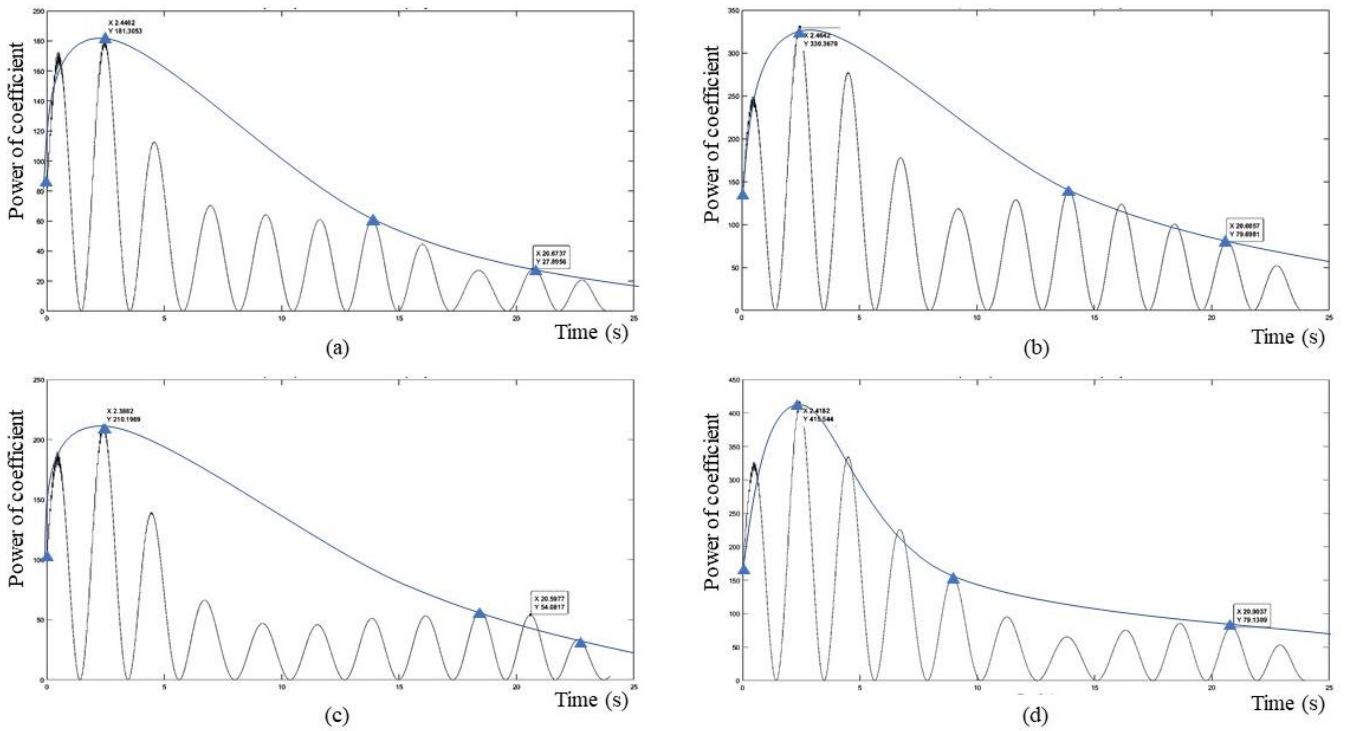


Fig. 10. Wavelet envelop of (a) channel 1 in direction 1 (b) channel 2 in direction 2 (c) channel 3 in direction 1 and (d) channel 4 in direction 2

TABLE IV. COMPARISON OF NATURAL FREQUENCY OF THE BUILDING FROM FFT & CWT WITH EMPIRICAL METHODS

Code	Natural Period (s)	Natural Frequency (Hz)
KBC (2009)	4.45	0.23
ASCE 7 -10	9.29	0.11
Eurocode 1	5.22	0.19
AS/NZS 1170	5.22	0.19
Hong Kong Design code	5.22	0.19
Lagomarsino	4.36	0.23
Yoon and Joo	4.62	0.22
Tamura	3.58	0.28
Using FFT	4.63	0.216
Using CWT	4.50	0.222

B. The damping ratio of the Building

Estimated Damping Ratio values of the two directions of the building using Fast Fourier Transformation and Continuous Wavelet Transformation are shown in Table V.

The average 1st mode Damping ratio from FFT analysis in Direction 1 is 0.64 % and Direction 2 is 0.34 %. Similarly, the average 1st mode Damping ratio from FFT analysis in Direction 1 is 0.68 % and Direction 2 is 0.42 %. In both methods, the Damping ratio in direction 1 is higher than the damping ratio in direction 2. Results have a slight difference. However, those are comparable with each other.

Calculated Damping ratio values according to the empirical methods that available in the literature are compared with the results in Table VI. Tamura [1] suggested the empirical value of $x/H \leq 2 \times 10^{-5}$ for use in the given equation. Considering the values in Table VI, estimation methods proposed in several codes have significant variation. Damping design values in Table VI are in the range from almost 0.5% to 2% for RC buildings, showing significant dispersion of design damping values.

Wavelet amplitude maps and wavelet envelopes for all four channels are shown in Fig. 9 and Fig. 10.

TABLE V. ESTIMATED DAMPING RATIO VALUES OF FOUR CHANNELS OF THE BUILDING USING CWT

	Damping Ratio (%)	
	Using FFT	Using CWT
Direction 1	0.64	0.68
Direction 2	0.34	0.42

TABLE VI. COMPARISON OF DAMPING RATIO VALUES FROM FFT AND CWT WITH EMPIRICAL METHODS

Code	Damping ratio (%)	
	Direction 1	Direction 2
ISO 4354	1.20	1.20
ASCE 7 -10	2.00	2.00
Eurocode 1	1.57	1.57
AS/NZS 1170	0.75	0.75
ESDU 83009	0.58	0.58
Yoon and Joo	0.75	0.80
Tamura	0.48	0.55
Using FFT	0.64	0.34
Using CWT	0.68	0.42

V. SUMMARY AND CONCLUSIONS

In this paper, Natural frequencies and Damping ratios of the first mode of a high-rise RC structure were evaluated. The acceleration data was acquired using wired accelerometer sensors for analysis. Random decrement method was applied for ambient signals to reduce the computational time. Normalized ambient vibration signals were analyzed using CWT and FFT.

A comparison study was done between results obtained in FFT and CWT, based on the results it can be concluded that the methodology proposed in this paper using CWT is more appropriate to estimate the Natural frequency and Damping ratio of tall buildings. Other than that, The CWT analysis is time-consuming compared to FFT. Further application of CWT based damping identification method is recommended to estimate damping of existing tall buildings in Sri Lanka.

Although Sharp peaks are provided in CWT to identify natural frequency in power of coefficient variation with frequency. These peaks showing a much better representation of the natural frequency of the building than Fourier amplitudes obtained from FFT while FFT provides several spikes. Furthermore, Empirical methods for estimate Natural frequency also show fair agreement with both measured values from FFT and CWT.

However, damping ratio values from empirical methods are in the range from almost 0.5% to 2% for RC buildings, showing significant dispersion of design damping values. Measured Damping values in this study are in good agreement with AS/NZS 1170 and amplitude-dependent estimation methods. Based on the results of this research frequency and amplitude-dependent estimation methods are recommended for the damping estimation of tall buildings.

REFERENCES

- [1] Y. Tamura, "Damping in Buildings and Estimation Techniques," *Advanced Structural Wind Engineering*, pp. 347–376, 2013, doi: 10.1007/978-4-431-54337-4_13.
- [2] R. Smith and M. Willford, "Damping in Tall Buildings – Uncertainties and Solutions," *IABSE Congress, Chicago 2008: Creating and Renewing Urban Structures – Tall Buildings, Bridges and Infrastructure*, 2008, doi: 10.2749/222137908796225618.
- [3] T. Arakawa and K. Yamamoto, "Frequencies And Damping Ratios Of A High Rise Building Based On Microtremor Measurement," *13th World Conference on Earthquake Engineering*, Aug. 2004.
- [4] Y. Kankanamge, Y. Hu, and X. Shao, "Application of wavelet transform in structural health monitoring," *Earthquake Engineering and Engineering Vibration*, vol. 19, no. 2, pp. 515–532, Apr. 2020, doi: 10.1007/s11803-020-0576-8.
- [5] T.-H. Le and Y. Tamura, "Modal Identification of Ambient Vibration Structure using Frequency Domain Decomposition and Wavelet Transform," *The Seventh Asia-Pacific Conference on Wind Engineering*, Nov. 2009.
- [6] D.-J. Yoon, W. J. Weiss, and S. P. Shah, "Assessing Damage in Corroded Reinforced Concrete Using Acoustic Emission," *Journal of Engineering Mechanics*, vol. 126, no. 3, pp. 273–283, Mar. 2000, doi: 10.1061/(asce)0733-9399(2000)126:3(273).
- [7] K. Gurley, T. Kijewski, and A. Kareem, "First- and Higher-Order Correlation Detection Using Wavelet Transforms," *Journal of Engineering Mechanics*, vol. 129, no. 2, pp. 188–201, Feb. 2003, doi: 10.1061/(asce)0733-9399(2003)129:2(188).
- [8] Y. F. Ji and C. C. Chang, "Nontarget Stereo Vision Technique for Spatiotemporal Response Measurement of Line-Like Structures," *Journal of Engineering Mechanics*, vol. 134, no. 6, pp. 466–474, Jun. 2008, doi: 10.1061/(asce)0733-9399(2008)134:6(466).
- [9] T. Ha, S.-H. Shin, and H. Kim, "Damping and Natural Period Evaluation of Tall RC Buildings Using Full-Scale Data in Korea," *Applied Sciences*, vol. 10, no. 5, p. 1568, Feb. 2020, doi: 10.3390/app10051568.
- [10] S. R. Ibrahim, "Random Decrement Technique for Modal Identification of Structures," *Journal of Spacecraft and Rockets*, vol. 14, no. 11, pp. 696–700, Nov. 1977, doi: 10.2514/3.57251.
- [11] M. Kolling, B. Rsnik, and A. Sargsyan, "Application of the random decrement technique for experimental determination of damping parameters of bearing structures."
- [12] Y. Tamura and S. Suganuma, "Evaluation of amplitude-dependent damping and natural frequency of buildings during strong winds," *Journal of Wind Engineering and Industrial Aerodynamics*, vol. 59, no. 2–3, pp. 115–130, Mar. 1996, doi: 10.1016/0167-6105(96)00003-7

Economic Feasibility of a Hybrid Energy System for Kalpitiya Peninsula from Selected Technologies

Kavinda R. Atapattu
Department of Mechanical Engineering
University of Moratuwa
Moratuwa, Sri Lanka
kavi.rukshan@gmail.com

Prof. Rahula A. Attalage
Emeritus Professor
University of Moratuwa, Sri Lanka
Dean Faculty of Graduate Studies &
Research, Sri Lanka Institute of
Information Technology (SLIIT)
rattalage@hotmail.com

Abstract— The technical potential and economic feasibility of an on-grid renewable energy based microgrid (MG) system in view of curtailing fossil fuel electricity generation was investigated in this study. Reducing the dependency on national grid could ensure economic benefits, improved supply reliability and cost effective grid interconnection of renewable sources. As a case study, Kalpitiya peninsula in Puttalam was selected after critically evaluating the available renewable potential of solar photovoltaic (PV), wind, biomass and municipal solid waste (MSW). Four (04) microgrid combinations were simulated in HOMER Pro (Hybrid Optimization of Multiple Electric Renewables) for a project life of 20 years. Economics of each optimised MG combination were compared with the base case where Kalpitiya peninsula is fed from fossil fuel based (i.e.: diesel) power transmitted through national grid. Most economical on-grid MG from a private investors' perspective consisted 12 nos. 850 kW wind turbines, 4 nos. 1 MW MSW plants & 2 nos. 1 MW biomass plants with a discounted payback of 2.68 years. From utility supplier's (i.e.: Ceylon Electricity Board-CEB) perspective, the most economical on-grid MG comprised of 12 nos. 850 kW wind turbines, 03 nos. 1250 kW wind turbines and 2 nos. 1 MW of biomass plants where annual cost saving against the base case was estimated as LKR 350.5 Mn equivalent to remove a 1 MW diesel generator for 353 days per year. On-grid MGs contribute towards increasing renewable energy share in the system cost effectively by curtailing the oil burning thermal power generation. The study methodology could also be referred when incorporating more renewables to utility grid to achieve national energy targets.

Keywords — Microgrid, Renewable energy, HOMER Pro, Kalpitiya peninsula

I. INTRODUCTION

Energy is becoming a basic need for almost every human being in 21st century since the human needs become more complex and sophisticated in this digital age. Evolving trend in world economic sector is to align with the sustainable development principles mainly due to conservation of limited resources which is now at prime importance. Therefore the energy sector, which has a direct impact on economic activities, is essentially moving towards sustainability hence the renewable energy share in the energy mix of many countries is increasing day by day. The estimated annual average expenditure of fossil fuel imports is about 25% of the Sri Lankan import expenditure and about 50% of income earned from export [1]. Therefore, the energy sector is obviously causing a huge impact on the balance of trade of the country and exchange rates as well.

In Sri Lanka, both conventional renewable energy sources such as major hydro and non-conventional renewable energy (NCRE) sources such as solar PV, wind power etc. are also

utilised consistently in the energy mix, which is positively influenced to the country's economic and environmental perspectives. Total installed power generation capacity of Sri Lanka is approximately 4,046 MW, consists 900 MW of coal power, 1,575 MW of oil burning thermal power, 1,379 MW of hydro power and 544 MW of NCRE sources such as mini hydro, solar PV, wind and biomass power plants. The annual total electricity demand of the country is about 15,374 GWh in 2018 and the expected annual demand growth is around 4-6% [2].

Intermittency is an inherent property of renewable energy technologies such as wind, solar PV which make several technical challenges on incorporating them to a utility grid. Rather than connecting NCRE's individually, a cluster of NCRE's could be connected to utility grid as a MG. A MG is a group of interconnected loads and Distributed Energy Resources (DERs) with clearly defined electrical boundaries that behaves as a single controllable unit with respect to the power system [3]. It can be viewed as a bunch of local electrical sources and electrical loads which are operated in a synchronized connection with a conventional power grid while it can also be functioned as an autonomous system in off-grid condition [4]. Being a regionally limited power system, microgrid optimize the power quality and economic benefits while increasing the reliability, sustainability of power supply through operating in on-grid, off-grid or in dual modes continuously by changing the characteristic of the connection with the grid [5].

The overall paper is presented in 06 sections. Literature review includes a summary of results obtained from MGs modelled in different configurations for various purposes in both foreign and local contexts. Problem definition describes the opportunity for a MG in Kalpitiya peninsula and the procedure of conducting the study aligning with aim, objectives is presented in methodology. Data on costs and resource availability of selected renewable energy technologies are presented in modelling of microgrid section. Subsequently the results obtained from HOMER Pro simulations are presented with economic comparison between each MG configuration and the base case. Final thoughts and further study opportunities on MG in Kalpitiya peninsula are suggested in conclusion and future work section.

II. LITERATURE REVIEW

Feasibility of having a hybrid energy system with solar PV-wind-diesel technologies for a rural area in Saudi Arabia was studied by S. Rehman, A.M. Mahbub, J. Meyer and L.M. Al-Hadhrani. It has concluded that, wind power generation would increase 5% for every 0.5m/s step increment of wind

speed while the levelised cost of energy (LCOE) of the hybrid power system showed a linear declination [6].

A. Shezan, R. Saidur, K.R Ula, A. Hossain, W.T. Chong and S. Julai of Department of Mechanical Engineering, University of Malaya had carried out a feasibility study of an off-grid hybrid energy system model for 02 hotels in a remote area, Cameron highlands, consisting of wind-battery storage-diesel using HOMER Pro. The study was conducted as a step towards eco-tourism in remote villages where 15 nos. of 10 kW wind turbines, 4 kW diesel generator with 02 battery storage units became the most economical and eco-friendly system [7].

A research on performance and feasibility of a wind-solar PV-diesel MG in rural areas of Bangladesh was carried out by M. Hasan and O. B. Momin. It was found that having a hybrid energy system with wind-solar PV-diesel has a total net present cost (NPC) less than diesel only system with less fuel consumption and reduces CO₂ emission by 60% rather than using utility grid energy [8].

Feasibility assessment of an off-grid solar PV-diesel hybrid energy scheme for a catholic church was conducted by A.V. Anayochukwu. Incorporation of solar PV to existing diesel generator system was the goal of this research and it was shown that a solar PV could be integrated to the system up to 53% where the generation from diesel could be reduced to 47% [9].

Hybrid energy system comprising of solar PV-wind-diesel-battery storage was proposed by M. Laidi, S. Hanini, B. Abbad, N. K. Merzouk and M. Abbas to electrify the remotely located houses in southern Algeria. MG with a renewable penetration of 47% was found to be the most economically viable alternative [10].

Technical and economic benefits of a hybrid energy system proposed for a rural area in Greece were studied by J. G. Fantidis, D. V. Bandekas and N. Vordos as an alternative for diesel power generation. To identify the critical parameters, sensitivity analysis was carried out and competitive technological scenarios in future were also discussed [11].

A review on optimal sizing techniques of hybrid energy systems done by V. O. Okinda and N. A. Odero proved that renewable power generation is a viable option to consider in place of utility grid power supply or a replacement for off-grid non fossil fuel based power generation for remote areas as well [12].

Further, optimally sized components of hybrid energy system is important for supply reliability and financial viability. Versatility of MGs make it financially and technically viable prospect hence a popular topic in research for electricity generation from renewable sources in the world.

In Sri Lankan context, a hybrid energy system with wind turbines and diesel generator was modelled by K. Ratneswaran for Eluvathiv island in Sri Lanka to run as an off-grid system. HOMER Pro was used to model the most economical and reliable system with 02 nos. diesel generators of 45 kW, 15 kW capacities, 80 kW wind turbine and battery storage along with a 16 kW AC-DC converter which has a payback period of 07 years [13].

A grid connected solar PV-wind MG model was investigated by M.V.P.G. Udayakanthi for a location selected

in Kirinda, Hambantota area after comparing the renewable energy potential of the particular site with the other parts of Sri Lanka. In that study southern coastal belt and north western coastal belt were identified as the best locations for MGs in terms of renewable potential availability. Finally, the study has modelled a solar PV-wind hybrid energy system with a payback period of 3-4 years using HOMER Pro software tool [14].

Mainly MGs (i.e.: hybrid energy systems) has been modelled, optimised and analysed for off-grid rural electrification schemes such as small islands with a community where the grid connection is distant. Few studies have discussed the optimisation techniques used to make the designed MGs much economical replacing fossil fuel fired systems. It could be found that HOMER Pro software tool, developed by National Renewable Energy Laboratory (NREL), Department of Energy in United States of America (USA), is the most commonly used microgrid modelling software for the optimisation, sensitivity analysis in comparison to other software packages such as HYBRID2, IHOGA etc.

III. PROBLEM DEFINITION

Most importantly the availability of renewable energy sources as well as the economics of the available energy sources would have to be considered when a MG is to be connected to existing system. In [14], north western coastal region was identified as one of the best locations to have a MG in terms of available potential of renewable energy sources such as wind, solar.

Kalpitiya peninsula is located in western coastal belt in Sri Lanka and administratively it is located in Puttalam district in North-Western province. Electricity to Kalpitiya peninsula is fed through Puttalam grid substation as per the existing arrangement of the local power distribution network. It is directly connected to the Anuradhapura & Kotugoda (Ja-ela) grid substations which are on 220 kV power transmission network where each substation is located approximately 100 km away from Puttalam grid substation. Therefore, generated power need to be transmitted more than 100 km for the end users in Kalpitiya peninsula where the transmission and distribution line losses generally accounts around 9% of generation. Hence, an opportunity of having a potential MG arises with abundantly available renewable energy sources in the particular geographical area to generate power locally and distribute within the Kalpitiya peninsula.

Therefore, it is important to evaluate the technical potential and economic feasibility of having a renewable energy based MG system that could be employed for Puttalam, Kalpitiya peninsula as a pilot project.

IV. METHODOLOGY

This research was aimed to evaluate the technical and economic feasibility of introducing a renewable energy based MG to Kalpitiya peninsula. Proposed MG scenarios were simulated to achieve the highest degree of autonomous control. Potential economic benefits of the proposed MG were also analysed over the conventional central grid electricity supply. In this study, a detailed and optimised model was suggested to be implemented as a pilot project by using a globally accepted software tool HOMER Pro.

Initially, a suitable location to implement a MG was selected based on the potential of harnessing renewable

energy resources such as solar energy, wind energy, biomass energy etc. The distance of the utility grid connection was also concerned. In this perspective, Kalpitiya peninsula was selected as the area of interest to implement the proposed MG system.

Then the actual hourly electrical load data set of Kalpitiya peninsula was collected to study the variation of power consumption throughout the day and throughout the year. The derived hourly electrical load profile was used for the modelling of proposed MG. Modelling and optimisation of MG was done from industrially accepted commercial MG modelling software called HOMER Pro.

Simulations were performed using wind resource data, solar resource data published in NREL database and National Aeronautics and Space Administration (NASA) surface meteorology and solar energy database, which are available in HOMER Pro as inbuilt libraries for Kalpitiya peninsula. Cost data of solar panels, wind turbines, biomass power generation and MSW power generation was manually included to the simulations. The particular global cost data trends of renewable energy technologies were referred from the publications of International Renewable Energy Agency (IRENA). Financial data such as inflation rate, nominal discount rate and exchange rate was extracted from recent publications of Central Bank of Sri Lanka (CBSL) to evaluate the economics of the optimised MG configuration. Evaluation of cost benefits for the proposed MG was performed in comparison with the base case of supplying power to Kalpitiya peninsula from existing grid connection.

V. MODELLING OF MICROGRID

In order to model the MG, hourly electrical load profile of Kalpitiya peninsula was derived from the existing 30 min interval readings. Available energy potential of each technology was evaluated along with the costs of each technologies in global market and Sri Lankan context.

Considering the present scenario, the power demand is currently being fulfilled through the national grid. In this research Kalpitiya peninsula is intended to become a virtual island as far as the power supply is concerned. Since the grid connection is already in place battery storage was not considered as a technological option in the proposed MG. Without battery storage, MG could generate power on its own and sell any excess power to national grid as well as draw power from national grid if there is any deficit in local power generation.

If any excess power is sold to national grid, it was assumed that it replaces the power generated from diesel/fuel oil. Therefore, power purchasing price from national grid is considered as Rs.36.00/kWh. Prevailing power purchasing, selling prices with national grid and the power generation costs of each technology related to each power source used in the MG had been studied in order to find out the most economical combination of sources based on their availability as well. Grid sell back price was taken as Rs.25.09 considering the MG is in the category of other non-conventional power producer according to the prevailing tariff announcement by Public Utilities Commission of Sri Lanka (PUCSL) with effect from 01.01.2012. Grid power purchasing and sell back rates were assumed to be the same within anytime of the day and throughout the project time period as well.

A. Load profile in Kalpitiya peninsula

As per the electrical single line diagrams it was understood that feeder 03 (33 kV feeder) of Puttalam grid substation is feeding the energy to Kalpitiya peninsula. Therefore, actual load demand data of Kalpitiya peninsula was obtained from Puttalam grid substation for each day in year 2018. The demand data were extracted from recorded in log sheets in Puttalam grid substation for every 30 min interval throughout each day. All the data were entered to microsoft excel and converted it to an hourly load profile.

Analysing the monthly average electrical load profile, it could be clearly observed that if the load demand in the month of April could be catered by the MG, power demand of almost all the other months of the year could be catered. Therefore, load demand of weekdays and weekends in the month of April is considered as annual load profile for further analysis.

B. Renewable power generation technologies

With the increasing popularity of power generation from renewable sources, massive continuous improvements had caused them to become competitive with fossil fuel technologies. Considering the cost values of onshore wind, offshore wind, solar and biomass projects implemented from 2010 onwards the costs had been reducing drastically to become more competitive against fossil fuel fired electricity generation in almost every part of the world [15][16]. Global weighted average cost of utility scale onshore wind power technology had been declined from 23% as a result of wind turbine price decreasing 39-58% from their peaks in 2007-2010 and developed turbines such as longer blades with bigger swept area, higher hub heights for higher power ratings per turbine [15]. As shown in Fig. 1, LCOE of solar PV has the highest reduction of 73% along with the reductions of concentrated solar power as well as onshore and offshore wind, biomass technologies [16].

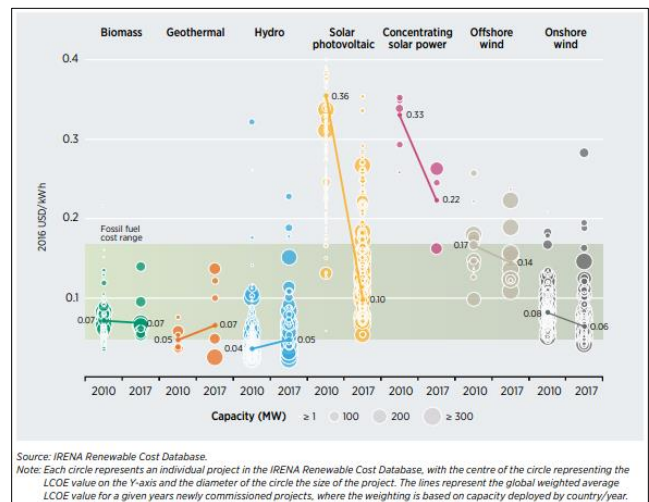


Fig. 1. LOCE of renewable energy technologies 2010-2017 [15]

1) Solar energy

Solar resource potential in Kalpitiya was compared to other parts of Sri Lanka in Table I, according to the solar resource maps developed by NREL. It is evident that west coast of Kalpitiya peninsula possesses 4.5 – 6.0 kWh/m²/day throughout the year which is close to average solar irradiance in Hambantota area.

TABLE I. DATA FROM SOLAR RESOURCES MAPS OF SRI LANKA DEVELOPED BY NREL [17]

Location	Average solar resource potential(kWh/m ² /day) as per NREL assessment (tilted at latitude)			
	South west monsoon (May to September)	North east monsoon (December to February)	1 st Inter monsoon (March to April)	2 nd inter monsoon (October to November)
South east near coastal area (eg : Hambantota)	5.0 – 5.5	5.5 – 6.0	6.0 – 6.5	5.5 – 6.0
Central hills (eg: Ambewela)	4.5 – 5.0	5.0 – 5.5	5.5 – 6.0	5.0 – 5.5
Jaffna peninsula	4.5 – 5.0	5.5 – 6.0	6.0 – 6.5	4.5 – 5.0
North west coast (eg : Kalpitiya)	4.5 – 5.0	5.0 – 5.5	5.5 – 6.0	4.5 – 5.0

Solar resource could be harnessed in Kalpitiya peninsula substantially as this is available throughout the year. Solar panel technologies such as all-black had been introduced in 2017 where the cost was competitive to other technologies. Crystalline and thin film technologies are becoming more economical year by year as a result of the technological improvements and market competition [16].

Typical global weighted average cost of utility scale solar power projects is around 1,210 USD/kW. The costs of 95th and 5th percentile of global weighted average for a utility scale solar power plant has dropped down from 3300 – 7900 USD/kW to 800 USD/kW and 2,700 USD/kW. Global weighted average cost had been reduced 74% from 2010 to 2018 period. Utility scale solar PV costs in different countries of the world had also been reduced by 66% - 84% from 2010 to 2018 period [16].

Elements in Table II were taken referring to global and local market data and used for HOMER Pro simulation.

TABLE II. COST OF SOLAR PANELS SELECTED FOR MICROGRID MODELLING [16]

Solar panel make & model	Capacity of a panel	Panel efficiency	Capital cost (USD/kW)	Annual O & M cost (USD/kW)
Sharp ND-250QCS	250 W	15.3	400	14

2) Wind energy

The wind resource availability and its variations had been studied by NREL in Sri Lanka. The resource availability in Kalpitiya is reviewed in comparison to other parts of the island in order to evaluate the possibility of wind power generation.

TABLE III. DATA FROM WIND RESOURCES ATLAS DEVELOPED BY NREL [18]

Location	Wind resource potential (Class)	Wind power density at 50 m elevation (W/m ²)	Wind speed at 50 m elevation (weibull parameter k=2)
South east coast (Hambantota to Kirinda)	Good	400 – 500	7.0 – 7.5
West coast (Puttalam, Mannar & islands near Jaffna)	Excellent	500 – 600	7.5 – 8.0
Central hills (Ambewela)	Excellent	500 – 600	7.5 – 8.0

According to the wind potential classification done by NREL, Kalpitiya peninsula possesses a considerable potential to harvest wind power compared to other areas of Sri Lanka with the annual average wind power density values 500 – 600 W/m² at 50 metre elevation (Excellent - Class 5).

NREL has published wind data in a wind potential assessment done in 2003. NASA has published monthly averaged wind speeds for 10 years (1983 – 1993) at 50m elevation in earth terrains similar to airports which was taken from Homer Pro libraries [18].

The measured wind speed data at 50 m elevation from the ground in Pawandhanavi wind power plant at Illanthadiya (Kalpitiya peninsula) shows a promising annual average of 6.63 m/s. However, the wind speed data given by NREL is much closer to onsite measurements while the data published by NASA showing a considerable under estimation from actual onsite measurements as compared in Table IV.

TABLE IV. COMPARISON OF WIND RESOURCE DATA IN PUTTALAM, KALPITIYA AREA

Month	Monthly average wind speed data (m/s) at 50 m elevation		
	NREL data (From HOMER Pro)	On site measurement (from Pawandhanavi)	NASA Data (From HOMER Pro)
January	5.60	5.25	4.84
February	3.80	6.04	4.09
March	4.60	4.58	3.56
April	5.20	2.99	3.61
May	9.10	6.17	5.39
June	9.90	12.22	6.65
July	9.30	10.21	5.83
August	9.70	9.32	5.97
September	8.70	7.68	5.17

October	7.00	6.92	4.15
November	5.20	3.75	3.79
December	5.60	4.32	4.59
Annual average	7.00	6.63	4.81

Typical global weighted average cost of utility scale onshore wind power projects is around 1,200 USD/kW. The cost of global weighted average for a utility scale wind power plants has dropped from 5,000 USD/kW in 1983 to 1500 USD/kW in 2018. Therefore, global weighted average total installation costs had been reduced 73% from 1983 to 2018 period. Typical country average of total averaged installed cost for wind power plants in India and China had come down to 1200 USD/kW while the costs in other countries varies in between 1660 USD/kW & 2250 USD/kW [16].

Annual operation and maintenance cost can be taken as 1.5% of total capital cost as recommended by PUCSL as well as the global energy data [19]. For the modelling of MG, wind turbines similar to Pawandhanavi plant (Gamesa-G58-850 kW) and Nirmalapura plant (Suzlon-S64-1250kW) were considered as given in Table V.

TABLE V. COST OF WIND TURBINES SELECTED FOR MICROGRID MODELLING [16]

Wind turbine make & model	Capacity of a turbine	Hub height (m)	Capital cost (USD)	Annual O & M cost per turbine (USD)
Gamesa-G58	850 kW	50	1,275,000	18,700.00
Suzlon-S64	1250 kW	50	1,875,000	27,500.00

3) Biomass energy

Staple food of Sri Lanka is rice and it is the crop for which highest land area was utilised for cultivation. Rice husk generated in paddy processing possesses a considerable potential for power generation in Ampara, Anuradhapura, Polonnaruwa & Kurunegala districts. As Puttalam is located as a bordering district to Anuradhapura and Kurunegala the rice husk is available for power generation. It is found that 30% of excess rice husk could be used for power generation with an annual energy potential of 180 GWh. [20]

The outer covering of paddy grain is called as rice husk and it accounts for about 20% of its weight. Availability of rice husk is the critical factor to decide whether it is possible to find the sufficient amount of fuel source to operate the power plant. Nearly 40 MT of paddy husk is needed per day for a 1 MW paddy husk fired power plant with a capital cost of 1250 USD/kW. [20]

In order to run 1 MW power plant with 90% plant factor 13,160 MT of paddy husk is needed. Even if the total paddy husk production in Puttalam district is collected for the power plant, the paddy production should be more than 65,800 MT per year. Paddy production statistics reveals that the availability of paddy husk in both yala, maha seasons within Puttalam district over recent years is marginal to run a 1 MW plant with a 90% capacity throughout a year (329 days) [21].

However, there is more paddy production in neighbouring districts such as Anuradhapura and Kurunegala where the paddy husk could be collected easily and transported to Puttalam [21]. In order to collect adequate amount of fuel there should be an organised mechanism unless the paddy husk would be used for other industrial purposes.

For a small scale power plant in which the capacity is less than 10 MW that operates on biomass or agricultural waste PUCSL has approved the capital cost should be around LKR 263 Mn/MW and annual operation and maintenance cost to be 5% of total capital cost [19]. Capital cost for paddy husk fired power generation was taken from [20] as depicted in Table VI.

TABLE VI. COST OF RICE HUSK POWER GENERATION FOR MICROGRID MODELLING [20]

Plant capacity	Capital cost	Annual O & M cost (5% of capital)	Fuel consumption	Plant life time
1 MW	1250 USD/kW	62.5 USD/kW	40,000 kg/day	20 years

4) Municipal Solid Waste(MSW) energy

A case study on economic and financial feasibility of MSW power generation from MSW based on western province of Sri Lanka was referred to identify viable MSW technologies in local context [22]. Direct incineration MSW was considered as the most suitable technology for this study to generate electricity without having a biogas, residual derived fuel (RDF) plant. Generation of waste amount in Sri Lanka has increased from around 6,400 ton/day in 1999 to 10,786 ton/day since 2009[23]. According to Table VII, most of the waste generation is collected from Western Province which accounts for 52% and smallest amount is collected from Uva Province.

TABLE VII. SOLID WASTE GENERATION & DISPOSAL SITES BY PROVINCES [23]

Provinces	Generation amounts (ton/day)	Collection amounts (ton/day)	Collection rates	Number of final disposal sites	
1. Northern	566	178	5%	31%	16
2. Eastern	785	347	10%	44%	40
3. North-central	616	91	3%	15%	35
4. North-western	1,134	187	5%	16%	45
5. Central	1,585	304	9%	19%	47
6. Sabaragamuwa	835	178	5%	21%	30
7. Uva	587	116	3%	20%	24
8. Western	3,502	1,793	52%	51%	52
9. Southern	1,158	264	8%	23%	60
Total	10,768	3,458	100%	32%	349

A survey conducted by Japan International Cooperation Agency (JICA) in 2016 has identified the status of several projects that were proposed in earlier studies. As per the report metro Colombo solid waste management project is underway after the completion of environmental impact assessment of the project. It is estimated to collect 1200 MT waste per day which are generated in metro Colombo region to Meethotamulla and transport them by train to Aruakkalu land filling site which is the quarry operated by Insee Cement, Puttalam. In that sense, the fuel source is already in the near proximity with the implementation of this project where a solid waste power generation facility would become feasible to be operated in the MG.[23]

For small scale MSW power plants, capacity under 10 MW, PUCSL had approved a capital cost value in NCRE tariff decisions as LKR 399 Mn/MW and about 7% of that capital costs as annual operation and maintenance cost as given in Table VIII[19].

TABLE VIII. COST OF MSW POWER GENERATION FOR MICROGRID MODELLING

Plant capacity	Capital cost	Annual O & M cost (7% of capital)	Fuel consumption	Plant life time
1 MW	2,216,666 USD/kW	155,160 USD/kW	100 Tons/day	20 years

C. Other constraints

In order to evaluate the financial viability of proposed MG configurations, financial data such as nominal discount rate, inflation rate and exchange rate had been given manually to HOMER Pro. Nominal discount rate is the interest rate where the money could be borrowed from a financial institution or from a bank. As per weekly financial indicators published by the CBSL, the average weighted lending rate (AWLR) specified for licensed commercial banks which had been varying around 14% in 2018, 2019 is taken as nominal discount rate and inflation rate is taken as 6% considering the annual average value of 2018. Exchange rate of 1 USD is taken as LKR 180 for the project life time of 20 years. Minimum renewable fraction and maximum annual capacity shortage were considered as 0%, 10 % (max.) respectively to ensure the reliability of supply during the unavailability MG components.

D. microgrid Simulation

The Optimal combination for utilising energy resources were obtained from HOMER Pro simulation with economics, emissions of each configuration. Configurations of MGs were considered as per Table IX and each of them were compared with the base case of supplying power from national grid.

TABLE IX. SIMULATED CONFIGURATIONS OF MICROGRID

Configuration	Included energy sources
A	Grid + wind 01 + wind 02 + solar
B	Grid + wind 01 + wind 02 + solar + biomass
C	Grid + wind 01 + wind 02 + solar + MSW
D	Grid + wind 01 + wind 02 + solar + biomass + MSW

Selected MG configurations with maximum 10,000 kW grid sales were compared with one another in order to develop more effective, economical and practical MG model. Sensitivity analysis for grid sale capacity in each configuration were also carried out in order to make the MG autonomous as much as possible while making the unmet load 0 kWh. Each optimised configuration was compared with the existing base case scenario of supplying power from national grid.

VI. RESULTS AND DISCUSSION

Simulation result of each microgrid configuration is summarized in Table X.

TABLE X. COMPARISON OF MICROGRID SIMULATION RESULTS

	MG Configuration A	MG Configuration B	MG Configuration C	MG Configuration D
Initial capital (USD)	26.6 Mn	23.4 Mn	24.2 Mn	26.7 Mn
Annual O&M cost (USD)	5.20 Mn	2.50 Mn	399,575	-1.99 Mn
LCOE (USD/kWh)	0.147	0.089	0.0489	0.00926
NPC (USD)	79.4 Mn	48.8 Mn	28.2 Mn	6.47 Mn
Renewable penetration (%)	42.6	67.2	87.6	97.5
Annual grid purchases (kWh/yr)	30,505,553	17,683,158	7,071,683	1,726,168
Annual grid sales (kWh/yr)	7,481,541	8,308,810	11,217,508	23,091,279
Annual CO ₂ emissions (kg/yr)	19,279,510	11,175,756	4,469,304	1,090,938
ROI (%)	10.9	24.6	32.3	37.8
IRR (%)	14.9	29.4	37.3	42.7
Simple payback (Years)	6.29	3.38	2.68	2.34
Discounted payback (Years)	8.86	4.05	3.11	2.68

One similarity is the exclusion of solar power and inclusion of 12 nos. 850 kW wind turbines into all economically optimised MG configurations. Additionally, MG configurations C, D did not include 1250 kW wind turbines where both included 04 nos. 1 MW MSW plants. MG configuration B included 03 nos. 1250 kW wind turbines and 02 nos. 1 MW biomass plants while MG configuration D also optimized with the latter. Referring to the Table X, it is clear that all projects are having a considerable IRR, discounted payback periods varying in between 2.68 to 8.86 years. Annual O&M cost in MG configuration D has become minus due to the grid sales counted 33.6% of consumed electricity [24].

When this MG is assumed to be an independent power producer (IPP), the economic benefits can only be calculated at the end of the year since there are many different energy sources integrated in the MG. Assume the revenue for MG operator is paid according to flat tariff given in Table XI announced by PUCSL.

TABLE XI. FLAT TARIFF FOR 01-20 YEARS FOR NCRE TECHNOLOGIES ANNOUNCED BY PUCSL ON 01.01.2012

Technology	All inclusive flat tariff for 1-20 years (LKR/kWh)
Mini hydro	16.70
Mini hydro - local	17.15
Wind	20.62
Wind - local	21.22
Biomass (Dendro)	25.09
Biomass (Agricultural and Industrial Waste)	17.71
Municipal Solid Waste	26.10
Waste heat	9.19

In the perspective of CEB, the cost could be different in each MG configuration when it is targeted to reduce the diesel power generation due to the localised power generation in MG as well as the net grid sales. Calculation in Table XII depicts the extra cost incurred by CEB even if the MG is operated as an Independent Power Producer (IPP) with the power purchasing agreement referred to current NCRE tariffs established by PUCSL in Table XI above.

TABLE XII. COMPARISON OF COST INCURRED BY CEB IN UTILITY GRID SUPPLY AND MICROGRID CASE

	Microgrid configuration A	Microgrid configuration B	Microgrid configuration C	Microgrid configuration D	
Base case	Total units consumed from grid (kWh/yr)	45,650,174	45,650,174	45,650,174	45,650,174
	Cost of grid power from diesel (LKR)	1,643,406,266	1,643,406,266	1,643,406,266	1,643,406,266
	Total cost for CEB (LKR)	1,643,406,266	1,643,406,266	1,643,406,266	1,643,406,266
Microgrid case	Grid purchases by microgrid (kWh/yr)	30,505,553	17,683,158	7,071,683	1,726,168
	Cost of power to feed microgrid from grid (LKR)	1,098,199,908	636,593,688	254,580,588	62,142,048
	Payments for grid sales by microgrid (kWh/yr)				
	Wind01 (kWh/yr)	14,783,581	14,783,581	14,783,581	14,783,581
	Wind02 (kWh/yr)	8,360,086	4,180,043	-	-
	Biomass(Rice husk) (kWh/yr)	-	17,520,000	-	17,520,000
	MSW (kWh/yr)	-	-	35,040,000	35,040,000
	Total cost incurred grid sales from microgrid (LKR)	477,222,414	701,309,127	1,219,381,440	1,529,660,640
	Total cost for CEB (LKR)	1,575,422,322	1,337,902,815	1,473,962,028	1,591,802,688
	Extra cost incurred by CEB for base case (LKR)	67,983,944	305,503,451	169,444,238	51,603,578

In terms of extra cost incurred for base case by CEB, MG configuration B is the having the best cost benefit while MG configuration D having the least benefit. Since the electricity is generated from diesel power plants in the base case, all MGs are beneficial in curtailing the power generation from diesel. From the benefit that CEB is getting by operating a grid connected MG in Kalpitiya peninsula, it is possible to calculate how many equivalent hours a particular diesel generator could be stopped in a calendar year as derived in Fig. 2.

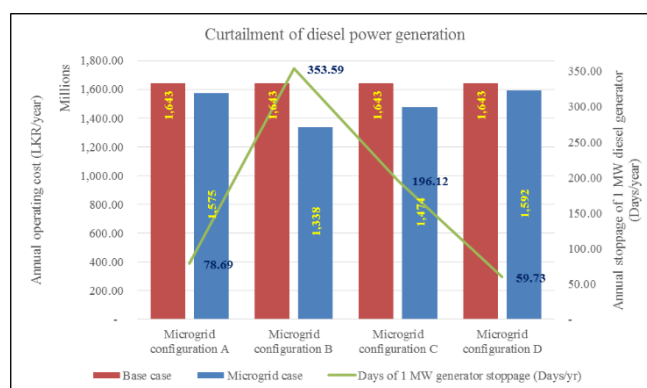


Fig. 2. Curtailment of diesel power generation

According to Fig. 2 above it is evident that 1 MW diesel generator could be almost left out if MG configuration B is implemented. It is equivalent to 01 month stoppage of 10 MW diesel generator per year without operating in the whole year when MG configuration B is considered. As far as the MG configurations A, C, D are concerned, the curtailment of diesel power generation is about 2.5 months, 6.5 months & 2 months respectively.

VII. CONCLUSION AND FUTURE WORK

The discounted payback periods of the simulated MGs were in the range of 2.68 to 8.86 years for the nearly same initial investments around 24.2 – 26.7 million USD which is promising. If the MG is planned to function as an IPP, the NPC of all the configurations are positive which means it is profitable.

MG configuration D comprising 12 nos. 850 kW wind turbines, 4 nos. 1 MW MSW plants & 2 nos. 1 MW biomass plants is the most profitable alternative for a private investor which offers an equivalent benefit for CEB to stop 1 MW diesel generator for 02 months. MG configuration B consisting 12 nos. 850 kW wind turbines, 03 nos. 1250 kW wind turbines and 2 nos. 1 MW of biomass plants is more attractive in CEB perspective as it gives the best financial saving which is equivalent to permanent curtailment of 1 MW diesel generator.

It could be clearly seen that increasing the contribution of renewable energy sources for distributed generation could serve loads with cost effective electricity generation and reduce the dependency on fossil fuel imports drastically. Reduction of fossil fuel imports can save huge expenditure and bring relief to the country's balance of trade. This study is an initial step towards the investigation of the most suitable strategy specially to integrate more renewable energy sources to Sri Lankan power system so as to provide quality, reliable, sustainable and affordable energy to every person while achieving economic prosperity of the nation.

During the HOMER Pro simulation, the availability of power generation from MSW and rice husk was assumed to be 100% due to the unavailability of data regarding the realistic maintenance schedules. Therefore, modelling of MG with realistic maintenance schedules would be a future work. Reliability improvement of electricity supply of Kalpitiya peninsula of each MG configuration could also be analysed. Further, financial benefits on energy savings by reduction of transmission energy loss could also be investigated as a future study.

REFERENCE

- [1] Sri Lanka Energy Sector Development Plan for a Knowledge-Based Economy 2015-2025, "Energy Empowered Nation", Ministry of Power and Energy, 2015
- [2] Long Term Generation Expansion Plan 2018-2037, Ceylon Electricity Board
- [3] P.Ferraro, E. Crisostomi, M. Raugi and F. Milano, "On the impact of Microgrid Energy Management Systems on Power System Dynamics", Department of Energy, Systems, Territory and Constructions Engineering, University of Pisa, Italy, 2016-2017.
- [4] D. Baghel, R. R. Tiwary, "Voltage balancing in solar based DC Micro-grid system," International Research Journal of Engineering & Technology (IRJET), vol. 04, issue. 01, pp. 964-968, January 2017.
- [5] Siemens AG, Microgrids, 2011.
- [6] S. Rehman, A. M. Mahbub, . J. Meyer and . L. M. Al-Hadhrami, "Feasibility study of a wind-solar PV-diesel hybrid power system for a village".
- [7] S. A. Shezan, R. Saidur, K. R. Ullah, W. T. Chong and S. Julai, "Feasibility analysis of a hybrid off-grid wind–DG-battery energy system for the eco-tourism remote areas," vol. 17, December 2015.
- [8] M. Hasan and O. B. Momin, "Performance Analysis and Feasibility Study of Solar-Wind-Diesel Hybrid Power system in Rural Areas of Bangladesh," International Journal of Engineering Research and General Science, pp. 410 - 420, September 2015.
- [9] A. V. Anayochukwu, "Feasibility Assessment of PV Diesel Hybrid Power system for an Isolated off Grid Catholic Church," Renewable Energies Reaseach Nucleus, pp. 49 - 63, 2013.
- [10] M. Laidi, S. Hanini, B. Abbad, N. K. Merzouk and M. Abbas, "Study of a Solar PV-Wind-Battery Hybrid Power System for a Remotely Located Region in the Southern Algerian Sahara: Case of Refrigeration," pp. 30-38, 2012.
- [11] J. G. Fantidis, D. V. Bandekas and . N. Vordos, "Techno-economical study of hybrid power system for a remote village in Greece," Recent Researches in Energy, Environment and Sustainable Development, pp. 30 - 35.
- [12] V. O. Okinda and N. A. Odero, "A review of techniques in optimal sizing of hybrid energy systems," International Journal of Research in Engineering, pp. 153 -161, November 2015.
- [13] K. Ratneswaran , "Hybrid Power System for Eluvaithivu Island Sri Lanka," Master of Science Thesis, pp. 1 - 61, 2011.
- [14] M.V.P.G. Udayakanthi, "Design of a Wind-Solar Hybrid Power Generation System in Sri Lanka," Master of Science Thesis, KTH School of Industrial Engineering and Management, pp. 1 - 61, 2015.
- [15] IRENA, "Renewable power generation costs in 2017," International Renewable Energy Agency, Abu Dhabi, 2018.
- [16] IRENA, "Renewable power generation costs in 2018," International Renewable Energy Agency, Abu Dhabi, 2019.
- [17] D. Renne, R.George, B. Marison and D. Heimiller, "Solar resource assessment for Sri Lanka & Maldives," National Renewable Energy Laboratory, U.S. Department of Energy, Colarado 80401-3393, 2003.
- [18] D. Elliot, M. Schwartz, G. Scott, S. Haymes, D. Heimiller and R. George, "Wind Energy Resource Atlas of Sri Lanka & the Maldives," National Renewable Energy Labortory, U.S. Department of Energy, Colarado - 804101 - 3393, 2003.
- [19] PUCSL, "Decision on Non-Conventional Renewable Energy Purchase Tariffs 2012-2013", Public Utilities Commission of Sri Lanka, 05th October 2012.
- [20] A. S. Rodrigo &. S. Perera, "Potential & viability of rice husk based power generation in sri lanka," Engineer, vol. XXXXVI, No. 04, pp. 9-17, 2013.
- [21] "www.ceicdata.com," CEIC, 2020. [Online]Available: <https://www.ceicdata.com/en>.
- [22] J. Senanayake, "Economic & Financial Feasibility of Power Generation from Municipal Solid Waste : A case study based in western province of Sri Lanka," University of Moratuwa, Katubedda, 2014.
- [23] Japan International Cooperation Agency(JICA), "Data Collection Survey on Solid Waste Management in Democratic Socialist Republic of Sri Lanka," Kokusai Kyogo Co. Ltd, 2016.
- [24] Homer Energy LLC, "Homer Pro 3.12 User Manual", [Online]Available:<https://www.homerenergy.com/products/pro/docs/3.12/index.html>, 13th August 2018.

PATH LOSS EXPONENT ESTIMATION FOR ESP8266 WIRELESS SENSOR NETWORK

D.S. De Silva
Senior Lecturer,
*Department of Electrical and
Information Engineering
Faculty of Engineering, University of
Ruhuna*
Galle, Sri Lanka
saman@eie.ruh.ac.lk

Nishshanka NMKH
*Department of Electrical and
Information Engineering
Faculty of Engineering, University of
Ruhuna*
Galle, Sri Lanka
kanishkanishshaka@gmail.com

Dineshika WMR
*Department of Electrical and
Information Engineering
Faculty of Engineering, University of
Ruhuna*
Galle, Sri Lanka
ruwaniwickramasinghe95@gmail.com

De Alwis TADYD
*Department of Electrical and
Information Engineering
Faculty of Engineering, University
of Ruhuna*
Galle, Sri Lanka
yashodealwis@gmail.com

Abstract—Wireless networks are an evolving technology that has been embraced in many applications currently. The study of radio propagation models plays an important role in these wireless systems, both in theoretical and practical terms. In this regard, one of the most important parameters that has been commonly considered in wireless communications research is the path loss exponent. In the literature, there are many theoretical evaluations of path loss exponents available for wireless networks in different environments such as free space, building and industrial. In this paper, in order to test the experimental analysis, the area where ESP8266 Wi-Fi modules are commonly deployed was chosen. Using the Obtained Signal Strength Indicator (RSSI), path loss and path loss exponents are determined and the standard deviation of path loss is also calculated based on them. The theoretical research available in the literature compares all the calculated parameters.

Keywords—path loss exponents, received signal strength indicator, wireless sensor network, esp8266

I. INTRODUCTION

Wireless sensor networks are evolving as a solution for monitoring and regulating a multitude of environments and it is important to characterize them because of the complexities of application scenario [1]. For many WSN applications, location-awareness is a requirement today. Location-aware wireless sensor networks have recently reached almost every area of life [2]. The most popular technique for gathering the location information of each sensor node is received signal strength indicator (RSSI) measurements. RSSI-based localization is an excellent alternative in terms of power requirements and hardware costs.

Although RSSI position estimation offers competitive advantages, but more research is required to improve the situation. Because the outcome can be inaccurate and inconsistent, especially in the indoor setting [3]. For an example, there are no of obstacles and reflectors inside an indoor. So, multipath propagation can be a significant source of error to get the inaccurate RSSI measurements because of the presence of these various reflection and dispersion bodies in the propagation scene [4]. In addition to that, deviation of

parameters which are caused to inaccurate measurements is triggered by environmental changes such as temperature, humidity, human activities, and object arrangement [3]. Therefore, all of these concerns are combined, leading to the need for improvement of specific radio range specifications.

When we are dealing with WSNs there are certain criteria that must be taken into account in both theoretical and functional research when designing the network because of the wireless existence. Since, they have a direct effect on the efficiency of the communication between the transmitter and the receiver [5].

Since the precision of the exponent of path loss directly affects the outcomes of the RSS-to-distance conversion, in distance-based wireless sensor network localization, where distance from the RSSI measurements is calculated, path loss exponent estimation (PLE) plays an important role [6]. Due to various phenomena such as free space path loss, reflection, diffraction, fading, shadowing path loss can occur [3]. To obtain an accurate estimate of the inter-sensor distance from the corresponding RSS measurement, accurate knowledge of the PLE is required.

There are a large number of theoretical analyses on path loss exponent estimation without taking account of realistic measurements and environmental factors. Existing methods either consider that the PLE is known a priori by assuming that the WSN environment is free space, or obtain the PLE by measuring both RSS and distances in the same WSN environment before device deployment by comprehensive channel measurement and modelling [3].

There are no of research which were done for analyse the behaviour of PLE at a wireless sensor Network. In [3] online-update small-to-big rectangular measurement, and online-update big-to-small rectangular measurement approaches was used to analyse the accuracy and stability of PLE for localization.

In [5] ,[7] they analysed PLE for different types of WSN environments.

TABLE I. PATH LOSS EXPONENTS FOR DIFFERENT ENVIRONMENTS

Environment	Path Loss Exponent
Free Space	2
Urban area cellular radio	2.7 to 3.5
shadowed urban cellular radio	3.0 to 3.5
In building line of sight	1.6 to 1.8
Obstructed in building	4.0 to 6.0
Obstructed in factories	2.0 to 3.0

Through this research we try to analyse accurate value for path loss exponent for this ESP8266 wireless environment.

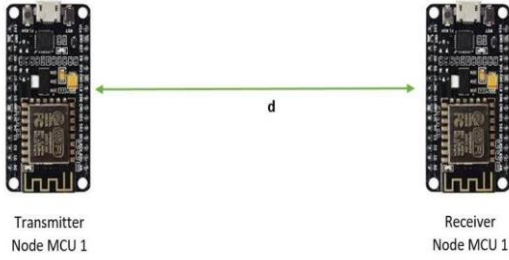


Fig. 1. Experimental Setup

II. PATH LOSS EXPONENT ANALYSIS

In a Wi-Fi network, the obtained electromagnetic wave power varies according to the distance between the transmitter and the receiver. RSSI value can be calculated using following formula.

$$p_d = p_{(d_0)} - 10n \log_{10}\left(\frac{d}{d_0}\right) \quad (1)$$

Where,

n - Path loss exponent

d - Distance between transmitter and receiver

$p_{(d_0)}$ Received signal strength at reference distance

Based on the studies available in literature and measurements, by minimizing the mean square error of the received power and the estimated power $(p - p^1)^2$ where p is the received power at distance d and p^1 is the estimated power of p , one can solve the equation in order to find n as follows:

$$f(n) = \sum_{i=1}^k (p_i - p_0 + 10 \log_{10}\left(\frac{d_i}{d_0}\right))^2 \quad (2)$$

Where k represents the number of transmitter distances. An approximation of path loss, n , can be found by equating the derivative of $f(n)$ to zero.

$$\frac{df(n)}{dn} = \sum_{i=1}^k 20 \log_{10}\left(\frac{d_i}{d_0}\right) (p_i - p_0 + 10 \log_{10}\left(\frac{d_i}{d_0}\right)) \quad (3)$$

When

$$\frac{df(n)}{dn} = 0 \quad (4)$$

$$\sum_{i=1}^k 20 \log_{10}\left(\frac{d_i}{d_0}\right) (p_i - p_0 + 10 \log_{10}\left(\frac{d_i}{d_0}\right)) = 0 \quad (5)$$

Let

$$E(n) = \sum_{i=1}^k (p_i - p_i^1)^2 \quad (6)$$

$E(n)$ be the summation of the difference between the received power and the estimated one. The standard deviation can be computed as:

$$\sigma = \sqrt{E(n)} / k \quad (7)$$

The path loss and standard deviation vary depending on the environmental conditions in various environments.

III. DATA COLLECTION AND ARRANGEMENT

Following figure 2 shows the experimental setup which we have used for collect data. We planned an indoor field (10 m x 10 m) with barriers in the field to conduct the tests with our proposed process. This is to prevent effects on our findings if it is extended to other environments. Because we use Wi-Fi sensor nodes (ESP8266 Wi-Fi module) for this experiment. When conducting field measurement activities, also we have minimized human interference.

Our suggested calculation method attempts to minimize the error of position caused by location-dependent parameters. In order to accomplish this aim, our recommended solution varies dramatically from the ordinary arrangement. Because in our proposal, receiver becomes fixed rather than adjusting the receiver's position we suggest that the position of the transmitters must be changed. The reason for keeping the receiver fixed and adjusting the transmitter location is to establish a situation such that the receiver appears at the middle of the transmitters at all times.

The field of calculation can be of any form. So we simply choose the circular shaped localization to prevent uncertainty by forming the circular region. For the transmitter and the receiver we used the ESP 8266 Wi-Fi module. We used the USB transfer for the receiver ESP266 module.

In here we used Wi-Fi network. So co channel interference is one of main problem that can be occurred. Because there were number of transmitters. This results in interference when esp8266 nodes operate in adjacent channels in same air

interface. Therefore, we focused our attention to preserve the space between operational channels by at least 20MHz to minimize the co-channel interference.

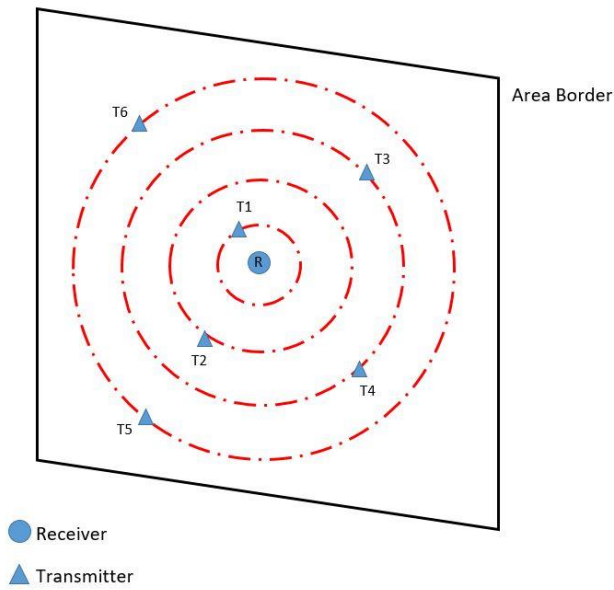


Figure 2: Circular Shaping

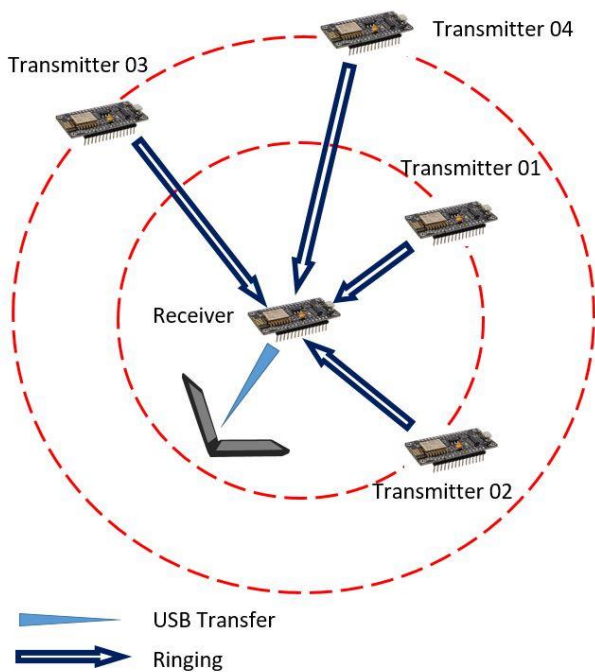


Figure 3: Interaction connections between receiver and the transmitter

For the data measurements gather during this task, we collect data for every each triggering signal provided. These received RSSI values were detected and transmitted to the

computer-attached to the base-station node (Receiver). The machine showed the RSSI value that received.

The whole process involves signal detecting, ranging, and data collecting. We marked a straight line along the center of the area. The measurement started with a distance of 50cm from transmitter to receiver until 800cm away from transmitter. Between the two ends, measurement was done in every 50 cm. We have got three measurements for each distance from three separate points of each circle. The test has been repeated for 16× 3 points. And calculated mean value of three measurements for the particular distance.

$$\text{mean RSSI value} = \frac{T_1 + T_2 + T_3}{3}$$

..

IV. RESULTS AND DISCUSSION

The ESP8266 Nodemcu Wi-Fi sensor nodes have been placed in a hostel room where some obstacles (ex: bunk beds, small cupboards, Tables and chairs) were existing and several Wi-Fi networks such as routers were operating.

TABLE II. DISTANCE VS MEAN OF RSSI READINGS

Distance (m)	Mean of RSSI (dB)
0.5	-23.15
1.0	-37
1.5	-45.10
2.0	-50.84
2.5	-55.31
3.0	-58.95
3.5	-62.03
4.0	-64.70
4.5	-67.05
5.0	-69.15
5.5	-71.05
6.0	-72.80
6.5	-74.40
7.0	-75.90
7.5	-77.25
8.0	-78.54

For the distance 1m apart from the receiver and the transmitter was measured at many locations by moving the transmitter for varies locations on the 1m apart circle. So the mean value for the 1m apart was found to be -37 dB. In this experiment we got the RSSI value received at the 1m as reference

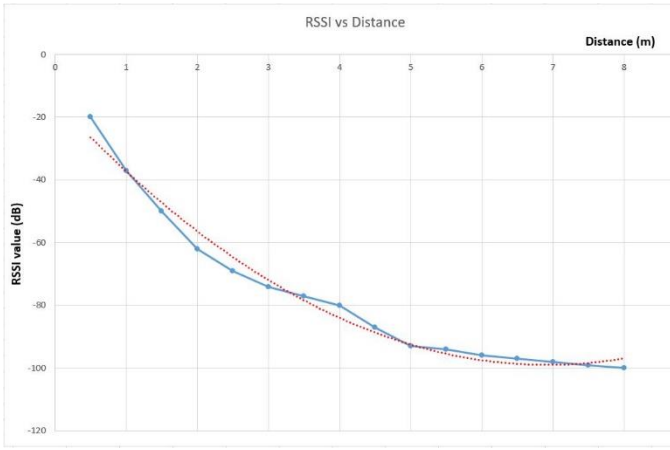


Figure 4: The graph of RSSI value Vs Distance

We have got three measurements for each distance from three separate points of each circle. Above figure 4 shows the average RSSI values vary for each distance. According to the graph shown in figure 4, the gradient of the graph is decreasing with the increase of distance. In the figure 04 experimental data points are shown in blue color.

From observation, the result is less variation and fluctuation. Its trace is also almost have a smooth line

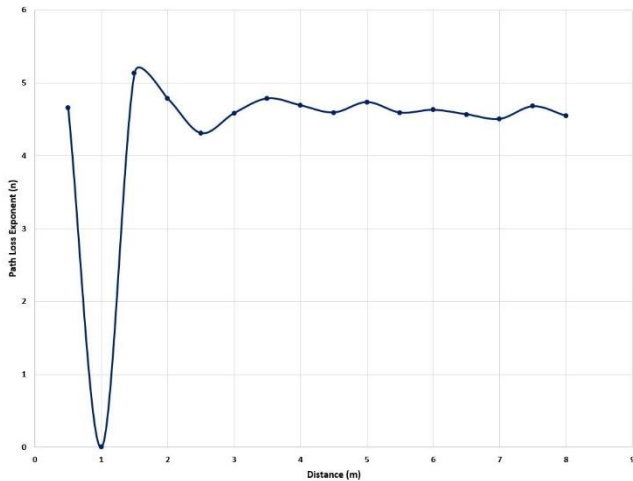


Figure 5: The Graph of Distance Vs Path Loss Exponent

The path loss exponent has been calculated using these average RSSI values. Figure 5 present the calculated pass loss exponent for each distance by using equation 1. According to the graph, the path loss exponent values has varied in between 4 and 5.

By using the average RSSI value that we analyzed using experimental data and equation 5, we have obtained average value for path loss exponent. Average path loss exponent for the selected environment is 4.6.

We have calculated the standard deviation using equation 6 and 7, when $n=2$, $n=4$, $n=4.6$ and $n=6$. Table 2 represents that standard deviation data

TABLE III: STANDARD DEVIATIONS FOR DIFFERENT PATH LOSS EXPONENTS

Path Loss Exponent	Standard Deviation
$n = 2$	4.095
$n = 6$	0.972
$n = 4.6$	0.156
$n = 6$	2.179

According to the table 1, PLE of an obstructed in building which has wireless sensor network is lies between 4 and 6. The obtained PLE for our case is 4.6 which is lies on that range.

Figure 6 contain the graphs of RSSI value vs distance at the free space (when $n=2$), when $n=6$ and $n=4.6$.

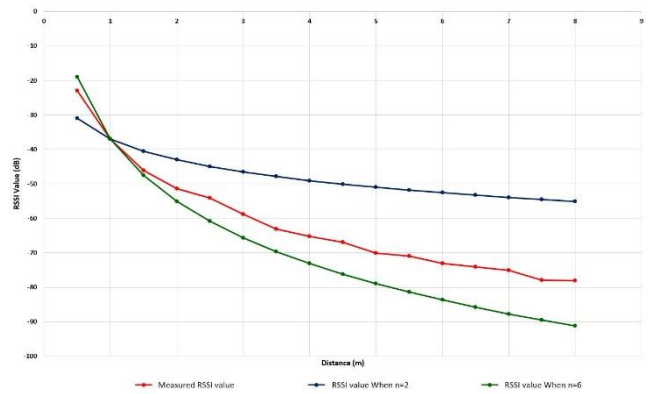


Figure 6: The graph of Distance Vs RSSI value at different path loss exponents

V. CONCLUSION

Our research has shown that changing the measurement arrangement will improve the accuracy of path loss exponent estimation in wireless sensor network environment. When compared to other estimation of path loss exponents in previous researches for different environments, the estimation accuracy can be increased even further using our proposed circular calculation for wireless sensor network environment. Table 3 summarizes the efficiency analysis of the outcome for the wireless sensor network with other environments.

TABLE IV: PATH LOSS EXPONENTS FOR DIFFERENT ENVIRONMENTS

Environment	Path Loss Exponent value
Free Space	2.0
Wireless Sensor Network	4.6
Obstructed in building	4.0 to 6.0

Based on the difference environments wireless sensor network has path loss exponent is higher than the free space and lies in the range of obstructed in building environment.

ACKNOWLEDGMENT

We would like to express our gratitude to recent module coordinator of Introduction to Research Dr. Anuradha Mendis, lecturer, Department of Electrical and Information Engineering, University of Ruhuna, former module coordinator of Introduction to Research Dr. Iromi Ranaweera, senior lecturer, Department of Electrical and Information Engineering, University of Ruhuna and Dr. Chandana Perera, senior lecturer, Department of Electrical and Information Engineering, University of Ruhuna. And we would like to extend our gratitude to our supervisor Mr. Saman De Silva, senior lecturer, Department of Electrical and Information Engineering, University of Ruhuna for guiding us to successfully accomplish this research.

REFERENCES

- [1] Y. Zhang, N. Meratnia, and P. Havinga, "Outlier detection techniques for wireless sensor networks: A survey," *IEEE Commun. Surv. Tutorials*, vol. 12, no. 2, 2010, doi: 10.1109/SURV.2010.021510.00088.
- [2] T. Nowak, M. Hartmann, T. Zech, and J. Thielecke, "A path loss and fading model for RSSI-based localization in forested areas," 2016, doi: 10.1109/APWC.2016.7738133.
- [3] C. C. P. -, P. C. O. -, and W. C. -, "Accuracy and Stability Analysis of Path Loss Exponent Measurement for Localization in Wireless Sensor Network," *Int. J. Digit. Content Technol. its Appl.*, vol. 7, no. 7, 2013, doi: 10.4156/jdcta.vol7.issue7.136.
- [4] S. Subedi, E. Pauls, and Y. D. Zhang, "Accurate Localization and Tracking of a Passive RFID Reader Based on RSSI Measurements," *IEEE J. Radio Freq. Identif.*, vol. 1, no. 2, 2017, doi: 10.1109/jrfid.2017.2765618.
- [5] G. Mao, B. D. O. Anderson, and F. Bariş, "Online calibration of path loss exponent in wireless sensor networks," 2006, doi: 10.1109/GLOCOM.2006.497.
- [6] J. Miranda *et al.*, "Path loss exponent analysis in Wireless Sensor Networks: Experimental evaluation," 2013, doi: 10.1109/INDIN.2013.6622857.
- [7] V. Dharmadhikari, N. Pusalkar, and P. Ghare, "Path Loss Exponent Estimation for Wireless Sensor Node Positioning: Practical Approach," in *International Symposium on Advanced Networks and Telecommunication Systems, ANTS*, 2018, vol. 2018-December, doi: 10.1109/ANTS.2018.8710123.

Development of Mechanical Ventilation Strategy to Achieve Thermal Comfort for Large Occupant Spaces

D. L. D. R Liyanage
*Department of Mechanical and
Process Engineering
Faculty of Engineering
University of Jaffna
Kilinochchi, Sri Lanka
2017e056@eng.jfn.ac.lk*

W. M. M. H. L De Silva
*Department of Mechanical and
Process Engineering
Faculty of Engineering
University of Jaffna
Kilinochchi, Sri Lanka
2017e023@eng.jfn.ac.lk*

K. Thurairaja
*Department of Mechanical
Engineering
Institute of Engineering Technology
Katunayake, Sri Lanka
kankeyan.t@gmail.com*

S. H. I Hameed
*Department of Mechanical and
Process Engineering
Faculty of Engineering
University of Jaffna
Kilinochchi, Sri Lanka
ifhaz@eng.jfn.ac.lk*

Abstract- Study and practical implementation of ventilation for the interior of buildings has been continuously evolving. It seems that as a result of the increase in global warming, people's tendency to work in indoor environments rises. This shows the need of establishing a ventilation system to provide the desired thermal comfort within the sets of limitations for buildings because being in a thermally comfortable environment can improve the effectiveness and efficiency of the people and hence the time spent inside can be more productive. To achieve the required thermal comfort level, mechanical ventilation systems are being used because of their higher reliability. In this paper, a design strategy is proposed by analysing 3D simulations of diffuser layouts in different configurations. The research investigates the airflow characteristics of vortex diffusers and their effect on thermal comfort. Modelling of the identified spaces was carried out using SOLIDWORKS and simulations were carried out using ANSYS Fluent. Mechanical Engineering Lecture Hall of the University of Jaffna was selected as the case study to interpret the strategies developed through this research. As another outcome of this study, the thermal comfort zone was developed to the Kilinochchi condition based on climatic data of the Kilinochchi district. The proposed strategy based on simulations provides a guideline to organize mechanical ventilation equipment for larger spaces to achieve the desired thermal comfort.

Keywords- *Thermal Comfort, Mechanically Ventilated Building, Computational Fluid Dynamics, Large occupant buildings, Diffuser layouts, Thermal comfort zones*

I. INTRODUCTION

Most of the time people stay inside and they are either in factories, offices, or academic institutes[1]. Due to the temperature and humidity, it is especially important to have a ventilation system in these places to provide people with thermal comfort. According to ISO 7730 thermal comfort is defined as the condition of mind which expresses satisfaction with the thermal environment. Being thermally uncomfortable affects the efficiency of the people and causes many other physical and psychological malevolent impacts; negative mood, symptoms of sick building syndrome, increments of heart rate and respiratory ventilation, etc[1][2][3]. Lack of ventilation can cause building up moisture, other pollutants, and odours inside a home, or a building[4]. There are mainly three types of ventilation systems; natural, mechanical, and hybrid. The typical ventilation process is done by Natural ventilation. For a large-scale building when many people are in the room, it will not be enough to provide good ventilation[5]. Further, considering the reliability of the ventilation systems, mechanical ventilation has the upper hand. Defining thermal comfort itself is a challenging task as thermal comfort can vary from person to person. Hence providing thermal comfort appropriately and evaluating it would be an even harder task. For the evaluation of thermal comfort PMV (Predicted Mean Vote) PPD (Predicted Percentage Dissatisfied) model is used. In that case, there are several factors to consider, mainly; air temperature,

air velocity, radiant temperature, humidity, clothing, and metabolic activity. Computational Fluid Dynamics (CFD) is beneficial because it is a user-friendly way to quickly solve many different types of flow problems. This provides users with a general understanding of fluid mechanics a tool to solve otherwise very complex fluid flow problems involving fluid-fluid, fluid-solid, or fluid-gas interaction. CFD analysis was carried out by researchers for various purposes such as studying the thermal comfort of occupants, optimization of the mechanical ventilation system, natural ventilation, and energy consumption in a building[6]. In this study, ANSYS FLUENT is used with the k- ϵ turbulence model for the CFD simulation.

Most of the previous research work has been done taking small spaces as the case study. In [6] the study has been done for a residential house. [7] considers a chamber of 40.3 m³ and In [8] kitchens are considered. The closest previous study is [9] which also considers a lecture hall. However, that study uses hybrid ventilation with ceiling fans and open windows. Four methods have been tested in that study while opening and while utilizing window rows and ceiling fans differently. Other than that, [10] analyses the influence of natural and forced ventilation on the thermal comfort of a lecturing room. In that study, the result has come as, when the lecture room is with full human capacity the available ventilation is not enough to provide thermal comfort to the hall. [5] States a method with smart windows which is still in the development stage. However, this study focuses on providing ventilation to large spaces such as university lecture halls with mechanical ventilation by considering different diffuser layouts and sizes which can be more generic. It is apparent that large spaces with a large number of occupants is not necessarily thermally comfortable. In this study a novel strategy of mechanical ventilation will be proposed to provide ventilation to such large occupant spaces. The study was carried based on the simulations done with computer software, mainly ANSYS FLUENT and SOLIDWORKS.

II. MATERIALS AND METHOD

A. CFD Simulations

SOLIDWORKS (2020 academic software) was used for developing the 3D models required for the airflow simulations and the models were saved in Parasolid format (*.x_t) to upload for the geometry model in ANSYS Fluent (2021 academic version) which was used for the airflow simulations. Developing the model of the air body was done by extruding the walls towards the inside of the room and subtracting the initial model. The dimension of the model with a single diffuser (figure 1) consists of four walls, ceiling, and floor. Each wall has 3.5 m height and 3 m width and outlet opening is of 0.45 m width and 0.3 m height. The ceiling consists of a vortex diffuser which has a 0.44 m diameter, in the center of it.

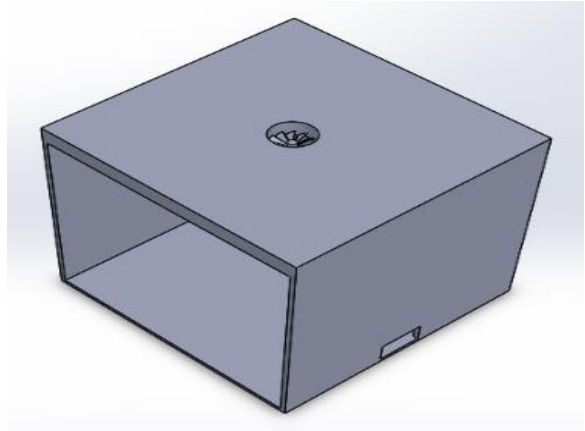


Fig. 1: Initial model of the room with one vortex diffuser

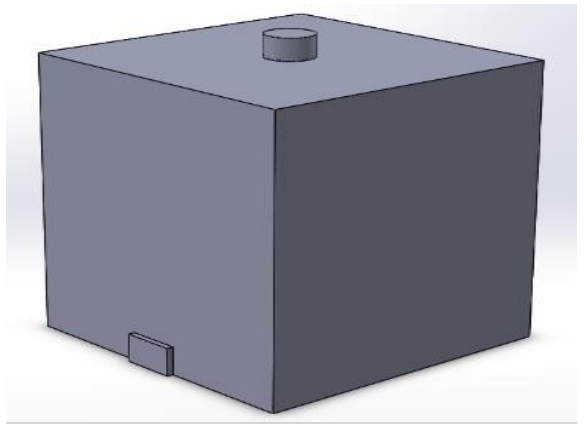


Fig. 2: Developed Air body

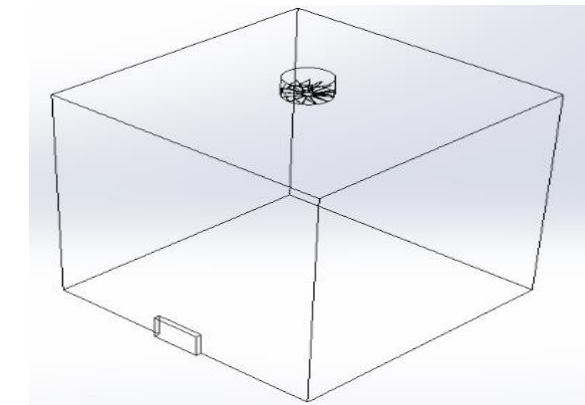


Fig. 3: Wireframe view of the air body

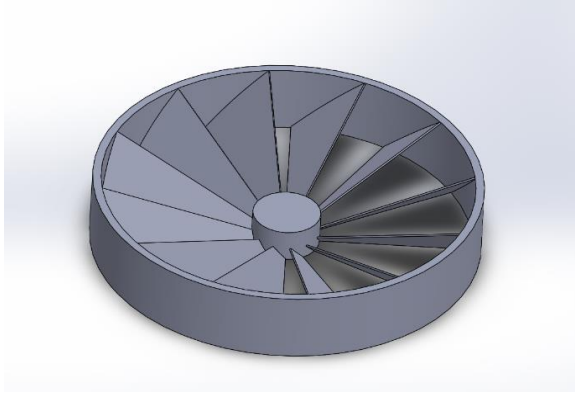


Figure 4: Vortex diffuser

The developed air body was imported to ANSYS Fluent for the airflow simulations. No-slip boundary conditions were used along the room walls, the ceiling, and the floor. All walls and ceilings were isothermal at room temperature (27 °C). All properties were assumed to be uniform across the inlet section. At the outflow boundary, environmental pressure is considered. The geometry model was meshed by using the Tetrahedron method because tetrahedral elements can fit better complex geometry and can create high-quality surface meshes essential for stable convergence[12]. the standard $k-\epsilon$ turbulence model was used to simulate because it consumes less computer power comparatively and provides reasonably accurate solutions[13][14][15]. The inlet air velocity was given as 4.5 m/s. Determination of whether the thermal comfort condition is achieved is done by obtaining a velocity distribution of the horizontal plane at 1m from the floor (Head Plane).

Other than this model the following diffuser configurations also were subjected to simulations.

- 1). 6m x 6m x 3.5m cuboid with 8 diffusers
- 2). 9m x 9m x 3.5m cuboid with 8 diffusers
- 3). 6m x 6m x 3.5m cuboid with 9 diffusers
- 4). 9m x 9m x 3.5m cuboid with 9 diffusers

After simulating different layouts with same inlet velocity, the layout which gives the best thermal comfort condition can be selected as the best diffuser layout.

B. Data acquisition and adaptation

Some adaptations had to be done for the data acquired from the meteorological department and other sources. The meteorological department of Sri Lanka doesn't collect data in the Kilinochchi district. Instead, the temperature and humidity reading of the Jaffna area were

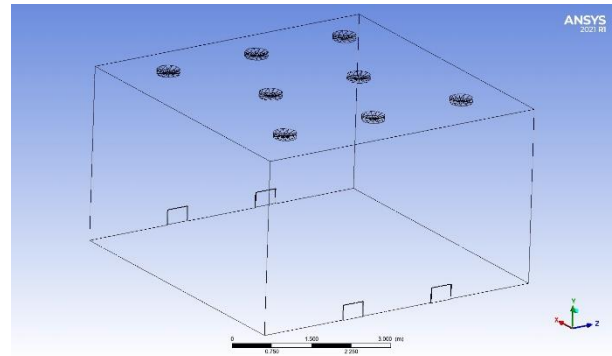


Figure 5: Wireframe model of 6m x 6m x 3.5m cuboid with 8 diffusers configuration

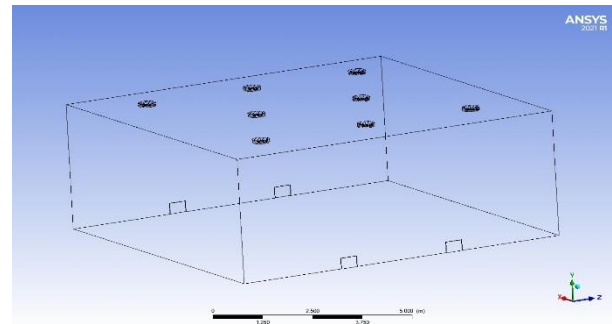


Figure 6: Wireframe model of 9m x 9m x 3.5m cuboid with 8 diffusers configuration

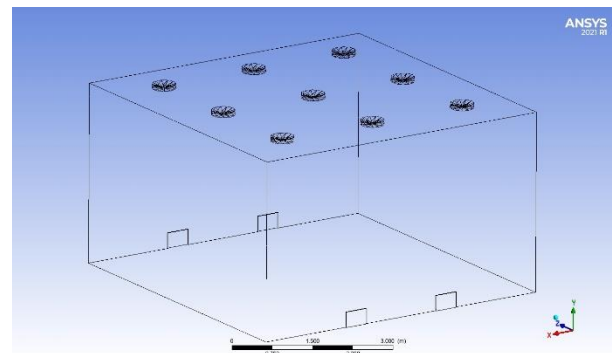


Figure 7: Wireframe model of 6m x 6m x 3.5m cuboid with 9 diffusers configuration

provided by that department. An online weather information provider, World Weather Online (WVO) was used to get the data of the Kilinochchi area. In [16], states that the data of WVO are reliable. Additionally, a statistical test has been done comparing readings of the meteorological department and WVO of the Jaffna area which also assured the reliability of using data of WVO.

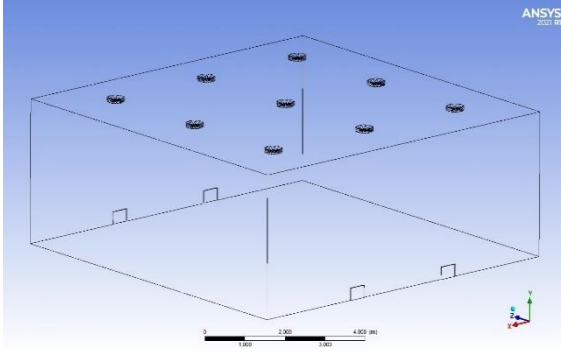


Figure 8: Wireframe model of 9m x 9m x 3.5m cuboid with 9 diffusers configuration

TABLE I: STATISTICAL TEST RESULT BETWEEN METEOROLOGICAL DEPARTMENT'S DATA AND WWO DATA

Variable	Observations	Min	Max	Mean	Std. deviation
Observation 1	144	26.000	30.000	28.278	1.149
Observation 2	144	23.442	32.253	28.413	1.936
Mann-Whitney test/ Two-tailed test					
U		9352			
U(standardized)		-1.443			
Expected value		10368.000			
Variance (U)		495172.474			
p-value (Two-tailed)		0.149			
alpha		0.050			

Test interpretation:

H_0 : The difference of location between the samples is equal to 0.

H_a : The difference of location between the samples is different from 0.

As the computed p-value is greater than the significance level $\alpha=0.05$, one cannot reject the null hypothesis H_0 .

XLSTAT was used for the statistical tests of data. Adaptation of data was done using MATLAB R2019 software. Further, to check the thermal comfort state of the hall, some readings had to be taken when the hall is occupied by a large number of people. However, the situation in the world when this study is being done was not favorable to take such reading as a closed space could not be occupied by a large number of people according to quarantine rules and regulations with Covid-19 pandemic. Hence some readings which were taken for a

previous study at the University of Moratuwa in 2014 had to be used. Those readings were also taken when people are occupying a hall in the daytime. Readings of that study were needed to be adapted for the conditions of the Kilinochchi area in 2020. Machine learning models were trained using MATLAB for the data adaptation. First, to adapt the temperature and humidity readings of 2014 to 2020 a linear regression model was trained with the data from WWO. To adapt reading from Moratuwa to Kilinochchi a non-linear regression model was trained. Using the parameters of those models the readings could be adapted.

C. Development of thermal comfort zone

The thermal comfort zone was developed for the Kilinochchi area as the case study lecture hall was in Kilinochchi. Temperature and humidity data of 20 years were obtained from the Meteorological Department of Sri Lanka. According to [17] the steps of developing a thermal comfort zone for a particular area are mentioned below.

Step 1. Determine the neutral temperature of the area using meteorological data with the equation

$$T_n = 17.6 + 0.31 T_0 \quad (1)$$

T_0 is the mean dry bulb temperature of the particular area. Step 2. Locate the intersection point of T_n dry bulb

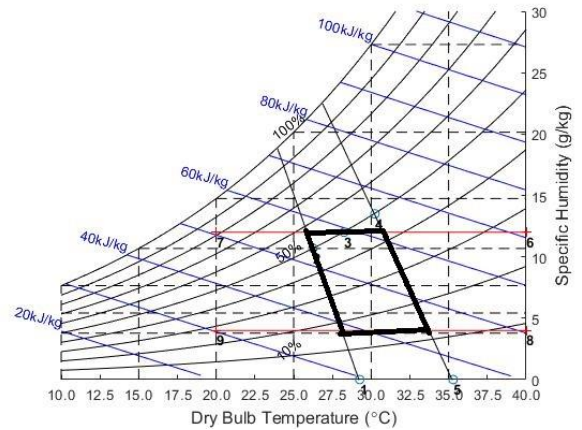


Fig. 9. Thermal comfort zone developed for Kilinochchi area

temperature line and 50% relative humidity line on the psychrometric chart. Step 3. Determine the left and right boundary points on the 50% RH line by

$$T_1 = T_n - 2^\circ C \quad \text{and} \quad (2)$$

$$T_2 = T_n + 2^\circ C \quad (3)$$

Step 4. Determine the Standard Effective Temperature (SET) lines corresponding to T_1 and T_2 . The baseline

interception point of the SET line corresponding to temperature T can be calculated by

$$T_{intercept} = T + 23(T - 14)HR_T \quad (4)$$

HR_T is the humidity ratio in kilogram scale corresponding to T and 50% RH. Step 5. The top and bottom boundaries are 0.012 and 0.004 humidity ratio lines.

III. RESULTS

A. Thermal comfort zone

According to the data from WWO, the average temperature of the Kilinochchi area is 28.2450C. Using that value and the equations aforementioned the thermal comfort zone for the Kilinochchi area was developed. Highlighted in black in Figure 9 is the thermal comfort zone. This comfort zone developed for an air velocity of 0.25 ms⁻¹. When the air velocity increases, this thermal comfort zone broadens.

B. CFD Simulations

According to different diffuser configurations, different air velocity distributions were obtained of a horizontal plane at 1m (Head plane).

In figure 10 it is apparent that right underneath the

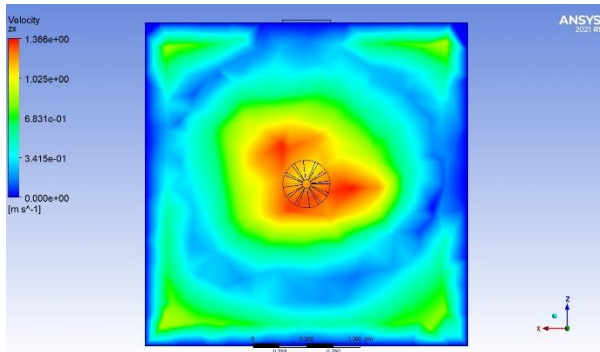


Figure 10. Velocity distribution of a head plane of single diffuser configuration

diffuser there is a high air velocity over 1.3 ms⁻¹. According to the ASHRAE standards, this doesn't comply as the occupants do not have any control over the airflow velocity. However, most of the area is having more the 0.6 m/s airflow velocity. A better velocity distribution can be seen from all other configurations. In 6m x 6m with 8 diffusers configuration (figure 11), most of the area is above 0.5 m/s. Less air distribution could be seen in the layout shown in figure 12 and most of the area has just above 0.3 m/s air velocity. The lowest maximum value could be seen in the layout shown in figure 14. Considering the obtained velocity

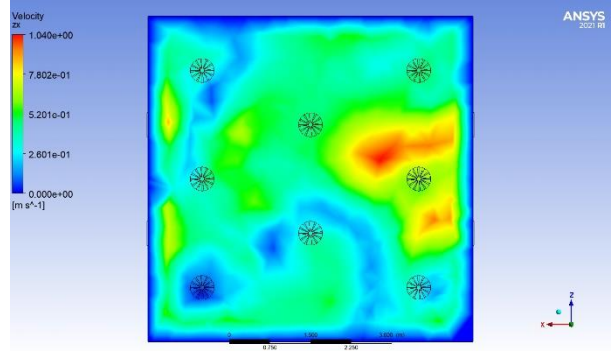


Figure 11. Velocity distribution of a head plane of 6m x 6m x 3.5m cuboid with 8 diffusers configuration

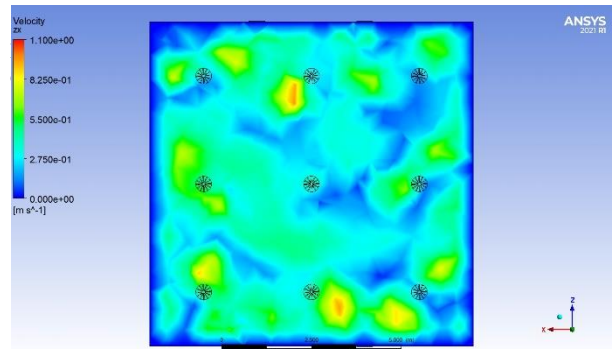
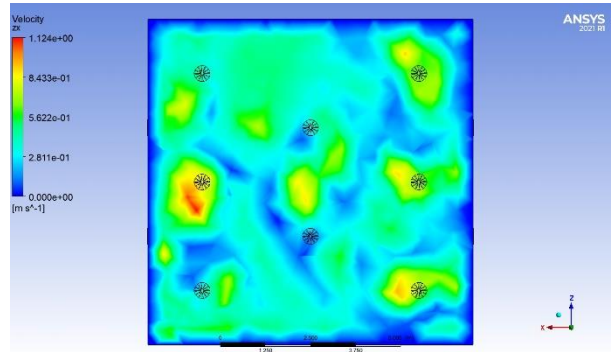


Figure 13. Velocity distribution of a head plane of 9m x 9m x 3.5m cuboid with 9 diffusers configuration

distribution, the layout in figure 11 has a higher chance of achieving thermal comfort as it has a higher velocity distributed more evenly.

C. Data adaptation

To convert data from 2014 to 2020, a linear regression model was trained using MATLAB. The parameters came out as for humidity [77.166645,

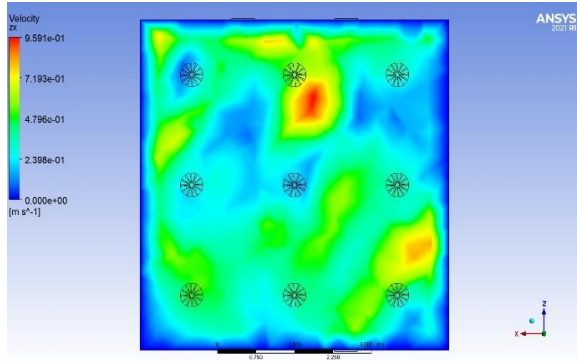


Figure 14. Velocity distribution of a head plane of 6m x 6m x 3.5m cuboid with 9 diffusers configuration

3.040133] and temperature [28.6667, 0.9847]. A non-linear regression model was trained using 'fitlm' function of MATLAB to convert readings from Moratuwa to Kilinochchi. The parameters came out as for humidity; $b_1=-0.8969$, $b_2=0.0618$, $b_3=-4.7988e-04$ and for temperature; $b_1=1.00$, $b_2=-6.7524e-11$, $b_3=1.1594e-12$ for the function

$$Y = (b_1 \times x_1 + b_2 \times x_2 + b_3 \times x_3) \quad (5)$$

IV. CONCLUSIONS

A. Comfort condition

To determine the comfort condition inside the hall, the gathered data points have to be plotted inside the psychrometric chart with the comfort zone marked.

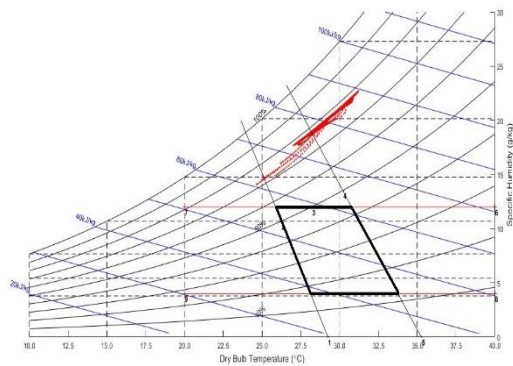


Fig. 15. Thermal comfort zone with data points marked

There are 8328 data points marked in this plot (Fig. 10). It is apparent that all the data points are clearly out of the thermal comfort zone. Thereby, it can be concluded that a ventilation system is vital to this type of hall for the occupants to be thermally comfortable.

When the PMV value is calculated for the layout in figure 11 taking approximate air velocity as 5 m/s, the value is 0.43 with a PPD value of 9% which can be acceptable. (Air temperature = 28.245°C, Relative

humidity = 75%, Metabolic rate = 1 met, Clothing level = 0.61 clo)

B. Future research work

Testing on more diffuser layouts to determine the layout which provides the best thermal comfort condition inside. Interpreting that layout for case study lecture hall to validate, hence proposing the strategy as that can be applied for any case study accordingly.

REFERENCES

- [1] Z. S. Zomorodian, M. Tahsildoost, and M. Hafezi, "Thermal comfort in educational buildings: A review article," *Renew. Sustain. Energy Rev.*, vol. 59, pp. 895–906, 2016, doi: 10.1016/j.rser.2016.01.033.
- [2] B. Chenari, F. B. Lamas, A. R. Gaspar, and M. G. Da Silva, "Simulation of Occupancy and CO₂-based Demand-controlled Mechanical Ventilation Strategies in an Office Room Using EnergyPlus," *Energy Procedia*, vol. 113, pp. 51–57, 2017, doi: 10.1016/j.egypro.2017.04.013.
- [3] L. Lan, P. Wargoeki, D. P. Wyon, and Z. Lian, "Effects of thermal discomfort in an office on perceived air quality, SBS symptoms, physiological responses, and human performance," *Indoor Air*, vol. 21, no. 5, pp. 376–390, 2011, doi: 10.1111/j.1600-0668.2011.00714.x.
- [4] S. J. Cao, C. W. Yu, and X. Luo, "New and emerging building ventilation technologies," *Indoor Built Environ.*, vol. 29, no. 4, pp. 483–484, 2020, doi: 10.1177/1420326X20909092.
- [5] B. Chenari, J. D. Carrilho, G. Botte, and M. G. da Silva, "Towards Energy-Efficient Ventilation in Buildings: Development of the Smart Window Ventilation System," *J. Clean Energy Technol.*, vol. 4, no. 6, pp. 457–461, 2016, doi: 10.18178/jocet.2016.4.6.332.
- [6] F. Usman and A. R. A. Bakar, "Thermal Comfort Study Using CFD Analysis in Residential House with Mechanical Ventilation System," *Lect. Notes Civ. Eng.*, vol. 53, no. June, pp. 1613–1628, 2020, doi: 10.1007/978-3-030-32816-0_124.
- [7] B. W. Olesen, A. Simone, M. Krajčič, F. Causone, and M. De Carli, "Experimental study of air distribution and ventilation effectiveness in a room with a combination of different mechanical ventilation and heating/cooling systems," *Int. J. Vent.*, vol. 9, no. 4, pp. 371–383, 2011, doi: 10.1080/14733315.2011.11683895.
- [8] S. Liu *et al.*, "Improving indoor air quality and thermal comfort in residential kitchens with a new ventilation system," *Build. Environ.*, vol. 180, p. 107016, 2020, doi: 10.1016/j.buildenv.2020.107016.
- [9] J. Song and X. Meng, "The Improvement of Ventilation Design in School Buildings Using CFD Simulation," *Procedia Eng.*, vol. 121, pp. 1475–1481, 2015, doi: 10.1016/j.proeng.2015.09.073.
- [10] M. A. Rahman and N. G. A., "Analysis of Lecturing Room using Computational Fluid Dynamics Natural and Forced Ventilation," *Int. J. Eng. Res. Technol.*, vol. 3, no. 3, pp. 653–659, 2014.
- [11] M. A. Aziz, I. A. M. Gad, E. S. F. A. Mohammed, and R.

- H. Mohammed, "Experimental and numerical study of influence of air ceiling diffusers on room air flow characteristics," *Energy Build.*, vol. 55, pp. 738–746, 2012, doi: 10.1016/j.enbuild.2012.09.027.
- [12] S. C. Tadepalli, A. Erdemir, and P. R. Cavanagh, "Comparison of hexahedral and tetrahedral elements in finite element analysis of the foot and footwear," *J. Biomech.*, vol. 44, no. 12, pp. 2337–2343, 2011, doi: 10.1016/j.jbiomech.2011.05.006.
- [13] B. Bjerg *et al.*, "Modelling of ammonia emissions from naturally ventilated livestock buildings: Part 2, air change modelling," *Biosyst. Eng.*, vol. 116, no. 3, pp. 246–258, 2013, doi: 10.1016/j.biosystemseng.2013.01.010.
- [14] E. Bustamante *et al.*, "Exploring ventilation efficiency in poultry buildings: The validation of computational fluid dynamics (CFD) in a cross-mechanically ventilated broiler farm," *Energies*, vol. 6, no. 5, pp. 2605–2623, 2013, doi: 10.3390/en6052605.
- [15] T. M. R. d. C. Curi, D. J. de Moura, J. M. Massari, M. Mesquita, and D. F. Pereira, "Computational fluid dynamics (CFD) application for ventilation studies in broiler houses," *Eng. Agric.*, vol. 37, no. 1, pp. 1–12, 2017, doi: 10.1590/1809-4430-Eng.Agric.v37n1p1-12/2017.
- [16] T. J. Doherty and E. Arens, "Title Evaluation of the physiological bases of thermal comfort models Publication Date EVALUATION OF THE PHYSIOLOGICAL BASES OF THERMAL COMFORT MODELS," 1988, [Online]. Available: www.ashrae.org.
- [17] M. T. . Jayasinghe and R. A. Attalage, "Comfort Conditions for Built Environments in Sri Lanka," *Eng. J. Inst. Eng.*, vol. 29, no. 1, pp. 12–23, 1999.

Surface Area Measurement of Porous Graphene: A Kinetics Study on Methylene Blue Adsorption Method

Ayesha Sandaruwani
Dep.of Materials Sci.& Eng.
University of Moratuwa
Sri Lanka
ayeshamkas@gmail.com

Hansinee Sitanimaluwa
Dep.of Materials Sci.& Eng.
University of Moratuwa
Sri Lanka
hansinees@uom.lk

Mahesh Rathnayaka
Dep.of Materials Sci.& Eng.
University of Moratuwa
Sri Lanka
maheshrathnay@gmail.com

Abstract— Studying methylene blue (MB) adsorption is a promising method to analyze the surface area of porous materials. However, understanding the characteristic adsorption mechanism for any particular porous material is essential to select the suitable kinetic model and adsorption isotherm (equilibrium) for surface area evaluation. In this study, several kinetic models were studied for MB adsorption of porous graphene. Porous graphene for this study was prepared by KOH activation of graphene oxide (GO), which was synthesized using Sri Lankan vein graphite as the carbon precursor. The MB adsorption tests for porous graphene were performed at 25°C, and the effect of the contact time and the initial MB concentration were discussed. It was observed that the 2nd order kinetic model clearly explained the adsorption mechanism than the 1st order kinetic model. The adsorption isotherms obtained for MB adsorption of porous graphene were tested with Langmuir, Freundlich and, Temkin adsorption models. Langmuir model showed more capability to describe the equilibrium state. Therefore, among the tested kinetic models and adsorption isotherms, the 2nd order kinetic model and Langmuir isotherm are most appropriate to describe the MB adsorption mechanism onto porous graphene. The specific surface area (SSA) value of porous graphene determined by the selected adsorption model was in excellent agreement with the SSA value determined by Brunauer-Emmett-Teller (BET) method.

Keywords— Porous graphene, specific surface area, adsorption kinetics, Sri Lankan graphite

I. INTRODUCTION

Materials which form cavities in their atomic structural geometry are categorized as porous materials. These porous materials are further studied according to the internal structural data. Variations in the internal structures cause the porous materials to exhibit different physical properties in nature. In order to improve the properties of porous materials, internal structures should be thoroughly investigated. Properties of porous structures depend on the pore size, pore shape, surface area and surface roughness. It is highly significant to establish the relationships between these pore characteristics and physical properties through proper experiments[1].

Among porous materials, porous carbon materials have been extensively investigated over the recent years in order to use in adsorbents, energy storage devices, thermal insulation, water and gas purification etc.[2],[3],[4]. Microporous (< 2 nm), Mesoporous (2-50 nm) and microporous(>50 nm) are three groups of porous materials which have been categorized by International Union of Pure and Applied Chemistry according to their sizes of pores.[5].

Porosity of the porous materials have been investigated using different techniques such as microscopic techniques, techniques of physical adsorption of a gas and dye adsorption techniques. Considering the adsorption based techniques, measurement of specific surface area has been affected by the molecule of adsorbate, crystallographic planes[6] on surface and temperature of the measuring environment. Relatively, various techniques have been explored in order to measure the surface area of a desired material at fixed scales and at room temperature. Brunauer-Emmett-Teller (BET) adsorption method, methylene blue (MB) adsorption, ethylene glycol monoethyl ether adsorption[7], protein retention[8], and electrokinetic analysis of adsorption[6] of complex ions have been commonly used.

MB dye has been used to calculate the surface area of porous materials for recent years. Chemical formula of MB is $C_{16}H_{18}ClN_3S$ where the molecular weight is 319.87 g/mol. Considering the MB dye, it can be identified as a cationic dye in the aqueous solution ($C_{16}H_{18}N_3S^+$) which is attracted in to the negatively charged particles on the surface of porous material. Because of this mechanism the specific surface area of materials can be calculated by the degree of MB absorption. As the MB particle can infiltrate through porous structures it is highly suggested way to determine specific surface area of porous materials[9]. However, there are less studies have been done to study the adsorption mechanism of MB dye onto activated graphene oxide (AGO). It is important to understand the adsorption kinetics before applying the adsorption capacities for any property calculation. Since, the adsorption kinetics are unique for any adsorbent, this study gives a clear understanding about the adsorption kinetics of MB onto AGO which were prepared from Sri Lankan graphite.

Porous graphene can be obtained using oxidation and reduction of graphene which is a honeycomb structure consist of carbon atoms forming 2D single sheets. Unique chemical and physical properties of graphene oxide(GO) has drawn significant attention from the industrial and research sectors over the last few years. Hence there are lots of successful studies in understanding its physical and chemical characteristics which encouraged various applications of GO. High surface area obtained from activated GO is an extensively used property in many industries such as energy storage devices, electronic devices and biomedical applications. Dye adsorption method is investigated as another successful process to study the surface area of activated graphene oxide. MB has drawn the attention over the past few years in order to demonstrate the adsorption efficiency of GO through removal of MB dye from aqueous solutions[10].

II. METHODOLOGY

A. Materials

GO was synthesized from Sri Lankan natural vein graphite by modified hummers method. Activation was done by following KOH/GO mass ratio at 4 under 800°C for 60 min. MB (Breckland scientific suppliers) was used as the adsorbate. Required MB solutions were prepared using distilled water.

B. Method

Spectrophotometer was used to determine the MB adsorption at full wavelength spectrum. The optimum wavelength was used for the calibration curve preparation and further adsorption measurements.

C. Adsorption Kinetics

Experimental values were fitted to the first order and second order kinetic models in order to investigate adsorption process. The equations for the kinetic rates are as follows.

$$\frac{dq_t}{dt} = K_n(q_e - q_t)^n \quad (1)$$

Here q_e is the mass of dye adsorbed by unit mass of adsorbent (mg g^{-1}) at the equilibrium state where q_t corresponds to the mass of dye adsorbed by unit mass of adsorbent after time t . The rate constant (k_n) is n^{th} order adsorption (at $n=1$ unit is min^{-1} and at $n = 2$ unit is $\text{mg g}^{-1}\text{min}^{-1}$). The equations can be written in linearized integrated forms as follows,

$n=1$; for the 1st order kinetics:

$$\ln(q_e - q_t) = \ln q_e - K_1 t \quad (2)$$

$n= 2$; for the 2nd order kinetics:

$$\frac{t}{q_t} = \frac{1}{K_2 q_e^2} + \frac{t}{q_e} \quad (3)$$

$\ln(q_e - q_t)$ vs t and t/q_t vs t graphs were plotted to calculate constants of rate and the coefficients of the 1st and 2nd order kinetic models. The best fitting kinetic model was chosen based on the linear regression coefficient (R_2) and the q_e values.

Intraparticle diffusion model was considered to determine the result of diffusion where in the adsorption process it is the rate controlling step.

$$q_t = K_p t^{\frac{1}{2}} + c \quad (4)$$

Here k_p is the inter particle diffusion rate constant. k_p is evaluated from the gradient of linear part of the curve q_t against $t^{1/2}$.

Models of Langmuir, Freundlich and Tempkin were investigated and tested considering the equilibrium conditions at ambient temperature. In Langmuir isotherms, theoretical assumption of monolayer adsorption on adsorbent surface is considered and interactions between the adsorbed molecules are neglected. The MB dye adsorption has successfully described and represented by the equation below.

$$q_e = \frac{q_{\max} K_L C_e}{1 + K_L C_e} \quad (5)$$

Here q_e is amount adsorbed per gram of adsorbent after equilibrium (mg g^{-1}) reached and C_e is solute concentration in the aqueous solution (mg L^{-1}) after point of equilibrium is reached. K_L and q_{\max} and are considered as constants correlated

to the adsorption energy (Lmg^{-1}) and to the capacity of maximum adsorption (mg g^{-1}). In Langmuir isotherm another characteristic parameter can be identified as dimension factor r (separation factor) which can be represented as follows.

$$r = (1 + K_L C_0)^{-1} \quad (6)$$

Here C_0 denotes the maximum value of commencing adsorbate concentration (mg L^{-1}). Type of the isotherm is affiliated to the value of r where the $r > 1$ means unfavorable, $r = 1$ linear, $0 < r < 1$ favorable and $r = 0$ means irreversible adsorption.

Empirical model based heterogeneous adsorption on independent active sites is given by the Freundlich's equation as follows,

$$q_e = K_F C_e^{\frac{1}{n}} \quad (7)$$

Here K_F is relative adsorption capacity ($\text{mg}^{1-(1/n)} \text{L}^{1/n} \text{g}^{-1}$) and n depicts intensity of adsorption where the $n > 1$ represents preferable adsorption.

When adsorption sites get filled, Temkin isotherm shows a linear depletion in the adsorption energy. Because of interactions between adsorbent and adsorbate the heat generated by adsorption of molecules in the layer tends to decrease linearly with the surface area. The characterization of the adsorption can be done by a uniform binding energies distribution until a maximum point. Tempkin isotherm is expressed as following equation.

$$q_e = \frac{RT}{b} \ln(AC_e) \quad (8)$$

Here the b is Temkin constant of heat adsorption (J/mol), A is Temkin isotherm constant (Lg^{-1}), T is absolute temperature (K), and R is universal gas constant ($8.314 \text{ J mol}^{-1} \text{ K}^{-1}$). Based on the nonlinear X^2 statistic determination test (SS) the best fit model for the distribution was selected where the SS depicts the comparison between experimental q_e and estimated q_e values.

$$SS = \sqrt{\frac{\sum (q_{e,calc} - q_{e,exp})^2}{N}} \quad (9)$$

Here the $N =$ Number of the experimental points.

III. RESULTS AND DISCUSSION

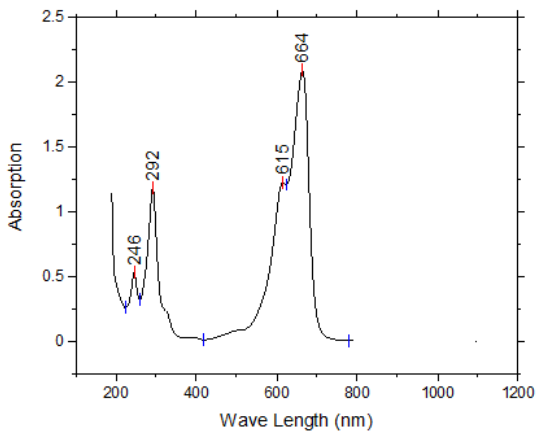
A. Methylene Blue Adsorption

The full range of UV-Vis absorption spectrum of MB aqueous solution was taken (Fig.1(a)), and the high intense absorbance peak is at 664 nm. Therefore, 664 nm was used to measure the absorbance values. Then, the calibration curve of MB dye was obtained at 664 nm is shown in Fig.1(b) and was used for determining the concentration of MB in the filtrates at different AGO samples. Fig.1(b) shows a plot of MB concentration versus spectrophotometer absorbance readings. Absorbance values are linearly proportional to MB concentration. The relationship is $y=0.11092x$ with $R^2=0.98621$.

Many research groups have given several hours to be settled with AGO with MB. However, in the present work, the adsorption of MB onto the AGO showed to be relatively high with equilibrium being attained after 120 min. Therefore, AGO and MB could adsorb for 3 hours and, then the

spectrophotometer reading was taken for the filtrate. The calibration curve was used to measure the filtrate MB concentration from the absorbance. Then, adsorbed MB mass per one gram of AGO was calculated.

(a)



(b)

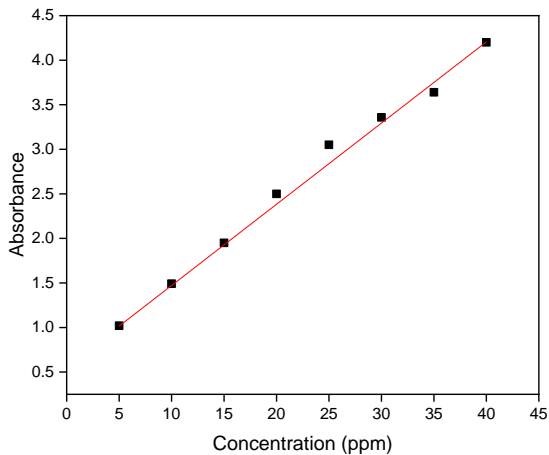


Fig. 1: (a) The spectrophotometer absorption curve of MB at $\lambda = 664\text{nm}$, (b) The spectrophotometer calibration curve of MB at $\lambda = 664\text{nm}$

The spectrophotometry readings of the filtrates were taken and it was converted to the milligrams of MB adsorbed by 1 gram of GO at equilibrium (q_{eq}) and the adsorption quantity at any state from the calibration curve. High absorbance values of the filtrate indicate poor adsorption of MB onto the AGO surface. Therefore, the filtrate absorbance is inversely related to q_{eq} values

B. Influence of the adsorbent dosage

Fig.2 depicts that the adsorption amount clearly correlated with the initial MB concentration. The amount of dye adsorbed per unit mass of adsorbent at equilibrium (q_{eq}) values show higher values when the initial MB concentrations are increased. q_{eq} gets higher probably due to an increase in driving force (concentration gradient) when the initial MB concentrations are increased. The diffusion of MB molecules onto the activated GO is definitely accelerated by the increase of the initial dye concentration of MB.

At a lower concentration of dye, the driving force seems less to adsorb MB. But when the initial concentrations reach 5 ppm, the q_{eq} values get increased at a higher rate of the gradient. At that point, the driving force may be sufficient enough to access most of the active sites of GO.

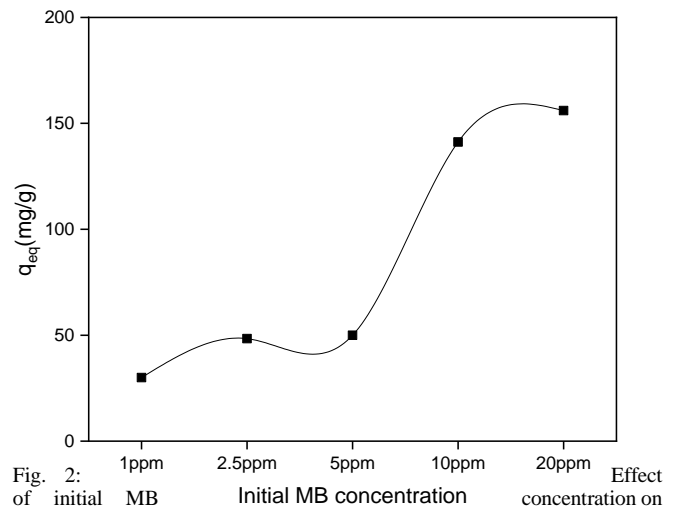


Fig. 2: Effect of initial MB concentration on q_{eq}

C. Adsorption Kinetics

According to Fig.3, initially adsorption rate is high for the AGO samples and equilibrium is reached around 120 min. The availability of larger surface area and the external activation sites which can be reached fast by dye molecules have contributed to the fast adsorption rate of AGO. The efficiency of dye adsorption is also high in AGO because the single layered atomic structure has removed the hindrance for the dye molecules to reach active sites. The saturation of dye adsorption occurs around 120 min and hereafter the graph shows constant adsorption quantity per 1g of AGO for the rest of time.

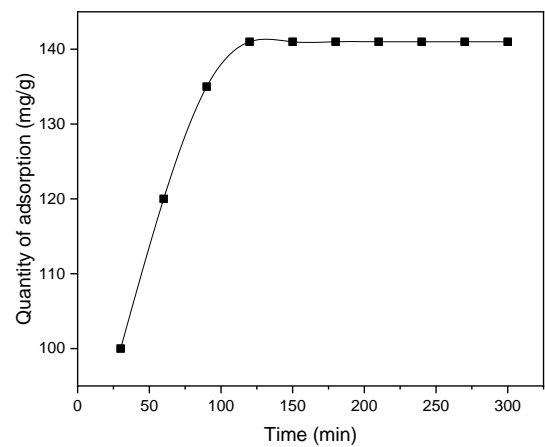


Fig. 3: Effect of activation time on the quantity of MB adsorption

It is noteworthy of demonstrating the equilibrium condition, rate of surface reactions, and intraparticle diffusion by kinetic models. But aforementioned models want to clearly understand the hidden adsorption mechanism to a certain extent, with their practical significance limiting to measure its effects. Therefore, adsorption time dependency is considered as the prevalent parameter to investigate the adsorption kinetics. It is proven that the long time adsorption and short time adsorption fit for 1st order kinetics and 2nd order kinetics models respectively.

The limiting mechanism of MB molecules adsorption on AGO was investigated by plotting the 1st order and 2nd order versions of kinetic rate equations, which are given by Eqn.2 and Eqn.3 correspondingly. The respective plots are

illustrated in Fig.4 and the respective kinetic parameters are tabulated in Table.1. The 1st order model predicts the q_e values with 16.23% of underestimation. But the 2nd order model precisely predicts those values with only 4.3% overestimation. Therefore, 1st order model does not fit for the MB adsorption onto the AGO surface. Thus, the 2nd order model reasonably describes the MB adsorption with that model having R^2 of 0.998. Thus, it can be inferred that the rate limiting step may be chemisorption promoted by either valency forces, through sharing of electrons between adsorbent and sorbate, or covalent forces, through the exchange of electrons between the parties involved.

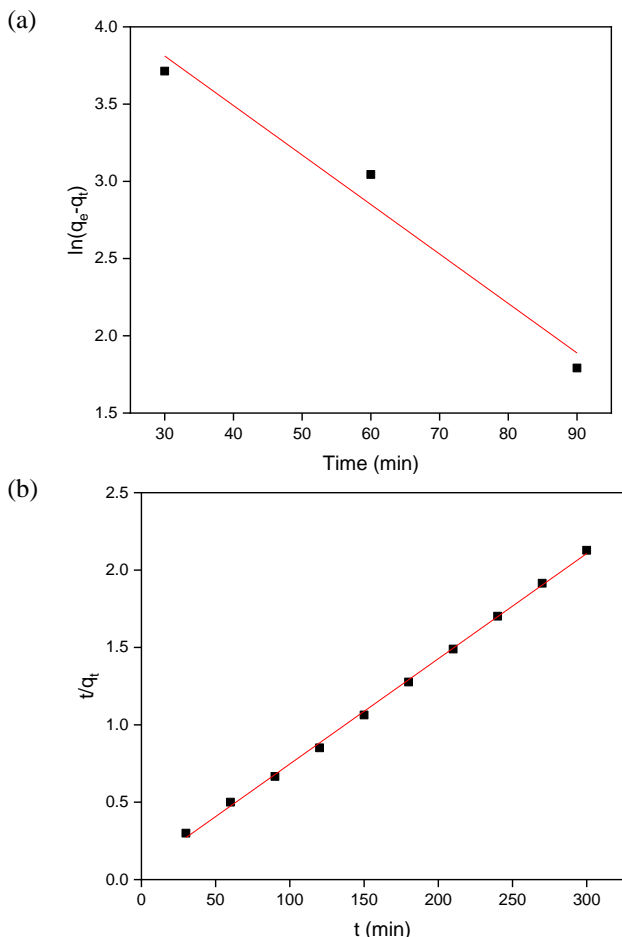


Fig. 4: (a) Plot for the 1st order kinetic model, (b) Plot for the 2nd order kinetic model.

TABLE I. SUMMERY OF THE KINETIC MODELS

Order	Plot equation	K	$q_{e, \text{calculated}}$	%difference	R^2
1 st order	$y = -0.032x + 4.7718$	$K_1=0.032$	118.13	-16.23 %	0.973
2 nd order	$y = 0.0068x + 0.0673$	$K_2=0.00075$	147.06	+4.3%	0.998

The effect of the intraparticle diffusion on the MB adsorption onto the AGO surface was evaluated based on the intraparticle diffusion model. This plot behaves having small curvature (mostly linear) initially and some equilibrium state throughout the plot. This initial curvature represents the bulk

diffusion, and the linear section represents the intraparticle diffusion. Normally, bulk diffusion depends on the initial adsorbent concentration. A special line is fitted by connecting the data points which behave slight linearly. The intercept of this line uses to predicts whether the interparticle diffusion is the rate controlling mechanism or not. In this Fig.5 the line is not passing through the origin, if it passes through the origin interparticle diffusion would be the rate controlling step. However, considering the calculated K_p and C values (Equation of $y = 8.7333x + 52.222$, K_p of 8.733, c at 52.22, R^2 of 0.99), MB adsorption onto the AGO has high impact from bulk diffusion and after few minutes adsorption is happened mainly due to intraparticle diffusion, but this doesn't say the rate controlling step as the intraparticle diffusion.

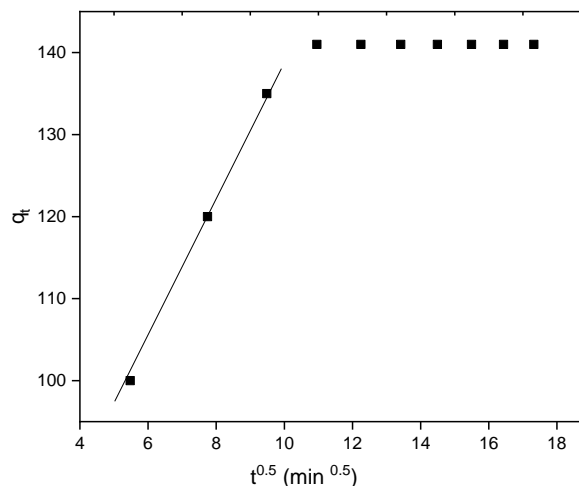


Fig. 5: Evaluation of intraparticle model for MB adsorption onto AGO.

D. Adsorption Equilibrium

As Fig.6, MB adsorption isotherms were evaluated by Langmuir, Freundlich, and Temkin adsorption models. Q_{max} value from the Langmuir isotherm represents the adsorption capacity, having a high value of 922.26 mg/g shows its high activation level which corresponds to satisfactory porosity. The separation factor (r) is the most important parameter which tells about the favorability of the isotherm for the adsorption behavior. Since r value is in-between 0 and 1, it gives good sight to the applicability of Langmuir modes to the MB and AGO adsorption mechanism. Though the Freundlich equation is an empirical model based on heterogeneous adsorption over independent sites, having n value larger than 1 demonstrates the pertinency of this model for our system. Statistical comparison (SS value) is the best option to select the suitable model for the adsorption mechanism for any situation. Therefore, the Langmuir model can be selected to precisely describe the adsorption of MB onto the AGO surface, considering the corresponding kinetic parameters and mainly from the SS value as illustrated in Table.II.

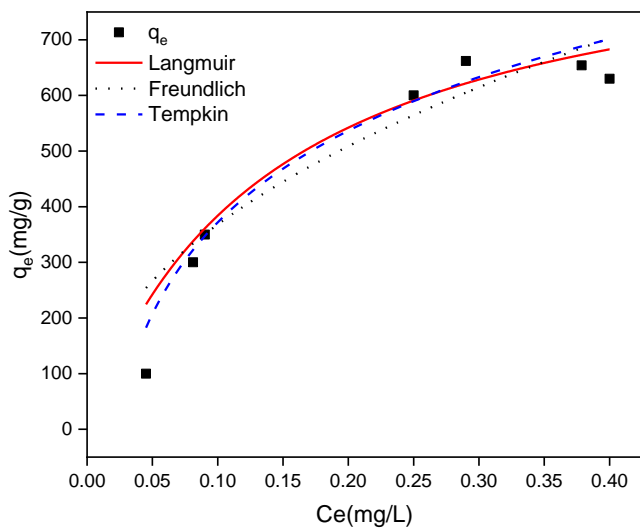


Fig. 6: Adsorption isotherms of MB on AGO at 25°C

TABLE II. SUMMARY OF THE ADSORPTION ISOTHERMS

Model	Constants
Langmuir	
K_L	7.13
Q_{max}	922.26
r	0.121
R^2	0.89
SS	0.98
Freundlich	
K_F	1078
n	2.14
R^2	0.78
SS	2.56
Temkin	
A	47.83
b	10.42
R^2	0.86
SS	1.96

IV. CONCLUSION

The experiment was conducted to investigate the capability of using the MB adsorption in surface area measurement of AGO. The 2nd order kinetic model was the most favorable kinetic model to describe the MB adsorption

onto the AGO surface. And the Langmuir isotherm was found as the best adsorption isotherm among the various adsorption isotherms, which explains this adsorption mechanism clearly. Therefore, having clear understanding of the unique adsorption kinetics of MB dye onto AGO, any surface area calculation would be feasible by following the 2nd order kinetic model and the Langmuir adsorption model.

ACKNOWLEDGMENT

This research work was funded by Senate Research Committee (SRC) grants at University of Moratuwa. Grant numbers: SRC/CAP/2019/01 and SRC/ST/2019/54.

REFERENCES

- [1] P. S. Liu and G. F. Chen, "Characterization Methods," *Porous Mater.*, pp. 493–532, 2014, doi: 10.1016/b978-0-12-407788-1.00010-1.
- [2] T. Hanai, "Separation of polar compounds using carbon columns," *J. Chromatogr. A*, vol. 989, no. 2, pp. 183–196, 2003, doi: 10.1016/S0021-9673(02)02017-4.
- [3] C. W. Huang, Y. T. Wu, C. C. Hu, and Y. Y. Li, "Textural and electrochemical characterization of porous carbon nanofibers as electrodes for supercapacitors," *J. Power Sources*, vol. 172, no. 1, pp. 460–467, 2007, doi: 10.1016/j.jpowsour.2007.07.009.
- [4] F. Su, F. Y. Lee, L. Lv, J. Liu, X. N. Tian, and X. S. Zhao, "Sandwiched ruthenium/carbon nanostructures for highly active heterogeneous hydrogenation," *Adv. Funct. Mater.*, vol. 17, no. 12, pp. 1926–1931, 2007, doi: 10.1002/adfm.200700067.
- [5] P. Schneider, "Adsorption isotherms of microporous-mesoporous solids revisited," *Appl. Catal. A, Gen.*, vol. 129, no. 2, pp. 157–165, 1995, doi: 10.1016/0926-860X(95)00110-7.
- [6] D. A. H. Hanaor, M. Ghadiri, W. Chrzanowski, and Y. Gan, "Scalable surface area characterization by electrokinetic analysis of complex anion adsorption," *Langmuir*, vol. 30, no. 50, pp. 15143–15152, 2014, doi: 10.1021/la503581e.
- [7] A. B. Cerato and A. J. Lutenecker, "Determination of Surface Area of Fine-Grained Soils by the Ethylene Glycol Monoethyl Ether (EGME) Method," *Geotech. Test. J.*, vol. 25, no. 3, pp. 315–321, Sep. 2002, doi: 10.1520/GTJ11087J.
- [8] O. Paykov and H. Hawley, "A Protein-Retention Method for Specific Surface Area Determination in Swelling Clays," *Geotech. Test. J.*, vol. 36, no. 4, pp. 606–611, May 2013, doi: 10.1520/GTJ20120197.
- [9] J. C. Santamarina, K. A. Klein, Y. H. Wang, and E. Prencke, "Specific surface: Determination and relevance," *Can. Geotech. J.*, vol. 39, no. 1, pp. 233–241, 2002, doi: 10.1139/t01-077.
- [10] N. Zaghbani, A. Hafiane, and M. Dhahbi, "Separation of methylene blue from aqueous solution by micellar enhanced ultrafiltration," *Sep. Purif. Technol.*, vol. 55, no. 1, pp. 117–124, 2007, doi: 10.1016/j.seppur.2006.11.008.

Precision Dual Axis Tracker for Solar Concentrator

Yomal Malinda
Department of Electrical and
Telecommunication Engineering
South Eastern University of Sri Lanka
Oluvil, Sri Lanka
yomalmalinda96@gmail.com

Damith Pushpika
Department of Electrical and
Telecommunication Engineering
South Eastern University of Sri Lanka
Oluvil, Sri Lanka
damithpushpika94@gmail.com

Mohamed Haleem
Department of Electrical and
Telecommunication Engineering
South Eastern University of Sri Lanka
Oluvil, Sri Lanka
mala_haleem@seu.ac.lk

Aslam Saja
Department of Electrical and
Telecommunication Engineering
South Eastern University of Sri Lanka
Oluvil, Sri Lanka
saja.aslam@seu.ac.lk

Safnas Kariapper
Department of Electrical and
Telecommunication Engineering
South Eastern University of Sri Lanka
Oluvil, Sri Lanka
safnas.mhm@seu.ac.lk

Sithy Juhaniya
Department of Electrical and
Telecommunication Engineering
South Eastern University of Sri Lanka
Oluvil, Sri Lanka
juhani90@seu.ac.lk

Fuhaid Alshammari
Mechanical Engineering Department
College of Engineering
University of Hail
Hail, Kingdom of Saudi Arabia
fu.alshammari@uoh.edu.sa

Mohamed Elashmawy
Mechanical Engineering Department
Engineering College
Suez University
Suez, Egypt
arafat_696@yahoo.com

Abstract—This paper presents an implementation of a precision dual axis tracking system for a parabolic solar concentrator. An example application of this solar concentrator is water purification using solar energy, or solar still. The tracking system developed in the work rotates the solar concentrator along two axes; vertically (in Altitude) and horizontally (in Azimuth), so that to orient the parabolic reflector to directly face the sun, throughout the day. Two axes tracking system is known to achieve higher efficiency compared to single axis trackers and fixed systems for solar energy harvesting. While flat panel photovoltaic (PV) energy harvesting systems benefit from dual axis trackers, the efficiency of solar concentrators of the type considered in this work is highly dependent on the accuracy of orientation toward the sun. The drive control designed and built in this work is of hybrid type. The sun position is calculated periodically using a sun-path computation algorithm and the orientation of the concentrator is changed incrementally. More precision is achieved using a sensor-based feedback control system. Four LDRs function in unison to generate error signals, indicating the deviations in the orientation of the solar concentrator from actual altitude and azimuth of the sun. These error signals are fed back to the controller for corrective rotations, of the altitude and azimuth motors. This secondary control is essential to compensate for errors due to backlashes in the mechanical drive system. The hybrid system enables robust and reliable operation throughout a day regardless the sky conditions.

Keywords—renewable energy, solar tracking, sun path, parabolic concentrator, solar water still

I. INTRODUCTION

The energy demand is increasing as the world population is increasing day by day. On the other hand, oil and coal reserves are getting depleted fast during the current century. Also, environmental problems such as pollution and global warming are accelerated by the use of oil and coal energy. Solar energy is becoming a desirable solution in this regard, although the initial installation cost still remains high.

The study leading to this paper arose in the context of an experimental solar powered water desalination system [1]. Fig. 1 shows the water desalination system which uses a

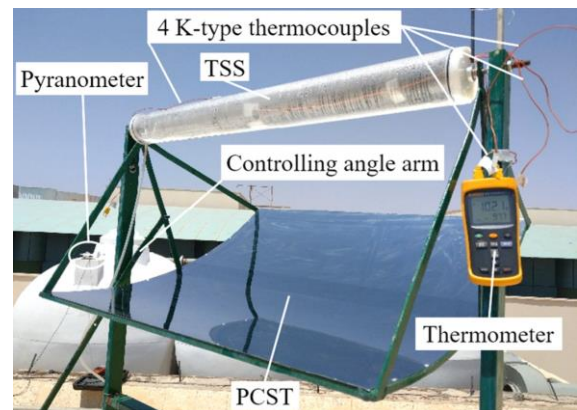


Fig. 1. Photograph of existing PCST-TSS.

tubular solar still (TSS) energized by a parabolic concentrator with solar tracking system (PCST) thus dubbed PCST-TSS.

Currently, solar tracking for this apparatus is achieved by periodic manual adjustments. A precision automated solar tracking system is sought necessary for the expedition of the TSS development process. The tracking system to be designed is required to be low cost, robust, and of minimal maintenance needs.

In [2], the author therein published analytical results on achievable energy gains of ideal (dual axes) tracker and single axis tracker in comparison to fixed panel. The results indicated gains up to 50% for ideal tracking. According to experimental studies, the gains brought by solar tracking for flat-panel photovoltaic (PV) systems in the annual energy productivity have been found to be in the range of 13–44% depending on the geographical location, mode of experiment, and the nature of apparatus [3],[4].

While the benefit of solar tracking systems for flat PV panels have been shown to be significant, precision tracking has a more profound impact in *concentrator based solar thermal energy systems*. Minor deviations in focusing the solar radiation to the position of energy harvesting device can cause loss of large proportion of collectable energy. The TSS considered in this paper is such a solar thermal energy

harvesting device requiring a precision sun tracking mechanism.

In [5], authors presented the analysis on the effect of small deviation of incident angle on thermal performance of parabolic solar concentrator. Fig. 2 illustrates the geometry of a parabolic solar concentrator of the type considered in their analysis as well as in our work. The heat absorbing device is placed at the focal line of the two-dimensional parabolic concentrator. The coefficient of angle deviation η_β is defined as the decreasing of collector's thermal performance due to small angle deviation of concentrator's focal plane related to the direction of the incident sun beams β ($^\circ$) and is shown to be given by

$$\eta_\beta = \begin{cases} 1, & \beta \leq \beta_{\min} \\ \frac{4f}{B} \sqrt{\frac{d}{2f \sin \beta}} - 1, & \beta_{\min} \leq \beta \leq \beta_{\max} \\ 0, & \beta > \beta_{\max} \end{cases} \quad (1)$$

Here β_{\min} is the minimum incident angle β so that all the beams still hit the heat absorber. When β exceeds β_{\max} , all reflected beams miss the heat absorber. It can be shown that these two limiting incident angles are given by

$$\beta_{\min} = \sin^{-1} \left[\frac{8df}{16f^2 + B^2} \right] \quad (2)$$

and

$$\beta_{\max} = \sin^{-1} \left[\frac{d}{2f} \right] \quad (3)$$

where d is the diameter of the heat absorbing tube, and f and B are respectively the focal length and width of the parabolic concentrator. We illustrate here the sensitivity of performance to incident angle deviation by computing the coefficient of angle deviation η_β for the dimensions of the parabolic concentrator built in our work. The selected dimensions being $B = 90$ cm, $L = 75$ cm, $f = 40$ cm, and $d = 10$ cm, the limiting incidence angles are $\beta_{\min} = 5.45^\circ$ and $\beta_{\max} = 7.18^\circ$. As indicated by the graph of η_β versus β in Fig. 3, the percentage of reflected rays hitting the heat absorber reduces from 100% at β_{\min} to 0% as the incident angle reaches β_{\max} . The parabolic concentrator needs to be pointed within 5.69° of the direction of the Sun to collect more than 90% of the reflected Sun rays. This range of angle may be increased by increasing the diameter of the heat absorber and by decreasing the focal length and/or width of the parabolic reflector. The diameter of the heat absorber is limited by the factors such as the temperature levels required in the solar still and the relative dimensions of the parabolic reflector. Decreasing the width of the reflector has implications in the amount of energy collected. Likewise decreasing the focal length cause difficulties in mounting the heat absorber conveniently.

The solar concentrator of the type considered in our work has to maintain the focal axis horizontal while tracking the sun. This in turn requires an *alta-azimuth* mount wherein the apparatus will be rotated horizontally (in azimuth) and vertically (in altitude) so that to face the sun directly throughout the day. A single axis tracker to rotate the reflector only in the east-west direction may focus a significant fraction of the incident solar radiation on to the heat absorber. However, the TSS horizontally placed in the north-south direction may not be perpendicular to the direction of the sun every day. A two-axis tracker will perform optimally by compensating for the daily changes in the sun path throughout the year.

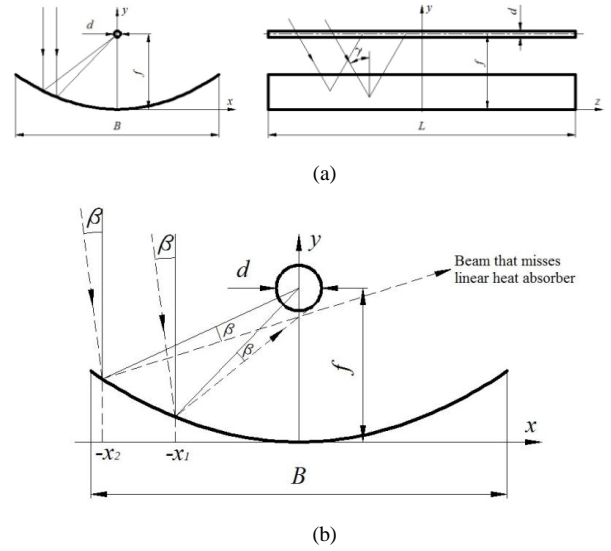


Fig. 2. Effect of deviation in incident angle in Parabolic Concentrator (a) Cross sectional and side views (b) Small deviation of incident angle of sun beam at parabolic concentrator.

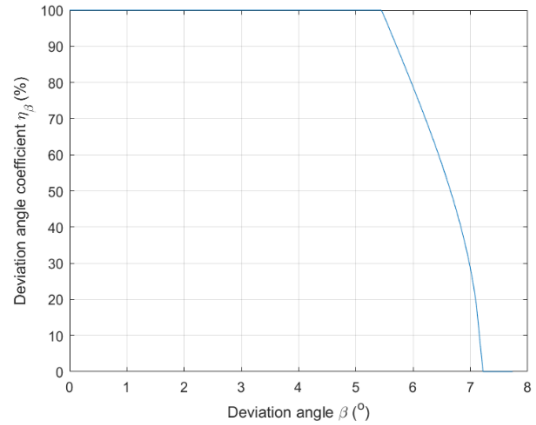


Fig. 3. Variation of deviation angle coefficient with incident angle.

With respect to tracking control strategies, solar tracking systems designed and built around the globe are of three categories; open loop, closed loop, and hybrid. Open loop system is simplistic and cost effective and is based on sound theoretical considerations of solar geometry with respect to time of the day and hence precision computation of the coordinates of the sun on the celestial sphere. However, a system solely operating in such an open loop mode should have mechanisms and structure of sufficient quality since there are no sensors and feedbacks to estimate the actual orientation of the parabolic concentrator. On the other hand, a closed loop system completely based on sensor feedback has its drawbacks because the sensors may lock into a reflected ray or stray light. Thus, a hybrid system based on sun path computation and tracking as the primary method and a periodic small-scale correction using sensor feedback is robust.

In what follows, we present the system design considerations and operational algorithms in Section II. The mechanical structure and the gear system of the solar tracker, electronic subsystems, and the program components are described and illustrated as they were fabricated, in Section III. The paper is concluded in Section IV.

II. SYSTEM DESIGN AND ALGORITHMS

A. Structural and Mechanical Design

Initially FreeCad software was used to design the system structure. Later the design was ported to SolidWorks so as to simulate the systems dynamics. Fig. 4 shows the CAD model. The tracker is driven by the azimuth and elevation motors via spur gear systems. The TSS is to be placed at the focal line of the parabolic reflector. The base and the vertical cylindrical column are of sufficient masses to keep the center of gravity low enough to achieve good stability. Although not shown in the design, a counter weight is to be included at the top of rotating parabolic reflector to balance the mass of the reflector. This will annul the static torque on the elevation motor. Thus, the torque requirement will reduce to that needed to overcome the inertia and friction.

The position sensor arrangement is exemplified at the right top. The tracker is to be eventually powered by solar cells mounted on the edges of the reflector as depicted.

B. Dual-axis tracking control system

A combination of open loop and closed loop control methods have been used in the tracking system thus resulting in a hybrid tracker. The block diagram of the controller is shown in Fig. 5. The open loop approach encompasses a sun path calculation algorithm so as to periodically orient the parabolic reflector to directly face the sun. The sun-path algorithm residing in the microcontroller obtains time from the Real Time Clock (RTC) module. Position of the sun at any given time is expressed in terms of either *equatorial coordinates* (right ascension and declination) or *alta-azimuth coordinates* (altitude and azimuth). The coordinates can be transformed from one to another considering the spherical geometry of the *celestial globe*, the apparent sky in which the celestial objects including the sun moves. The sun path calculation involves the consideration of earth's daily rotation around the north-south axis and the yearly orbit around the sun. The approximately 23.44° tilt of the earth's rotational axis with respect the orbital axis causes the apparent daily sun path on the celestial globe to shift throughout the year with respect to far objects such as stars.



Fig. 4. Structural and mechanical design of the PCST-TSS with dual-axis tracking.

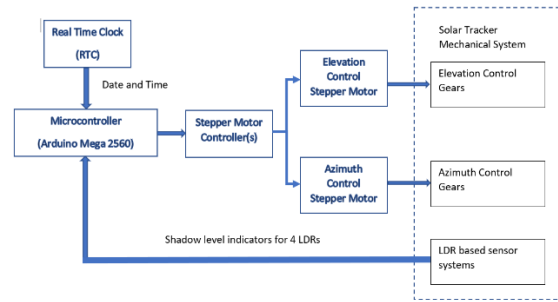


Fig. 5. Functional block diagram of the dual axis solar tracking controller.

Hence the position of the sun at solar noon moves with a yearly cycle along the *ecliptic* which is at an angle of 23.44° with respect to the *celestial equator*. The celestial equator lies in the same plane as the earth's equator. Formulations of sun path algorithms is found in literature such as [6]. In addition to the earth's rotation and orbit, earth's axis wobbles periodically with a much longer time constant of 26,000 years. This is known as *precession*. The *nutation* is the minute oscillation of the axis within the precession which has a period of 16.8 years. Implementation of sun path algorithms considering these and other factors have been available for adoption in our solar tracking system. NREL's Solar Positioning Algorithm (SPA) [7] is an example implementation that makes use of tabulations in the popular book by J. Meeus [8].

The closed loop control is achieved by the inclusion of a sensor module to detect any error in the orientation and by repositioning the reflector in altitude and azimuth via an iterative algorithm. We use stepper motors in the system designed and built due to the versatility and accuracy. Stepper motors with high torques and precision have become relatively inexpensive compared to traditional servomotors of equal torque and precision. However, an external sensor module and feedback is needed when using stepper motors since there are no built-in encoders in stepper motors as in servo motors. The closed loop control is required in order to compensate for positioning errors due to backlashes in the gear system and the inaccuracies in the structural elements of the tracking mechanisms. The parabolic reflector position sensing module we built consists of four Light Dependent Resistors (LDRs) mounted on a rigid board as in Fig. 6. Readings from electronic circuitry associated with the four LDRs are systematically used in the computation of errors. The overall control process with sun path computation and sensor feedback is illustrated in Fig. 7.

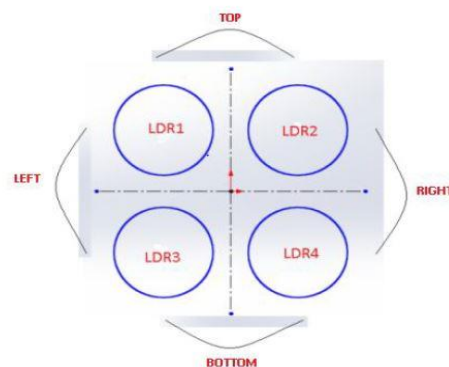


Fig. 6. Schematic arrangement of the sun position sensor module.

TABLE I. MATERIALS AND COMPONENTS

Material/Component	Size/Specs	Cost (LKR)
1 x Reflective sheet	75cm x 90cm (2.5' x 3')	360
2 x Steel box bars	Length-18 ft, 1" x 1", thickness-1.4mm	2500
Flat iron rods	Widths of 1/2" and 3/4"	590
2 sets of gear wheels	96mm/24mm (62:14 teeth)	3000 ^a
2 x NEMA 17 stepper motors	1.8° step angle (200 steps/revolution), 40Ncm, 1.2 A at 4 V	2980
2 x A4988 stepper motor drives	35 V and ± 2 A	530
DS3231 RTC modules	Leap-Year Compensation Valid Up to 2100, Accuracy ±2ppm from 0°C to +40°C	295
4 x LDR	8 to 12 ms response time, ~10Ω to 1k Ω typical from bright light to dark	72
Arduino Mega 2560 micro-controller board	ATmega2560, μC, 7-12V input, 5V logic, 256K flash	1890
DC power supply (12V/10A) -for testing	AC/DC converter	1290
Breadboard, Veroboard	Breadboard with Embedded metal clips and perf board	160
2 x Limit switch		260
Wires, headers and passive components	miscellaneous	121
Replenishable workshop tools, solders, and welding rods	miscellaneous	1450
Total cost		15498

^aestimated

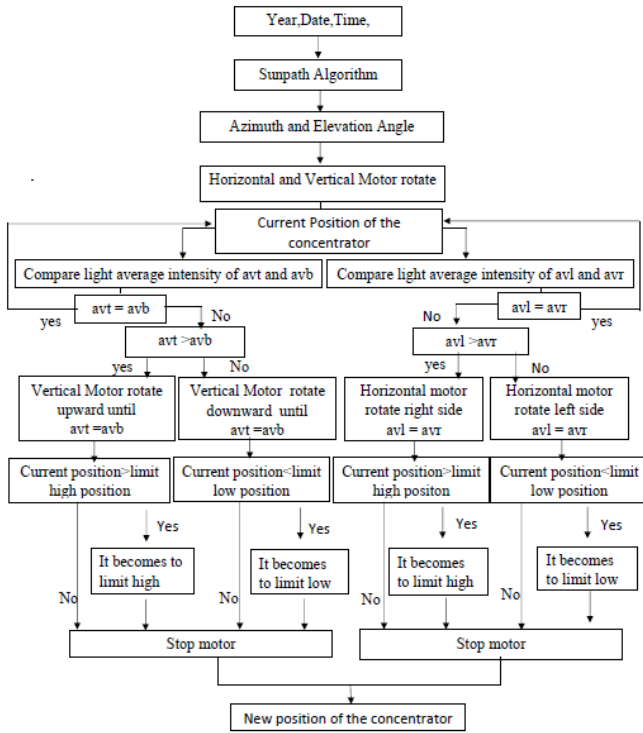


Fig. 7. Flow chart of the hybrid dual axis solar tracking algorithm.

In the hybrid sun tracking and motor actuation algorithm depicted in this flow chart, the variables avt, avb, avl, and avr refer to average values of the readings from LDRs as follows.

- avt : average of the measurements from top two LDRs
- avb : average of the measurements from bottom two LDRs
- avl : average of the measurements from Left two LDRs
- avr : average of the measurements from Right two LDRs

Thus, the comparisons are made between avt and avb to correct positioning error in the elevation. Likewise, comparison is made between avl and avr to correct the azimuthal error.

III. MECHANICAL AND ELECTRONIC SUBSYSTEMS

A. Mechanical constructions of tracker components

Most of the materials required for prototyping the structure of the solar tracker, the gear systems and the parabolic reflector were collected from local hardware stores and used items stores (na-dar shop). Some materials such as aluminum blocks for gear cutting were available at the mechanical engineering workshop of SEUSL. The electronic components were purchased through mail orders placed at electronic part supply stores in Kandy and Colombo cities. The parts list along with the costs are listed in TABLE I. The total cost has been well within the expected budget of LKR 20,000.

The mechanical components were fabricated at the mechanical engineering workshop of SEUSL with the support of workshop engineer and the technical staff using machineries available at the workshop. Materials and replenishable tools were provided by us to the workshop. Fig. 8 and Fig. 9 show the parabolic reflector, the base, and the altitude and azimuth gear wheels as they were fabricated at the workshop. Aluminum sheet of good reflective characteristics was used to build the parabolic concentrator. The spur gears were cut from aluminum bars since it was the viable material among the available stock for the machineries.

Some used parts were also included in the fabrication. The cylindrical pipe used as the vertical pier and the base plates are examples.



Fig. 8. Reflector (left) and the base (right) of the solar concentrator fabricated at SEUSL mechanical engineering workshop.

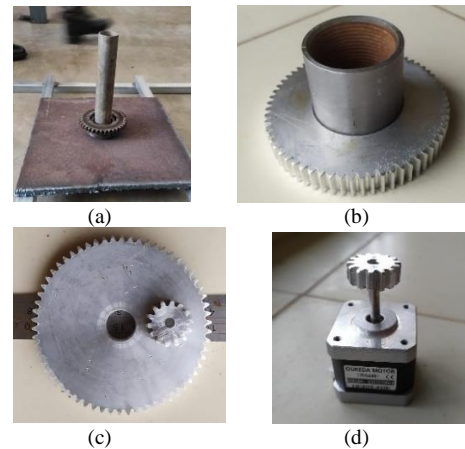
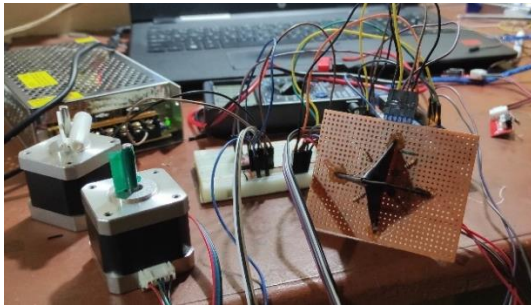


Fig. 9. Gear wheels and mounts fabricated at SEUSL mechanical engineering workshop (a) azimuth gear on rotatable tube (b) altitude gear wheel fixed around the rotatable pipe (c) spur gear wheel pair for a gear ratio of 4 (d) smaller gear wheel on stepper motor spindle.

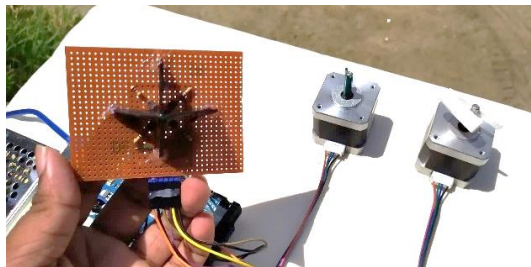
B. Hybrid controller electronics and program codes

The control electronics were assembled on a bread board. The sensor module was built on a Vero board. The 4 LDRs were mounted close to the 4 corners of the cross shaped shading arrangement so that to achieve good sensitivity. The sensor module operation was verified in outdoor environment by pointing to the sun and observing that the motors rotate as the sensor module was tilted (Fig. 10).

The hybrid control algorithm for the dual axis solar tracker was implemented in Arduino language for compiling and uploading into the Arduino Mega 2560 board. While there are less expensive microcontroller board available, the choice has been due to the availability with our personal stocks at the time of prototyping. The programming tasks involved customizing the sun path algorithm program obtained from sources such as [7], writing codes to process LDR sensor output as well as for stepper motor control. Eventually, all program components were combined to follow the logic of flow chart in Fig. 7. The sensor readings are used to make decision on which way to turn the altitude and azimuth motors. In doing so an error tolerance has been introduced to avoid excessive movement of the tracker during a corrective cycle following repositioning based on sun path algorithm.



(a)



(b)

Fig. 10. (a) Assembled operational hybrid solar-tracker control system (b) testing the operation of sensor module with LDRs in the sunlight.

IV. CONCLUSION

This paper presented the design and prototyping of a solar concentrator with dual axis tracking to be used for harvesting solar energy for water purification. Based on the prior art in research topic, a hybrid control tracking system was introduced. We completed the fabrication of all necessary components namely the mechanical structure, gear systems, electronic control system along with the stepper motor and the parabolic reflector. Due to the COVID 19 pandemic the university has been continuously closed during the last several months of our senior year research project. Therefore, we were unable to attend to the workshop within the university premises to complete the system integration and testing of the complete electro-mechanical system as of now. Refinements to the hardware and software are to be made following the tests to be carried out on the completed system.

ACKNOWLEDGMENT

Authors thank the engineer and the technicians of mechanical engineering workshop for the effort taken to support us to fabricate the mechanical components of the prototyped solar tracker.

REFERENCES

- [1] M. Elashmawy, "Improving the performance of a parabolic concentrator solar tracking tubular solar still (PCST-TSS) using gravel as a sensible heat storage material," *The Int. J. Sci. and Tech. of Desalting and Water Purification*, Elsevier, vol. 1, Jan. 2020, doi.org/10.1016/j.desal.2019.11.4182.
- [2] R. C. Neville, "Solar Energy Collector Orientation and Tracking Mode," *Solar Energy*, vol. 20, no. 1, pp. 7–11, 1978, 10.1016/0038-092x(78)9013-4-2.
- [3] A. Şenpınar and M. Cebeci, "Evaluation of Power Output for Fixed and Two-Axis Tracking PV arrays," *Applied Energy*, vol. 92, pp. 677–685, 2012, doi:10.1016/j.apenergy.2011.07.043.
- [4] S. Abdallah, "The Effect of Using Sun Tracking Systems on the Voltage–Current Characteristics and Power Generation of Flat Plate Photovoltaics," *Energy Conversion and Management*, vol. 45, no. 11–12, pp. 1671–1679, 2004 doi:10.1016/j.enconman.2003.10.006.
- [5] T. Simonovic, M. Stamenic, N. Tanasic, and M. Trinic, "Effect of small deviation of incident angle on thermal performance of parabolic-trough solar collector," *4th International Symposium on Environmental Friendly Energies and Applications (EFEA)*, Belgrade, Serbia, Sep. 2016, pp. 1–4, doi: 10.1109/EFEA.2016.7748815.
- [6] R. Walraven, "Calculating the position of the sun," *Sol. Energy*, vol. 20, no. 5, pp. 393–397, 1978, doi: 10.1016/0038-092X(78)90155-X.
- [7] Solar Position Algorithm (SPA) (nrel.gov)
- [8] J. Meeus, *Astronomical Algorithms*. Second edition 1998, Willmann-Bell, Inc., Richmond, Virginia, USA.

Performance Analysis of Hierarchical Software Defined Network (SDN) Controller Arrangements in SDNs

Fernando W.T.P.N.

*Department of Electrical and Electronic Engineering
University of Peradeniya
Peradeniya, Sri Lanka
nishakawith@gmail.com*

Jayaweera M.N.R.S

*Department of Electrical and Electronic Engineering
University of Peradeniya
Peradeniya, Sri Lanka
jayaweerasanga@gmail.com*

Pathirana P.R.N.

*Department of Electrical and Electronic Engineering
University of Peradeniya
Peradeniya, Sri Lanka
rusirunuwan1995@gmail.com*

Dr. Maheshi B. Dissanayake

*Department of Electrical and Electronic Engineering University of Peradeniya
Peradeniya, Sri Lanka
maheshid@eng.pdn.ac.lk*

Anuradha Udunuwara

*Research and Development Sri Lanka Telecom PLC Kandy,
Sri Lanka
anuradhau@slt.com.lk*

Abstract—The traditional architecture of a typical data network in general and in Telecommunication network environment in particular has legacy issues such as manageability, scalability and flexibility. Network administrators do not have much power to control and monitor their networks. Therefore, a new network architecture, software-defined networking (SDN), has emerged to address these challenging issues by redefining the network to make it programmable. SDN relies on decoupling the control plane from the data plane so that it is central and programmable. OpenFlow protocol, which is an open-source protocol adopted by the Open Networking Foundation, is empowered to facilitate the communication between controller and switch and to enable agile management of the network. The controller is the vital component of the SDN architecture. Therefore, there is a necessity to assess and compare the different existing controllers in the market and research domains. A comparative performance analysis of hierarchical SDN controller arrangement implemented on networks is done with the ODL (OpenDaylight) and Open Network Operating System (ONOS) on a Mininet virtual test environment. The test-bed topologies are methodically created as traditional hardware defined networks (HDNs), with the default SDN controller in Mininet emulator and with the ODL, ONOS controllers. Each method is analyzed with a non-hierarchical and hierarchical SDN controller arrangement, respectively. The initial packet latency, minimum, maximum, and average round-trip time (RTT), and Transmission Control Protocol (TCP) bandwidth are measured and analyzed with respect to network topology in Mininet under HDN and SDN scenarios.

I. INTRODUCTION

Software define network (SDN) is an architecture with logically centralized controller with intelligence, typically used for a telecommunication network. with intelligence. These SDNs are implemented and managed through group of SDN controllers and the arrangement of these controllers in a network plays a crucial role similar to the controller selection and topology selection. In a flat or horizontal architecture, the

controllers are positioned horizontally on one single level. In other words, the control plane consists of just one layer, and each controller has the same responsibilities at the same time and has a partial view of its network. In a hierarchical or vertical architecture, the controllers are positioned vertically [1]. They are portioned among multiple levels, which means that the control plane has several layers, generally two or three. The controllers have different responsibilities, and they can take decisions based on partial or complete view of the network.

There can be seen various kinds of SDN controllers used in the industry. They can be multi-vendor SDN controllers or multi-techno SDN controllers[6]. For a particular implementation, customer, especially telecom service providers might have to use a mix of those controllers according to their need or due to financial constraints. In such a case, there can be inconsistencies between controllers and weaker communication between SDN controllers will force the network to a low performance state.

To overcome these bottlenecks, we propose a hierarchical SDN controller architecture arrangement and traditional network performance parameters such as initial packet latency, average round-trip time, Transmission Control Protocol (TCP) bandwidth and jitter are examined to observe the reliability of our proposed architecture. Assessment of hierarchical controller setup with different SDN controllers is the main objective of this analysis.

II. PROBLEM DEFINITION

One of the biggest shortcomings of traditional networks is its rigid structure and low flexibility, especially at expansion stages. Hardware based physical infrastructures with manual configurations fails to address the rapid explosion in the demand for telecom services, demands for a flexible, fast and low-cost networking solutions. SDN provides virtualized,

software based solutions to these bottlenecks. Out of many SDN controllers in the market, Open Network Operation System (ONOS) and OpenDayLight (ODL) are two popular choices with network architects.

Single and distributed controller are the general models for control plane. A single SDN controller faces with some problems such as scalability and single point of failure. Distributed model is introduced to solve these problems. Hierarchical model is known as one of the main kinds of distributed SDN controllers. In this paper, hierarchical SDN models with a combination of ODL and ONOS controllers are analyzed with the performance matrices. In this study, we evaluate the performance of the ONOS and ODL SDN controllers in hierarchical network arrangement under four different topologies.

III. LITERATURE SURVEY

According to literature, there exist few studies with the aim of comparing SDN controllers. These studies have been designed to identify the baseline performance of controllers and determine which controller outperforms the others in certain specific test environments.

In [7] a comparative performance analysis of ONOS and ODL SDN controllers are carried out by considering different network topologies with unloaded and loaded network conditions. An impartial experimental analysis based on active measurement has been done for the selected Standalone reactive mode controllers by executing ‘ping’ and ‘iperf’ commands in the Mininet console. The experimental evaluation of ONOS and ODL indicates that ONOS outperforms ODL for throughput and latency with different network topologies.

In 2015, Khattak et al conducted a preliminary study of the Floodlight and ODL controllers using Cbench [2]. They evaluated the performance of these two controllers in terms of throughput and latency. They have stated in [2] that they choose Floodlight due to its maturity as an SDN controller. The authors noticed that ODL has unexpectedly poor responsiveness in throughput and latency tests compared to Floodlight. Further, they have observed that ODL failed to produce acceptable level of result in many of the tests, and the failure increased when scaling up the number of switches. They speculated that this could be due to memory leakage of the ODL controller. They also proposed modifications in Cbench to support data center traffic models for SDN architecture as well.

Bhargavi Goswami [3] focused on Experimenting with scalability of SDN. They specifically used ONOS controller and have observed that with time ONOS controller was able to achieve stability under varying number of nodes and was able to handle the network blast to some extent.

Bulumulla [8] developed an algorithm to identify link congestion. Bulumulla observed that by reducing link congestion, network throughput could be increased. The algorithm designed forwards traffic to unused or low utilized links. According to the developed algorithm, the SDN controller can change the traffic flow automatically.

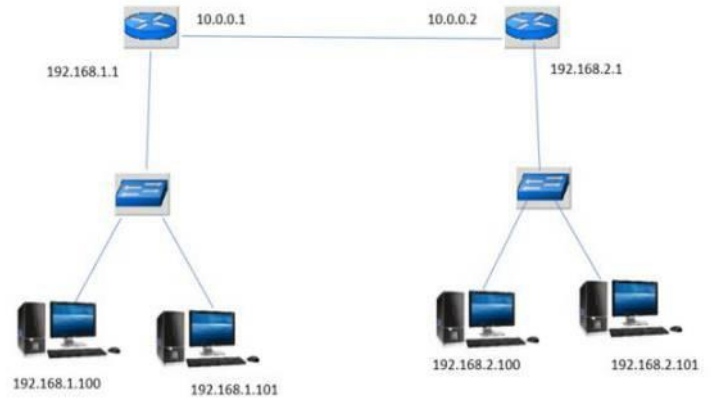


Fig. 1. Legacy Custom topology with two routers

B. Implementation of default topologies with an external con-troller

In the test setup a virtual network was designed with two OpenFlow switches that are controlled by either ODL or ONOS SDN controllers. We have adopted ODL SDN controller, Versions ODL-0.8.4 (Oxygen) and ONOS SDN controller, ONOS-2.3.0 (Toucan) in the test setup. This network has an ODL/ONOS SDN controller on top and two OpenFlow switches that are controlled by the SDN controller [4]. Each host is connected to a switch as shown in in Fig.2.[9]

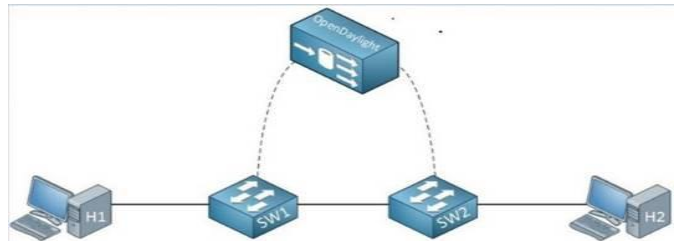


Fig. 2. Minimal default topology

C. Implementation of custom topologies with an external controller

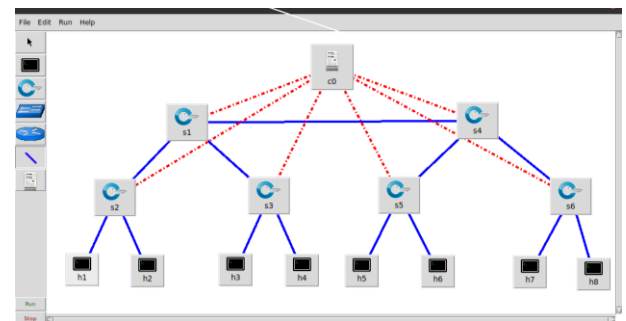


Fig. 3. Topology implemented with the default Mininet controller

To create various topologies for testing purpose, separate python scripts were developed and made them to be controlled through a remote controller. Initially one ODL controller which is installed in separate virtual machine was connected to topology as shown in Fig.3 and tested for the seamless operation.

D. Implementation of custom topologies with two external controllers

In most of the references there was only a central controller to manage every switch in the topology. To model a hierarchical controller setup, next concern is to connect C0 and C1 controllers separately to a network as in the in-Fig.4 [5]. Here two ODL controllers are used as C0 and C1.

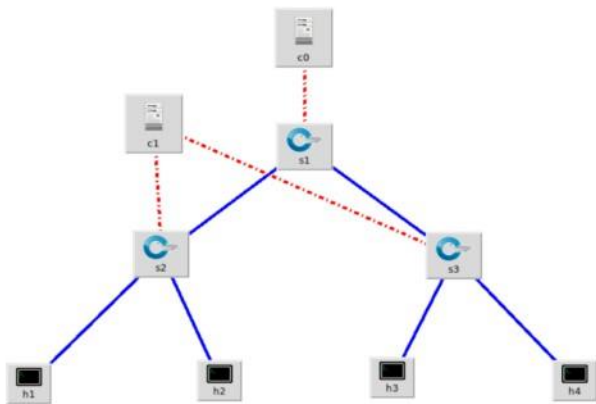


Fig. 4. Two external controller setup

E. Implementation of the hierarchical controller setup

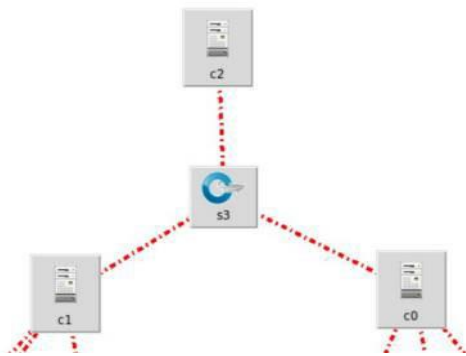


Fig. 5. Hierarchical controller setup

In order to create the hierarchical architecture, the setup that was created by using two controllers is extended by introducing third SDN controller C2 that connects to central OpenFlow switch S3 as illustrated in in Fig.5.

The tests were carried out with ONOS and ODL SDN controllers connected hierarchically to span three network topologies of OpenFlow based virtual switches (OpenVswitch) as in Fig.6. These basic topological arrangements were spanned as in Fig.8 to create 12 instances. Complex networks are mostly derivatives of basic single, tree and linear topologies.

Accordingly these three basic configurations were tested for the final analysis. Tests were carried out to evaluate the effects of hierarchical SDN controller arrangements and the correlation of controllers from different vendors[6]. Latency, jitter, and throughput parameters were examined in the hierarchically connected three ODL controller arrangement and two ODL controllers connected as a flat architecture that are installed in separate virtual machines. The same tests were repeated on a non-hierarchical (flat) architecture with ODL and ONOS controller setup, and then by connecting an ODL controller hierarchically to the same setup. The non-hierarchical architecture is utilized as the reference network. In presenting the results, the outcomes of the hierarchical and flat architectural setups were presented with the same order of controllers in one graph (latency, jitter analysis) to facilitate comparison of results and to avoid having repetitive figures.

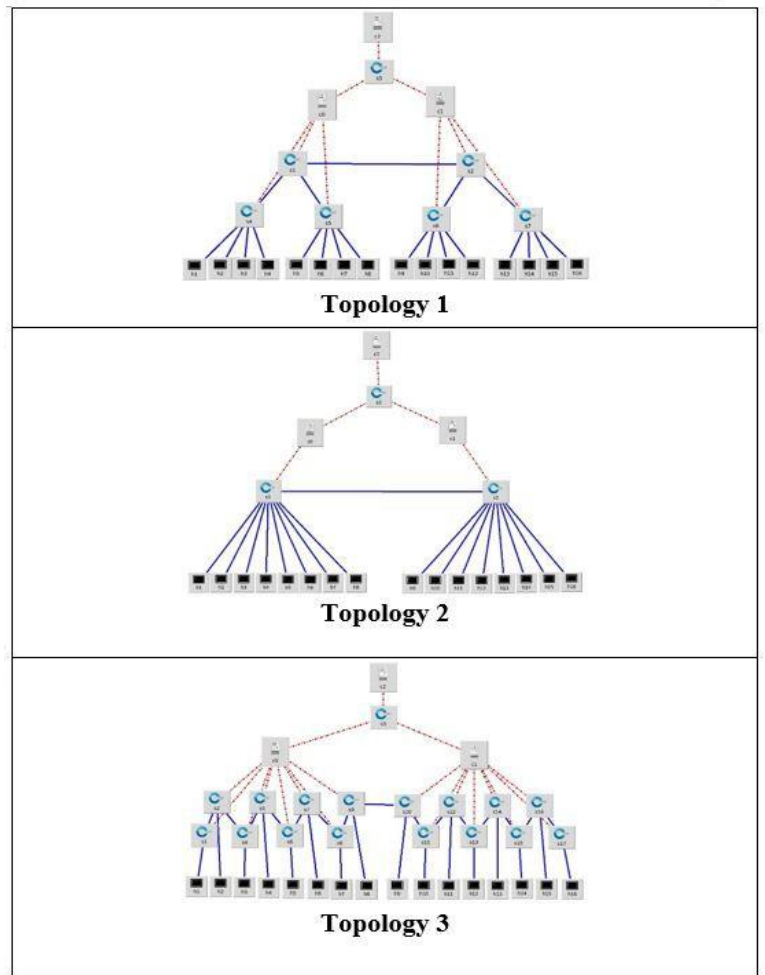


Fig. 6. Test topologies

V. RESULTS

A. Throughput Comparison

This section presents the results of throughput tests on ONOS and ODL connected hierarchical and non-hierarchical topologies. Here the network topology is varied while keeping the number of hosts around 16 to maintain the same network

Time(s)	Throughput Comparison for Topology 1((Gbps)															
	h1-h2				h1-h5				h1-h9				h1-h13			
	Topology				Topology				Topology				Topology			
	1-1	1-2	1-3	1-4	1-1	1-2	1-3	1-4	1-1	1-2	1-3	1-4	1-1	1-2	1-3	1-4
1	30.6	23.5	28.2	27.2	11.44	18.2	13.3	13.2	1.78	1.13	1	1.65	1.5	1.08	1.17	1.5
2	30.2	26.9	26.8	29.1	12.35	18.4	12.8	13.4	1.84	1.53	0.973	1.6	1.09	1.39	1.12	1.75
3	31.5	28.2	27.1	32	14.8	13.6	12.7	13	1.95	1.53	0.807	1.49	0.41	1.27	1.07	1.46
4	32.8	29.6	23.8	32.2	15	13	13.3	13.4	2.03	2.14	0.758	1.87	1.49	1.31	1.16	1.22
5	31.9	26.7	25.7	31	14.7	15.9	13.8	14.3	2.01	2.48	0.813	1.77	1.01	1.37	1.2	1.58
6	31.9	23.4	29.9	29.6	13.8	16.6	12.8	13.3	1.94	2.34	0.981	1.61	1.09	1.22	1.01	1.67
7	34.2	24.7	28	30.6	15.1	16.5	13	14.2	1.93	2.27	0.78	1.59	1.68	1.45	1.46	1.34
8	33.2	27.2	26.4	30.7	13.8	19.1	12.4	13.7	1.86	3.91	0.746	1.74	1.84	1.28	1.49	1.43
9	31.6	27.1	26.2	28.4	14.6	18.4	13.5	13.3	1.91	5.09	0.845	1.85	2.14	1.52	1.59	3.5
10	31.1	32.1	25.3	26.1	15.6	18.2	13.8	13.7	2.6	4.75	0.913	1.79	1.87	1.99	1.6	2.3
11	32.4	26.5	30.9	30	15.8	18.7	8.24	12.5	2.59	5.05	0.887	1.63	2.09	1.92	1.41	1.55
12	30.2	33.5	26.8	27.1	15.5	18.1	12.6	13.6	2.48	3.32	1.05	1.63	2.17	1.91	1.6	1.25
13	32.2	32.6	27.8	32.6	17.5	17.3	13.8	14.2	2.48	2.61	1.15	1.72	2.02	2.05	1.62	2.09
14	30.9	27.8	28.8	33	17.1	18.7	13.9	14.7	2.72	2.44	1.03	1.66	2.28	2.26	1.56	1.32
15																

Topology	Number of Nodes					No. of links (Host-Switch, Switch-Switch)
	Switches in forwarding plane	Hosts	Controller			
			C0	C1	C2	
Topology 1-1	6	16	ODL	ODL	ODL	21
Topology 1-2	6	16	ODL	ODL	-	21
Topology 1-3	6	16	ODL	ONOS	ODL	21
Topology 1-4	6	16	ODL	ONOS	-	21
Topology 2-1	2	16	ODL	ODL	ODL	17
Topology 2-2	2	16	ODL	ODL	-	17
Topology 2-3	2	16	ODL	ONOS	ODL	17
Topology 2-4	2	16	ODL	ONOS	-	17
Topology 3-1	16	16	ODL	ODL	ODL	31
Topology 3-2	16	16	ODL	ODL	-	31
Topology 3-3	16	16	ODL	ONOS	ODL	31
Topology 3-4	16	16	ODL	ONOS	-	31

Fig. 8. Topology configurations used in performance Analysis

scale, which eases the comparison of controller performance with respect to a topology change. “iperf” bandwidth-testing tool on the Mininet is used for this experiment. This tool produced an estimate of network throughput for each topology-controller combination, providing an alternate means of measuring the network’s potential to send traffic quickly. This command outputs two element array of defined server and client terminals of selected hosts and these are taken as the measurements of throughput. Although this metric represents data plane performance of the virtual testbed, which does not contain any physical component and setup with equal resources made available to both controllers, it should be noted that the output results solely depend on controller setup performance.

The measured TCP throughput of the hierarchically connected topologies and non-hierarchically connected topologies are subjected to less variations as shown in Fig.7. Performance of the throughput in the nodes decline with the combination of different controllers in hierarchical and non-hierarchical instances

When two different types of controllers are connected, it leads to a better utilization of the throughput over time. This is the obvious reason for the increment of the throughput value over the time.

B. Latency Analysis - Average Round Trip Time

The experiment was carried out by running the ping command fifteen times on a specific path in each of the topology presented in Fig.8. Each path used was logically different from each other. The test environment with hierarchically connected topology-3 in Fig.6 has considerably lower round trip time (RTT) value than non-hierarchically connected topology-3.

It is evident that the hierarchical controller has a better algorithm to find the shortest path to reach the destination. Anyhow, RTT value increases with the combination of ONOS and ODL controllers in hierarchical and non-hierarchical instances as seen in Fig.9-10.

Topology 3- Average RTT Comparison

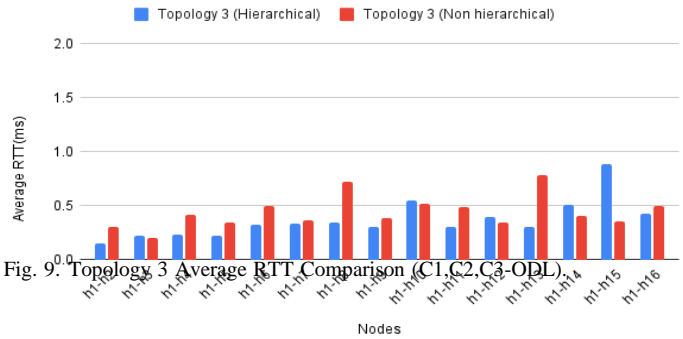
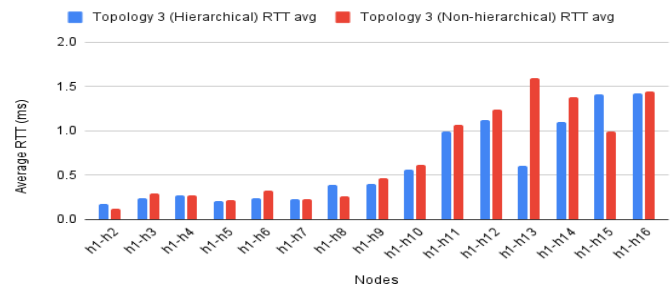


Fig. 9: Topology 3 Average RTT Comparison (C1,C2,C3-ODL).

Topology 3- Average RTT Comparison - (C1-ONOS)



Average round trip time was calculated by using eq (1).

$$Average\ Round\ Trip\ Time = \frac{\sum_{i=1}^n RTT(i)}{n} \quad (1)$$

C. Latency Analysis - Initial Round Trip Time

The initial RTT tracks the time taken for the very first ping that is sent after the topology is established in Mininet network emulator. The first ping is always higher than the next one

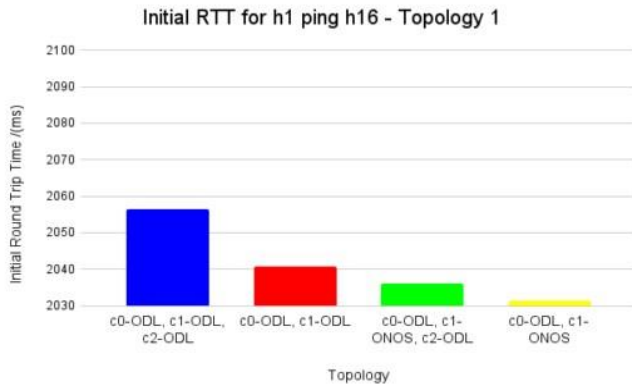


Fig. 11. Initial Round Trip Time for Topology 1.

Topology 1 - Jitter Comparison

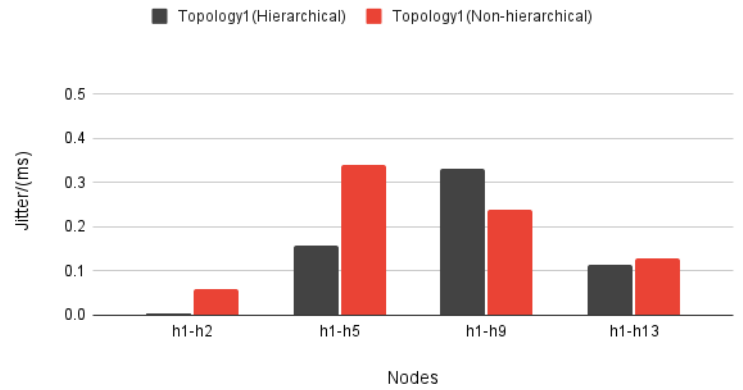


Fig. 13. Jitter comparison- Topology 1 (C1,C2,C3-ODL)

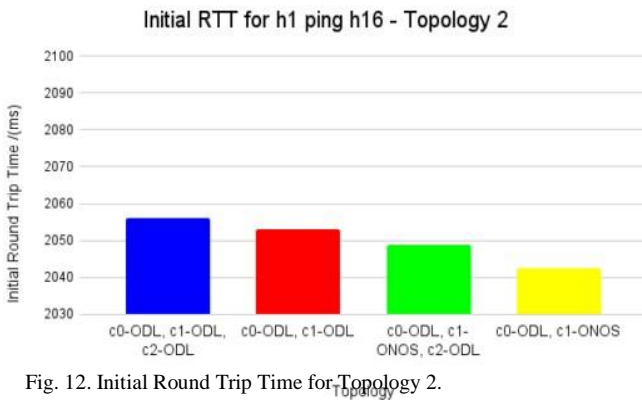


Fig. 12. Initial Round Trip Time for Topology 2.

Topology 1 - Jitter Comparison- (C1-ONOS)

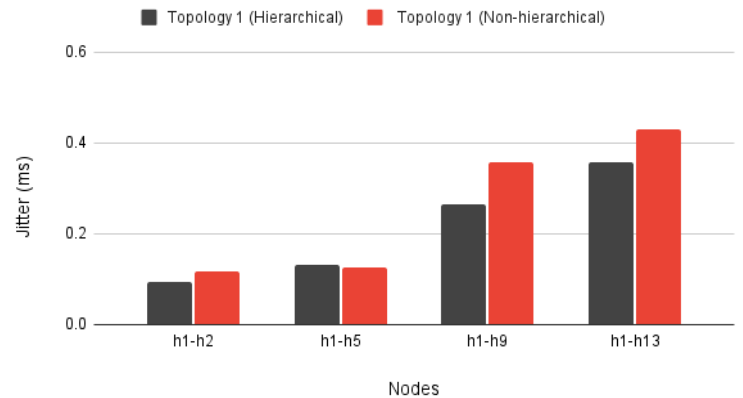


Fig. 14. Jitter comparison- Topology 1 (C1-ONOS)

because it is the first time that a packet traverses the network. The initial RTT gives an estimate of how much time each controller algorithm must take in processing time, to come to terms with the underlying network topology.

Initial RTT decreases with the combination of ONOS and ODL controllers in hierarchical and non-hierarchical instances as seen in Fig.11-12 .In general, initial RTT increases with the hierarchically connected topologies, specially when all three controllers are of the same type.

D. Jitter Comparison

Voice and video transmission over the network has become popular and attracted more attention recently. Jitter has become a very important network performance parameter in multimedia communication. Jitter is the irregular time delay while sending data packets over a network. In an Internet Protocol (IP) network, packets are sent in a continuous stream with the packets spaced evenly apart at the sending side. However, due to network congestion, improper queuing, or configuration errors, this steady stream can become uneven, causing the delay between each packet to vary instead of remaining constant. Jitter of each topology is calculated using 15 individual ping messages. In these tests, the hierarchical setups of SDN controllers (control plane) is varied while keeping the forwarding plane as it is.

Topology 3 - Jitter Comparison

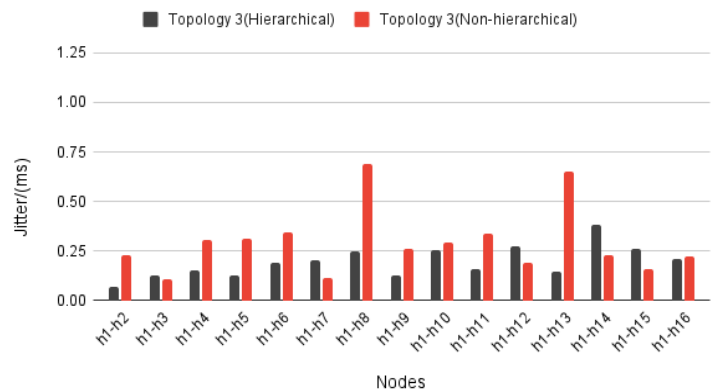


Fig. 15. Jitter comparison- Topology 3

Topology 3 - Jitter Comparison- (C1-ONOS)

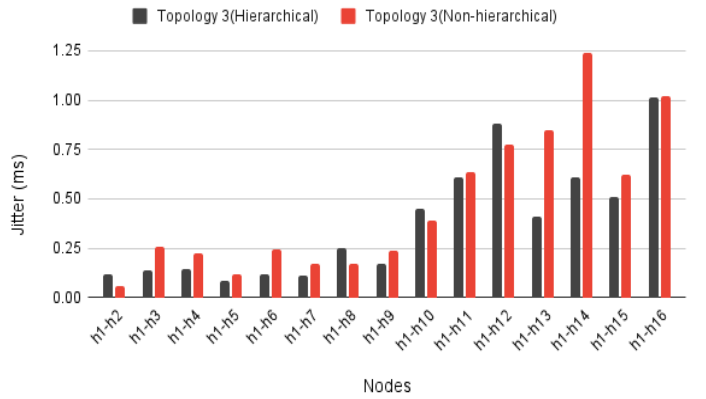


Fig. 16. Jitter comparison- Topology 3 (C1- ONOS)

When considering Jitter of Topology 1 and Topology 3 as in Fig.13-16, setup with hierarchical SDN controller shows lower Jitter values than the one with non-hierarchical. This observation indicates that hierarchical controller setup is more consistent and leads to a more stable network connection when considering topology 1 and Topology 3 even with the combination of ONOS and ODL controllers. Jitter is defined as given in eq. (2).

$$Jitter = \frac{\sum_{i=1}^n |T_{i+1} - T_i|}{n} \quad (2)$$

VI. CONCLUSION

SDN makes the network programmable, agile, and flexible by separating the data and control traffic. Since controller is the key component of the SDN architecture, there is a necessity to assess and compare different controllers in the market and research domains. This study carries out a comparative performance analysis of hierarchical SDN controller arrangement, realized using the ODL and ONOS open-source controllers on a Mininet emulator virtual test environment. Each possible hierarchical arrangement is analyzed with a non-hierarchical and hierarchical SDN controller layout. The initial packet latency, minimum, maximum, and average round-trip time, and Transmission Control Protocol (TCP) bandwidth are compared with respect to hardware defined network (HDN) and SDN scenarios under different Network topologies in Mininet.

The predominately in this analysis, the hierarchically connected topologies and non-hierarchically connected topologies are subjected to less variations in terms of the TCP throughput. In few cases the non-hierarchical controller architecture shows an improvement over hierarchical controller architecture. Hence it can be inferred that, the combination of controllers leads to high throughput. Furthermore, the topologies with less number of switches are subjected to low variations in average RTT, while in topology 3 with the hierarchical controller exhibited promising performance. When considering initial RTT, non-hierarchical controller

architecture with controllers of same vendors performed extremely well. In the jitter analysis, the hierarchical controller architecture exhibited less variations showcasing that they are stable.

As an overall picture, hierarchical SDN controller setup outperforms non-hierarchical setup according to the measured performance parameters.

VII. FUTURE WORK

The study presented is carried out in Mininet emulating environment. The actual traffic in a telecom network heavily depends on the network layout such as selection of transmission mediums as well as on the amount of traffic present in the network (loading of the network). As a future direction, the proposed setup could be tested in real-test environment with deployed test SDN network with actual network traffic.

REFERENCES

- [1] Othmane Bliat, Mouad Ben Mamoun, Redouane Benaini, "An Overview on SDN Architectures with Multiple Controllers", Journal of Computer Networks and Communications, vol. 2016, Article ID 9396525, 8 pages, 2016.
- [2] Z. Khattak, M. Awais, and A. Iqbal, "Performance Evaluation of OpenDaylight SDN Controller," in In Proceedings of the 20th IEEE International Conference on Parallel and Distributed Systems (ICPADS), Hsinchu, Taiwan, December 2014.
- [3] Sameer, M. and Goswami, B., 2018. Experimenting with ONOS scalability on software defined network. Journal of Advanced Research in Dynamical and Control Systems, 10(14-Special Issue), pp.1820-1830.
- [4] Pal, C., Veena, S., Rustagi, R.P. and Murthy, K.N.B., 2014, February. Implementation of simplified custom topology framework in Mininet. In 2014 Asia-Pacific Conference on Computer Aided System Engineering (APCASE) (pp. 48-53). IEEE.
- [5] Zhou, Y., Zheng, K., Ni, W. and Liu, R.P., 2018. Elastic switch migration for control plane load balancing in SDN. IEEE Access, 6, pp.3909-3919.
- [6] Rashma, B.M. and Poornima, G., 2019, February. Performance evaluation of multi controller software defined network architecture on mininet. In International Conference on Remote Engineering and Virtual Instrumentation (pp. 442-455). Springer, Cham.
- [7] Dissanayake, M.B. Kumari, A. L. V. and Udunuwara, U.K.A., "Performance Comparison of ONOS and ODL Controllers in Software Defined Networks Under Different Network Topologies", J. Res. Technol. Eng. volumn 2 (3) ,94-105, 2021.
- [8] Bulumulla, W.R.W.M.Y.S.B. (2020). Enhanced Resilience for Software Defined Network Enabled Data Center Networks. University of Peradeniya, Sri Lanka.
- [9] <https://networklessons.com/cisco/ccna-routing-switching-icnd2-200-105/introduction-to-sdn-opensdylight>

Design an Ocean Wave Energy Converter for Srilanka

Raveendran Gowrishankaran
Department of Mechanical Engineering
Faculty of Engineering
University of Sri Jayewardenepura
Nugegoda
Gowrishankaran.eng@gmail.com

Dulini Yasara Mudunkotuwa,
Department of Mechanical Engineering
Faculty of Engineering
University of Sri Jayewardenepura
Nugegoda
dulini@sjp.ac.lk

Abstract— Sri Lanka has pledged to increase the use of renewable energy sources in order to meet UNDP Sustainable Development Goals. Being an island nation, power generation by extracting wave energy could be a sustainable solution. The climatic conditions of Sri Lanka produce strong wave (20 – 30 kW/m) in certain coastal areas during monsoon period. Even during non-monsoon period it is possible to generate power of 10 to 15 kW/m. In this study the Asymmetric partially submerged buoy is used as an energy conversion device, and it generates electrical energy due to the heave motion. The governing equations of the motion and hydrodynamics parameters are solved for one degree of freedom system using ANSYS Aqua. Three different geometric shapes are tested and adding supplemental mass and optimization of hydrodynamic parameters for different sea states is conducted to determine the performance of each buoy shapes. From the overall results, pinched cone buoy produced average power of 81kW (for 2.98m) and 120kW (for 4.05m), outperforming hemispherical and conical shape buoys.

Keywords— wave energy, convertor, Buoys, Power takeoff, Aqua, CFD.

I. INTRODUCTION

In order to meet the Sustainable Development Goals, set by UNDP, Sri Lanka needs to look into renewable energy sources in power generation. Therefore, there arise a need to develop clean energy sources. The wave and tidal power extraction methodologies have not developed considerably compared to other renewable resources [1].

About 71% of earth's surface is covered with water and the ocean holds about 96.5% out of them. Therefore, the possibility of extracting energy from water surfaces can be maximized compared to the energy extraction from the land surfaces. The new technologies to extract energy from ocean includes tidal power, wave energy, ocean thermal energy conversion, ocean currents, ocean winds and salinity gradients. Among them, the most feasible technologies are tidal power, wave power and ocean thermal energy conversion. The Ocean thermal energy conversion cannot be implemented, without a significant temperature difference [2]. Therefore, the technologies such as wave energy and tidal energy are more feasible for extracting energy from the ocean.

Tides are the rise and fall of the sea levels caused by the combination of gravitational force of moon and sun and the rotation of earth. The height differences (Potential energy) of the tides are used to generate electricity hence, method is called as 'Tidal energy extraction'. Unlike solar and wind energy tidal energy can be predicted easily. This is because, the tide phenomena occur twice in each lunar day (24h) and each tidal phenomenon will happen for 50 minutes and 28 seconds [2]. There exist methods to derive electrical energy using tidal power such as Tidal barrages, Tidal fences, and

tidal turbines. However, this tidal energy requires significant amount of head differences between high tides and low tides.

Wave energy is quite different from tidal energy. Waves are generated by wind. There exist several methods to generate electricity using the movement of the wave. They are Oscillating water columns(OWC), Overtopping devices, and Oscillating body devices. In such methods Air turbines, Low head water turbine and linear electrical generators are used to convert the wave energy into electrical energy [3]. However, the wave energy will vary with time. This is because they depend upon on climatic conditions. Therefore, climatic analysis of the location is mandatory to determine the feasibility of a wave power plant.

In Sri Lanka, the two major monsoon periods are dominating the wave climate in coastal areas. From the studies of energy utilization in Sri Lanka, it shows that the southern coastal area is more feasible to setup wave energy power plant (WEPP) [1].

II. LITERATURE SURVEY

A. Wave Energy and Srilankan wave climate

There is a high possibility to have short wave in Sri Lanka, which has the wave period of 10 to 12 seconds [1]. Also, Sri Lanka is a very special location having a good swell with the power density of 20kW/m and the maximum wave height is below 6 meters. Therefore, Sri Lanka is a very suitable place to utilize the wave energy for the commercial purpose [2].

Sri Lanka is affected by two major monsoon periods namely: Northeast monsoon and Southwest monsoon. Usually, the southern coastal area is affected by both of the monsoon periods. Therefore, it is a good opportunity to have strong wave climate in Sri Lankan Southern coastal area. wave energy flux power is 15kW/m, and the swell wave period is between 8 to 17 seconds [3].

B. Wave Energy Extraction Methods

There are three major types of extracting energy from waves. Which are OWC, Overtopping devices, and oscillating body devices. In all the method the wave movement is used to rotate the turbine. In Sri Lanka the oscillating body devices are more suitable than other types [3].

C. Governing Equation.

There will be some limitations in Wave energy convertor (WEC) designing process based on Wave condition. Initially the maximum possible capture width is determined based on the wavelength for particular area wave condition. To

determine the maximum possible capture width the equation was derived by Falnes in [4].

$$L_{max} = \frac{\lambda}{2\pi} \quad (1)$$

Furthermore, the capture width ratio was derived by Shadman. For a successful device must satisfy a relationship which contains capture width ratio C_{wr} :

$$C_{wr} = \frac{L_{max}}{D} \geq 3 \quad (2)$$

Where, D is the buoy diameter of the WEC. Using this relationship, the buoy diameter will be selected according to the wave condition of the location [5]. Alternatively, Falnes recommended, that the buoy diameter should be between 5 to 10% of the incident wavelength [4].

Shadman established a relationship between wave frequency ω_n , Surface area A_{wp} , Buoy mass m_b , Added mass m_a , and density ρ .

$$\omega_n = \sqrt{\frac{\rho g A_{wp}}{m_b + m_a}} \quad (3)$$

Based on equation (3), the optimum added mass value can be obtained to match the heave resonance of the buoy frequency with wave natural frequency. Therefore, the optimum power will be developed by the design [5]. When the period of wave changes, the buoy no longer achieves the resonance, and it does not produce the maximum power output as well. Therefore, to achieve the resonance at any wavelength, there will be a separate analysis to be done on PTO damping and Added mass using different techniques.

Static equilibrium equation when there is no external force applied on a Spring mass damper system is given below,

$$\sum F_z = ma + bv + cx = 0 \quad (4)$$

III. METHODOLOGY

A. Data Collection

As discussed earlier, in Sri Lanka wave climate is affected by two major annual cyclic weather conditions. namely,

1. South-west monsoon – May to September
2. North-east monsoon – December to February

The monthly average wind speed of Sri Lankan coastal zone is higher than 4m/s, thus reasonable wave will be created during the normal period except monsoon periods [3]. However, during monsoon period the strength and height of the wave will be increased. Specially south and western areas will be affected by south-west monsoon period.

In order to analyze wave strength and height (energy) in Sri Lanka, the wave data was collected from two different major sources: Satellite data and Wave buoy measured data.

1. Wave buoy measured data.

This wave data measurement was carried out in southwest coastal ocean in Sri Lanka by Coast Conservation Department. A pitch and roll type buoy were used to measure the wave data in off Galle harbor at a water depth of 70m. It provides raw data of wave in the form of time series for swell wave and sea wave at the location where the buoy was deployed. The wave data had been recorded for 30 minutes for each 3 hours [6].

The wave data height of the wave, time period, and the direction of the wave are only available between 1989 to

1995. However, there are some data missing during 1989 to 1995 as well. Therefore, the analysis will be based on annual time series.

2. Satellite Data

NASA associated satellite data was downloaded using TOPEX altimeter sensor data record from Physical Oceanography Distributed Active Archive Centre (PODAAC) [7]. This data was measured twice a day.

B. Data Comparison

In order to get precise data analysis, the data comparison was carried out between satellite data and measured buoy data. Here, monthly average significant wave height and time period were used for analysis. Thus, the comparison will be providing a proper understanding about the feasibility of each data set.

The deviation between measured wave data and satellite wave data was analyzed in figure 1, and the satellite wave data also used for further calculation because of unavailability of wave data.

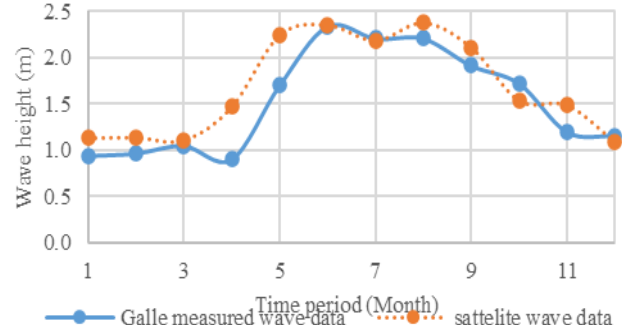


Fig. 2. Measure wave data using buoy and satellite altimeter

The climatic conditions vary with time; therefore, it is mandatory to compare the current wave data with the previous wave data. In order to do the analysis, the current wave data was obtained from a web site called ‘Magic seaweed’ [6]. They provide wave height, wave period and the wave direction for every 3 hours from places in Sri Lanka. The wave data has been collected from February onwards around South coastal Area. Figure 2. shows the wave height deviation along the time series.

In Sri Lanka average wave height is between 0.5m and 2.5m and the average wave period is between 10s and 13s. Therefore, the new wave data set was used for further calculation and decision making. However, the new data set was compared with old wave data set and both of them are showing similar attributes [8].

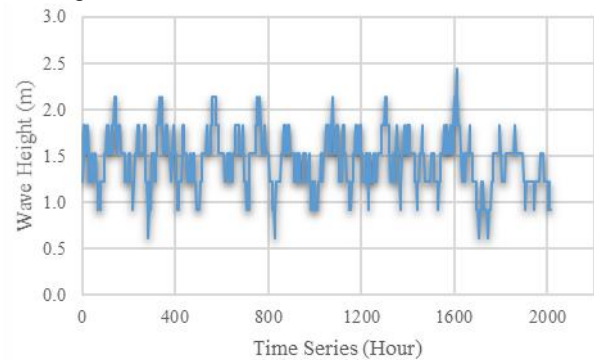


Fig. 1. Wave height variation data (New) along Time series

C. Wave Power Calculations

Significant wave height (H_s), Zero-crossing period T_z , and peak period T_p , were defined by following equations [8].

$$H_s = 4\sqrt{m_0} \quad (5)$$

Where,

H_s - Significant wave height (m)
 m_0 - Initial Spectral moment (m^2)

$$T_z = \sqrt{\frac{m_0}{m_2}} \quad (6)$$

Where,

T_z - Zero crossing wave period (s)
 m_2 - Second Spectral moment (m^2s^{-2})

$$T_m = \frac{m_0}{m_1} \quad (7)$$

Where,

T_m - Mean wave period (s)
 m_1 - First Spectral moment (m^2s^{-1})

$$T_p = \frac{1}{f_p} \quad (8)$$

Where,

T_p - Peak wave period (s)
 f_p - Peak Frequency (Hz)

m_n ($n = 0,1,2$) are the spectral moments of spectral density [3].

The wave power in deep water will be expressed by following equation.

$$P = \frac{\rho g^2}{64\pi} H_s^2 T_E \quad (9)$$

Where,

P - Power of the wave per width (W/m)
 ρ - Density of sea water (kgm^{-3})

$$T_E = \frac{m_{-1}}{m_0}$$

From further simplification of (5), ($\rho = 1025 kgm^{-3}$)

$$P = 0.49H_s^2 T_E \quad (10)$$

D. Selection process of Wave energy converter type

According to table 1, Oscillating wave columns (OWC) and Over topping Devices (OTD) require more than 2m of wave height to produce considerable amount of power. Therefore, these two types of WECs cannot be used in Sri Lanka. Considering Impact type of WECs, it should need 2m/s speed of wave to generate significant amount of power and it has lower efficiency (20 to 30%) than other existing WEC. Therefore, this process is also not suitable in Sri Lanka. Even though Tidal barrages have higher efficiency, 5m of head differences cannot be achieved. Therefore, Buoy Type is the most suitable WEC for Sri Lanka. It can extract power with reasonable efficiency (45-50%) and with minimum of 0.2m wave height which is sufficient to extract significant amount of power. The buoy type WTC is the most suitable option for Sri Lankan wave climatic condition which was shown in table 2.

TABLE I: COMPARISON OF WAVE ENERGY EXTRACTOR [9]

Type	Requirements	Efficiency
OWC	Minimum wave height 4m.	30-40%
Buoy	Minimum wave height 0.2m.	45-50%
OTD	Minimum wave height 3 to 5m.	20-25%
Impact	Minimum wave impact velocity $2ms^{-1}$	20-30%
Tidal Barrages	Minimum tide Head different 5m	60-65%

TABLE II: WAVE CLIMATIC CONDITION IN SRI LANKA

Data	Available in Sri Lanka
Average wave height (H)	1.1 m
Average wave period (T)	11 s
Average wave energy (P)	15 kW/m
Average Tide head different	0.8 m

E. Selection Process of PTO System

TABLE III: TYPES OF PTO SYSTEMS [9]

PTO Type	Efficiency (%)
Hydraulic	65
Air Turbine	55
Water Turbine	85
Mechanical Drive	90
Direct Drive to Linear Generator	95

Power Take off System is working like power transmission system of WEC. Because the buoy make oscillation due to wave movement and it should transfer to the Power Generator. There will be a system between buoy and power generator to transfer mechanical energy for the conversion.

Buoy type WEC supports with Hydraulic, Mechanical and Direct drive to linear Generator. therefore, out of these types a best option should be selected. Hydraulic PTO system is very expensive and very complex. It gives lower efficiency, and it requires high attention in maintenance since the hydraulic pipes comes through the sea water. When considering Direct drive to Linear generator, it provides higher efficiency and less complexity than other types. However, it cannot produce continuous electricity for every stroke. the extracted power varies between 0 to maximum. Finally, when considering the mechanical PTO, it can provide higher efficiency with reasonable cost and also continuous power can be produced from Hydraulic type PTO system when it is used with proper Mechanical motion Rectifier (MMR) [9].

F. Mechanicam Motion Rectifier (MMR)

Mechanical motion Rectifier is used to produce continuous power. The Main task of the MMR is to convert the Bidirectional movement of the wave into unidirectional movement. Therefore, the Bidirectional oscillation of the wave produces unidirectional output shaft rotation. Following figure shows an MMR which can work as mentioned earlier [9].

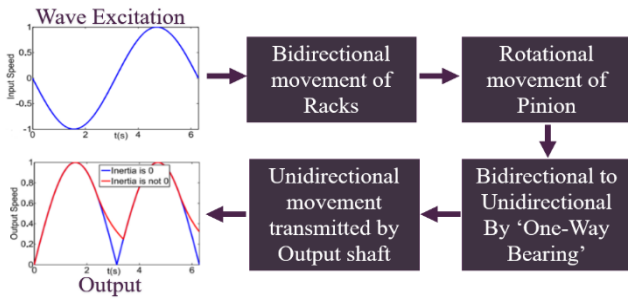


Fig. 3. MMR working principle.

G. Model Development and Simulation

1) Design of Buoy

The design of the buoy plays a major role to maximize the extracted power. There are some existing buoy designs which are used to convert wave energy into electrical energy. The extracted power is directly dependent upon the wave energy and the buoy design. In order to select the best design for Sri Lanka, 3 designs were tested using simulations. For each design different set of diameters were chosen and tested via 'Ansys Aqwa'. The selected design and its specifications are shown below,

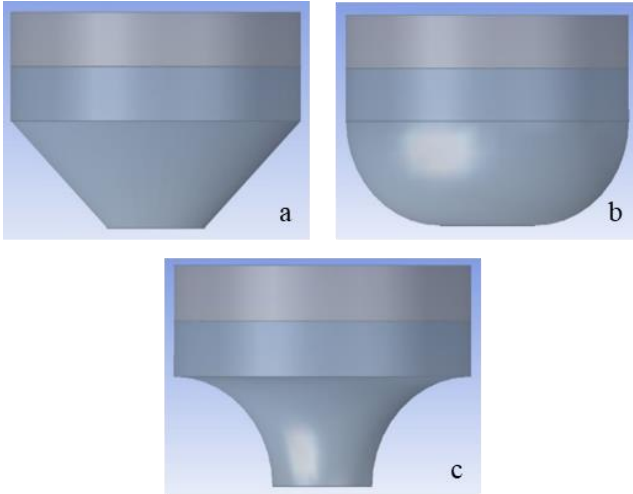


Fig. 4. (a) Conical; (b) Hemispherical; (c) Pinched Conical.

2) Dimension selection of buoy

There are some limitations in buoy design which are directly dependent on wave conditions of a particular location. According to the Sri Lankan wave conditions, the maximum buoy diameter has been calculated as 5.31m. Since it is a floating buoy the reaction of buoyancy forces also should be considered to verify buoy stability in designing. The stability of the geometries should be verified when loading the inputs to the Aqwa solver and then it will determine the mass and the level of the buoy.

Therefore, as a preliminary calculation 4 different diameters were chosen to check the stability of the buoy under buoyancy reactions. Which is elaborated in the table 4.

Initially, the larger distance (0.75 and 1 m) was chosen above water level because for the smaller diameter designs (1.55m and 2.98m) it is not stable under the buoyancy reaction. Finally, 0.5m was determined through trial-and-error methodology. However, the buoy with 1.55m diameter was identified as not stable. In order to stabilize the 1.55m buoy, the distance above water level should be kept 0.23m. But at this height there is a huge possibility of over topping waves. Therefore, the distance above water level is set to 0.5m for all the buoys.

Considering the buoy design with 5.20m diameter of buoy design, it requires more added mass to achieve the natural frequency of the wave to produce significant amount of power. When it comes to manufacturability of this buoy, it is very costly and complex. Therefore 2.98m and 4.05m diameter design have been selected for further analysis.

After finalizing the geometries, the models were imported into Aqwa (Hydrodynamics Diffraction) analysis system. Then the Hydrodynamic parameters were determined using hydrodynamic diffraction. Initially some of the compulsory boundary conditions were used to get the results from Hydrodynamics Diffraction. As an initial step of the analysis, the buoy has been connected with the sea bottom floor with inbuilt mooring function in the Hydrodynamic Diffraction of Aqwa workspace. The value of the mooring cable stiffness is determined as 500N/m by iterative method. Thus, the buoy did not move (drag) too much during the wave excitation. During the iterative method higher stiffness values also were used to fully submerge buoy under the water level. Lower

TABLE IV: BUOY DIMENSION AND STABILITY

	Diameter (m)	Height (m)	Distance Above water Level (m)	Distance Below water Level (m)	Center of Gravity from Upper surface (m)	Center of Buoyancy (m)	Stability
Conical	1.55	1.05	0.50	0.55	0.34	0.3	Not Stable
	2.98	1.99	0.50	1.49	0.77	1.04	Stable
	4.05	2.53	0.50	2.03	0.90	1.172	Stable
	5.20	3.49	0.50	2.99	1.04	1.32	Stable
Hemi-Spherical	1.55	1.05	0.50	0.55	0.44	0.39	Not Stable
	2.98	1.99	0.50	1.49	0.89	1.15	Stable
	4.05	2.53	0.50	2.03	1.09	1.35	Stable
	5.20	3.49	0.50	2.99	1.32	1.58	Stable
Pinched Conical	1.55	1.05	0.50	0.55	0.33	0.29	Not Stable
	2.98	1.99	0.50	1.49	0.66	0.94	Stable
	4.05	2.53	0.50	2.03	0.71	1.01	Stable
	5.20	3.49	0.50	2.99	0.77	1.07	Stable

values also were used but the buoy moved unfavorably due to wave excitation.

3) Initial conditions

Initial conditions were chosen for the analysis from the wave data collected during February 2021 to May 2021, which is shown in figure 3. From the wave data set the average wave amplitude was determined as 1.1m and the simulation was performed for a range of wave period between 8s to 14s. A range of wave period is used since the depth of the sea may vary from one place to another.

4) Hydrodynamic Parameters and Power output

The hydrodynamic diffraction will solve the excitation force, added mass and damping coefficient in the simulation. However, the aim of hydrodynamic response analysis is to determine the simulated power by each buoy with different diameters. Therefore, Additional radiation damping force 15kN/m/s is added into the system using the stiffness matrix option in the z direction. This will represent the Power Take Off (PTO) system which is placed somewhere in the WTC in 'Z' direction.

The additional PTO damping coefficient will affect the velocity profile and the oscillation of the buoy. According to the equation of motion, more damping causes the buoy velocity to drop. Thus, to give some counter reaction against the additional PTO damping, the addition of supplemental mass in z direction is mandatory. This will speed up the buoy during the wave excitation. However, this supplement mass will be determined through a trial-and-error methodology. Supplemental mass should be added or subtracted to achieve peak velocity. In this system, the approximate peak velocity is achieved when the added mass is nearly 1000kg in z direction. However, both PTO damping coefficient value and added mass value will be optimized to achieve peak velocity and peak power.

There are several settings in Hydrodynamic diffraction analysis to test the buoy under regular and irregular wave conditions. However, this study mainly focused on optimizing the buoy parameters to achieve maximum power under regular waves. The buoys will also be tested under irregular wave condition. The results will be discussed below.

5) Optimization of the parameters under regular wave conditions

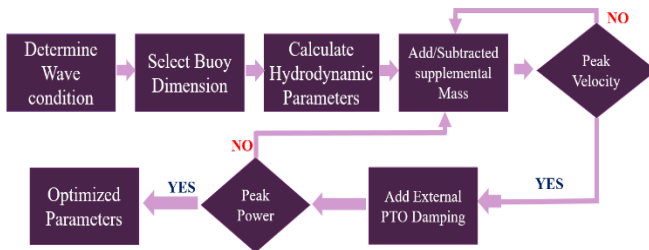


Fig. 6. Optimization process

The optimization process is very important to achieve maximum power. It consists of a few steps in order to optimize the parameter, as is shown in figure 9.

- a) The supplemental mass will be added in an ascending way and the velocity profile will be notified.

- b) By proceeding some iterations, the maximum velocity profile will be identified from the supplemental mass value.
- c) Then test it by increasing the PTO damping value and check the overall improvement of power capturing by the device.
- d) After the peak power capture was identified, the supplemental mass is adjusted by $\pm 10\%$ in either direction to check whether any significant variation occurs in the power captured. If any significant variations are identified the whole process must be repeated.

IV. RESULTS AND DISCUSSION

The aim of this study is to design a wave energy extractor for Sri Lankan wave climatic condition. It is identified that the most suitable WEC design is the buoy type. In order to select a better shape of the buoy with a suitable diameter, the analysis was done using ANSYS Aqwa.

A. Geometry based Excitation force.

As mentioned in earlier chapters, the Excitation force was approximated by the Froude-Krylov force. Following figures show the excitation force variation with wave frequency for different shape of buoy with same diameter.

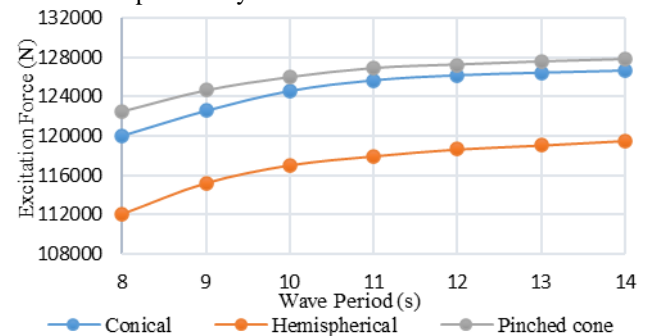


Fig. 7. Excitation forces on different buoy shapes with a diameter of 4.05m

Figure 6 shows that the excitation force is minimum for hemispherical and maximum for pinched cone designs. However, the decision cannot be taken only from these results.

B. Radiation Damping coefficient.

Radiation damping coefficient is another hydrodynamic parameter which could be solved by Aqwa. It directly affects the buoy oscillation, and it depends on the frequency. The following figures show how the radiation damping

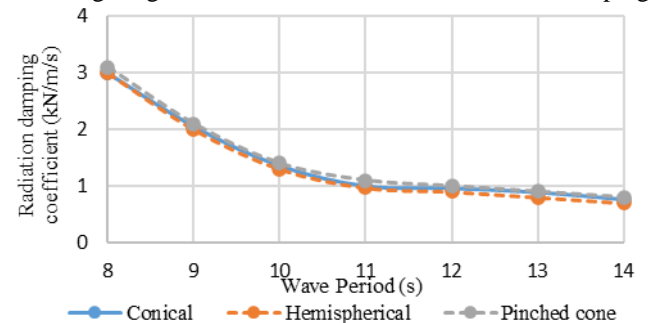


Fig. 5. Radiation damping coefficient of different buoy geometries with the diameter of 4.05m.

coefficient change with different buoy shapes for same diameter.

From the radiation damping results, the trends for both excitation and radiation damping are related. Here, the pinched cone gets a higher value, and the hemispherical cone gets a lower value. Furthermore, each graph converges rapidly when the wave period approaches 10s to 14s. Therefore, the significant difference is identified during the shorter wave periods.

C. Added Mass

The final hydrodynamic parameter solved by Aqwa was added mass. The value of the mass is added to the system in order to match the oscillation of the buoy with the wave natural frequency to achieve maximum oscillation. The manufacturing cost and manufacturability are directly dependent on the added mass of the system and this value is compulsory to analyze the Hydrodynamic Diffraction. Following figure 8 show the added mass variation with wave period for different shapes of same diameter.

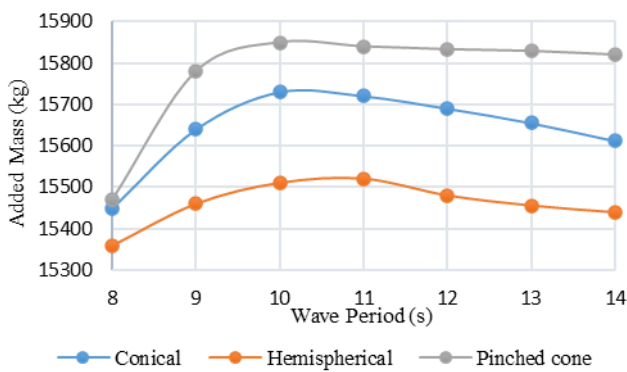


Fig. 9. Added mass of different buoy geometries with the diameter of 4.05m.

From the observation above, pinch conical design obtained with highest added mass and hemispherical is obtained with lowest added mass. This trend is not similar to other parameter results found previously

D. Optimization of Velocity with Supplemental Mass

This is an optimization process during the analysis and here the supplemental mass will be calculated using the equation (3) for each buoy at a specific wave frequency. Then the process will be done by increasing supplemental mass from zero to maximum levels and the velocity profile will be noticed. Then the Peak velocity variation will be recorded by gradually increasing the supplemental mass. Finally, the peak velocity and its corresponding mass values will be identified from the results.

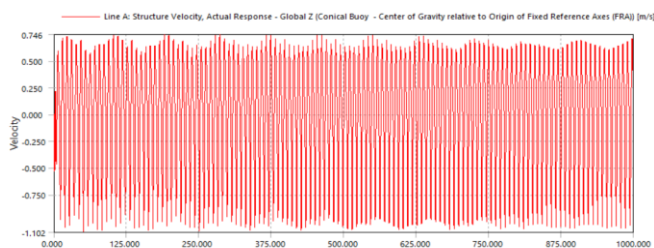


Fig. 10. Optimization of peak power with PTO damping

Once the Peak power is estimated, keep the PTO damping constant, the supplemental mass is adjusted by $\pm 10\%$, and checked if the Peak power shows any significant variation. If it is not varied, then the parameters are fully optimized.

However, if there are any significant variations then the optimization process must be done again from the supplemental mass step. The response of Peak power with added PTO damping is shown in the figure 10.

From the observation in both diameter cases, the lower peak power is obtained by conical shape buoy and the highest value of peak power is obtained by hemispherical buoy (9% more than conical shape buoy) in 2.98m diameter case and Pinched conical (12.5% more than conical buoy) in 4,05m diameter case. However, the peak power obtained by the buoys must be tested under the range of wave periods.

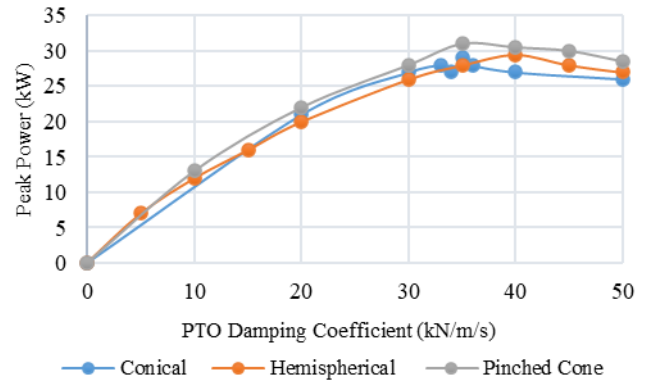


Fig. 8. Peak power optimization for different geometries with increasing PTO damping 4.05m.

E. Overall Peak power

According to the previous peak power performance of the buoys, the decision cannot be taken due to irregularities in the trends. In smaller diameter cases the hemispherical shape produces the highest peak power among others and in the 4.05m case Pinched cone produces the highest peak power. In order to finalize the decision, the test results were found for a range of wave periods. Following figures 11 showing the overall peak power performance.

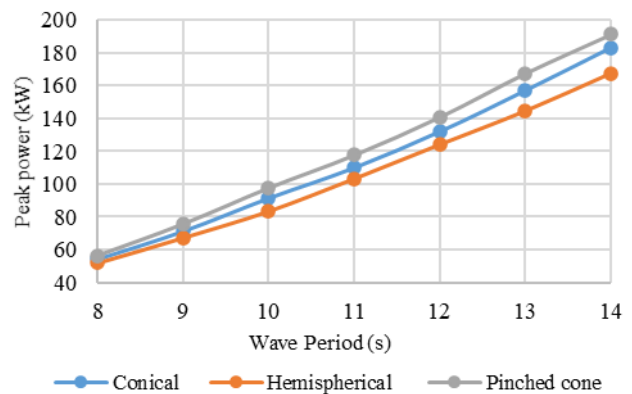


Fig. 11. Developed peak power by different geometries with the range of wave period for 4.05m.

Here, both results are showing similarity with the excitation force obtained previously. This provides reasonable proof within the constraints of the study. The following tables 5 and 6 elaborate the percentage difference of the peak power produced by different shapes of the buoy with respect to hemispherical buoy.

Considering 2.98m diameter case there are some significant differences between different geometries. The conical shape buoy produced average power of 75.36kW, which is 18.4% higher than the same diameter hemispherical buoy. The Pinched cone shape buoy produced average power of 81kW, which is 27.5% high than same size hemispherical buoy and 7.5% higher than conical shape. Considering 4.05m diameter case, the conical shape buoy produced average power of 114.3kW, which is 7.2% higher than the same diameter hemispherical buoy. The Pinched cone shape buoy produced average power of 120.9kW, which is 13.4% higher than same size hemispherical buoy and around 6% higher than conical shape.

In both cases the pinched cone produced high power than other shapes. However, comparison of the maximum power between two cases (2.98m and 4.05m) is bit complicated, hence the 4.05m diameter pinched cone buoy produced around 50% more power than 2.98m diameter pinched cone. In order to analyze both cases some extra parameters should be considered, such as manufacturability, manufacturing cost, return on investment.

F. Cost Analysis

Wall volume is mainly considered to do the cost analysis, because the higher percentage of the material will be used to build the wall of the buoy. The table is showing the wall volume of each buoy.

TABLE V: WALL VOLUME OF BUOY BODY

	Wall volume (m ³)		
	Conical	Hemispherical	Pinched cone
2.98m	0.46	0.55	0.74
4.05m	0.72	1.29	1.37

Fabrication cost of the conical shape is relatively lower than other shapes. However, other components such as Generator,

PTO system and MMR will affect the total manufacturing cost of each system.

Initially only the fabrication cost (without Generator, PTO, and MMR) is considered to perform an initial cost analysis. Basically, cost of fabrication is directly proportional to the cost of material. Therefore, a ratio was determined between Average peak power and wall volume (Power/Volume). This ratio can be considered as a ratio between Peak power and cost of fabrication.

TABLE VIII: RATIO BETWEEN PEAK POWER AND WALL VOLUME

	Peak power/Volume		
	Conical	Hemispherical	Pinched cone
2.98m	163.8	120.1	110.0
4.05m	158.3	82.2	88.6

From this initial estimate, the conical buoy shows higher efficiency. However, the proper cost analysis must be performed with all components to determine efficient design. Because when it comes to the whole system it consists of body, PTO system, MMR, power transmission and etc. So, the overall cost will be affected by those factors as well.

When only Considering the pinched cone shape, the smaller size (2.98m) of buoy gives higher power for unit cost of fabrication of the body. As mentioned previously, the final decision cannot be taken without performing a proper cost estimation. Also, further analysis should be performed for different diameter between 2.98m and 4.05m.

V. CONCLUSION

In this research three different geometries were chosen for the analysis and their characteristics were analyzed using ANSYS Aqwa. In order to perform the analysis, the Hydrodynamic parameters were used to determine some

TABLE VI: COMPARISON OF PEAK POWER FOR DIFFERENT GEOMETRIES WITH THE DIAMETER OF 2.98M.

Wave Period (s)	Hemispherical	Conical		Pinched Cone	
	Power (kW)	Power (W)	% Difference	Power (kW)	% Difference
8	12.3	17.3	40.65%	18.0	46.34%
9	28.3	34.8	22.97%	37.3	31.80%
10	44.2	50.9	15.16%	58.4	32.13%
11	63.2	72.4	14.56%	78.3	23.89%
12	83.7	92.4	10.39%	99.7	19.12%
13	104.1	117.3	12.68%	126.3	21.33%
14	126.5	142.4	12.57%	149.4	18.10%
	Average	75.36	18.43%	81.06	27.53%

TABLE VII: COMPARISON OF PEAK POWER FOR DIFFERENT GEOMETRIES WITH THE DIAMETER OF 4.05M.

Wave Period (s)	Hemispherical	Conical		Pinched	
	Power (kW)	Power (kW)	% Diff	Power (kW)	% Diff
8	52.1	54.4	4.41%	56.2	7.87%
9	67.4	71.4	5.93%	75.5	12.09%
10	83.6	91.5	9.45%	97.5	16.63%
11	103.4	110	6.38%	117.6	13.73%
12	124.2	132	6.28%	140.8	13.37%
13	144.6	157.4	8.58%	167.5	15.84%
14	167.4	183.3	9.32%	191.3	14.28%
	Average	114.3	7.19%	120.9	13.40%

important parameters (Excitation force, added mass and Radiation Damping coefficient) under small amplitude of waves.

The excitation forces are directly proportional to the diameter of the buoy and the frequency. Iterative optimization process has been used to optimize each level to produce a reasonable and repeatable result. After finalizing the added mass to achieve the peak velocity, the PTO damping will be added to the system to get the peak power. The PTO damping level would be gradually increased until the peak power is detected. The identified power will be compared with all the other devices.

Based on the experiment it is identified that the modified shape has an increment of 18.43% and 27.53% for 2.98m diameter and 7.19% and 13.4% for 4.05m diameter of Conical and Pinched cone respectively in the peak power capture of the devices compared with the hemispherical buoy. This is conducted under regular wave conditions. The average power is also compared with it and found out that it has a significant improvement in the performance of the design..

VI. REFERENCES

- [1] A. E. a. Y. Emani, "Electricity Generation by Tidal barragers," *ICSGCE Energy Propedia 12*, pp. 928 - 934, 2011.
- [2] T.Watabe, "Priliminary Study on Wave Energy Utilization in Srilanka," *Proceeding of the Eleventh (2001) International Offshore and polar Engineering conferance*, pp. 597-603, 2001.
- [3] P. A. H.W.K.M. Amarasekara, "A Prefeasibility study on ocean wave power Generation foe the southern coast of SriLanka : Electrical Feasibility," *International Journal of Distribution Energy Resouces and Smart Grids*, pp. 80-93, 2014.
- [4] F. J., " Ocean Waves and Oscillating Systems," no. 2004, pp. 233-242, 2004.
- [5] Shadman, "A geometrical optimization method applied to a heaving point absorber.," *Energy Procedia*, vol. 20, no. 2012, pp. 148 - 155, 2012.
- [6] "Magic SeaWeed," MSW, [Online]. Available: <https://magicseaweed.com/>. [Accessed November 2020].
- [7] P. M. a. H. K. e. al., "Investigation on Ocean Wave Energy Assesment for Srilanka," *National Energy Symposium 2019*, pp. 150 - 160, 2019.
- [8] R.N.Chamara, "Wave Energy Resoource Assesment for the Southern coast of Srilanka," *6th International Symposium Advances in Civil and Environmental Engineering (ACEPS - 2018)*, pp. 41 - 46, 2018.
- [9] L. Z. Changwei Liang Junxiao Ai, "Design, fabrication, simulation and testing of an ocean wave energy converter with mechanical motion rectifier," *Ocean Engineering*, vol. 136, no. 2017, pp. 190-200, 2017.
- [10] Y. C. a. Z. Liu, "Effects of Solidity Ratio on Performance of OWC Impulse Turbine," no. 2015, 2014.
- [11] B. Cahill, "Characteristics of the wave energy resouce at the Atlantic marine energy test site," no. 2013, pp. 34-57, 2013.
- [12] D. A. S. Bruno S. Frey, "Behavior under Extreme Conditions: The Titanic Disaster," *Journal of Economic Perspectives*, vol. 25, pp. 209-222, 2011.
- [13] I. Riley, "Geometric Optimization of a Heaving Point Absorber Wave Energy Converter," *Electronic Theses and Dissertations*, 2018.

Boiler Accidents Reported in Sri Lanka

Uvindu Eranjana Thilakarathne
Department of Mechanical Engineering
Faculty of Engineering
University of Sri Jayewardenepura,
Ratmalana, Sri Lanka
uvindura1995@gmail.com

Minura Malalanayake
Department of Mechanical Engineering
College of C.S. and Engineering
University of Michigan,
United States
minura@umich.edu

Tharaka Ruwan Bandara
Department of Mechanical Engineering
Faculty of Engineering
University of Sri Jayewardenepura,
Ratmalana, Sri Lanka
tharaka.bandara@sjp.ac.lk

Abstract— Boilers are used in many industries for the purpose of steam generation by heating water, to temperatures above its boiling point and pressures above the atmospheric pressure. Despite boilers being widely used in industries, there is still a risk of accidents as a result of not following proper safety and maintenance procedures. When high pressures are combined with high temperatures, the energy stored in steam is also high. Therefore, the release of such steam in the case of a rupture can be catastrophic. Health and safety hazards of leaking boilers include fires, explosions, poisoning due to exposure to toxic gases in combustion products, and burns. According to data collected from reliable sources, it is understood that avoidable accidents do occur due to lack of knowledge of boiler hazards. In this paper, collected data on boiler accidents in Sri Lanka such as information from boiler experts, reported information to authorized organizations, information available on media, etc. are organized to prepare an investigation report for each accident. The accidents are analyzed through the investigation reports prepared. Based on those analyses, a set of common causes that lead to such accidents are identified. Recommendations are put forth which will be helpful in taking preventive measures to reduce future boiler accidents.

Keywords—Pressure vessels, boilers accidents, explosions, boiler failure, process safety

I. INTRODUCTION

Boilers are identified as a type of pressure vessel and are associated with high operating pressures which are greater than atmospheric pressure and high temperatures greater than 110°C [1]. Fatal accidents can happen where a boiler explodes or a component of the boiler fails. Rupture failures of boilers can be catastrophic, causing considerable damage to life and property. Such incidents have led to generating flying projectiles of debris or released dangerous materials such as hot steam. Boiler inspection and operation are regulated by factory ordinance and the Department of Labour in Sri Lanka. Furthermore, the authority taking legal actions for the responsible parties of an accident is also the Department of Labour in Sri Lanka.

There are nearly a total of 40 boiler-related accidents reported in Sri Lanka as stated by the Department of Labour since 1985 [2]. The number of boiler accidents is considered to be higher than that reported as there are unreported accidents [2]. Since the 8th of July 2001 to November 2020, fifteen accidents related to boilers have been reported to the responsible authorities in Sri Lanka; the Department of Labour and Police. When conducting the research, some common reasons for boiler accidents were identified.

Control systems, gauge glasses, and safety valves are some of the basic components which lead to the safe operation of the boiler. A lack of periodic maintenance of the above-mentioned critical components could ultimately lead to an accident. Abrupt pressure differences generated from

unexpected chemical reactions, heating, cooling, or vacuum inside a boiler are potential dangers when a boiler is operating. According to the factory ordinance, steam boilers should be tested every year, while steam receivers should be tested every two years [3]. The boiler operator certificate is mandatory for the boiler operation, and the certification is given under three classes according to the experience of the boiler operator [2].

The motivation behind the research is to organize and analyze the information on boiler accidents such that useful recommendations can be provided to reduce boiler accidents in Sri Lanka. Even though investigations have been conducted by the responsible authorities in Sri Lanka, the data collected by them have not been organized and was not made accessible to the general public.

II. COLLECTION OF INFORMATION AND METHODOLOGY

The research was divided into five sections as identification of sources, data collection, data organizing, accident analysis, and providing recommendations. Of the sources identified, first data were primarily collected from the Department of Labour in Sri Lanka and Sri Lanka Police, as they are considered as reliable sources in the Sri Lankan legal system. Collected data were also enriched from secondary sources such as local media and professionals from the industry. Any contradicting details were noted within this study where information on an incident was collected from multiple sources. The gathered information for each accident was then organized according to an investigation report template. Next the organized data of accidents were categorized according to different criteria such as according to the area or region, the cause of the accident, the type of industry, etc. Finally, an analysis was conducted for each such category, and recommendations to reduce boiler accidents were put forth by identifying issues within these individual categories.

III. STUDIED CASES

A. Case I - Boiler explosion at Lanka Rice Mill in Dambulla

1) *Incident*: On 21/03/2003 at the Lanka Rice Mill premises, a boiler exploded and three persons died including the operator and an authorized boiler inspector. The boiler house was damaged and the outer shell of the boiler skyrocketed and landed in a bushy area over half a kilometer away from the boiler house (Fig. 1). Such heavy metal parts could have caused significant damage to the people and properties if they fell into a crowded area.

2) *Details of the Investigation*: One of the steam boilers from the Lanka Rice Mill exploded while doing the periodic boiler test by an authorized boiler inspector. The boiler inspector made one or two prior visits to the facility and had

to leave disappointed that the boiler was fired every time. When he arrived at the premises for the last time, again the boiler was fired up. As the boiler was fired, the authorized boiler inspector could not do the cold test unless the boiler was turned off and cooled.

When testing a boiler, two tests must be conducted which are the cold test followed by the hot test. The cold test is the test that is done at room temperature. Initially, water is filled to the boiler tank and is pressured up to 1.5 times the boiler working pressure. Material failures such as failed welded joints, if present, could be identified as the pressure is higher than the operating pressure of the boiler. For instance, if failed welded joints are present, then cold-water leakages can be observed from those failed welded joints. Leaking of pressurized cold water is less hazardous than that of pressurized hot water or steam. If no leakages or failures are noted after the cold test, then the hot test can commence. The failure pressure is only applicable to a correctly manufactured boiler. If the welds have become faulty then the vessel can fail at pressures well below the design pressure. The hot test is done when it is under normal operating pressure and to check that the safety valve is adjusted properly to prevent pressure from rising above the maximum permissible working pressure [3].

Instead of conducting the cold test first which required time for the boiler to cool down, the authorized boiler inspector started doing the hot test, bypassing the first step. While the hot test was performed, the boiler inspector was checking the pressure gauge and the operator was asked to raise the pressure. The operator added more biomass to increase the fire to raise the pressure. The process was carried out for some time. Since the cold test was bypassed, material failures were not identified. After some time, the boiler exploded with three fatalities including the authorized boiler inspector who was a Chartered Engineer. It was also found that the pressure relief valve had not opened [2].

Another possible reason for the explosion is, as stated by Surasena [4] who had investigated this accident as a third party, the authorized officer gave instructions to the operator to increase the pressure, to check whether the pressure relief valve of the boiler was working properly. Therefore, the operator was adding more fuel (biomass) to the boiler furnace. However, the pressure of the steam was not increasing accordingly. Eventually, the boiler operator identified that the water level of the boiler was low and that was the reason behind this unexpected behavior. Therefore, the boiler operator had turned on the feed water supply [4].

When operating with low water levels, internal components such as metal tubes start to absorb heat from flue gas due to the absence of water. Consequently, internal metal parts of the boiler start to heat, and if it continues unknowingly, internal metal parts could rise to temperatures more than 500°C which is the maximum working temperature of medium carbon steel, also known as boiler steel, that is used in boiler manufacturing [5]. The internal parts will bulge, and peak stresses will occur. Peak stress can be identified as the highest stress in a region produced by a

concentration such as a notch or a weld discontinuity and also by certain thermal stresses [1]. Peak stresses do not cause significant distortion but may cause fatigue failure.

In such kind of a situation, the boiler should be turned off and cooled. After cooling, an inspection has to be done by a professional to check whether the boiler is safe to restart. Instead of that, if the cold feedwater is introduced to the heated boiler core, liquid water will suddenly change its phase to gas, since the boiler was running with low water and the boiler core has already heated up to temperatures above the boiling point. When water is changing its phase, it expands in a volume ratio of 1:1600 [2]. This expansion ratio ultimately leads to an explosion due to abrupt pressure differences inside the boiler core. Stresses due to rapid change in the temperature of the tubes, and stress at local structural discontinuity due to bulging will lead the boiler to fail. This could result in a catastrophic explosion.

3) *Concluding remarks of the accident:* This accident happened for several reasons. The designed relief valve was replaced with another one and the new relief pressure had a higher relief pressure than the rated maximum operating pressure. Furthermore, the replacement had been done by a third person who was not authorized to do so, but the reason for the replacement was not revealed as the operator was also died. As the relief pressure of the new pressure relief valve is different than the rated value, it did not open at the maximum allowable working pressure which led to the boiler explosion. It was also stated by Jansz [2] that, welding joints of the boiler were not up to the standard which was found in investigations after the accident. These substandard welding joints could have been identified by the authorized boiler inspector if the cold test was performed. Any records of work were not found. Records of work are critical to ensure work is done properly and safely, and also to facilitate future failure investigations.

As stated by Surasena [4] this was an accident that happened due to operating with low water conditions where the feed water was suddenly introduced into the heated boiler which ultimately led to an explosion of the boiler. This explanation is more realistic than the previous, which suggested that the explosion was due to the malfunctioning of the pressure relief valve. In Sri Lanka, most of the boilers used are operated around the maximum permissible working pressure of 10 bar [4]. If a safety factor of 4 is used when manufacturing boilers, then the boiler could withstand a maximum pressure of 40 bar before exploding. As the above-mentioned boiler was a biomass boiler, it is not possible to reach up to such pressures [6] even with the pressure relief valve not functioning. But, along with the replacement of the pressure relief valve, welding joints were also repaired. Such welding joints, if not repaired properly, could eliminate all the above-mentioned pressure value requirements and lead to an explosion.

When testing high-risk equipment such as boilers, safety procedures must be followed. As the place was surrounded by three people including the owner, the explosion cost three lives.

4) Photographs of evidence:



Fig. 1: Debris (parts of boiler) from the Lanka Rice Mill incident [2]



Fig. 2: Foundation of the exploded boiler from the Lanka Rice Mill [9]

B. Case II - Shantha Rice Mill boiler accident in Polonnaruwa

1) *Incident:* In 2002, at the Shantha Rice Mill premises, a cylindrical vertical boiler was used to generate steam to boil the paddy (rice before threshing). The person who was operating the boiler suffered burn injuries due to a broken steam outlet. The Department of Labour was compelled to take legal actions as the operator was not instructed properly by responsible managers on how to work around high-risk equipment and to respond to an emergency [2].

2) *Details of the Investigation:* The foundation of the boiler was near a paddy field. Due to the instability of the land, the steam boiler tilted over and caused the rupture of steam pipe while in operation. The operator was untrained and did not have the boiler operator certificate which is a must for people to be employed as boiler operators.

He tried to control the steam leak near the broken outlet and it burnt 60% of his body [2]. He did not cut off the fuel supply in order to let the boiler cool. Due to injuries, he was admitted to Polonnaruwa general hospital. After receiving treatments for more than two weeks he died [2].

3) *Concluding remarks of the accident:* This accident happened mainly due to the unawareness of the operator about the operating procedures of high-risk equipment such as steam boilers. According to the Sri Lankan factory ordinance, it is mandatory to test boilers every 12 months [3]. If such inspections took place, an authorized boiler inspector could have identified the unstable condition and recommended to make the necessary changes. Conducted investigation also lacks detail.

4) Photographs of evidence:



Fig. 3: The Boiler in the Shantha Rice Mill related to accident [9]



Fig. 4: The collapsed boiler foundation at the Shantha Rice Mill [2]

C. Case III - Sewagama Rice Mill boiler accident in Polonnaruwa

1) *Incident:* On 23/05/2002, at the Sewagama Rice Mill premises, a vertical rice husk boiler was operating in the nighttime and it backfired. The person who was sleeping near the boiler suffered burn injuries. Department of Labour took legal actions as the operator was not instructed properly by responsible managers on how to work around high-risk equipment [2] according to factory ordinance section 34. 3A, 3B, 5 and 6 [3].

2) *Details of the Investigation:* Rice husk was used as the fuel. The concrete foundation of the boiler (Fig. 5) was 2-3 feet high. As it is a vertical boiler, the furnace of the boiler is just above the top of the foundation [9].

On the night of the accident, the operator overfilled the furnace with rice husk so that he could avoid rechecking the furnace throughout the night. The operator had slept near the boiler. As he had unintentionally blocked the air and fuel (rice husk) inlet of the furnace with excessive rice husk, sufficient air was not passing through to the furnace for complete combustion to take place. Further, there were blockages in exhaust lines due to improper preventive maintenance practices [2, 9].

When operating a boiler, some daily checkups must be carried out. Checking the condition of the boiler furnace, exhaust blockages, pressure gauges, feed water inlets, steam outlets, etc. are some of those. When the furnace fuel is biomass, the furnace and exhaust conditions must be thoroughly examined before firing up the boiler as

combustion of biomass is not always complete. Therefore, solid carbon residues, unburnt fuel particles present in the exhaust gas could deposit on the surface of exhaust pipe walls and with time an excessive amount of deposits could block the flow path of exhaust gas. Due to the blocked path of the flue gas outlet (exhaust pipe), flue gas could pass out from the only remaining opening which is the air/fuel inlet in the boiler furnace. As the rice husk is burning in the furnace, pressurized flue gas will force the fired rice husk out from the furnace opening which could be fatal if the burning material makes contact with a person.

In the investigations, it was found that a backfire occurred [2]. As the exhaust pipes were clogged, the hot exhaust escaped out from the furnace area. Flames and hot ash came out from the furnace opening. The operator was severely burnt and injured. He was admitted to Polonnaruwa general hospital as 60% of his skin had suffered burns. After receiving treatments for two weeks, he died [2, 9].

3) *Concluding remarks of the accident:* This accident was mainly due to the unawareness of the operator about operating a steam boiler. Also, the boiler exhausts were clogged due to improper maintenance routines [9]. The untrained operator was not aware of the risks related to steam boilers and accidents such as backfires. If a qualified and trained operator was employed, the accident could have been prevented.

4) *Photographs of evidence:*



Fig. 5: The boiler foundation and the boiler at Sewagama Rice Mill [2]

D. Case IV - Tea factory boiler explosion in Galle

1) *Incident:* On 12/02/2011 the boiler in a tea factory exploded in Galle. Further, a metal plate of the boiler was thrown away due to high pressure exposing the employees to a hazard. The feed water supply to the boiler was cut off which ultimately drove into an explosion.

2) *Details of the Investigation:* The boiler was in a tea factory in Koggala, Galle. On the day of the accident, the trained boiler operator was on leave and a trained person was

not present in the factory to operate the boiler [4]. The boiler was operating from 8:00 AM as usual. According to Surasena [4] it was operating around the pressure of 8 bar. At around 3:00 PM, the overflowing of the feed water tank was noticed by workers. The mechanic of the factory was informed about the incident. After his inspection, he noticed that the feedwater pump had been turned off. Therefore, he turned on the feedwater pump and after a few seconds, the furnace tubes failed with a loud noise. Fire bar and grid plate of the boiler was thrown away from the boiler. No one was injured [4]. A photograph of the boiler after the accident is shown in Fig. 6.

3) *Concluding remarks of the accident:* The reason for the feed water tank to overflow was because the condensed water supply from the boiler was continuously filling the feed water tank. There was no outflow from the tank because the feedwater pump to the boiler was switched off by an unknown person for an unknown reason according to Surasena [4]. After some time, due to interrupted water circulation, the boiler reached its minimum water level which resulted in a higher portion of the heat generated from the furnace being absorbed by the internal metal parts of the boiler instead by water. Due to this the furnace tubes experienced thermal stresses. With the sudden introduction of water by turning on the feed pump, the swift change in temperature resulted in failure of metal tubes [4]. Further, when cold feedwater was introduced into the heated boiler shell, the sudden expansion of water into steam has led to an explosion as also explained in case I.

As stated by Surasena [4], this boiler was fitted with low water and dangerous low water alarms which were found functional during the post-accident investigation, providing adequate evidence to prove the boiler failure was due to not being compliant with requirement of the factory ordinance i.e., boiler to be operated only by licensed operators.

Any automatic shutdown mechanisms, which would have indicated the low water level in the boiler or indicated that the feedwater pump was switched off, were also not available. Such automatic safety alarming systems are not mandatory in the guideline of factory ordinances in Sri Lanka [3].

4) *Photographs of evidence:*



Fig. 6: Exploded boiler at Galle tea factory [2]

E. Case V - Tea factory boiler explosion in Demodara

1) *Incident:* On 13/08/2011 the boiler in the tea factory of Demodara tea estate exploded. Further, a metal plate of the boiler which weighs around 300 kg was thrown causing a threat to the people working in the tea factory as well as in the tea estate [2].

2) *Details of the Investigation:* The boiler under investigation was in operation for more than 12 hours for withering green leaves, when the dryer was connected to the boiler [4]. Operator noted that they could not attain the temperature required and estate mechanic was informed. He rectified the electrical fault in the control circuit which made the feed pump to operate and the boiler exploded within few seconds at around 7:30 AM [4, 8]. A metal plate covering the boiler was thrown away. Three people who were near the boiler were died [8]. Injured people were admitted to the provincial general hospital, Badulla [7].

3) *Concluding remarks of the accident:* This accident was due to a combination of several reasons. That means, the feedwater pump was not working for an unknown reason and the operation was continued as normal [4]. The reason behind the boiler failure was, as it was heated up to high temperatures without water, furnace tubes were under thermal stresses, and with the introduction of water by turning on the feed pump, abrupt change in temperature results in the failure of metal tubes. The accident is similar to that in Case IV. As the boiler operator was on leave, management did not have another employee who was trained. The boiler was operated by an unknown employee [4] for which the factory management should be responsible.

4) Photographs of evidence:



Fig. 7: Front view of the exploded boiler at Demodara tea factory [9]

F. Case VI - Poultry farm boiler explosion in Valvettithurai

1) *Incident:* On 03/11/2020 the boiler in a poultry farm in Urikkadu, Valvettithurai exploded. Further, a metal plate weighing about 200 kg of the boiler was found 900 m from the location of the accident [10]. It was projected due to high pressure, exposing the employees to a hazard causing an injury to a worker.

2) *Details of the Investigation:* The boiler was in a poultry farm in Urikkadu, Valvettithurai bearing the address, Mailathenna, Thondamanaru. At the time of the accident, the boiler operator, an employer, and a vehicle were nearby. Due to the boiler explosion, a nearby wall collapsed and one person was injured.

3) *Concluding remarks of the accident:* The relevant boiler started operations a year ago. But, it was not registered according to the government regulations. As mentioned by Police [10] it was not up to standards and has not been tested since it started operation. The owner was charged according to penal code ordinance statements 280,327,328. Further information is not present as the case is still under investigation. Fig. 8 shows the photograph of the evidence.

4) Photographs of evidence:



Fig. 8: Exploded boiler at the Valvettithurai poultry farm [12]

IV. ANALYSIS OF THE ACCIDENT CASES

Since the 8th of July 2001 to 3rd of November 2020, fifteen accidents related to boilers have been reported to the responsible authorities in Sri Lanka; the Department of Labour and Police. When analyzing the accident cases, it was found that not employing trained and qualified operators, utilizing used imported boilers without degrading and no regular inspection by authorized persons are important causes that ultimately leads to boiler accidents in Sri Lanka.

Table II contains details of the reported accidents in Sri Lanka from 2001 to the present day as a summary. After studying the reported cases, those can be categorized into different categories, where further analysis is done under each category. The categories are determined by considering their importance when making recommendations. Fig. 9 shows the flow chart of how categorization is done.

TABLE I: SUMMARY OF THE ANALYSIS

	According to area		According to the cause of the accident		According to the type of the accident	According to industry
	Province	City	Main cause	Contributing causes		
Accident percentage	North Central Province 60%	Polonnaruwa 47%	Low water 72%	Lack of maintenance 60%	Explosions 87%	Rice Mills 67%

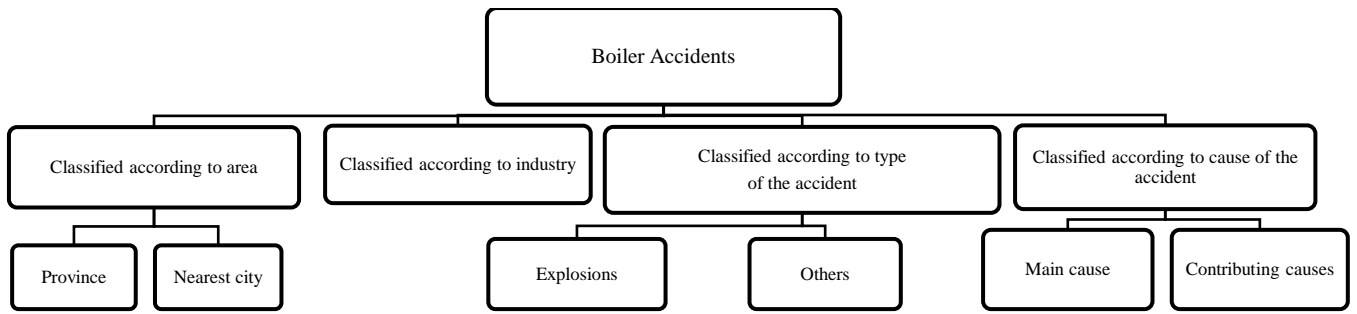


Fig. 9: Categorization flow chart

TABLE II: SUMMARY OF REPORTED ACCIDENTS FROM 2001 TO PRESENT [2, 4, 6, 9]

Location		Date	Severity			Nature of the pressure vessel
Destination	Industry (Name and address of organization)		Deaths	Injuries	Type of the boiler (Firetube, Water-tube)	Shape (Cylindrical with flat ends/spherical ends, Spherical,)
Anuradhapura	Sweet manufacture	2/03/2017	No	No	Firetube boiler	Cylindrical Vertical
Galle	Tea - Koggala	12/05/2011	No	No	Firetube boiler	Cylindrical Horizontal
Demodara	Tea	13/08/2011	3	No	Firetube boiler	Cylindrical Horizontal
Kantale	Manjula rice mill	2012	1	No	Firetube boiler	Cylindrical Horizontal
Polonnaruwa	Haalith rice mill	8/07/2001	2	Unknown	Firetube boiler	Cylindrical
Polonnaruwa	Hasna rice mill	25/07/2001	1	Unknown	Firetube boiler	Cylindrical
Polonnaruwa	Sewagama rice mill	23/05/2002	1	Unknown	Firetube boiler	Cylindrical Vertical
Polonnaruwa	Shantha rice mill	2002	1	Unknown	Firetube boiler	Cylindrical Vertical
Dambulla	Rice mill - Lenadura	21/03/2003	3	Unknown	Firetube boiler	Cylindrical
Rathnapura	Tea - Galaboda	2012	No	No	Firetube boiler	Cylindrical
Polonnaruwa	Suriya rice mill	2013	No	No	Firetube boiler	Cylindrical
Valvettithurai	Poultry farm - Urickadu	03/11/2020	No	1	Firetube boiler	Cylindrical

*Boiler explosions in New Lanka rice mill – Polonnaruwa, Ranmuthu rice mill – Kaduruwela, and Gamini rice mill – Anuradhapura is included in the analysis. But excluded from the table due to unavailability of information.

A. Classified according to the area or region

1) *Province*: When analyzing the cases as a whole, it is identified there is a tendency for more boiler related accidents in some areas than in the rest of the country. According to the details in Table II, accidents have been reported from several provinces of the country. Anuradhapura, Polonnaruwa, Kaduruwela, and Dambulla cities are in North Central province. Further, Kanthale is in the Eastern province but, that area is so close to North Central province. Galle, Demodara, Rathnapura, and Valvettithurai cities are in Southern, Uva, Sabaragamuwa, and Nothern provinces respectively.

Of all the accidents, 60% (9 accidents) of accidents have taken place in the North Central province or in close proximity to its borders. In the other five provinces mentioned above, the accident percentage is approximately 7% in each. In the North Central province, almost all the accidents were in rice mills. As the province supplying a higher portion of rice requirement in the country, rice mills are abundant in the region.

2) *Nearest city*: If the locations where the accidents occurred are classified according to the nearest city to that location, it is significant that around 47% (7 accidents) of

accidents have taken place close to the city of Polonnaruwa. All accidents that took place in Polonnaruwa were in rice mills. Around 12% of total accidents have been close to the city of Anuradhapura of which 50% of the accidents in Anuradhapura were also in rice mills. Therefore, the area around Polonnaruwa city must be considered as an area of importance in regards to boiler accidents and necessary actions have to be taken.

B. *Classified according to the industry*: It can be seen that there are two significant industries when analyzing the boiler accidents reported. Around 67% (10 accidents) of accidents were in rice mills and 20% (3 accidents) of accidents were in tea factories. 9 deaths were reported from accidents in rice mills where as 3 deaths were reported from those in tea factories.

C. Classified according to the type of accident:

1) *Explosions*: A common type of accident is an explosion which can be a boiler core explosion or a firebox explosion. Approximately 87% (13 accidents) of all reported accidents are explosions and related damages. Overpressurizing the boiler could result in core explosions where as incomplete combustion or combustion issues might lead to firebox explosions. During an explosion, steam inside

may splash and that is a hazard as the temperature of the steam is higher than 110°C.

2) *Backfire and Steam leaks*: For steam leaks and backfires a single case has been reported for each.

D. Classified according to the cause of the accident: Accidents can be categorized according to the immediate cause which is the most recent cause behind the accident and preliminary causes which led to the accident. Even though there are fifteen accidents reported, the immediate causes are investigated in seven accidents according to information collected from references [2, 4, 6, 9 and 10]. The analysis below is based on those seven cases rather than all the reported cases.

1) *Main cause*: Approximately 72% (5 accidents) of accidents have occurred due to operating the boiler with low water levels. The scientific background of this has been explained in **section III. A. 2)**. This cause could lead to the deadliest explosions due to the lack of training and knowledge on boiler operation, which can be seen in every accident reported. Main causes of other accidents analysed were due to clogging of inlets and outlets of the furnace, and damaged steam lines.

2) *Contributing causes*: As explained earlier, several contributing causes could lead to the occurrence of a single accident. But, most of those can be identified with the daily checklists and periodic maintenance. According to the available details, 60% of accidents have happened due to poor maintenance or due to the unavailability of periodic maintenance procedures. As a summary it can be identified that the contributing causes which led to accidents are:

- Modification/ periodic maintenance done by non-qualified personals [2].
- Not employing operators who have the necessary qualifications to operate boilers [9].
- No proper and regular inspection by authorized persons since there have been accidents just after inspections also [8].
- Using imported boilers that are rejected by others after several years of use without degrading the boiler [4].

V. RECOMMENDATIONS

Recommendations to avoid future boiler accidents are provided based on the analysis done according to the area, the industry, the type of the accident, and the main and contributing causes of the accident.

The Northcentral province, especially the Polonnaruwa area, has the highest accident occurrence, of which most are accidents in rice mills. Therefore, the existing regulatory and inspecting authorities must focus more on this area and rice mill industry. Even if unregistered boilers are currently used, the government must implement new methods to examine the industries where the responsible authorities have direct access to them whether they are registered or not.

A. *Implementing new methods for the registration process of boilers in responsible authorities*: In some accident cases, it is identified the boilers are not registered in responsible authorities, consequently not tested as recommended. The reasons for not registering the boilers needed to be identified as a whole. Accident case VI is an example of that. Since the boilers are not registered, the operations of such boilers cannot be monitored by government authorities. A new method to collect details of such cases must be implemented. There are two methods where information regarding boilers can be collected instead of relying on owners to do the registration.

- Getting direct information from local boiler manufacturers
- Getting direct information from Sri Lanka customs

Boilers are manufactured within Sri Lanka and also imported. Even though the boilers are not registered by the owners, the manufacturers can provide the details of the boiler they have manufactured, the industry, and all the details of their customers. Such a system can also be implemented for imported boilers where Sri Lanka customs gets every detail from the importer and that information is directly sent to the Department of Labour. Then, that information should be passed to relevant local government organizations. So, the relevant local government organization could be in touch with the industry where the boiler is operating. A computer-integrated system (a database) could fulfill the requirement here.

B. *Educating employers and employees of industries on boiler hazards*: In most cases, the cause of the accident is a combination of negligence over time and lack of knowledge regarding the hazard. The deaths or injuries have happened due to unawareness of people rather than the severity of the explosion. The boiler room should not be considered an all-purpose storage area or a free area where everyone can stay around. Being near a boiler can be dangerous. It is always a must to have limited number of people around the boiler. Unnecessary gatherings of people near the boiler must be avoided.

According to the analysis of different accident types, it is significant that boiler explosions do more harm over a wide range which includes significant property damages. As identified in the incidents discussed, not conducting daily checkups are one of the main reasons which ultimately leads to an accident. Following routine maintenance and inspection is the best way to prevent a boiler accident. The factory management should take the responsibility to ensure that high-risk machinery like a boiler should be operated carefully by trained persons as stipulated in the factory ordinance [3].

Awareness sessions must be conducted that are more focused on boiler-related accidents and their severity specially focused on employees. Because, if the employees are aware of the hazards of operating boilers without proper training and qualifications, they will resist working in risky, unsafe environments even though

employers ask them to do so. Furthermore, employers also should be equally informed and explained the repercussions of such actions. A severe code of conduct in operating boilers for both employers and employees must be implemented. With the support of local government organizations, the responsible authorities must undertake educating the employees and employers of the area and making information materials available.

C. Boiler Inspectors must report to the Department of Labour periodically on boiler tests conducted: As explained in **Section V. A.** if a computer database is established, information regarding boilers used will be readily available. By having every possible detail on a relevant boiler, the testing process can be directly monitored. Further, the same system can be used to record inspections conducted by authorized boiler inspectors.

Since managing the database is controlled by the government, periodic testing of boilers as mentioned in the factory ordinance [3] is not bypassed or neglected. Then issues regarding the boilers can be tracked on an annual basis. Even if a computer database cannot be established, at least a manual system has to be implemented by the Department of Labour to monitor and record details of inspections and boiler testing processes conducted by authorized boiler inspectors. This eliminates corruption with boiler testing procedures. Also, authorized boiler inspectors must always follow ethical practices as any misconduct would ultimately cost human lives.

D. Introducing laws that state mandatory boiler safety controls: Having an automatic alarming system or shutdown system with boilers would be costly, however the added safety outweighs the cost. Laws have to be imposed to make such kinds of safety systems mandatory

E. Improving the process of conducting investigations and making information on investigations accessible to the general public: Even though investigations are conducted in accident locations, properly documented reports are not available in Sri Lanka for general public. Therefore, actions taken for responsible parties of accidents are questionable. Further, having analyzed investigations pave the path to understand major issues and addressing those issues. In some other countries, the reports are readily available on the official web pages of responsible authorities which educates people on hazards with machinery and possible causes for hazards. U.S. Chemical Safety and Hazard Investigation Board (CSB) is an example of such an authority. Also, conducting investigations according to international standards will be helpful when analyzing and maintaining documents with the accident cases.

VI. CONCLUSION

In Sri Lanka, over 60% of reported accidents have occurred due to the ignorance of preventive maintenance as well as daily checkups by both operators as well as owners. More than 70% of accidents can be avoided if the operators were educated on boiler operations. Most boiler accidents were recorded from the Northcentral province, especially in

the Polonnaruwa area. All accidents from Polonnaruwa took place in rice mills and boiler operators were not trained and qualified in most of those cases. We cannot fully eliminate boiler accidents but can work towards reducing the risk of their occurrence by educating people about boiler accidents. Periodic inspection and maintenance routines are highly recommended to ensure safety in industries that use boilers. If provided recommendations are implemented, a significant reduction in the number of accidents recorded in the future is possible.

ACKNOWLEDGMENT

The authors are grateful for the insightful comments of this study offered by Prof. Douglas Swinbourne of RMIT University, Melbourne, Australia. The authors are also thankful to Mr. Mahinda Dissanayake (SSP, Sri Lanka Police) and Mr. Padmasiri (CI, Sri Lanka Police) for the kind support rendered in data collection.

DISCLAIMER

The content of this article such as text, tables, figures, images, and any other material(s) created by authors are intended for informational and educational purposes only and cannot be used in any legal proceedings or otherwise. The material on this article does not in any means constitute as legal advice.

REFERENCES

- [1] "Overview of pressure vessels," 2004, doi: 10.1201/9780203492468.ch1.
- [2] L. Jansz, "Industrial Safety Procedures in High Risk Machinery including Steam Boiler," *IESL - Public Lecture*, 2017. <https://www.youtube.com/watch?v=4XHxlaIPhn0&feature=youtu.be> (accessed Nov. 20, 2020).
- [3] Department of Labour, "Factory Ordinance," pp. 131–198, 1942.
- [4] U. Thilakarathne, "An interview with a boiler industry expert on boiler accidents(Mr. N. Surasena)", Dec. 2020.
- [5] S. Xue *et al.*, "Analysis of the causes of leakages and preventive strategies of boiler water-wall tubes in a thermal power plant," *Eng. Fail. Anal.*, vol. 110, p. 104381, Mar. 2020, doi: 10.1016/j.engfailanal.2020.104381.
- [6] D. Palmer, I. Tubby, and G. Hogan, "Biomass heating : a guide to medium scale wood chip and wood pellet systems Introducing automatically fed systems," *Energy*, 2011.
- [7] adaderana, "Boiler explodes killing three in Badulla," TV Derana, Sri Lanka, 2011.
- [8] U. Thilakarathne, "An Interview with Chief Factory Inspecting Engineer(Eng. E Abeyesiriwardhana) of the Department of Labour of Sri Lanka", Nov. 2020.
- [9] L. Jansz, "Online Lecture: 'Industrial Safety Procedures in High-Risk Machinery including Steam Boiler,'" *IESL - Public Lecture*, 2020. <https://www.youtube.com/watch?v=2iuVcNf4IHM>.
- [10] U. Thilakarathne, "Phone call interview with Officer in charge, Sri Lanka Police - Valvettithurai," 2021.
- [11] "Hiru News," 2020. <https://www.hirunews.lk/english/253975/boiler-explosion-injures-3-in-valvettithurai>.

The Design Optimization and 3D Printing Technique of Biomimetic Cellular Gyroid Lattice Structure in Fused Deposited Modelling Method

Silva K M A

*Mechanical Manufacturing And
Process Engineering
Department of interdisciplinary studies
University of Jaffna
Sri Lanka
2017e107@eng.jfn.ac.lk*

Bandara G K G E S

*Mechanical Manufacturing And
Process Engineering
Department of interdisciplinary studies
University of Jaffna
Sri Lanka
2017e016@eng.jfn.ac.lk*

Weerasekara N W S M

*Mechanical Manufacturing And
Process Engineering
Department of interdisciplinary studies
University of Jaffna
Sri Lanka
2017e122@eng.jfn.ac.lk*

Mugilgeethan V

*Mechanical Manufacturing And Process E
ngineering
Department of interdisciplinary studies
University of Jaffna
Sri Lanka
mugil@eng.jfn.ac.lk*

Abstract - The automotive and aerospace industries rely on lightweight components for their competent performance in terms of power availability. The bioinspired cellular lattice structures seem to be the most prominent strategy to optimize the structural element's strength while depreciating the weight. However, designing and developing the lattice structure for the actual application level is still challenging. Furthermore, the additive manufacturing technique that has shown an excellent capability to fabricate lightweight regular lattice structures, are still facing certain process limitations in terms of the geometrical capability, minimum printable size and support requirement in printing the gyroid lattice structures in the Fused Deposition Modelling (FDM) technique. Therefore, this study explored a comprehensive guide on the development of a gyroid unit cell to define the least printable size of a unit cell of 4 mm using FDM technology. This study, further, described the appropriate size and number of gyroid cells that can be used for the elementary shapes of 3D printing. The printing defects and the design improvement and printing technique also were considered to generate and print lightweight gyroid lattice structures efficiently. Overall findings of this study proved that the gyroid unit cell can be printed soundly maintaining the retraction speed between 40 mm/s and 50 mm/s and print speed between 20 mm/s and 30 mm/s with minimal errors.

Keywords- 3D printing, Gyroid, Lightweight, Fused Deposition Modelling, Least Printable Size.

I. INTRODUCTION

Recently, heightened dependence on oil and severe climate change have been scrutinized in several industries to decrease fossil fuel consumption and greenhouse gas emissions. Increased fuel economy would achieve through a combination of reductions in vehicle size, weight,

aerodynamic drag, and rolling resistance and increased powertrain efficiency or replace the conventional materials with lightweight alloys [1]. In previous studies, alternative alloys were proposed as a potential replacement of steel structures. However, the cost benefits are questionable. Therefore, the aluminium space frame structures have been employed. Nevertheless, studies revealed that the space frame structure required fastening parts and other fittings for mounting the outer panels and various functional parts, and that these would not reduce cost [2]. There are many approaches used in previous studies to reduce the overall weight of the vehicle by maintaining the required mechanical properties [3][4].

Rather the redesigning process can fulfil the requirements of the component than material replacement. Hence, with the general understanding, there are few other conditions that make effects on the output characteristics such as; strength, chemical reactivity, and thermal properties [5].

A lattice structure, made of space-filling unit cell can be faceted along any axis with no gaps between cells. This structure is recognised as an emerging solution to considerably reduce the weight, energy and manufacturing time. In natural lattice generation of the bone, it was observed that there were two regions namely cancellous bone and cortical bone. It shows that the lattice design becomes smaller itself near to the surface of the bone and creates a rigid cover called the cortical region [6]. It is challenging to produce a method to design the lattice structure as the natural design using evolving technology. Past studies attempted to develop these structures manually using Octet trusses and Rhombi cuboctahedrons, and mathematically considering Nodal approximation, Variational level set approaches and

Weierstrass formulas [7]. Manually generated structures consists of basic geometric patterns like a triangle or hexagonal. While mathematically generated structures are designed as hyperbolic surfaces that is generally called as triply periodic minimalistic surfaces (TPMS) [8]. In previous studies, the TPMS was implemented as a tensile specimen or cubic lattice structure such as I-graph-Wrapped Package (IWP), Neovius, Gyroid and Diamond shapes, and experiments were performed using a few numbers of 3D printed specimens [6]. The gyroid lattice structures are more prominent considering printing ability, strength, and density. Notably, the gyroid model can be generated with a simple trigonometric equation [7][9].

The benefits of lattice structures are employed in various applications, in particular, the medical industry. In literature, much focus has been drawn into studying the variation of density scaling parameters, particularly optimising characterisation and modelling for additive manufacturing to recreate the cancellous and cortical bone structures accurately [10]. Applications of lattice structures in the automotive industry have also been prioritized to decrease noise conduction, enhance weight reduction, and increase the ease of recycling automotive parts [11]. The aerospace and aeronautic industries also exploit the advantages of lattice structures aiming to improve the performance-to-weight ratio of parts. This eventually leads to increase the efficiency of aeronautical and aerospace vehicles [12].

With the development of additive manufacturing technology, 3D printing has become more and more popular in various sectors, including the automotive industry [13][14]. There is a comprehensive spread list of technologies in additive manufacturing with some unique procedures and benefits for each one. Fused Deposition Modelling (FDM) is more prevalent than other techniques due to its ease of manufacturability and decent printing quality [15][16]. Therefore, in this study, FDM technology was adapted since this method provide a validate information on printing properties including strength, printing speed, infill pattern and printing temperature [18][19]. Several properties of the printed part were discussed with some experimental data such as; tensile strength, surface roughness, build time. Large nozzle diameter of the printer, high layer thickness and high extrusion velocity can make significant improvement on the strength and surface roughness according to [20]. Moreover, it spends addition build time. Consideration of the building direction and if there any possibility to reinforcement on the part; such as using resins, can improve the strength of the relevant part [21]. Optimization of the printing parameters of the FDM technology will directly affect to the final quality of the printed object. Layer height is considerable printing parameter that can affect the print quality. Reduce the layer height instigated to increase the dimensional accuracy [22].

A study proposed synthetic bone designed using the combination of additive manufacturing and lattice structures [6]. The lattice structures produced with additive manufacturing could be beneficial to characterising and

producing optimised scaffolds for tissue and bone replacement to encourage osteointegration [7]. Existing studies have not well defined the concept of utilising gyroid cells in industrial applications. In this study, the following procedures considered for the realisation of this concept. Initially, the range of gyroid cell cubes was designed and printed. Subsequently, printing cells were evaluated, and they were optimised through design and 3D printing techniques. At the final step, confirm the number of cells covering the curves of each shape, the ascertained cell was activated into different three-dimensional basic shapes.

Most of the studies in the literature doesn't converge on all the optimization with a proper way of application of 3D printed gyroid cell. This study become a reference that appeared in credible for optimizing the printing parameters of the gyroid cells with assistance for the utilization of gyroid cells. Furthermore, with the advancement of the FDM 3D printed technology, it can be utilized for lightweight mass production applications such as aerospace engineering and aircraft manufacturing industries.

II. MATERIALS AND METHOD

In this study, all the computer aided design (CAD) models of the gyroid lattice structures were designed using Creo (v 7.0.2, student version) software, and post-processing were then performed with Geomagic Studio (v 12.0 free version) software. After that, designed CAD models were converted into Stereolithography (STL) format using the same Creo software. Then, Ultimaker Cura (v 4.8.0) software was adapted to generate the g-code file to print the gyroid lattice cells. The designed gyroid lattice cells were printed using Ultimaker 3 extended 3-D printer (Netherlands) with 2.85 mm diameter black PLA filaments. Afterwards, samples of printed gyroid unit cells were categorized to perform the defect analysis. An optical microscope (Euromex IS.1052-PLMi, The Netherlands) with 10X and 5X optical magnifying lenses was used to analyze the defects in the printed gyroid unit cells. Further, images of defects were captured using a 64 MP, f/2.0, 29mm (telephoto lens) mobile camera (Samsung Galaxy S20+). Fig 1 illustrated the overall setup practiced for the aforementioned proceeding.



Fig. 1. Morphology investigation setup (Iscope microscope, 10X and 5X magnifying lens kit, 64 Mega Pixel, f/2.0, 29 mm (telephoto lens) mobile camera (Samsung Galaxy S20+).

Initially, gyroid cells were designed using Creo software by identifying the cell boundaries. Subsequently, CAD models were generated various sizes of gyroid cells. The generated CAD models were printed using Ultimaker 3 extended 3D printer. Afterwards, deficiencies in the printed gyroid cells were observed selecting specific orientations in the printed unit cell. Subsequently, recorded deficiencies were analysed, and printing parameters were altered accordingly. Finally, cubical unit cells were reprinted with the improved printing parameters and observed through the optical microscope to validate the optimised printing parameters.

III. DESIGN PROCESS

The gyroid, a triply periodic minimal surface with zero mean curvature, was identified by Alan Schonon in 1970. It has the topology of an open-celled foam, which is sketched in Fig. 2(a). The close resemblance to the gyroid is given by Equation (1) [10].

$$\sin X \cos Y + \sin Y \cos Z + \sin Z \cos X = K \quad (1)$$

Where, $X=2\pi x$, $Y=2\pi y$, and $Z=2\pi z$. x , y , and z are directional coordinates, and K is constant.

It is possible to obtain a family of surfaces possessing the symmetrical and topology of the same TPMS by changing the constant K in the range of $-1.5 < K < 1.5$. However, it changes the volume fraction of the lattice phase [10]. Therefore, this study uses $K=0$ for all the gyroid cell designs.

The Creo software used to generate 3 mm cells as the minuscule cell size with 0.64 mm wall thickness. As indicated in Fig.2(b), it produced a solid cube when the size is 2 mm or less.

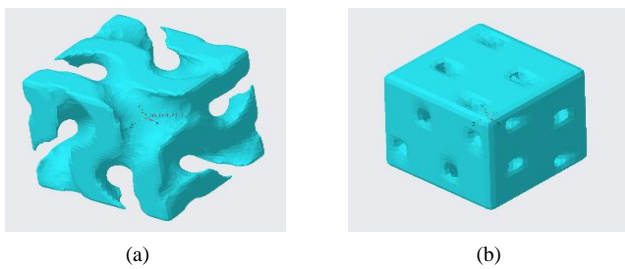


Fig. 2. (a) 2 mm Gyroid cell CAD Model (b) 3 mm Gyroid cell CAD model.

Therefore, gyroid cells were designed in 3 mm to 10 mm with an increment of 1 mm and were printed using PLA material. Initially, the printing parameters were set by 0.4 mm nozzle diameter, 165 °C extruder temperature, 70 mm/s printing speed, 50 mm/s extruder speed, 100% infill, and 0.1 mm layer height. Next, the printed cells were observed in an optical microscope to characterise the flaws in the lattice. Similar solid cubic structures also were reprinted to compare the weight deviation, as indicated in Fig.3.

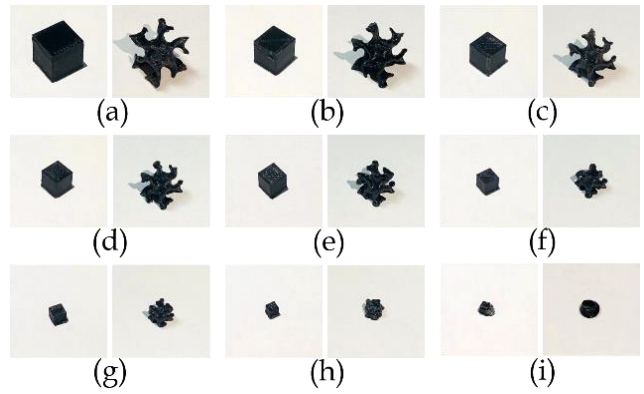


Fig. 3. Printed solid and Gyroid unit cells; (a) 10 mm; (b) 9 mm; (c) 8 mm; (d) 7 mm; (e) 6 mm; (f) 5 mm; (g) 4 mm; (h) 3 mm; (i) 2 mm

Further, optimized minimal size cell was implemented in selected basic shapes to optimize the implementation of lattice structure compared to a solid structure. Fig 4 represents the selected shapes; 30 mm cube, sphere of 30 mm diameter, 15 mm width and 30 mm length spheroid, 30 mm pyramid, 30 mm cone, and 15 mm depth hexagon with 15 mm of the length of aside.

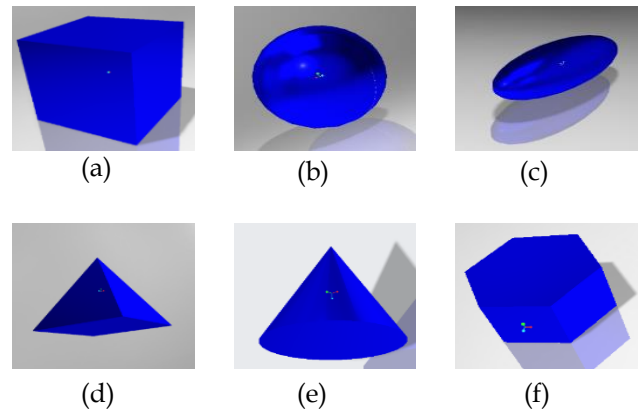


Fig. 4. Minimum printable size gyroid lattice applied basic shapes; (a) Cube; (b) Sphere; (c) Spheroid; (d) Pyramid; (e) Cone; (f) Hexagonal prism.

IV. EXPERIMENTS

For a comprehensive understanding, few experiments were performed on weight deviation. As mentioned earlier, nine cells were printed in a range of 2 mm to 10 mm with an incremental of 1 mm. Later, printed parts were analysed to categorise the gyroid properties among the samples. Weight comparison between the solid and gyroid infill cubic unit cells was assessed using axis electronic chemical balance (0.0001 g of least count) based on the results.

TABLE I. PRINTING SPEEDS AND RETRACTION SPEEDS USED TO PRINT THE 4 MM GYROID CELL VIA MAINTAINING OTHER PARAMETERS AS

Test number	Printing Speed (mm/s)	Retraction Speed (mm/s)
1	20	40
2	25	40
3	25	25
4	30	45
5	30	40
6	35	40
7	35	35
8	40	35
9	40	30
10	45	30

The 4 mm cell was primarily selected for the next set of experiments as it was the most diminutive printable size in the available printer. Next, selected cells were observed in the microscope to identify the possible flaws in the printed cells. The observation was recorded, and accordingly, the root cause of the imperfection in the unit cell was identified and generalized with the printing parameters. Further, repetitious models of unit cells with varying printing parameters were printed for each size. TABLE I contains the detail of printing parameters chosen for the experiment. A range of 20 mm/s – 50 mm/s was used for both printing and retraction/travel speed to analyse dimension accuracy in literature [23]. There for initially, an average value used to print the Gyroid cell in this study as 20 mm/s of printing speed and 40 mm/s of retraction speed. Subsequently, the experiment was continued by changing both the print speed and the retraction speed by 5 mm/s. Later, a similar analysis was performed to categorize the unit cells' flaw correction based on the printing parameters.

Finally, optimized cells were implemented in selected basic shapes and observed the effect of cell size on the weight reduction. The optimal level of gyroid cell could be implemented for a given shape with a defined dimension.

V. RESULTS

Fig. 3. (g) and Fig. 3. (h) show the printed 4 mm and 3 mm cells. As considering the outcome, 4 mm gyroid cells demonstrated better geometric quality than the 3 mm gyroid cell for Ultimaker 3 extended printer. Further, the 4 mm gyroid cell had some imperfections for the initial printing parameters. Fig. 5 illustrates the weight comparison of designed and printed gyroid unit cells. As indicated in Fig. 5, a prominent inequality was observed between printed and software-based weights measurements. The contrast of weight was attributed to the defects in the printed gyroid cells. As shown in Fig.6, mainly six types of defects were identified in the printed gyroid cells namely, voids, strings, excessive material, layer shift, non-uniform layer width, and shape deformation. These imperfections can be categorized into two divisions. One type of defect occurs due to apparatus

error, and another type occurs due to the geometrical complexity. However, this study focused on the defects that occurred due to the complexity of the gyroid design.

As discussed earlier, these imperfections can be eliminated by choosing the optimal printing parameters. Mostly, non-uniform layer width, excessive material, and voids depend on the material feed rate or printing speed. Low retraction speed and length result in formation of strings and shape deformation errors. Accordingly, altering the feeding rate, retraction speed, and length led in reducing these imperfections. However, the non-optimal value of the printing parameters could produce more defects in the printed cells.

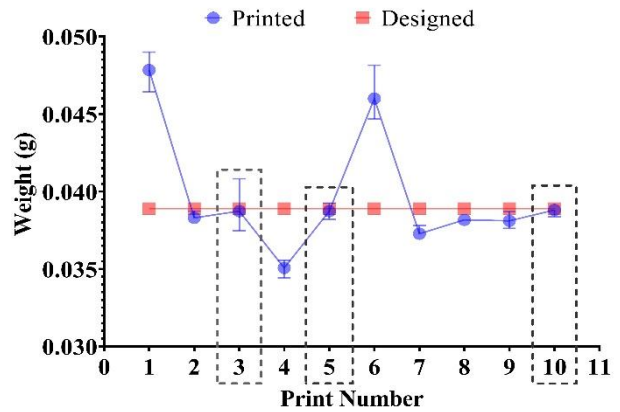


Fig. 5. Graph of weight deviation in different printed Gyroid cells Vs CAD design; 4 mm

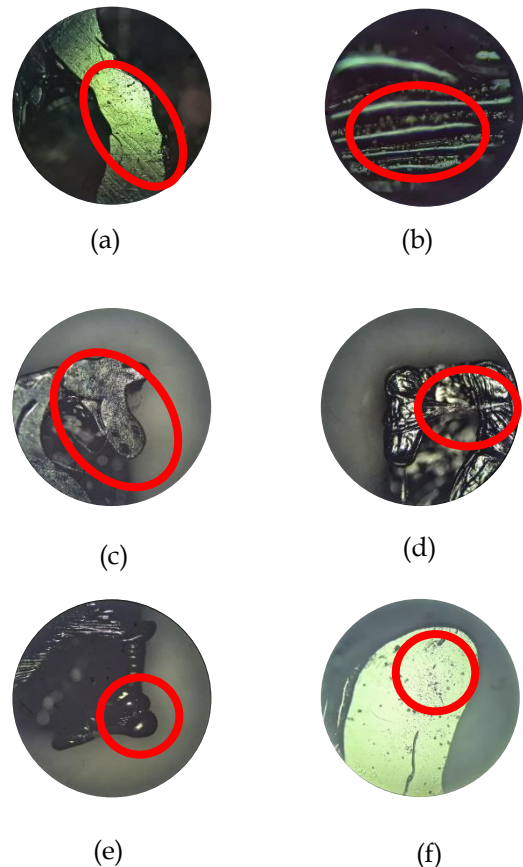


Fig. 6. Basic defects of a printed gyroid cell (Observed using Iscope microscope with 5X and 10X magnifying lens kit); (a) Nonuniform layer width; (b) Layer shift; (c) Shape deformation; (d) String; (e) Excessive material; (f) Voids.

Fig. 7 shows the 4 mm gyroid cell printed with 25 mm/s printing speed and 40 mm/s retraction speed while other printing parameters were kept constant.

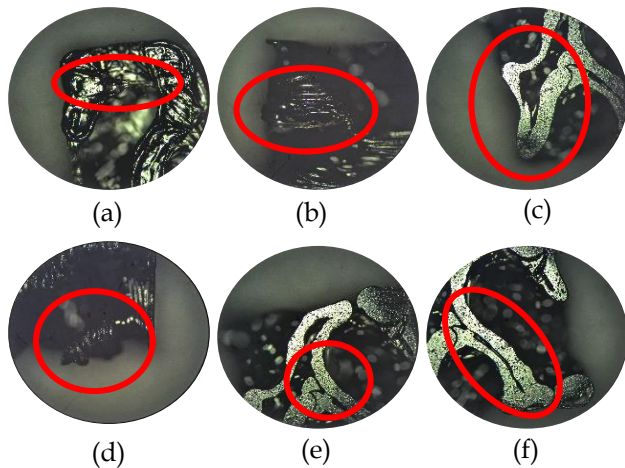


Fig. 7. Test 2; P.S.-25 mm/s, R.S.- 40 mm/s; (a) String; (b) Layer shift; (c) Shape deformation; (d) Excessive material; (e) Voids; (f) Nonuniform layer width

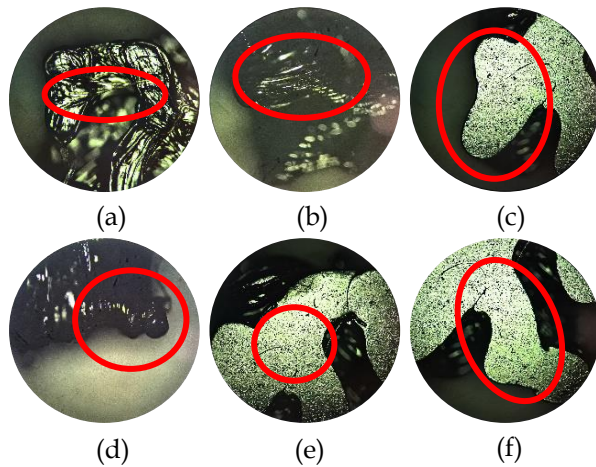


Fig. 8. Test 1; P.S.-20 mm/s, R.S.- 40 mm/s; (a) String; (b) Layer shift; (c) Shape deformation; (d) Excessive material; (e) Voids; (f) Nonuniform layer width

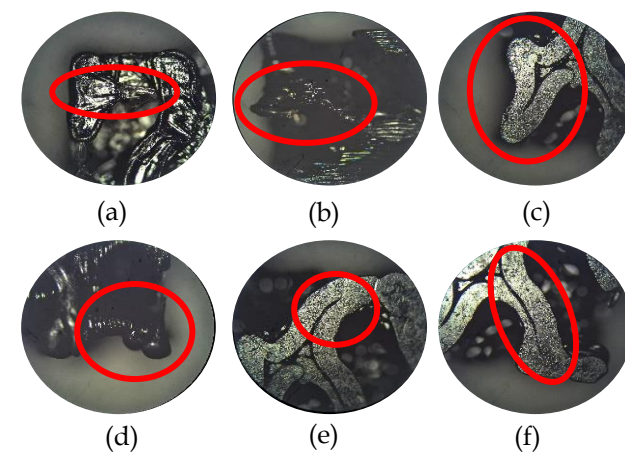


Fig. 9. Test 5; P.S.-30 mm/s, R.S.- 40 mm/s; (a) String; (b) Layer shift; (c) Shape deformation; (d) Excessive material; (e) Voids; (f) Nonuniform layer width.

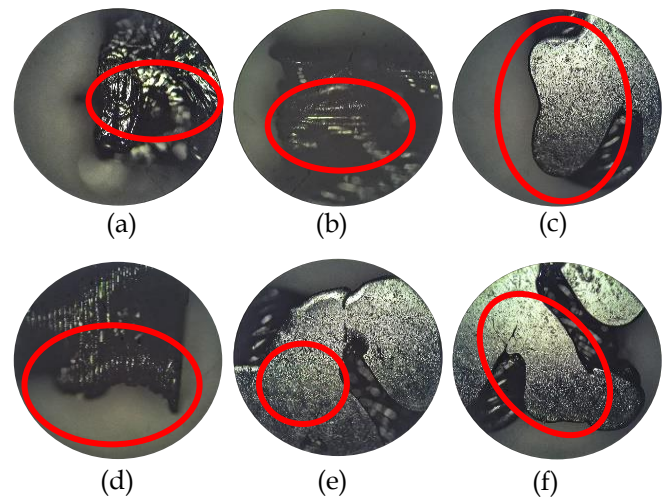


Fig. 10. Test 3; P.S.-25 mm/s, R.S.- 45 mm/s; (a) String; (b) Layer shift; (c) Shape deformation; (d) Excessive material; (e) Voids; (f) Nonuniform layer width

However, due to the complexity of the cell production, this model exhibited some imperfections. In this test, voids, string and excessive material were noted as significant defects, and the indication of layer shift and shape deformation were comparatively low.

Next, printing speed further decreased to 20 mm/s in order to subdue high void concentration. This change benefited to reduce the voids and increase the dimensional accuracy. However, the excess material and string defects remained the same. Further, the layer showed uniform pattern throughout the cell, as shown in Fig. 8. Another printed sample was considered with 30 mm/s printing speed and 40 mm/s retraction speed to validate the results. As shown in Fig. 9, model exhibited more defects than previous tests.

Next, printed model with the 25 mm/s printing speed and 45 mm/s retraction speed was considered. As shown in Fig. 10, selected parameter values overcame most imperfections, mainly strings, excessive material, voids, and layer shifting. It had some minor changes in layer width compared with the first experiment, which can be negligible. Fig 11 justified that it had the least number of defects among all the other tests.

Fig. 12 illustrates the average weight comparison between the same volume gyroid and solid unit cell. Implementing the gyroid lattice as a replacement for a solid structure would give a positive outcome. Further, noticeable weight changes can be observed in unit cell having the size more than 7 mm

With the implementation of lattice into designed shapes, a clear mass reduction could be observed with results in Fig. 13. With the increment of capacity of the object, the reduction of the mass showed a greater value.

Another important finding in this study is presented in Fig. 12. As previous results optimized the flawless printable gyroid lattice, it was always challenging to implement it on basic shapes practically. It could be attributed that the density

of gyroid cells in a defined volume was permanently restricted based on optimal gyroid implementation. As in Fig.12, the weight reduction can be obtained. implementing large size cells, however, it was controlled by the dimension and type of shape that can be used. The spheroid model can only reach up to 11 mm gyroid cell, and its dimension limited that level. Therefore, it was essential to know that the most apparent size of the gyroid unit cell that must be implemented in various complex shapes.

Another crucial observation is presented in Fig.14. A cube (30 mm) and a sphere (R=18.61 mm) were designed with an identical volume and it was observed the weight deviation. As indicated in Fig.14, there was a significant change for small sizes of gyroid cells, and the rate of change reduced as the size of the cell increased. This result implied the necessity for the optimized gyroid cells in basic shapes for real applications.

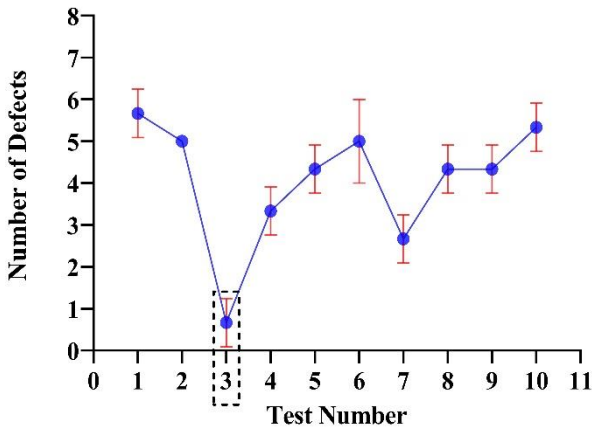


Fig. 11. Graph of number of defects comparison (average values) between tests (All tests were performed by changing the print speed and retraction speed while keeping all other parameters constant)

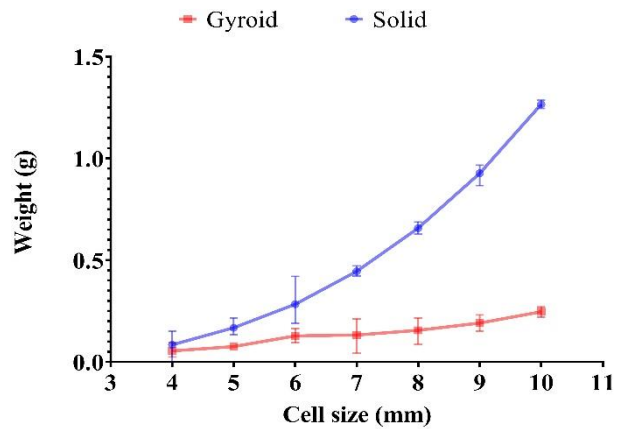


Fig. 12. Graph of weight comparison (average values) between solid and Gyroid unit cells

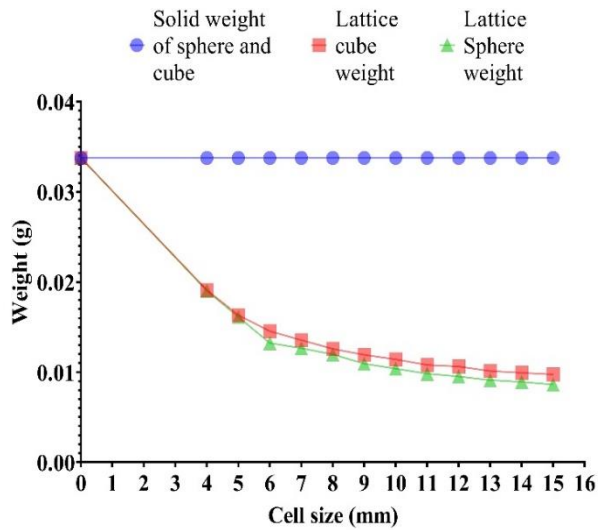


Fig. 14. Weight measurements on cubic and sphere shapes with solid and gyroid infill vs different dimensions of Gyroid unit cell.

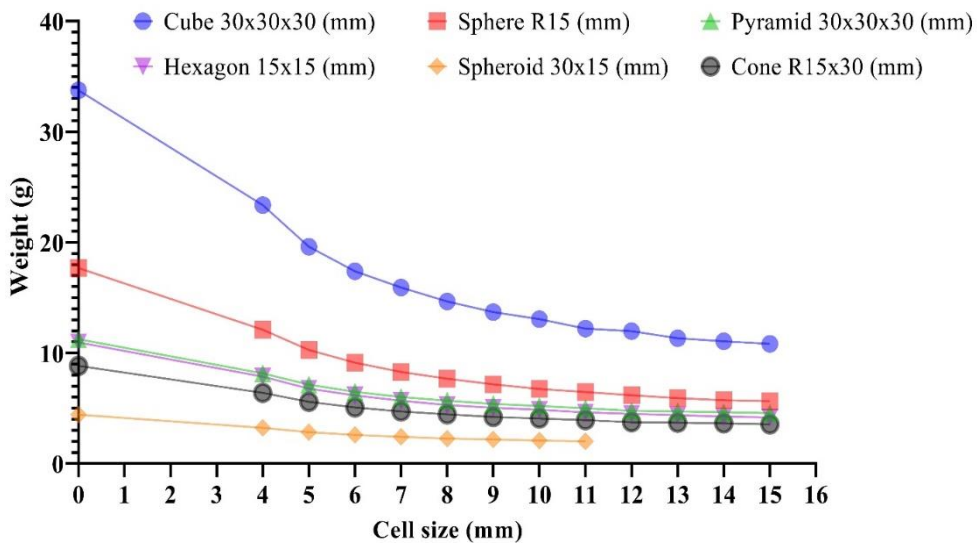


Fig. 13. Weight measurements on basic shapes with different dimensions of Gyroid unit cell

VI. CONCLUSION

The gyroid lattice structure is the most superior technique to reduce the weight of solid structures. Also, the additive manufacturing technique can be achieved with the implementation of gyroid lattice structures at the application level. The printing parameters and optimal size selection for a different shape is also the essential context that measures the feasibility of weight reduction.

This study primarily discusses the control parameters to avoid or reduce the defects in printed lattice structures and the optimal size selection for a given shape based on the weight comparison. There are six printing defects; Strings, Nonuniform layer width, Voids, Layer shift, Excessive material can find with printed 4 mm Gyroid cell using FDM technique.

The defects can control with printing speed and retraction speed. From selected speeds, results showing a clear deviation of the weight comparison. It seems three sets printing and retraction speeds show the best results on weight deviations. With the consideration of weight deviation and number of defects, most accurate printed cell shown as 25 mm/s of both printing and retraction speeds.

As was expected, weight reduction has significant performance with the Gyroid lattice structure. Adapting a proper wall thickness in the Gyroid cell, cause to achieve the required reduction of the component.

Further, the study recommends to perform a comprehensive finite element study based on the experimental results to validate the weight to strength ratio as future work.

REFERENCE

- [1] Jarod C. Kelly, John L Sullivan, Andrew Burnham, Amgad Elgowainy (2015). Impact of Vehicle Weight Reduction via Material Substitution on Life-Cycle Greenhouse Gas Emissions. *Environmental Science and Technology*. Vol (20), pp 12535-12542
- [2] Masaaki Saito, Shuuichiro Iwatsuki, Kunihiro Yasunaga, Kimitaka Andoh (2000). Development aluminum body for the most fuel-efficient vehicle. *JSAE Review*. Vol (21:4A) February, pp 511-516
- [3] Mayur Mhapankar (2015). Weight Reduction Technologies. *Analyst, Technology and patent research*, p 12
- [4] Yohimi Tamaki (1999). Research into Achieving a Lightweight Vehicle Body Utilizing Structure Optimizing Analysis. *Technical Notes/JSAE*. Vol (20) March, pp 555-561
- [5] Hirak Patel, Khushbu C. Panchal, Chetan S. Jadav (2013). Structural Analysis of Truck Chassis Frame and Design Optimization for Weight Reduction. *International Journal of Engineering and Advanced Technology (IJEAT)*. Vol (2:4) April, pp 665-668
- [6] D Barba, E Alabortc, R.C. Reed (2019). Synthetic bone: Design by additive manufacturing. *Acta Biomaterialia* Vol (20) April, pp 637-656
- [7] Dong-Jin Yoo (2011). Computer-aided Porous Scaffold Design for Tissue Engineering Using Triply Periodic Minimal Surfaces. *International Journal of Precision Engineering and Manufacturing*. Vol (12:1) February, pp 61-71
- [8] Mark Helou, Sami Kara (2017). Design, analysis and manufacturing of lattice structures an overview. *International Journal of Computer Integrated Manufacturing*. Vol (3), pp 243-261
- [9] Diab W. Abueidda, Mohamed Elhebeary, Cheng-Shen (Andrew) Shiang, Siyuan Pang, Rashid K. Abu Al-Rub, Iwona M. Jasiuk (2019). Mechanical properties of 3D printed polymeric Gyroid cellular structures. *Materials and Design*. Vol (165) March, p 9
- [10] Dumas M, Terriault P, Brailovski V (2017). Modelling and Characterization of a porosity graded lattice structure for additively manufacturing biomaterials. *Material and design*. Vol (121), pp 383-392
- [11] Borsellino C, Bella G.D (2009). Paper-reinforced biomimetic cellular structure for automotive applications. *Materials and design*. Vol (10), pp 4054-4050
- [12] Frulloni E, Kenny J.M, Conti P, Torre L (2007). Experimental study and finite element analysis of the elastic instability of composite lattice structure for aeronautic applications. *Composite Structures*. Vol (4), pp 519-529
- [13] V.Sreehitha (2017). Impact of 3D printing in automotive industries. *Procedia Manufacturing*. Vol (5) February, pp 91-94
- [14] N. Shahrubudina, T.C. Leea, R. Ramlana (2019). An overview on 3D printing technology: technological, materials, and application. Vol (2), pp 1286-1296
- [15] Thabiso Peter Mpofo, Cephas Mawere, Macdonald Mukosera (2012). The impact and Application of 3D printing Technology. Vol (3), pp 2148-2152
- [16] Revilla-León, M. (2019). *Metal additive manufacturing technologies: literature review of current status and prosthodontic applications*, p. 13
- [17] Alan C S Dantas, Debora H Scalabrin, Roberta De Farias, Amanda A. Barbosa, Andrea V. Ferraz, Cynthia Wirth (2016). Design of Highly Porous Hydroxyapatite Scaffolds by Conversion of 3D Printed Gypsum Structures-a Comparison Study. *Procedia CIRP*. Vol(49), pp 55-66
- [18] Arup Dey, Nita Yodo (2019). Asystematic Survey of FDM process Parameter Optimization and Their Influence on Part Characteristics. *Manufacturing and Materials Processing*. Vol (3) July, pp 64
- [19] Chamil Abeykoon, Pimpisut Sri Amphorn, Anura Fernando (2020). Optimization of Fused Deposition Modelling Parameters for Improve PLA and ABS 3D Printed Structures. *International Journal of Lightweight Materials and Manufacture*. Vol (3), pp 284-297
- [20] Leipeng Yang, Shujuan Li, Yan Li, Minghun Yang, Qilong Yuan (2019). Experimental Investigations for Optimizing the Extrusion Parameters on FDM PLA Printed parts. *Journal of Materials Engineering and Performance*. Vol (28/1) January, pp 169-182
- [21] Ilmars Brensons, Svetlana Polukoshko, Andris Silins, Natalija Mozga (2015). FDM Prototype Experimental Research of Processing Parameter Optimization to Achieve Higher Tensile Stress. *Solid State Phenomena*. Vol (220-221), pp 767-773
- [22] Junhui Wu (2018). Study on optimization of 3D printing parameters. *Materials Science and Engineering*. Vol (392-6)
- [23] Reazul Haq Abdul Haq, Omar Mohd Faizan Marwah, Mohd Nasrull Abdol Rahman, Ho Fu Haw, Haslina Abdullah, Said Ahmad (2019). 3D Printer parameters analysis for PCL/PLA filament wire using Design of Experiment (DOE). *IOP Conf. Series: Materials Science and Engineering*. Vol (607) May

TECHNICAL PAPERS

Session 2

Assessment of Engineering Properties of Expansive Soils for Subgrade of Pavements

Ayomi W.A.W.¹
Undergraduate Research Assistant
Dept. of Civil Engineering,
University of Peradeniya
Kandy, Sri Lanka
wimalsha.ayomi1996@gmail.com

Premachandra D.G.T.P.²
Undergraduate Research Assistant
Dept. of Civil Engineering
University of Peradeniya
Kandy, Sri Lanka
tharinduntc47@gmail.com

Rathnayke R.M.P.³
Postgraduate Research Assistant
Executive Engineer
RDA Nalanda
Matale, Sri Lanka
rpanchula@yahoo.com

Athapaththu A.M.R.G.⁴
Senior Lecturer,
Dept. of Civil Engineering,
University of Peradeniya.
Kandy, Sri Lanka
rasikaathapaththu@gmail.com

Abstract— Expansive soils are one of the most problematic soils encountered in several dry zones of Sri Lanka. Considering its characteristics, civil engineers need to find solutions for any transportation facilities or buildings planned in such areas. Expansive soils swell significantly when it absorbs water and shrink when water is squeezed out or removed. Roads built on this soil undergo large uplifting forces due to swelling. These forces will cause cracking and breakage. Among the available treatment methods, replacement of subgrade and chemical stabilization with fly ash or lime are widely used to improve expansive soil conditions. In Sri Lanka, expansive soils can be found widely in Anuradhapura, Dambulla, Puttalam and Kataragama areas. The presence of such soil conditions in the road subdivisions caused severe damage to the pavement. The purposes of this research are to, identify the swell characteristics, assess the swelling potential, identify suitable treatment material and determine a non-destructive treatment method. Identification of the swelling potential of the soil is important for taking countermeasures. Application of improvement methods will expand the frequency of road repairs and will also be able to control and rectify cracks in the pavement. Soil samples were extracted from selected locations around Dambulla, Sri Lanka. Laboratory experiments such as compaction, California bearing ratio (CBR), free swell index, and swelling pressure tests were performed on the obtained natural soil samples.

Keywords— Expansive soil, Subgrade, Swell Potential

I. INTRODUCTION

The Road Development Authority (RDA) maintains over 12,500 km from the available national road network of nearly 120,000 km in Sri Lanka. Over the last decade, about 6,000 km long RDA maintained roads have been rehabilitated to the asphalt surface finish. This has been carried out to maintain and to improve the safety, comfort and efficiency of the road network. However, cracks appeared before reaching the design lifetime of the roads. There are several reasons for such pavement failures before reaching the design life of newly rehabilitated roads. Rutting failure, alligator cracking, design failure, material failure and cracking due to swell and heave are some of them. Among them, cracks caused by swelling and shrinkage due to occasional change in humidity, or cracks caused by the presence of a subgrade with poor or expansive soils are considered in this study. Injection of lime slurry is focused mainly in this research as a non-destructive treatment method.

Expansive soils are predominant around the world. Expansive soils are fine-grained soil or decomposed rocks that show significant volume change when subjected to the fluctuations of the water table. It absorbs water during the rainy season and swells, and during the dry season the water evaporates and shrinks [18]. This marginal volume change can be seen in the cracks and fractures of roads and other buildings on expansive soils [9]. Expansive soils are most likely to be unsaturated and have montmorillonite clay minerals [12] and due to their chemical composition, the expansive volume and strength of the soil vary at different humidity. Numerous studies have shown that this change in soil volume causes significant structural damage to foundations, including pavements. According to reports [2], lateral swelling pressure may vary in magnitude with vertical swelling pressure, and lateral swelling pressure is higher. In Sri Lanka, as well as in many arid and semi-arid areas of the world, soil pavements are widely used. Such soils are generally unsaturated and contain large amounts of clay. Roads built on this clay are subject to large lifting forces due to swelling scenarios. These forces cause the soil to swell or shrink, and researches have been conducted for different soil stabilizing techniques.

Soil stabilization is used to minimize or eliminate the harmful effects of swell potential. Soil stabilization is defined as mechanical or chemical treatments which increase or maintain the stability of soil or improve its engineering properties in favour of its usage. In mechanical stabilization, the grading of soil is changed by mixing it with other types of soils of different grades which hardly possess any expansive properties. In chemical stabilization, chemically active materials are added to modification of soil properties. Mechanical stabilization cannot use on existing roads without damaging the road. Chemical stabilization for expansive soil can be achieved using waste by-products or natural materials, such as; lime [14],[19], cement [5], fly ash [10], coffee husk ash [4], coir and coir pith [11], bagasse ash [13], micro silica fumes [6], marble dust and beas sand [6], geogrid and jute geotextiles [7] to improve soil properties and find solutions to problems caused by expansive soil. But, many of the waste by-products that have been mentioned above cannot be found easily in Sri Lanka and marble dust and beas sands are highly expensive. Most of the literatures reviewed were based on the chemical stabilization method. Stabilisation of expansive soil using one of the above-mentioned methods has shown

satisfactory results in changing the swell potential of expansive soils.

In this research, cracks on roads were observed in Inamaluwa – Sigiriya (B-162) road and Dambulla to Habarana road section in A6 road which was rehabilitated during 2012 and 2014 respectively. A close observation indicated that some cracks appearing on the roads and most of the cracks are wider than 2 mm. Some road sections are situated near paddy fields. Therefore, samples were taken from selected locations and Sieve Analysis, Atterberg Limits, Compression, Free Swell Pressure, Free Swell Index tests were carried out to identify the properties of untreated soil samples. Comprehensive laboratory tests were done to identify the clay content, mineral composition and physical, chemical and mechanical properties of the existing soil such as; Plasticity Index (PI), Liquid Limit (LL), Swell Index and CBR values. The soil type of the samples collected were found as clayey SAND having main clayey mineral as kaolinite /montmorillonite mixed layer which possesses low to medium swelling and shrinking potential. Detailed test results are discussed in the Testing and Interpretation section below. With the completion of checking of soil samples for each subgrade, soils were identified as expansive soils in selected locations.

II. TESTING & INTERPRETATION

A dynamic cone penetration test was carried out in the field at the time of sample collection. The CBR values were obtained using a correlation taken from TRL (Transport Research Laboratory). The other required data were taken by conducting necessary laboratory tests. The in-situ samples collected from the selected locations were subjected to standard proctor test, Atterberg limit test and swell pressure test. The detailed results of the tests are given in the following sections.

A. Dynamic Cone Penetration

This test was conducted on the site by well-trained professionals in the soft shoulder of the road. Mainly it was possible to identify two distinctive layers; subbase and subgrade. Table I contains the interpretation of the results based on DCP test. The CBR value was calculated based on the following empirical formulae (1) recommended by TRL (Transport Research Laboratory).

$$\text{Log}_{10}(\text{CBR}) = 2.48 - 1.057 \text{Log}_{10}(\text{DPI}) \quad (1)$$

$$\text{DPI} = \frac{\text{Penetration (mm)}}{\text{No. of blows}}$$

The CBR values of subgrade in all the selected locations were determined using the DCP test results and are shown in Figure 1.

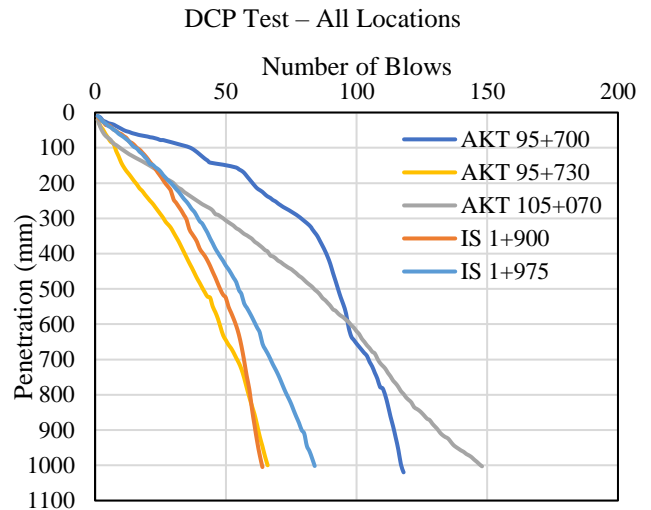


Fig. 1. DCP test results of all the locations

According to [16], the calculated CBR values satisfied the design CBR requirement in both the subbase and subgrade almost in all the samples except AKT 95+730. It is possible that the subbase material in this location may have not met with the required properties and to be certain it is expected to conduct DCP test again closer to that chainage.

B. Sieve Analysis

This was conducted to identify the content of the soil under the guidelines stated in BS 1377: Part 2: 1990 in the selected locations and it was revealed that the soil contains sand in higher percentages.

According to the Unified Soil Classification System (USCS), the soil type was clayey SAND with low to medium plasticity properties. Figure 2 clearly illustrates the particle size distribution curves drawn for each sample collected.

TABLE I. CBR VALUES OF SUBGRADE FROM DCP TEST

Location	Layer	Start at (mm)	Finish at (mm)	Layer Thickness (mm)	No. of Blows	CBR %
AKT 95+700	1	0	660	660	101	41.5
	2	660	1020	360	17	12.0
AKT 95+730	1	0	750	750	57	19.8
	2	750	1000	250	9	9.0
AKT 105+070	1	0	300	300	49	44.5
	2	300	1003	703	99	8.5
IS1+900	1	0	380	380	-	-
	2	380	1385	1005	64	16.4
IS1+975	1	0	530	530	-	-
	2	530	1535	1005	84	21.9

*AKT - Ambepussa - Kurunegala - Trincomalee Rd
*IS - Inamaluwa - Sigiriya Rd.

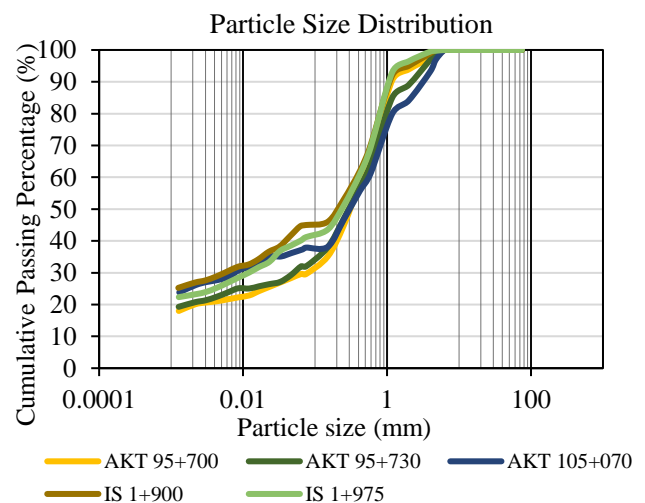


Fig. 2. Particle size distribution curves for selected locations

C. Compaction test

The test was adopted to determine the optimum moisture content of the soil corresponding to the maximum dry unit weight of the soil. For each soil category, five soil samples with different weights and different water content have been prepared and compacted according to the BS 1377: Part 4: 1990.

The behavioural pattern of soil changes with fluctuations in its saturated status. These values shown in Table II could be used to compare the virgin soil sample with a stabilized soil sample. Variations of soil properties with the addition of stabilizers; lime, cement, fly ash, etc. have been studied widely [3].

TABLE II. MDD AND OMC RESULTS

	Location	Maximum Dry Density		Optimum Moisture Content (%)
		(kN/m ³)	(Mg/m ³)	
AKT	95+700	17.9	1.82	14.5
	95+730	18.1	1.84	14.5
	105+070	19.0	1.94	12.7
IS	1+900	17.3	1.76	15.0
	1+975	17.2	1.75	16.0

D. Atterberg Limit

Atterberg limit test plays a crucial role in soil identification and classification. This was conducted to the methods described in BS 1377: Part 2: 1990 and the results of the soil samples are shown in Table III.

TABLE III. ATTERBERG TEST RESULTS

Road	Chainage	Side	LL (%)	PL (%)	PI (%)
AKT	95+700	LHS	32	14	18
AKT	105+070	RHS	42	18	24
IS	1+900	LHS	42	17	25

Based on the above results and the chart obtained from [8] (Figure 3), soil classification and swelling potential could be categorized as mentioned in Table IV.

TABLE IV. CLASSIFICATION AND SWELL POTENTIAL

Road	Chainage	USCS	Swell Potential
AKT	95+700	SC*	Low
AKT	105+070	SC	Medium
IS	1+900	SC	Medium

* SC – Clayey SAND

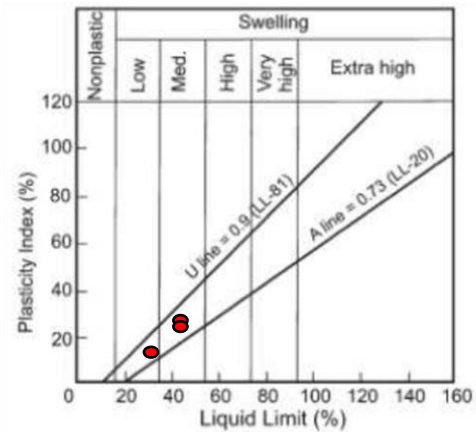


Fig. 3. Classification of swell potential based on Dakshananth and Raman (1973)

The soil samples possess swelling potential changing from “low” to “medium”. This confirms the availability of problematic soils with a considerable potential swell.

E. Free Swell Index

This was conducted to the standards described under IS 2720: Part 4: 1985 and the results are shown in Table V were obtained. With the classification proposed by [15] the dominant clay type also was determined. This is shown in Table VI. It can be concluded that the main clayey mineral was a kaolinite/montmorillonite mixed layer which possesses low to medium swelling and shrinking potential with test results and USCS.

TABLE V. DOMINANT CLAY TYPE BASED ON FREE SWELL RATIO

Road	Chainage	FSI	FSR	Dominant Clay Mineral Type
AKT	95+700	0	1.0	Kaolinite and Montmorillonite
AKT	95+730	0	1.0	
AKT	105+070	0	1.0	
IS	1+900	20	1.2	
IS	1+975	10	1.1	

TABLE VI. CLASSIFICATION OF DOMINANT CLAY TYPE (PRAKASH AND SRIDHARAN, 2004)

Free Swell Ratio (FSR)	Soil Expansivity	Clay Type	Dominant Clay Mineral Type
< 1.0	Negligible	Non-swelling	Kaolinite
1.0 – 1.5	Low	Mixture of Non-swelling and swelling	Kaolinite and Montmorillonite
1.5 – 2.0	Moderate	Swelling	Montmorillonite
2.0 – 4.0	High	Swelling	Montmorillonite
> 4.0	Very high	Swelling	Montmorillonite

With the identification of the dominant clay type, the problematic nature of the subgrade soil can be asserted.

F. Swell Pressure

The standard oedometer (BS 1377: Part 5: 1990) was used to measure swelling pressure. The swelling potential has been

used to describe the ability of a soil to swell in terms of volume change, and it is defined as the ratio of increasing height to the original height due to increased moisture content. Swelling pressure is designated as the pressure required to return the sample to its original volume.

The classification of degree of expansion was determined referring to the studies conducted by [17] and the final outcome is shown in Table VII.

TABLE VII. SWELL PRESSURE TEST RESULTS

Location	Swell pressure	Max. Swell %	Degree of Exp.
IS 1+900	97.02	2.13	Medium
IS 1+975	63.13	0.98	Low

G. Summary

The outcome of the conducted tests was that the available subgrade soil possesses a significant expansive property and the crack appeared on the surface of the observed area is mainly due to the availability of expansive soil subgrade. Continuous observational details and analytical data collected from RDA has confirmed that the design failures or material failures are not possible. This observation leads the above-mentioned outcome to be prominent in the case of development of cracks.

H. Field Measurement of Crack Width

Two points were permanently marked across a section of cracks selected by concrete nails and the width of the cracks were recorded separately from time to time under both wet and dry weather conditions. It was observed, the width of the cracks is reduced during the wet period and vice versa. Furthermore, during the dry period, the exposed subgrade material showed rock hard property and it was very soft during the wet weather period. These crack width variations are shown in following Figure 4, 5 and 6.

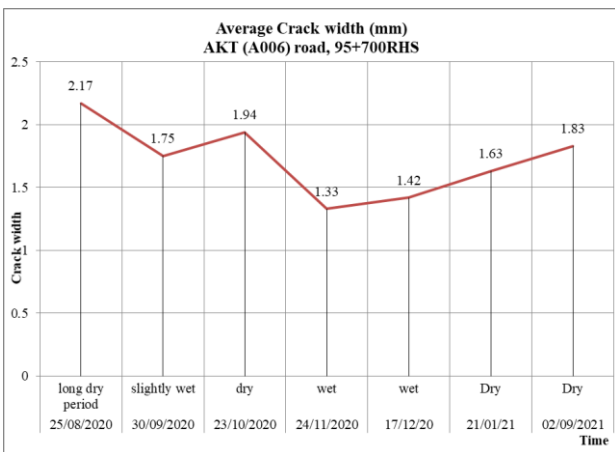


Fig. 4. Seasonal Average Crack Width Measurement Ambepussa Kurunegala Trincomalee road at chainage 95+700 (RHS)

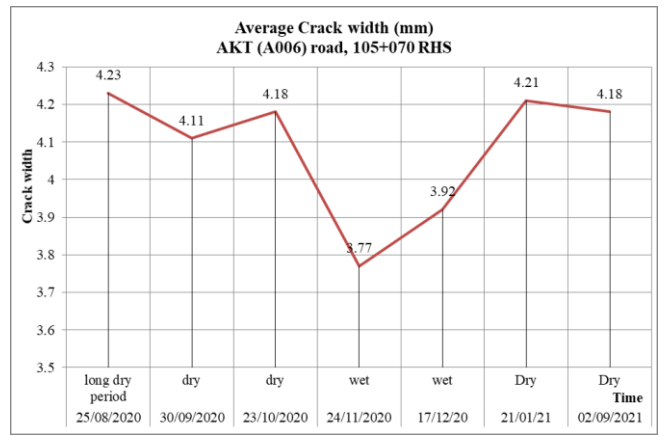


Fig. 5. Seasonal Average Crack Width Measurement in Ambepussa Kurunegala Trincomalee road at chainage 105+070(RHS)

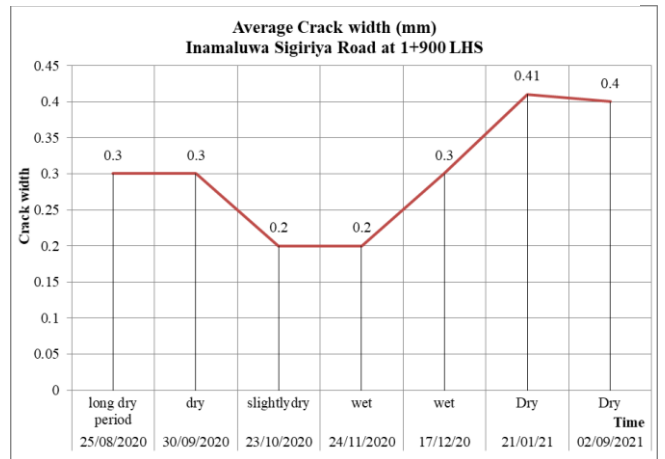


Fig. 6. Seasonal Average Crack Width Measurement in Inamalawa – Sigiriya road at chainage 1+900(RHS)

Comparing the crack width variation of AKT 105+070 and IS 1+900, it can be observed that, even the both soil samples possess medium swell potential, the numerical values of crack width showed considerable difference. The possible reason for this was found as the pavement design maintained on each of the road. IS road had a thick dense overlay related to that of AKT road. Hence, a large surcharge acting upon the subgrade of IS road, have limited the ability to swell, unlike in AKT road, resulting development of smaller crack widths.

III. CONCLUSIONS

Following conclusions are drawn based on the above findings and it is expected to obtain samples from uncracked locations in order to compare the properties of soils in both the cracked and uncracked locations.

- The soil type of each location according to the USCS and BS standards has been identified as clayey SAND. The liquid limit, plastic limit, and plasticity index vary in the ranges of 32-42%, 14-18%, and 18-25%, respectively.
- Samples obtained from the subgrade have shown substantial swelling potential which varies from low to medium.

- The width of the crack varies with the seasonal water content of the soil. According to the field experimental results, it was observed that the crack width increases in the dry season. These changes can be observed due to the presence of expansive soil in the subgrade.
- It can be concluded that the availability of expansive soil in the subgrade causes a major impact to the deterioration of the road pavement.

ACKNOWLEDGMENTS

The authors highly appreciate the assistance provided by the laboratory assistants in the Geotechnical laboratory of the Faculty of Engineering, University of Peradeniya and staff members of the Road Development Authority office in Naula, Matale.

REFERENCES

- [1] Adel Djelai, Abdelkader Houam, Behrooz Saghafi, Ali Hamdane and Zied Benghazi, "Static analysis of flexible pavements over expansive soils", Iran University of Science and Technology, 2016.
- [2] Andy B.F, (1989), Laboratory evaluation of lateral swelling pressure journal of Geotechnical Engineering, ASCE, vol. 115, No. 10 pp. 1481-1486.
- [3] Asgari M.R, Baghevbanzadeh Dezfali, Bayat M, (2013), Experimental study on stabilization of a low plasticity clayey soil with cement /lime, Saudi Society for Geosciences
- [4] Atahu M.K, Saathoff F, A. Gebissa A, (2018), Strength and compressibility behaviours of expansive soil treated with coffee husk ash, Journal of Rock Mechanics and Geotechnical Engineering 11 (2019) 337-348
- [5] Bandara W.W, Mampearachchi W.K, K. Sampath K.H.S.M, (2017), Cement stabilised soil as a Road base material for use in Sri Lankan roads, ENGINEER-Vol. L, No. 01.pp.[21-29],2017
- [6] Chayan Gupta, (2013), Influence of Micro Silica fumes on subgrade characteristics of expansive soil, researchgate.net/publication/292982499
- [7] Choudhary A, Gill A, J Jha, Sanjay Shukla, (2012), improvement in CBR of the expansive soil subgrades with a single reinforcement layer, ECU publication 2012
- [8] Dakshanamant V, Raman V, (1973), A simple method of identifying an expansive soil, Soils and Foundations, Japanese Society of soil mechanics and foundation engineering, 13 {1}, pp. 97-104
- [9] Das B.M, (2011), Principles of Geotechnical Engineering, 7th edition, Cengage Learning, Stanford.
- [10] Dissanayake T.B.C.H, Senanayake S.M.C.U, Nazvi M.C.M, (2017), Comparison of the Stabilization behaviour of fly Ash and Bottom Ash Treated Expansive Soil, ENGINEER-Vol. 1, No. 01, pp. [11-19]
- [11] Leema Peter, Jayasree P.K, Balan K, Alaka Raj S, (2014), Laboratory investigation in the improvement of Expansive Soil Stabilised with Coir Waste, Transportation Research Procedia 17 92016) 558-566
- [12] Liet Chi Dang, Hayder Hasan, Beza Fatah, Hadi Khabbaz, (2015), Influence of Bagasse ash and hydrated lime on strength and mechanical behaviour of stabilized expansive soil,
- [13] Liet Chi Dang, Hayder Hasan, Behzad Fatahi, Robert Jones, Hadi Khabbaz, (2016), International Journal of GEOMATE, Sept 2016, Vol. 11, Issue 25, pp. 2447-2454
- [14] Magdi M Zumrawi, Omer S.M. Hamza, (2013), Improving the characteristics of Expansive Subgrade Soils using Lime and Fly ash, researchgate.net / publication / 322165737
- [15] Prakash K, Sridharan A, (2004), Free swell ratio and clay mineralogy of fine-grained soils, www.researchgate.net/publication/245403715
- [16] RDA Srilanka, Pavement Design Report – Revision 1, Kandy-Jaffna Road (A009) (Naula Town)
- [17] Seed H.B, Woodward R.J. Jr, Lundgren. R, (1962) , Study of swell and swell pressure characteristics of compacted clays, Highway Research Bulletin No.313, pp. 12-39
- [18] Snethen D.R et al, (1975) , A review of engineering experience with expansive soils in highway subgrades, Report No. FHWA-RD-75-48, Federal Highway Administration, Washington D.C
- [19] Thyagaraj T, Sudhakara M. Rao, P. Sai Suresh, Salini U, (2012), Laboratory Studies on stabilization of an Expansive Soil by Lime precipitation Technique, J. Mater. Civ.Eng, 2012, 24(8): 1067-1075

Validation of HCM model to estimate the delays in minor roads of unsignalized T - junctions in suburban areas under mixed traffic conditions

Rupasingha, W. A. M. J.
Department of Civil Engineering,
University of Peradeniya
Peradeniya, Sri Lanka
malrupasingha@gmail.com

Dharmarathna W. R. S. S
Department of Civil Engineering
University of Peradeniya
Peradeniya, Sri Lanka
samal@eng.pdn.ac.lk

Abstract - Vehicle controlling at unsignalized intersections is a complicated procedure since each driver in the minor road of the junction must make his/her own decisions when entering to the major road, as it is influenced by many reasons. Driver on the minor road should scan for an acceptable gap before entering to the junction. When they do not see significant gaps, it would cause for a heavy delay in minor road. Highway Capacity Manual (2010) and Tanner (1962) provide two approaches to estimate the aforementioned-delay, which have been developed for the homogeneous traffic flow conditions in developed countries. Traffic flow conditions in developing countries like Sri Lanka are heterogeneous since they consist of large number of light vehicles mixed with heavy vehicles. Therefore, this research aims to validate a model to estimate the delays in minor roads of unsignalized intersections. Three unsignalized T-junctions in Kurunegala district were selected for the case study and the respective field data were collected as video records in a weekday. Those observed delays were compared with the theoretical values calculated from HCM (2010) and Tanner (1962) models. The HCM model showed more similarity, and hence it was identified as the most suitable model. An improvement method given in HCM (2010) was also checked to incorporate the mixed traffic conditions into the HCM model. Theoretical delays were recalculated and compared with actual delays. Statistical analysis showed that there is no significant difference between the delays calculated with adjusted method and actual values compared to the original HCM model.

Keywords— Delays in minor road, T-Junction, HCM, unsignalized intersections, heterogeneous traffic,

I. INTRODUCTION

Delay is defined as the excess time consumed in a transportation facility compared to that of a reference value. More specifically, it is the difference between the time it would take to traverse a road section under ideal conditions and the actual travel time. Delay is often considered as one of the most important measures of the effectiveness of unsignalized intersections as perceived by road users [1].

The total delay for two-way stop-controlled (TWSC) intersections can be divided into two parts, namely queue delay and service delay. Queue delay is the time between the vehicle's arrival at the end of the queue and the time when the vehicle arrives at the stop line. Service delay is the time between the arrival at the stop line and the departure from the stop line [2]. When an unsignalized T-junction is considered, there can be an unavailability of acceptable gaps in the main road traffic stream at peak times, which can cause a heavy delay to vehicles in the minor road when entering to the main

road. Accordingly, longer queues can be occurred in the minor road.

There are two commonly used methods to calculate the delays in minor road, as proposed by Tanner [3] and Highway Capacity Manual [4]. These models have been developed in countries with different vehicle mix compositions than in developing countries like Sri Lanka. Further, those methods have been developed for homogeneous traffic conditions available in most of the developed countries. Traffic flow conditions in many developing countries like Sri Lanka are heterogeneous due to the consistency of higher percentage of lighter vehicles such as motorbikes, three-wheelers and heavy vehicles. Therefore, it is necessary to modify these models to estimate the delays in minor roads connected to intersections under mixed traffic condition.

II. LITERATURE REVIEW

There are two main theoretical methods available in the literature to calculate delays in minor roads.

- Tanner method (1962)
- Highway Capacity Manual (HCM) method (2010)

A. Tanner's model [3]

Tanner's model has developed based on three assumptions as minor road vehicle arrivals at the junction are randomly distributed, major road traffic flow forms an alternating renewal process with the time taken for a group of vehicles to cross the junction having an arbitrary distribution and the gaps among bunches are being distributed exponentially, and minor street vehicles pass the major street at equally spaced instants during a gap provided that there is at least a time constant before the start of the next group.

The developed model to estimate the average delays for vehicles on the minor street at unsignalized junctions is represented by the following set of equations.

$$W_2 = \frac{0.5 \frac{E(y^2)}{Y} + q_2 * Y * \exp(-\beta_2 q_1) * \frac{\exp(\beta_2 q_1) - \beta_2 q_1 - 1}{q_1}}{1 - q_2 Y (1 - \exp(\beta_2 q_1))} \quad (1)$$

Where,

$$E(y) = \frac{\exp(q_1(\alpha - \beta_1))}{q_1(1 - \beta_1 q_1)} - \frac{1}{q_1} \quad (2)$$

$$E(y^2) = 2 * \frac{\exp(q_1(\alpha - \beta_1))}{q_1^2 * (1 - \beta_1 q_1)^2} - (\exp(q_1 * (\alpha - \beta_1)) - \alpha q_1 * (1 - \beta_1 q_1) - 1 + \beta_1 q_1 - \beta_1^2 q_1^2 + \frac{0.5 * \beta_1^2 q_1^2}{1 - \beta_1 q_1}) \quad (3)$$

$$Y = E(y) + \frac{1}{q_1} \quad (4)$$

q_1 - Flow in the major road (veh/sec)

q_2 - Flow in the minor road (veh/sec)

β_1 - Minimum time headway of the traffic stream in the major road (sec)

β_2 - Minimum time headway of the traffic stream in the minor road (sec)

α - The average lag or gap in the major road traffic stream accepted by the minor road drivers when entering the major road traffic stream (sec)

W2 - delay to minor road (sec)

The application of Tanner's model as given in equation (1) to (4), to estimate delays of vehicles in minor road traffic, requires lot of information on the characteristics of both minor and major road traffic streams as the flow rates of the traffic on both minor and major roads, critical gap, and headways in both the major road and minor road traffic stream.

Ali Sahraei et al (2014) [5] used Tanner's model to investigate delays to the minor road vehicles at priority junctions located in suburban areas in Malaysia and showed that the observed delays were in a good agreement with values estimated using the Tanner's model for the twilight time, but not for the day time data.

Generalization to several lanes of Tanner's formula was done considering the capacity of a nonpriority movement at an isolated intersection accommodating the possible bunching of major road traffic and different critical gaps for different lanes [7]. Heidemann (1991) [6], coupled Tanner's model with queueing-theory approach subjected to the assumption of the vehicle arrivals in both the minor and the major road flows being distributed according to the Poisson law.

B. HCM model [4]

HCM model provides the below equation in order to estimate the average delays for vehicles on the minor street at unsignalized junctions.

$$D = \frac{3600}{C_{m,x}} + 900T \left(\frac{V_x}{C_{m,x}} - 1 + \sqrt{\left(\frac{V_x}{C_{m,x}} - 1\right)^2 + \frac{(3600)}{450T} \left(\frac{V_x}{C_{m,x}}\right)} \right) + 5 \quad (5)$$

Where; D - Control delay (sec/veh),

V_x -Flow rate for movement x (veh/h),

$C_{m,x}$ - Capacity of movement x (veh/h),

T - Analysis period (h)

The constant value of 5 (s/veh) is included in the equation for the deceleration of vehicles from the free flow speed to the speed of vehicle in the queue and the acceleration of vehicles from the stop line to free flow speed.

Capacity of the movement can be calculated using following equation.

$$C = V_{c,x} \frac{e^{-V_{c,x} T_{c,x} / 3600}}{1 - e^{-V_{c,x} T_{f,x} / 3600}} \quad (6)$$

Where, $V_{c,x}$ = Conflicting flow rate (veh/h)

$T_{c,x}$ = Critical gap (s)

$T_{f,x}$ = Follow up time (s)

The model proposed in HCM [4], is much simpler when compared with the Tanner's model [3]. In general, the HCM model only requires two main inputs for its application as flow rate of the movement and corresponding capacity.

Box and Worth (1967) [8] recommend another method for calculation of control delay at priority [8]. Based on this method, vehicles were counted in queue length during 15 min intervals and control delay in term of vehicle per hour was measured.

Lu and Lall (1995) [9] determined a non-linear multivariable model for TWSC junctions by using 34 h data collected through video cameras in Alaska. This model evaluated minor road control delays as a function of the subject minor road traffic volume and the major road traffic volume.

Kyte et al. (1996) [10] attempted to establish a new practical model for estimation of delay based on queueing theory at priority junctions. In this regard, Kyte et al. (1996) used two specific times which were service time (automobile spend time at the stop line position on minor road until departure to the major road) and move up time (the minimum time for automobile to arrive to the stop line after the previous automobile leaves the stop line). Therefore, vehicle will spend time on the minor road based on the sum of these two periods.

III. METHODOLOGY

Three unsignalized T junctions which are located in Kurunegala - Kuliypitiya (B247) and Narammala - Negombo (B308) roads in the Northwestern province of Sri Lanka, were selected for the case study. Site selection was done based on three criteria as, acceptable traffic volumes on

both major road and minor road, reasonable sight distances and better access and safety for the data collectors and equipment during the data collection.

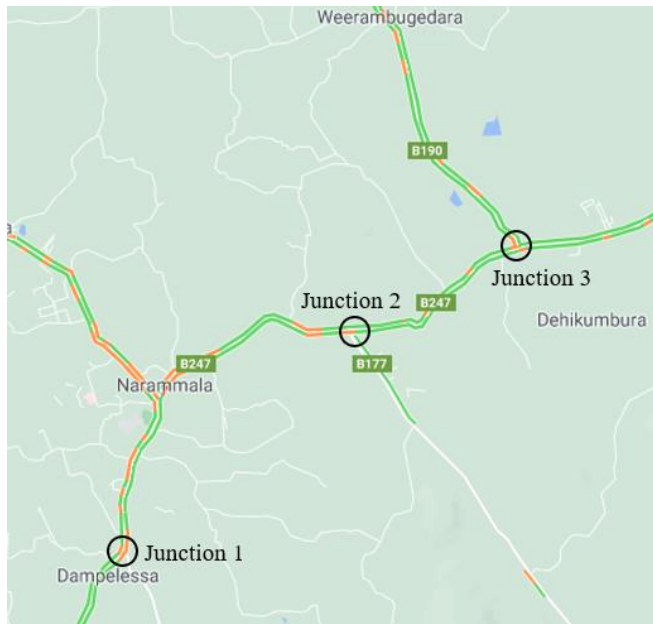


Fig. 1. Selected junctions

Data collection was done by video recordings at the respective junctions as two hours in the morning peak and two hours in the evening peak in a weekday. Selected time periods were 7.00 am to 9.00 am and 4.00 pm to 6.00 pm.

Delays of the vehicles in the minor road and other relevant data such as major road flow rate, minor road flow rate, minimum time headway in the major road traffic stream, minimum time headway in the minor road traffic stream and critical gap were collected manually by scrutinizing the recorded videos.

Then, the theoretical delays were calculated by using the HCM model [4] and Tanner’s [3]. Finally, the theoretical values and actual values were compared.

Actual delays were estimated manually using the recorded videos collected in selected peak hours. Four hour durations were divided in to 15 minutes intervals and calculated the average delay within respective intervals.

Delays are calculated by the HCM model, Tanner’s model were compared with actual delays. The results showed in Fig. 2 to Fig. 4 indicate a significant difference between the theoretical and actual delays. Highest difference showed by Tanner’s model with respective actual delays.

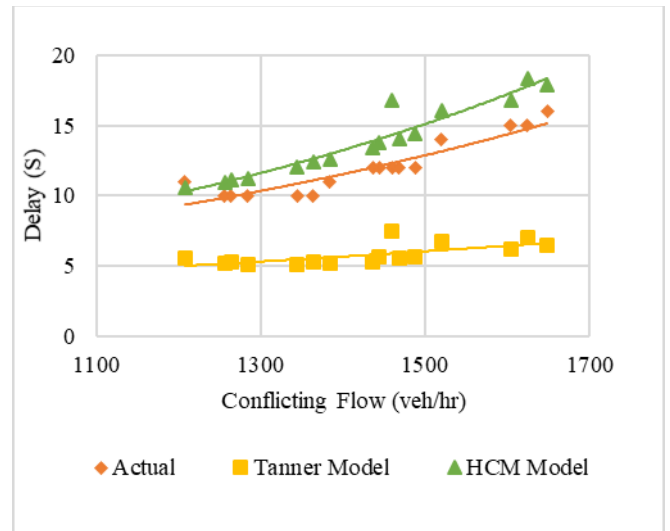


Fig. 2. Delay variation in junction 1

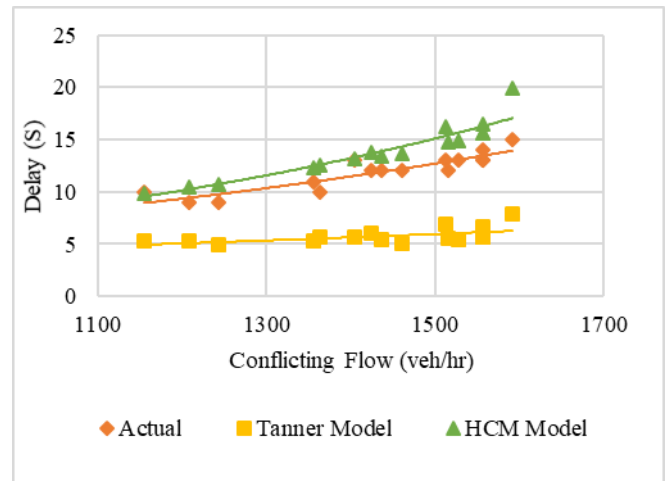


Fig. 3. Delay variation in junction 2

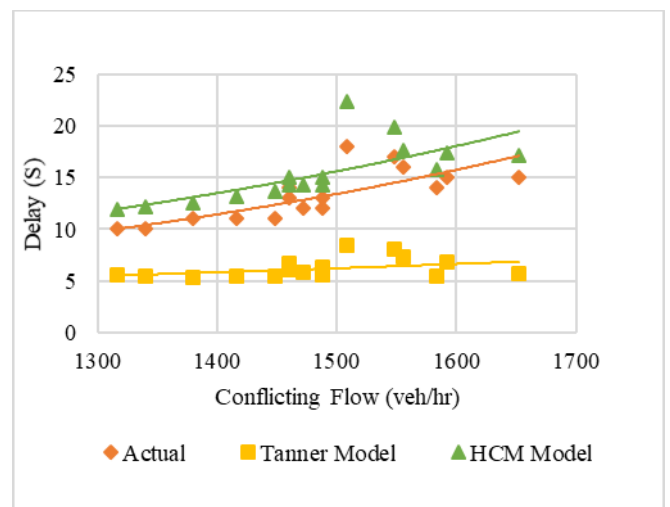


Fig. 4. Delay variation in junction 3

Other than that, Root Mean Square Error and percentage bias were calculated for both HCM model values and Tanner model values.

TABLE I. RMSE AND PBIAS VALUES FOR HCM AND TANNER MODELS

	RMSE	PBIAS
HCM Model	2.27	16.41 %
Tanner Model	6.65	52.20 %

In both cases Tanner model shows a higher error compared to HCM model.

Therefore, the HCM model was identified as the most suitable model for Sri Lankan mixed traffic conditions.

A. Mixed traffic adjustment methods

There are two basic methods for mixed traffic adjustment given in HCM and SIDRA (Signalized & unsignalized Intersection Design and Research Aid) method based on the Passenger Card Equivalent (PCE) factors and percentage of vehicles.

However, the PCE factors vary from country to country depending on vehicle mix by type, make and age, road design and driving habits. Kumarage (1996) [11] established statistically acceptable values for different traffic movements, and design of highways in Sri Lanka.

Percentages of vehicles were calculated using the data obtained. Mixed traffic flow at the selected junctions consists 48% of motorcycles 22% of three-wheelers, 19% of car/jeep category and rest of 11% with other vehicles.

1) Adjustment method 1

Following equation given in HCM was used in adjustment method 1.

$$\text{Ad. factor 1} = \frac{1}{1 + P_1(E_1 - 1) + \dots + P_n(E_n - 1)} \quad (7)$$

Where, P = Proportion of vehicle type

E = PCE factor

2) Adjustment method 2

As per the SIDRA method, below relationship was used in the adjustment method 2.

$$\text{Ad. factor 2 (for } P > 0.05) = \frac{1}{1 + (E - 1)(P - 0.05)} \quad (8)$$

Ad. Factor 2 = 1 (for $P \leq 0.05$)

Where, P = Proportion of vehicle type

E = PCE factor for relevant vehicle type

TABLE II. CALCULATED ADJUSTMENT FACTORS

	Junction 1	Junction 2	Junction 3
HCM - Modification	1.07	1.07	1.08
SIDRA - Modification	1.18	1.16	1.20

Then, the flow rates were adjusted using the two adjustment factors separately to calculate the delays using HCM model again.

IV. RESULTS

Results obtained through the above analysis are shown in Fig. 5 to Fig. 7.

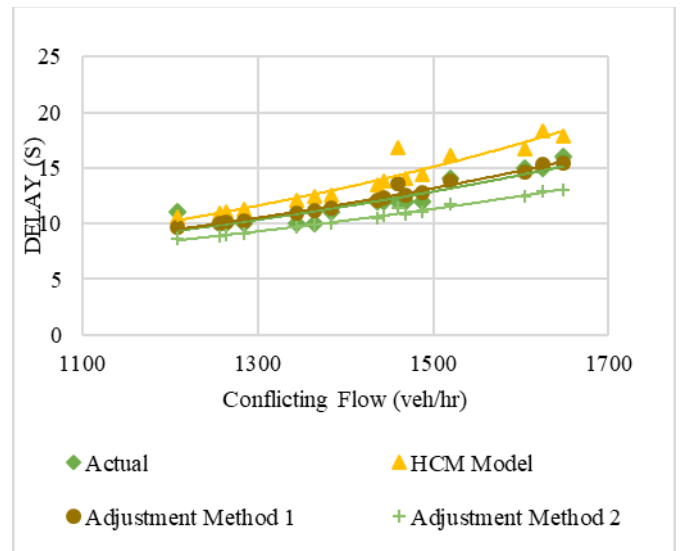


Fig. 5. Delay variation in junction 1

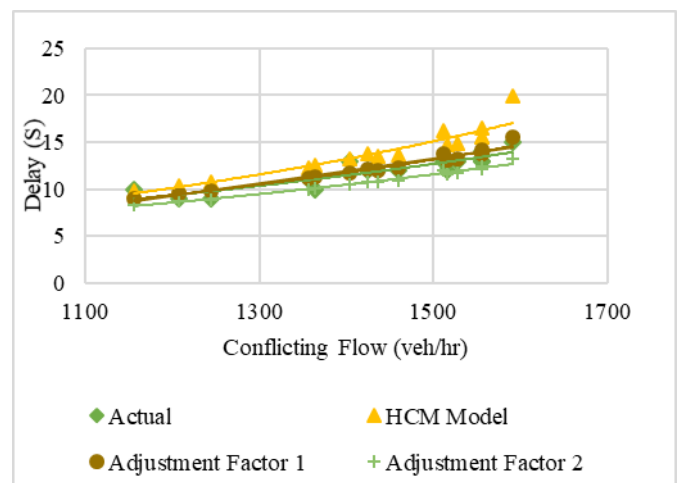


Fig. 6. Delay variation in junction 2

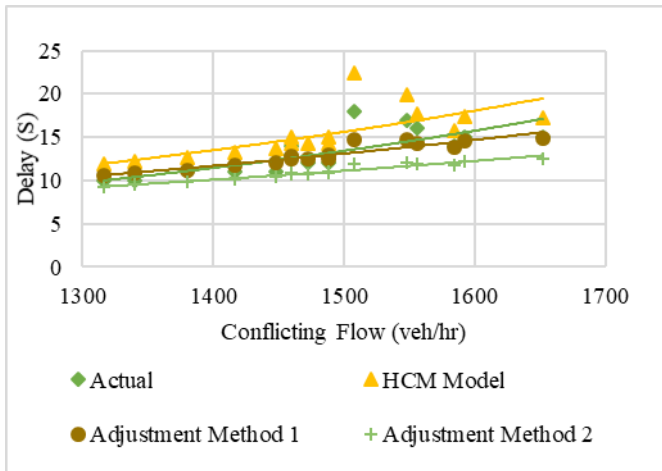


Fig. 7. Delay variation in junction 3

When the above figures are compared, there is a significant difference between actual delays and updated HCM model values with adjustment factor 2. But it does not show a significant difference between actual values and updated HCM model values with adjustment factor 1, which is given in HCM (2010).

Here again Root Mean Square Error and percentage bias were calculated for both adjustment method 1 and 2.

TABLE III. RMSE AND PBIAS VALUES FOR ADJUSTMENT METHODS

	RMSE	PBIAS
Adjustment method 1	0.93	0.65 %
Adjustment method 2	1.99	12.75 %

In both cases adjustment factor 2 shows a higher error compared to adjustment factor 1.

V. CONCLUSION

The paper discusses results of a study carried out to estimate the delays of minor road vehicles at unsignalized junctions located in suburban areas under mixed traffic condition. The paper makes a comparative assessment between Tanner model [3] and the HCM model [4]. The results showed that the actual delays on peak hours were higher than Tanner model results and lower than the HCM

model results. Both Tanner model and HCM model gives a significant difference with actual delay values. Therefore, it implies that both HCM model and Tanner model cannot directly applicable to the analysis of delays in unsignalized junctions in developing countries like Sri Lanka which has a mixed traffic condition. When adjustment factors were used, it does not show a significant difference between actual values and updated HCM model values with adjustment factor 1, which is given in HCM (2010). Therefore, this adjustment factor 1 can be directly used to calculate delays of the minor road vehicles at unsignalized junctions located in suburban areas under mixed traffic condition from HCM default method. Further, it is recommended that the HCM method should be checked for unsignalized junctions located in urban areas in the future studies.

ACKNOWLEDGMENT

We express our sincere gratitude to the academic and non-academic staff of the Department of Civil Engineering University of Peradeniya, and all who supported us in the data collection stage.

REFERENCES

- [1] Ciro Caliendo, "Delay Time Model at Unsignalized Intersections", *Journal Of Transportation Engineering*. Vol. 140. Pag.1-13, 2014
- [2] Michael Kyte, Chris Clemow, Naseer Mahfood, B. Kent Lall, And C. Jotin Kristy, "Capacity and Delay Characteristics of Two-Way Stop-Controlled Intersections" *Transportation Research Record*, 1991
- [3] Tanner, J. C. 1962. "A Theoretical Analysis of Delays at an Uncontrolled Intersection", *Biometrika*. 49(1/2): 163-170.
- [4] Transportation Research Board (TRB). 2010. *Highway Capacity Manual*. National Research Council, Washington, D.C.
- [5] Mohammad Ali Sahraei, Othman Che Puann "Minor Road Traffic Delays at Priority Junctions on Low Speed Roads in Suburban Areas" , Article in *Jurnal Teknologi* . 2014
- [6] Heidemann, D. "Queue length and waiting-time distributions at priority intersections" 1991
- [7] Caroline S.Fisk, "Priority intersection capacity: A generalization of Tanner's formula", 1989
- [8] Box, P. C. , & Worth, W. A. Warrants for traffic control. *Signals* . 22-29. 1967
- [9] Lu, J. J. and Lall, B. K. 1995. "Empirical Analysis of Traffic Characteristics at Two-Way Stop-Controlled Intersections in Alaska", *Transportation Research Record*. 49-56.
- [10] Michael Kyte, Wayne Kittelson, Zong Z Tian, Bruce Robinson, Mark Vandehey, "Analysis of Traffic Operations at All-Way Stop-Controlled Intersections by Simulation" *Transportation Research Record Journal of the Transportation Research Board*, 1996
- [11] Kumaraage, "PCU Standards for Sri Lanka Highway Design" Annual Sessions, Institute of Engineers Sri Lanka, 1996

Discrete Choice Modeling Approach for Understanding the Mode Choice Variability

M.I.M.M.H. Adheeb

Department of Civil Engineering
Faculty of Engineering
University of Peradeniya
Peradeniya, Sri Lanka
mimmhadheeb95@gmail.com

A.M.A. Ilahi

Department of Civil Engineering
Faculty of Engineering
University of Peradeniya
Peradeniya, Sri Lanka
abzalilahi@gmail.com

W.R.S.S. Dharmarathna

Department of Civil Engineering
Faculty of Engineering
University of Peradeniya
Peradeniya, Sri Lanka
samal@eng.pdn.ac.lk

Abstract— Number of transportation planning techniques have been implemented in the global context for forecasting the mode share variability among the available transport modes. Accordingly, the approaches of mode choice modeling play an important role in public transport development, especially in developing countries including Sri Lanka. Hence, this study is set up to look at the variability of mode choice parameters based on different modes of transport which are commonly used in Kandy district, such as cars, taxis, buses, motorcycles, shared vehicles, bicycles, etc. Trip purposes were identified as work, education, shopping, health, leisure etc. under different socioeconomic variables, such as age, gender, car ownership, and monthly income which have a significant impact on the selection of transport mode. Raw data was gathered using an online questionnaire, and face-to-face interviews. Cross sectional analysis showed 48% of the trip-makers are under 25 years of age and are expected to represent the educational trips. About 49% are between 25 to 60 and expected to be the main contributor for the work trips. 38% travelers are public transport users and are having less than 25,000 LKR monthly income. In addition, 26% individuals earning over 75,000 LKR as their monthly income are using private vehicles. Hence the data set is significantly representing the most categories of travelers in Kandy district and the estimated parameters can be highly utilized in the development of city transport planning. Travel time, travel cost, access time, waiting time are considered as main parameters and estimated under the utility maximization theory in Multinomial logit (MNL) modeling approach in RStudio platform. All the estimated parameters are found to be significant. Study indicates that people well aware of travel time, travel cost, access time and waiting time in public transport. The estimated parameters stressed the necessity of improving all the considered time related parameters in order to bring the travelers back to the public transport modes.

Keywords— *Multinomial logit model, mode choice, parameter estimation, utility maximization*

I. INTRODUCTION

Transportation has become an essential part of the day-to-day life of people and sparked with the current substantial industrialization, and decentralization nature of the improvement of cities. Being a South Asian country together with India, Pakistan, Bangladesh, etc., Sri Lanka also has subjected to the increasing horizontal spread of cities which has led to increased travel demand. Hence proper transportation planning arrangement is needed to deal with all requirements and provide smooth traffic along the local road network. Accordingly, the mode choice modeling has become crucial as it is one of a very significant components in the urban transportation planning and policy making.

The aggregate and disaggregate models to mode choosing research in transit are generally differentiated. The modal difference is easily examined using data aggregated at the township level or for a set of passengers in the bulk method. Bulk models attempt to represent the usual behaviour of

passengers instead of just a single individual. Independent mode choice behavior and decision rules, on the other end, are especially crucial in disaggregate simulation. As a result, this could represent changes in decision-making behavior as a result of changes in personal features and rival qualities [1]. Independent travelers are the ruling element in a disaggregated system. The model must be directed by the passengers' behavioral principles, which is a crucial prerequisite for simulating consumption patterns. To put it another way, it will reflect the choices that passengers undertake when faced with a difficult conclusion [2].

Being the second largest and fastest-growing city in Sri Lanka, Kandy faces acute transport problems. As a result, the goal of this research is to create a discrete choice model based on a well-established utility function for evaluating passengers' mode choice characteristics based on visits to Kandy.

II. LITERATURE REVIEW

In Nanjing, China, Ling Ding and Ning Zhange looked for public transportation and private vehicles. Travelers' personal data including travel details were collected using a reveal preference survey and a stated preference survey [3]. Financial condition, land usage, aging, salary, trip duration, and transport costs have considered as influencing factors for making travel decisions. MNL estimations were done using walking time, waiting period, in-vehicle time, fare, comfort, and travel time cost as factors in utility functions. The untenable transport infrastructure in Klang Valley been analyzed as a case analysis in Malasia [4]. A questionnaire technique has used to perform a review opinion study. Using the gathered characteristics of choice, mode shifting study was used to create discrete choice models to assess the chance of passengers switching from their present state to public transit.

Demetsky and Tatineni (2005) investigated a distribution network relying on modeling methodology for territorial cargo traffic management, in which the mode choice analysis was conducted utilizing four different classifiers: binary logistic concept, linear regression, polynomial analysis of variance, and tree characterization [5]. The logistic regression simulations gave the most discoverable findings among the existing empirical choice models, while the polynomial classifier and classifying trees offered the most precise modal split amongst those four empirical models. Zenina and Borisov (2012) used multiple regression, decision trees, and MNL models to classify transit mode preference [6]. For the investigation, five different means of transportation were considered: private car, mass transit, pedestrian, cycling, and cab. The multinomial logit model calculations have demonstrated how distinct utility requirements and the predicted parameters associated with them will be utilized to forecast decision probabilities based on trip variables and replacement features.

For the Egyptian city of Mansoura, a mode choice model is being developed by Elharoun, Shahdah and El-Badawy (2018) [7]. They had collected 10,000 trip data using online questionnaires covering private vehicle, taxi, microbus, walk, and other forms of city transportation. The model was developed using logit modeling approach, and the quality of fit was determined using the chi-square test. A case study of work trip mode choice modeling conducted in Kolkata [8], measurable parameters like as journey duration, transport costs, processing time, and others were combined with qualitative aspects such as dependability, relaxation, and efficiency. The usefulness of each additional source was obtained through a sample survey using a logit model that was developed based on a utility function, taking into account Indian work commutes as transit, para-transit, and personal vehicles. Another study undertaken in Latvia looked at three options: a vehicle, a rail, and a bus [9]. They have developed two discrete choice models including the model allows the prediction of the choice between using a car and using public transport, and the model focusing choice between using a bus and using a train.

Almasri and Alraee (2013) investigated the method of travel in Gaza city work commutes utilizing information gathered from surveys and face-to-face interactions [10]. Their research focused on the influence of macroeconomic factors on mode choice models, such as wage, car owning, location, and maturity level as significant drivers, and the model they developed had a 95% confidence precision. Own vehicle, shared taxi, taxi, motorbike, bicycle, and having to walk have been the methods studied, and a log - linear model based on utility maximization was utilized. The null hypothesis was developed after evaluating the model's validity using the likelihood linear interpolation. In Dresden, Germany, students choose their mode of transportation to school were analyzed [11]. Pupils may move from low-cost means of transportation such as bicycle, public transit, while distance, vehicle ownership, and climate were the main influential elements that influence the choice behavior. They used a MNL technique for model estimations. They suggested a system for disaggregating travel data collected using GIS, and were using a questionnaire to collect details on every pupil's home state, school attended, maturity, gender, vehicle availability, as well as availability of driver license, and the desired mode of travel from home to school and return. A study focused on developing transcontinental transportation planning models for Saudi Arabia, with the main goal of developing interstate travel mode patterns for KSA was done [12]. In airports, bus stations, and railway stations, all relevant data was gathered using a standardized assessment. The mode choice model has been developed for business, Aumera (Pilgrimage), and personal travels, taking into account aspects such as demographics, distance traveled, trip duration, commuter nationality, and out-of-pocket expenses.

Rahman and Consultant (2020) estimated the impact of time and mode choice behavior of Dhaka city people through disclosed desire and expressed preference data [2]. They investigated ten various patterns in all, including two modes (Mass rapid transit and Bus rapid transit). For mode choice analysis, a MNL model was established, and a numeric logistic regression was utilized to quantify the amount of time.

Holland (2000) used a fuzzy inference approach to estimate modal split, which was used to establish choice for a set of observable trip features [13]. In this investigation,

Mizutani and Akiyama (2001) employed a hybrid model that included fuzzy logic as well as the logit model [14]. In a fuzzy-logit model, a utility function is defined using fuzzy argumentation rather than arithmetic operations to represent people judgments with ambiguity in a discrete choice model. Teodorovic and Kalic (1996) developed and used an approximation logic technique to address the travel mode phenomenon [15].

III. METHODOLOGY

The online questionnaire study focused trips related to Kandy city. Kandy is Sri Lanka's second biggest city, with a population of 1,452,000 people as of 2017 [16] which is growing day by day. Different areas are congested due to various purposes such as academic, business, and leisure as a result of the growing populace and interests. The city is situated on the Kandy highland, which extends across an area of tropical tea estates. Kandy is the capital of Sri Lanka's central region and a religious and commercial powerhouse.

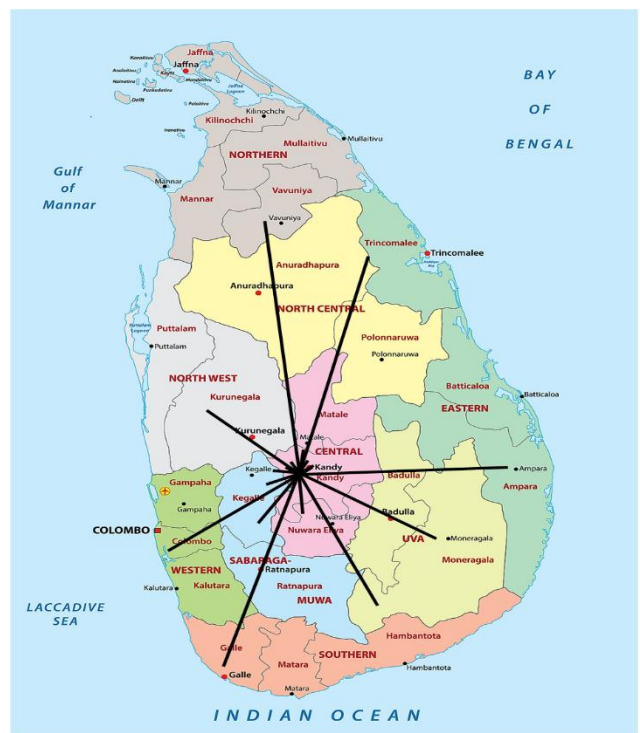


Fig. 1. Trip distribution of respondents

Devised and implemented a commuter survey to gather data on their preference method of transportation. An online questionnaire was distributed among diverse group of people, including undergraduates, university staff, school teachers, students, parents of students, officers, and the general public, in order to receive their responses. Each respondent fill out 37 questions in the questionnaire during the online survey. A total of 691 people from diverse fields took part in the study. Origin – destination of the travelers indicated that the data set is fulfilled with trips from most parts of the country as shown in Figure 1. Surveys were gathered over the course of one month, and hence we consider our data to be connected to a single time period.

IV. THEORETICAL BACKGROUND

Logit model is one of the most widely used approaches for mode choice assessments. It is the most widely utilized

multiple regression model, based on the premise that standard errors (ε_{ni}) are distributed independently and consistently, with high values for all i . The unseen variables are independent across options and have the same deviation for all choices, which is a key aspect of the concept. The logit model's popularity stems from its ease of use.

Each option would provide a specific amount of value to the decision-maker. The decision-maker is aware of this usefulness, but the researcher is not. The decision-maker selects the option that gives the most benefit. Hence a utility function must be created before it can be used in the logit model. The utility function is defined in general as:

$$U = \beta_0 + \beta_1 X_1 + \beta_2 X_2 + \dots + \beta_n X_n + \varepsilon \quad (1)$$

Where,

U is the utility

X_1, X_2, \dots, X_n are the attributes of alternatives

$\beta_0, \beta_1, \beta_2, \dots, \beta_n$ are the respective parameters

ε is the random error term

The logit model is used to calculate the likelihood of a specific mode being chosen. This model estimates the likelihood of a commuter choosing a certain mode based on the utility maximization. Probability model is calculated as:

$$p(k) = \frac{e^{U_k}}{\sum_x e^{U_x}} \quad (2)$$

Where,

$p(k)$ is the likelihood of a passenger selecting an option k

U_k is the utility of mode k .

The maximum likelihood technique is used to estimate the variables. According to Kleinbaum and Klein (2000), maximum likelihood is frequently employed to estimate a variable in a straight or quadratic model. [17].

If a sample of N decision-makers is obtained for the purposes of estimation. The probability of person n choosing the alternative that he was actually observed to choose can be expressed as:

$$\prod_i (P_{ni})^{y_{ni}} \quad (3)$$

Where $y_{ni} = 1$ if person n choose i and zero otherwise. It simply gives the probability of the chosen alternative.

Presuming that every selection maker's is unaffected by the choices of others, the likelihood of every individual in the pool picking the option that he was seen to choose is:

$$L(\beta) = \prod_{n=1}^N \prod_i (P_{ni})^{y_{ni}} \quad (4)$$

Where β is a vector containing the model parameters. The log likelihood function is then expressed as:

$$LL(\beta) = \sum_{n=1}^N \sum_i y_{ni} \ln (P_{ni}) \quad (5)$$

This finds β which maximizes the log likelihood value.

Goodness of fit is measured using likelihood ratio index (ρ^2) test. Using discrete choice models, the likelihood ratio index is widely used to determine how much the models match the observations. The likelihood ratio index is calculated as follows:

$$\rho^2 = 1 - \frac{LL(\hat{\beta})}{LL(0)} \quad (6)$$

Where $LL(\hat{\beta})$ is the final value of the log likelihood function while $LL(0)$ represents the value when all the parameters are zero (initial value).

As a result, the metrics have limited utility in evaluating the effectiveness of an estimated model and should be used with precaution although when comparing various parameters' comparative adequacy. Another issue with rho-squared measurements is that they progress regardless of whatever parameter is introduced to the model and how important it is. As a result, a modified rho-squared ratio is used instead of the rho-squared ratio. The adjusted likelihood ratio index is:

$$\bar{\rho}^2 = 1 - \frac{LL(\hat{\beta}) - k}{LL(0)} \quad (7)$$

Where k is the number of degrees of freedom (parameters) used in the model.

Individual parameters are tested and validated using t-statistic approach. The t-statistic function is defined as:

$$t\text{-statistic} = \frac{\hat{\beta}_k - \beta_k^*}{S_k} \quad (8)$$

Where $\hat{\beta}_k$ is the estimate for k^{th} parameter

β_k^* is hypothesized value for the k^{th} parameter

S_k is the standard error of the estimate.

The null hypothesis that the variable is equal to the hypothesized value is rejected when the absolute values of the t-statistic are big enough. Small magnitudes of the t-statistic indicate that the parameter does not contribute greatly to the model's predictive value and should be eliminated.

V. CROSS SECTIONAL ANALYSIS

A cross-sectional analysis was carried out by scrutinizing the gathered data before moving in to the parameter estimation. Fig. 2 shows that 62% of respondents use public transportation (bus + train) and 35% use their own cars for transportation. Here the private vehicle include: car, van, motorbike, bicycle and own three-wheeler while other modes include: office vehicles, walking etc. Based on the usual travel patterns in Kandy, the amount of walking and bicycling is quite low and it also represents in the collected data as well. Considering the purpose of the journey, the duration of the trip, and the degree of income, their likelihood is virtually negligible for distances more than 6 km distance.

Fig. 3 demonstrates that the majority of survey respondents are from low-income households where their monthly income is less than 25,000 LKR. The poll drew less attention from those with higher incomes.

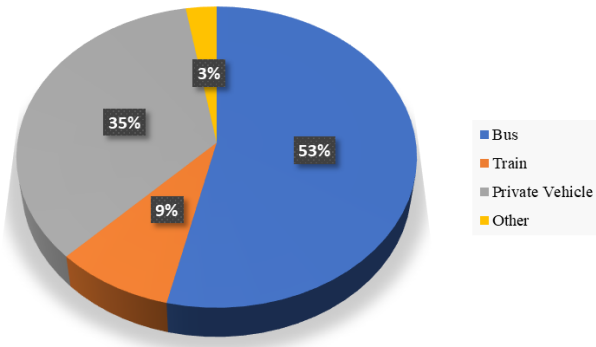


Fig. 2. Number of person trips in different modes

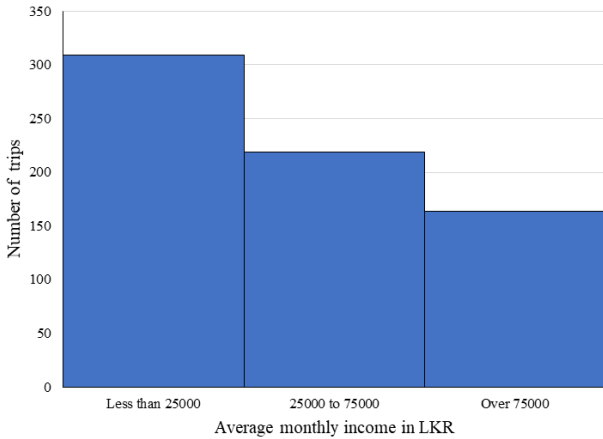


Fig. 3. Average monthly income of the respondents

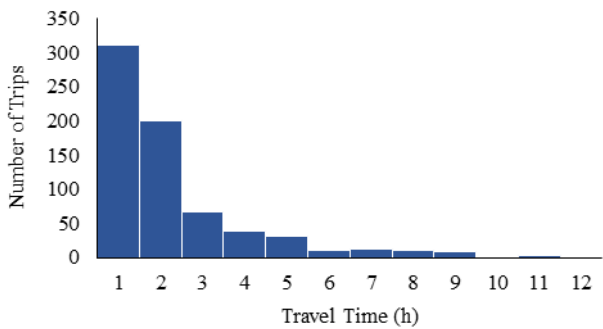


Fig. 4. Histogram of travel time

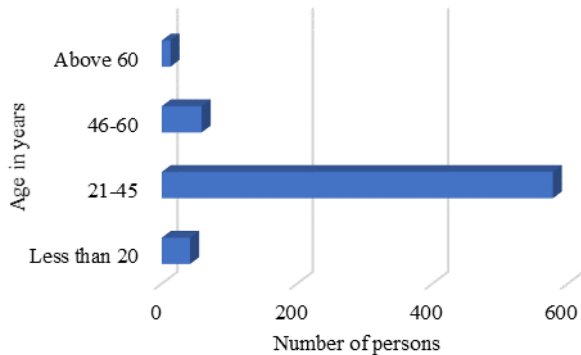


Fig. 5. Age characteristics of commuters

The majority of the trip data as showed in Fig. 4 are clearly short excursions as large percentage of trip data has a journey time of less than one hour. These represents the daily commuters to the city. Fig. 5 shows that the age of the travelers

varies from 14 to 67 years with maximum commuters in the range of 21 to 45 years from the survey.

According to the study, one third of overall visits are undertaken for educational purposes, as illustrated in Fig. 6. Schools, tuitions, and university excursions are all covered educational travels. Kandy is a city having a university with 12,000 students and many city-based schools and tuition classes.

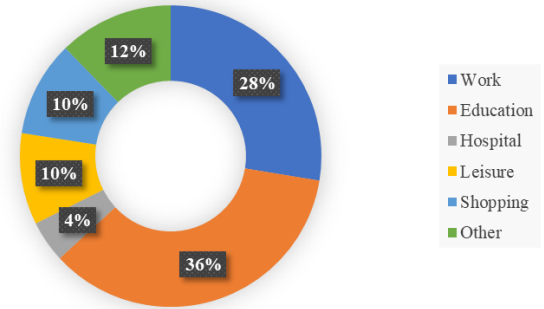


Fig. 6. Trip purposes of the respondents

Work travels, which account for 28% of all trips, are the second most important reason for the trips. Kandy, Sri Lanka's second biggest business city, is home to a number of offices and organizations. As a result, work travels are significant in the region. It is also appealing for leisure outings, shopping trips, and medical visits within the city. In the pie chart, the category other purpose includes home visits from family and friends, funerals and wedding visits, and non-mentioned travel purposes.

Fig. 7 indicates that low-income people are mostly chosen public transport (bus and train) for their traveling while medium income people and high-income people are using their own vehicle regardless of the distance and cost.

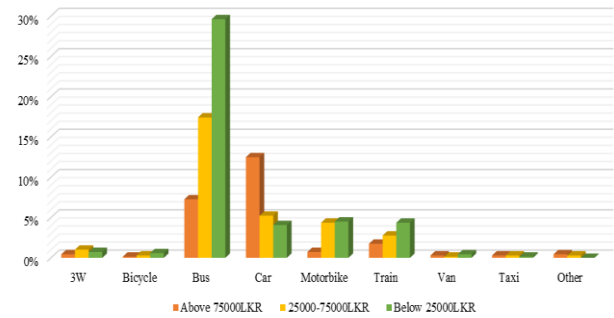


Fig. 7. Mode choice of different level of income people

VI. ESTIMATION RESULTS

The developed model is a discrete choice model for travelers choosing a mode of travel in Kandy from the available alternatives. Table 1 shows the parameter estimation results. The pool was weeded out of surveys with missing responses and inaccurate information. The likelihood ratio index is 0.493 and the adjusted likelihood ratio index is 0.477. Both these indicators show a high goodness of fit with model data and establish the model for estimating parameters. Each parameter's absolute t-value is significant, being more than 1.96 at a 95% significance threshold.

TABLE I. MODEL ESTIMATION RESULTS

	Estimates	t - value
Travel Time	-0.01805	-7.75
Travel Cost	-0.00507	-4.81
Access Time	-0.00110	-4.64
Waiting Time	-0.00066	-4.40
Sample		691
Initial LL		-932.626
Final LL		-472.982
ρ^2		0.493
$\bar{\rho}^2$		0.477

In the constructed model, all significant coefficients have intended signs, indicating proper effect paths. Table 1 displays parameter values, t-values for testing the insignificance hypothesis, the likelihood ratio index, and the adjusted likelihood ratio index. There were substantial parameter estimations and logical signs for all of the variables. It is predicted that the variable trip cost would be negative. Because as the cost of travel for a specific mode rises, the likelihood of choosing that mode decreases. A positive coefficient in the table shows that the elements have a beneficial effect on utilities, implying that the option is more likely to be chosen. The negative sign of variables implies that as the number of factors increases, the likelihood of selecting a mode decreases.

Another major consideration is the expense of travel. People are very conscious about out-of-pocket travel expenses. Commuters are more inclined to choose a low-cost method of transportation in the majority of situations, according to the poll. This is reflected in the parameter estimate findings as well. The fact that the trip cost parameter has a negative sign indicates that when the cost of a specific method rises, individuals are less likely to select that mode.

In addition, the parameters access time and the waiting time are well significant. Both these parameters are highly related with the public transport as private transport is not dealing with either of them. Hence, it is very clear and proved that the authorities should take necessary actions to improve the bus and train frequencies in addition to provide easy access in order to attract travelers towards the public transport.

VII. CONCLUSIONS

The research was conducted based on 691 trips in Kandy that were obtained through an online and face-to-face questionnaire. According to the poll, commuters are well-versed on the various modes of transportation and their features, such as expense and trip time. According to the findings, low-income persons are more likely to use public transportation than middle- and high-income people. Kandy is attracting more visitors for educational and business purposes. It also has some appeal for leisure excursions. MNL model was used to estimate the parameters using utility maximization theory in RStudio platform. Travel time, travel cost, waiting time, and access time are estimated as parameters and found that all are significant. The sign showed negative as expected, indicating the likelihood of choosing that particular mode is decreased, when those factors are increased. Accordingly, it is recommended for authorities to take

necessary actions with respect to those parameters, in order to improve the public transportation in the city. Few such suggestions are increase bus and train frequencies, provide easy access to their terminals, and improve the travel time. With these findings, an effective elasticity analysis can be performed to forecast commuter decision behavior in the event of a transportation system change and that will be our next step.

REFERENCES

- [1] F. S. Koppelman and C. Bhat, "A Self Instructing Course in Mode Choice Modeling: Multinomial and Nested Logit Models," *Elements*, 2006.
- [2] F. I. Rahman and I. Consultant, "Analysis of Mode Choice Behavior and Value of Time in Dhaka City, Bangladesh," *Int. J. Traffic Transp. Eng.*, vol. 10, no. 2, pp. 138–152, 2020, doi: 10.7708/ijtte.2020.10(2).02.
- [3] L. Ding and N. Zhang, "A Travel Mode Choice Model Using Individual Grouping Based on Cluster Analysis," *Procedia Eng.*, vol. 137, pp. 786–795, 2016, doi: 10.1016/j.proeng.2016.01.317.
- [4] O. Chiu Chuen, M. R. Karim, and S. Yusoff, "Mode choice between private and public transport in Klang Valley, Malaysia," *Sci. World J.*, vol. 2014, no. Figure 1, pp. 7–9, 2014, doi: 10.1155/2014/394587.
- [5] M. J. Demetsky and V. C. Tatineni, "Supply Chain Models for Freight Transportation Planning," *Cent. Transp. Stud. Univ. Virginia*, 2005.
- [6] N. Zenina and A. Borisov, "Transportation Mode Choice Analysis Based on Classification Methods," *Sci. J. Riga Tech. Univ. Comput. Sci.*, vol. 45, no. 1, pp. 49–53, 2012, doi: 10.2478/v10143-011-0041-2.
- [7] M. Elharoun, U. E. Shahdah, and S. M. El-Badawy, "Developing a mode choice model for mansoura city in Egypt," *Int. J. Traffic Transp. Eng.*, 2018, doi: 10.7708/ijtte.2018.8(4).10.
- [8] R. CHANDA, S. SEN, and S. KUMAR, "Mode Choice Modelling of Work Trips A Case Study of Kolkata Urban Transportation Planning," no. December, pp. 41–45, 2016, doi: 10.15224/978-1-63248-114-6-20.
- [9] D. Pavlyuk and V. Gromule, "Application of a discrete choice model to analysis of preferred transport mode for Riga-Daugavpils route," *Transp. Telecommun.*, vol. 12, no. 1, pp. 40–49, 2011.
- [10] E. Almasri and S. Alraee, "Factors Affecting Mode Choice of Work Trips in Developing Cities—Gaza as a Case Study," *J. Transp. Technol.*, 2013, doi: 10.4236/jts.2013.34026.
- [11] S. Müller, S. Tscharktschiew, and K. Haase, "Travel-to-school mode choice modelling and patterns of school choice in urban areas," *J. Transp. Geogr.*, 2008, doi: 10.1016/j.jtrangeo.2007.12.004.
- [12] H. M. Al-Ahmadi, "Development of intercity work mode choice model for Saudi Arabia," 2007, doi: 10.2495/UT070641.
- [13] S. Pulugurta, A. Arun, and M. Errampalli, "Use of Artificial Intelligence for Mode Choice Analysis and Comparison with Traditional Multinomial Logit Model," *Procedia - Soc. Behav. Sci.*, vol. 104, pp. 583–592, Dec. 2013, doi: 10.1016/J.SBSPRO.2013.11.152.
- [14] K. Mizutani and T. Akiyama, "Construction of modal choice model with a descriptive utility function using fuzzy reasoning," *Annu. Conf. North Am. Fuzzy Inf. Process. Soc. - NAFIPS*, vol. 2, pp. 852–856, 2001, doi: 10.1109/NAFIPS.2001.944715.
- [15] D. Teodorovič and K. Vukadinovič, "Generating and Tuning the Fuzzy Logic Systems Developed in Transportation Applications," pp. 303–365, 1998, doi: 10.1007/978-94-011-4403-2_5.
- [16] "Kandy District Information." https://www.aidscontrol.gov.lk/index.php?option=com_content&view=article&id=35&Itemid=172&lang=en (accessed Aug. 03, 2021).
- [17] A. Efendi and H. W. Ramadhan, "Parameter estimation of multinomial logistic regression model using least absolute shrinkage and selection operator (LASSO)," *AIP Conf. Proc.*, vol. 2021, no. 2016, pp. 1–6, 2018, doi: 10.1063/1.5062766.

A Comparative Study of ADT Estimation Models Developed for Sri Lankan Road Network

R.D.N.D. Kumari
Department of Civil Engineering,
University of Peradeniya, Peradeniya,
Sri Lanka
nupamadulmini@gmail.com

P.M. Jayarathna
Department of Civil Engineering,
University of Peradeniya, Peradeniya,
Sri Lanka
prasadmadranga81@gmail.com

W.R.S.S. Dharmarathna
Department of Civil Engineering,
University of Peradeniya, Peradeniya,
Sri Lanka
samal@eng.pdn.ac.lk

I.M.S. Sathyaprasad
Department of Civil Engineering,
University of Peradeniya, Peradeniya,
Sri Lanka
imssatya@gmail.com

Abstract - Average Daily Traffic (ADT) data are mostly used in transportation engineering for the purpose of planning and designing roads, pavement capacity designing, prioritizing road maintenance investments, accident studies, etc. In conceptual planning stage, it is sufficient to use estimated ADTs obtained from a model, which saves time and cost. ADT estimation models have been developed using different methods such as regression analysis, and neural networks. This paper aims to make a comparison between three recently developed models to estimate the ADT at any location of the class-A road network in Sri Lanka. These models assume that the ADT at a specific location is contributed by local traffic, regional traffic, and inter-district traffic across the measurement location. The first model considered has been developed based on the travel distance and incorporated six input variables. The model parameters have calibrated through regression analysis. The second model considered is based on the travel time, and calibrated using the regression analysis method. It was identified that at some locations the estimated ADT is distorted because of the presence of expressways and important class-B links which facilitate inter-district traffic. Therefore, the model is further developed, incorporating important class-B road links, AB road links, and expressways to the link node system. A generalized cost function, representing the travel time, distance, and toll cost, is used instead of travel distance which has resulted in an improved Network Connectivity Factor through the revised link node system. The paper presents a comparison of the pros and cons of each ADT estimation model and recommends the most appropriate model for different conditions.

Keywords — ADT estimation, regression analysis, neural networks, origin-destination data, generalized cost function

I. INTRODUCTION

Identification of traffic flow characteristics and their behavior is much important in transportation planning and traffic engineering. ADT is referred to the total traffic volume within 24 hours at a selected section of a highway and it is considered as a main parameter for analyzing traffic flow behavior. ADT data is important in developing road infrastructures, designing pavements, bridges and other highway facilities, improving roadway conditions and roadway safety. Further, it can be used as an indicator of pollution level and accident rates. ADT is affected by many factors such as, relative location and the size of the urban centers, nature and the function of the road, regional economy and urban development. ADT can be

measured either manually or mechanically. Manual methods incur large man power and time while mechanical methods incur high cost. Therefore, for the conceptual designs it is useful to take an estimated ADT value from an ADT estimation method which takes low cost, low time and no man power. Another advantage of an ADT estimation model is that its capability of predicting ADT at any given unobserved location.

Following methods are usually practiced for developing ADT estimation models;

1. Ratio/Expansion factor method
2. Regression analysis method
3. Neural network method

This paper compares three models that have developed using regression analysis method. The method is acceptable compared to the expansion factor method. Further, the use of statistical knowledge is also less than that of the neural network method. Regression analysis is a reliable method of identifying which variables have impact on a topic of interest. The process of performing a regression allows to confidently determine the factors that most significant, their influence on each other and factors need to be ignored.

The paper makes an attempt to compare a current study by the authors with two previous models. The previous models only consider the class-A road network in their studies while the current study considered the class-A road network, important class-B roads and available expressways. Important class-B links were selected considering the ADT values of that particular links and local knowledge.

II. LITERATURE REVIEW

ADT estimation models play a crucial role in current conceptual traffic planning works as their results are easily obtainable in addition to the effortless data accessibility, least cost and reliability. Generalized cost function is used by many researchers in order to find the shortest path between given any origin and destination. Reference [1] considered emission factors length, travel time and travel time fluctuation of

respective road segment in order to construct a generalized cost function. Each weight of the generalized cost function was determined by using a stated preferences survey. Two variables as travel time cost and fuel consumption have used in travel cost estimation.

An attempt to compare different AADT forecasting techniques was found in [2]. Accordingly, linear regression, multiple regression, Idaho (USA) method, and growth factor method have used to find the best method. Maximum absolute error and average absolute error were used to compare the methods among each other.

Number of lanes, regional accessibility to employment, population and employment in the buffer zone of a counting station, and direct access to expressways have identified as input variables [3]. Influence of regional economic activities on road traffic has reflected through the regional accessibility to employment centers. Population and employment were calculated in order to account the effects of local land use developments on AADT.

AADT has estimated using non-linear regression and used to estimate intersection performance across Kentucky state in United States. Results of the study indicated that the estimates generated can be effectively used for safety assessment and countermeasure prioritization [4]. A new approach was made based on the FHWA method in order to estimate the ADDT for truck vehicles and introduced mechanisms to deal with the vagueness of boundaries between individual road groups and adopts measures of uncertainty to solve the difficulties of identifying the group which matches the given road section [5]. Another AADT estimation was found in [6] where they introduced a feasible systematic methodology for generating nationwide AADTs, their distribution, and the associated emissions by integrating existing census data, geographical data, traffic counter data, vehicle fleet data and emission factors in Dublin.

III. METHODOLOGY

The current study by the authors compares the Network Connectivity Factor (NCF) based on travel time, travel distance and the generalized travel cost to identify the most effective stable parameter for estimating ADT for different types of road classes and locations. The total traffic volume through a location consists of the following three types of traffic components;

- Local traffic component (urban trips due to local urbanization effect)
- Regional traffic (intra-district trips due to regional urbanization effect)
- National level traffic (inter-district trips represented by NCF)

In a study by the authors (the third model of the comparison) above three types of traffic components were represented by

six input variables similar to [7]. Build-up areas of two cities (A1, A2) to the either side of the location measured in km² and the distances to each city center from the counting location (d1, d2) measured in km were used to represent the local traffic which occurs due to the urbanization effect. These four variables were collected through the Google maps. The district population densities (person/sq.km) were extracted from the census of population and housing 2012, by the Department of Census and Statistics, Sri Lanka and applied a growth rate [8] in order to represent the regional traffic. It is based on the assumption that the population density of a district is an indicator of its urbanization and the regional trips. The national level traffic was represented by the NCF.

The NCF mainly indicate the total number of inter district trips through a given location. The study [7] calculated the NCF based on travel distance by assuming all the trip paths follow the shortest path based on the distance. In the study of [9], assumed all the trip paths follow the quickest path which take lesser time to reach their destination and have calculated the NCF based on travel time. Both above works have used the following schematic diagram of Sri Lankan road network which contents 51 nodes and 79 links.

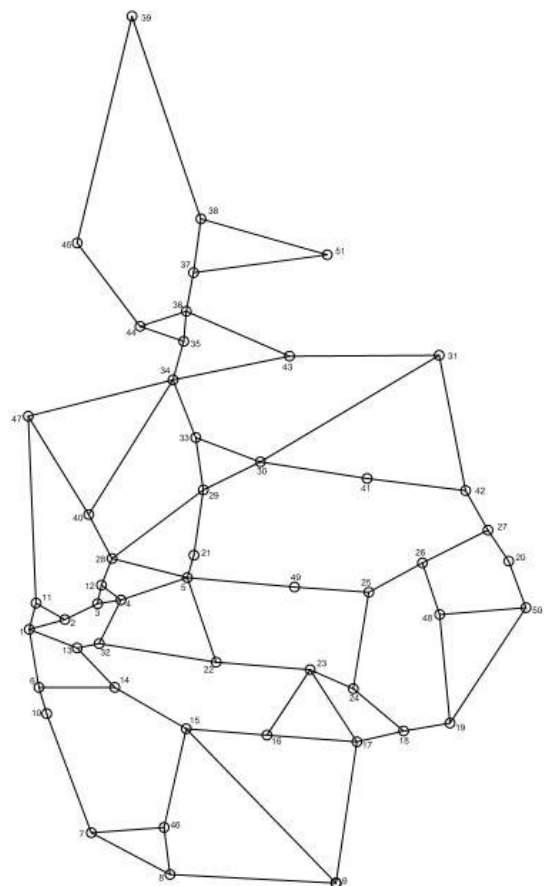


Fig. 3.1. Schematic diagram of class-A road network [9]

We improved the schematic diagram shown in Figure 3.1 by adding important class-B links and expressways. Figure 3.2 shows the modified schematic diagram of Sri Lankan road network. It includes 96 nodes and 162 links. The study

focused on the behavior of route choice based on generalized cost path and calculated NCF assuming all the trips follow route estimated through the lowest generalized cost. Generalized cost was calculated by using, travel time, travel distance and the travel cost (toll cost).

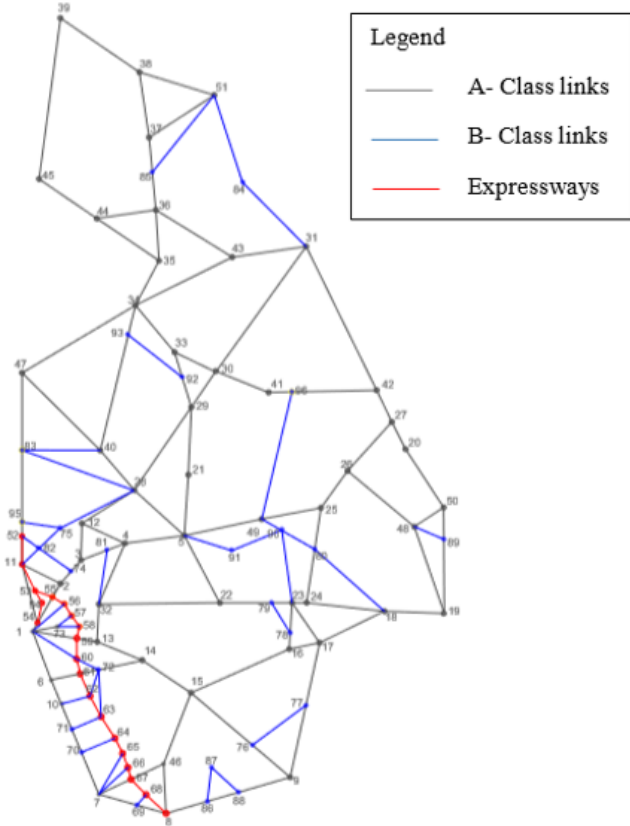


Fig. 3.2. Schematic diagram of road network with class-B links and expressways

It is assumed that the total inter district trips follow the shortest, quickest or the lowest generalized cost path. For each origins and the destinations, the best route was found by applying Dijkstra's Algorithm [10] in python platform. After identifying the best route, NCF was calculated using equation 1 shown below. Trips were assigned using all-or-nothing assignment and the inter-district trip volume through a given road link is compared by summing up the shortest/quickest or lowest generalized cost trips that go through the given road link.

$$NCF_{pq} = k \sum_j \sum_i \left(\frac{P_i * P_j}{t_{ij}^2} \right) C_{ijl} \dots (1)$$

Where,

- NCF_{pq} = Network connectivity factor of pq link
- P_i, P_j = Population densities of districts i and j
- t_{ij} = Travel time/ Travel distance/ Generalized cost between p and q
- k = Number of quickest/shortest/lowest generalized cost paths going through the pq link
- $C_{ijl} = 1$ if i-j shortest path/quickest path/cheapest path goes across link 'l'

- $C_{ijl}=0$ if i-j shortest path/quickest path/cheapest path does not go across 'l'

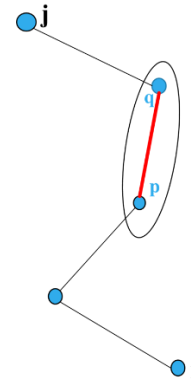


Fig. 3.3. Path from i to j goes through the link l

After finding all six variables, regression analysis was done using Minitab statistical software in order to estimate model parameters.

The first study of the comparison [7] that has developed based on the travel distance is;

$$ADT = 4561 + 284 A1 - 111.1 d1 + 1637 A2 - 104.1 d2 + 4.118 DP + 2147 \ln(NCF) \dots (2)$$

The second study of the comparison [9] that has developed on the travel time is;

$$ADT = 5081 + 3.264 * DPD + 894 * A2 - 151.4 * d1 - 170.3 * d2 + 2528 * \ln(NCF) \dots (3)$$

The third study of the comparison, which is referred as the study of the authors that developed based on the generalized cost [11].

$$ADT = 8303 + 1581 \ln(A1) + 2185 \ln(A2) - 69.3D1 - 169.6D2 + 5.260DPD + 239.6NCF \dots (4)$$

ADT - Average Daily Traffic

D1 - Longest distance from counting location

D2 - Opposite distance from counting location

A1 - Buildup area of the city that belongs to longest

distance (D1)

A2 - Buildup area of the city that belongs to opposite

distance (D2)

DPD - District population density of the district in which measurement station is located

NCF - Network Connectivity Factor of the link on which the measurement station is located

Common links for all three networks were extracted and compared the statistical parameters of the models to identify the most suitable model to estimate the ADT at a given location in the Sri Lankan road network.

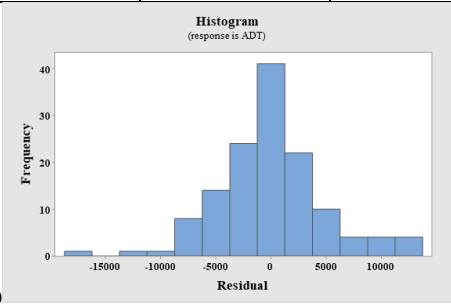
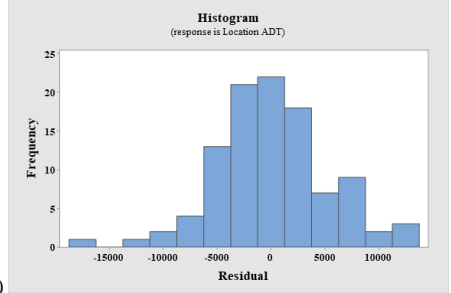
IV. RESULTS AND DISCUSSION

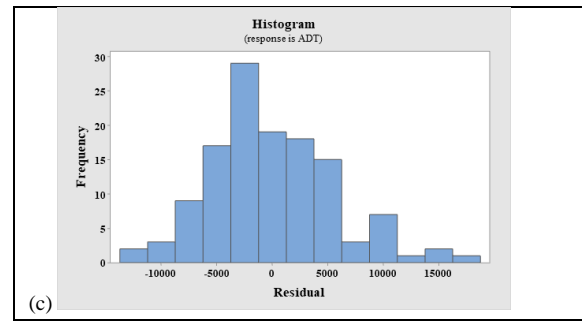
Using backward elimination method, the software detects p-value and removes the insignificant independent variables. Accordingly, A1 was identified as an insignificant variable in [9]. Therefore, it does not include in their respective ADT model. But A1 includes in the ADT model which was introduced by [7]. It is clear that significance of A1 in the ADT model varies with the NCF. In our case, [11] all input variables are significant. Different link-node system is used in the current study in comparison with the recent past models [9] & [7].

Comparison 01

It is difficult to compare three researches directly. Thus, 75 common locations which can be used to predict ADT by using all three models were selected for the model comparison.

TABLE I. COMPARISON OF THREE REGRESSION MODELS

Results of ADT model with NCF based on distance (a) [7]	Results of ADT model with NCF based on travel time (b) [9]	Results of ADT model with NCF based on generalized cost (c) [11]
$ADT = 4561 + 284 A1 - 111.1 d1 + 1637 A2 - 104.1 d2 + 4.118 DPD + 2147 \ln(NCF)$	$ADT = 5081 + 3.264 DPD + 894 A2 - 151.4 d1 - 170.3 d2 + 2528 \ln(NCF)$	$ADT = 8303 + 1581 \ln(A1) + 2185 \ln(A2) - 69.3 D1 - 169.2 D2 + 5.262 DPD + 239.6 NCF$
R-square =0.58	R-square = 0.61	R-square = 0.65
PBIAS = 9.592075%	PBIAS = 4.425623%	PBIAS = -0.76461%
		
		



In 1st comparison, R-square value was observed as 0.65 in the current study by the authors [11]. It is better than 0.61 and 0.58, which were observed in the previous models [9] and [7] respectively. In addition, percentage BIAS has a very less value in the current analysis. Hence, it is neither under estimating nor over estimating.

Histograms are used to display numeric data. Data should be symmetric in histograms. In the present model [11], there is no outliers in comparison with the other two models.

Comparison 02

In this case R square values are nearly same. Therefore, above 75 links were separated in to three ranges based on the road length of class – A roads.

Range 1 - 0 km to 120 km

Range 2 - 120 km to 300 km

Range 3 - 300 km to 440 km

There are 27 links in range 01, 26 links in range 02 and 22 links in range 03.

According to above ranges regression analysis was done for the all three models. The respective R square and Percentage BIAS values are tabled in Table II.

TABLE II. RANGE BASED REGRESSION MODEL

		Range 1	Range 2	Range 3
Based on distance model (a)	R square	0.6317	0.4802	0.599115
	PBIAS	8.822213	7.952831	10.24271
Based on travel time model (b)	R square	0.6937	0.2658	0.687199
	PBIAS	7.656306	5.537683	-1.60276
Based on generalized cost function model (c)	R square	0.8528	0.3329	0.5451
	PBIAS	5.016416	-0.86626	-2.54732

- For the range 01 (0 – 120 km) model (c) has higher R square value and lower PBIAS value.
- For the range 02 (120 km – 300 km) model (a) has higher R square value and lower PBIAS value.
- For the range 03 (300 km – 440 km) model (b) has higher R square value and lower PBIAS value.

V. CONCLUSION

In comparison 01, regression analysis based on the generalized cost function has higher R square value, lower PBIAS value and no outliers. Based on the aforementioned facts, NCF based on generalized cost can be recommended as the most stable parameter for estimation of ADT. Furthermore, the schematic diagram of road network was created by including important Class-B links and expressways. Accordingly, if a user wants to find ADT at a given location on a Class-B link or on an expressway, the best model is model c which is developed based on generalized cost function.

If a user wants to find ADT at a given location on Class-A road, the best model can be selected using PBIAS values and R square values, based on the second comparison. As a result of that, suitable model for the A-class roads is chosen according to separated ranges.

1. For the range 01 (0 – 120 km), the best model is model c (regression analysis based on generalized cost function)
2. For the range 02 (120 – 300 km), the best model is model a (regression analysis based on distance).
3. For the range 03 (300 – 440 km) best model is model b. (regression analysis based on travel time).

VI. RECOMMENDATION FOR FUTURE DEVELOPMENT

This paper compares three models as two previous models and a current study by the authors. Two previous models have used only class-A road network while the current study by the authors considered class-A roads, important Class-B road links and expressway links.

The intensity the economic development of a city has been considered as represented by the two-dimensional spatial built-up area for the A1 and A2 in the all three studies. However, as the trip attractiveness of a city is better represented by the multi-storied development in urban areas with an appropriate weightage factor to accommodate the vertical development would be more accurate.

ACKNOWLEDGEMENT

Our sincere thanks go to the Road Development Authority for their assistance in collecting traffic data. We shall also acknowledge previous researchers for providing information about respective studies.

REFERENCES

- [1] F. Yu-qin, L. Jun-qiang, G.-e. X. and Y. H. He, "Route choice model considering generalized travel cost based on game theory," Hindawi Publishing Corporation Mathematical Problems in Engineering, vol. 2013, no. 5, 2013.
- [2] T. Sliupas, "Annual average Daily Traffic Forecasting using different techniques," Transport, pp. 38-43, 2006.
- [3] F. Zhao and N. Park, "Using Geographically Weighted Regression Models to Estimate Annual Average Daily Traffic," Journal of the Transportation Research Board, p. 99–107, 2004.
- [4] Staats, William Nicholas, "Estimation of annual average daily traffic on local roads in kentucky," Theses and Dissertations--Civil Engineering. 36, 2016.
- [5] R. Rossi, M. Gastaldi, G. Gecchele, S. Kikuchi, "Estimation of Annual Average Daily Truck T Traffic Volume. Uncertainty treatment and data collection requirements," 15th meeting of the EURO Working Group on Transportation, Procedia - Social and Behavioral Sciences 54(845 – 856), 2012.
- [6] Miao Fu, J. Andrew Kelly, J. Peter Clinch, "Estimating annual average daily traffic and transport emissions for a national road network: A bottom-up methodology for both nationally-aggregated and spatially-disaggregated results", Journal of Transport Geography 58 (186–195), 2017.
- [7] B. Balasooriya, A. Wijekoon and I. Sathyaprasad, "Estimation of average daily traffic based on urbanization effect and network connectivity," ICSECM2017-151, 2017.
- [8] Department of Census and Statistics Sri Lanka, "Census of population and Housing," 2012.
- [9] M. Hafza, W. Jayathilaka and I. Sathyaprasad, "A comparative study travel time and distance in the estimation of inter district trips," ICSBE1018-492, 2018.
- [10] E. Dijkstra, "A Note on problem in connexion with graphs," Numerische Mathematics 1, pp. 269-271, 1959.
- [11] R.D.N.D Kumari , P.M. Jayarathne , W.R.S.S. Dharmarathna , I.M.S. Sathyaprasad, "Improvement of an adt estimation model developed for a-class roads in sri lanka by incorporating national expressways and important b-class links," ICSBE2020-026,2020

Mix Design and Pavement Analysis of Thin Surfaced Asphalt Pavements for Low Volume Roads

J. Arjoon Moses
Department of Civil Engineering
University of Moratuwa
Colombo, Sri Lanka.
150408f@uom.lk

W.K. Mamppearachchi
Department of Civil Engineering
University of Moratuwa
Colombo, Sri Lanka.
wasanthak@civil.mrt.ac.lk

Abstract— Low-volume roads (LVR) are the beginning of the world’s economy and the lifelines of rural communities. As more than 65% of the road network consists of rural LVR in Sri Lanka which are mostly unpaved gravel roads, the rural communities and tourism are adversely affected. Even the traditional asphalt (TA) pavements are long-lasting, they are not recommended for LVR as TA pavements are over-designed and not financially feasible. So, “Thin Surfaced Asphalt (TSA) Pavements” are suggested for LVR as they hold longer life and less cost; but there are no proper mix design guidelines in Sri Lanka. Therefore, this research is focused on developing mix design guidelines and pavement analysis for TSA pavements. Marshall samples were prepared for dense graded (DG) asphalt concrete of 7 mm and 10 mm nominal maximum size aggregates (NMSA) and, the properties of both types (DG-7 & DG-10) of specimens were concluded to fulfill the required criteria and the optimum bitumen contents were defined. With the defined parameters, the properties of materials were determined, and mechanistic pavement analysis was carried out using computer software for a selected road (0.11 million CNSA) of Kurunegala i-Road project. Pavement analysis determined that the 20 mm of DG-7 and 25 mm of DG-10 layers have adequate structural thicknesses. From the cost comparison, the DG-7 and DG-10 pavements were found to reduce the material cost for the asphalt layer by 48.69% and 39.29% respectively when compared with TA pavements. Thus, TSA pavements are found to be more suitable for LVR.

Keywords—Low volume roads; Traditional asphalt pavements; Thin surfaced asphalt pavements; Dense graded asphalt concrete; Mechanistic pavement analysis

I. INTRODUCTION

Low volume roads (LVR) can be defined as the roads with annual average daily traffic (AADT) of 1000 vehicles per day or less than that [1]. Roads contribute to the economy especially by facilitating transportation and tourism sectors and, the total contribution to gross domestic products (GDP) from these two sectors was 11.4% for the year 2016 according to the report of World Travel & Tourism Council [2]. The impact from LVR is significant for the GDP of Sri Lanka because more than 64000 km (approximately 65%) of the road network are LVR [3]. Therefore, it is vital to provide better surfacing for LVR even though they consist lesser volume of vehicles and the majority of them are light vehicles.

Currently, the LVR are over-designed in Sri Lanka as they are constructed with traditional asphalt (TA) pavements (an asphalt layer thickness of 50 mm or higher) since the pavement designing is based on empirical codes “Overseas Road Note 31” [4] or “AASHTO Green Book” [5] which were published several decades ago. As a result, the expense on roads is about 700 billion rupees from 2015 to 2018 [6] which

is a considerable amount of money for a country like Sri Lanka which usually incurs a deficit budget. Actually, the LVR do not need a higher thickness of the asphalt layer since they consist of low traffic; thus, thin surfaced asphalt (TSA) pavements are recommended. Unfortunately, our country does not have proper mix design guidelines for TSA pavements, and the codes of other countries cannot be directly applicable due to the different testing methods, materials used, climatic and environmental conditions. Therefore, mix design development and investigation on the suitability of TSA pavements (structurally and financially) were the two main focuses of this study.

II. LITERATURE REVIEW

A. Thin Surfaced Asphalt (TSA) Pavements

The TSA pavements are found to be satisfactory for LVR with recently done researches; especially, the design executed in the view of the non-linear behaviour of unbound granular material for TSA pavements (thickness less than 40 mm) [7]. Also, the durability of TSA (AC-TL) pavements for secondary roads (LVR) was concluded to be the same as TA (AC) pavements [8] as shown in Fig. 1. The Austroads guidelines [9] recommend TSA pavements over TA pavements for rural roads (LVR) with CNSA ≤ 1 million as presented in TABLE II.

Even though many countries are pioneers in TSA pavements, the codes of Australia and New Zealand were chosen due to the close trend of climatic conditions when compared with Sri Lanka [10] as illustrated in Fig. 2. The Marshall design criteria are given in TABLE I for DG 7, DG 10, and WCT 2 (Wearing Course Type 2 – Sri Lanka [11]). Dense graded (DG) asphalt mixtures with nominal maximum size aggregates (NMSA) of 7 mm and 10 mm were chosen for the study as they do not require any modified or special materials and, the minimum paving thicknesses of those types (DG 7, DG 10) are 20 mm and 25 mm respectively according to Australian specifications [12].

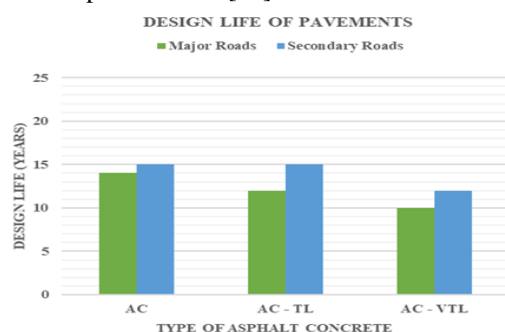


Fig. 1. Design life of pavements

TABLE I. DESIGN REQUIREMENT OF MARSHALL PROPERTIES

	NZ / AUS		SL
	DG 7	DG 10	WCT2
Stability (kN)	6.5	6.5	5.34
Flow (0.25 mm Units)	8 to 18	8 to 18	8 to 18
Voids in Mineral Aggregates (For 4% Design Air voids)	16	15	13
Air voids %	3 to 5	3 to 5	3 to 5

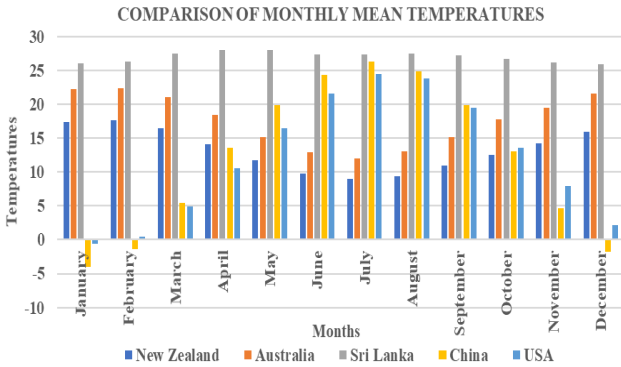


Fig. 2. Comparison of monthly mean temperatures

TABLE II. SUITABILITY OF PAVEMENT TYPES FOR RURAL ROADS

Road Class		1	2	3	4	5
Design Traffic (ESAs)		$10^6 - 10^8$	$10^6 - 10^7$	$10^5 - 10^6$	$10^4 - 10^5$	$< 10^4$
Pavement Type	Granular/ Thin Asphalt	✓b	✓b	✓	✓	✓
	Granular/ Thick Asphalt	✓	✓	✓	✗	✗
	Full Depth Asphalt	✓✓	✓✓	✗	✗	✗
	Concrete	✓✓	✓	✗	✗	✗
	Concrete Segmental Pavers	✗	✗	✗	✗	✓

symbols in TABLE II represent:

- ✓✓ Most Suitable
- ✓ Adequate Performance
- ✗ Not Recommended
- b: Can be used successfully in this road class but very good quality control of materials and construction processes with good maintenance are required.

B. Pavement Analysis – Mechanistic Approach

The mechanistic analysis was carried out using “Circlly 7.0” software. Fatigue of asphalt concrete and rutting of subgrade were examined using the (1) and (2) respectively.

$$N = \frac{SF}{RF} \left(\frac{6918 \times (0.856 V_b + 1.08)}{E^{0.36} \times \mu \epsilon} \right)^5 \quad (1)$$

Where,

- N – Allowable number of repetitions of the standard axle
- $\mu \epsilon$ – Load-induced horizontal tensile strain at the base of the asphalt (microstrain)
- V_b – Percentage of bitumen by volume in asphalt (%)
- E – Asphalt modulus (MPa)
- SF – Shift factor between laboratory and in-service fatigue lives
- RF – Reliability factor for asphalt fatigue

$$N = \left(\frac{9150}{\mu \epsilon} \right)^7 \quad (2)$$

Where,

- N – The allowable number repetition of standard axle
- $\mu \epsilon$ – The vertical compressive strain developed under a standard axle at the top of the subgrade

The resilient modulus values of subgrade, subbase, and base course were determined using (3) which was provided by the U.K. Transportation Research laboratories [13]. Dynamic modulus of asphalt concrete was determined using (4) which was established by Witczak and Fonseca [14]. The effects of pavement temperature, the viscosity of bitumen, and vehicle speed (or loading frequency) were concerned and the resilient modulus was derived using the relationship between resilient modulus and dynamic modulus which was established by Xiao [15].

$$M_R = 2555 \times (CBR)^{0.64} \quad (3)$$

- Where, M_R – Resilient modulus (psi)
- CBR – California bearing ratio

$$\begin{aligned} \log E = & -0.261 + 0.008225 p_{200} - 0.00000101 (p_{200})^2 + 0.00196 p_4 - \\ & 0.03157 V_a - 0.415 \frac{V_{beff}}{V_{beff} + V_a} + \\ & \frac{(1.87 + 0.002808 p_4 + 0.0000404 p_{38} - 0.0001786 (p_{38})^2 + 0.0164 p_{34})}{1 + e^{(-0.716 \log f - 0.7425 \log \eta)}} \end{aligned} \quad (4)$$

Where,

- E – Dynamic modulus of asphalt mix in psi
- η – Bitumen viscosity in 10^6 poise
- f – Loading frequency
- V_a – Percent air voids in the mix by volume
- V_{beff} – Percent effective bitumen content by volume
- P_{34} – Percent retained on 19 mm sieve, by total agg. weight
- P_{38} – Percent retained on 9.5 mm sieve, by total agg. weight
- P_4 – Percent retained on 4.76 mm sieve, by total agg. weight
- P_{200} – Percent passing 0.075 mm sieve, by total agg. Weight (Here, agg. Means aggregates)

Here, the average heavy vehicle speed (one of the parameters which defines the loading frequency) was selected as 30 kmph even though 60 kmph was recommended in Austroads; as it gives a conservative design and represents the actual condition of Sri Lanka. The Poisson’s ratio was selected as 0.40 for both types of asphalt concrete layer (DG 7 and DG 10) according to ‘Guide to Pavement Technology – Part 2’ of Australia [16] while relevant values for granular layers were obtained from the journal paper published by Xu [17].

III. RESEARCH METHODOLOGY

The methodology consists of the following steps:

- The aggregates gradation was determined, and properties of aggregates were examined.
- After testing the properties of bitumen, the Marshall samples were prepared for each type of asphalt mixture. The optimum bitumen content was established by investigating the Marshall properties.
- With the determined optimum bitumen content, the allowable minimum layer thicknesses of asphalt concrete for the selected LVR were defined (by analyzing LVR with (0.11 – 0.2 million CNSA) using computer software “Circlly 7.0”).
- Finally, the cost comparison was performed between the original design for selected the LVR and the proposed design with the thin surfaced asphalt (TSA) layer.
- The decision was taken whether to adopt TSA pavements for LVR of Sri Lanka with considerations on the durability and financial viability.

IV. EXPERIMENTAL STUDY

A. Tests on Aggregates

The specific gravities and absorptions of coarse aggregates (2600 g aggregates retained on 4.75 mm sieve selected as per the proportion of gradation of sizes) and fine aggregates (1100 g aggregates passing on 4.75 mm sieve selected as per the proportion of gradation of sizes) were determined as per “ASTM C 128 – 68” and “ASTM C 127 - 68” respectively. The results are presented in TABLE III and TABLE IV.

The aggregates’ gradation was derived after the examination of the specifications of Australia and New Zealand and, it is presented in TABLE V.

B. Tests on Bitumen

Even though bitumen 80/100 was recommended in New Zealand specifications for TSA pavements [18], this study was done using bitumen 60/70 as it holds a higher softening point; thus, suitable for Sri Lanka (tropical country) [19] because the pavement temperatures are higher (approximately 55°C).

The viscosity of bitumen was determined at 135°C and 160°C [20] for plotting graph shown in Fig. 3 and then the standard temperatures on which the bitumen has a viscosity of 170±20 cSt and 280±20 cSt were selected for mixing and compaction of Marshall sample correspondingly (given in TABLE VI).

TABLE III. PROPERTIES OF COARSE AGGREGATES

Properties of Coarse Aggregates	DG 7	DG 10
Bulk specific gravity	2.701	2.719
Apparent specific gravity	2.753	2.751
Absorption %	0.699	0.433

TABLE IV. PROPERTIES OF FINE AGGREGATES

Properties of Fine Aggregates	DG 7	DG 10
Bulk specific gravity	2.589	2.57
Apparent specific gravity	2.779	2.716
Absorption %	2.648	2.079

TABLE V. SELECTED GRADATION OF AGGREGATES

Size (mm)	DG 7 (% PASSING)	DG 10 (% PASSING)
12.5	-	100
9.5	100	79-100
6.3	80-100	68-87
4.75	70-87	50-76
2.36	44-75	32-61
1.18	29-60	22-48
0.6	19-47	15-36
0.3	12-33	10-26
0.15	8-22	6-17
0.075	5-12	4-11

TABLE VI. VISCOSITY OF BITUMEN

Temperature (°C)	Viscosity (cSt)
135	425.9
160	156.3

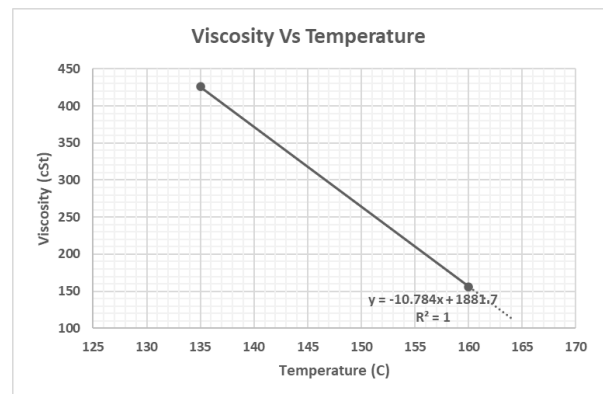


Fig. 3. Viscosity of bitumen vs temperature

C. Preparation of Marshall Samples

Oven-dried – sieved aggregates and bitumen were kept in the oven until they came to 160°C of stable temperature and then the aggregates were mixed with 6 different amounts of bitumen while holding the temperature in the range of 156.9°C to 160.6°C for mixing. After mixing thoroughly with a bench mounting asphalt mixer, the mixed sample was placed in a mould and compacted by giving 50 blows per side using a manual Marshall compactor while maintaining the temperature not less than 135°C. (Even the standard compaction temperature was determined as 146.7°C to 150.4°C, the compaction temperature maintained not less than 135°C because of the difficulties in controlling the temperature). Three samples were prepared for each bitumen content; thus, a total number of more than 36 samples were prepared for both types of asphalt concrete DG 7 and DG 10.

D. Determination of Maximum Theoretical Specific Gravity

1800 g of oven-dried aggregates were mixed with 6% of bitumen within the temperature range from 157°C to 160°C and, after cooling to 25±1°C the maximum theoretical specific gravity test was performed as per ASTM D2041 – 03a [21]. The results are stated in TABLE VII.

E. Testing Marshall Properties

The Marshall properties were tested as per ASTM D6927 – 15 [22]. The results of DG 7 mixtures are illustrated in Fig. 4 to Fig. 8 while the results of DG 10 mixtures are illustrated in Fig. 9 to Fig. 13.

Results of DG 7 Samples

1) Stability

For 5.5% to 7.5% of bitumen content, the stability requirement was attained as shown in Fig. 4 and the maximum stability occurred at 6.35% (≈ 6.4%).

2) Flow

For 5% to 7.3% of bitumen content, the flow was acceptable. The flow and bitumen content is plotted as in Fig. 5.

1) Bulk Specific Gravity

Maximum bulk-specific gravity occurred at 7.07% (≈ 7.1%) of bitumen content. The relationship between bulk specific gravity and binder content is presented in Fig. 6.

2) Air Voids

The air voids content 3% to 5% was achieved at 6.37% (≈ 6.4%) to 7.25% (≈ 7.2%) of bitumen content and the relationship between air voids and bitumen content is presented in Fig. 7. The 4% of design air voids was achieved at 6.75% (≈ 6.8 %) bitumen content.

3) Voids in Mineral Aggregates (VMA)

The VMA requirement was satisfied in the entire tested bitumen content range. The voids in mineral aggregates vs bitumen content plot is given in Fig. 8.

The bitumen content range from 6.4% to 7.2% was found to satisfy all the Marshall criteria as stated in TABLE VIII. The optimum bitumen content (OBC) was derived as 6.8% according to the Asphalt Institute method [23] and, OBC falls within the acceptable range of bitumen content.

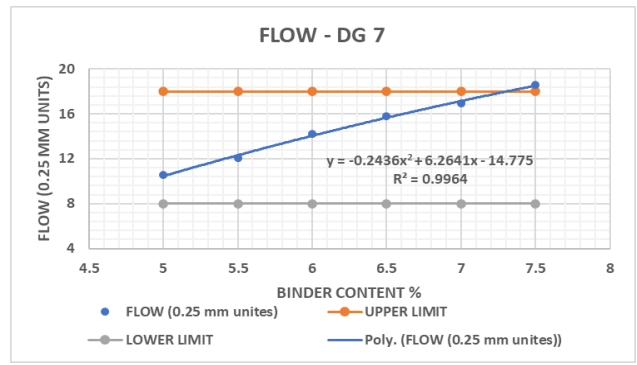


Fig. 5. Flow vs binder content for dg7 samples

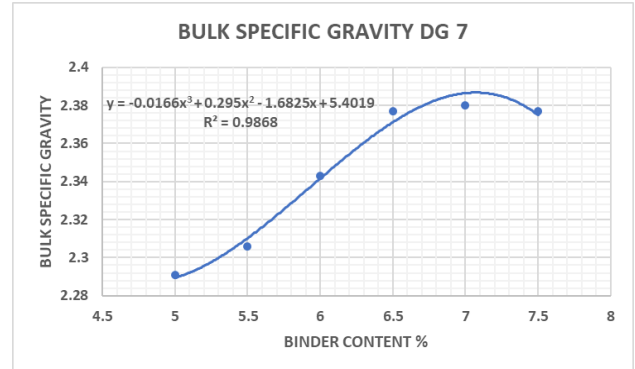


Fig. 6. Bulk specific gravity vs binder content for dg7 samples

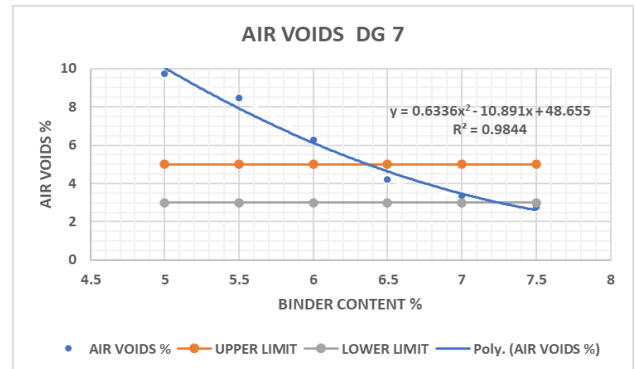


Fig. 7. Air voids vs binder content for dg 7 samples

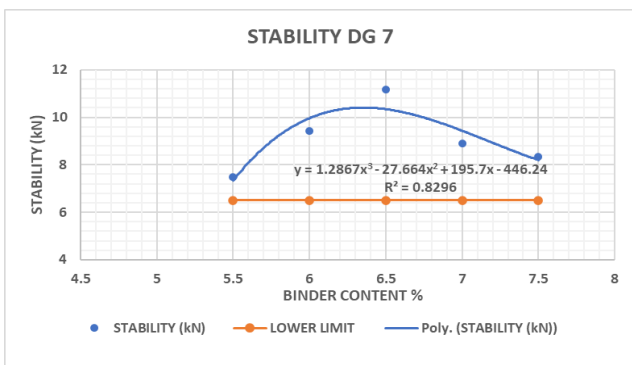


Fig. 4. Stability vs binder content for dg7 samples

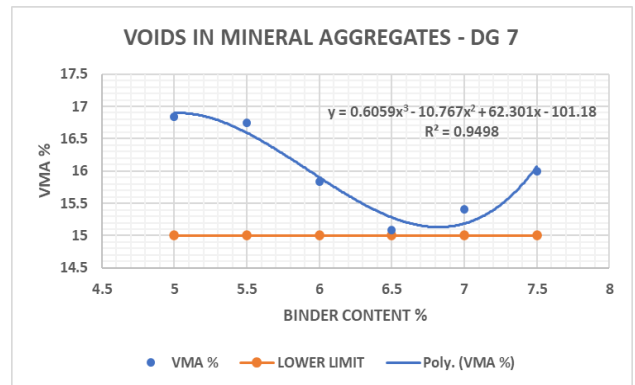


Fig. 8. Voids in mineral aggregates vs binder content for dg7 samples

Results of DG 10 Samples

1) Stability

For 5% to 7% range of bitumen content, the required stability was attained as shown in Fig. 9. The maximum stability occurred at 6.40%.

2) Flow

For 4.5% to 6.8% of bitumen content, the flow was acceptable. Flow vs binder content is plotted as given in Fig. 10.

3) Bulk Specific Gravity

Maximum bulk specific gravity occurred at 6.67% (\approx 6.7%) of bitumen content. Bulk-specific gravity vs binder content is presented in Fig. 11.

4) Air Voids

The air voids content 3% to 5% was accomplished at 5.55% (\approx 5.6%) to 6.37% (\approx 6.4%) of bitumen content and the relationship between air voids and bitumen content is displayed in Fig. 12. The 4% of design air voids was achieved at 5.92% (\approx 5.9 %) bitumen content.

5) Voids in Mineral Aggregates (VMA)

The VMA requirement was satisfied in the entire tested bitumen content range. The voids in mineral aggregates vs bitumen content plot is given in Fig. 13.

TABLE VII. MAXIMUM THEORETICAL SPECIFIC GRAVITY

	DG 7	DG 10
Gmm	2.4997	2.4815

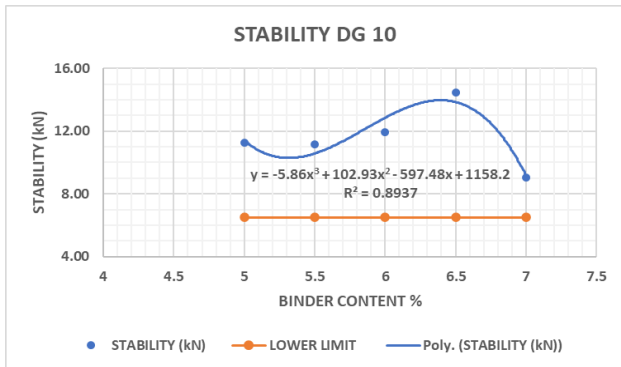


Fig. 9. Stability vs binder content for dg10 samples

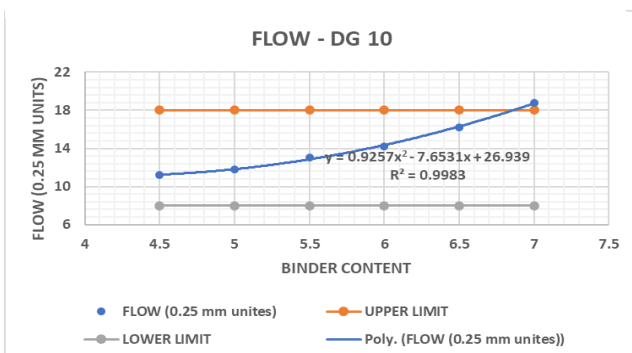


Fig. 10. Flow vs binder content for dg10 samples

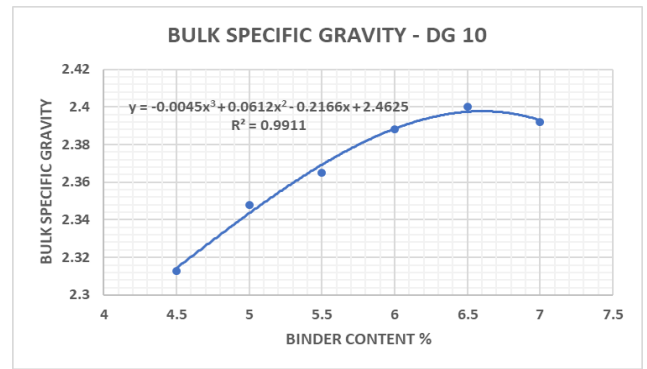


Fig. 11. Bulk specific gravity vs binder content for dg10 samples

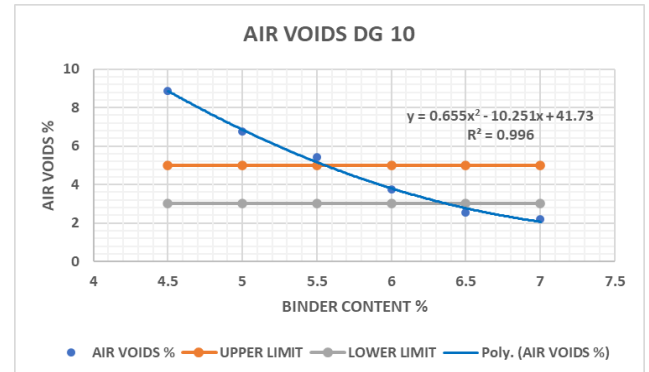


Fig. 12 . Air voids vs binder content for dg10 samples

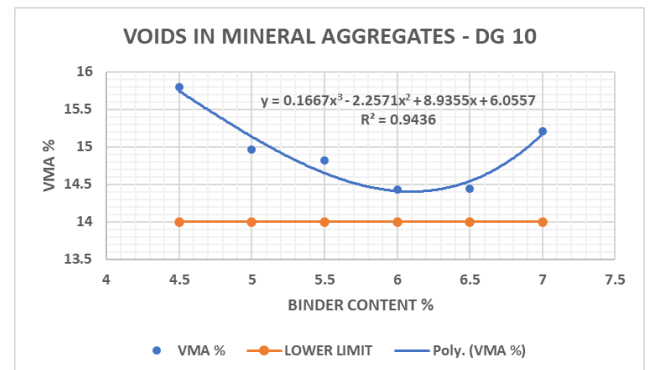


Fig. 13. Voids in mineral aggregates vs binder content for dg10 samples

TABLE VIII. OPTIMUM BINDER CONTENT AND ACCEPTABLE RANGES

	BINDER CONTENT %	
	DG 7	DG 10
Maximum Stability	6.40	6.40
Maximum Specific Gravity	7.10	6.70
4% Design Air voids	6.80	5.90
Optimum Binder Content	6.80	6.33
Stability range	5.50 to 7.50	4.50 to 7.00
Flow (0.25 mm units) range	5.00 to 7.31	4.50 to 6.86
3% to 5% Air voids range	6.37 to 7.25	5.55 to 6.37
VMA range	5.00 to 7.50	4.50 to 7.00
Selected Binder Content	6.80	6.30

The bitumen content range from 5.6% to 6.4% was found to satisfy all the Marshall criteria as stated in TABLE VIII. The optimum bitumen content (OBC) was derived as 6.3% for DG10 mixture according to the Asphalt Institute method [23] and, OBC falls within the acceptable range of bitumen content.

Thus, the Marshall requirements were found to be satisfied by both types of mixtures and the relevant OBC were determined. With the defined OBC and other properties, the applicability of TSA pavements for LVR was examined using mechanistic software by analyzing typical LVR in Sri Lanka and it is explained under ‘V’.

V. PAVEMENT ANALYSIS (MECHANISTIC APPROACH)

The mechanistic pavement analysis software ‘CIRCLY 7.0’ was used to assess the structural performance of TSA pavements. For the mechanistic analysis, road number ‘ID-98’ which is a ‘C’ class road that belongs to Kurunegala phase 01 of ‘Integrated Roads Investment Project’ (i-Road project) was selected. The road ‘ID-98’ was selected as a typical LVR because it consists of AADT of 485 vpd (which is less than 1000 vpd) and CNSA of 1.1×10^5 for the design life of 10 years (more than 70% of the i-Road project of KU2, KU3 and KU4 consist of CNSA less than 1.1×10^5). The material parameters and axle load data were determined to perform a precise mechanistic analysis.

The material properties were assessed as illustrated in ‘II. B’ and, (5) & (6) were used in addition. (5) which is recommended by the Federal Highway and Administration (FHWA) Department of United States of America [24] used with the parameters concluded by Witczak and Mirza [14] to account for the aging of the asphalt pavement. (6) was established by Molenaar [25] for determining the loading frequency.

$$\log(\log(\eta)) = A + VTS \log(T_R) \quad (5)$$

Where,

η - Viscosity (cP)

A - Intercept of temperature susceptibility relationship

VTS- Slope of temperature susceptibility relationship

T_R - Temperature in Rankine

$$\log(f) = -0.6 - 0.5 h_a + 0.94 \log(v) \quad (6)$$

Where,

f - Loading frequency (Hz)

h_a - Thickness of asphalt layer (m)

v - Average speed of heavy vehicles (kmph)

The determined material properties of granular materials are shown in TABLE IX while that of asphalt layers are shown in TABLE X. The input parameters for (4) are also included in TABLE X.

The axle load data were not readily available for the selected LVR; thus, the axle load survey data of Katugastota – Kurunegala - Puttalam (A010) highway at Wariyapola junction which is located near LVR was used to establish the axle load distribution for the road ‘ID-98’ and the locations are expressed in Fig. 14. CNSA of ID-98 was calculated as 1.0943×10^5 with the axle survey data of A010. (Here, the LVR was assumed to have 65% of the total axle distribution of A010.)

TABLE IX. PROPERTIES OF UNBOUND GRANULAR MATERIALS

	Resilient Modulus	Poisson's Ratio
Subgrade	82	0.40
Subbase	105	0.35
Base Course	211	0.35

TABLE X. INPUT PARAMETERS AND MATERIAL PROPERTIES OF ASPHALT CONCRETE

	DG 7	DG 10
Optimum bitumen content (%)	6.8	6.3
P 200 (%)	7	7
P 4 (%)	26	37
P 34 (%)	0	0
P 38 (%)	0	11
Va (%)	3.15	3.89
Vb,eff (%)	11.374	11.2072
Visosity (million poise)	0.13102	0.13592
f (Hz)	6.00	5.97
DYNAMIC MODULUS (Mpa)	1507	1651
RESILIENT MODULUS (Mpa)	1468	1608
POISSON'S RATIO	0.4	0.4

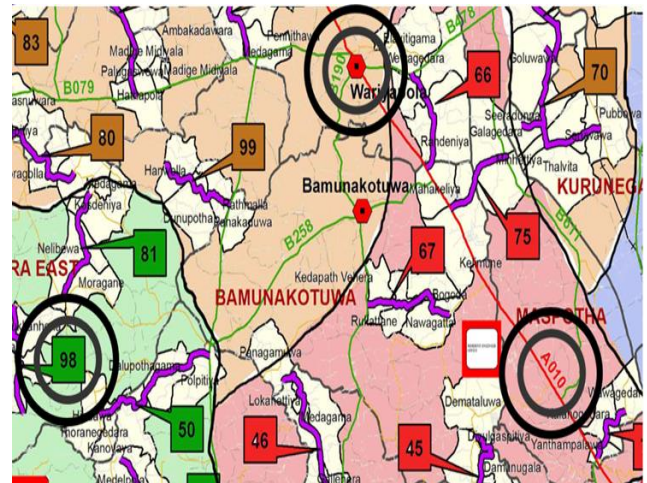


Fig. 14. Locations of axle load survey and road id98

The minimum paving thickness of pavements 20 mm for DG 7 and 25 mm for DG 10 were applied while assuming the 125 mm thick base course and 100 mm thick subbase layers according to the original design. The evaluations were yielded satisfactory solutions for both DG 7 and DG 10 TSA pavements as the cumulative damage factors (CDF) for asphalt layers and subgrade were lesser than 1.0. Thus, the thickness of pavements 20 mm for DG 7 and 25 mm for DG 10 were verified to have adequate structural thicknesses. The mechanistic analysis result is displayed in Fig. 15 and Fig. 16. Therefore, with the defined properties and result of pavement analysis, the TSA pavements were found to be durable. The financial viability was investigated as illustrated in section ‘VI’.

No.	ID	Title	Current Thickness	CDF
1	150408F DG 7	Size 7- WMAPT 44.53 C- 30 kmph	20.00	5.12E-03
2	150408F Base C...	Granular, E=211MPa	125.00	
3	150408F Subbase	Granular, E=105	100.00	
4	150408F Subgrade	E=82MPa	0.00	1.43E-01

Fig. 15 Pavement analysis of 20mm dg7

No.	ID	Title	Current Thickness	CDF
1	150408F DG 10	Size 10, WMAPT 44.33 C - 30 kmph	25.00	1.64E-01
2	150408F Base C...	Granular, E=211MPa	125.00	
3	150408F Subbase	Granular, E=105	100.00	
4	150408F Subgrade	E=82MPa	0.00	1.04E-01

Fig. 16. Pavement analysis of 25mm dg10

VI. COST COMPARISON

Cost estimation was done for the asphalt concrete materials only because, the base, sub-base materials, and their thicknesses were assumed to be the same as the original i-Road ID-98 design data. The TABLE XI shows the cost estimation for a 1 km roadway, which was performed with highway schedule of rates 2020 of North-Western Province. From the table, it is obvious that the 20 mm of DG 7 and 25 mm of DG 10 pavements reduce the cost by 46.30% and 38.63% respectively when compared with WCT 2 (wearing course type 2- original design).

(Note: General note 26.4 – the factor 1.378 was selected to convert the compacted volume to loosen volume with the assumption of 97% compaction of the base course layer. General note 29.9 – Density of wearing course was selected as 2.450 metric tons per cubic meter.)

TABLE XI. COST COMPARISON OF DG7, DG10 LAYERS WITH WCT2 LAYER

	WCT 2	DG 7	DG 10
Thickness of asphalt layer (mm)	50	20	25
Road width (m)	6.2	6.2	6.2
Bulk Volume (m ³)	310	124	155
Mass of Asphalt concrete (ton) General Note 29.9	744.31	289.478	364.824
Binder %	4.7	6.8	6.3
Binder mass (ton) -	34.983	19.685	22.984
Aggregate mass (ton)	709.327	269.793	341.84
Binder % (volume)	10.85	15.26	14.26
Aggregate loose volume (m ³)	367.439	139.364	176.362
General Note 26.4			
Binder cost (BO - 355C) (Million SLR)	3.009	1.693	1.977
Aggregate cost (million SLR)			
19 mm aggregate BO - 308A	0.895	0.31	0.393
12.5 mm aggregate BO- 309			
9.5 mm aggregate BO - 316			
Total Material Cost (million SLR)	3.904	2.003	2.370
Cost reduction % related to WCT 2		48.69	39.29

VII. DISCUSSION AND CONCLUSION

The Marshall test showed satisfactory results and, the OBC for DG7 and DG10 were defined and, the properties of materials were derived. The mechanistic analysis proved that the 20 mm of DG7 and 25 mm of DG10 were structurally adequate. After the verification of structural feasibility, the cost comparison was performed and, the TSA pavements were found to reduce the cost considerably (as 48.69% for DG7 mixtures and 39.29% for DG10 mixtures) when compared with traditional asphalt pavements.

Therefore, the TSA pavements are recommended over TA pavements to be used for the LVR of Sri Lanka.

ACKNOWLEDGMENT

I offer my sincere gratitude to the research supervisor Prof. W.K. Mamparachchi, Department of Civil Engineering, the University of Moratuwa for his guidance and encouragement to carry out my research work productively. I would like to appreciate the assistance and guidance of Eng. Mr. M. Mariyathan and Eng. Mr. M.J. Arulhasan. Also, my sincere thanks to my colleagues Mr. R.W.D.K. Bandara, Mr. B. Kingston and Mr. M. Parasuram for supporting me in the successful completion of the research.

REFERENCES

- [1] A. Faiz, "The Promise of Rural Roads," *Promise Rural Roads*, no. September, 2012.
- [2] World Travel & Tourism Council, "Travel & Tourism Economic Impact 2017: Sri Lanka," *World Travel Tour. Counc.*, 2017.
- [3] G. J. Kinigama, "Development of Methodology to Estimate Esal Vaules for Low Volume Roads in Provincial Sector," no. March, 2010.
- [4] Transport Research Laboratory, *A guide to the structural design of bitumen- surfaced roads in tropical and sub-tropical*, Fourth. 1993.
- [5] AASHTO, *A Policy on Geometric Design of Highways and Streets, 5th Edition*, Fifth edit. Washington, D.C. 20001, 2004.
- [6] "Sri Lanka: Budget 2019 - Roads and Expressways - Sri Lanka Guardian." [Online]. Available: <http://www.srilankaguardian.org/2019/03/sri-lanka-budget-2019-roads-and.html>. [Accessed: 05-Jan-2020].
- [7] S. Leischner, F. Wellner, G. C. Falla, M. Oeser, and D. Wang, "Design of Thin Surfaced Asphalt Pavements," *Procedia Eng.*, vol. 143, no. Ictg, pp. 844–853, 2016.
- [8] E. Beuving, "Use of SMA in Europe," no. February, 2018.
- [9] A. guide to pavement technology 2009, *Part 3: Pavement Surfacing*. 2009.
- [10] "Climate data for cities worldwide - Climate-Data.org." [Online]. Available: <https://en.climate-data.org/>. [Accessed: 13-Jan-2020].
- [11] ICTAD, *Standard specifications for construction and maintenance of roads and bridges*, Second. Colombo 7: Institute for Construction Training & Development (ICTAD), 2009.
- [12] A. guide to pavement technology 2014, "Part 4B: Guide to Pavement Technology," Second., R. John and P. Laszlo, Eds. Sydney: Austroads Ltd. Level 9, 287 Elizabeth Street Sydney NSW 2000 Australia, 2014, p. 139.
- [13] R. B. Mallick and T. El-Korchi, *Pavement Engineering: Principal and Practice*. 2018.
- [14] M. W. Witezak and O. A. Fonseca, "Revised Predictive Model for Dynamic (Complex) Modulus of Asphalt Mixtures," *Transp. Res. Rec.*, no. 1540, pp. 15–23, 1996.
- [15] Y. Xiao, "Evaluation of engineering properties of hot mix asphalt concrete for the mechanistic-empirical pavement design," 2009.
- [16] Austroads, *Guide to Pavement Technology Part 2: Pavement Structural Design*, no. c. Austroads Ltd. Level 9, 287 Elizabeth Street Sydney NSW 2000 Australia, 2018.

- [17] L. Xu, "Typical values of Young's elastic modulus and Poisson's ratio for pavement materials."
- [18] New Zealand Transport Agency, "Specification for Dense Graded and Stone Mastic Asphalt," vol. 1, pp. 1–30, 2014.
- [19] W. K. Mampearachchi, G. S. Mihirani, B. W. P. Binduhewa, and G. D. D. Lalithya, "Review of asphalt binder grading systems for hot mix asphalt pavements in Sri Lanka," vol. 40, no. 4, pp. 311–320, 2012.
- [20] ASTM D 4402-15, "Standard Test Method for Viscosity Determination of Asphalt at Elevated Temperatures Using a Rotational Viscometer," 2015.
- [21] ASTM D2041/ D2041M, "Standard test method for theoretical maximum specific gravity and density of bituminous paving mixtures," *Am. Soc. Test. Mater.*, p. 4, 2011.
- [22] "ASTM D6927 - 15 Standard Test Method for Marshall Stability and Flow of Asphalt Mixtures | Road Surface | Asphalt." [Online]. Available: <https://www.scribd.com/document/358806748/ASTM-D6927-15-Standard-Test-Method-for-Marshall-Stability-and-Flow-of-Asphalt-Mixtures>. [Accessed: 13-Jan-2020].
- [23] I. Kett, "MARSHALL METHOD of MIX DESIGN," *Asph. Mater. Mix Des. Man.*, pp. 102–119, 1998.
- [24] "Appendix A: Processing Asphalt Binder Viscosity Data - LTPP Computed Parameter: Dynamic Modulus , September 2011 - FHWA-HRT-10-035." [Online]. Available: <https://www.fhwa.dot.gov/publications/research/infrastructure/pavements/ltp/10035/008.cfm>. [Accessed: 04-Jan-2020].
- [25] A. Molenaar, "Lecture Notes on the Design of Flexible Pavements." European Asphalt Pavement Association, 2018.

Evaluation of Parking Patterns and the Parking Behavior of the Drivers in Kandy, Sri Lanka

P.M.G.D.M. Herath
Department of Civil Engineering
University of Peradeniya
Peradeniya, Sri Lanka
dhanushkamadusanka1995@gmail.com

P.M. Hewamallikage
Department of Civil Engineering
University of Peradeniya
Peradeniya, Sri Lanka
pasindumenuka93@gmail.com

A.G.H.J. Edirisinghe
Department of Civil Engineering
University of Peradeniya
Peradeniya, Sri Lanka
jayalath@eng.pdn.ac.lk

Abstract— Roadside parking is one of the major factors which causes traffic congestion in most of the roads in Sri Lanka. It is a normal practice for roadside buildings in Sri Lanka to provide their own parking facilities facing main roads. Due to this, often vehicles have to reverse to main road to start their journey. This is one of the main reason to disturb the smooth traffic flow and also for road accidents. The purpose of this research is to identify the parking patterns and the parking behavior of the drivers in Kandy municipal area. In this research, commercial buildings in Kandy city are categorized into four main categories according to the service provide by the building. Parking frequency and parking duration of the vehicles according to the building category is assessed. The parking behavior of the drivers is categorizing into four categories according to the parking and leaving direction of vehicles. The maneuvering time of the vehicles when leaving is studied for the four behavioral categories. The results show that about 70% of drivers are reversing their vehicle to the main road when leaving, which causes more traffic disturbance to the traffic flow in the road.

Keywords— Roadside, Parking, Reversing, Traffic

I. INTRODUCTION

Kandy is one of the highly urbanized cities in Sri Lanka. With the highly growing number of vehicles in Sri Lanka, the number of vehicles entering and leaving the Kandy municipal area is increasing day by day. Due to that, parking has become a very important requirement in Kandy town area. This causes various problems for the traffic flow in the city such as traffic congestion, accidents etc.

Sri Lanka is one of the countries which is suffering from financial and labor time losses due to traffic congestion. The economic loss due to traffic congestion in Sri Lanka is Rs. 40 billion per annum in 2012. This is about 1.5% of the Gross Domestic Production (GDP) of Sri Lanka [5]. The traffic congestion occurs when the volume of the traffic generates is higher than the capacity of the road segment. The capacity of the roads in Sri Lanka is increasing with a rate of 2-3% annually. But the increasing of the traffic flow in the road network is about 10% annually [5]. Therefore, the traffic congestion is one of the major issues in Sri Lanka.

There are many factors which effect the traffic congestion in roads. Among them, parking is one of the major issues which causes a huge impact on road traffic. With the increasing number of vehicles and parking demand, most of the commercial buildings are providing parking facilities for their own customers. Those parking facilities can be in various types according to the available space, parking demand and some other factors. Off-street parking, roadside parking and

curb side parking are some of them. Among these types of parking, most of the roadside buildings are providing their own parking facilities directly facing the main road. Due to this most of the vehicles entering to the parking have to reverse the vehicle to the main road when they leave. This may cause a serious issue for the traffic flow by leading to traffic congestion and accidents.

Although many studies have been done to identify the problems which causes traffic congestion in Kandy municipal area, very less number of studies were done to identify the parking patterns and the parking behavior of the drivers in Kandy municipal area. Therefore, this study focuses on the parking patters and the parking behavior of the drivers considering Kandy municipal area.

II. LITERATURE REVIEW

Kandy city is located at about 500m above the mean sea level and situated 116km from Colombo, where the financial capital of Sri Lanka. Three sides of the Kandy municipal area are surrounded by the Mahaweli river and the other side, the boundary is Hanthana mountain range [6]. About 56,000 vehicles and 318,000 people enter the Kandy city daily [1]. Among the total number of vehicles, 50% of the vehicles are cars/vans. About 40% of the vehicles are coming to the city and about 15-20% of vehicles are going through the city for other destinations [3]. There are three peak times in the city where the maximum peak is occurred from 07.00 – 08.30, second highest peak occurs from 16.00 - 17.45 and other peak is from 13.00 - 15.00 [3].

Parking demand is very high in the grid city area of Central Business District (CBD) where the parking mode is roadside parking (curb parking). Very high parking demand can be seen in Colombo street, Kotugodella veediya, D.S. Senanayaka veediya etc. from about 8.30 - 18.00. In some times, the parking demand is increasing about 150% of the legal parking capacity [6].

Among the daily parking in Kandy CBD area, 22% is motor bicycles, 30% three wheelers, 24% car/ jeep, 15% vans, 6% buses and 5% goods vehicles [6]. Average parking duration of Kandy CBD is varying from less than 30 minutes to 105 minutes. The average 85th percentile parking duration is 90 minutes. But in some areas it is about four hours and some areas it is about two hours. Total number of parking bays available in CDB is 825 and 118 spaces or 14.3% among them are occupied for about eight hours or more [6].

According to Kandy City transport study [6], it was found that the average speed of a vehicle during the peak time of CDB area is 16.7km/h and it is 25.7km/h during the off peak time.

When the vehicles are reversing to the main road from a roadside parking, the width of the road may reduce or the total width of the road may be used by the reversing vehicle. With that, the speed of the vehicles travelling in the road may reduce or the vehicle may be stopped totally. This speed reduction due to on-street parking has a significant effect on vehicle speed in local streets, but the effect is not meaningful in narrow streets [2]. The mean speed of a vehicle falls down from 1km/h for an increase of roadside parking from 10%. Furthermore, it says that the speed of vehicles which are travelling at a speed more than the average speed has a significant effect of on-street parking for their speed.

One major factor which causes traffic congestion is parking. On-street parking has a major effect on traffic congestion than the off street parking. Among the on-street parking, illegal parking causes a significant effect on traffic congestion. Illegal parking results in temporary congestion caused by the reduction of the road width and sudden reduction of speed. The congestion is caused because of the bottleneck caused with the entering and leaving of the vehicles from a parking. The effect becomes high when the level of traffic flow is moderate and high [7].

Parking pattern is another considerable factor which effects for the traffic congestion. Angled parking with reverse maneuvers requires more time and more road space resulting more traffic congestion. Reversing of vehicles from angled parking causes bottleneck effect and results in traffic congestion and accidents [7]. For parallel parking, required maneuvering space should be provided in order to reduce the congestion.

Madushanka et. al. (2020) studied about the effect of roadside parking maneuvers on traffic flow using PVT VISSIM micro simulation software [4]. According to the research, it was observed that the capacity will reduce by a percentage of approximately 7% per 100 parking maneuvers and the capacity dropped by a value of approximately 17% when there were 250 parking maneuvers per hour

To study about the effect of the roadside parking for the traffic congestion in roads, it is very important to identify the parking patters and the parking behavior of the drivers. Therefore, this study is carried out to identify the parking patterns and the parking behavior of the drivers in Kandy municipal area.

III. STUDY AREA

The focus of this research is to study the parking patterns and the parking behavior of roadside parking facilities where vehicles are reversing to the main road in Kandy municipal area. The study is done for the main three roads in Kandy municipal area which is bounded by Peradeniya bridge and Katugastota bridge. The three road segments are,

1. Kandy – Katugastota (A9 Road)
2. Kandy – Getambe junction (William Gopallawa mawatha)
3. Kandy – Getambe junction (Sirimawo Bandaranayaike mawatha)

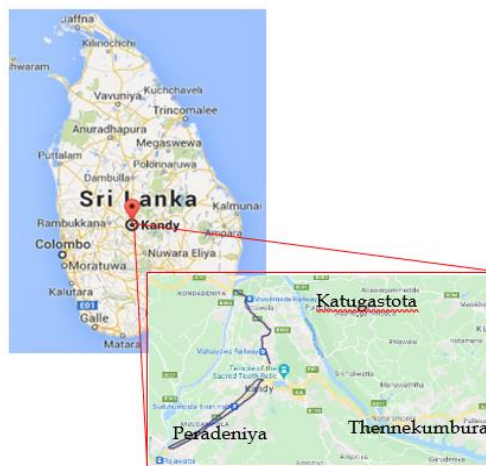


Fig. 1. Study Area

IV. METHODOLOGY

The methodology of this study is consisting of five main steps as shown in Fig. 2.

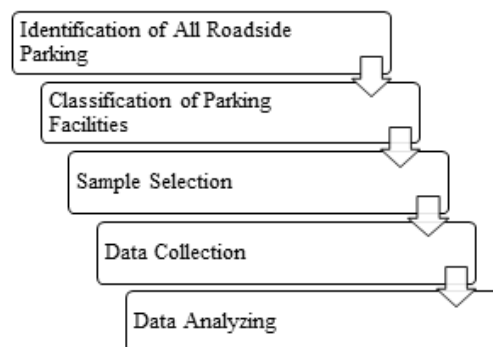


Fig. 2. Research methodology flow chart

A. Identification of All Roadside Parking

All the roadside buildings with the parking facilities were identified within the three road segments. All the locations were marked on a map of Kandy municipal area with the identification of the purpose of the building related to each parking facility. Google map and the Google street view (2015) was used for the initial identification of the places and a field survey was done for the confirmation of the data.

Following details of the parking facilities were recorded in the identification stage.

1. Location
2. Number of parking bays
3. Category of the building
4. Parking pattern of the vehicles

B. Classification of Parking Facilities

All the buildings related to parking facilities were classified according to the facilities which are provided by the building. The building categories were as follows,

1. Super Markets (SM)
2. Shopping Centers (SC)
3. Food Courts (FC)
4. Financial Centers (Bank)

The classification was done in order to categorize the parking facilities with respect to the peak time and the parking frequency.

C. Sample Selection

A sample from all the places marked in the map was selected for further collection of data. For a better sample selection, reconnaissance video survey was done in order to get an idea about parking facilities.

18 buildings were selected for the detailed data collection.

D. Data Collection

Data collection was done manually and using video records.

Following Sections were covered under manual data collection.

1. Date
2. Time
3. Name of the organization and the address
4. Function of the building
5. Number of parking bays
6. Arrangement of parking bays
7. Direction of closest lane to the building

Video records were done to cover both peak and off peak time. The duration of each video was two hours. Following data were taken by using the video records.

1. Total number of vehicles parked during the selected time interval
2. Parking direction and behavior of parking
3. Entering time and leaving time of each vehicle
4. Maneuvering time of each vehicle when leaving with respect to leaving direction
5. Entering direction and leaving direction of each vehicle with respect to lane direction

V. RESULTS AND DISCUSSION

The number of vehicles enter and leave during a unit time period is varying with the facility provide by the building. The variation of the average parking frequency with the Service provide by the building is shown in Fig. 3. The variation of average parking duration of vehicles with the service provide by the building is shown in Fig. 4. The highest parking frequency can be observed in super markets while the parking duration of super markets show lower values. Parking duration in shopping centers and food courts show higher

values than other categories which implies that the customers spend more time in those places than the others.

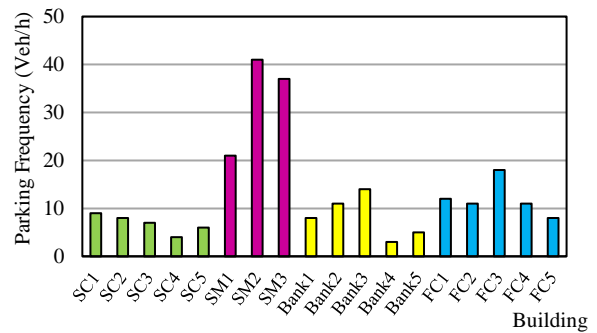


Fig. 3. Variation of average parking frequency with the service provide by the building

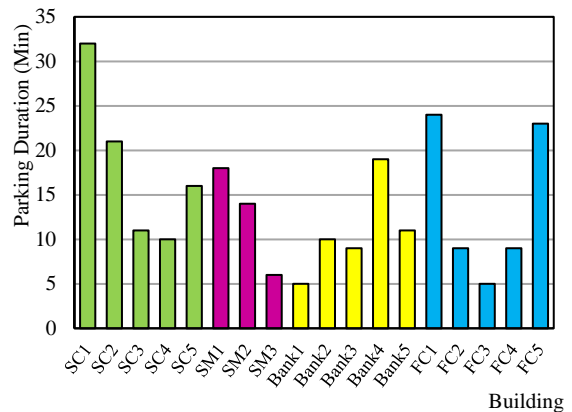


Fig. 4. Variation of average parking duration with the service provide by the building

The maneuvering time of a vehicle depends on various factors. Parking behavior, road width, vehicle volume in the road are some of them. The variation of average maneuvering time of vehicles in each building is shown in Fig. 5. According to the figure, it can be seen that the maneuvering time is more than 20s in every place and also in some places it takes an average maneuvering time of more than one minute which may cause a significant disturbance to the traffic flow in the road.

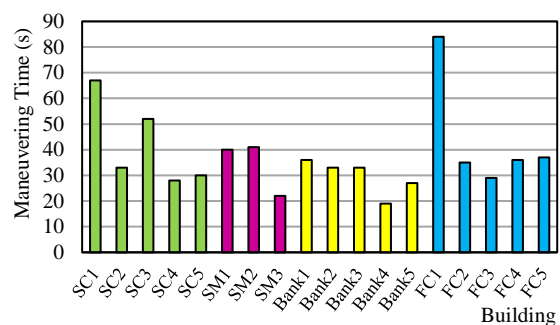


Fig. 5. Variation of average maneuvering time in each building

The maneuvering time of a vehicle depends on the travel direction of the vehicle. Whether it travels in the adjacent lane or in the opposite lane. Variation of average maneuvering time with the travelled direction is shown in Fig. 6.

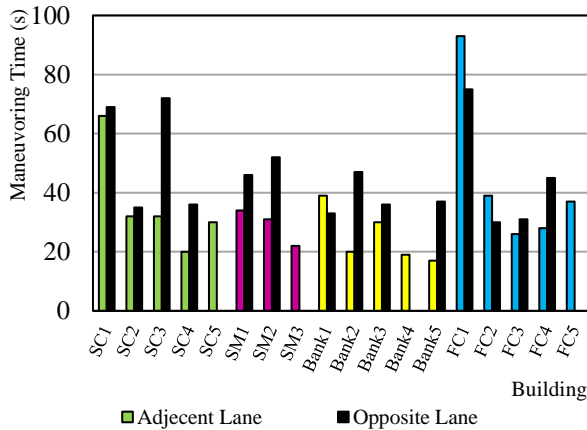


Fig. 6. Variation of average maneuvering time with travelled direction

According to Fig. 6, it can be clearly identified that the maneuvering time of the vehicles which are travelling in the opposite lane of the parking after leaving the parking is higher. The reason for this is, those vehicles have to cross the road when leaving and it may take more time. This also cause a significant disturbance to the traffic congestion in the road.

The variation of the parking behavior of the drivers with the Service provide by the building is shown in Fig. 7. According to the figure, highest percentage of drivers are reversing their vehicles to the main road when they are leaving. This may take a higher maneuvering time which cause more traffic disturbance and leads to accidents.

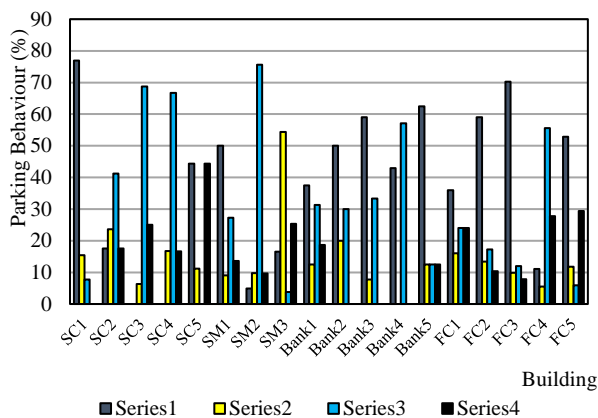


Fig. 7. Variation of parking behavior with the service provide by the building
Parking behavior –

- Series 1 - The vehicle reverse to the main road when leaving
- Series 2 - Parking the vehicle facing the main road
- Series 3 - Use the shoulder of the road to reverse the vehicle
- Series 4 - The vehicle turns inside the parking

There is a considerable effect of parking behavior of the drivers for the maneuvering time of the vehicles when leaving the parking facility. Fig. 8 shows the variation of maneuvering time with the parking behavior of the drivers.

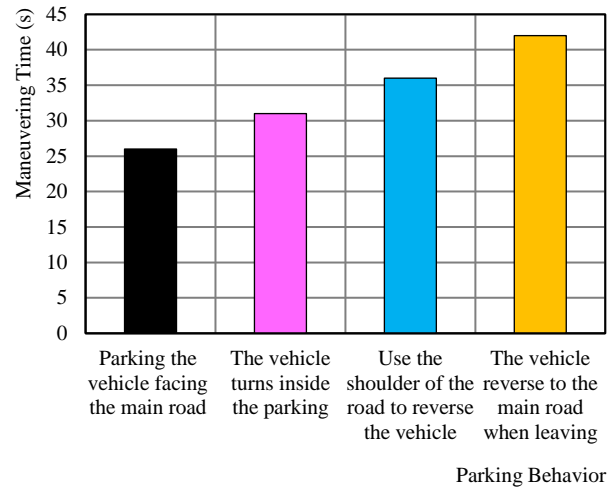


Fig. 8. Variation of maneuvering time with the parking behavior

According to Fig. 8, highest maneuvering time can be seen when the vehicle reverse to the main road when leaving while the lowest can be seen when the vehicle parks facing the main road and leave the parking directly. Although, reversing to the main road is identified as an illegal behavior in driving, most of the drivers tend to reverse their vehicle to the main road when leaving a roadside parking. This may take a higher maneuvering time causing a significant disturbance to the traffic flow in the road.

It is very important to identify the parking frequency and parking durations of different building categories when studying about the parking patterns as shown in Table I. Highest parking frequency is observed in super markets which implies that a large number of vehicles are entering and leaving to the super markets in a unit time. This may cause a significant effect on the traffic flow in the road. Therefore, more attention has to be paid to those parking facilities to minimize the disturbance to the traffic flow. Proper entering and leaving paths should be implemented in those parking facilities to minimize the traffic disturbance. The highest parking duration can be identified in shopping centers which implies that the customers spend more time in those categories of organizations. With the high parking duration, there should have enough parking lots to park all the vehicles entering to the organization. Otherwise, drivers tend to park their vehicles in the side of the road which leads to the traffic congestion in the road. Therefore, more attention should be paid to the number of parking lots in the parking facilities in shopping centers.

TABLE I. AVERAGE PARKING FREQUENCY AND AVERAGE PARKING DURATION FOR EACH BUILDING CATEGORY

Building Category	Average Parking Frequency (Veh/h)	Average Parking Duration (min)
Shopping Centers	7	18
Super Markets	33	13
Financial Centers	8	11
Food Courts	12	14

Different parking behaviors and their percentages which were obtained from all the collected data are shown in Table II.

TABLE II. PARKING BEHAVIOR OF VEHICLES

Parking Behavior	Percentage (%)	Maneuvering Time (s)
The vehicle reverse to the main road when leaving	38	42
Parking the vehicle facing the main road	14	26
Use the shoulder of the road to reverse the vehicle	32	36
The vehicle turns inside the parking	16	31

VI. CONCLUSIONS

In this study, parking patterns and the parking behavior of the drivers in Kandy municipal area was investigated based on the service provide by the building. Four main categories of building were identified base on the service provide by the building and the parking frequency, parking duration, maneuvering time and the parking and leaving behavior of the vehicle was studied.

According to the results, it has been identified that the service provide by the building has a considerable effect on parking frequency and the parking duration. The maneuvering time of the vehicles which are leaving through the opposite lane is almost higher than the maneuvering time of the vehicles which are leaving through the adjacent lane and it leads to more traffic disturbance. About 70% of drivers are reversing their vehicle to the main road which identifies as an illegal behavior of drivers. About 14% of drivers are parking their vehicle facing the main road which shows the least maneuvering time.

Accordingly, policy makers can use the results to propose suitable measures to minimize traffic congestion when building approval is granted. Some measures can be taken to reduce the proportion of vehicles that reverse to the main road.

Several possible future developments of the study were identified. The study was limited only to Kandy municipal area. But it can expand to the other areas too. Only four major building categories were considered for the study. Some more other building categories can be considered further.

ACKNOWLEDGMENT

The authors would like to acknowledge the guidance given by the academic staff of Faculty of Engineering, University of Peradeniya.

REFERENCES

[1] Amal S. Kumarage (2017). Sustainable Transport plan for Kandy. Civil Engineering Society University of Peradeniya

[2] G. Praburam (2015). Effect of On-street parking on Traffic Speeds. IPENZ Transportation Group Conference, Rydges Hotel, Christchurch; 22-24 March 2015

[3] K.M. Jayathilake (2004). Traffic problems in Kandy Metropolitan Area, Department of Civil Engineering, University of Moratuwa.

[4] Madushanka, P.H.S., Jayaratne, D.N.D. and Pasindu, H.R., 2020, July. Study of the impact roadside parking has on traffic flow characteristics- a vissim simulation based approach. In *2020 Moratuwa Engineering Research Conference (MERCOn)* (pp. 419-424). IEEE.

[5] Massive Rs 32 bln loss due to traffic congestion: Transport expert, Sundaytimes.lk, (2016).

[6] University of Moratuwa in association of University of Peradeniya (2011). Kandy city transport study

[7] Yousif, Samaher & PhD, Purnawan. (1999). "On-street parking: Effects on traffic congestion. *Traffic Engineering & Control*". 40.

Colloid Mobilization and Transport in Saturated Porous Media: Laboratory Column Experiments and Numerical Verification

Thilini Gunawardhana
Dept. of Civil Engineering
University of Peradeniya
Peradeniya, Sri Lanka
thil.nima@gmail.com

Banithy Balakrishnan
Dept. of Civil Engineering
University of Peradeniya
Peradeniya, Sri Lanka
banithy93@yahoo.com

Chamindu Deepagoda
Dept. of Civil Engineering
University of Peradeniya
Peradeniya, Sri Lanka
chaminduk@pdn.ac.lk
<https://orcid.org/0000-0002-8818-8671>

Abstract—Contaminant migration in subsurface may potentially lead to severe health and environmental problems. In classical contaminant migration studies, only two mobile phases (liquid and gas) are explored. The presence of a third and a hidden mobile phase, the so-called colloidal phase, has been largely overlooked and its potential to carry contaminants have been under-explored in relation to severe health concerns associated with contaminant movement to groundwater (e.g., CKDu problem in North Central province in Sri Lanka). This study investigated the effect of ionic strength (as a chemical perturbation) on transport of water-dispersible soil colloids (i.e., particle size from 1 nm – 10 μ m) as a potential mode of contaminant transport. A series of column studies were conducted to investigate the transport of soil colloids (Stokes' diameter < 10 μ m) extracted from a CKDu affected area (high-endemic) and a less affected area (low endemic) in a sand-packed saturated column (7.40 cm diameter, 25 cm height) by varying the ionic concentration (0.01 M, 0.05 M, 0.1 M). Effluent samples were collected and tested to estimate the colloid concentrations and a series of breakthrough curves for different combinations of ionic strengths and flow rate were obtained. Experimental results were numerically characterized based on the advection-diffusion-dispersion modeling framework coupled with attachment, detachment and straining parameters which were inversely estimated using the software - 'HYDRUS 1D'. Observed colloid breakthrough curves showed higher attachment for high ionic strengths. Numerical results identified the attachment as the key colloid retention mechanism in saturated sand in an ionic solution.

Keywords—Colloid transport, Chemical perturbation, Column experiment, Numerical modeling

I. INTRODUCTION

Naturally soil has three phases; solid, liquid and gas. While solid is an immobile phase and the liquid and gas are mobile phases. Most of the approaches which describe and predict the movement of contaminants treat groundwater as a two-phase (i.e., mobile phase and immobile phase) system. Contaminants that are sparingly soluble in water and that have a strong tendency to bind to aquifer (liquid) media are assured to be retarded to move much more slowly than the rate at which groundwater flows [1]. Based on this approach, many contaminants that readily adsorbed solid – solid phase were considered to present little danger to groundwater pollution [2]. The frequent appearance of contaminants, those were considered to be immobile, were observed to travel (at astonishingly) longer distance higher than the distance which is predicted by two phase system and even at rates higher than the mobile aqueous phase.

Later, a third phase is identified as the colloidal phase which is a hidden mobile phase in a soil-water system and has been underrepresented as a potential contaminant transport pathway. It can potentially facilitate the transport of numerous contaminants in soil including radionuclides, hydrophobic organic compounds (HOCs), heavy metals, pesticides, pathogens etc. A wide range of environmentally harmful heavy metals/metalloids including Lead (Pb), Mercury (Hg), Arsenic (As), Chromium (Cr), Zinc (Zn), Copper (Cu), Cadmium (Cd) and Nickel (Ni) are found in subsurface [3]. These metals, typically considered to be immobile or slowly mobile, were found to be mobile with higher rates in the presence of colloids. For example, Zn and Cu is transported 5 to 50-fold more in the presence of colloids than in the absence of it [4]. Similarly, mobility of Pb increased 10 to 3000 times with colloids than without colloids [5]. Further, studies evidenced that the transport of Zn, Pb and Cu facilitated by readily-dispersible soils [6]. Moreover, Chen et al. [6] observed colloid facilitated transport of Cesium (Cs).

Extreme metal accumulation in the human body is a consequence of long term metal intake at either low or high levels. The bio-accumulated metals can cause severe non-communicable diseases and disorders, for example the chronic kidney disease (CKD), which has become a challenging issue for the medical sector in developed and developing countries, such as Egypt, India, Sri Lanka and Central Asia [7]. Notably, it is reported that drinking contaminated water is a common cause of CKD. Further, the use of heavy metal-contaminated water for irrigation has also shown to contribute heavy metal accumulation in crops, which later become severally toxic to the functioning of vital human organs, kidneys and liver. Cd and Pb damage the renal tubules and lead to severe neurotoxin effects on the human kidneys [8].

Another major public health problem in Sri Lanka is Chronic Kidney Disease of unknown etiology (CKDu). It has become a significant threat to people in several countries worldwide as well during last few decades [9]. The CKDu problem has a strong prevalence in North Central Province of Sri Lanka which extends over 10530 m² in the dry zone with agricultural dominance and a well-established network of irrigation reservoirs. Pathetically the farmers (especially males) from poor socio-economic backgrounds in this province become victims of the disease, exceeding the number of patients 30,500 by the year 2017 [10]. Early studies showed a prevalence of 3.7% in Madawachchiya and 3.2% in Huruluwewa [11] but later evidence suggested this to be around 15%-23% in Anuradhapura and Polonnaruwa districts

[12]. Extensive studies carried out from various perspectives such as morphological, epidemiological, socio-economical, hydrological, toxicological and agricultural, no conclusive causative factor for CKDu in Sri Lanka has not been characterized yet [13]–[16]. Nevertheless, prima facie evidences link the CKDu problem to the impact of agrochemicals in the groundwater which is the prime drinking source of the agricultural community of North Central province.

Then a question arises, how these contaminants such as agrochemicals, heavy metals etc. end up in groundwater. One of the significant mechanisms whereby the strongly – sorptive contaminants can potentially migrate to groundwater is referred as Colloid Facilitated Transport (CFT). Small mobile particles of nanometer scale consisting of mineral fragments, microbes, plant decay debris are ubiquitous in pore waters [17]. These Nano-scale particles are collectively called colloids. A colloid, with particle size 1 nm – 1 μm, has a lower limit to make sure they are larger than dissolved molecules, while the upper limit ensures that they are small enough to be suspended in the percolating water. Colloids can potentially sorb chemicals with high affinity and carry them to groundwater. The high charge and large specific surface area are two attributes which promotes adsorption of contaminants and carry them to groundwater faster than the dissolved contaminants. The mobilization, sorption/desorption and transport of colloids and contaminants are highly sensitive to physical properties of soil and the chemistry of soil-water.

Despite the extensive research related to the CKDu problem [18]–[20], there is no scientifically based systematic study which has been investigated the role of colloids - mobilization and transport in CKDu-affected regions in North Central province. Therefore, this study provided an experimental and numerical investigation of mobilization and transport of colloids extracted from soils from CKDu affected area and compared with those from a less-affected area in North central province of Sri Lanka. The objective of this research is to investigate the potential of soil colloid mobilization in agricultural soils in selected CKDu-affected regions in North Central Province in Sri Lanka and examine the effects of flow rate and ionic strength of irrigated water on colloid mobilization and transport in subsurface in those areas in Sri Lanka. Furthermore, numerical simulations and parameterizations were done to predict the extent of contaminant migration mediated by soil colloids.

II. MATERIALS AND METHODS

A. Material

River sand was used as the porous media in all column experiments. Soil colloids were extracted from soil samples, which were collected from CKDu affected area in North central province in Medawachchiya (referred hereafter as high-endemic soil) and also from a less-affected area in Horowpothana (referred hereafter as low-endemic soil) where the higher number of CKDu patients and relatively lower number of CKDu patients have been reported, respectively [10]. All the other chemicals used (i.e., NaCl, HNO₃, NaOH) in the experiments are of analytical grade.

B. Methods

First, the river sand was sieved out to select the fraction passing through 2 mm sieve and retaining on 425 μm sieve. Then, sand was washed thoroughly several times with water

until the acidity and turbidity was completely removed and the neutral pH was achieved. The washed sand was then oven dried at 105°C for 24 hours and air dried for another 24 hours to decrease the temperature before packing in the column to be used in the column experiments.

To prepare the colloidal solution, soil samples were air-dried for 24 hours and sieved by 2 mm sieve. Then, 150 g of sieved soil was added to the container and filled with water. Then, the solution was shaken manually for 15 minutes in order to break the soil aggregates. Next, the solution was kept undisturbed for 20 hours at 25°C to allow coarser particles to settle and the particles smaller than 10 μm were gently siphoned. Stokes' law was used to compute the depth of extraction as shown in (1) below;

$$v = \frac{(\rho_s - \rho_w)d^2g}{18\eta} \quad (1)$$

where ρ_s is the density of particles (2.65 g/cm³), ρ_w is the density of water (0.998 g/cm³ at 20°C), g is gravitational acceleration (981 cm/s), d is particle diameter (2×10^{-3} mm) and η is viscosity of the medium (1×10^{-3} Pa s at 20°C). The main steps of preparation of colloidal solution are illustrated in the Fig. 1.

C. Experimental setup

The column experimental apparatus mainly consists of two Mariott tanks and a sand column. Two number of Mariott tanks which were custom-built using 0.5 mm thick plexi glass, have diameter and height of 74 mm and 800 mm, respectively. One of the Mariott tanks was filled with tap water which was used as the influent and the other one was filled with the colloidal solution. The two tanks were hydraulically connected at the bottom to the inlet of sand-packed column through a common three-way valve. Fig. 2 shows the assembly of Mariott tanks and column.

The column made of acrylic having a diameter and height of 74 mm and 250 mm, respectively was used to contain the porous media. Two number of 3 mm thick rubber O-rings were inserted to the grooves at the top and bottom lids to make sure a watertight joint. All joints were sealed and checked for complete water-tightness prior to experiments.

D. Column Packing

The sand column was divided into the layers from the bottom of the column. At the beginning, water was allowed to flow upward from the bottom of the vertically oriented column. A 10 mm thick gravel layer was placed at the bottom to ensure equal distribution of water. Four number of 50 mm thick sand layers were wet-packed (i.e., keeping the water level above the sand layer being packed) ensuring the same density. At each layer, the column was gently tamped to achieve the expected density of 1.63 g/cm³, to liberate the

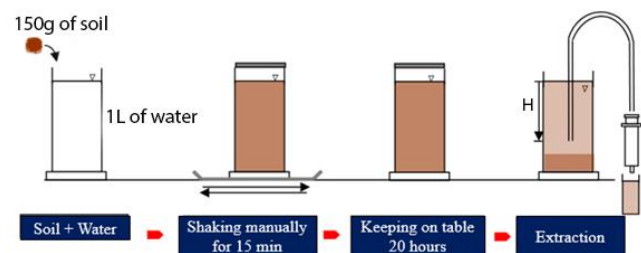


Fig. 1. Major steps associated with the preparation of colloidal solution



Fig. 2. Experimental Setup

entrapped air and to maintain a leveled surface. Tamping numbers were done equally for each sand layer. Another 10 mm thick gravel layer was placed on the topmost sand layer and the top lid was gently fixed into the column while water flowing in the upward direction.

The elevation of the column with respect to the Mariott tank was adjusted to alter the hydraulic gradient and thereby obtained the required flow rate. The colloidal solution was continuously stirred to keep colloids dispersed evenly (i.e. to prevent the colloid deposition at the bottom of the tank). Initially about one pore volume (i.e., the volume of total pores inside the soil column – estimated using bulk density of soils and porosity) of water was applied downward to precondition the column, to estimate the Darcy flow rate and fraction collection time. Then, four pore volumes of colloidal solution were applied. Again, the three-way valve was switched to allow water to pass through the sand column for another three to four pore volumes. Therefore, the application sequence of the solutions is; one pore volume of irrigated water, four pore volumes of water extractable colloidal solution, three to four pore volumes of irrigated water.

The effluent samples were collected in predetermined time intervals, measured the electrical conductivity (EC) and turbidity using EC meter (Eutech CON 700) and turbidity meter (Hach Benchtop 2100N Laboratory Turbidimeter, EPA, 230 Vac) respectively.

E. Numerical verification

The HYDRUS 1D (version 4.17) was utilized to model and parameterize the obtained results by the experimental study. HYDRUS 1D is a computer software package which simulates water, heat and multiple solutes movement in one dimensional variably saturated media [21]. The governing flow and transport equations are numerically solved using Galerkin-type linear finite element schemes [22]. The governing equation for colloid transport was simplified to be used in the model as follows;

$$\frac{\partial C}{\partial t} = -v_x \frac{\partial C}{\partial x} + D_L \frac{\partial^2 C}{\partial x^2} - \left(k_{att} C - \frac{\rho_b}{\theta} k_{det} S_{att} \right) - k_{str} \psi_{str} C \quad (2)$$

where C is the colloid concentration in the aqueous phase at a distance x and time t , v_x is the interstitial particle velocity, D_L is the hydrodynamic dispersion coefficient, k_{att} is the attachment rate coefficient, ρ_b is the dry bulk density of the

porous medium, θ is the porosity of the porous medium, k_{det} is the detachment rate coefficient, S_{att} is the attached particle concentration, k_{str} is the straining coefficient and ψ_{str} is the dimensionless colloid straining function [23].

III. RESULTS AND DISCUSSION

A. Characterization of sand and colloids

Table I shows the properties of sand and colloids used in the column experiments. Particle densities of packed sand and high endemic soil is similar and low endemic soil showed relatively a smaller particle density. Also, the bulk density values of high endemic and low endemic soils are comparatively same and somewhat smaller than the value showed for packing material.

Particle size distribution (PSD) curves for sand, high endemic soil colloids and low endemic soil colloids are shown in Fig. 3. The effective diameter (d_{50}) of sand can be identified from Fig. 3 as 2 mm. Other two PSD curves show the distribution of colloidal particles of high endemic and low endemic soils. Particle size of both colloidal samples are less than 10 μm hence can be technically considered as the colloidal samples.

In the particle size distribution curves the symbols represent the experimental data while the solid lines give model predictions which were fitted to the modified Rosin Rammler equation used by Rosin and Rammler, 1933 [24] as shown in (3).

$$p(x) = 100 \left[1 - e^{-\ln^2 \left(\frac{x}{D_{50}} \right)^\beta} \right] \quad (3)$$

where x is the particle size, D_{50} is the mean particle diameter and β is an empirical constant of the distribution.

B. Colloid Stability

Investigating the stability of colloids has a significant importance when studying colloidal behavior in subsurface. The colloid-facilitated contaminant migration processes significantly affect with colloidal stability. The occurrence of the state of dispersions, from stable to unstable, or vice-versa is important in many non-engineering applications as well, for example in food industries at large level, in medicinal field, in water purification, paints and cosmetics etc. [25].

The colloidal stability is controlled by the interactions between the particles, mainly through electrostatic or steric phenomena. In this study, the main focus was on the former method which can be achieved through changes in ionic concentrations in the colloidal solution. In addition, the ion

TABLE I. PROPERTIES OF SAND AND COLLOIDS

Sand / Soil	Particle size	Particle density (g/cm ³)	Bulk density (g/cm ³)
Sand	Particles smaller than 2 mm and greater than 425 μm	2.65	1.76
High endemic area Soil (Medawachchiya)	Particle size < 2 μm	2.65	1.70
Low endemic area soil (Horowpothana)	Particle size < 2 μm	2.63	1.69

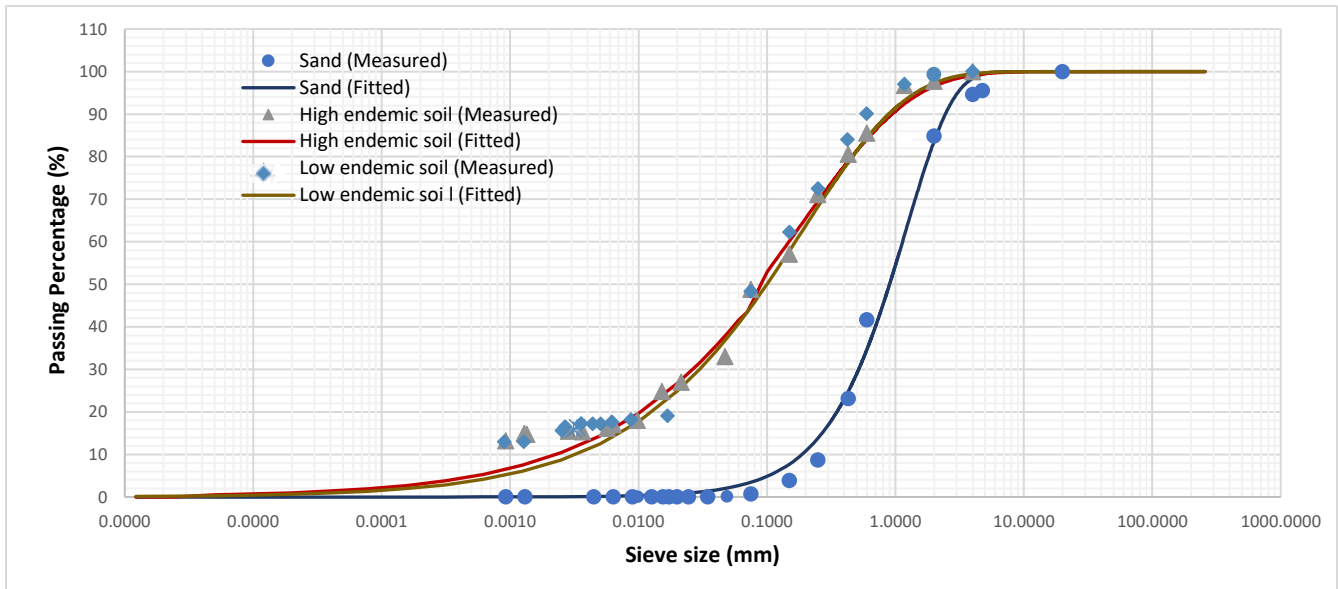


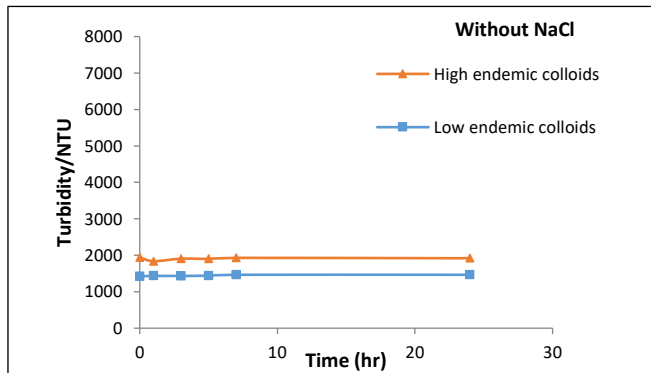
Fig. 3. Particle size distribution curves for sand and soil colloids

valence and pH could also make a significant impact on colloid stability.

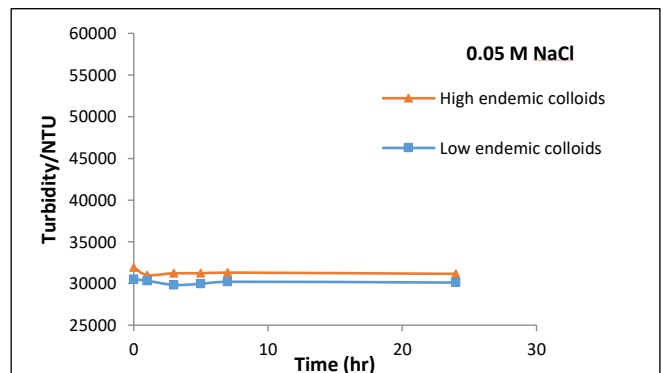
The observed high stability of both high and low endemic soils as shown in Fig. 4, confirmed the applicability of colloidal solutions in 8-hour column experiments as was subsequently done with these colloid suspensions (explained later) without continuous stirring.

C. Experimental results obtained by the column experiments

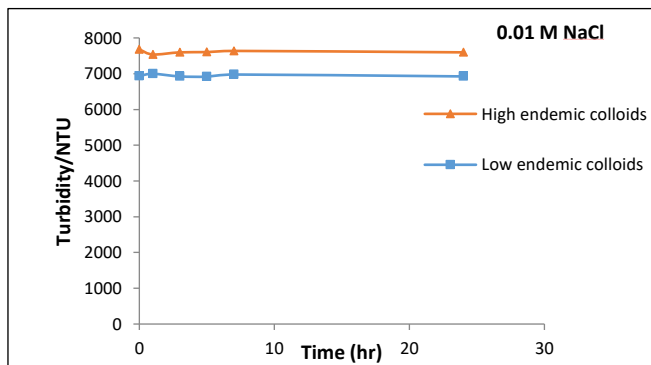
All experiments were conducted at a constant flow rate ($2.75 \text{ cm}^3/\text{s}$) with changing ionic concentrations. The flow rate was purposely selected to mimic a worst-case scenario for conservative analysis. The changes in ionic strength was achieved by adding different concentrations of NaCl to investigate the effect of ionic strength in colloid transport.



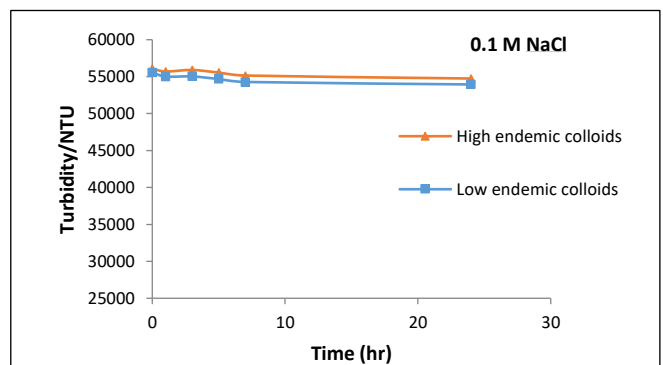
(a)



(c)

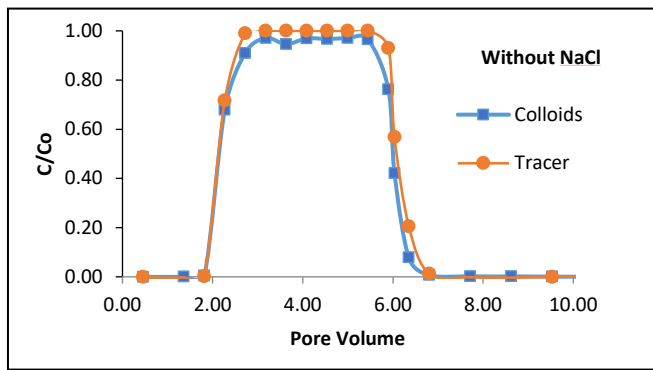


(b)

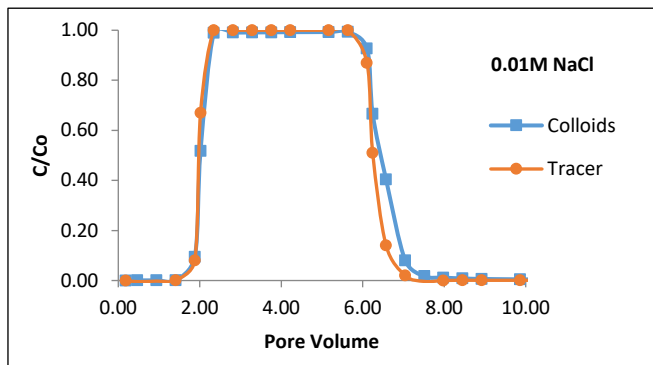


(d)

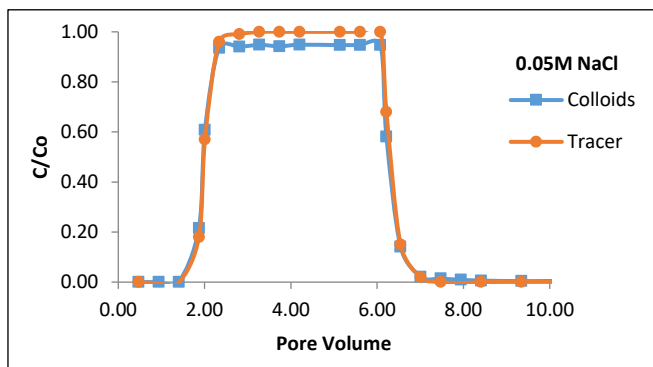
Fig. 4. Colloid stability curves (a) without NaCl, (b) 0.01 M NaCl, (c) 0.05 M NaCl, (d) 0.1 M NaCl



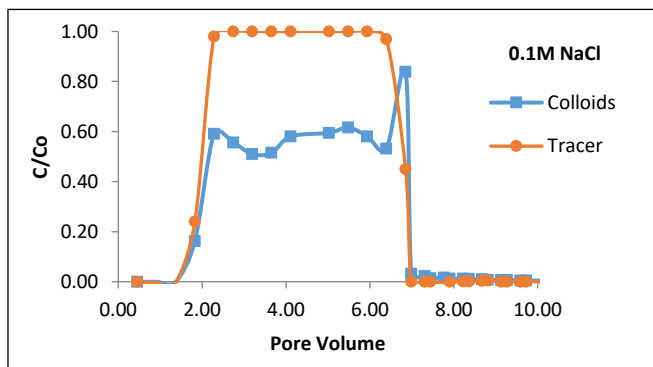
(a)



(b)



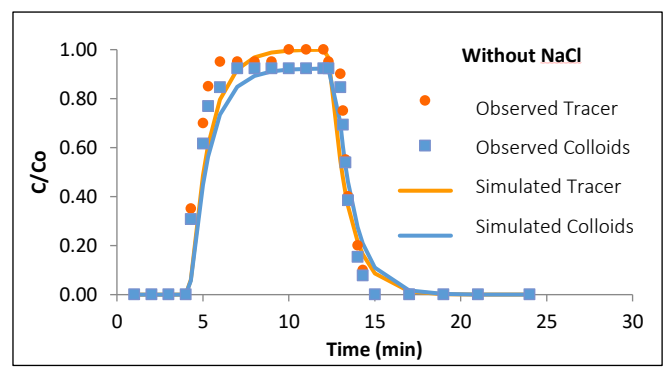
(c)



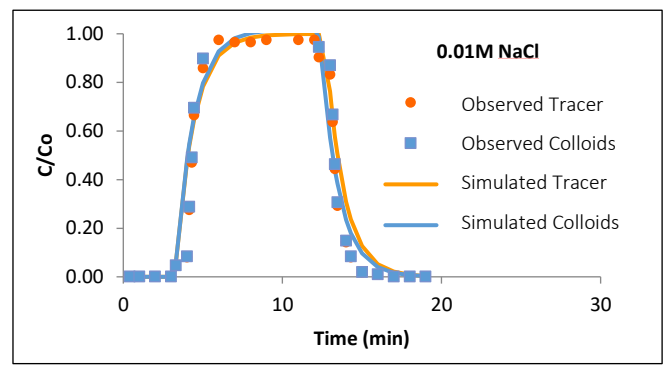
(d)

Fig. 5. Breakthrough curves obtained by the column experiments for $2.75 \text{ cm}^3/\text{s}$ (a) without NaCl, (b) 0.01 M NaCl, (c) 0.05 M NaCl, (d) 0.1 M NaCl

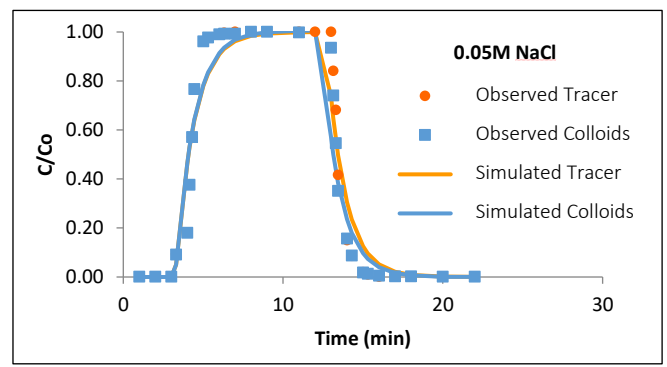
The breakthrough curves were observed for different ionic strengths as illustrated in fig. 5. Breakthrough curves of colloids and tracers were obtained from measuring the turbidity and electrical conductivity of the collected samples respectively. With no ionic solution (i.e., 0 M NaCl), colloid



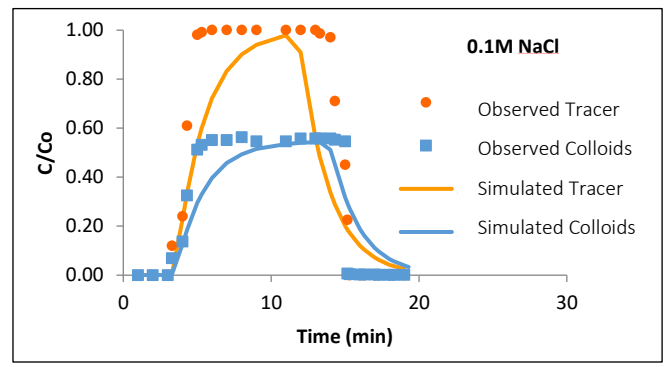
(a)



(b)



(c)



(d)

Fig. 6. Breakthrough curves comparison between the experimental data and the current models fitting for $2.75 \text{ cm}^3/\text{s}$ (a) without NaCl, (b) 0.01 M NaCl, (c) 0.05 M NaCl, (d) 0.1 M NaCl

retention seems to be low (Fig. 5a). With the increase of ionic strength from 0.1 M (Fig. 5b), 0.05 M (Fig. 5c) and 0.01 M (Fig. 5d), retention of colloids also increased because the range of repulsive forces increases due to the expansion of the diffuse ions surrounding colloids. This is

well agreed with the simulation done by Ryan and Elimelech, 1996 [26].

D. Modelled breakthrough curves and parameters

Simulated breakthrough curves obtained via HUDRUS 1D was illustrated in fig. 6 for the flow rate of 2.75 cm³/s without NaCl (as a reference) and also for three different ionic strengths of high endemic soil (Note that only high endemic soils were considered here due to its high importance). For both cases the tracer and colloids breakthrough curves were well fitted with the simulated data.

Table II shows the inversely-estimated parameters (attachment coefficient, detachment coefficient and straining coefficient) for different ionic strengths. The fitted attachment coefficient confirms that the colloid attachment decreases when decreasing ionic strength.

TABLE II. MODELLED PARAMETERS

Scenario	Hyd. Conductivity (m/s)	Dispersivity (m)	Att S ₂ (hr ⁻¹)	Att S ₁ (hr ⁻¹)	Det S ₁ (hr ⁻¹)
Without NaCl	0.373	215.93	2.99 E-03	2.99 E-03	0.263
0.01 M NaCl	0.358	217.42	3.81E-03	1.1798	6.804
0.05 M NaCl	0.749	98.55	1.76 E-03	3.1583	6.076
0.1 M NaCl	0.409	104.98	0.13979	3.7402	51.317

IV. CONCLUSIONS

This experimental and numerical study investigated the transport of soil colloids (< 10 μm) in saturated sand (d₅₀ = 2 mm) for different ionic strengths for a particular flow rate using a series of column experiment. Colloid transport and retention parameters were estimated using HYDRUS 1D software based on the breakthrough curves generated for different ionic strengths. The estimated attachment coefficients and straining coefficients were significantly higher in high ionic strength. Hence, the results of numerical analysis identified attachment as the key retention mechanism in saturated porous sand in an ionic solution. Overall, the results provided useful implications to estimate colloids (and hence colloid-facilitated transport of contaminants) to reach groundwater under varying ionic strengths.

ACKNOWLEDGMENT

This work was supported by the Department of Civil Engineering, University of Peradeniya. We also acknowledge Eng. Anthony, technical staff of the Geotechnical Laboratory and Engineering workshop for the guidance and assistance provided throughout this study.

REFERENCES

- [1] Mccarthy, Zachara "ES&T Features: Subsurface transport of contaminants," J. E. S. and Technology 1989, vol. 23, pp. 496-502.
- [2] J. Zhuang, Y. Jin, M. J. Flury, "Comparison of Hanford colloids and kaolinite transport in porous media," V. Z. J. 2004, vol. 3, pp. 395-402.
- [3] E. M. Alissa, G. A. J. Ferns, "Heavy metal poisoning and cardiovascular disease," J. O. T. 2011.
- [4] A. J. Karathanasis, "Subsurface migration of copper and zinc mediated by soil colloids", Soil Sci. Soc. Am. J. 1999, vol. 63, pp.830-838.
- [5] A. J. Karathanasis, "Colloid - mediated transport of Pb through soil porous media," I. J. O. E. S. 2000, vol. 57, pp. 579-596.
- [6] G. Chen, M. Flury, J. B. Harsh, P. C. Lichtner, "Colloid-facilitated transport of cesium in variably saturated Hanford sediments," J. E. S. and Technology 2005, vol. 39, pp. 3435-3442.
- [7] M. Almaguer, R. Herrera and C. M. J. M. R. Orantes, "Chronic kidney disease of unknown etiology in agricultural communities," vol. 16, pp. 09-15, 2014.
- [8] L. Järup, "Hazards of heavy metal contamination," J. B. M. B. 2003, vol. 68, pp. 167-182.
- [9] World health statistics 2012, 1.Health status indicators. 2.World health. 3.Health services - statistics. 4.Mortality. 5.Morbidity. 6.Life expectancy. 7.Demography. 8.Millennium development goals - statistics. 9.Statistics. I.World Health Organization, 2012.
- [10] A. V. Ranasinghe, G. W. G. P. Kumara, R. H. Karunarathna, A. P. De Silva, K. G. D. Sachintani, J. M. C. N. Gunawardena, S. K. C. R. Kumari, M. S. F. Sarjana, J. S. Chandraguptha, M. V. C. De Silva, "The incidence, prevalence and trends of Chronic Kidney Disease and Chronic Kidney Disease of uncertain aetiology (CKDu) in the North Central Province of Sri Lanka: an analysis of 30,566 patients," BMC Nephrology 2019, pp. 20-338.
- [11] R. Chandrajith, S. Nanayakkara, K. Itai, T. Aturaliya, C. Dissanayake, T. Abeyssekera, K. Harada, T. Watanabe, A. J. E. G. Koizumi, "Chronic kidney diseases of uncertain etiology (CKDu) in Sri Lanka: geographic distribution and environmental implications," Health 2011, vol. 33, pp. 267-278.
- [12] C. Jayathilake, V. Rizliya, R. Liyanage, "Antioxidant and free radical scavenging capacity of extensively used medicinal plants in Sri Lanka," J. P. F. S. 2016, vol. 6, pp. 123-126.
- [13] C.B. Dissanayake and R. Chandrajith, "Groundwater fluoride as a geochemical marker in the etiology of chronic kidney disease of unknown origin in Sri Lanka", C. J. of Science 2017, vol. 46(2), pp. 3-12.
- [14] W. P. R. T. Perera, M. D. N. R. Dayananda, J. A. Liyanage, "Exploring the Root Cause for Chronic Kidney Disease of Unknown Etiology (CKDu) via Analysis of Metal Ion and Counterion Contaminants in Drinking Water: A Study in Sri Lanka", J. of Chemistry 2020, vol. 2020, Article ID 8670974.
- [15] L. Harada, L. Hellström, T. Alfvén, "Low level exposure to cadmium and early kidney damage: the OSCAR study," O. and E. Medicine 2000, vol. 57, no. 10, pp. 668-672.
- [16] S. Thijssen, J. Maringwa, C. Faes, I. Lambrichts, and E. Van Kerkhove, "Chronic exposure of mice to environmentally relevant, low doses of cadmium lead to early renal damage, not predicted by blood or urine cadmium levels," Toxicology 2007, vol. 229, no. 1-2, pp. 145-156.
- [17] N. M. Denovio, J. E. Saiers, J. N. J. Ryan, "Colloid movement in unsaturated porous media," V. Z. J. 2004, vol. 3, pp. 338-351.
- [18] S. Satarug, M. Nishijo, J. M. Lasker, R. J. Edwards, and M. R. Moore, "Kidney dysfunction and hypertension: role for cadmium, p450 and heme oxygenases?," T. J. of Experimental Medicine, 2006, vol. 208, no. 3, pp. 179-202.
- [19] A. Menke, P. Muntner, E. K. Silbergeld, E. A. Platz, and E. Guallar, "Cadmium levels in urine and mortality among U.S. adults," Environmental Health Perspectives 2009, vol. 117, no. 2, pp. 190-196.
- [20] S. D'iez, "Human health effects of methylmercury exposure," Reviews of Environmental Contamination and Toxicology 2009, vol.198, pp. 111-132.
- [21] J. Šimůnek, M. Šejna, H. Saito, M. Sakai, and M. Th. van Genuchten, "The HYDRUS-1D Software Package for Simulating the Movement of Water, Heat, and Multiple Solutes in Variably Saturated Media," Version 4.17, HYDRUS Software Series 3, Department of

Environmental Sciences, University of California Riverside, Riverside, California, USA, 2013, pp. 343, 2013.

- [22] J. Šimůnek, C. He, L. Pang, S. J. Bradford, "Colloid-facilitated solute transport in variably saturated porous media," *V. Z. J.* 2006, vol. 5, pp. 1035-1047.
- [23] S. A. Bradford, J. Simunek, M. Bettahar, M. T. V. Genuchten, S. R. Yates, "Modeling Colloid Attachment, Straining, and Exclusion in Saturated Porous Media," *Environ. Sci. Technol.* 2003, vol. 37, pp. 2242-2250.
- [24] P. Rosin, E. Rammler, "The laws governing the fineness of powdered coal", *J. Inst. Fuel.* 1933, vol. 7, pp. 29-36.
- [25] J. Matusiak and E. G. M. Curie-Sklodowska, "Stability of colloidal systems – a review of the stability measurements methods" 2017, *Sq.* 3, pp. 20-031.
- [26] J. N. Ryan, M. Elimelech, "Colloid mobilization and transport in groundwater," *Colloids and Surfaces, Physicochemical and Engineering Aspects* 107, 1996, vol. 1, pp. 5.

Density Effects on Soil Gas Diffusivity in Agricultural Soils

Tharindi Lakshani
Department of Civil Engineering
University of Peradeniya
Peradeniya, Sri Lanka
mmtharindilakshani@gmail.com

Chamindu Deepagoda
Department of Civil Engineering
University of Peradeniya
Peradeniya, Sri Lanka
chaminduk@pdn.ac.lk

Abstract—Accurate prediction of soil- gas diffusivity (D_p/D_o : where D_p and D_o are gas diffusion coefficients in soil and free air, respectively) and its variation with soil physical conditions (e.g., soil type/texture, soil density, soil moisture status) are important prerequisites for simulating subsurface gas migration and emission of greenhouse gases across soil-atmosphere continuum. Literature is abundant with studies using repacked soils for estimating soil-gas diffusivity, however they are unlikely to mimic realistic conditions in the subsurface, thereby leading to a marked mischaracterization of subsurface gas transport. In this study, measured soil-gas diffusivity in undisturbed soils sampled from differently characterized Danish soil profiles (total of 150 undisturbed soil samples) were used to investigate soil density effects on diffusive gas migration. The selected soils represent a wide range of natural and anthropogenic origins, including agricultural soils, forest soils, urban soils, landfill cover soils, etc. The measurements were within a selected range of matric potentials (-10 to -500 cm H_2O) typically representing natural field conditions in subsurface soil. The soils used for this study subjected to five different density categories (1.0-1.2, 1.2-1.4, 1.4-1.6, 1.6-1.8, 1.8-2.0 $g\ cm^{-3}$) and showed peak diffusivity within the range of 1.4-1.6 $g\ cm^{-3}$ as critical density window at a given suction. A series of predictive and descriptive gas diffusivity models were tested against the measured data for a model comparison. Results clearly distinguished the effect of soil structure status due to the accurate performance of SWLR model on measured diffusivity data.

Keywords— soil density, soil gas diffusivity, soil types, Predictive models

I. INTRODUCTION

According to the Intergovernmental Panel on Climate Change (IPCC) [1], emission of greenhouse gases (primarily carbon dioxide, methane, and nitrous oxide) lead to significant regional and global climate changes. Although main greenhouse gas production occurs in natural systems, anthropogenic sources such as landfills, agricultural fields, and constructed wetlands also have contributed to an increased atmospheric presence [2]. As a high potent greenhouse gas, Mosier [3] has mentioned that CH_4 contributes nearly 25% of anticipated global warming, nearly one-third of which occurs in terrestrial ecosystems [4]. Among anthropogenic sources, landfills are responsible for approximately 7 - 20% of CH_4 emissions [5]. The gas migration through soil system is linked to soil physical properties such as soil texture and soil structure (e.g. soil density/compaction) and is mainly controlled by the physical, chemical, and biological processes in unsaturated soil layers. Subsurface migration of gases through the soil air phase and their subsequent emission across the soil-atmosphere interface occurs predominantly by diffusion and, to a lesser degree, by near-surface pressure fluctuations as explained by Penman [6] and Poulsen et al. [5], respectively.

Asia-Pacific Network for Global Change Research (APN) grant – CRRP2020-07MY-Deepagoda.

Soil gas diffusivity (the ratio of gas diffusion coefficients in soil and free air, D_p/D_o) is the key parameter which describes the diffusive transport of gases in partially saturated soils. Since, measurement of D_p/D_o is complicated to perform and instrumentally challenging in situ with sufficient control of the initial and boundary conditions (Rolston et al. [7]; Rolston and Moldrup [8]; Werner et al. [9]), descriptive/predictive models are frequently used to estimate D_p/D_o values from easily measurable parameters such as air-filled porosity and total porosity. Notwithstanding the presence of a wide range of predictive models, soil density and its associated changes to soil structure have been sparsely investigated in literature, although some general studies about effects of soil density on soil aeration are available. Buckingham [10], Stepniewski [11], Currie [12], Xu [13], Shimamura [14], Fujikawa and Miyazaki [15] have examined the direct effect of soil density on the gas transport parameters. According to the studies by Stepniewski [11] and Xu [13] on gas diffusion in differently textured soils, the effect of bulk density on the relationship between D_p/D_o and ϵ was less and have showed contradictory conclusions. Moreover, the observation by Fujikawa and Miyazaki [15] and Hamamoto [16] at a given air-filled porosity ϵ , D_p/D_o increased with the increment of bulk density. As explained by Currie [12], there was not any single relationship which can describe the changes in D_p/D_o with ϵ at different bulk densities. In this study, density effects on soil gas diffusivity were examined using undisturbed soils with different levels of density/compactness sampled across Denmark representing urban, agricultural, forest sites and as well as a final landfill cover soil.

II. MATERIALS AND METHODS

A. Soils, sampling sites, and data

In this study, total of 150 literature data on undisturbed soil samples were considered. Soil samples were taken from eight different locations across Denmark, representing a wide range of soil texture, total porosities, and horizons. Undisturbed soil samples were collected using 100 cm^3 annular cores with 0.061 m internal dia., and 0.034 m length. Care was taken to ensuring minimum disturbance during sampling by driving the sharpened edge of annular core into the soil by means of a hammer. To prevent preferential air flow through the annular gap between the core and the sample, the end surfaces were trimmed, and the edges were kneaded with a knife. After that, the samples were end-capped and stored at 2°C. In the following text, soils are referred to as their sampling location (Skellingsted, Hjørring, Rønhave, Foulum, Jyndeved, Mammen, Gjorslev, and Poulstrup).

Urban soils were sampled at Skellingsted site which was located adjacent to an unlined municipal landfill operated as a dump of municipal solid and industrial waste from 1971 to 1990. According to Christophersen and Kjeldsen [17], the

landfill was covered with 80 cm of sand and 20 cm of topsoil at the final closure and soil samples were collected at 70 cm depth. Hjørring also represents an urban soil which were sampled from a deep vadose zone profile from 4 to 5 m and 6 to 7 m depths at a former municipal gas work site. Both gas diffusivity data for Skellingsted and for Hjørring were partly presented by Poulsen [5] and Moldrup [18].

Under agricultural soils, Mammen and Gjorslev agricultural field soils and three lysimeter soils (Rønhave, Foulum, and Jyndeved) were included from Kawamoto [19,20]. Three lysimeter soils were excavated from the three locations, soils were air dried, crumbled to aggregates < 20 mm, and then packed in the bins incrementally in 10 cm layers to the same dry bulk density as occurred in the field located at Aarhus University, the Faculty of Agricultural Sciences at Research Centre Foulum. For further details on management and treatment practices of soils before sampling and packing procedure Kawamoto [20] and Lamandé [21] were referred respectively. Notably, Mammens and Gjorslev agricultural soil sites have been in agricultural use for centuries. Forest soil data from two medium-organic sandy layers collected in a natural mixed hardwood forest at Poulstrup representing two depth intervals, 10 to 15 cm depth and 15 to 20 cm depth (Kruse [22], Moldrup [23]). Details of each layer for selected soils are given in Table I.

The distribution of soil textural classes for all 150 soil samples is illustrated in Fig 1. This Figure indicates that, except one clay layer from Hjørring (at 4.10 m depth), almost all the soil samples/layers from eight different locations can be texturally characterized as sand or sandy soils.

B. Measurement methods

To obtain the desired soil matric potentials for all soil samples, the method proposed by Klute [25] was used as follows. First, 100 cm³ undisturbed soil cores were saturated inside sand boxes and samples were drained to the intended

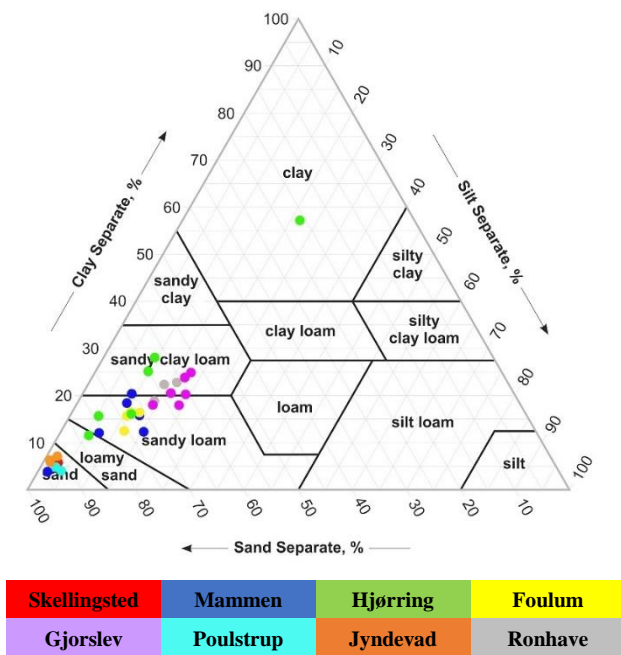


Fig. 1. Distribution of soil texture classes of 150 soil samples considered in this study

matric potential (ψ) using either hanging water columns or suction and pressure plate systems for $\psi > -100$ cm H₂O and for $\psi < -100$ cm H₂O, respectively. Matric potentials were selected in the range of -10 to -500 cm H₂O.

Using the one-chamber experimental setup initially presented by Taylor [26] and further developed by Schjønning [27], the values of D_p/D_0 through soil samples were obtained. First, the chamber was flushed with 99.99% N₂ gas to make the chamber free of O₂. Then undisturbed soil core was placed on the chamber allowing atmospheric O₂ to diffuse through the soil sample into the chamber. Following the method outlined by Rolston and Moldrup [9], O₂ diffusion coefficient in soil (D_p) was calculated. As explained by Schjønning [28], time taken for each measurement differed due to the applied matric potential on soil sample and O₂ depletion due to microbial consumption can be neglected.

III. STATISTICAL ANALYSIS

To compare and test for general accuracy and tendency for overprediction or underprediction of existing models for gas diffusivity, two statistical indices were used as follows. RMSE was used to evaluate the model overall fit to the measured data.

$$RMSE = \sqrt{\frac{1}{n} \sum_{i=1}^n (d_i)^2} \quad (1)$$

Bias was used to evaluate whether a model over-estimated (positive bias) or under-estimated (negative bias) the observed data.

$$bias = \frac{1}{n} \sum_{i=1}^n (d_i) \quad (2)$$

where n is the number of measurements in the data set and d_i is the difference between the observed and predicted diffusivity values.

IV. EXISTING MODELS FROM LITERATURE

Among the wide range of gas diffusivity models, the pioneering empirical model was introduced by Buckingham [11] as per (3).

$$\frac{D_p}{D_0} = \varepsilon^2 \quad (3)$$

To prove this relationship, Buckingham used four different soils with varying moisture content and compactness, leading to conclude that gas diffusion in soils is not greatly affected by soil type. A series of single-parameter models were developed later by Penman [6]; Marshall [29]; Millington [30] in the given order. Later, by accounting density effects (implicitly) and soil type with the total porosity, Milington and Quirk [31,32] models were developed as soil type dependent models. Milington and Quirk 1960 [31] model is shown by (4):

$$\frac{D_p}{D_0} = \frac{\varepsilon^2}{\phi^{2/3}} \quad (4)$$

As per (5), Milington and Quirk 1961 [32] model is shown below:

TABLE I. SAMPLING LOCATIONS, DEPTHS, AND SOIL PHYSICAL CHARACTERISTICS

Location	Depth (m)	Texture	Clay %	Silt %	Sand %	Organic matter %	Total porosity #	Reference
Skellingsted	0.70	Sand	5.1	2.0	92.9	1.7	0.359 (0.020)	Poulsen [5]
Hjørring	4.00-4.50	Sandy clay loam	24.8	9.2	65.9	0.2	0.449 (0.040)	Moldrup [18]
Hjørring	4.10	Clay	56.6	21.0	22.3	0.2	0.502	Moldrup [18]
Hjørring	4.50-5.00	Sandy clay loam	26.9	9.2	63.9	0.2	0.456 (0.032)	Moldrup [18]
Hjørring	6.00-6.50	Sandy loam	15.7	10.8	73.4	2.1	0.382 (0.042)	Moldrup [18]
Hjørring	6.50-7.00	Loamy sand	11.2	5.0	83.8	1.6	0.404 (0.052)	Moldrup [18]
Gjorslev	0.05-0.25	Sandy clay loam	17.4	18.6	64.1	2.6	0.378 (0.013)	Kawamoto [19,20]
Gjorslev	0.33-0.53	Sandy clay loam	17.2	14.1	68.7	0.3	0.369 (0.008)	Kawamoto [19,20]
Gjorslev	0.80-1.00	Sandy clay loam	19.3	19.1	61.6	0.2	0.338 (0.013)	Kawamoto [19,20]
Gjorslev	2.05-2.25	Sandy clay loam	24.1	17.3	58.6	0.2	0.321 (0.006)	Kawamoto [19,20]
Gjorslev	3.50-3.70	Sandy clay loam	22.8	17.0	60.1	0.3	0.291 (0.008)	Kawamoto [19,20]
Gjorslev	4.65-4.85	Sandy clay loam	19.7	15.6	64.7	0.4	0.306 (0.037)	Kawamoto [19,20]
Mammen	0.05-0.25	Sandy loam	11.6	14.8	73.6	3.4	0.435 (0.005)	Kawamoto [19,20]
Mammen	0.30-0.50	Sandy clay loam	15.2	12.4	72.4	0.4	0.347 (0.013)	Kawamoto [19,20]
Mammen	1.10-1.30	Sandy clay loam	19.5	9.0	71.5	0.1	0.322 (0.005)	Kawamoto [19,20]
Mammen	2.05-2.15	Sandy clay loam	17.9	8.6	73.5	0.1	0.321 (0.010)	Kawamoto [19,20]
Mammen	3.40-3.60	Sandy loam	11.3	6.7	82.0	0.1	0.352 (0.010)	Kawamoto [19,20]
Mammen	5.40-5.60	Sand	3.6	0.9	95.5	0.0	0.389 (0.011)	Kawamoto [19,20]
Rønhave	0.00-0.30	Sandy clay loam	17.9	13.1	69.0	2.3	0.450 (0.025)	Kawamoto [19,20]
Rønhave	0.30-0.70	Sandy clay loam	21.7	13.5	64.8	0.5	0.436 (0.012)	Kawamoto [19,20]
Rønhave	0.70-1.40	Sandy clay loam	21.8	15.8	62.4	0.3	0.415 (0.010)	Kawamoto [19,20]
Foulum	0.00-0.30	Sandy loam	11.8	11.3	77.0	2.3	0.539 (0.020)	Kawamoto [19,20]
Foulum	0.30-0.60	Sandy loam	15.0	10.2	74.9	0.5	0.389 (0.017)	Kawamoto [19,20]
Foulum	0.60-0.90	Sandy clay loam	16.0	12.0	71.9	0.2	0.393 (0.002)	Kawamoto [19,20]
Foulum	0.90-1.40	Sandy clay loam	16.3	10.5	73.2	0.1	0.350 (0.005)	Kawamoto [19,20]
Jydevad	0.00-0.30	Loamy sand	5.9	2.1	91.9	1.9	0.469 (0.019)	Kawamoto [19,20]
Jydevad	0.30-0.70	Loamy sand	6.0	0.5	93.5	0.7	0.458 (0.010)	Kawamoto [19,20]
Jydevad	0.70-1.40	Loamy sand	5.2	0.7	94.1	0.2	0.438 (0.013)	Kawamoto [19,20]
Poulstrup	0.10-0.15	Sand	3.7	3.1	93.2	3.7	0.519 (0.021)	Kruse [22]
Poulstrup	0.15-0.20	Sand	4.3	2.6	93.1	4.1	0.539 (0.031)	Moldrup [23]

Average values are given. Values in parentheses are standard deviations.

† Soil textures are classified based on the International Soil Science Society (ISSS) standard (Verheye and Ameryckx, [24])

$$\frac{D_p}{D_0} = \frac{10}{\varepsilon^3} \frac{1}{\Phi^2} \quad (5)$$

Normally wet soils show large tortuosity for gas diffusion due to the generation of narrow pore throats between soil particles. Considering a water-induced linear reduction (WLR) of gas diffusivity in the presence of water, WLR–Marshall model (Moldrup [33]) was developed. The WLR model is expressed as (6):

$$\frac{D_p}{D_0} = \varepsilon^{1.5} \left(\frac{\varepsilon}{\Phi} \right) \quad (6)$$

With the lack of clear guidelines for model choice at a given soil state, the new structure-dependent WLR model (SWLR) was developed. By assuming a difference between the structureless soil state and the intact soil state, a porous media complexity factor, C_m , was introduced for the extension

of WLR model. Using 290 soils representing well across soil depths, compaction, and texture, Moldrup [34] observed an excellent performance of SWLR model with $C_m = 2.1$ for gas diffusion of intact soils. As per (7), The SWLR model takes the form of:

$$\frac{D_p}{D_0} = \varepsilon^{(1+C_m\Phi)} \left(\frac{\varepsilon}{\Phi} \right) \quad (7)$$

V. RESULTS AND DISCUSSION

A. Effects of density and air-filled porosity

Fig. 2 shows measured D_p/D_0 plotted against air filled porosity for all soil samples divided into five density categories in the ranges of 1.0-1.2, 1.2-1.4, 1.4-1.6, 1.6-1.8, 1.8-2.0 g cm⁻³. As commonly observed D_p/D_0 increased with the increase of air-filled porosity irrespective of the density. It can be seen that except for range E which had its data confined to the lower ε region ($\varepsilon < 0.06$), all the density categories had

D_p/D_0 values that ranged across the entire ϵ with relatively little scatter. This behavior can be explained by agreeing well with Fujikawa and Miyazaki [15]. The increase in D_p/D_0 with bulk density is due to the changes in the soil pore configuration (i.e., change in shape of soil pores) due to the natural compaction, resulting in a relative increase in the effective pore space. With the density increment of soils, volumetric solid content is increased with less water content, which creates less water bridging between particles and less water-induced tortuosity, leading to higher diffusivity values. As shown in Fig. 2, density category C gives the highest D_p/D_0 values with the less effect of ineffective pore space. Thereafter D_p/D_0 values again started to decrease due to less effective pore space since close packing and pore configuration.

Further to discuss the effect of bulk density, diffusivity data at two soil water matric potentials were selected. Fig. 3(a) and (b) illustrate the two dimensional graphical representations of soil gas diffusivity vs bulk density at suction levels corresponding to $pF = 1.7$ (-50 cm H₂O) and 2.0 (-100 cm H₂O), respectively (note: $pF = \log |\Psi, \text{cm H}_2\text{O}|$).

Millington Quirk (1961), Buckingham (1904), WLR-Marshall, and SWLR predictive models for gas diffusivity were presented by solid lines. Maximum air filled porosity values at 1.40 g cm⁻³ bulk density for $pF = 1.7$ and 2.0 were used as reference values to generate predictive model lines. Selected models were able to capture the measured diffusivity values at middle range of density values, while overpredicting those at less and high densities. Note that the air-filled porosity variations (ϵ) across the bulk density are illustrated using 10 and 9 different air-filled porosities at $pF = 1.7$ and 2.0, respectively. Fig. 3(a) and (b) clearly demonstrate the presence of a density window which resulted a peak in gas diffusivity. This is against the generally expected tendency of decreasing gas diffusivity with increasing density. At a given suction, water is held in lower densities (1.1-1.3 g cm⁻³) with high total porosity within larger pores creating additional water induced tortuosities for gas diffusion. Therefore, even at the same air-filled porosity, lower densities yielded lower diffusivities than higher densities due to the presence of high-water content surrounding the air-filled pores. At very high densities (1.6-1.8 g cm⁻³) (with smaller total porosity), although the presence of water is less, the air-filled pore space is also less, and water is held in capillary-dominated smaller pores thus constraining the gaseous phase pore connectivity.

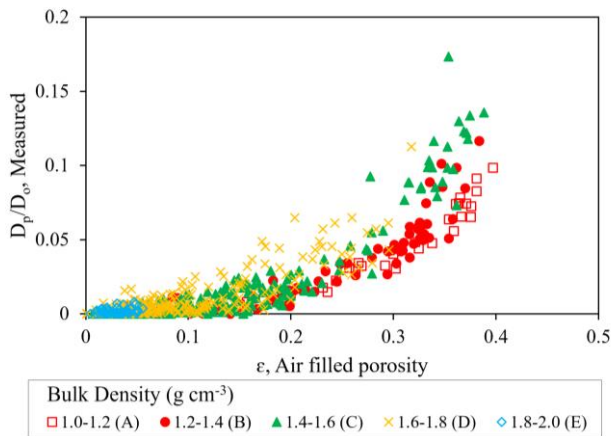


Fig. 2. Measured Gas diffusivities (D_p/D_0) against air - filled porosity (ϵ) for selected soils based on different density levels.

As a result, a diffusivity peak occurred at a medium-dense soil (1.4-1.6 g cm⁻³)

The observed peaks, however, did not occur under the same density for the two selected suction levels, implying that the peak location is moisture dependent. At higher suction ($pF = 2.0$), the D_p/D_0 peaked at a higher density as compared to the peak occurred at the lower suction ($pF = 1.7$). This is due to the fact that more and more small-sized pores get drained at higher suction levels thus shifting the peak location towards the high-density direction.

B. Gas diffusivity model performances

The predicted gas diffusivity plotted against the measured soil gas diffusivity are shown in scatterplots in Fig. 4, using Buckingham (1904) (3), Millington Quirk (1961) (5), WLR - Marshall model (6), and SWLR model (7). Using RMSE (1) and bias (2) model performances were statistically evaluated. The detailed statistical analysis is given in Table II. According

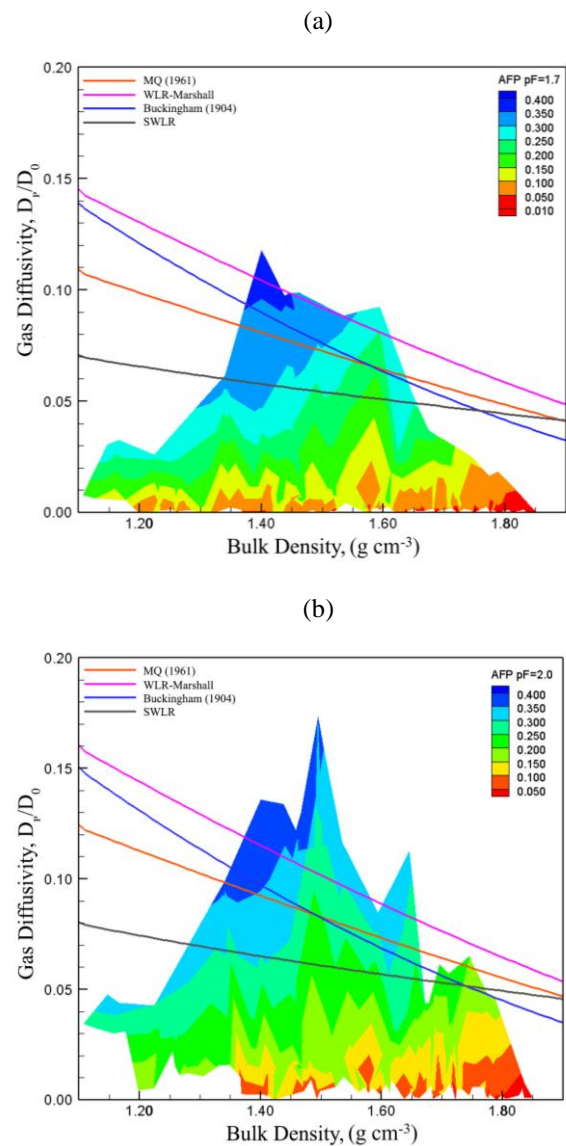


Fig. 3. Variation in soil gas diffusivity (D_p/D_0) for different bulk densities under different air-filled porosities (AFP) (a) at $pF = 1.7$ (-50 cm H₂O) soil water matric potential (b) at $pF = 2.0$ (-100 cm H₂O) soil water matric potential. The solid lines illustrate the predictions from selected gas diffusivity models.

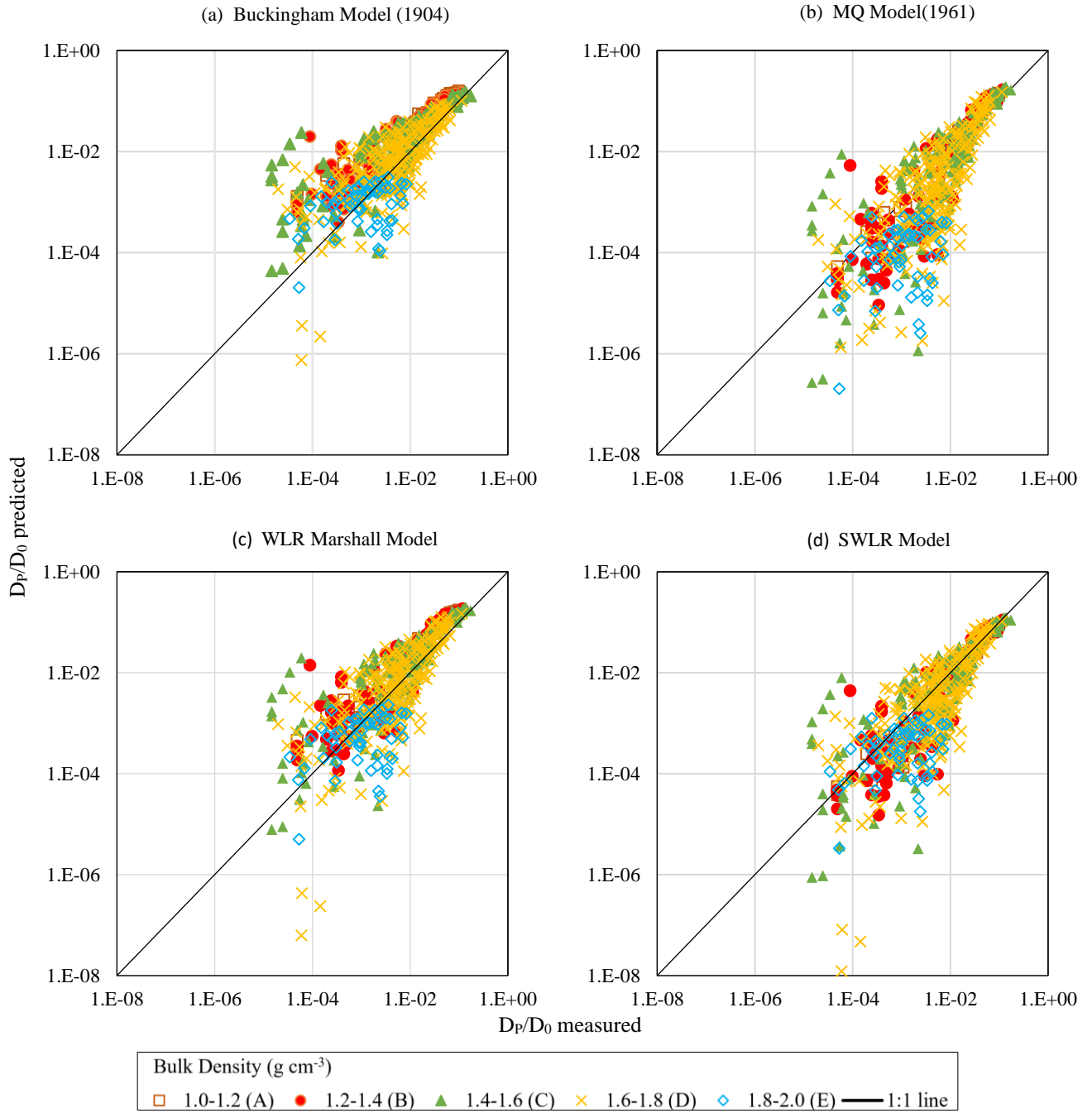


Fig. 4. Scatterplot comparison of measured and predictive D_p/D_0 data points of A, B, C, D and E bulk density ranges for four existing models: (a) the Buckingham model (1904) (3), (b) Millington Quirk (1961) model (5), (c) the WLR-Marshall model (6), and (d) SWLR model (7)

to the statistical analysis WLR-Marshall (Moldrup [33]), indicates the weakest performance among the existing models with a significant overprediction. The Millington and Quirk (1961) model markedly overpredicted D_p/D_0 at higher air-filled porosities and grossly underpredicted D_p/D_0 at low air-filled porosities, as typically observed in the literature. Buckingham (1904), one of the earliest work on soil gas diffusivity, performed well on most of the soil than MQ (1961). Overall, above mentioned classical models (WLR-Marshall, MQ (1961), Buckingham) lead to a marked bias of estimated values as compared to observations, probably due to the lack of provisions to structure dependability of the soils. Notably, structure dependent water induce linear reduction (SWLR) model, outperformed the other classical models, yielding minimum RMSE and bias values as the best performed one to capture gas diffusivity behavior across soil

texture and compaction levels accurately. Less-dense soils are better predicted than high dense soils by SWLR model. Normally at high densities, micropores are dominant and even at high suction levels water is held by capillary action. Due to this, water induced effects on diffusivity are high and leads to large scatter at high densities.

TABLE II. PERFORMANCE OF SELECTED MODELS AGAINST THE MEASURED D_p/D_0 DATA EXPRESSED IN TERMS OF RMSE AND BIAS

Model	Equation	RMSE	Bias
Buckingham (1904)	$D_p/D_0 = \varepsilon^2$	0.0208	0.0109
Millington Quirk (1961)	$D_p/D_0 = \varepsilon^{10/3}/\Phi^2$	0.0177	0.0056
WLR – Marshall	$D_p/D_0 = \varepsilon^{1.5}(\varepsilon/\Phi)$	0.0268	0.0137
SWLR	$D_p/D_0 = \varepsilon^{(1+C_m\Phi)}(\varepsilon/\Phi)$	0.0083	-0.0003

VI. CONCLUSIONS

This study investigated the density effects on soil gas diffusivity of agricultural soils subjected to matric potentials between -10 cm to -500 cm H₂O as usual subsurface moisture conditions. Total 150 Danish soil samples were studied to evaluate the effect of density, air filled porosity, D_p/D_o and comparison of predictive model performances. Results identified a critical density window (1.4-1.6 g cm⁻³) which resulted in a peak in D_p/D_o at a given suction status. The location of peak shifted to a higher density at higher suction level, and hence was moisture dependent. The measured data were compared with three existing models for estimating soil diffusivity which yielded a marked disparity since none of them considered the soil structure status. The SWLR model accurately characterized the measured D_p/D_o data and statistically outperformed the other three models. Overall, the results confirmed a pronounced effect of soil density on diffusive transport of gases in partially saturated soils and emphasized the need of selective model applications to accurately characterize soil density effects.

ACKNOWLEDGMENT

The authors gratefully acknowledge the financial support from Asia -Pacific Network for Global Change Research (APN) grant – CRRP2020-07MY- Deepagoda.

REFERENCES

- [1] Intergovernmental Panel on Climate Change. 2007. Observations: Surface and atmospheric climate change. In *Climate change 2007: The physical science basis*. Cambridge Univ. Press, Cambridge, UK.
- [2] Bartlett, K.B., and R.C. Harriss. 1993. Review and assessment of methane emissions from wetlands. *Chemosphere* 26:261–320.
- [3] Mosier, A.R. 1998. Soil processes and global change. *Biol. Fertil. Soils* 27:221–229.
- [4] Smith, K.A., T. Ball, F. Conen, K.E. Dobbie, J. Massheder, and A. Ray. 2003. Exchange of greenhouse gases between soil and atmosphere: Interactions of soil physical factors and biological processes. *Eur. J. Soil Sci.* 54:779–791.
- [5] Poulsen, T.G., M. Christophersen, P. Moldrup, and P. Kjeldsen. 2001. Modeling lateral gas transport in soil adjacent to old landfill. *J. Environ. Eng.* 127:145–153.
- [6] Penman, H.L. 1940. Gas and vapor movements in soil: The diffusion of vapors through porous solids. *J. Agric. Sci.* 30:437–462.
- [7] Rolston, D.E., R.D. Glauz, G.L. Grundmann, and D.T. Louie. 1991. Evaluation of an in-situ method for measurement of gas diffusivity in surface soils. *Soil Sci. Soc. Am. J.* 55:1536–1542.
- [8] Rolston, D.E., and P. Moldrup. 2002. Gas diffusivity. p. 1113–1139. In J.H. Dane and G.C. Topp (ed.) *Methods of soil analysis*. Part 4. SSSA Book Ser. 5. SSSA, Madison, WI.
- [9] Werner, D., P. Grathwohl, and P. Hohener. 2004. Review of field methods for the determination of the tortuosity and effective gas-phase diffusivity in the vadose zone. *Vadose Zone J.* 3:1240–1248.
- [10] Buckingham, E. 1904. Contributions to our knowledge of the aeration of soils. *Bur. Soil Bull.* 25. U.S. Gov. Print. Office, Washington, DC.
- [11] Stepniewski, W. 1981. Oxygen diffusion and strength as related to soil compaction. *Pol. J. Soil Sci.* 12:3–13.
- [12] Currie, J.A. 1984. Gas diffusion through soil crumbs: The effects of compaction and wetting. *J. Soil Sci.* 35:1–10.
- [13] Xu, X., J.L. Nieber, and S.C. Gupta. 1992. Compaction effect on the gas diffusion coefficient in soils. *Soil Sci. Soc. Am. J.* 56:174.
- [14] Shimamura, K. 1992. Gas diffusion through compacted sands. *Soil Sci.* 153:274–279.
- [15] Fujikawa, T., and T. Miyazaki. 2005. Effects of bulk density and soil type on the gas diffusion coefficient in repacked and undisturbed soils. *Soil Sci.* 170:892–901.
- [16] Hamamoto, S., P. Moldrup, K. Kawamoto, and T. Komatsu. 2009a. Effect of particle size and soil compaction on gas transport parameters in variably saturated, sandy soils. *Vadose Zone J.* 8:1–10.
- [17] Christophersen, M., and P. Kjeldsen. 2001. Lateral gas transport in soil adjacent to an old landfill: Factors governing gas migration. *Waste Manage. Res.* 19:579–594.
- [18] Moldrup, P., T. Olesen, P. Schjønning, T. Yamaguchi, and D.E. Rolston. 2000b. Predicting the gas diffusion coefficient in undisturbed soil from soil water characteristics. *Soil Sci. Soc. Am. J.* 64:94–100.
- [19] Kawamoto, K., P. Moldrup, P. Schjønning, B.V. Iversen, T. Komatsu, and D.E. Rolston. 2006a. Gas transport parameters in the vadose zone: Development and tests of power-law models for air permeability. *Vadose Zone J.* 5:1205–1215.
- [20] Kawamoto, K., P. Moldrup, P. Schjønning, B.V. Iversen, D.E. Rolston, and T. Komatsu. 2006b. Gas transport parameters in the vadose zone: Gas diffusivity in field and lysimeter soil profiles. *Vadose Zone J.* 5:11.
- [21] Lamandé, M., P. Schjønning, and F.A. Tøgersen. 2007. Mechanical behaviour of an undisturbed soil subjected to loadings: Effects of load and contact area. *Soil Tillage Res.* 97:91–106.
- [22] Kruse, C.W., P. Moldrup, and N. Iversen. 1996. Modeling diffusion and reaction in soils: II. Atmospheric methane diffusion and consumption in forest soil. *Soil Sci.* 161:355–365.
- [23] Moldrup, P., C.W. Kruse, D.E. Rolston, and T. Yamaguchi. 1996. Modeling diffusion and reaction in soils: III. Predicting gas diffusivity from the Campbell soil water retention model. *Soil Sci.* 161:366–375.
- [24] Verheye, W., and J. Ameryckx. 1984. Mineral fractions and classification of soil texture. *Pedologie* 2:215–225.
- [25] Klute, A. 1986. Water retention: Laboratory methods. p. 635–662. In A. Klute (ed.) *Methods of soil analysis*. Part 1. 2nd ed. SSSA Book Ser. 5. SSSA, Madison, WI.
- [26] Taylor, S.A. 1949. Oxygen diffusion in porous media as a measure of soil aeration. *Soil Sci. Soc. Am. Proc.* 14:55–61.
- [27] Schjønning, P. 1985. A laboratory method for determination of gas diffusion in soil. (In Danish with English summary.) Rep. S1773. Danish Inst. of Plant and Soil Sci., Tjele.
- [28] Schjønning, P., I.K. Thomsen, J.P. Møberg, H. de Jonge, K. Kristensen, and B.T. Christensen. 1999. Turnover of organic matter in differently textured soils: I. Physical characteristics of structurally disturbed and intact soils. *Geoderma* 89:177–198.
- [29] Marshall, T.J. 1959. The diffusion of gases through porous media. *J. Soil Sci.* 10:79–82.
- [30] Millington, R.J. 1959. Gas diffusion in porous media. *Science* 130:100–102.
- [31] Millington, R.J., and J.M. Quirk. 1960. Transport in porous media. p. 97–106. In F.A. Van Beren et al. (ed.) *Trans. Int. Congr. Soil Sci.*, 7th, Madison, WI. 14–21 Aug. 1960. Vol. 1. Elsevier, Amsterdam.
- [32] Millington, R.J., and J.M. Quirk. 1961. Permeability of porous solids. *Trans. Faraday Soc.* 57:1200–1207.
- [33] Moldrup, P., T. Olesen, J. Gamst, P. Schjønning, T. Yamaguchi, and D.E. Rolston. 2000a. Predicting the gas diffusion coefficient in repacked soil: Water induced linear reduction model. *Soil Sci. Soc. Am. J.* 64:158.
- [34] Moldrup P., Chamindu Deepagoda T.K.K., Hamamoto S., Komatsu T., Kawamoto Rolston D.E. & Wollensen de Jonge L. (2013) Structure-dependent water-induced linear reduction model for predicting gas diffusivity and tortuosity in repacked and intact soil. *Vadose Zone Journal* 12. doi: 10.2136/vzj2013.03.0061.

A Study on Impact of Three-wheelers in Urban Traffic Congestion

Tharamasinghe A.I.
Department of Civil Engineering
University of Peradeniya
Peradeniya, Sri Lanka
tharamasinghai@gmail.com

Jayasooriya J.A.D.G.
Department of Civil Engineering
University of Peradeniya
Peradeniya, Sri Lanka
dumidu3@gmail.com

Dharmarathna W.R.S.S.
Department of Civil Engineering
University of Peradeniya
Peradeniya, Sri Lanka
samal@eng.pdn.ac.lk

Edirisinghe A.G.H.J.
Department of Civil Engineering
University of Peradeniya
Peradeniya, Sri Lanka
jayalath@eng.pdn.ac.lk

Abstract— Three-wheelers have become one of the most famous informal public transport systems in South Asia and identified as a major factor for causing urban traffic congestion. According to the Department of motor traffic, 1,159,158 registered three-wheelers exist in Sri Lanka at the end of 2018 and it is approximately 15% of the total vehicle population during the considered period. Accordingly, this study is formulated to examine the effect of three-wheelers on urban traffic. Kandy Municipal area was selected for the case study and video surveys were carried out to examine the impact of three-wheeler parking issues. Data regarding three-wheeler volume were extracted from the Traffic Survey at Gatambe Junction, Kandy conducted by RDA in 2018. In addition, a questionnaire survey was conducted among 203 three-wheeler drivers to study their demographic details, habits and driving carrier information. From the analyzed results, it was revealed that only 18.7% of three-wheeler drivers have properly learnt to drive three-wheelers from qualified trainers. 61.6% of them have learnt within less than 30 days. This confirms that they are suffering from a lack of proper training towards their career. Also, it is clearly visible from the results that three-wheelers are highly contributing to the traffic congestion. By providing a proper training and recognition for the drivers who drive three-wheelers as a profession and introducing separate parking facilities with the intervention of local government by avoiding on-street parking may help drastically to reduce the prevailing traffic congestion due to the three-wheelers.

Keywords— *three-wheelers, urban traffic, drivers' behaviour, informal public transportation*

I. INTRODUCTION

Three-wheelers were introduced to Sri Lanka in 1978, due to lack of the last-mile transport facilities in rural areas. Gradually it has become the most famous Informal Public Transport (IPT) system in Sri Lanka [1]. Many people especially who are living in urban areas use three-wheelers for fulfilling their day to day traveling purposes. Low cost, promptness, flexibility in door-to-door service and easiness of online taxi services make the three-wheeler more popular among general public. According to the records of Department of motor traffic, it can be clearly visible that year by year three-wheeler population has increased. Figure 1 shows the increase of three-wheeler population from 2007 to 2019 based on data obtained from the Department of motor traffic [2]. Increasing three-wheeler volume is highly effective to the urban traffic congestion since it is main IPT system in Sri Lanka.

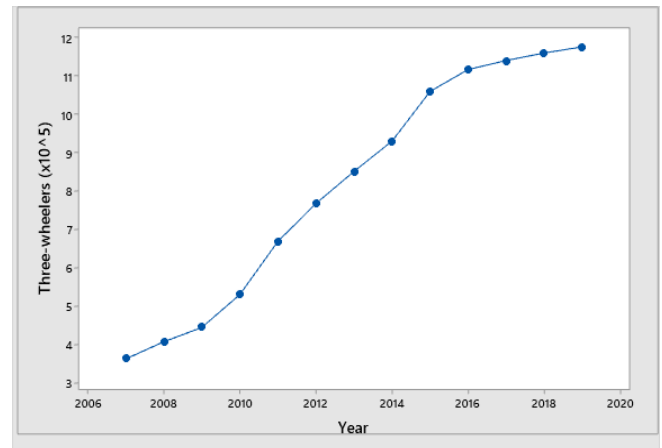


Fig. 1. Annual variation of three-wheeler population from 2007 to 2019

Three-wheelers make negative impacts on the urban transport system in many ways such as illegal or improper parking, aggressive driving, overloading, and creating situation to end up with traffic accidents etc. As calculated in 2012, Sri Lanka lost 40 billion LKR per annum due to the traffic congestion which is about 1.5% of their Gross Domestic Production (GDP) [3]. Hence, it is timely worth to examine how the three-wheelers influence on the urban traffic. Such influences are hardly examined in the literature with limited studies have been carried out on three-wheeler crashers, effect of three-wheeler parking near intersections and negative and positive impact to the society from three-wheelers etc.

This study was conducted in highly urbanized Kandy Municipal Council (KMC) area. Kandy traffic congestion have had a significant social and economic impact on the residents of Kandy through causing inconvenience. Within the KMC territory, about 0.18 million people live, and more than 50,000 vehicles pass through on a daily basis [4]. 169 three-wheeler parks are located in KMC area and 1813 three-wheeler drivers have registered in these three-wheeler parks.

Objectives of this study are to examine the effect of three-wheeler drivers' behaviour on urban traffic and identify the most affected factors, to examine the three-wheeler parking issues on urban traffic with their parking type and location, to examine the volume of three-wheelers which enter to KMC through the main roads and giving most effective solutions to reduce the traffic congestion.

II. LITERATURE REVIEW

Three-wheelers are used in many developing countries in the world with different names; Tuk-tuk in Thailand, Tempo in Nepal, Auto-rickshaw in India, Tricycle in Bangladesh etc. [5]. Three-wheelers are used as a paratransit transport in those countries. Thaghaisankun & Nakamura described paratransit is an efficient road utilized mode, which handle many passengers, the excessive numbers and undisciplined driving which create more congestion and traffic accidents on the road [6]. In Sri Lankan context, three-wheelers play a major role in transportation modes.

Studying of three-wheeler drivers' behaviour is very important to perceive the social impacts to the traffic congestions.

Questionnaire survey carried out in five identical cities in Southern province of Sri Lanka revealed that three-wheeler drivers' behaviours cause a less reputation in the industry [7]. Further, the driver factors that affect the road traffic accidents have examined based on the characteristics of three-wheeler drivers [8]. In addition, it was identified that the nervousness and aggression on the roads are gradually rising which lead towards of congestion and possible fluidity of traffic flow [9]. A similar study carried out at signalized and un-signalized junctions during both peak times and off-peak traffic conditions further proved the effect of aggressive driving behaviour which influence the urban traffic flow [10]. Hence this confirmed that the characteristics of three-wheeler drivers significantly affect to the traffic congestion.

In Sri Lanka most of three-wheeler parks have been located either side of the road as on-street parks. Therefore, the issues in these parks always effect on traffic flow along the main road.

Purnawan & Yousif, (1999) conducted video survey to investigate the effect of on-street parking for traffic congestion [11]. They have observed parking maneuver time for parallel on-street parking, angle on-street parking and illegal on-street parking and found that angle on-street parking has more impact on traffic congestion rather than other two parking styles. Praburam & Koorey, (2015) investigated the impact of on-street parking on traffic operations through the traffic survey [12]. They have chosen ten roads with various widths to observe the vehicular speed and shown that on-street parking has a noticeable effect on traffic speed. Three-wheeler parks which located in narrow roads and near intersections lead to the traffic congestion and accidents. Because of the limited public transportation system available on minor roads, many three-wheeler parks are located around such intersections in Sri Lanka. Gopallawa & Weerasekera, (2014) have carried out a traffic survey in selected locations to observe the influence of three-wheeler parking near intersections [13] and found that three-wheeler parks near intersections have negative impact on the road users.

Most three-wheelers are used to travel in town limits for fulfilling daily transport needs of people. Accordingly, it increases the number of three-wheelers in town limits and it is caused for the rapid development of the traffic congestion on urban traffic. KMC is already suffering from traffic problems [14] and three-wheelers are one of the major contributing factors.

The need for mobility in Sri Lanka increases due to high urbanization [15] and obviously bring more people to the road

network. The issue become more crucial when people move more towards the private transport.

III. DATA COLLECTION

Data collection was conducted under characteristics of three-wheeler drivers, three-wheeler parking issues that effect to urban traffic and volume of three-wheelers in KMC area.

Personal interviews using questionnaire and online questionnaire surveys were conducted among three-wheeler drivers to identify their characteristics. Demographic parameters of three-wheeler drivers, habits, aggressive behaviour on road and details of their driving career are the considered areas in the questionnaire. Target sample size was calculated as 190 using Cochran formula considering 85% confidence level [16]. However, with the pandemic situation of the country 150 samples were collected from personal interviews and 53 were collected from online questionnaire survey. So total sample size is 203.

Since most of three-wheeler parks are located as on-street parks it influences to urban traffic congestion. Video surveys were conducted to identify the three-wheeler parking issues on urban traffic and parking maneuvering time was observed. Two hours video survey was conducted for each three-wheeler park covering five three-wheeler parks. Both entering and leaving maneuvering times were observed in peak and off-peak time period. Figure 2 shows the three-wheeler park locations near the main roads in KMC area.

Three-wheeler volume data were gathered from a survey done in 2018 at Gatambe junction by Road Development Authority (RDA) [17]. Gatambe junction is one of the main entrance point to Kandy city because vehicles enter to KMC through both Sirimavo Bandaranaike Mawatha (A1) and Colombo-Kandy road on William Gopallawa Mawatha (AB42).

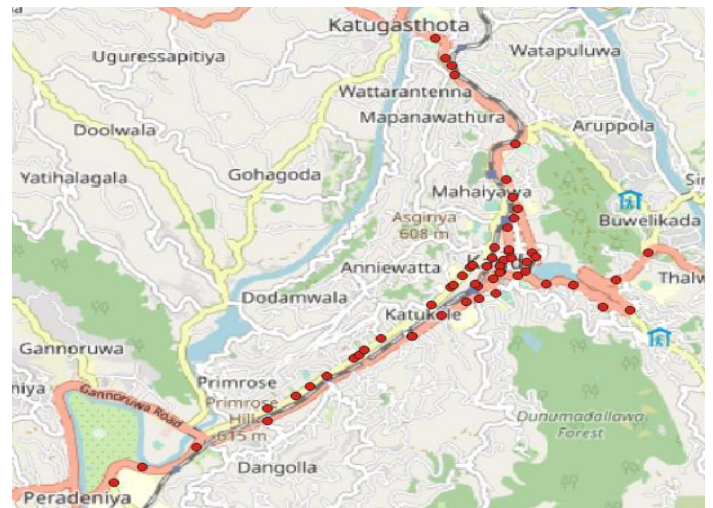


Fig. 2. The three-wheeler parks near to the main roads in KMC area

IV. DATA ANALYSIS AND RESULTS

Data analysis part was done for all three sections separately.

A. Effect of Three-wheeler Drivers' Behaviour

Questionnaire survey data collection was used to analyze their characteristics effect on urban traffic congestion. TABLE I shows the frequency percentage of factors under demographic parameters and driving career.

TABLE I. FREQUENCY PERCENTAGE OF FACTORS CONSIDER UNDER DEMOGRAPHIC PARAMETERS AND DRIVING CAREER

Factor	Demographic parameters		
	Variable	Frequency	Percentage
Gender	Male	203	100%
	Female	0	0%
Age	18 -28	25	12.3%
	29 - 58	161	79.3%
	Above 58	17	8.4%
Educational level	GCE A/L qualified	30	14.8%
	GCE O/L qualified	73	36.0%
	Below GCE O/L	100	49.3%
Daily income	Less than 1000	54	26.6%
	1001 - 2500	138	67.1%
	More than 2500	11	5.4%
Marital status	Bachelor	35	17.2%
	Married	166	81.8%
	Divorced	1	0.5%
	Widower	1	0.5%
Other income	Yes	52	25.6%
	No	151	74.4%
Other skills	Non skilled	113	55.7%
	Skilled (plumbing, carpenter, farmer, etc.)	90	44.3%
Job type	Part time	17	8.4%
	Permanent	186	91.6%
Driving career			
Factor	Variable	Frequency	Percentage
License	Yes	203	100%
	No	0	0%
License category	Heavy vehicles & TW	59	29.1%
	Light vehicles & TW	100	49.3%
	TW only	42	20.7%
	Other	2	1.0%
Method of training to obtain license	Friend or Relative	71	35.0%
	Qualified trainer	38	18.7%
	Self-Study	94	46.3%

Driving career			
Factor	Variable	Frequency	Percentage
Ownership	own	157	77.3%
	Relative	28	13.8%
	Friend	10	4.9%
	Out sider	8	3.9%
Register to park	Yes	168	82.8%
	No	35	17.2%
Traffic fines paying	Several week	3	1.5%
	Per month	5	2.5%
	Several month	37	18.2%
	Per year	56	27.6%
	Several years	102	50.2%

In addition to above categorical data, number of accidents have been reported for last five years, working hours, number of trial test faced, days spent to learn three-wheeler driving, years of experience and number of family members were collected as numerical variables.

When the above raw data is analyzed, it is evident that all 203 interviewers are male. According to the responses of three-wheeler drivers most of them are in 29 – 58 years range and it is 79.3% from all responses. It hints that most of them are highly experienced in driving career. The education level of three-wheeler drivers, 49.3% of them are below G.C.E (O/L) educational range. Only 14.8% of them have qualified G.C.E. (A/L) examination. It clearly shows that majority of three-wheeler drivers have not possessed a good education. Most of them lies in 1000 – 2500 LKR in their daily income and it is 67.1% of all the responses. 91.6% of them are driving three-wheelers as their permanent job and 74.4% of them don't have any other source of income to maintain their families. When investigating on their family background, 81.8% of them are married and 96% of them have to foster more than three family members. Furthermore, 55.7% of them don't have any other skills like plumbing, carpentering, farming etc. So the results that have been collected depict that their economical background is not much facilitate. Since most of them don't have other skills, they have to carry on this job and run behind money.

All respondents have driving license while 49.3% of them have light vehicle license and 29.1% have heavy vehicle license. However, 46.3% of drivers have learnt to drive by self-studying and only 18.7% of three-wheeler drivers have learnt to drive three-wheelers from qualified trainers. 61.6% of them have learnt three-wheeler driving less than 30 days of period. It can be clearly visible that majority of three-wheeler drivers haven't had a good training on three-wheeler driving. But 95 % of them have passed trial examination in their first try. Positive side is that, 77.83% of them have more than five years' experience in their job carrier and 62% of them have not faced any accident within last five years. There are 38% of drivers who have faced just one accident while, most of those accidents have happened because of the uncontrol of the vehicle.

Fig. 3 Three-wheeler drivers' habits

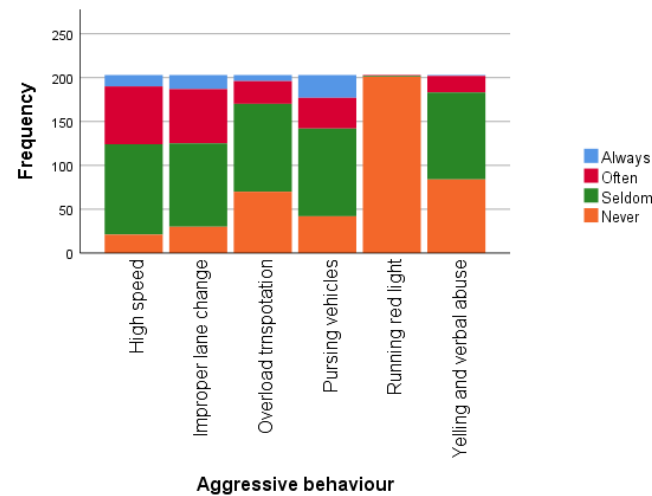
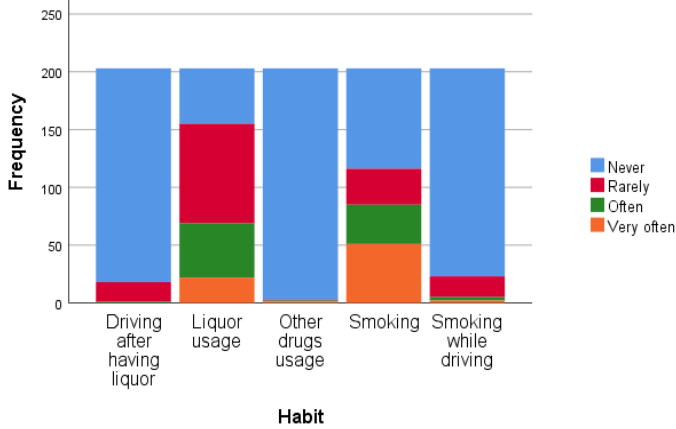


Fig. 4. Aggressive behaviour of three-wheeler drivers

Figure 3 and 4 shows the frequency distribution of three-wheeler drivers' habits and their aggressive behaviour on the road. Scrutinizing their habits, it was revealed that more than 86% of them have addicted to liquor and more than 57% have addicted to smoking. However, 91.2% of them don't drive after having liquor and 88.7% of them don't smoke while driving. The best part is 98.5% of them don't use any other drugs.

Six aggressive behaviours that usually caused by drivers were included in the questionnaire and it was scaled as never, seldom, often and always. Dummy variable called "drive mode" was created using how they have answered those questions. This marking scales was followed, 4 marks for "always", 3 mark for "often", 2 marks for "seldom" and 1 marks for "never". Then total marks and percentage of marks were calculated for each driver. So, it can be clearly understood that if one driver has less percentage value of drive mode, he is less contributing to traffic congestion. However, if percentage value is $\geq 60\%$ take him as "Un-safe" driver, if percentage value is between 60% and 45% take him as "Ordinary safe" driver and if percentage value is $< 45\%$ take him as "Safe" driver. Then drive mode can be taken as a dependent variable and others can use as an independent variable. TABLE II shows the frequency of drive mode variable.

TABLE II. FREQUENCY OF DRIVING MODE VARIABLE

Drive mode variable		
Rank	Frequency	Percentage
Safe	71	35.0%
Ordinary Safe	109	53.7%
Un Safe	23	11.3%

Since dependent variable is ordinal, ordinary logistic regression analysis carried out by taking "Drive mode" as the independent variable. General equation of OLR is as follows.

$$\text{Log} \left(\frac{P}{1-P} \right) = \beta_0 + \beta_1 X_1 + \beta_2 X_2 + \dots + \beta_n X_n \quad (1)$$

Here β_0 represented the intercept of the model and X_1, X_2, \dots, X_n are explanatory variables. $\beta_1, \beta_2, \dots, \beta_n$ represent the co-efficient of each of the explanatory variables. In this scenario SPSS statistics version 25 software package was used to carry on the OLR analysis. Stepwise Logistic regression was performed for OLR analysis and statistically insignificant variables were removed. Here confidence interval was assumed as 90%. Then p value should be less than 0.1 ($p < 0.1$) to be significant variable. For interpreting the results, if one of the variables in the same parameter category was significant ($p < 0.1$) those variables were retained in the model [18]. Proceeding stepwise OLR analysis, it was found four statically significant variables. TABLE III shows the parameter estimate of the OLR model. Here "Exp(B)" value is odd ratio, "sig." value is p value and "B" values are log odds with a unit change in X variables. The odd ratio for OLR represent how the odds change with unit increase in that variable holding all other variables constant.

TABLE III. PARAMETER ESTIMATION

Variable	B	Exp (B)	Sig.
Driving after having liquor			
Never	2.292	9.893	0.000
Often	1.644	5.176	0.408
Rarely	0 ^a	1	
Smoking			
Never	0.720	2.055	0.051
Often	0.159	1.172	0.723
Rarely	0.309	1.362	0.503
Very often	0 ^a	1	
Method of training to obtain license			
Friend or Relative	0.044	1.045	0.891
Qualified trainer	0.936	2.549	0.021
Self-study	0 ^a	1	
Ownership			
Friend	-0.360	0.698	0.637
Outsider	1.801	6.058	0.027
His own	0.999	2.717	0.019
Relative	0 ^a	1	

When considering the “driving after having liquor” variable odd ratio of “never” is 9.893. It means the cumulative probability of drivers those who never drive after having liquor is 9.893 times more than those who rarely drive after having liquor. It shows that those who never drive after having liquor are most safety drivers and they are less contributive to traffic congestion.

The smoking frequency odd ratio of “never” is 2.055 and p value is 0.051 which is less than 0.1. It can be understood that three-wheeler drivers those who never smoke are most safe drivers and those who smoke very often are most un-safe in the comparison of odd ratio.

When comparing the odd ratio of “Method of training to obtain license” variable, the highest odd ratio has to be ‘drivers those who learn from qualified trainer’ and it is 2.549. P value is 0.021 and it is significant. Three-wheeler drivers those who learn from qualified trainer are safer drivers rather than drivers who self-study and learn from friend or relative. They are less contributive to traffic congestion.

When the ownership of the three-wheeler is taken into count, the highest odd ratio can be seen in those who used three-wheeler from outsider. It is 6.058 and it means that three-wheeler drivers who use three-wheeler from outsider are safer drivers than those who use their own one or relatives’ one or friends’ one. Furthermore, p value is 0.027 and it is less than 0.1.

The Result of OLR analysis proves that driving after having liquors, smoking, methods they used to learn three-wheeler driving and ownership of the three-wheeler affect to the traffic congestion.

B. Effect of Three-wheeler Parking

Three-wheeler parking maneuver time was observed for the analysis. Leaving and entering maneuver times can be defined as time taken by one three-wheeler to exit from parking slot to middle of the road lane and time taken by one three-wheeler enter to parking slot from middle of the road lane. This is also can be called as disturbance time for the road traffic flow.

Parking maneuvering time of a three-wheeler is depending on various factors. Parking type, parking location, vehicle volume on the road are some of that factors. Here parking type and parking location consider for the analysis. TABLE IV shows the details of locations where video survey has done.

TABLE IV. DETAILS OF LOCATIONS

Park no.	Three-wheeler Park location	Parking type	Location type
L1	Infront of Peradeniya hospital	Angle Parking	Main road (A1)
L2	Near Gatambe Water Board	Parallel Parking	Junction, Minor Road
L3	P.L.P Alwis Mawatha junction on A26 road	Angle Parking	Junction, Minor Road
L4	Near Court in Kandy	Parallel Parking	Junction, Minor Road
L5	Near D.S. Senanayake Collage, Kandy	Angle Parking	Main road (A26)

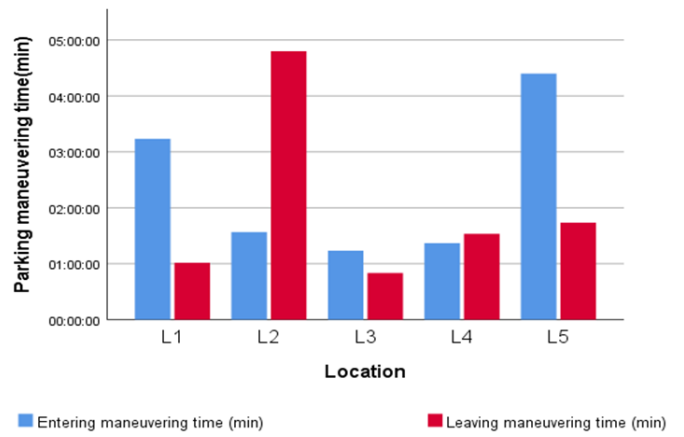


Fig. 5. Total parking maneuvering time for each location in peak time

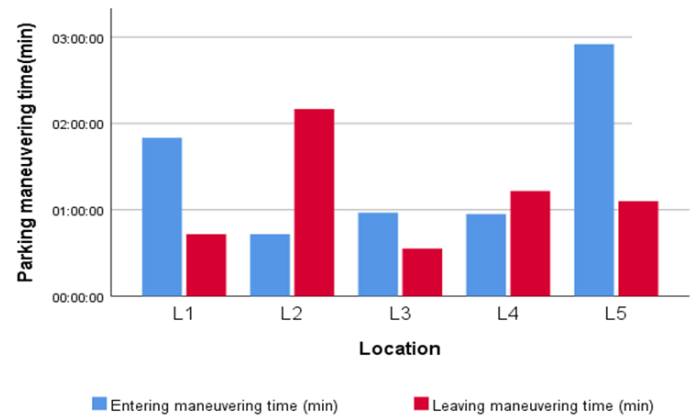


Fig. 6. Total parking maneuvering time for each location in off-peak time

Total parking maneuvering time in both peak and off-peak time can be graphically represented for each location as it can be seen in figure 5 and figure 6. Accordingly, higher entering maneuvering time have angle parking type than parallel parking type. Park L5 has highest entering maneuvering time in both peak time and off-peak time. In both peak and peak-off time highest leaving maneuvering time has in park L2. Total maneuvering time depends on the total number of turns. Therefore, it is necessary to find average parking maneuvering time (APM) per turn. It can be calculated as;

$$(APM)_{\text{per turn}} = \frac{\sum_{i=1}^n (\text{Parking maneuvering time})_i}{\sum_{i=1}^n i} \quad (2)$$

Here “i” is turn number. APM per turn was calculated for each park and TABLE V shows those results.

TABLE V. APM PER TURN FOR EACH LOCATIONS

Park no.	APM per turn / sec. (Entering)	APM per turn / sec. (Leaving)
L1	39	13
L2	4	12
L3	10	5
L4	7	9
L5	26	8

If APM per turn value increases then contributes traffic congestion also should be increased. When the above result is considered, APM per turn for entering values are as $L1 > L5 > L3 > L4 > L2$. Here L1, L5, L3 all have located as angle parking. L1 and L5 have located as on-street parks in main road and L3 has located in junction minor road. It can be clearly visible that if three-wheeler park located as angle parking in main road it is highly effected to the urban traffic congestion. Furthermore, the APM per turn value for leaving L1 takes highest value but L5 take lowest value. When comparing these two locations, L1 location traffic volume is higher than L5. Therefore, it can be occurred.

C. Effect of Three-wheeler Volume

Percentage of three-wheelers entering to KMC through the Sirimavo Bandaranaike Mawatha (A1) and Colombo-Kandy road on William Gopallawa Mawatha (AB42) are illustrated here. Figure 6 shows volume of three-wheelers entering to KMC through the A1 and AB42 routes and figure 7 shows the probability that the entering vehicle will be a three-wheeler.

By studying the figure 7 and 8, it can be clearly visible that every hour more than 20% of total number of vehicles enter to KMC through the A1 road and AB42 road are three-wheelers. However highest number of three-wheelers which enter to KMC through A1 at 7.00am to 8.00am and through the AB42 at 8.00am to 9.00am. When comparing probability of hourly three-wheeler entering, maximum probability can be seen at 2.00pm to 3.00pm in both routes

Furthermore, it can be clearly visible that the probability the entering vehicle be a three-wheeler get higher value in A1 road in most hours because of the availability of food courts, financial centers, schools are located in A1 route more than AB42.

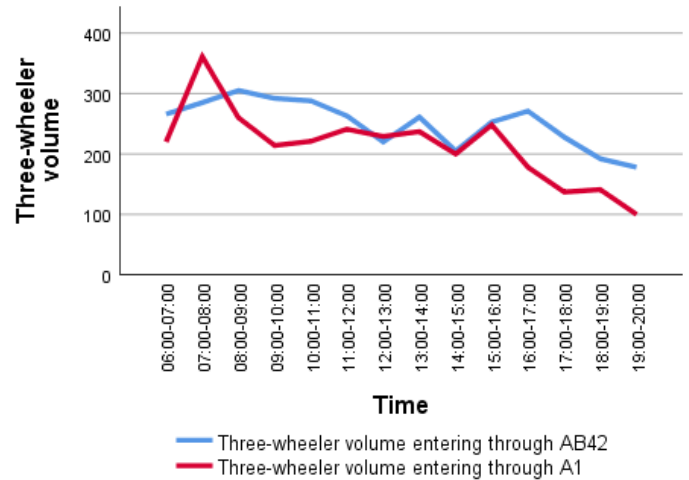


Fig. 7. Volume of three-wheelers entering to KMC through the A1 and AB42 routes

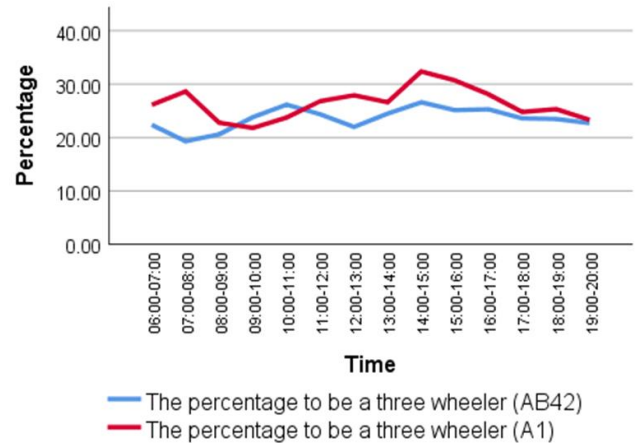


Fig. 8. The percentage that the entering vehicle will be a three-wheeler through AB42 and A1

V. CONCLUSION

Based on the above analysis, it can be concluded that three-wheelers are negatively affected on urban traffic. Driver behavioral habits like smoking, driving after having liquor, and improper training on driving are leading towards causing urban traffic congestion. Hence it is recommended to provide them a good training on their job career as well as driving performance in order to achieve a more effective solution to reduce traffic congestion created by three-wheelers. Regarding the three-wheeler parking issues on urban traffic, it can be visible that angle parking on main roads is positively influenced to the traffic congestion. If three-wheeler parks can be located as parallel parking or if it can be located in area with enough space, aforementioned traffic congestion can be considerably reduced. In addition, three-wheelers occupied a significant percentage of the traffic volume entering to the KMC. Hence, it is recommended to improve the public transport systems in order to reduce such three-wheeler volume.

ACKNOWLEDGMENT

Authors would like to acknowledge the support given by the Faculty of Engineering, University of Peradeniya during the data collection. Also, special gratitude to the Road Development Authority and staff of Kandy Traffic Police and for granting the permission of collecting data from roadways of the city.

REFERENCES

- [1] M. Samarakoon, B. Wijewardhana and Shayamali, "A sociological study of the socio-economic background of three wheel drivers in rural Sri Lanka: Special reference to Rathnapura, Ambilipitiya and Wallavaya areas," *International Journal of Academic Research and Development*, vol. 3, no. 1, pp. 659-662, 2018.
- [2] Total vehicle population, "Department of motor traffic," 2019. [Online]. Available: <http://www.motortraffic.gov.lk.pdf>. [Accessed 18 October 2020].
- [3] Y. Bandara and C. Jayasooriya, "Measuring the Economic Costs of Traffic," in *IEEE*, 2017.
- [4] K. M., "Loss of Manpower due to Road Traffic Congestion in Sri Lanka:," *Applied Economics & Business*, vol. I, pp. 55-69, 2019.
- [5] V. Phun , T. Yaib, "State of the Art of Paratransit Literatures in Asian Developing Countries," Tokyo Institute of Technology , Tokyo, 2016.
- [6] A. Tangphaisankun, F. Nakamura and T. Okamura, "Study on Role of Paratransit as a Feeder Mode in Urban Transportation in Developing Countries," Yokohama National University. , Yokohama, 2016.
- [7] A. Somasundaraswaran, M. Kumari and D. Siriwardana, "Three-wheeler drivers view in small cities in Sri Lanka," Department of Civil and Environmental Engineering, Faculty of Engineering, University of Ruhuna, 2006.
- [8] H. Sampath and P. Fonseka, "Characteristics of three-wheeler drivers, and driver factors associated with road traffic accidents of three wheelers registered in the urban council Panadura," *Journal of Community Physicians of Sri Lanka*, vol. 15, no. 1, pp. 33-44, 2010.
- [9] A. Kalasova and Z. Krchova, "Effect of aggressive driving on formation of congestion," Katowice-Ustron, Poland, 2011.
- [10] R. Gheorghiu, A. Cormos, V. Iordache and V. A. Stan, "Analysis of driver behaviour's influence in urban traffic flows," Iasi, Romania, 2018.
- [11] Purnawan and Yousif, "A study into on-street parking: Effects on traffic congestion," Department of Civil and Environmental Engineering, University of Salford, Manchester M5 4WT, United Kingdom., 1999.
- [12] Praburam and Koorey, "Effect of on-street parking on traffic speeds," Christchurch, New Zealand, 2015.
- [13] U. A. Gopallawa and K. S. Weerasekera, "Effects of three-wheeler parks near intersections," *Journal of Engineering and Technology of the Open University of Sri Lanka*, vol. 2, no. 1, pp. 1-16, 2014.
- [14] K. Jayatilaka and A. Kumarage, "Survey of conditions regarding traffic problems in Kandy metropolitan area," University of Moratuwa, Sri Lanka, 2003.
- [15] A. Sandaruwan, T. Karunaratne, J. Edirisinghe and V. Wickramasinghe, "Carpooling: A Step to Reduce Traffic Congestion in Sri Lanka," Battaramulla, Colombo, 2019.
- [16] B. A.G., *Elementary Statistics*, New York: McGraw-Hill, a business unit of The McGraw-Hill Companies, 2012.
- [17] RDA, "RDA Traffic Survey at Gatambe Junction," Kandy, 2018.
- [18] Chowdhury, Uddin and Taraz, "Identifying Important Features of Paratransit Modes in Sylhet City,," *Civil Engineering Journal*, vol. IV, 2018.
- [19] Afrin and N. Yodo, "A survey of road traffic congestion measures towards a sustainable and resilient transportation system," Department of Industrial and Manufacturing Engineering, North Dakota State University, USA, 2020.

Pavement Degradation Model for Road Infrastructure in Sri Lanka

Nadun T Meghasooriya
Department of Civil Engineering
University of peradeniya
Sri Lanka
nadun.meghasooriya@gmail.com

Nadeeshika M Jayarathna
Department of Civil Engineering
University of peradeniya
Sri Lanka
nadeemadu610@gmail.com

Sinniah K Navaratnarajah
Department of Civil Engineering
University of peradeniya
Sri Lanka
navask@eng.pdn.ac.lk

Abstract—Pavement degradation prediction is essential for road management systems to predict the most effective maintenance time. The existing degradation prediction models are calibrated for different countries; therefore, they cannot be used directly for the local condition to predict the maintenance requirements. In Sri Lanka, this is causing many difficulties during the maintenance activities of road infrastructure and drainage systems running along the roadways. Therefore, in this study, the pavement degradation models for unpaved road infrastructure in Sri Lanka are proposed using Markov analysis. The analysis consists of identifying performance parameters, condition stages of the road sections, TPM (Transition Probability Matrix), and finally prediction of the road lifetime and level of maintenance requirements. UPCI (Unpaved Condition Index) is proposed for the unpaved road as the performance parameter which includes all the possible deterioration types of gravel roads such as potholes, corrugations, overexposed aggregates, erosion, roadside drainage, and rutting. Development of the TPM is proposed based on the data collected at three gravel roads in Dambulla Pradesiya Sabha. Model calibration and validation were done using the collected data for Sri Lankan unpaved roads.

Keywords—Pavement degradation, Maintenance, Markov Model, Unpaved Condition Index

I. INTRODUCTION

Pavement maintenance is one of the most important roles after the construction. Every country adopts various pavement management systems (PMS) which are consist of many prediction models developed in their state or calibrated models from other states. Model is depending on the road types such as unpaved, paved, and rigid pavements. Among various models that developed in many countries, Australian Road Research Board (ARRB) models, Highway Development and Management (HDM) models, Technical Recommendations for Highway Manual 20 (TRH20) model, Unpaved Condition Index (UPCI) evaluation, Pavement Condition Index (PCI) evaluation and Distress Rating (DR) evaluations are widely used.

Sri Lanka is a tropical country situated near the equator with more variability in climate and various geological regions. Climate zones are defined as wet, intermediate, and dry according to the annual rainfall. All three types of flat, rolling, and mountainous terrains can be identified in Sri Lanka due to the geological variation. Also, traffic is congested near main cities and heavy vehicles are used to transport factory productions even in some rural areas. Therefore more diversity of traffic can be observed in Sri Lanka causing many difficulties in using the same degradation model for entire Sri Lanka faced by relevant road

development authorities. These situations make many inconveniences of maintenance scheduling, funding, durability, and waste of money.

Pavement degradation models are widely used in PMSs to predict when maintenance will be required. Models can predict the degradation with time as well as the lifetime economic evaluation. After the construction, long-term funding requirements for pavement maintenance can be estimated with the sense of the lifetime of the road [1]. And also, models are used to decide the best maintenance type such as re-graveling, blading, reconstruction, and major drainage repair considering cross-section, roadside drainage, rutting, potholes, loose aggregates, dust, corrugation, and ride quality [2]. The model can be used for any country after it is calibrated to local conditions. Calibration is essential because universal degradation models can vary from country to country with many factors. Better prediction can be obtained by calibrated models for local conditions.

Age of the pavement, traffic volume, and weight, thickness of last overlay, strength, and condition of pavement structure, surface deflection, and construction quality are the affecting factors for pavement degradation [1]. Among them, age was identified as significant in predicting pavement deterioration. Plasticity factors, traffic, rainfall, and material properties can be considered as the affecting factors [3]. Furthermore, pavement material properties, climate, and road geometry can be considered as the affecting factors [4] for TRH-20, HDM-4 and ARRB models. HDM-4 and ARRB models incorporate all four major fields of input, but geometry is omitted from the TRH-20 Model. For road geometry, HDM-4 uses the gradient and the curvature whereas ARRB incorporates only the gradient. Gravel lose prediction models such as TRRL Model, South African Model, Australian Model, and Highway Design and Maintenance Model show a comparison of gravel loss prediction [5]. That concludes positive sensitivity of more than 0.6 for traffic and climate for all models. HDM-4 and TRRL Models account for vertical alignment and the South African Model for maximum aggregate size. Except for TRRL Model, all other models are sensitive to fines content and plasticity. When considering all these works of literature, a summary of the affecting factors can be identified as traffic volume age of pavement, the thickness of last overlay, material properties of wearing course (plasticity factor, material type, practical size distribution), climate (rainfall, wet zone, and dry zone, Weinert N-value, wind), road geometry (average rise and fall, gradient of the road, average curvature).

Combined performance parameters for the researches can be used to study the deteriorations as in [1, 6, and 7]. Some research papers reported individual performance parameters

to rate the condition of the road as in [3, 5, 8, and 9]. Combined performance parameters are related to the overall condition of the road which is suitable for combined maintenance procedures. Individual performance parameters identify each degradation individually and individual maintenance such as blading and re-graveling.

Actual ride quality and gravel loss variations are higher than the predicted ride quality and gravel loss variations using degradation models [4]. Some models show different complete degradation times under different distresses and washboards and potholes show the lesser degradation time [8]. But some researchers have reported, transverse and ride indices show faster deterioration [2].

II. MARKOV APPROACH

Prediction of performance can be done in two types of models: deterministic and stochastic (probabilistic). Deterministic models include primary response, structural performance, functional performance, and damage models [1]. Stochastic models are based on probability which is applied widely because of the consideration of uncertainty. Markov approach and survivor curves are two main approaches for stochastic models [11, 12]. Markov approach is mainly consisting of four main steps: performance parameter selection, condition stages identification, transition probability matrix development, and finally Markov chain development to predict the lifetime of a road. Markov chains can be identified as homogeneous and non-homogeneous chains based on the transition probability matrix used. The homogeneous Markov model assumes steady-state transition probabilities over the entire analysis period which presents a major drawback for predicting future pavement conditions [7]. The non-homogeneous Markov model deploys different transition probabilities for each transition which can lead to superiority in predicting future pavement conditions. But this required more data and time to develop TPM for each transition [13]. In this research homogenous Markov modeling is used for final analysis.

A. Performance Parameter Selection

Some research papers reported individual performance parameters to rate the condition of the road [3, 5, 8, and 9]. Several combined performance parameters were also developed as well as individual performance parameters. [1, 6, 7]. Individual performance parameters identify each degradation individually and individual maintenance such as blading and re-graveling are proposed. Therefore separate models are needed to identify specific deterioration types. According to the used performance parameter required maintenance will be done. Maintenance activity might recover many degradations but some other deteriorations might not be recovered. Combined performance parameters are related to the overall condition of the road which is suitable for combined maintenance procedures. Prediction is done considering all the degradation types including all parameters into one model. Both types of performance parameters are presented in Table I.

Unpaved Road Condition Index (URCI) combined performance parameter was developed by the U.S. Army Corps of Engineers [10]. This index consists of properties of

TABLE I. PERFORMANCE PARAMETERS

Individual Performance Parameters	Combined Performance Parameters
Roughness Rating	Unpaved Road Condition Index (URCI)
Structural Strength Rating	Unpaved condition Index (UPCI)
Rutting Rating	Unpaved Pavement Condition (UPC)
Cracking Rating	
Stone Loss Rating	

cross-section. Roadside drainage, corrugations, dust, potholes, rutting, and loose aggregate into a value between 0 and 100. Common Unpaved Condition Index (UPCI) model for both gravel and earth roads with and without roughness was used in some papers [6]. But Unpaved Pavement Condition (UPC) was defined only as a function of age [2].

B. Condition Stages

Condition stages represent the level of road degradation. Each stage has a fixed range of performance parameter ratings useful in identifying the transitions from one stage to another. In the literature, the authors were concluded that the number of stages depends on the degradation rate of the road. Five condition stages and seven condition stages are the most ideal number of stages.

Rutting (RT) or transverse deformations caused by the loose aggregate, measured as the mean vertical deformation for each 5 m sections of 50 m section using a straight bar in centimeters. Exposed oversized aggregate (OA) is another dummy variable, considered as 1 when oversized aggregates with mean diameters greater or equal to 10 cm are observed as a generalized phenomenon within the sample section. Crown condition (CW) which is the average between drainage and transverse profile condition, both defects are rated as 0 when observed in good condition, 0.5 in fair condition, and 1 in poor condition. It was observed that no drainages were supplied for roads which caused for increment in road degradation.

C. Transition Probability Matrix (TPM)

The transition probability matrix (TPM) consists of the probabilities of transitions from upper stages to the same stage or lower stages after a considerable period. Each probability is computed as a percentage of the total number of sections transferred to the total number of sections considered. TPM which is composed of the diagonal probability in addition to extra probabilities concerning the first row of the TPM has been used in [8, 14]. Along the main diagonal represent the probabilities of pavements remaining in the same condition states after the elapse of one transition. Entries above the main diagonal denote the probabilities of pavements transmitting to the worse condition states after one condition. Similarly, entries below the main diagonal indicate the probabilities of pavement transiting to the better condition [15]. Normally, that cannot happen if there is no maintenance was done. This is the most common method of developing the transition probability matrix. But cumulative probability matrixes are also defined by calculating the cumulative probability per row in each TPM [6].

D. Markov Chain

Markov chain is developed to predict life by calculating the transferring fractions for the considered period in TPM. Homogenous TPM assumes that the transition probabilities for each period are equal. Therefore, the prediction of the condition rating for an equal period can be computed by continuing the multiplication using the same TPM. Equally distributed TPM is needed to predict the actual lifetime of a road. Otherwise, the Markov chain will converge to a higher rating.

III. DATA COLLECTION

To develop the deterioration model using Markov analysis, a case study was conducted for selected three unpaved roads located in the Naula Pradeshiya Saba area as shown in Fig. 1. Lion Rock Road (1) is situated around Sigiriya Fortress maintained by Sigiriya Fortress Maintenance Unit which is funded by Naula Pradeshiya Sabha. Both Naula Road (2) and Inamaluwa Road (3) are maintained directly by Naula Pradeshiya Sabha. The selected roads should have many characteristics to implement the analysis. Road sections should not be improved by any maintenance work during the data collection period. Also, the selected roads should represent all the introduced stages. Straight road sections were selected to avoid degradation due to additional friction forces imposed on the horizontal curves of the roads. Nearby three roads were selected to represent the dry zone of Sri Lanka to minimize the environmental alternation. Therefore the developed model applies only to the dry zone of the country and can be developed for other zones following the same procedure.

Unpaved Condition Index (UPCI) was selected as the most appropriate performance parameter to rate the gravel roads in Sri Lanka because it consists of many degradation parameters which give overall condition with less use of measuring instruments. The index consists of six degradation measurements such as corrugation, potholes, erosion, rutting, exposed oversized aggregate, and crown condition. First, each road was divided into 100 m sections and three sections

among them were selected which represent the condition of the entire road. UPCI values were assigned to subdivided sections with 10m in length. UPCI needs several in situ measurements to calculate the current condition of each section. Three data sets were collected in three time periods, two for TPM development and the other one for validation.

UPCI has performed a technique of reducing the maximum possible condition by the measured degradations. The maximum condition rating of any road is identified as 10 and 6 parameters are used to measure the road condition as shown in (01). UPCI shows a linear variation for each parameter. But the effect of each parameter on the overall condition is different and proportional to the magnitude of parameter coefficient showing higher coefficients for highly affecting parameters in road degradation. All coefficients should be negative to reduce the rating from 10 to null, but should not be less than 0. Corrugations (CR) are measured as the mean vertical deformation observed in a section in centimeters. But corrugation was not observed in any section of selected three roads during the entire investigation time. Potholes (PT) are calculated as the product of the mean diameter in meters, maximum depth in meters, and the number of potholes in a sample section. Erosion (ER) is a dummy variable, considered as 1 if either erosion depth or width is greater than or equal to 5 cm. Depth and width measuring of the erosion can be conducted as same as pothole diameter and depth measurements. Rutting (RT) or transverse deformations caused by the loose aggregate, measured as the mean vertical deformation of five readings for each 10 m subsection using a straight bar in centimeters. Exposed oversized aggregate (OA) is another dummy variable, considered as 1 when oversized aggregates with mean diameters greater or equal to 10 cm are observed as a generalized phenomenon within the sample section. Crown condition (CW) which is the average between drainage and transverse profile condition, both defects are rated as 0 when observed in good condition, 0.5 in fair condition, and 1 in poor condition.

$$UPCI = 10 - 1.16CR - 2.25PT - 1.47ER - 0.33RT - 1.56OA - 1.58CW \quad (1)$$

IV. DATA ANALYSIS

UPCI model is calibrated to United States road conditions. Therefore model calibration is required for Sri Lankan conditions before lifetime prediction in Sri Lankan gravel roads. To find the actual rating of the road, a Visual and Direct Measurement method was used [14]. Using one set of data collected, the model was calibrated considering variables considered only in the UPCI model. But it was observed that the R-sq is only 44% indicates that something remains in the residuals that can be removed by a more appropriate model. Therefore all variables, their multiples, and square terms were subjected to stepwise regression. Concluding the analysis results, the authors are proposed a developed model (Developed Unpaved Condition Index-DUPCI) for gravel road condition rating in Sri Lanka which was calibrated for the dry zone.

$$DUPCI = 9.009 - 1.169RT - 0.752ER - 0.6264RT \times OA + 1.602RT \times CW - 0.1232PT \times ER - 2.465CW^2 \quad (2)$$

$$R^2 = 78\%$$

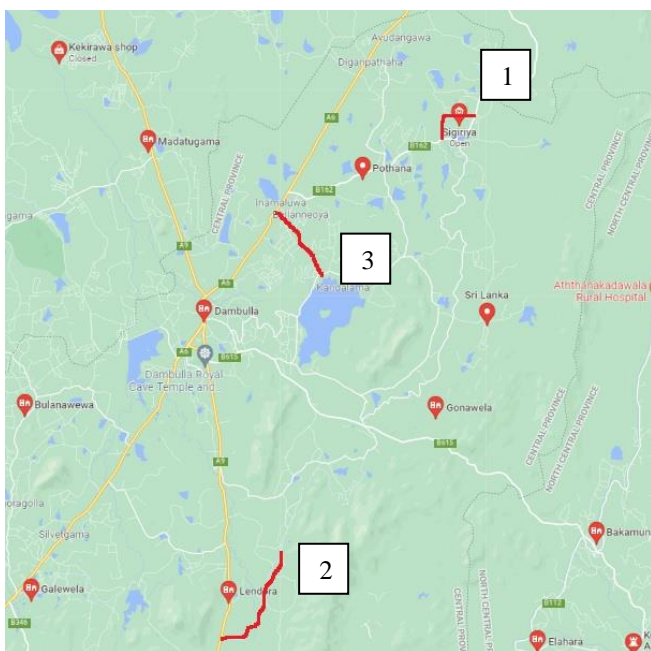


Fig. 1 Map of the selected roads

DUPCI shows a maximum rating of 9. Therefore the number of condition stages was reduced to 4 including very good, good, poor, and fail stages and new ranges of ratings were proposed by the author as showed in Table II. Initially, separate analyses were conducted for each road preparing 3 transition probability matrixes. Table III shows TPM for Lion Rock road which consists of transitions only between middle condition stages. Table IV is concluded the TPM for Naula Road clearly showing the transitions only between higher condition stages. The road is not degraded for lower conditions during the study period. Inamalua Road was in poor condition during the first visit. According to the TPM entire 3 sections were transferred within lower condition stages as shown in table V. Fig. 2, 3, and 4 show the lifetime predictions of Lion Rock Road, Naula Road, and Inamalua Road respectively. Fig. 2 shows better variation at the beginning and middle but the end might be not having a better prediction because the TPM only consists of values in the top and middle of the matrix. Therefore the acceptable region of the prediction is limited to the beginning and middle portions. The lifetime of the Naula Road consists of better prediction during the 1st few months as shown in Fig. 3 because the TPM consists of values for higher stage transitions. Therefore curve is converged to a higher value after the first few months. According to Fig. 4, the Inamalua Road demonstrate higher deterioration in the beginning because of the less high stage transitions. All three roads selected for the analysis do not show complete behavior during the entire life because the number of transitions is not enough. The main reason for this is an inadequate number of sections selected for the analysis. Also, the selected period might be not enough to show each stage's transitions.

Combined analysis was conducted to overcome difficulties and data deficiency faced during the individual road analysis. All data were concluded to build one TPM which defines the entire selected region as shown in Table VI. The developed Markov chain is shown in Table VII. The time difference between the first two data collections is 2.5 months. Therefore chain was developed for 2.5 month time intervals.

TABLE II. CONDITION STAGES

Stage	UPCI Range
Very good	9 - 7
Good	7 - 5
Poor	5 - 3
Fail	3 - 1

TABLE III. TRANSITION PROBABILITY MATRIX LION ROCK ROAD

	TPM			
	VG	G	P	F
VG	0.421053	0.526316	0.052632	0
G	0	0.909091	0.090909	0
P	0	0	0	0
F	0	0	0	0

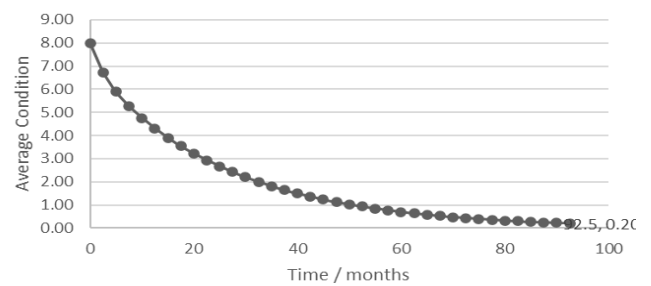


Fig. 2. Pavement lifetime prediction Lion Rock Road

TABLE IV. TRANSITION PROBABILITY MATRIX NAULA ROAD

	TPM			
	VG	G	P	F
VG	0.545455	0.318182	0.090909	0.045455
G	0	1	0	0
P	0	0	0	0
F	0	0	0	0

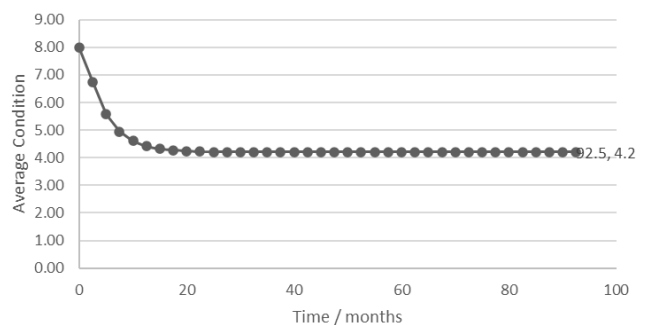


Fig. 3. Pavement lifetime prediction Naula Road

TABLE V. TRANSITION PROBABILITY MATRIX INAMALUWA ROAD

	TPM			
	VG	G	P	F
VG	0.4	0.2	0	0.4
G	0	0.5625	0.4375	0
P	0	0	0.75	0.25
F	0	0	0	1

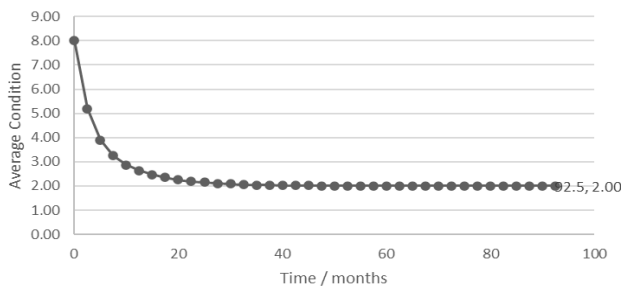


Fig.4. Pavement lifetime prediction Inamaluwa Road

TABLE VI. TRANSITION PROBABILITY MATRIX FOR T1 TO T2

	TPM			
	VG	G	P	F
VG	0.468	0.404	0.064	0.064
G	0	0.771	0.229	0
P	0	0	0.75	0.25
F	0	0	0	0

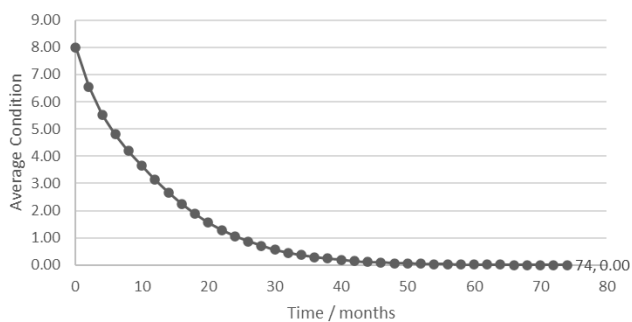


Fig. 5. Pavement lifetime prediction

Two data sets were used to build the Markov chain from 1st data collection until the fail condition. The Markov chain can predict future conditions with time but not backward. Therefore the predicted lifetime is not included in the time from construction to 1st data collection. According to the data records of Naula Pradeshiya Sabha, all the roads were graveled in February 2019. The third data set was used to validate the proposed model for Sri Lankan gravel roads. Considering the condition rating of a gravel road just after the construction is 9, all four data sets were plotted in the lifetime prediction graph for validation as shown in Fig. 6. The predicted lifetime and actual mean rating with the time of selected 3 roads were matched confirming the model is applicable. According to the results, a gravel road in the dry zone, Sri Lanka is completely failed within 7 years. But with the experience at the site, the author proposes rehabilitation when a road reaches rating 5, the stating rating of poor condition stage. Therefore rehabilitation should be done after 2.5 years after construction. Reconstruction is proposed when the road reached to fail condition stage which starts at a rating of 3.

TABLE VII. MARKOV CHAIN

Stage	Month	VG	G	FA	P	F	Average Condition
0	0	0.0000	1.0000	0.0000	0.0000	0.0000	8.00
1	2	0.0000	0.4680	0.4040	0.0640	0.0640	6.55
2	4	0.0000	0.2190	0.5006	0.1705	0.0460	5.53
3	6	0.0000	0.1025	0.4744	0.2565	0.0566	4.81
4	8	0.0000	0.0480	0.4072	0.3076	0.0707	4.20
5	10	0.0000	0.0225	0.3333	0.3270	0.0800	3.65
6	12	0.0000	0.0105	0.2661	0.3230	0.0832	3.14
7	14	0.0000	0.0049	0.2094	0.3039	0.0814	2.67
8	16	0.0000	0.0023	0.1634	0.2762	0.0763	2.26
9	18	0.0000	0.0011	0.1269	0.2447	0.0692	1.89
10	20	0.0000	0.0005	0.0983	0.2127	0.0612	1.57
11	22	0.0000	0.0002	0.0760	0.1820	0.0532	1.29
12	24	0.0000	0.0001	0.0587	0.1539	0.0455	1.06
13	26	0.0000	0.0001	0.0453	0.1289	0.0385	0.86
14	28	0.0000	0.0000	0.0349	0.1070	0.0322	0.70
15	30	0.0000	0.0000	0.0269	0.0883	0.0268	0.57
16	32	0.0000	0.0000	0.0208	0.0724	0.0221	0.46
17	34	0.0000	0.0000	0.0160	0.0591	0.0181	0.37
18	36	0.0000	0.0000	0.0124	0.0480	0.0148	0.30
19	38	0.0000	0.0000	0.0095	0.0388	0.0120	0.24
20	40	0.0000	0.0000	0.0073	0.0313	0.0097	0.19
21	42	0.0000	0.0000	0.0057	0.0251	0.0078	0.15
22	44	0.0000	0.0000	0.0044	0.0202	0.0063	0.12
23	46	0.0000	0.0000	0.0034	0.0161	0.0050	0.09
24	48	0.0000	0.0000	0.0026	0.0129	0.0040	0.08
25	50	0.0000	0.0000	0.0020	0.0102	0.0032	0.06
26	52	0.0000	0.0000	0.0015	0.0081	0.0026	0.05
27	54	0.0000	0.0000	0.0012	0.0065	0.0020	0.04
28	56	0.0000	0.0000	0.0009	0.0051	0.0016	0.03
29	58	0.0000	0.0000	0.0007	0.0040	0.0013	0.02
30	60	0.0000	0.0000	0.0005	0.0032	0.0010	0.02
31	62	0.0000	0.0000	0.0004	0.0025	0.0008	0.01
32	64	0.0000	0.0000	0.0003	0.0020	0.0006	0.01
33	66	0.0000	0.0000	0.0002	0.0016	0.0005	0.01
34	68	0.0000	0.0000	0.0002	0.0012	0.0004	0.01
35	70	0.0000	0.0000	0.0001	0.0010	0.0003	0.01
36	72	0.0000	0.0000	0.0001	0.0008	0.0002	0.00
37	74	0.0000	0.0000	0.0001	0.0006	0.0002	0.00

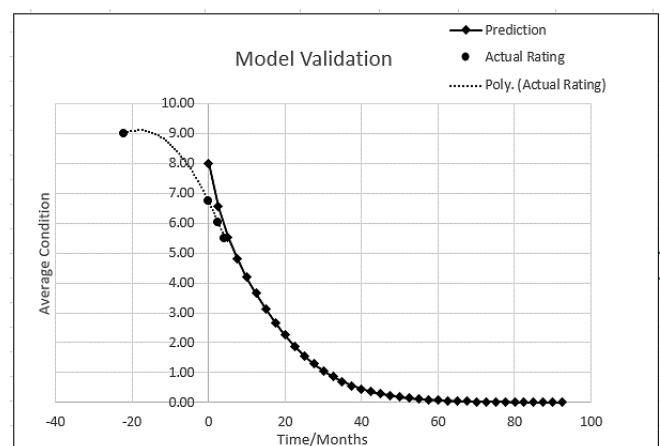


Fig. 6. Pavement lifetime prediction validation

V. CONCLUSIONS AND RECOMMENDATIONS

The main objective of the research was to identify the degradation rate and lifetime of gravel roads in Sri Lanka. The following conclusions were made from the study based on the data collected in three selected unpaved roads in Sri Lanka.

1. Corrugations were not observed during the entire investigation period on all roads.
2. Considerable variation was happened in rutting and potholes making them the most significant factors affecting road degradation. The effect of erosion is only considered after a certain depth. But the same impact is considered in UPCI and DUPCI for different scales of erosion.
3. According to the measured ratings, the road does not show any noticeable degradation during the first 7 months.
4. Noticeable degradation was observed during higher condition stages and degradation of road sections which having lower stages showed slow degradation.
5. It was observed, after some time of degradation happened, the silt accumulation in potholes begins reducing the depth of the potholes.
6. Small potholes were combined with the time making larger potholes. Therefore the number of potholes was reduced.
7. UPCI and DUPCI don't consider the smaller exposed over-size aggregates. This might be caused for errors in calculations of rating. Therefore it is recommended to consider the factor OA as a function of the area or diameter of exposed aggregates.
8. Rutting is measured as the maximum depth relative to the road centerline and edge. Road edge can degrade only due to environmental factors such as rainfall. But the center can be degraded due to traffic causing errors in rutting depth measurements. Taking rutting depths relative to the reference point by using a leveling instrument can avoid this error.
9. Proper TPM can be defined using data of more sections. The number of transitions from each stage to lower stages contributes to proper distributions in transition probabilities. Also, it is recommended to take a higher number of lengthy sections rather than selecting small sections to observe better degradation.
10. Several TBMs can be obtained using data from more roads for different climatic zones or TBM can be developed road vice.
11. The final rating was converged to rating 2 nearly after 75 months confirming the lifetime of the road is 6 years.
12. Selected gravel roads had average daily traffic of less than 50. The predicted lifetime is relevant to less ADT and the same analysis can be conducted to higher ADT ranges.

ACKNOWLEDGMENT

The authors would like to appreciate the support of the Road Development Authority (RDA), Provincial Road Development Authority (PRDA), Kundasale, and Naula.

REFERENCES

- [1] K. P. George, A. P. Rajagopal, and L. K. Lim, "Models for Predicting Pavement Deterioration," Department of Civil Engineering, University of Mississippi, 1989, Miss 38677.
- [2] P. Saha and K. Ksaibati, "Developing an Optimization Model to Manage Unpaved Roads," Journal of Advanced Transportation, Volume 2017, Article ID 9474838.
- [3] G. J. Giummarra, T. Martin, Z. Hoque, and R. Roper, "Establishing Deterioration Models for Local Roads in Australia," Journal of the Transportation Research Board, No. 1989, Vol. 2, Transportation Research Board of National Academies, Washington, D.C., 2007, pp. 270-276.
- [4] G. V. Zyl, R. Uys, and M. Henderson, "Applicability of Existing Gravel Road Deterioration Models Questioned," Journal of the Transportation research board, No. 1989, Vol. 1, Transportation Research Board of the National Academies, Washington, D.C., 2007, pp. 217-225.
- [5] L. V. Wijk, D. Williams, and M. Serati, "Roughness deterioration models for unsealed road pavements and their use in pavement management," International Journal of Pavement Engineering.
- [6] A. Chamorro and S. L. Tighe, "Condition Performance Models for Network-Level Management of Unpaved Roads," Journal of the Transportation research board, No. 2204, Transportation Research Board of the National Academies, Washington, D.C.2011, pp. 21-28.
- [7] K. Abaza, "Simplified Staged Homogenous Markov Model for Flexible Pavement Performance Prediction," Department of Civil Engineering, Road Materials and Pavement Design, 2015, Vol. 17, No. 2, 365-381.
- [8] W. Aleadelat, S. Wulff and K. Ksaibati, (2019). "Development of Performance Prediction Models for Gravel Roads Using Markov Chains," American Journal of Civil Engineering, vol 7, no. 3, 2019, pp. 73-81.
- [9] R. Uys, "Evaluation of Gravel Loss Deterioration Models Case Study," Transportation Research Record: Journal of the Transportation Research Board, No. 2205, Transportation Research Board of the National Academies, Washington, D.C., 2011, pp. 86-94.
- [10] R. A. Eaton, S. Gerard, and R. S. Datillo, "A Method for Rating Unsurfaced Roads," Transportation Research Record Journal of the Transportation research board, No 1106, Washington, D.C., 1987, USA.
- [11] J. V. Carnahan, W. J. Davis, M. Y. Shahin, P. L. Keene, and M. I. Wu, "Optimal Maintenance Decisions for Pavement Management," Journal of Transportation Engineering, ASCE, Vol. 113, No. 5, 1987, pp. 554-572.
- [12] R. L. Lytton, "Concepts of Pavement Performance Prediction Modeling," Proc. North American Conference on Managing Pavements, Toronto, Canada, Vol. 2, 1987.
- [13] A. Butt, M. Shahin, K. Feighan, and S. Carpenter, "Pavement Performance Prediction model using the Markov Process," Transportation Road Research Board, 1123, 12-19.

TECHNICAL PAPERS

Session 3

Quality Analysis on Spent Filter Backwash Water of Drinking Water Treatment Plants in Sri Lanka for Reuse

Rislan A.W.M.
Projects
Veolia Water Technologies
Colombo, Sri Lanka
mdrislan@gmail.com

Herath G.B.B.
Department of Civil Engineering
University of Peradeniya
Peradeniya, Sri Lanka
gemunuh@pdn.ac.lk

Abstract— As a developing nation, Sri Lanka has committed towards the Sustainable Development Goal (SDGs) of becoming a low water stressed country. In this connection, this study on water treatment plant residual management, especially the Spent Filter Backwash Water (SFBW) management aims to find the current status and to make recommendation for reusing and protection of the environment from their unsafe disposal. In Sri Lanka, so far there is neither a guideline nor detailed studies carried out to regulate the SFBW water disposal. Therefore, this study will also be a baseline to understand the current situation of SFBW handling in Sri Lanka both in dry & wet zones. Altogether 22 Drinking Water Treatment Plants (DWTPs) were evaluated using a questionnaire, raw water and SFBW water testing for Turbidity, pH, TOC and residual metal contents. Raw water TOC was found to be much higher than acceptable limits risking a high potential to form high DBPs. In addition, SFBW show residual Aluminum (Al) levels as high as 2.25 mg/L on average. 70% of SFBW was found to be disposed to environment with inadequate treatment. Hence, proper SFBW management is essential and combined equalization and sedimentation can be a good basic option in this regard.

Keywords— Raw water, Spent Filter Backwash (SFBW) water, TOC, Residual Aluminium, pH, Electrical Conductivity (EC), Water Treatment, Sri Lanka.

I. INTRODUCTION

With the growth of world population, water use is increasing by 1% every year [33]. Further, unsafe discharge of wastewater is a serious problem as globally 80% of wastewater from industries, agriculture and cities are returned to nature without treating or reuse [34]. In Sri Lanka, the Kelani River is considered to be threatened by the release of untreated or insufficiently treated wastewater and solid waste [27]. In this regard, the DWTPs without facilities for SFBW water treatment also contribute to wastewater discharge into environment.

National Water Supply and Drainage Board (NWSDB) mostly uses surface water sources to provide drinking water. Due to impurities, water [35] need to be treated up to drinking water standard using water treatment facilities all around the country. Currently NWSDB operates more than 300 DWTPs in the country and cover about 51.2 % of population with piped drinking water supply [22].

A. Study Focus

Most DWTPs in Sri Lanka has conventional water treatment systems, which include a filtration step. Filter backwashing (BW) is mandatory with rapid sand filters. During BW process large amount of SFBW water is produced as a residual stream [8]. Globally many studies carried out on SFBW show that they contain high concentration of solids and

chemicals [20]. As a result, it can harm the environment as well as human if disposed to environment directly [37]. Further the produced SFBW water volume varies from 3 % to 10% of DWTPs total production [32].

SFBW water recycling can ensure improved sustainability of water. Therefore, many studies are carried out on safe recycling methods for SFBW water using conventional and non-conventional water treatment techniques [2][19]. However, varying raw water quality influences SFBW water. Further treatment and recycling methods differs with financial viability. Hence it is vital to investigate the SFBW water handling methods accordingly, depends on a countries' priority.

B. Problem Identification

Access to safe drinking water is one of the goals of SDGs where government of Sri Lanka has set priorities to increase the pipe borne water coverage in the country. However, lack of funds from public sector leads to partnerships with private sector to achieve the intended goals. Therefore, especially with foreign investors, clear procedure of DWTPs residual management is essential to obtain their cooperation. As of now in Sri Lanka, there is no study carried out to evaluate the quality of SFBW water or any guidelines on how to handle them in a sustainable way.

Even though NWSDB has its own policy on sludge management, it recommends recycling the SFBW water after careful evaluation of the quality [24]. However, no detailed materials are available on SFBW water quality and its management at DWTPs in Sri Lanka. As an initial step to attend this issue, this research is initiated with an aim of preparing a reference document on SFBW water quality and status of it for designing water treatment plants with SFBW water management systems in Sri Lanka for interested parties.

II. LITERATURE REVIEW

All water treatment plants generate a waste stream from water treatments processes. Mainly from sedimentation & filter backwashing processes, large amount of wastewater and sludge are produced as residuals from DWTP [32]. However, the pollutant content of those residuals varies from source to source and country to country [32]. Hence, not all the parameters are presence in SFBW water as mentioned in the EPA report since pollutant depends on raw water quality and chemical used for treatment.

In order to conduct analysis on SFBW water for reuse or safe disposal options, knowing about residuals produced from rapid sand filter (RSF) is necessary. Further, the treatment of residuals are gradually emerging as an important part of the water treatment process, as the cost of residuals treatment is

increasing in order to meet the more stringent effluent water quality standards [5][6]. Generally, 3 % to 6 % of produced clean water from DWTP is used for BW [32]. When DWTPs capacity is large, consumed proportion for BW water will be large.

A. Quality of generated SFBW water

SFBW water contains particulates including clay and silt particles, microorganisms (bacteria, viruses, and protozoan cysts), colloidal and precipitated humic substances, and other natural organic particulates from the decay of vegetation. At conventional and direct filtration plants, filter backwash also contains precipitates of aluminum or iron used in coagulation [6].

One of the core objective of this research is to analyze the quality of this SFBW water of DWTPs in Sri Lanka. In terms of turbidity, conventional DWTPs generally produce SFBW water with turbidity ranges from 150 to 250 NTU [12]. During BW, SFBW water turbidity varies between 0.57 and 97 NTU [5]. Other contaminants like, TOC, aluminum, manganese, and iron concentrations in the SFBW water can be higher than those found in both the raw water before and after chemical addition [16].

Form the studies of DWTPs across United States shows that particulate matter are highly concentrated in SFBW water compared to the raw water samples, as such TOC, Turbidity and TSS values are higher than raw water values. This confirms the previous studies outcomes that organic material in SFBW water is contained in the particulate phase. It may also contain a high concentration of pathogens that were originally present in the surface water. Discharging such a stream to the environment can represent a problem, especially in large filtration systems [37]. Studies indicates that SFBW water from a conventional treatment plant generally has a turbidity of 150 to 250 NTU [12]. It should be noted that, the quality of the spent filter backwash water also depends on the volume of backwash water used. The more water used, the more diluted the spent backwash water will become.

B. Presence of residual coagulant chemical

Most DWTPs follow coagulation, flocculation, and sedimentation with filtration to remove finer solid particles such as suspended solids, colloids, and color (indicative of dissolved organic material) [32]. As NWSDB operates RSFs for most of the plants as final particle removal process, all the particles that remain from previous process will trapped in the RSF. Mainly coagulant residuals are of concern in this research as they can harm human and environment. As Aluminium (Al) metal salt is used for coagulation process, there is possibility of presence of particulate Al in SFBW water as filtration process removes considerable amount of residual Aluminium from settled water [13].

Excessive consumption of Al becomes threat to health. Reported minor symptoms of the high level of residual Al in drinking water are nausea, vomiting, diarrhea, mouth and skin ulcers, rashes and arthritic pain [39]. Further consumption of Al may cause Alzheimer's disease as suggested by [21]. Not only Al has influence on human but also on environment because Al becomes more soluble and, hence, potentially more toxic to aquatic biota at acidic pH [9]. There are studies on removal of Al in the SFBW water globally [38] [11].

C. Presence of Natural Organic Matters (NOM)

According to [4], NOM is normally present in raw and treated water but does not pose a human health risk. However, NOM reacts with free chlorine and chloramines to form Disinfection by Products (DBPs). Common DBPs are Trihalomethanes (THMs), Haloacetic acids (HAAs), and Haloacetonitriles (HANs). Therefore, chlorine has the potential to combine with organic precursors present in water to form DBPs [18].

In order to estimate the presence of NOM, Total organic carbon (TOC) is a measurement of total amount of carbon in organic compounds in an aqueous system. TOC of a water or wastewater indicates its pollutant levels & characteristics of the system [30]. As DBPs are of potential concern when recycling SFBW water, study carried out by [20] shows SFBW water samples have high TOC concentrations (20-85 mg/ L) in different DWTPs.

In Sri Lankan context, there are no studies available on SFBW water treatment with quality analysis. However, globally many researches are being carried out to reuse the SFBW water since they are large in volumes. Studies on SFBW water suggest some treatment options similar as raw water treatment methods [2]. Each treatment option has advantages and disadvantages, operational considerations and cost benefits. Country like Sri Lanka need a solution not to compromise the financial benefits of the plants in long term run. Hence adopting an equalization tank would be a least, cost-effective solution to prevent the water loss and to protect environment.

Whatever said, it should be noted that, quality of SFBW water should be evaluated before recycling as all the studies have done. In addition, it may contain harmful microbial pathogens [8] and may increase particle and cyst loadings and hydraulic surges to DWTPs [17]. It is also reported that recycling untreated waste streams can increase concentrations of iron, Mn, NH₃-N and DBPs of filter effluent [36][40]. Hence, SFBW water quality evaluation was conducted in this research on selected parameters

III. METHODOLOGY

In order to evaluate the existing DWTPs in the country in detail, a questionnaire was prepared which includes the plant processes data pertaining the SFBW quality. Initially, parameters for analysis were selected. One of the core objectives of this research is to analyze raw water & SFBW water to prepare a data set for decision makers in water treatment sector of the country. Therefore, following parameters were chosen to evaluate with the help of Filter Backwash Recycling Rule (FBBR), considering the resources available. Same parameters were analyzed in both samples. Those were turbidity, pH, TOC and residual coagulant (Al³⁺).

Then, 22 DWTPs in dry and wet zones in Sri Lanka were selected. Those are from Nuwera Eliya, Kandy, Matale, Anuradhapura and Polannaruwa districts. DWTPs in these districts cover major climate zones of Sri Lanka with different water sources from small spring to large rivers and reservoirs. Fig. 1 shows the selected DWTPs in each districts.

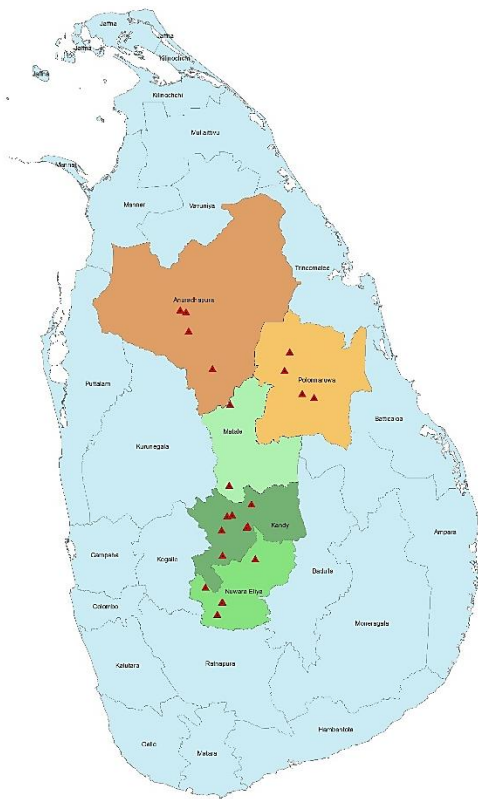


Fig. 1. Selected DWTPs locations

After selection of plants, with questionnaire, SFBW water samples and raw water were collected into 1.5-Liter new PET (polyethylene terephthalate) bottles. SFBW water samples were collected at the initial stage of rinsing process as water quality varies with time during BW rinsing. Hence, the worst case is represented. Collected samples were brought to University of Peradeniya environmental laboratory for turbidity, pH and TOC analysis. Afterwards, SFBW water samples were brought to NWSDB regional laboratory for residual coagulant chemical analysis. Samples were kept refrigerated until the testing. All testing were done according to AWWA standard methods.

To prepare tables, charts and descriptive and inferential statistical analysis Microsoft Excel 2016 software version was used. Due to small sample size and assumed the distribution is normal, commonly used parametric test, the Student's t-test is conducted [1][29] for TOC and turbidity of both samples to see the relationship between them. Since measurements are made on the same water source before and after a treatment, they become dependent samples and paired t-test is conducted. In addition, regression analysis also conducted to see the relationship between those two parameters in both samples [25].

IV. RESULTS AND DISCUSSIONS

Table 1 shows the DWTPs in both climate zones chosen for study with their raw water quality parameters. Spaces are left blank due unavailability of data.

TABLE I. SELECTED DWTPS AND THEIR MONTHLY AVERAGE VALUES OF RAW WATER QUALITY PARAMETERS

WTP	Climate Zone	Water Source	Daily Basis Tests (Monthly Avg.)			
			Turbidity, (NTU)	pH	Conductivity, (µS/cm)	Color, (Pt.co)
Maskeliya	Wet Zone	Stream	3.08	6.61	41.2	
Rikillagaskada		Stream	3.16	7.5	55.6	
Ginigaththene		Stream	3.91	7.25	49.1	
Hatton Low Level		Stream	2.8	6.7		
Hatton High Level		Stream	3.11	6.87		
Paradeka		Stream	30.6	7.1	36	20
Arattana		Stream	1.98	7.47		
Matala		River	27	7.1		
Meewathura		River	30	7	50	
Greater Kandy		River	13.5	7.12	83.8	53
Polgolla		Reservoir	76	7.17		
Balagolla		Reservoir	43.21	7.2		
Haragama		Reservoir	45	7.25		
Nuwerawewa	Dry Zone	Reservoir	10.25	8.2	525	
Thuruwila		Reservoir	13	7.9	430	
Tissa Wewa		Reservoir	28	8.5	400	
Kalawewa		Reservoir	8	7.3	230	
Minneriya		Reservoir	4	7.59	175	
Maderigiriya		Reservoir	5.5	8.1		
Greater Dambulla		Reservoir	3.76	8	210	
Polonnaruwa		Reservoir	4	7.84		
Gallella	River	20	7.4	230		

Comparing the turbidity and pH values of water sources in each zone, turbidity values of wet zone water sources are higher than dry zone water sources (Fig. 2). This may be due to rivers are the main water sources for wet zone while reservoirs are for dry zone. Reservoirs are stagnated water bodies where suspended particles could settle, compared to moving water. pH values of dry zone water sources are higher than wet zone water sources. Presence of alkali metals such as Na/K could be a reason for high pH in dry zone [7]. Fig. 3 shows the pH variation of water sources in each zones.

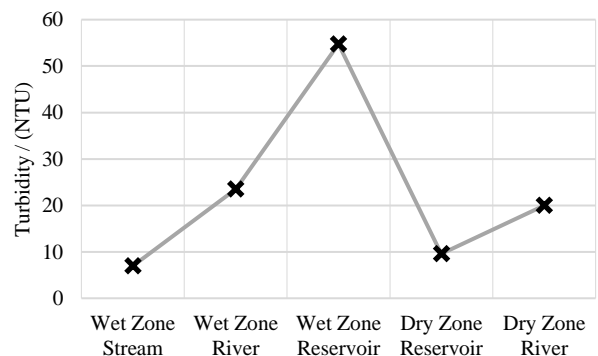


Fig. 2. Comparison of monthly average turbidity with water sources

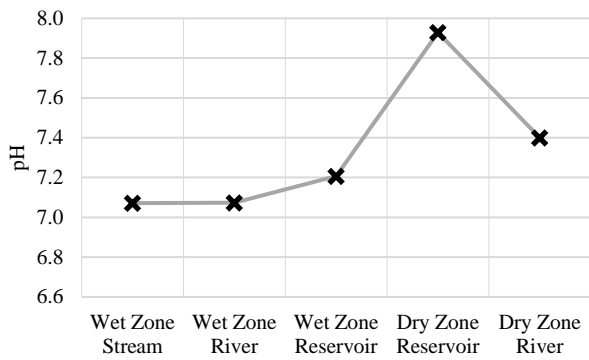


Fig. 3. Comparison of monthly average pH values with water sources

Electrical conductivity (EC) of dry zone water sources were higher than wet zone. Especially dry zone reservoirs shows high EC levels. High evaporation rates, droughts, water draining agricultural lands, accumulation of waste matters etc. could be possible reasons for higher EC in dry zone waters. Studies of [7] also confirm that dry zone water sources have high EC values. Fig. 4 shows the variation of EC. No EC data available from wet zone reservoirs. Each DWTPs operating in Sri Lanka keeps a record of daily data of raw water parameters. Turbidity and pH are mainly recorded while other parameters are occasionally tested. However, modern plants provided with instruments.

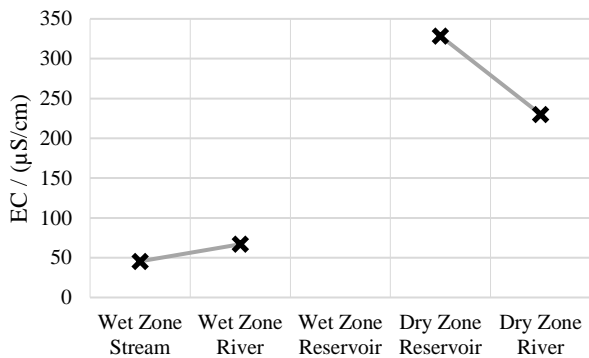


Fig. 4. Comparison of monthly average EC of water sources

According to the pre-chlorination practice, it was observed that 31% of WTPs in wet zone use pre chlorination process while 67% of plants in dry zone. High value in dry zone is the presence of toxigenic cyanobacteria in most dry zone fresh water sources [14]. In addition, [26] have reported higher diverse populations of cyanobacteria recorded from the dry zone reservoirs while lower densities recorded from those of the intermediate zone. Hence, pre chlorine is common in dry zones to control algae presence in raw water.

When it comes to BW, in these 22 plants, 21 DWTPs use RSF filter for filtration process. Sand is the common filter media in all WTPs. Backwash frequency of each plant varies depend on the raw water quality. On average wet zone plants perform backwashing once in 48 hours. In dry zone plants, it was once in 36 hours. Fig. 5 shows the variation of BW frequency of DWTPs in each zones. This shows the backwashing frequency is depend on the raw water quality. When there is low turbidity, filters run long hours compared to high turbidity.

Out of 22 DWTPs, 16 DWTPs use chlorinated water for filter backwashing with residual chlorine. This could lead to formation of DBPs as SFBW water contains organic matters. Other 6 WTPs use filtered water before chlorination for BW making these plants less prone to DPBs formation. However, there is possibility of DBPs in this water due to pre chlorination process.

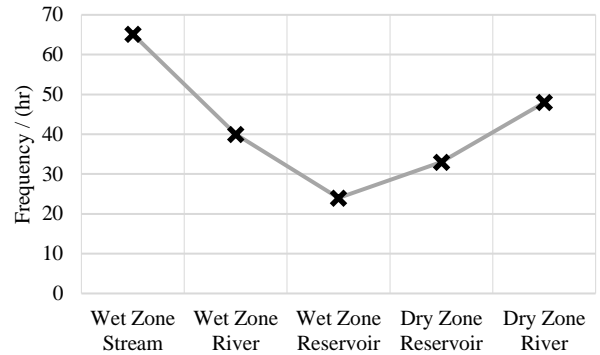


Fig. 5. BW frequency of filters compared to water sources

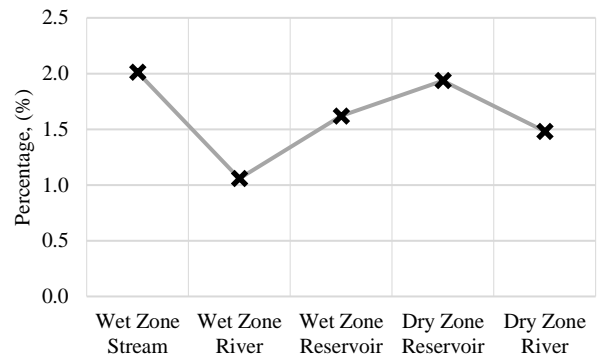


Fig. 6. Estimated average percentage of water used for a backwash event compared to plant daily production capacity

In total about 4200 m³ of water is used on daily basis for BW process in studied 22 WTPs in Sri Lanka (2850 m³ of treated water & 1350m³ of filtered water). Further, average water consumption for backwashing compared to production capacity of the plant is 1.78 % per BW event. Fig. 6 shows the percentage of water used for backwashing in dry and wet zone.

Proper handling of produced SFBW water during BW event is mandatory. Even though there is no regulation in Sri Lanka, WTPs have adopted some strategies to handle this water. There were three major recycling and disposal options observed. Those are (1) do recycling the SFBW water with recirculation tank after settling down the suspended particles (2) direct them to drying beds and dispose to environment (3) directly discharge to environment. From 4200 m³ of SFBW water, about 1200 m³ (29%) is brought back for recycling purpose. About 1500 m³ (35%) directed to drying bed before releasing into environment. Rest of it, about 1500 m³ discharged into the environment without any treatment.

Results of tested parameters are further evaluated to understand the present conditions of SFBW water further. Measured TOC values represent the dissolved organic carbon content in the raw water as the samples filtered through 0.45µm filter papers. Hence, particle matters are separated and

only dissolved matters are measured as TOC. TOC of raw water used for drinking water purpose should be less than 4 mg/L [8]. Fig. 7 shows the raw water TOC variation of studied DWTPs. Here, raw water of 9 DWTPs (41%) exceeds the limits from tested 22 WTPs. According to Fig. 8, water sources in the dry zones have higher organic carbon contents represent the highest level of organic matter content. In addition, wet zone river sources too show a high level of TOC values. This may due to high algae presence in them. Further agriculture sector too contribute in adding more organic compounds to the source water in dry zones [2].

Now, TOC values of SFBW water were compared with raw water respectively. They are shown in Fig. 9. From studied WTPs 6 plants use filtered water (non-chlorinated) and 16 plants use treated water (chlorinated) for backwashing. Hence, initial TOC values of filtered water is expected to be lower compared to the raw water due to possible reduction in organic content during treatment. From the statistical analysis, Pearson correlation value 0.701 shows positive relationship between SFBW water and raw water TOC. Further from paired T test the p-value, 0.305 (>0.05) confirms that there is no significant difference between them. In addition, $R^2 = 0.492$ shows that there is 50% linear relationship between TOC of raw water & SFBW water.

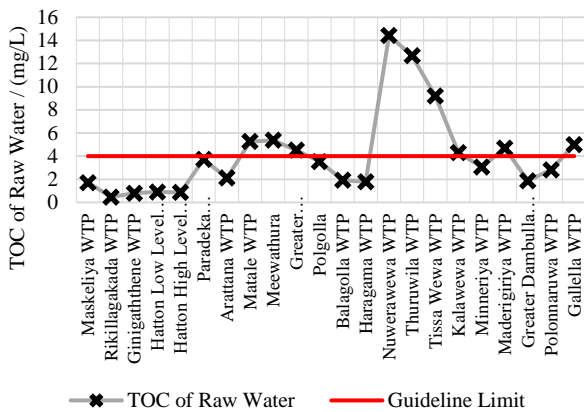


Fig. 7. TOC values of raw water

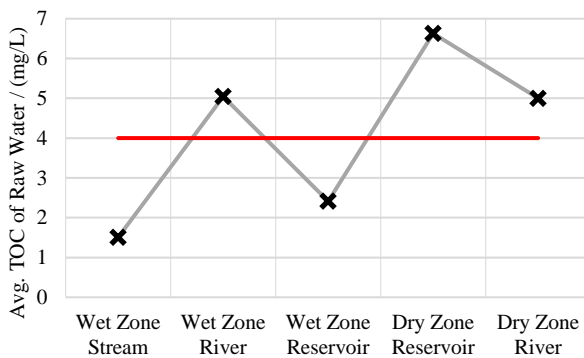


Fig. 8. Average TOC values of water sources

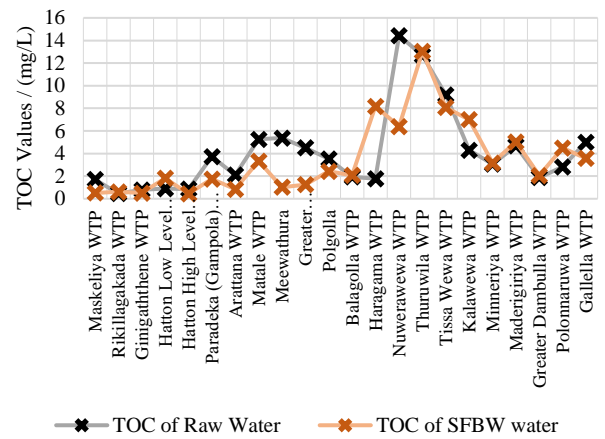


Fig. 9. SFBW water TOC values compared to raw water

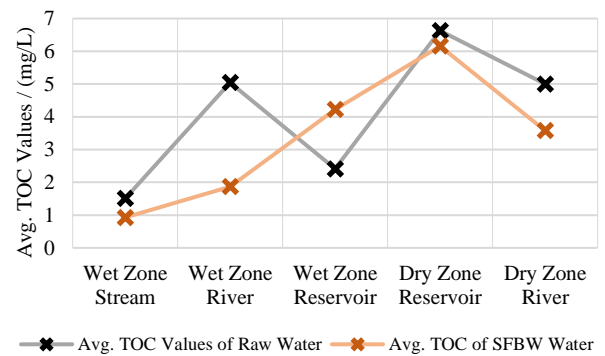


Fig. 10. Average TOC values comparison for raw & SFBW water

Fig. 10 shows the mean TOC values comparison with raw and SFBW water. Further, this was compared with previous studies about TOC values of raw water and SFBW water. They shows no significance difference between them [28] [20] [19]. Therefore, SFBW water TOC values reflect the raw water TOC values. In Sri Lanka, Al based coagulants are used in all studied DWTPs. Thus, SFBW water was analyzed for residual Al content for the possibility of existence of them. USEPA has recommended acute criterion of 750 $\mu\text{g/L}$ (0.75 mg/L) for protection of aquatic species when discharging wastewater into surface water or land. Further SLS 614:2013 has limitation on drinking water as 0.2 mg/L. In addition, Uganda has regulated Al on wastewater discharge and maximum permissible level is 0.5 mg/L. Fig. 11 shows the residual Al content in SFBW water from studied WTPs. Further, these are grab samples collected at the beginning of backwashing process. As a whole volume, there could be dilution of Al concentration. Comparing to the USEPA regulations, SFBW water cannot be discharged directly to the environment, as most of the samples are much higher than 0.75 mg/L. Many studies confirms the toxicity of Aluminium that harmful to humankind due to unprotected discharge [15].

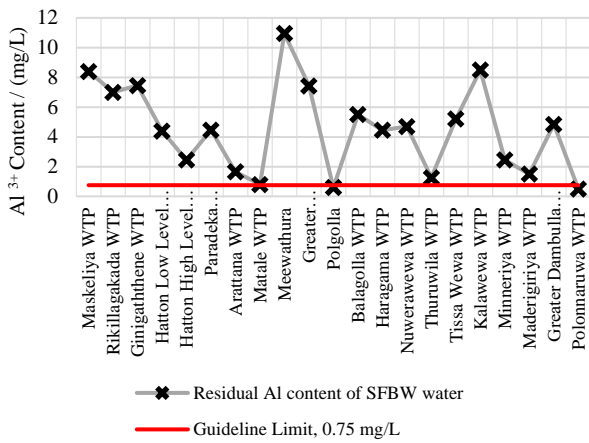


Fig. 11. Aluminium concentration in SFBW water

Further, initial concentration of Al was estimated at the beginning of BW, using collected samples to estimate the pollutant loading to environment. Final concentration was assumed as zero. Because during BW, SFBW water quality varies from extreme to clean. Therefore, simple arithmetic average concentration was used to calculate the weight of Al. From all 22 DWTPs approximately 10 kg of Al generated per backwash event. Fig. 12 shows the discharged weight of Al from each plant. Further, about 7 kg of Al is disposed to environment.

Finally, turbidity of raw water and SFBW water samples were measured and compared using a multiplying factor. For this, SFBW water turbidity was compared to respective raw water to see how many multiple increases are SFBW water turbidity. Fig. 13 shows the multiplying factor of each DWTP.

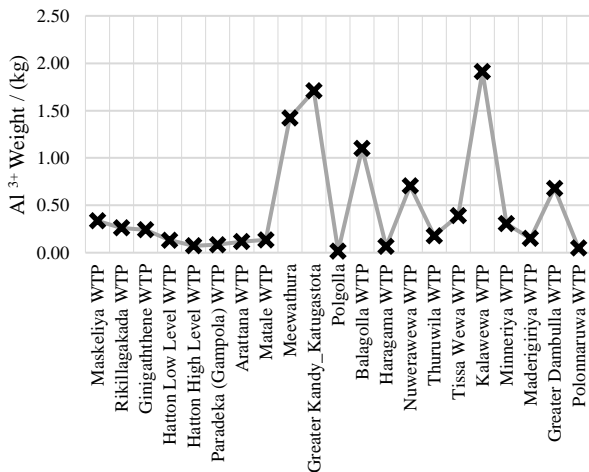


Fig. 12. Generated Al weight in each plant per backwash

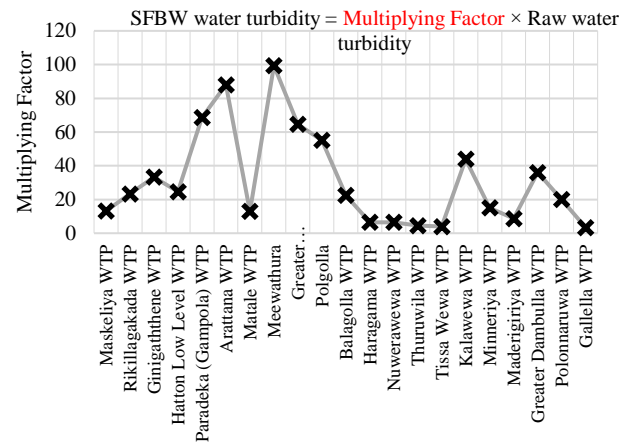


Fig. 13. Multiple increase of turbidity of SFBW water compare to raw water

Wet zone plants have high multiple increase compare to dry zone plants. They show about 47 times higher turbidity of SFBW water compared to raw water where dry zone show about 16 times. This variation in multiple increase may be due to backwashing frequency of filters. Because, 56 % of dry zone DWTPs do backwashing once in a day where only 34 % of plants in wet zone do so. Further maximum filter running time is 2 days in dry zone. Some plants in wet zone run more than 2 days. So this could be a reason for turbidity increase in wet zone plants SFBW water. In addition, statistical analysis shows that there is no good relationship between turbidity of SFBW water and raw water. Paired T test the p-value equals to 0.000, which means there is a significant difference between those values. However, Pearson correlation value shows 0.295 and $R^2 = 0.09$ which means there is a poor linear relationship between them. High turbidity values of SFBW water depends on many reasons hence it is difficult relate them [31][12][8].

Results of this study on selected parameters are promising the possibility of recycling in comparison with previous studies on this subject. In Sri Lanka, NWSDB produces 1.5 million m³ of drinking water per day and 2% of it, 30,000 m³ of SFBW water is generated all over the country [23]. For a sustainable future, it is mandatory to reuse it. TOC values of SFBW water do not have significant difference from respective raw water TOC values. TOC values are determined after removal of particulate matters. Hence, SFBW water can be considered as raw water after removal of particulate matter in terms of organic content. Past studies has concluded that recycling of SFBW water could enhance the removal of TOC, DOC during sedimentation process [41][10].

Al content in SFBW water is beyond the regulation for disposal into the environment. SFBW water residual Al content varies between 0.5 ppm to 11 ppm. Studies have shown that presence of residual Al in SFBW water helped in reduction of coagulant addition during recycling process. It is obvious that turbidity of SFBW water is very high compared to raw water soon after BW event. However, it is possible to bring the turbidity to acceptable range compared to raw water after sedimentation process with 5 hours of retention time [3]. As such, samples of SFBW water of this study were left for 5 hours after mixing well. This exercise confirmed the turbidity of SFBW water could be reduced drastically after a sedimentation process.

As suggested by FBRR, an equalization tank is the best option for DWTPs in Sri Lanka for recycling of SFBW water. Minimum volume of the equalization tank will be 2% of the plant production capacity.

V. CONCLUSIONS

Following conclusions are reached under this study,

- Waters of wet zones have high turbidity (28 NTU) and low pH (7.12) in comparison to dry zone with turbidity (15 NTU) and pH (7.66). Average EC in wet zone is 57 $\mu\text{S}/\text{cm}$ where 280 $\mu\text{S}/\text{cm}$ in dry zone
- TOC of raw water in dry zone are higher than recommended levels. Hence, pre and post chlorination activities need to be regulated for DBPs.
- About 70% of SFBW water is discharged to the environment without proper treatment. This is about 3000 m^3 of water from 18 WTPs per backwash event.
- TOC in SFBW water show similar variation compared to raw water TOC content.
- Residual Al^{3+} content in SFBW water is beyond the discharge standards, 0.75 mg/L [8]. It has an average of 2.25 mg/L considering all 22 WTPs. It is about 10 kg of Al is generated from single backwash event in studied DWTPs.
- Turbidity of SFBW water shows the trend of raw water turbidity. Wet zone plants show about 47 times higher turbidity of SFBW water compared to raw water where dry zone plants show about 16 times.

VI. RECOMMENDATIONS

As SFBW water contains high level of coagulant chemicals and very high turbidity values compared to regulations, disposal to environment without treatment is not possible. As a simple option, filter back wash recycling rule of USEPA need to be applied in all WTPs with Equalization Tank as a treatment option. Biological contaminants such as protozoa especially *Cryptosporidium* and *Giardia* in SFBW water samples has to be evaluated further.

Due to high levels of TOC content in raw water, disinfection with chlorine gas need to be controlled for safe levels of DBPs in treated water for consumption. This area need to be further studied on DBPs and causes for the high dosage. Finally, NWSDB must put effort to implement FBRR in all its upcoming water supply schemes to protect the environment and reuse the sources towards the sustainable goals of UN.

ACKNOWLEDGMENT

The author would like to acknowledge the support of Academic and non-academic staff members of Environmental Engineering laboratory, Department of Civil Engineering, University of Peradeniya, and the DWTPs technicians of NWSDB.

REFERENCES

[1] Ali, Z., & Bhaskar, S. B. (2016). Basic statistical tools in research and data analysis. *Indian journal of anaesthesia*, 60(9), 662–669.

[2] Amarasiri, S., *Caring for water*. 2008

[3] Arendze S. and Sibiya M., "Filter backwash water treatment options," *J. Water Reuse Desalin.*, vol. 4, no. 2, p. 85, 2014.

[4] Chaulk, M. and Sheppard, G., *Study on Characteristics and Removal of Natural Organic Matter in Drinking Water Systems in Newfoundland and Labrador*. Newfoundland Labrador Department of Environment and Conservation Division WM; 2011 August 2011. Report No. Contract, (103047.00)

[5] Cornwell, D., Bishop, M.M. and Dunn, H.J. (1984). 'Declining-rate filters: regulatory aspects and operating results.' In: *Journal American Water Works Association*, vol. 76, no. 12, p. 55

[6] Cornwell, D., MacPhee, M., McTigue, N., Arora, H., DiGiovanni, G., LeChevallier, M., Taylor, J., 2001. *Treatment Options for Giardia, Cryptosporidium, and Other Contaminants in Recycled Backwash Water*. American Water Works Association Research Foundation (AWWARF), Denver, CO, USA.

[7] Dissanayaka C.B., "Water Quality in the Dry Zone of Sri Lanka-Some Interesting Health Aspects", *J. Natn.Sci.Foundation, Sri Lanka*, 2005 33(3): 161-168.

[8] EPA, "Filter Backwash Recycling Rule. Technical Guidance Manual EPA 816-R-02-014," 2002.

[9] Gensemer R. W. and Playle R. C., "The bioavailability and toxicity of aluminum in aquatic environments," *Crit. Rev. Environ. Sci. Technol.*, vol. 29, no. 4, pp. 315–450, 1999.

[10] Gottfried, A., Shepard, A., Hardiman, K. & Walsh, M. 2008 *Impact of recycling filter backwash water on organic removal in coagulation–sedimentation processes*. *Water Research* 42 (18), 4683–4691

[11] Jahan .I, *Removal of aluminium from filter backwash water using adsorbents and a geotextile*, Master of applied science thesis, 2016

[12] Kawamura S. (2000). *Integrated Design and Operation of Water Treatment Facilities*. 2nd Ed. New York: John Wiley & Sons, Inc

[13] Kim Y. H., Eom J. Y., Kim K. Y., Lee Y. S., Kim H. S., and Hwang S. J., "Applicability study of backwash water treatment using tubular membrane system with dead-end filtration operation mode," *Desalination*, vol. 261, no. 1–2, pp. 104–110, 2010.

[14] Kulasooriya S. A., "Toxin producing freshwater cyanobacteria of Sri Lanka," *Ceylon J. Sci.*, vol. 46, no. 1, p. 3, 2017.

[15] Lenntech B. V. (2015). *Aluminium - (Al) - Chemical properties, Health and Environmental effects*.

[16] Levesque, B.R. et al, 1999. *Filter Backwash Recycle: Quality Characteristics and Impacts on Treatment*. Proc. 1999 AWWA Ann. Conf., Chicago.

[17] Liu Z., Xu Y., Yang X., Huang R., Zhou Q., and Cui F., "Does the recycling of waste streams from drinking water treatment plants worsen the quality of finished water? A case assessment in China," *Water Sci. Technol. Water Supply*, vol. 17, no. 2, pp. 597–605, 2017.

[18] Madabhushi, B.S., 1999, "What are trihalomethanes?," *Tap*, 1999.

[19] Mahdavi M., Ebrahimi A., Azarpira H., Tashauoei H. R., and Mahvi A. H., "Dataset on the spent filter backwash water treatment by sedimentation, coagulation and ultra-filtration," *Data Br.*, vol. 15, pp. 916–921, 2017.

[20] McCormick N. J., Porter M., and Walsh M. E., "Disinfection by-products in filter backwash water: Implications to water quality in recycle designs," *Water Res.*, vol. 44, no. 15, pp. 4581–4589, 2010.

[21] McLachlan, D., Bergeron, C., Smith, J. E., Boomer, D. and Rifat, J. L. (1996). "Risk for Neuropathologically Confirmed Alzheimer's Disease and Residual Aluminum in Municipal Drinking Water Employing Weighted Residential Histories." *Neurology* 46: 401–5.

[22] National Water Supply and Drainage Board, "Corporate Action plan", 2019.

[23] National Water Supply and Drainage Board, "Corporate Action plan", 2014.

[24] National Water Supply and Drainage Board, "Sludge Management Policy for Water Treatment Plants," no. December, p. 8, 2012.

[25] Niroumand H., Zain M. F. M., and Jamil M., "Statistical Methods for Comparison of Data Sets of Construction Methods and Building Evaluation," *Procedia - Soc. Behav. Sci.*, vol. 89, pp. 218–221, 2013

[26] Perera, M. B. U. and Yatigammana, S. K. (2014) *Distribution and composition of cyanobacteria in Sri Lankan reservoirs* In: Illeperuma, O. A. et al. (eds) *Symposium Proceedings, International Symposium on Water Quality and Human Health: Challenges Ahead*, 27 and 28 June, PGIS, Peradeniya, Sri Lanka: p14

[27] Ratnayake, R.M.S.K. 2010. "Urbanization and Water Quality Control for the Source of Water in Colombo City, Sri Lanka." Paper submitted to the 1st WEPA International Workshop, Hanoi, Viet Nam, 8-9 March.

- [28] Suman S. and Sulekh C., "Effect of Filter Backwash Water when blends with Raw Water on Total Organic Carbon and Dissolve Organic Carbon Removal," *Res. J. Chem. Sci.*, vol. 2, no. 10, pp. 38–42, 2012
- [29] Takona, J.P. (2002). *Educational Research: Principles and Practice Book*. Writers Club Press.
- [30] Tchobanoglous, G, Burton, F.L, 2003. George Tchobanoglous, Franklin L. Burton, H. David Stensel, *Wastewater Engineering Treatment & Reuse*, 4th edition. Metcalf & Eddy, Inc., New York: McGraw-Hill. DCN DW00871.
- [31] U.S. Epa, "Drinking Water Treatment Plant Residuals. Management Technical Report. Summary of residuals generation, treatment and disposal at large community water systems.," no. September 2011, p. 378, 2011.
- [32] U.S. Epa, "Drinking Water Treatment Plant Residuals. Management Technical Report. Summary of residuals generation, treatment and disposal at large community water systems.," 2002
- [33] United Nations (2019) 'Leaving no one behind: Facts and Figures', *Highways*, 88(5), p. 3. doi: 10.2307/j.ctvnjbdm2.22.
- [34] United Nations, *Millennium Development Goals Country Report 2014: Sri Lanka*. 2015.
- [35] UNESCO (United Nations Educational, Scientific and Cultural Organization) and MoAIMD (UNESCO and Ministry of Agriculture, Irrigation and Mahaweli Development). 2006. *Sri Lanka Water Development Report*
- [36] Wang, L., Ferons, D. P., Ma, W., Nessler, M. B., Peterson, J. D., Jin, Y. & Ikehata, K. 2012 Health effects associated with wastewater treatment, reuse, and disposal. *Water Environment Research* 84 (10), 1824–1855.
- [37] Wilf M., Pearce G., Allam J., Suarez J., *Reclamation of sand filter backwash effluent using capillary ultrafiltration*, *Membr. Technol.* 3 (2003) 6–9.
- [38] Wood .M.E, 2014, *Removal of aluminum in filter backwash water: a treatment optimization case study*, Master of applied science thesis.
- [39] World Health Organization, 2018. *Alternative drinking-water disinfectants: bromine, iodine and silver*.
- [40] Zazouli, M.A. and Kalankesh, L.R., 2017. Removal of precursors and disinfection by-products (DBPs) by membrane filtration from water; a review. *Journal of Environmental Health Science and Engineering*, 15(1), p.25
- [41] Zhou, Z., Yang, Y., Li, X., Su, Z., Liu, Y., Ren, J. & Zhang, Y. 2015 Effect of recycling filter backwash water on characteristic variability of dissolved organic matter in coagulation sedimentation process. *Desalination and Water Treatment* 53 (1), 48–56.

Comparative Evaluation of The Spatial Distribution of Rainfall for Accurate Runoff Modeling; A Case Study in Upper Kelani River Basin

D.W.V.M. Perera
Department of Civil Engineering
University of Peradeniya
Kandy, Sri Lanka
vishakap6@gmail.com

D.T.H.K. Karunarathne
Department of Civil Engineering
University of Peradeniya
Kandy, Sri Lanka
teshanikarunarathna@gmail.com

M.M.G.T. De Silva
Department of Civil Engineering
University of Peradeniya
Kandy, Sri Lanka
gouri@eng.pdn.ac.lk

Abstract — Runoff models are used to illustrate the mathematical relationship between rainfall and runoff. Modeling runoff helps to understand, control and monitor the streamflow. However, the accuracy of the modeling results heavily depends on the quality of the input data. Rainfall is one such major input and the spatial distribution of rainfall plays a key role. This research aims to evaluate the impact of spatial distribution of rainfall for accurate runoff modeling over the upper Kelani river basin. Three commonly used interpolation methods namely; Arithmetic mean, Thiessen polygon, and Inverse Distance Weighting (IDW) were used for this purpose. The runoff was then simulated using HEC-HMS for each rainfall series obtained from each spatial distribution method. Model calibration is done for 1989-2006 and validated for 2007-2016. The simulated hydrograph at Hanwella outlet was compared with the observed runoff hydrograph with the use of goodness of fitting statistics such as; Nash–Sutcliffe Efficiency (NSE), Relative Root Mean Square Error (RRMSE) and Percentage Bias (PBIAS). Final step was to identify the most reliable rainfall interpolation method with corresponding catchment characteristics for the upper Kelani river basin. IDW method gave the best performance with reference to PBIAS (11.01%), whereas arithmetic mean method performed well with NSE (0.74). However, even though the Thiessen polygon method showed balance performance with RRMSE (0.53), all three methods are capable of simulating the runoff very close to the actual. Hence, this study concludes that the interpolation method used for spatial distribution of rainfall is not a critical factor for the accurate runoff modeling in upper Kelani river basin.

Keywords— rainfall-runoff modeling, spatial distribution, HEC-HMS

I. INTRODUCTION

Rainfall-runoff modeling is one of the major components in a hydrological study, which is essential to understand, control, monitor and manage the water resources. Therefore, accurate modeling of runoff is crucial and the accuracy highly depends on the quality of input data. Rainfall, soil moisture, evapotranspiration, surface runoff and temperature are the major factors influencing runoff simulations while rainfall is the major driving force among them. However, rainfall measurements cannot be taken in every single point and gauges are not evenly distributed. Hence, interpolation techniques are needed to calculate the spatial distribution of rainfall. However, rainfall distribution is not spatially

uniform. Hence, the assumption of spatially uniform rainfall distribution in hydrological modeling is not always correct. Besides the large-scale atmospheric circulations, topographic features such as latitude, longitude, altitude, slope, and direction of slope have variable effects on the spatial distribution of rainfall. Therefore, it is worth to investigate a reliable spatial interpolation scheme for a selected area to provide accurate spatial distributions of rainfall. Several other studies were also carried out to identify the best fitting spatial distribution method to distribute rainfall in river basins all over the world such as Uttarakhand region in the Himalayas [1], Mula and Mutha Rivers [2], and mountainous region in tropical island, O‘ahu, Hawai‘i [3]. However, the most reliable interpolation method differs from one basin to other. According to past literature, Inverse Distance Weighting (IDW) and the spline interpolation give better results in small basins with high rain gauging density [4]. Further, Keblouti et.al, concluded that IDW is the best fitting interpolation technique to distribute rainfall over the coastal city of Annaba located in eastern Algeria [5]. However, no research was conducted to upper Kelani river basin to analyze the influence of rainfall interpolation technique for the accuracy of runoff simulations. Hence, this study aims to identify the most reliable spatial distribution technique to distribute rainfall over the upper Kelani river basin for accurate runoff simulation.

II. STUDY AREA

This research, considers Upper Kelani river basin. Kelani river is the second largest river by volume of discharge and fourth-longest river (145 km) in Sri Lanka. It originates from the central hills and flows to the west coast through the commercial capital of the country, Colombo city. It is bounded by 6°47'–7°05' North latitudes and 79°53' to 80°13' East longitudes while passing through Nuwara Eliya, Rathnapura, Kegalle, Gampaha and Colombo districts. The upper basin approximately covers 1,887 km² [6], [7]. Fig.1 shows the map of upper Kelani river basin with the rainfall gauging stations used for the analysis.

The Kelani basin receives about 3,718 millimeters of annual average rainfall while it varies from 500 mm to 5,000 mm in the dry season to wet season. The total annual volume of the Kelani river is approximately 8,600 million cubic meters and 65% of the total volume is discharged into the sea. The peak flow in the river varies between 800 – 1,500 m³/s during monsoon periods [7]. Lower and middle reaches of the Kelani river flows through Colombo and Gampaha districts, where they bear the highest population density and the commercial hub of the country.

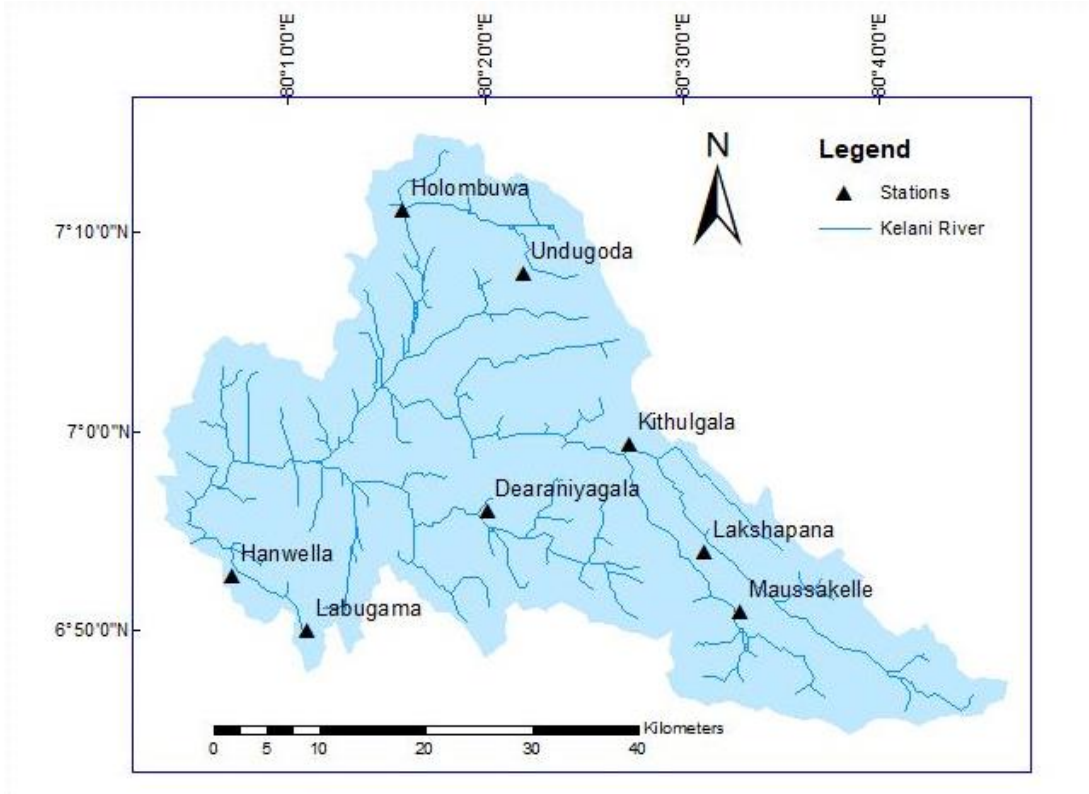


Fig. 1. Upper Kelani river basin

The flood damage in the Kelani river basin is comparatively high. Therefore, identifying reliable modeling technique to simulate river discharge and floods is vital.

III. METHODOLOGY

A. Data

The daily rainfall data at eight rainfall-gauging stations located in the upper Kelani river basin namely, Hanwella, Labugama, Dearaniyagala, Holombuwa, Undugoda, Kithulgala, Lakshapana and Maussakelle were obtained from the Department of Meteorology, Colombo for the period from 1989 to 2016 (27 years). Daily stream flow data at Hanwella gauging station was obtained from the Irrigation Department, Colombo for the same period. Missing rainfall data were calculated at each station by using normal ratio method because of the difference between the average annual rainfall at other adjacent stations and the missing data station is greater than 10% [8].

B. Research flow

Rainfall data were spatially distributed by applying each selected interpolation method. Three simple and widely using methods namely; arithmetic mean method, Thiessen polygon method and IDW method were considered for this analysis.

Then the rainfall-runoff simulations were carried out for each interpolated rainfall series. Following the similar literature [9, 10, 11, 12] this research used Hydrologic Engineering Center – Hydrologic Modeling System (HEC-HMS) software for runoff simulation in upper Kelani basin. Finally, the simulation results were compared with the observed discharge data at Hanwella station. Fig. 2 shows the stepwise methodology adopted. Here, the rectangular shapes, parallelogram shapes and diamond shape are used to represent process steps, input or output, and decisions respectively.

C. Arithmetic mean method

This is the simplest technique use to estimate mean rainfall over a river basin by only taking the rain gauging stations inside the basin into account. Here, the mean rainfall is calculated by using the (1). The calculations are based on the assumptions that the uniform distribution of rain gauges within the basin and no large variation of gauge measurement compared to the mean.

$$P = \sum_{i=1}^n \frac{P_i}{n} \quad (1)$$

Here, P is average rainfall depth, P_i is rainfall depth at gauge i and n is the number of gauging stations.

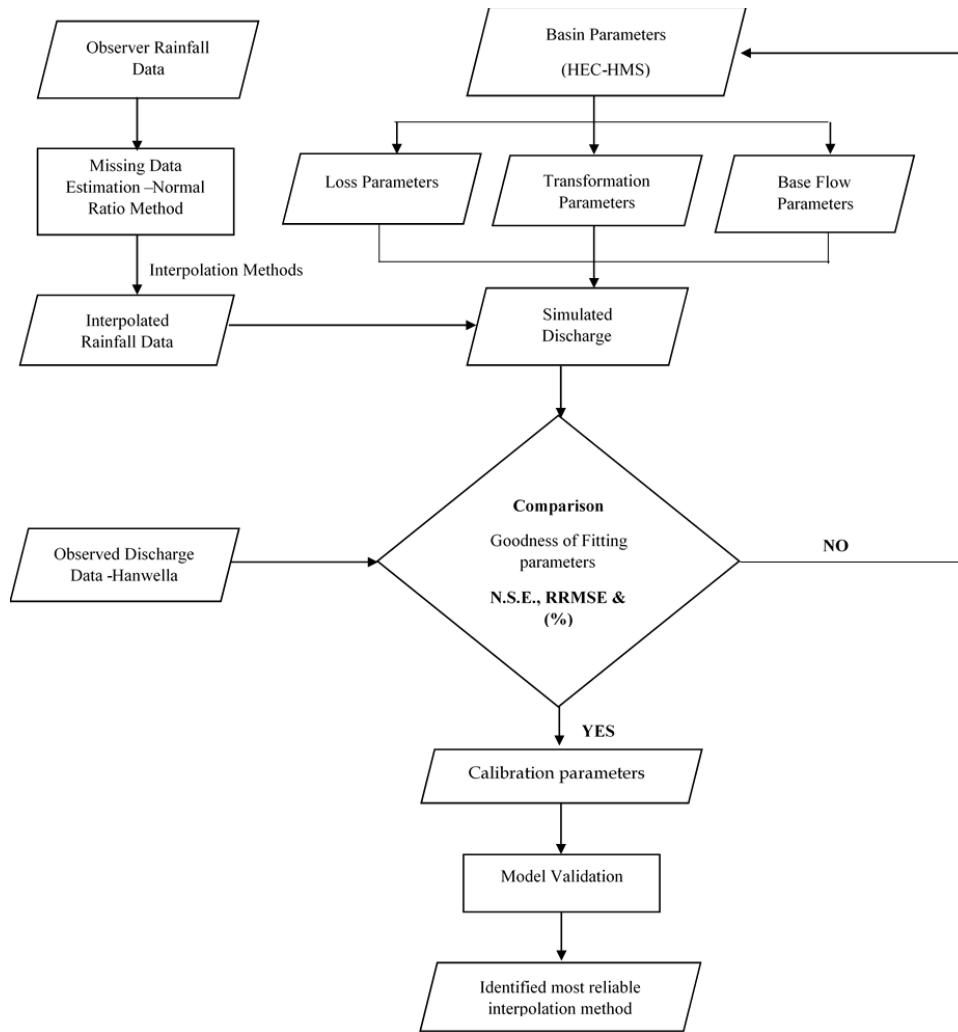


Fig. 2. Methodology

D. Thiessen polygon method

Thiessen polygon method is one of the simple and popular method to compute the mean areal rainfall. A graphical technique calculates station weights based on the relative areas of each measurement station in the Thiessen polygon network. The station observations are multiplied by the individual weights and the values are summed to obtain the areal average rainfall. The mean areal rainfall (P) is calculated by (2).

$$P = \frac{P_1 \cdot A_1 + P_2 \cdot A_2 + \dots + P_n \cdot A_n}{A_1 + A_2 + \dots + A_n} \quad (1)$$

Where $P_1, P_2 \dots$ are observed rainfall at the stations inside or outside of the basin and $A_1, A_2 \dots$ are the areas of polygons around each station.

E. Inverse Distance Weighted method (IDW)

IDW is a very flexible, spatial, deterministic interpolation method. The nearby known points are more influenced by the estimated value of a point rather than those farther away points. It estimates the values of points using a linear combination of values at sampled points weighted by an inverse quadratic function of the distance from the point

of interest to the sampled points. The weights are a decreasing function of distance [13]. Equation (3) is used to calculate the rainfall at any point (P_x). Where; W is equal to $\frac{1}{D^2}$.

$$P_x = \frac{\sum P_i \cdot W}{\sum W} \quad (2)$$

Here, D is the distance between the considered point (x) and the station with known rainfall whereas P_i is rainfall at station with known rainfall.

F. Rainfall-runoff modeling

The rainfall time series derived from each interpolation method was then used in rainfall-runoff model to generate the flow at Hanwella gauging station. The rainfall-runoff modeling software used in this study is, HEC-HMS 4.7.1, which is developed by the United States Army Corps of Engineers. HEC-HMS model setup consists of a basin model, meteorological model, control specifications, and input data (time series data) [11]. Table I shows the selected method with basin parameters

TABLE I. HEC-HMS PARAMETERS

Parameter	Method
Modeling precipitation losses	Soil Moisture Accounting Method
Modeling direct runoff	Clark Unit Hydrograph Method
Modeling base flow	Recession Method

a) Modeling rainfall losses

The HEC-HMS software includes a several methods to compare infiltration losses, such as deficit and constant method, exponential method, Green and Ampt method, initial and constant method, Soil Conservation Service (SCS) curve number method, and soil moisture accounting method. Among these methods, the deficit and constant method and soil moisture accounting method are designed for continuous simulations while the other methods are for short term simulations [14]. In this study Soil Moisture Accounting loss method is used as the loss method and Table II shows the values for calibrated parameters for rainfall loss.

b) Modeling Direct Runoff

Clark unit hydrograph method, Kinematic wave method, SCS unit hydrograph method, and Snyder unit hydrograph method are the available unit hydrograph methods in HEC-HMS. This study considered Clark Unit hydrograph method and it requires few parameters namely time of concentration and storage coefficient. Those parameters were calculated using (4) and (5) and T_c and R values for upper Kelani basin were calculated as 28h and 40h respectively..

$$T_c = \frac{0.0179 \times L^{0.77}}{S^{0.385}} \quad (4)$$

$$T_c + R = 142.2 \times (DA)^{0.081} \times S^{0.539} \quad (5)$$

Where L , s , DA and S are length of flow path (m), average slope of watershed, drainage area (km^2), and channel slope (m/km) respectively [14].

c) Modelling Base Flow Method

There are three alternative base flow methods in HEC-HMS, namely Constant monthly base flow method, linear reservoir method, and Recession Base Flow method. After simulating some trials, the base flow modelling parameters such as initial discharge, recession constant and ratio were fixed to $112 \text{ m}^3/\text{s}$, 0.7 and 0.5 respectively.

TABLE II. PARAMETERS FOR LOSSES

Calibrated Parameters	Value
Soil (%)	70
Groundwater 1 (%)	45
Groundwater 2 (%)	80
Max Infiltration (MM/HR)	55
Impervious (%)	40
Soil Storage (MM)	200
Tension Storage (MM)	75
Soil Percolation (MM/HR)	1
GW 1 Storage (MM)	60
GW 1 Percolation (MM/HR)	1.2
GW 1 Coefficient (HR)	100
GW 2 Storage (MM)	150
GW 2 Percolation (MM/HR)	1
GW 2 Coefficient (HR)	1

IV. RESULTS AND DISCUSSION

Data from 1st October 1989 to 30th September 2006 were used for model calibration and the data from 1st October 2006 to 31st May 2016 were used for validation. The hydrological model results were compared with the observations. Nash-

Sutcliffe Efficiency (NSE), Relative Root Mean Square Error (RRMSE), and percentage bias (PBIAS) were considered to check the reliability of the simulations [1, 2, 6, 9, 15]. Table III shows the limitation ranges of the NSE, RRMSE, and PBIAS [12].

TABLE III. RANGES FOR VALIDATION

Performance rating	N.S.E.	RRMSE	$\delta_b(\%)$
Very good	0.75 to 1	0 to 0.5	$\leq \pm 10$
Good	0.65 to 0.75	0.5 to 0.6	± 10 to ± 15
Satisfactory	0.50 to 0.65	0.6 to 0.7	± 15 to ± 25
Unsatisfactory	< 0.50	≥ 0.7	$> \pm 25$

A. Nash–Sutcliffe Efficiency (NSE)

The NSE value is calculated as one minus the ratio of the error variance of the modeled time-series divided by the variance of the observed time-series. In the situation of a perfect model with an estimation error variance equal to zero, the resulting Nash-Sutcliffe Efficiency equals to 1 (NSE=1). NSE value is calculated by using the (6).

$$NSE = 1 - \frac{\sum_{i=1}^N (O_i - M_i)^2}{\sum_{i=1}^N (O_i - \bar{O})^2} \quad (6)$$

O_i is the i^{th} observation value, M_i is the i^{th} predicted value and N is the total number of observation.

C. Percentage bias (PBIAS)

Percentage bias (PBIAS) measures the average tendency of the simulated values to be larger or smaller than their observed one. Bias is the difference between the mean of the estimates and the actual value. PBIAS value is calculated by using (8).

$$PBIAS = 100 * \frac{\sum_{i=1}^N (O_i - M_i)}{\sum_{i=1}^N O_i} \quad (8)$$

O_i is the i^{th} observation value M_i is the i^{th} predicted value and N is the total number of observation. There are several limitations for this validation.

B. Relative Root Mean Square Error (RRMSE)

The RRMSE value is relative to what it would have been if a simple predictor had been used. By taking the square root of the relative squared error, one reduces the error to the same dimensions as the quantity being predicted. Equation (7) shows the RRMSE equation.

$$RRMSE = \sqrt{\frac{\sum_{i=1}^N (M_i - O_i)^2}{N}} \quad (7)$$

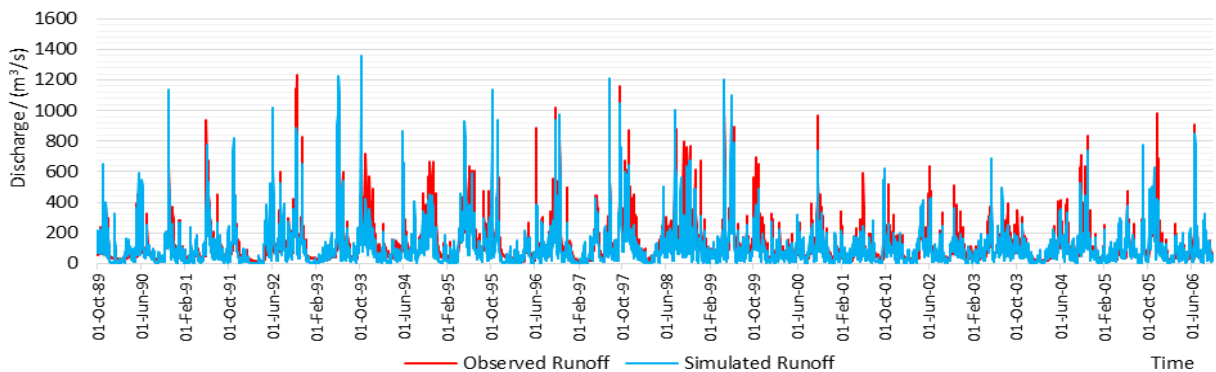
Where; O_i is the i^{th} observation value, M_i is the i^{th} predicted value and N is the total number of observation.

The HEC-HMS model was calibrated and validated by comparing the simulated daily runoff of each rainfall time series with the observed streamflow at the Hanwella gauging station. Fig. 3, Fig. 4 and Fig. 5 indicate the comparison between observed and simulated hydrographs for both calibration and validation under each interpolation method.

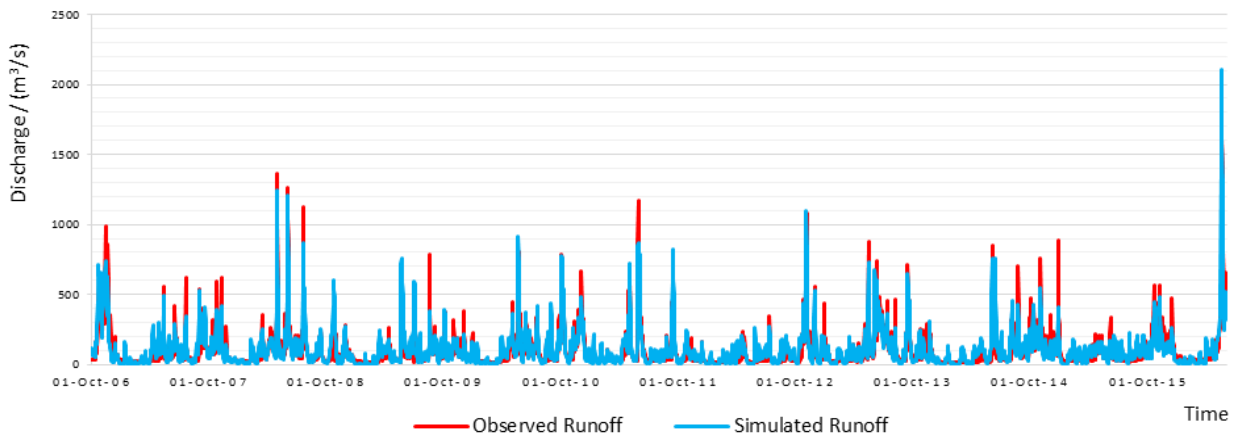
The model performance was evaluated through statistical parameters such as; NSE, PBAIS, and RRMSE. Table IV shows the performance evaluation results for calibration and validation of each interpolation scheme.

TABLE IV. COMPARISON OF PERFORMANCE EVALUATION RESULTS

Performance evaluation method	Arithmetic mean method		Thiessen polygon method		Inverse Distance Weighted method (IDW)	
	Calibration	Validation	Calibration	Validation	Calibration	Validation
Nash–Sutcliffe Efficiency (NSE)	0.74	0.76	0.73	0.76	0.73	0.74
Relative Root Mean Square Error (RRMSE)	0.57	0.71	0.53	0.76	0.58	0.74
Percentage bias (PBIAS)	13.01	13.02	15.87	7.39	11.01	12.44

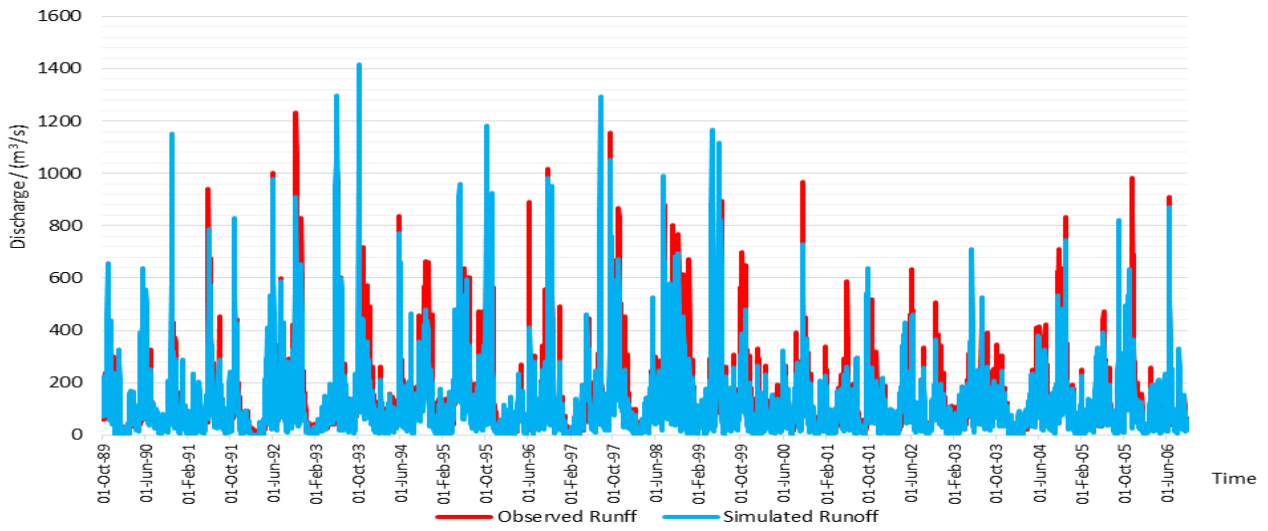


(a)

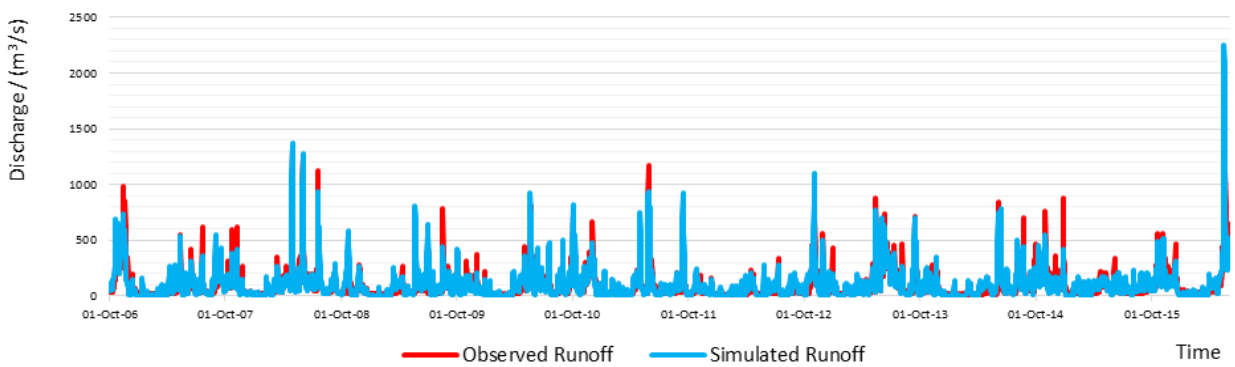


(b)

Fig. 3. Observed runoff at Hanwella and simulated runoff at upper Kelani basin by using Arithmetic Mean Method: (a) Calibration; (b) Validation



(a)



(b)

Fig. 4. Observed runoff at Hanwella and simulated runoff at upper Kelani basin by using Inverse Distance Method: (a) Calibration; (b) Validation

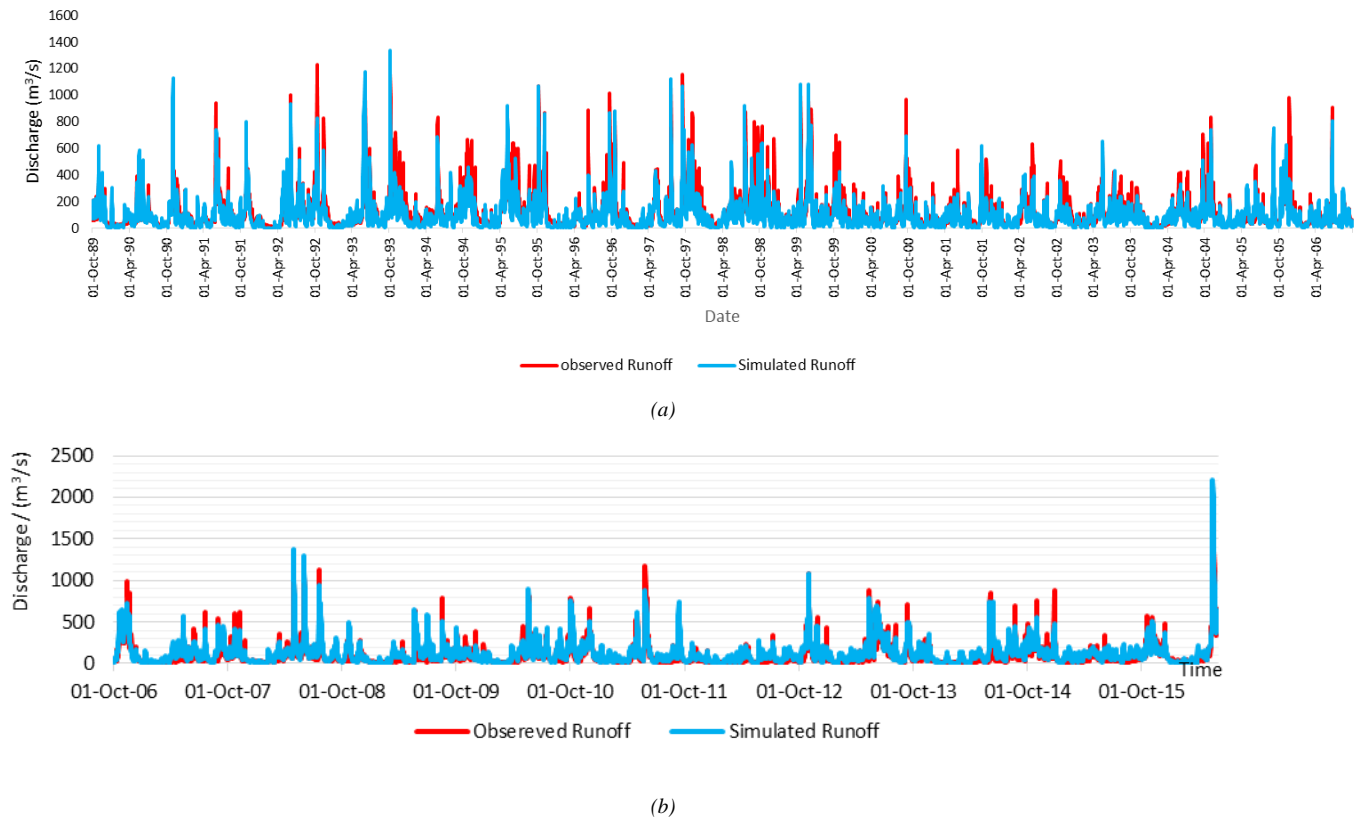


Fig. 5 Observed runoff at Hanwella and simulated runoff at upper Kelani basin by using Thiessen Polygon Method: (a) Calibration; (b) Validation

CONCLUSION

This study considered arithmetic mean method, Thiessen polygon method and IDW method as rainfall interpolation techniques to spatially interpolate the rainfall observations of eight rain gauging stations in upper Kelani river basin. HEC-HMS was used as the rainfall-runoff model. Rainfall losses, direct runoff transformation and base flow were simulated in HEC-HMS by considering soil moisture accounting model, Clark unit hydrograph and recession method respectively. Reliability of the calibration and validation was analyzed through the performance evaluation parameters; NSE, RRMSE, and PBIAS.

NSE values were nearly equal for all the interpolation methods and they were in the range of very good or good category. However, RRMSE values were in the satisfactory range for calibration period correspond to all the interpolation techniques whereas they deviate from the satisfactory range for validation. Similar to NSE, PBIAS also performed well with all the interpolation techniques. All the statistical parameters show satisfactory performance for calibration, while only one parameter deviates from the satisfactory condition for validation. As a summary, IDW method gave the best performance with reference to PBIAS (11.01%), whereas arithmetic mean method performed well with NSE (0.74). Even though the Thiessen polygon method shows balanced with RRMSE (0.53), all three methods are capable of simulating the

runoff reasonably well. Hence, this study concludes that the interpolation method used for spatial distribution of rainfall is not a crucial factor for the accurate runoff modeling in upper Kelani river basin.

ACKNOWLEDGMENT

We extend our sincere gratitude to those who helped and guided for us. Special thanks should goes to Prof. K.P.P. Pathirana and Mr. D.D. Dias for their constructive criticisms. Rainfall data and stream flow data were obtained from department of meteorology and irrigation department respectively.

REFERENCES

- [1] A.Basistha, D.S. Arya, and N.K.Goel, "Spatial Distribution of Rainfall in Indian Himalayas A Case Study of Uttarakhand Region," *Water Resource Manage*, p. 22:1325–1346, 2008.
- [2] P.D.Wagner, P.Fienera, F.Wilkena, S. Kumarc, and K.Schneidera, "Comparison and evaluation of spatial interpolation schemes for daily rainfall in data scarce regions," *Journal of Hydrology*, p. 388–400, 2012.

- [3] A.Mair, and A. Fares, "Comparison of Rainfall Interpolation Methods in a mountainous region of a Tropical Island," *Journal of Hydrologic Engineering*, pp. 371-383, 2011.
- [4] T.A.O.Tao,C.H.O.C.A.T.Bernard, L.I.U.Suiqing, and X.I.N. Kunlun, "Uncertainty Analysis of Interpolation Methods in Rainfall spatial Distribution -A Case of Small Catchment in Lyon," *Journal of Environmental Protection*, pp. 50-58, 2009.
- [5] M. Keblouti, L. Querdachi and H. Boutaghane., "Spatial Interpolation of Annual Precipitation in Annaba-Algeria - Comparison and Evaluation of Methods. Energy Procedia," vol. 18, p. 68 – 475, 2012.
- [6] M.M.G.T.De Silva, S.B. Weerakoon, and S. Herath., "Modeling of Event and Continuous Flow hydrographs with HEC-HMS :Case Study in the Upper Kelani River Basin, Sri Lanka," *Journal of Hydrologic Engineering*, pp. 800-806, 2014.
- [7] K.D.C.R.Dissanayaka, and R.L.H.L. Rajapakse, "Climate extremes and precipitation trends in Kelani river basin, Sri Lanka and impacts on streamflow variability under climate change," *Proceedings of the 2nd International Conference on Climate Change*, vol. Vol. 2, no. Issue 2, pp. pp. 01-17, 2018.
- [8] R.P.De Silva, N.D.K. Dayawansa, and M.D. Ratnasiri, "A comparison of methods used in estimating missing rainfall data," *The journal of Agricultural Science*, vol. Vol 3, no. No 2, pp. 101-108, 2007.
- [9] T. Chen, L. Ren, F. Yuan , and X. Yang, "Comparison of Spatial Interpolation Schemes for Rainfall Data and Application in Hydrological Modeling. Water," 2017.
- [10] E. Sardoi, N. Rostami., S. Sigaroudi and S. Taheri, "Calibration of loss estimation methods in HEC-HMS for simulation of surface runoff (Case Study: Amirkabir Dam Watershed, Iran.," *Advances in Environmental Biology*, pp. 343-348, 2012.
- [11] L.G.Sintayehu,Department of Natural Resources Management. , "Application of the HEC-HMS Model for Runoff Simulation of Upper Blue Nile River Basin," *Hydrological Current Res* 6, 2015.
- [12] G.R.M.B. Gunathilake, P.S. Panditharathne, G.R.A.S. Gunathilaka and N.D. Wragoda, ".Application of HEC-HMS model to simulate long term streamflow in the Kelani River Basin,Sri Lanka.," *10th International Conference on Structural Engineering and Construction Management (ICSECM)*, 2019.
- [13] N.Khorsandi, M.H. Mahdian, E. Pazira, D. Nikkami, and H. Chamheidar, "Comparison of Different Interpolation Methods for Investigating spatial Variability of Rainfall Erosivity Index," *Pol. J. Environ. Stud. Vol. 21*, vol. 21, no. 6, pp. 1659-1666, 2012.
- [14] A.D.Feldman, "Hydrological modelling system HEC-HMS Technical Reference Manual.U.S. Army Corps of Engineers.Hydrologic Engineering Center," 2000.
- [15] M Hassim, A Yuzir , M.N Razali , F.C Ros , M.F Chow , and F. Othman, "Comparison of Rainfall Interpolation Methods in Langat River Basin," *Earth and Environmental Science*.

Development of Damage Curves for Flood Risk Assessment in Rathnapura

H.A.M.H.G.U.I.S. Bandara
Department of Civil Engineering
University of Peradeniya
Kandy, Sri Lanka
e15031@eng.pdn.ac.lk

S.P. Chandrathilake
Department of Civil Engineering
University of Peradeniya
Kandy, Sri Lanka
sasiriprathapa1@gmail.com

M.M.G.T. De Silva
Department of Civil Engineering
University of Peradeniya
Kandy, Sri Lanka
gouri@eng.pdn.ac.lk

Abstract — The practices of living with floods and make use of them while minimizing the losses have introduced the flood management concept against the traditional flood control. Accordingly, damage assessment has become an important tool for decision making in flood risk management and disaster mitigation. Every year most of the major river basins in Sri Lanka are subjected to floods during monsoon seasons. Rathnapura district is one such highly vulnerable area for frequent floods and associated huge economic losses due to the overflowing of the Kalu river. Hence, this study is an attempt to develop damage curves for flood risk assessment in Rathnapura area as a decision support tool. This analysis is based on household questionnaire survey data related to the flood in 2017. A multiple linear regression technique was used to develop damage function relating the relative flood damage with flood characteristics and socio-economic characteristics of the households. The results suggest that the relative flood damage is a function of inundation depth, distance from the river to the household, and the household income status. According to the established regression equation, relative flood damage is highly influential to the households locate near to the river and having low income. Hence, this study concludes that flood damage is not only a function of flood characteristics but also a result of socioeconomic and geographical characteristics of a household. These findings give insights for the policymakers to think beyond the traditional structural adaptation measures.

Keywords: Flood risk assessment, Damage curves, Multiple linear regression

I. INTRODUCTION

In today's context, flood control has been replaced by flood management concept in terms of living with the floods, making benefit of it, and minimizing the losses. The success of flood management in any region depends on the evaluation of different types of flood losses. Development of stage-damage functions for different subcategories is a widely applicable method for flood damage assessment [1]. The stage-damage function is one of the important techniques in flood damage assessment. A Flood Risk Assessment (FRA), incorporates with the accurate assessment of decision making on risk management and risk transfer. It focuses on four main components; flood hazard, exposure, vulnerability and performance on effective flood protection [2]. Flood damage can be in different aspects; economic damage (national, community or individual) causing a certain number of properties affected, damage to individuals (deaths, injuries) ecological and environmental damages (occasionally expressed in monetary terms) and emotional impacts (depression). Those damages can be classified into two distinct categories namely tangible and intangible. The tangible impacts are measurable in monetary terms whereas the intangible impacts such as people injuries or deaths are generally assessed in different terms [3].

Many past researchers have developed flood damage curves for different areas all over the world by considering flood characteristics [4, 1, 5, 6, 7, 8]. However, traditional

approaches focused more on buildings in urban areas, and the basic tools to carry out this task are the so-called flood damage curves or functions [3]. A study carried out by Dias, et al., (2017) to assess the flood damage in the Colombo area was considered (i) building fabrics, (ii) building contents (iii) distributed infrastructure (e.g., electricity, telephone, water supply, roads, and flood protection) and (iv) vehicles by considering flood depth as the major elements of the damage assessment [9]. Our study is based on household-level data and compared to previous studies this study considered geographical and socioeconomic characteristics of households, beyond the traditional consideration of flood characteristics to analyze the flood damage. The main objective of this study is to develop damage functions to obtain damage curves by analyzing the factors influencing to flood risk. So that the policymakers can think of adaptation measures beyond the traditional structural approach.

II. STUDY AREA

This study considers Rathnapura, Sri Lanka, a highly flood-prone area which locates in the wet zone and receives a high amount of rainfall. This high rainfall has resulted in rich vegetation and an environment of greenery interspersed with streams and waterfalls. The climate of Rathnapura is tropical and receives rainfall throughout the year, though the main contributor is Southwestern monsoons. The average annual rainfall is about 4,000 to 5,000 mm while the average temperature varies from 24 to 35 °C coupled with high humidity levels. In every year floods affect the area while some of them are critical. The Irrigation Department defines 'critical' as the floods that exceed 24.4 m MSL at Rathnapura stream flow measuring gauge. There were critical floods in 1913, 1940, 1941, 1947, 2003, and 2017. [10]

The Rathnapura district, which covers approximately 3,275 km², is about 100 kilometers from Sri Lanka's commercial capital, Colombo. Rathnapura and its adjoining area are biophysically diverse – mountain areas with steep slopes, river valleys, lowlands, and plains together form a highly complex natural environment. Due to its geological and geographical features, approximately 90% of the region has underground gem deposits [11].

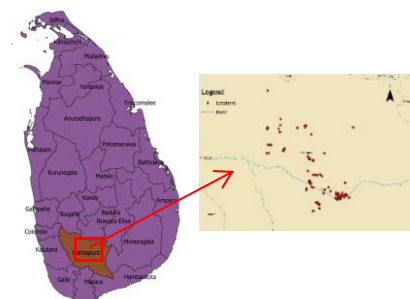


Fig. 1. Study Area

III. DATA

This research is mainly based on questionnaire survey data collected from 275 randomly selected households in Ratnapura area. However, the effective sample became 231 after removing the incomplete and inappropriate data sets. This face-to-face interview type questionnaire survey was carried out to have a good understanding of the local-scale effects of the 2017 flood in the Rathnapura area. The questionnaire was designed according to three scopes; demographic data, information on asset ownership, and damage data. Factors such as gender, age, race, education level, location, occupation, and household income data were collected as the demographic data, whereas house ownership status, house type, numbers of stories, construction materials, land area, etc. were considered under the scope of asset ownership. The flood depth, flood duration, and the financial damage due to the flood were considered to understand the tangible flood impact and damage.

IV. METHODOLOGY

Collected questionnaire survey data were used to develop damage curves through the multiple linear regression method in Minitab software.

Minitab is a statistical package that provides a broad range of basic and advanced data analysis techniques. It includes regression techniques (general and logistic), analysis of variance, experimental design, control charts, and quality tools, survival analysis, multivariate analyses (principal components, cluster, and discriminant), time series, descriptive and non-parametric statistics, exploratory data analysis, power and sample-size calculations. In addition, Minitab supports a wide range of graph and chart types [12]

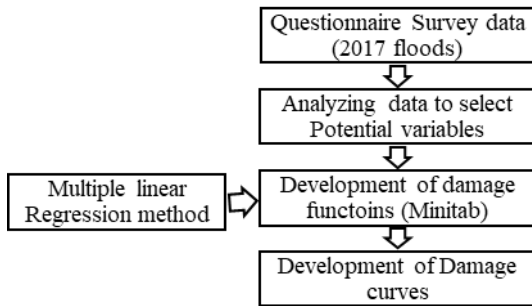


Fig. 2. Methodology

A. Cross section analysis

It is important to keep careful records of survey data for effective usage and analysis. Many successful researchers recommend the use of a computer to sort and organize the data [13, 5]. Data such as household location, the house type, (single-storey or two-storeyed), house construction material, roofing material, land size, occupations of the household members, per capita income, flood inundation duration, maximum inundation depth, total financial loss under flood 2017 were collected and managed with the use of Excel spreadsheet.

One of the major floods of the last two decades, the 2017 flood was taken into account. The distribution of flood-affected populations among subgroups is shown in Table 1. It demonstrates 227 households (99 percent of the entire sample) were hit by the 2017 flood.

The sample size validity was tested using data from the 2011 Census and Statistics Department. A probability sampling approach was used to compute the sample size validity. According to Crandall & Crandall [13], a confidence level of 80–99 percent is appropriate, while Cochran suggests a 4–6% error limit [14]. For a population of 1,088,007 (2011 census data), the minimum valid sample size was 224 for a 90% confidence level and a 5.5 percent error. As a result, the sample size of 231 households can be considered as reasonable [11]. In the sample of 231 households, 81 (35%) had a monthly per capita income of less than 10,000LKR, which is equivalent to the World Bank's absolute poverty level of US\$1.9 per day [15]. However, more than 75% of the households are located within 1 km of the river. Further, more than 80% of the households were inundated beyond 5 feet while the average inundation height is 9 feet.

TABLE I. NUMBER OF HOUSES AFFECTED BY FLOOD

	2017 flood
Poor (n=81)	80 (99%)
Non-poor (n=150)	147 (98%)
Grand total (n=231)	227 (99%)

B. Regression method

Regression analysis is a group of statistical techniques used to approximate the relationships between one or more independent variables and a dependent variable. There are many variants of regression analysis, such as linear, multiple linear, and nonlinear [16]. Simple linear and multiple linear techniques are the most common regression techniques whereas the nonlinear regression analysis is widely used for complex data sets in which dependent and independent variables display a nonlinear relationship.

Simple linear regression is a model that assesses the relationship between a dependent variable and an independent variable. Multiple linear regression analysis is essentially similar to the simple linear model, with the exception that multiple independent variables are used in the model [16]. Equation (1) represents the general equation for regression analysis for flood damage estimations.

$$\text{Relative flood loss} = f(x_{i1}, x_{i2}, x_{i3}, \dots, \dots, \dots + x_{ip}) \quad (1)$$

Multiple regression method was used in this study to model the relationship between flood damage and the influencing independent variables. Flood characteristics (number of day the house is under flood, maximum inundation depth) geographical characteristics (elevation, distance from the river to household) and socioeconomic characteristics (education level, dependent ratio, poor/non-poor condition, land size, single/double story) were considered as the independent variables whereas the relative flood damage was considered as the dependent variable.

C. Select potential variables and develop damage functions

The best fitting independent variables among the questionnaire survey data has to be identified before the regression analysis. There are various procedures for that purpose. In this study, damage data such as a number of day the house is under flood, maximum inundation depth, geographical characteristics such as elevation, distance from the river to household and socioeconomic characteristics such as education level, dependent ratio, poor/non-poor condition

(dummy), land size, single/doublestorey (dummy) were considered as independent variables and multi-collinearity checking was done to identify the correlation among the independent variables.

The relative flood loss was considered as the dependent variable. The average cost of damage caused by the flood is referred to as the absolute loss. The financial loss suffered in relation to average annual income (2) is referred to as the relative loss. This measure represents the maximum amount of loss a household can bear; the more the relative loss, the greater the impact, even if the absolute loss is not significant. If a wealthy family and a poor family both lose the same amount in a tragedy, the poor family's relative loss will be greater because their lower income.

$$\text{Relative flood loss} = \frac{\text{Flood loss}}{\text{Annual average income}} \times 100\% \quad (2)$$

D. Model development and validation

The primary problems connected with the limited availability of data are model development and validation. In order to overcome this issue, considering the past literature [17], random sampling was employed to divide the whole sample into 10 subsamples. Each sub sample contains randomly generated 150 data points. One model was development using the first random samples and kept it as the control. The remaining nine samples were used for validation. Similar to sample 1, separate models were developed for all the other nine samples. Then the percentage deviation of each coefficient correspond to each independent variable was calculated with respect to the values of control model to check the reliability of it.

E. Goodness of fitting parameters

Reliability of each model was checked by using the model fit parameters namely; probability level, Root Mean Square Error Approximation (RMSEA), Goodness of Fit Index (GFI), Adjusted Goodness of Fit Index (AGFI), Comparative Fit Index (CFI), Normed Fit Index (NFI) and Tucker-Lewis Coefficient (TLI). Table II indicates the most appropriate range for each model fit parameter.

TABLE II. MODEL FIT PARAMETERS

	Acceptable range
Probability level	Closer to "0"
RMSEA	Closer to "0"
GFI	Closer to "1"
AGFI	Closer to "1"
CFI	Closer to "1"
NFI	Closer to "1"
TLI	Closer to "1"

V. RESULTS AND DISCUSSION

A. Model development

First, linear regression models were developed for each selected independent variable with the dependent variable to understand the direct impact of each variable on relative flood loss. P values for each model were obtained and shown in table III. The significance level of the relationship is high when the P-value less than 0.05 ($P \leq 0.05$). Table III shows the results of the single linear regression between relative

flood loss and each independent variable (distance from the river to household, inundation depth, number of days house is under flood, high education level, dependent ratio, poor/non-poor condition, land size, single/double story). Dependent ratio, single double story and land size were rejected because the high P values beyond the acceptable range. Then many combinations of the remaining independent variables were checked with relative flood loss (dependent variable) through multiple linear regression in Minitab and the results are shown in table IV. Multi-collinearity among independent variables were also checked in this stage. Finally, inundation depth, distance to river and poor/non-poor condition were selected as the best fitting combination of independent variables as they showed the highest significance.

TABLE III. INFLUENCING VARIABLES WITH RELATIVE FLOOD LOSS

Independent variable	P-Value
Distance from the river to household	0.005
Dependent ratio	0.226
Single/Double Stories house	0.226
High Education Level	0.007
Number of days the house is under flood	0.023
Inundation Depth	0.002
Land size	0.612
Poor/Non poor	0.017

TABLE IV. INFLUENCING COMBINATION OF VARIABLES WITH RELATIVE FLOOD LOSS

Combination	P-value
Inundation depth	0.012
Distance from the river to household	0.03
Poor/ Non poor	0.004
<hr/>	
Inundation depth	0.053
Distance from the river to household	0.008
High Education Level	0.004
<hr/>	
Inundation depth	0.074
Distance from the river to household	0.023
High Education Level	0.086
Number of days the house is under flood	0.26
Poor/ Non poor	0.081
<hr/>	
Inundation depth	0.019
Distance from the river to household	0.021
High Education Level	0.081
Poor/ Non poor	0.084

B. Model validation

Validation of the model was carried out by using the other nine random samples. Reliability checking of the validation process was also checked through the model fit parameters. Relevant model fit parameters and their values are shown in table V. Model fit parameters for the validation lie within a reasonable range, meaning the selected independent variables are appropriate. However, in order to check whether the remaining nine models used for validation are compatible with the controlled model, further comparison was made for the coefficients correspond to each independent variable with the controlled model. Here, the percentage variation of each coefficient with respect to controlled model was calculated and shown in Table VI. All the percentage deviations are in between -21% and 21% confirming that the model parameters are stable around the controlled model.

C. Regression equation

Regression equation of the control sample which explain the relationship of each independent variable with relative flood loss is shown below (3).

$$RL = 7.69 + 0.372 \times ID - 0.002046 \times DR - 3.24 \times PNP \quad (3)$$

In (3) “*RL, ID, DR and PNP*” are the relative flood loss, the inundation depth in feet, the distance from the river to household in meters and the Poor/Non-Poor condition (dummy, non-poor = 1, Poor = 0) respectively. Equation 3 represents that the relative flood loss is with high inundation depths and low distance from the river. Further, it indicates that the relative flood loss is high for poor households than non-poor households.

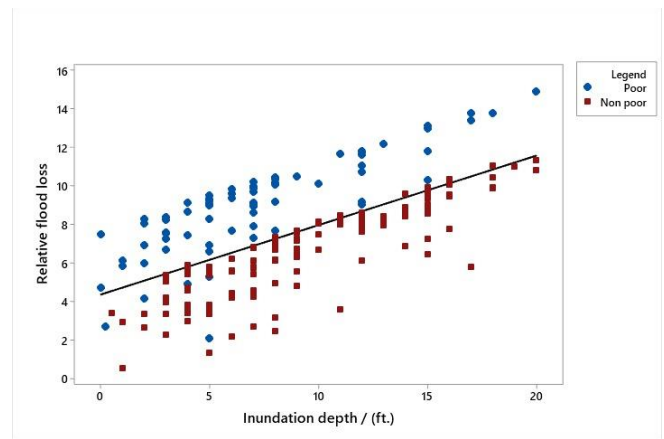


Figure III. Variation of Inundation depth vs Relative flood loss

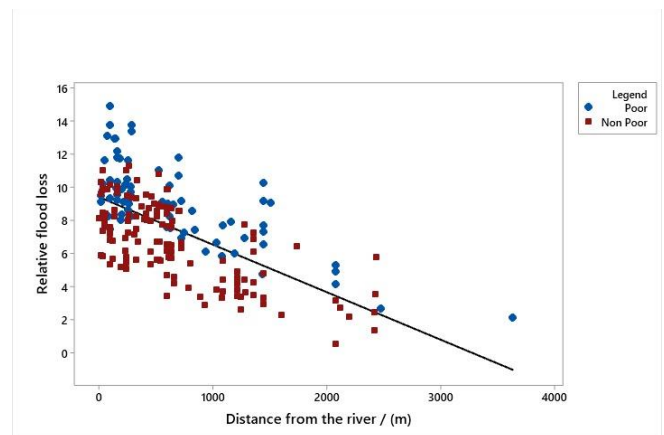


Figure IV. Variation of Distance from the river to household vs Relative flood loss

Figure III and IV are partial representations of the multiple linear regression result. Figure III shows that the relative flood loss is increasing with the increase of inundation depth. However, it indicates that the poor households are subjected to considerable relative loss even with low inundation depths. Figure IV indicates that the relative flood loss is decreasing with the increase of distance to the river from the household. In other words, the relative flood loss is high, when the households are closer to the river. That impact is high for the poor households compared to non-poor households.

TABLE V. MODEL FIT PARAMETERS OF MODEL VALIDATION

Parameter	S 1	S 2	S 3	S 4	S 5	S 6	S 7	S 8	S 9	S 10	Acceptable range
Probability level	0	0	0	0	0	0	0	0	0	0	Closer to "0"
RMSEA	0.074	0.054	0.034	0.094	0.076	0.058	0.097	0.054	0.058	0.079	Closer to "0"
GFI	0.913	0.89	0.943	0.901	0.921	0.889	0.879	0.95	0.932	0.905	Closer to "1"
AGFI	0.851	0.862	0.81	0.841	0.879	0.81	0.832	0.889	0.811	0.874	Closer to "1"
CFI	0.901	0.78	0.867	0.891	0.811	0.831	0.843	0.9	0.912	0.827	Closer to "1"
NFI	0.771	0.788	0.712	0.79	0.771	0.79	0.843	0.721	0.732	0.8	Closer to "1"
TLI	0.734	0.698	0.721	0.811	0.832	0.79	0.901	0.911	0.784	0.821	Closer to "1"

TABLE VI. PERCENTAGE BIAS VALUES OF MODEL AND SAMPLE

Sample No	Constant	Coefficient			Percentage Bias			
		Inundation Depth	Distance from the river to household	Poor/Non-poor	Constant	Inundation Depth	Distance from the river to household	Poor/Non-poor
1	8.03	0.402	0.0022	2.98	-4.42	-8.06	-6.06	8.02
2	7.82	0.412	0.0021	3.08	-1.69	-10.75	-1.66	4.93
3	8.03	0.371	0.0018	3.56	-4.42	0.26	12.51	-9.87
4	7.78	0.361	0.0018	2.94	-1.17	2.95	10.55	9.25
5	8.21	0.308	0.0022	3.27	-6.76	17.20	-9.48	-0.92
6	6.94	0.340	0.0016	2.77	9.75	8.60	20.91	14.50
7	8.24	0.376	0.0022	3.27	-7.15	-1.08	-9.48	-0.92
8	7.56	0.409	0.0015	3.63	1.69	-9.95	28.00	-12.03
9	8.20	0.380	0.0015	3.90	-6.63	-2.15	29.13	-20.37
10 (control)	7.69	0.372	0.0020	3.24	0	0	0	0

VI. CONCLUSION

This study aims to develop flood damage function model based on questionnaire survey data. The model considered not only the effects of flood characteristics but also the geometric and socioeconomic characteristics. The relative flood damage was found to be depend on household income, inundation depth and distance from the river to household. According to the established regression equation, relative flood damage positively correlates with the inundation depth while there is a negative relationship with the distance from river. Further, it represents that the poor households suffer more due to floods compared to the non-poor. Hence, these results support to conclude that the local scale flood damage is not only a function of flood characteristics but also a result of socioeconomic and geographical characteristics of a household. These findings give insights for the policymakers to think beyond the traditional structural adaptation strategies to develop flood management system.

Moreover, only inundation depth has been considered as the variable representing flood characteristics that affects to the physical damages. However, some other factors such as velocity, flooding duration, the polluting, or sediments load

conveyed by water can be affected and should be studied in future studies. Furthermore, flood damages can be tangible or intangible, where tangible impacts can be measured in monetary terms and intangible impacts are generally as human injuries or deaths. Therefore, a future research may be conducted by considering intangible damages as well.

VII. ACKNOWLEDGMENT

The authors would like to convey their sincere gratitude to those who helped and guided in many ways. Special thanks should go to Prof. K.P.P. Pathirana and Mr. D.D. Dias for their constructive criticisms. Our gratefulness further extended to the household members who spent their valuable time to respond our questionnaire.

REFERENCES

- [1] N. S. Romali, S. K. Sulaiman, Z. Yusop and Z. Ismail, "Flood Damage Assessment: A Review of Flood Stage–Damage Function Curve," *Springer Science+Business Media Singapore*, 2015.
- [2] National Research Council, *Tying Flood Insurance to Flood Risk for Low-Lying Structures in the Floodplain*, Washington, DC: The National Academies Press, 2015.
- [3] E. Martínez-Gomariz, M. Valentin, B. Russo, P. Sánchez Hernández and J. Montes, "Methodology for the damage assessment of vehicles exposed to flooding in urban areas," *Floods risk management*, 2018.
- [4] M. M. Fernandes, "Flood damage estimation beyond stage-damage functions:," *Journal of Flood Risk Management*, 2010.
- [5] L.-F. Chang, J.-L. Kang and M.-D. Su, "Industrial and Commercial Depth-Damage Curve Assessment," *WSEAS Transactions on Environment and Development*, 2009.
- [6] E. M. Gomariz, E. F. Ortiz, M. G. Hidalgo, S. Castán and M. Gómez, "Flood Depth-Damage Curves for Spanish," *Sustainability*, 2020.
- [7] V. Grama, A. Avanzi, C. Lucia, E. Frank and D. Vitalie, "Flood Vulnerability Usage for Flood Risk Assessment in the Republic of Moldova.," 2016.
- [8] J.-L. Kang, M.-D. su and L.-F. Chang, "Loss functions and framework for regional flood damage estimation in residential area," *Journal of marine science and technology*, vol. 13, pp. 193-199, 2005.
- [9] P. Dias, N. Arambepola, K. Weerasinghe, K. Werrasinghe, D. Wagenaar, L. M. Bouwer and H. Gehrels, "Development of damage functions for flood risk assessment in the city of Colombo(Sri Lanka)," *Procedia Engineering*, pp. 332-339, 2017.
- [10] T. Rathnaweera, M. Palihawadana, H. Rangana and U. Nawagamuwa, "Effects of global warming on landslide frequencies in ratnapura district, Sri Lanka," in *Civil Engineering Research Exchange Symposium 2012*, 2012.
- [11] M. De Silva and A. Kawasaki, "A local-scale analysis to understand differences in socioeconomic factors affecting economic loss due to floods among different communities," *International Journal of Disaster Risk Reduction*, vol. Volume 47, 2020.
- [12] K. Lawrence, "Information Technology," [Online]. Available: <https://technology.ku.edu/software/minitab>. [Accessed 24 July 2021].
- [13] J. Crandall and C. Crandall, "Computer Systems and Methods for Surveying a population," *United States Patent Application Publication*, 2008.
- [14] W. G. Cochran, *Sampling Techniques*, 3 ed., Jogh Wiley & Sons, 1997.
- [15] F. Jane and N. Ceema, "Social Poverty A Relative and Relevant Measure," *World Bank*, 2017.
- [16] V. Krotov, "A Quick Introduction to R and RStudio," 2017.
- [17] A. S. Singh and M. B. Masuku, "Sampling techniques and determination of sample size in applied statistics research," *International journal of economics, Commerce and management*, vol. Voll. 2, no. 11, 2014.
- [18] D. Smith, "Flood damage estimation-A review of urban stage-damage curves and loss functions," 1994.

Water Quality Variation in Cascade Irrigation System; A Case Study in Thirappane Tank Cascade System, Anuradhapura, Sri Lanka

S. R. M. A. K. D. Rajapaksha
Department of Civil Engineering
University of Peradeniya
Peradeniya, Sri Lanka
kushanidrajapaksha@gmail.com

H. N. D. Chandrasinghe
Department of Civil Engineering
University of Peradeniya
Peradeniya, Sri Lanka
nayomidarshika299@gmail.com

B. A. N. Jayalath
Provincial Irrigation Department,
North Central Province
Anuradhapura, Sri Lanka
banjayalath@yahoo.com

N. K. L. C. Rupasinghe
Department of Civil Engineering
University of Peradeniya
Peradeniya, Sri Lanka
lahiruru@eng.pdn.ac.lk

B. U. Kaushalya
Department of Civil Engineering
University of Peradeniya
Peradeniya, Sri Lanka
uthpala.kaushalya@eng.pdn.ac.lk

K.G.N.Nanayakkara
Department of Civil Engineering
University of Peradeniya
Peradeniya, Sri Lanka
nadeen@eng.pdn.ac.lk

Abstract— The tank cascade system (TCS) is a water management technique that was designed to balance the nature of Sri Lanka's rainfall and landscape. Thirappane tank cascade system is one of the prominent cascade systems in the Anuradhapura district with seven small tanks. The water quality of this cascade has a significant impact on human lives and the aquatic resources of this area since it is widely used for irrigation, agriculture, recreational activities and bathing. This study focuses on studying the variation of water quality along with a selected TCS for Dissolved Oxygen (DO), Conductivity, Salinity, Turbidity, Total Dissolved Solids, pH, Temperature, Phosphate, Nitrate, TSS, BOD, COD, Zn, Sulphate, Total nitrogen and Mn. Water samples were collected monthly basis from January 2021 to April 2021. Water quality was compared with Sri Lankan ambient water quality guidelines. CCME WQI and WA WQI were used to analyze the results. EC, TDS, and Salinity showed an upward trend along the cascade while Turbidity, Nitrate, BOD, and TSS showed a decreasing trend along the cascade. DO concentration of all the tanks did not meet the required limit while the COD concentration of all the tanks exceeded the permissible level for drinking water with simple treatment, bathing and recreational activities, aquatic life and agricultural activities. CCME WQI did not show any variation along the cascade. WA WQI showed variation along the cascade for all categories except irrigation and agricultural activities. Correlations between the water quality and rainfall were analyzed using the Pearson correlation analysis. It can be stated that 35.7%, 14.3%, 7.1%, 21.5%, 14.3%, 7.1% parameters showed “Very strong positive”, “Strong positive”, “Weak Positive”, “No or negligible”, “Weak negative”, “Strong negative” relationships respectively. In addition to that, the correlations between water quality parameters were identified. From the studied parameters, it can be seen that 14.8% of parameters showed “Significant linear correlation” with selected parameters while 6.7% of parameters showed “Very strong linear correlation”.

Keywords— Tank Cascade System, Thirappane Cascade, Water Quality, Water Quality Index, Pearson Correlation Analysis

I. INTRODUCTION

There are three climatic zones in Sri Lanka known as wet, intermediate and dry zone. The annual rainfall of the dry zone is less than 1250 mm (From October to January). Annual

average evaporation in the dry zone ranges between 1700 - 1900 mm, which exceeds the average annual rainfall implying the water stress [1].

Agriculture is the main livelihood of the people in the North Central Province (NCP), which is located in the dry zone of Sri Lanka. Tank cascade irrigation systems provide continuous water flow from the upper tank to lower tanks through cultivated lands. A cascade is a “connected series of small irrigation tanks organized within a meso-catchment of the dry zone landscape, storing, conveying, and utilizing water from an ephemeral rivulet” [2]. Due to population growth, expanding cultivation land, deforestation, and industrialization water quality in TCS may not be suitable for some applications. Therefore, it is important to review the water quality of tank cascades in Sri Lanka for their sustainability.



Fig 1: Location of Thirappane Tank Cascade System

Figure 1 shows the location of the Thirappane tank cascade system. Thirappane cascade is one of the cascades in the Malwathu Oya river basin and it is located about 20 km south of Anuradhapura city in the NCP. It is a typical medium density small TCS with seven connected tanks representing a linear type cascade. The main tanks located along the main axis in the Thirappane cascade are namely, Thirappane tank, Alisthana tank, Meegassagama tank, Bulankulama tank, Badugama tank, Vendarankulama tank, and Gulupetta tank [1,

3]. The total extent of the Thirappane TCS is approximately 283 ha. A total of around 350 families live within the upper part of the cascade. The upper part of the Thirappane TCS is a residential area while the middle part and lower part are agricultural area and forest land, respectively.

II. NEED OF THIS STUDY TO THE PRESENT CONTEXT

The physical, biological, and chemical parameters of water determine the quality of water. Variation in water quality is not unique to all tanks in the cascade system. Therefore, each tank requires a separate water quality analysis. Despite the fact that Thirappane TCS has had water quantity assessments and various models developed, no studies have been conducted to assess the water quality variation with the area's rainfall.

This study focuses on studying the variation of water quality in the Thirappane TCS in the dry zone of Sri Lanka for bathing and recreational activities, aquatic life, irrigation, and agricultural activities and drinking water with simple treatment. In addition, two different water quality indices are developed and water quality variation with rainfall is investigated.

III. LITERATURE REVIEW

A. Tank Cascade System

TCS is considered an advanced water conduction mechanism developed in ancient irrigation history to avoid water scarcity problems in the dry zone [4]. Sri Lanka's TCSs are different in many ways from modern reservoirs. Two main differences are smaller basin sizes and higher sustainability. The water flow along a small drainage course is intercepted by placing an earth dam, which creates a tank. Each small tank has its catchment area. The head tank of the TCS is fed mainly by rain and conversion from the river, while the irrigation canals distribute the water downstream through the rice fields [5].

During the last two or three decades, with the expansion of the population, human intervention in these irrigation systems has been very high. The natural habitat of tank ecosystems is being impacted by urbanization and deforestation, as well as inappropriate land use and trash dumping [6]. The application of agrochemicals such as fertilizers and pesticides are now severely affecting the TCS ecosystems. However, these contamination events were not evident in the older TCS, although there is a high probability of contaminating the tank water in the cascade by excess nutrient input. Farmers used animal dung as a source of fertilizer for their crops in the past. There was also a specific feature called "Thaulla" in the ancient TCS. It acts as a wetland that not only removes nutrients, suspended particles and heavy metals but also regulates the flow of water in the TCS during the rainy season. It also acts as a windbreaker, reducing excessive evaporation [7].

B. Water Pollution and Effects

The natural water consists of common anions and cations such as bicarbonate, carbonate, sulphate, chloride, fluoride, nitrate, and phosphate, as well as calcium, magnesium, sodium, and potassium, iron, manganese, and other minerals. Nevertheless, excess of these minerals is not good for humans as well as the environment. Most agrochemicals (weedicides,

insecticides, and fungicides) contain extremely high levels of Cadmium (Cd^{2+}), Arsenic (As^{3+}), and other heavy metals. [8].

Chronic Kidney Disease (CKDu) is one of the greatest problems in NCP, which recorded the highest mortality and morbidity rates [9]. In addition to that, the presence of *Salmonella*, *Shigella*, *Escherichia coli*, and *Vibrio* in water bodies may cause water-borne diseases such as typhoid fever, diarrhea, dysentery, gastroenteritis, and cholera.

In these aquatic bodies, excess nutrients (particularly nitrogen and phosphorus) can induce algal blooms, eutrophication, and even fish mortality. Some algae blooms may produce poisons that harm human health, wildlife, and livestock when swallowed. In many countries, salinization is recognized as the primary threat to environmental resources and human health. It is affecting almost 1 billion ha worldwide/globally representing about 7% of the earth's continental extent [10]. Salinity decreases agricultural production. Furthermore, soil salinity causes ion toxicity, osmotic stress, nutrient (N, Ca, K, P, Fe, Zn) deficiency, and oxidative stress in plants limiting water uptake from soil. According to Larry's research (2006), more than 14,000 people are dying daily in the world due to water-related diseases.

C. Studies on Cascade Systems

Generally, water sampling is performed in two methods; grab sampling and composite sampling. In most of the researches, samples were collected from the surface of the water body [3, 11, 12]. The sampling stations were selected based on their contamination vulnerability, population density, and areas of industrial and anthropogenic activity such as minerals and mining in the catchment area [13, 14]. To minimize errors, the number of sampling locations is increased in proportion to the size of the reservoir. In most of the researches, the sampling was done on a seasonal basis during Yala (May to August) and Maha seasons (September to March) in Sri Lanka [3, 11, 12].

D. Water Quality Parameters and Analysing techniques

Table I shows the water quality parameters and their analysing techniques reported in the literature.

TABLE I WATER QUALITY PARAMETERS AND ANALYSING INSTRUMENTS AND METHODS

Parameter	Instrument
pH	pH probe, Multi-Parameter Analyzer, Potentiometry
Temperature	Multi-Parameter Analyzer, DO Meter, Temperature probe
Electrical conductivity	Multi-Parameter Analyzer, Conductometry
Turbidity	Turbidity Meter
TDS	Multi Parameter Analyzer
DO	Multi Parameter Analyzer, DO Meter, Oximeter
BOD	BOD Test, BOD meter
COD	UV-VIS Spectroscopy, COD meter
Nitrate	Colorimeter
Sulphate	Colorimeter
Total Nitrogen	Atomic Absorption Spectrophotometry

Parameter	Instrument
Phosphate	Molybdate blue colorimeter, Ascorbic acid method, Colorimeter
Zn	Atomic Absorption Spectrophotometry
Mn	Atomic Absorption Spectrophotometry,
Ca ²⁺	Atomic Absorption Spectrophotometry
Mg ²⁺	Atomic Absorption Spectrophotometry
Na ⁺	Flame Photometer
K ⁺	Flame Photometer
Parameter	Method
Alkalinity	Acid base titration, Potentiometric Titration
Salinity	Multi Parameter Analyzer
Carbonate and Bicarbonate	Acid base titration
Total and fecal coliform	Membrane Filtration method
TSS	Oven dry method, Gravimetric
Chloride	Standard AgNO ₃ titration

Horton (1965) developed the WQI in the United States by selecting ten of the most commonly used water quality variables such as DO, pH, coliforms, specific conductance, alkalinity, chloride, etc. Water quality is rated as Excellent, Good, Medium and Poor according to the selected water quality index. There are different water quality indices such as Weight Arithmetic Water Quality Index (WAWQI), National Sanitation Foundation Water Quality Index (NSFWQI), Canadian Council of Ministers of the Environment Water Quality Index (CCMEWQI) and Oregon Water Quality Index (OWQI). According to the reviewed literature, available indices have many variations and limitations based on the number of water quality variables used, and they are not universally accepted. Hence, it needs worldwide acceptability with a varying number of water quality variables [15].

The quality of water is a powerful environmental factor that determines the health of humans. Therefore, various national agencies have established water quality standards that specify the chemical, microbial, and radiological characteristics of safe water that are permissible. In water quality standards there are different categories such as bathing and recreational activities, Drinking, Aquatic life, Irrigation, and Agricultural activities, etc. CEA Ambient water quality guideline [16] and the United States Environmental Protection Agency (EPA) guidelines are some of these guidelines.

IV. MATERIAL AND METHODS

A. Sample Collection

The grab sampling method was used to collect the water samples. In this study, water quality was analyzed monthly basis over four months period (From January to April). Sampling was done inside the reservoir near the outlet. To avoid the turbulent effect, samples were taken several feet away from the tank bunt. Daily rainfall data of the Mahailuppallama meteorological station during the study period were also collected. In this study, Nitric acid and Sulfuric acid were used for the preservations. In addition to

that, HACH COD vials were used to analyze the COD in water samples. HACH Phosphate powder pillows, nitrate powder pillows and Sulphate powder pillows were used to analyse Phosphate, Nitrate and Sulphate respectively. Distilled water was used in all experiments. Filter papers with pore size 0.45 µm were used in filtering the samples.

B. Measuring Instruments and Methods

Temperature, EC, pH, TDS, DO, Salinity were tested in-situ and TSS, COD, BOD, Nitrate, Phosphate, Sulphate, Mn, Turbidity, Temperature, Total nitrogen and Zn were tested in the Environmental Laboratory of the University of Peradeniya. Table II shows measuring Instruments and Methods.

TABLE II MEASURING INSTRUMENTS AND METHODS

Parameter	Instrument	Method
DO, EC, Salinity, TDS, pH, Temperature	Multi-parameter Analyzer	Electro Chemical
Zn, Mn	Shimadzu AA7000 Atomic Absorption Spectrophotometer	Atomic Absorption
Nitrate, Sulphate, COD	HACH DR900 Colorimeter	Cadmium Reduction
Phosphate, Total Nitrogen	UviLine 9100C Spectrophotometer	Light Absorption
COD	UV-VIS Spectroscopy	Colorimetric
Turbidity	HACH 2100N Turbidity Meter	Nephelometry
TSS		Gravimetric
BOD	BOD - DO Meter	

C. Analyzing the Variation of Water Quality Parameters

a) Comparison of Data with CEA Guideline

The Government of Sri Lanka has published Gazette No. 2148/20 including the ambient water quality standards. In this research water quality of the tanks was analysed under four categories namely, Water that requires simple treatment for drinking, bathing and recreational activities, aquatic life, irrigation and agricultural activities based on the above standards.

b) Water Quality Index

In this study, two Water Quality indices were selected considering the available water quality parameters.

- Weighted Arithmetic Water Quality Index

$$WQI = \sum Q_i W_i / \sum W_i \quad (1)$$

$$Q_i = 100 [(V_i - V_o) / (S_i - V_o)] \quad (2)$$

$$W_i = K / S_i \quad (3)$$

$$K = 1 / (\sum 1 / S_i) \quad (4)$$

Q_i - Quality rating scale

W_i - Unit weight for each water quality parameter

V_i - Estimated concentration of i^{th} parameter in the analyzed water

V_o - Ideal value of this parameter in pure water

$$V_o = 0 \text{ (except pH = 7.0 and DO = 14.6 mg/l)}$$

S_i - Recommended standard value of i^{th} parameter

K - proportionality constant

Table III shows the water quality rating as per weighted arithmetic water quality index.

TABLE III WATER QUALITY RATING AS PER WEIGHTED ARITHMETIC WATER QUALITY INDEX METHOD

WQI Value	Rating of Water Quality
0-25	Excellent
26-50	Good
51-75	Poor
76-100	Very Poor
Above 100	Unsuitable

- Canadian Council of Ministers of the Environment Water Quality Index method

F1 (Scope) represents the percentage of parameters that are not within the guideline

$$F1 = \left[\frac{\text{Number of failed variables}}{\text{Total number of variables}} \right] \times 100 \quad (5)$$

F2 (Frequency) signifies the percentage of individual tests within each parameter that exceeded the guideline

$$F2 = \left[\frac{\text{Number of failed tests}}{\text{Total number of tests}} \right] \times 100 \quad (6)$$

When the test value must not exceed the objective

$$\text{Excursion} = \left[\frac{\text{Failed test value}}{\text{Guideline value}} \right] - 1 \quad (7)$$

For the cases in which the test value must not fall below the objective, the equation is followed;

$$\text{Excursion} = \left[\frac{\text{Guideline value}}{\text{Failed test value}} \right] - 1 \quad (8)$$

Normalized sum of excursions (nse) = $\frac{\sum_{i=1}^n \text{Excursion}}{\text{Total number of te}}$ (9)

F3 (Amplitude) represents the extent (excursion) to which the failed test exceeds the guideline.

$$F3 = \left[\frac{\text{nse}}{(0.01)\text{nse}+0.01} \right] \times 100 \quad (10)$$

$$\text{CCME WQI} = 1 - \left[\frac{\sqrt{F1^2+F2^2+F3^2}}{1.732} \right] \quad (11)$$

Table IV shows the water quality rating as per CCME water quality index.

TABLE IV WATER QUALITY RATING AS PER CCME WATER QUALITY INDEX METHOD

WQI Value	Rating of Water Quality
0-25	Excellent
26-50	Good
51-75	Poor
76-100	Very Poor
Above 100	Unsuitable

D. Pearson Correlation Analysis

a) Correlation Analysis with rainfall

In this research, water quality variation with rainfall was analyzed using Pearson correlation analysis. The Pearson correlations return a value between -1 and 1.

To obtain Pearson correlation this equation 12 was used.

$$r = \frac{\sum(x_i - \bar{x})(y_i - \bar{y})}{\sqrt{\sum(x_i - \bar{x})^2 \sum(y_i - \bar{y})^2}} \quad (12)$$

r - Correlation coefficient

x_i - Values of the x variable in a sample

\bar{x} - Mean of the values of the x variable

y_i - Values of the y variable in a sample

\bar{y} - Mean of the values of the y variable

b) Correlation Analysis Among Water Quality Parameters

In this study, correlation analysis was conducted among water quality parameters to identify the relationship between different parameters. The correlation coefficients for different water quality parameters are calculated using the following equation.

$$r = \frac{N \sum XY - \sum X - \sum Y}{\left[\{N \sum X^2 - (\sum X)^2\} \{N \sum Y^2 - (\sum Y)^2\} \right]^{\frac{1}{2}}} \quad (13)$$

X and Y are two water quality parameters and N is the total number of water quality parameters. In this study N=17

The values of the correlation coefficient up to 0.5 do not show any significant correlation between the pair of parameters considered.

$r \geq \pm 0.5$ - Significant linear correlation between the two parameters considered

$r \geq \pm 0.8$ - Very strong linear correlation between the two parameters considered

V. RESULTS AND DISCUSSION

A. Minimum, Maximum and Average Values of water quality parameters

Sixteen (16) water quality parameters were analysed for all water samples and the minimum, maximum, average and standard deviation values of each parameter for all sampling stations are listed in Table V.

TABLE V MINIMUM, MAXIMUM, AVERAGE AND STANDARD DEVIATION

Parameter	Unit	Minimum	Maximum	Average	SD
Temperature	°C	25.6	30.3	27.74	1.68
PH	-	6.89	8.22	7.31	0.36
Conductivity	µS/cm	74.48	680.8	299.98	186.53
TDS	mg/l	38.64	352.6	155.89	96.88
Salinity	mg/l	1.59	628	267.75	178.66
DO	mg/l	0.18	3.9	1.28	1.16
NO ₃ ⁻	mg/l	0.4	4.7	1.85	1.15
SO ₄ ²⁻	mg/l	0	29	1.76	6.28
COD	mg/l	0	41	17.76	9.7
TSS	mg/l	2	214	18.86	45.03
Turbidity	NTU	4	163	22.67	35.32
Zn	ppm	0.04	0.12	0.06	0.03
Mn	ppm	0.01	0.62	0.1	0.15
PO ₄ ³⁻	ppm	0.06	1.23	0.41	0.33
TN	ppm	0	2.15	0.97	0.59
BOD	ppm	-3.07	2.14	0.48	1.28

a) pH

Table V shows that in the Thirappane cascade system the pH is varied between 6.89 – 8.22. In the Ulagalla tank cascade system, which is located near the Thirappane cascade system,

pH variations were reported as 6.88 – 7.51 [12], 5.8 – 8.2 [17] and 6.79 – 7.47 [18]. Therefore, the pH variation of the Thirappane cascade system in this research is compatible with that of the Ulagalla cascade system. Moreover, the average pH value of Malwathu Oya Cascade-I was 7.4 during 2011-2012 [19] which is in good agreement with the current study. Tissa tank is located near the Thirappane cascade and capacity is nearly equal to the Thirappane tank [20]. During 2004, pH was varied from 7.84 - 8.22 in the Tissa tank. While the maximum value of the pH of Thirappane Cascade and the Tissa tank is the same. The minimum pH of the Tissa tank is more alkaline. The pH value of the Ulankulma tank which is situated in the Thirappane Divisional Secretariat of the Anuradhapura district had varied between 6.26 - 9.14 during 2016-2017 [18]. This tank had the highest pH value recorded compared to any study reported above.

b) Electrical Conductivity

In general, water hardness is prevalent in Sri Lanka's dry zone. As a result, EC value must be higher in the water sources of Anuradhapura District. Variation of EC in Ulagalla cascade were reported as 96.2 $\mu\text{S}/\text{cm}$ - 299 $\mu\text{S}/\text{cm}$ [12] and 94.25 $\mu\text{S}/\text{cm}$ - 806.33 $\mu\text{S}/\text{cm}$ [16]. However, the minimum and maximum EC of the Thirappane cascade system during the study period were 74.48 $\mu\text{S}/\text{cm}$ and 680.8 $\mu\text{S}/\text{cm}$ respectively. Malwathu Oya cascade-I had 530 $\mu\text{S}/\text{cm}$ average EC during 2011-2012 [18]. The average EC of the Ulankulama cascade was 613.54 $\mu\text{S}/\text{cm}$ in the 2016-2017 studied period [6]. According to these two kinds of research, EC was very large compared with the average EC (299.98 $\mu\text{S}/\text{cm}$) of the Thirappane cascade. EC of Tissa tank had been varied from 290 $\mu\text{S}/\text{cm}$ to 840 $\mu\text{S}/\text{cm}$ in 2004 [17]. Therefore, it can be stated that the minimum and maximum EC of the Thirappane tank is less than the Tissa tank. Compared to other literature, the present study reported the minimum EC values and it was obtained in Thirappane tank.

c) Phosphate

Phosphate concentration of surface water had been varied in Ulagalla cascade system as 0.02 mg/l - 0.34 mg/l [17] and 0.08 mg/l - 0.18 mg/l [16]. However, the maximum phosphorus of the Thirappane cascade system was 1.23 mg/l during the study period and it is comparatively higher than the previous studies.

d) TDS

In Ulagalla cascade TDS was varied from 40.2 mg/l to 151.3 mg/l during 2018 [12, 16]. In the present study, the highest TDS was recorded as 352.6 mg/l. However, according to the Mahagama & Manage surface water in Madawachchiya, Padaviya and Kebithigollewa areas in Anuradhapura District had varied between 214 mg/l to 453 mg/l [21] which is in good agreement with the present study.

e) Nitrate

A research which was done on the Thirappane cascade system using 3 main tanks such as Thirappane, Alistana and Meegassagama during 2010 -2011 revealed that the variation of Nitrate concentration was from 1.41 mg/l to 6.77 mg/l. From January to April Nitrate of these three tanks had varied from 3.04 mg/l to 5.11 mg/l [3]. However, the present study recorded much lower values in those tanks. Another research that was done from 2011 to 2012 on Malwathu Oya Cascade

1 reported that the average nitrate concentration was 2.01 mg/l [18]. It was approximately equal to the results in the present research (1.85 mg/l). Similar results (2.23 mg/l) for surface water had been reported in Madawachchiya, Padaviya and Kebithigollewa areas in Anuradhapura District during 2016 [21]. A study which was conducted on Ulankulama cascade reported low nitrate concentrations (0.36 mg/l – 1.1 mg/l) [22]. Nitrate concentration of Ulagalla cascade during 2018 had varied from 0.12 mg/l to 1.97 mg/l [16].

B. Comparison of Water Quality with CEA Ambient Water Quality Guideline

During April, the water temperature was quite higher due to hot environmental conditions. The average temperature of the cascade was 27.7 °C. The water temperature values in this study area varied from the lowest value of 25.6 °C at the Alistana tank and the highest value, which was 30.3 °C at Bulankulama and Meegassagama tanks. The average pH of the cascade system varied from 7.04 to 7.65, the lowest pH value was recorded at the Vendarankulama tank (6.89) whereas the highest was detected from the Badugama tank (8.22). Therefore, all water samples were within the permissible limits prescribed by CEA standards for drinking (6-8.5), bathing and recreational activities (6-9), Agriculture (6-8.5) and Aquatic life (6-8.5). During the study period, EC reported an increasing trend along the cascade. The test results were compared with the CEA guidelines of drinking, irrigation & agriculture respectively while no guidelines on recreation and fish & aquatic life in the Sri Lankan context. The highest conductivity was recorded in the Thirappane tank as 680.8 $\mu\text{S}/\text{cm}$ and the minimum was recorded in the Gulupeththewa tank as 74.48 $\mu\text{S}/\text{cm}$. Therefore, EC was shown to be within acceptable limit as per CEA guidelines for irrigation agricultural activities (<700 $\mu\text{S}/\text{cm}$). This sudden increase of DO concentration was observed during February along the cascade. Minimum DO concentration was recorded in the Meegassagama tank (0.18 mg/l) and the highest was recorded in the Badugama tank (3.9 mg/l). It is speculated that due to the high surface vegetation of the tanks DO concentration did not meet the required limit as per the CEA standard for drinking water with simple treatment (6 mg/l), bathing and recreational activities (5 mg/l), aquatic life (5 mg/l) and irrigation and agricultural activities (3 mg/l). During the study period, high turbidity (163 NTU) was recorded in the Vendarankulama tank compared to the other tanks. When compared with the precipitation of the study area during this period, it could be stated that turbidity had been increased with the precipitation. The highest precipitation was recorded in April and turbidity may increase due to the embankment erosion, surface runoff and lack of vegetation. The lowest value of turbidity was 8 NTU which was recorded at Bulankulama and Meegassagama tanks. According to the CEA guideline, all the tanks have exceeded the maximum Turbidity level for Category A; drinking water with simple treatment (5 NTU). A decreasing trend of Nitrate was observed along the cascade. The Thirappane tank which was located in the lowest part of the cascade recorded the minimum value which was 0.4 mg/l. The highest Nitrate concentration of 4.7 mg/l was reported in the Vendarankulama tank. This can be due to the surface runoff from the agricultural areas. However, the Nitrate

concentration of seven tanks of the cascade did not exceed the permissible level which was 10 mg/l. The average BOD₅ of the cascade system was recorded as 0.48 ppm. The maximum BOD₅ was recorded at the Vendarankulama tank, which was 2.14 ppm. Considering the study area, it can be seen that all the samples were within the permissible level as per the CEA standard for Category A; drinking water with simple treatment (4.2 mg/l), Category B; bathing and recreational activities, C; aquatic life (5.6 mg/l) and Category E; irrigation and agricultural activities (17 mg/l). During January and March Sulphate was not detected in the tanks. However, during April, a considerable concentration of Sulphate was found in the Vendarankulama tank (29 mg/l). This could be due to the high precipitation in April and the resulting agricultural runoff. During the sampling period, the Alistana tank reported zero Sulphate concentration. All the tests did not exceed the permissible level as per the CEA guideline in terms of Sulphate. Phosphate had varied between 0.06 – 1.23 mg/l, where the highest value was recorded in January at the Gulupetta tank and the lowest value was observed in March at the Thirappane tank. The variation had been considerably decreased from Vendarankulama tank to Meegassagama tank. The results revealed that the available phosphate in 70% of the tanks was well below the critical level as per CEA guideline for Category A; drinking water with simple treatment and B; bathing and recreational activities (0.7 ppm) and Category C; aquatic life (0.4 ppm).

C. Water Quality Index Analysis

Results obtained from WQI analysis were shown in Table VI.

TABLE VI SUMMARY OF WQI

Tank Name	CCME WQI				WA WQI			
	Category				Category			
	A	B	C	E	A	B	C	E
Gulupetta	F	F	F	G	VP	P	P	G
Vendarankulama	F	F	F	G	U	P	P	G
Badugama	F	F	F	G	G	G	G	G
Bulankulama	F	F	F	G	G	G	G	G
Meegasagama	F	F	F	G	E	G	G	E
Alistana	F	F	F	G	G	G	G	E
Thirappane	F	F	F	G	E	E	E	E

VP – VERY POOR, P- POOR, U- UNSUITABLE, F – FAIR, G – GOOD, E – EXCELLENT

According to the WA WQI, the Gulupetta and Vendarankulama tanks were found to be “Very Poor” and “Unsuitable” as drinking water sources respectively. Furthermore, according to the WA WQI rankings, the upper tank water was identified as “Good” and lower tank water was identified as “Excellent” for irrigation activities. 28.5% of the tanks had “Poor” quality water while 57% of the tanks had “Good” water for both bathing and recreational activities and aquatic life as per the WA WQI. According to the CCME WQI, all of the tanks had “Fair” water quality for drinking with simple treatment, bathing and recreational activities and aquatic life and “Good” water quality for irrigation and agricultural activities. There was no water quality variation along the cascade based on CCME WQI.

In the CCME WQI model, the influence of all parameters can be seen in the results since it has no restriction on the number of parameters. The greater the number of elements, the better the accuracy of the estimation. Furthermore, it has a poor level of sensitivity when it comes to missing data. But WA WQI had been conducted only for the selected water quality parameters (based on CEA guideline) and it did not include all the parameters which can describe the quality of a water body. Further, CCME WQI has given the same importance to the variables in the determination of the water quality index but the WA WQI model was different since it used the weighting factors for each parameter [23]. Moreover, in the CCME WQI model, there are five water quality levels but in WA WQI there are only four water quality levels. In addition to that, to get better accuracy in WQIs, the sampling period can be extended while increasing the sampling frequency and sampling locations. Figures 2 and 3 show the variation of WA WQI and CCME WQI respectively.

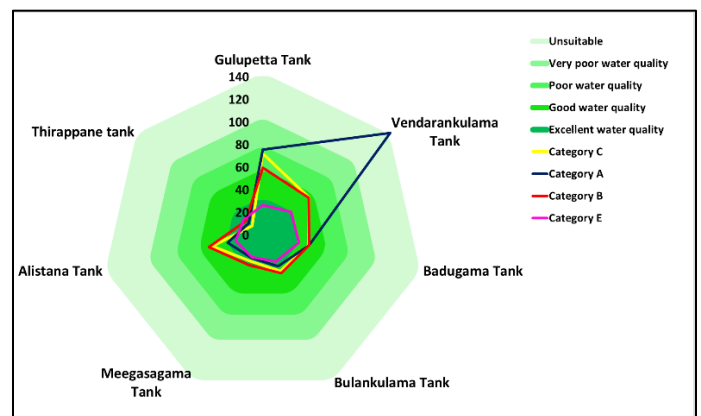


Fig 2: Variation of WA WQI

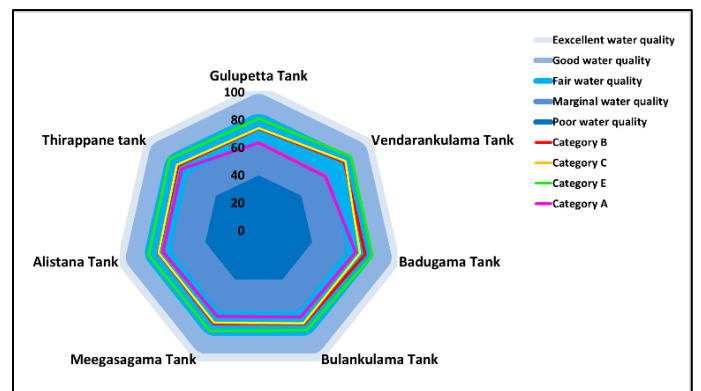


Fig 3: Variation of CCME WQI

D. Pearson Correlation Analysis

a). Correlation Analysis with Rainfall

Table VII shows the identification of the correlation and table VIII shows the summary of correlation analysis with rainfall.

0.7 or Higher	Very strong positive relationship
0.4 to 0.69	Strong positive relationship
0.3 to 0.39	Moderate positive relationship
0.2 to 0.29	Weak positive relationship
0.01 to 0.19	No or negligible relationship
0.00	No relationship
-0.01 to -0.19	No or negligible relationship
-0.20 to -0.29	Weak negative relationship
-0.30 to -0.39	Moderate negative relationship
- 0.40 to -0.69	Strong negative relationship
-0.7 or Higher	Very strong negative relationship

TABLE VII IDENTIFICATION OF THE CORRELATION

Parameter	Gulupetta tank	Vendarankulama tank	Badugama tank	Bulankulama tank	Meegassagama tank	Alistana tank	Thirappane tank	Thirappane cascade system
Tem.	0.74	0.99	0.93	0.58	0.99	0.93	0.99	0.82
pH	0.55	0.99	0.88	0.54	-0.84	0.47	0.01	0.77
EC	-0.63	0.99	-0.55	0.27	0.77	0.71	0.83	-0.20
TDS	-0.62	0.98	-0.57	0.27	0.78	0.84	0.83	-0.19
Sali.	-0.65	0.55	-0.54	0.25	0.79	0.68	0.83	-0.12
DO	-0.34	-0.63	0.23	-0.47	-0.65	-0.66	-0.66	-0.22
NO ₃ ⁻	0.91	0.99	0.93	0.99	0.99	-0.58	0.95	0.99
SO ₄ ²⁻	0.58	0.58	0.58	0.58	0.58	0.00	0.58	0.58
COD	-0.65	-0.62	-0.66	0.06	-0.45	0.22	-0.93	-0.51
TSS	0.76	0.59	0.58	0.01	-0.26	0.58	-0.26	0.56
Turb.	0.94	0.77	0.96	-0.91	0.09	0.64	0.01	0.87
Zn	0.41	0.99	0.41	0.41	0.41	0.41	0.41	0.72
Mn	0.24	0.60	0.33	-1.00	0.41	-0.92	-0.57	0.21
PO ₄ ³⁻	-	-	-	-	-	-	-	-0.13

TABLE VIII SUMMARY OF CORRELATION ANALYSIS WITH RAINFALL

From the selected fourteen (14) parameters Gulupetta, Vendarankulama, Badugama, Bulankulama, Meegassagama, Alistana and Thirappane tanks had 21.5%, 84.6%, 69.2%, 76.9%, 76.9%, 76.9% and 69.2% “Positive relationships” with rainfall respectively. Considering the Thirappane cascade system it can be stated that temperature, pH, nitrate, turbidity and Zn showed a “Very strong positive relationship” with rainfall. Sulphate and TSS showed a “Strong positive relationship” while Mn showed a “Weak positive relationship”. A positive relationship indicates that the concentration or parameter values are increasing with rainfall. This can be caused by embankment erosion, surface runoff, fertilizer use, and air pollution. Further, TDS, salinity and phosphate showed a “No or negligible relationship” with rainfall. EC and DO had a “Weak negative relationship while COD had a “Strong negative relationship” with rainfall.

This could be due to high water contamination or a lack of sunlight reaching the water body, reaction of oxygen in water with the contaminant and dilution of parameters due to an increase in tank water level.

b). Correlation Analysis Among Water Quality Parameters

According to the analysis it can be stated that TN, DO and BOD have a “Significant linear correlation ($\pm 0.5 \leq r \leq \pm 0.8$)” with temperature”. Also, it can be seen that phosphate and resistivity had a “Significant linear correlation” with pH. In addition to that, EC had a “Very strong linear correlation ($r \geq \pm 0.8$)” with TDS, salinity and resistivity, and “Significant linear correlation” with BOD. Further, Salinity showed a “Very strong linear correlation” with resistivity and “Significant linear correlation” with BOD. Moreover, resistivity illustrated a “Significant linear correlation” with phosphate. DO has a “Significant linear correlation” with Mn and TN.

Nitrate had a “Significant linear correlation” with Sulphate, TSS, Turbidity, Zn and TN. Sulphate showed a “Very strong linear correlation” with TSS and turbidity. Also, it showed a “Significant linear correlation” with Zn. COD didn’t show any relationship with any water quality parameter. TSS had a “Very strong linear correlation” with turbidity and “Significant linear correlation” with Zn. Table IX shows the summary of correlation analysis among water quality parameters. According to table IX, it can be seen that 14.8% of parameters showed “Significant linear correlation” with selected parameters while 6.7% of parameters showed “Very strong linear correlation”. Further, 78.5% of parameters did not show any linear relationship.

TABLE IX SUMMARY OF CORRELATION ANALYSIS AMONG WATER QUALITY PARAMETERS

	Tem	pH	EC	TDS	Sali.	Resi.	DO	NO ₃ ⁻	SO ₄ ²⁻	COD	TSS	Turb.	Zn	Mn	PO ₄ ³⁻	TN	BOD
Tem.	1																
pH	0.36	1															
EC	0.11	-0.38	1														
TDS	0.12	-0.38	0.99	1													
Sali.	0.13	-0.33	0.98	0.98	1												
Res	-0.02	0.59	-0.90	-0.90	-0.86	1											
DO	-0.56	0.04	-0.18	-0.19	-0.15	0.18	1										
NO ₃ ⁻	0.40	0.41	-0.47	-0.48	-0.41	0.48	0.12	1									
SO ₄ ²⁻	0.32	-0.11	-0.13	-0.13	-0.11	-0.03	-0.15	0.59	1								
COD	-0.09	-0.28	-0.66	-0.05	-0.09	-0.17	-0.43	-0.28	0.02	1							
TSS	0.29	-0.08	-0.18	-0.18	-0.15	0.01	-0.14	0.61	0.99	0.06	1						
Turb.	0.31	0.08	-0.34	-0.34	-0.30	0.22	-0.07	0.79	0.92	-0.03	0.94	1					
Zn	-0.04	-0.02	-0.31	-0.31	-0.33	0.17	0.33	0.67	0.54	-0.34	0.55	0.65	1				
Mn	-0.03	0.34	-0.31	-0.31	-0.27	0.40	0.73	0.28	0.40	-0.27	0.42	0.41	0.38	1			
PO ₄ ³⁻	0.08	0.54	-0.49	-0.49	-0.46	0.54	0.17	0.41	0	-0.47	0.12	0.31	0.19	-0.09	1		
TN	0.60	0.30	-0.02	-0.01	0.02	0.08	-0.56	0.51	0.38	0.13	0.41	0.46	0.30	0.10	0.09	1	
BOD	-0.53	0.43	-0.64	-0.63	-0.65	0.46	0.33	0.25	-0.14	-0.04	-0.07	0.10	0.43	0.07	0.13	0.02	1

VI. CONCLUSIONS

Variation of each water quality parameter was checked along the cascade and compared with the CEA ambient water quality guideline. Analysis results were compared with literature related to surface water of the study area during the past 10 years. According to the results, Phosphate and total nitrogen concentrations had been considerably increased.

WA WQI and CCME WQI were calculated for all tanks considering drinking water with simple treatment, bathing and recreational activities, aquatic life and irrigation and agricultural activities. CCME water quality did not show any variation along the cascade. WA WQI also did not show any variation along the cascade for irrigation and agricultural activities. But It could be observed an increased trend of water quality along the cascade for drinking water with simple treatment, bathing and recreational activities, aquatic life.

Variations of water quality parameters were observed with rainfall. Correlation analysis was conducted to find the relationship of the parameters with rainfall. Out of 14 parameters, 8 parameters demonstrated a “Positive relationship” with rainfall (temperature, pH, nitrate, turbidity, Zn, Sulphate, TSS and Mn) while 3 parameters demonstrated a “Negative relationship” (FC, DO, COD). In addition, 3 parameters showed a “No or negligence relationship” with the rainfall (TDS, Salinity and Phosphate).

Further, the correlations between water quality parameters were identified. From the studied parameters, it can be seen that 14.8% of parameters showed “Significant linear correlation” with selected parameters while 6.7% of parameters showed “Very strong linear correlation”. Further, 78.5% of parameters did not show any linear relationship.

REFERENCES

- [1] Panabokke, C.R., Sakthivadivel, S. and Weerasinghe, A.D. (2002). Small Tanks in Sri Lanka: Evolution, Present State and Issues. International Water Management Institute, Colombo, Sri Lanka.
- [2] Madduma Bandara, C.M., 1985, Catchment ecosystems and village tank in the dry zone of Sri Lanka: A time-tested system of land and water management. In: Lundquist, J., Lohm, U. & Falkenmark, M. (Eds.), Strategies for river basin development. D. Reidel Publishing Company, Germany (1985), 99-103.
- [3] Wijesundara, W.M.G.D., Nandasena, K.A. and Jayakody, A.N. (2012). Spatial and Temporal Changes in Nitrogen, Phosphorus and Potassium Concentration in Water in the Thirappane Tank Cascade in Dry Zone of Sri Lanka. Journal of Environmental Professionals Sri Lanka, Vol. 5, pp.70-81.
- [4] Mahatantila, K., Chandrajith, R., Jayasena, H.A.H. and Ranawana, K.B. (2008). Spatial and temporal changes of hydro geochemistry in ancient tank cascade systems in Sri Lanka: Evidence for a constructed wetland. Water and Environment Journal, Vol. 22(1), pp.17-24.
- [5] Bandara, C.M.M. (1985). Catchment Ecosystem and Village Tank Cascades in the Dry Zone of Sri Lanka: A Time Tested System of Land and Water Resource Management. Peradeniya: Reidel Publishing Company.
- [6] Varol, M., Gokot, B., Bekleyen, A. (2012). Spatial and temporal variations in surface water quality of the dam reservoirs in the Tigris River basin, Turkey. Vol. 92, pp 11-21.
- [7] Mahatantila, K., Chandrajith, R., Jayasena, H.A.H. & Ranawana, K. B. (2007). Spatial and temporal changes of hydro geochemistry in ancient tank cascade systems in Sri Lanka: evidence for a constructed wetland. Water and Environment Journal.
- [8] Keil, D.E., Ritchie J.B & MacMillin, G.A. (2011). Testing for toxic elements: A focus on Arsenic, Cadmium, lead and Mercury. Laboratory Medicine. Vol. 42, pp. 735–742.
- [9] Alwis, A. & Panawala, S., 2019 . A review of the national response to CKDu in Sri Lanka. Sri Lanka journal of social sciences , 42 (2), pp. 83-100.
- [10] The United States Environmental Protection Agency, 2016
- [11] Dahanayake, A.C. & Rajapakse, R.L.H.L. (2019). Water Quality Deterioration in the Malwathu Oya Basin. Moratuwa Engineering Research Conference (MERCon). pp. 307-313.
- [12] Kumari, M.K.N., Sakai, K., Kimura, S., Yuge, K., and Gunarathna M.H.J.P., 2019. Classification of Groundwater Suitability for Irrigation in the Ulagalla Tank Cascade Landscape byGIS and the Analytic Hierarchy Process. 1 July, pp. 1-14.
- [13] Ahmed, A., Baroudya, Fullenb, M.A., El-beshbeshya, T.R., Ramadanc, A.R., Halima, A., Guerrad, A.J.T., and Maria, C.O.J. (2016). Spatial distribution of heavy metals in the middle Nile delta of Egypt. International Soil and Water Conservation Research, Vol. 4, pp. 237-314.
- [14] Rahmanian, N. et al., 2015. Analysis of Physiochemical Parameters to Evaluate the Drinking Water Quality in the State of Perak, Malaysia. Hindawi Publishing Corporation Journal of Chemistry, pp. 1-10.
- [15] Tyagi, S., Sharma, B., Singh, P. and Dobhal, R. (2013). Water Quality Assessment in Terms of Water Quality Index. American Journal of Water Resources, 1. Vol. 3, pp.34-38.
- [16] Central Environmental Authority (2019). Proposed Ambient Water quality Standards for Inland Waters of Sri Lanka. Environment Action 1 Project. Colombo.
- [17] Wanasinghe W.C.S., Gunarathna M.H.J.P., Herath H.M.P.I.K. and Jayasinghe G.Y. (2018). Drinking water quality on Chronic Kidney Disease of Unknown aetiology (CKDu) in Ulagalla Cascade, Sri Lanka. Sabaragamuwa University Journal, Vol .16(1), pp.17-27.
- [18] Kumudumali, M. and Nirmanee, K.G. (2019). Assessment of Surface Water Quality for Irrigation in Ulagalla Cascade, Sri Lanka. International Journal of Latest Technology in Engineering, Management & Applied Science (IJLTEMAS), Volume VIII
- [19] Gunarathne, M. and Kumari, M. (2014). Water quality for Agriculture and Aquaculture in Malwathu Oya Cascade-I in Sri Lanka. Rajarata University Journal, Vol.2, pp.33-39.
- [20] Silva, E. I. L., 2004. Quality of irrigation water in Sri Lanka - status and. Asian Journal of Water, Environment, and Pollution, 1(1), pp. 5-12.
- [21] Mahagamage, Y. & Manage, P., 2019. Water quality and microbial contamination status of Madawachchiya,. Journal of Water and Land Development, iv-ix(45), pp. 1-11
- [22] Gunapala, K. G. M. J. W. & Abeysingha, N. S., 2019. Chemical Retention Function of Thaula Area of Small Reservoir; A Case Study in Ulankulama Tank, Anuradhapura, Sri Lanka. Resources and Environment, 9(3), pp. 49-57.
- [23] Mădălina, P. & Gabriela, B.I., 2014. Water Quality Index – An Instrument for Water Resources Management. Directory of Open Access Journals (new), pp. 391-398.

TECHNICAL PAPERS

Poster Session

Surface Urban Heat Island Effect and Vegetation Cover Analysis of Colombo Metropolitan Area (1997-2020), Sri Lanka, Based on Remote Sensing: A Review

Jayaweera B.P.D.V.
Department of Earth Resources
Engineering
Faculty of Engineering, University of
Moratuwa
Katubedda, Sri Lanka
vasudeshanjala@gmail.com

Abstract— The Surface Urban Heat Island (SUHI) effect is one of the crucial results of rapid and unplanned urbanization and reduction of vegetation around urban areas. The decrease of vegetation in city lands are often replaced by impervious elements such as buildings and at the expense of vegetation, the growth of impervious surfaces results in the formation of SUHIs. Motivated by the national tendency of green approaches in the construction field carrying out with the aim of mitigating the desolation of vegetation cover, this paper provides a detailed review of the SUHI effect within the Colombo Metropolitan Area (CMA) which is a rapidly urbanizing city in Sri Lanka with the main objective of resembling the past data and results of remote sensing studies in order to derive on a conclusion for a more continuous timeline (1997-2020) and the general objectives of studying the conceptual background and derive the limitations of SUHI observations via remote sensing techniques in Sri Lankan context. Within the timeline of 1997-2020, the reduction of vegetation is steep in CMA and the spatial patterns of SUHI formation in the area constantly show that the Colombo coastal belt and harbor areas are in an environmentally critical position indicating by the increasing ECI values and by the years hot spots have been emerging towards the other parts of CMA. Also, the aforesaid areas of optimal micro-climate and emerging hotspots require strong SUHI mitigation measures and green spaces can provide environmentally sustainable solutions to CMA. Thus, the findings of the overall study, including two decades of timeline would be useful in future sustainable urban planning and landscape development.

Keywords: Surface Urban Heat Island effect; sustainable urban planning; NDVI; NDBI; Colombo metropolitan area, Sri Lanka

I. INTRODUCTION

Continuous growth of population around the world and rapid urbanization cause changes in land use patterns and significant number of constructions are commencing with the demand of the corresponding level of urbanization. With the higher level of deforestation and removal of vegetation cover in urban areas in order to build impervious elements such as roads, buildings and parking lots, the level of formation of greenhouse gases are increasing and also as a result the surrounding temperature keep increasing day by day.

According to the global perspective, urbanization is occurred due to the higher demand and tendency of people to live in capital cities due to many social and economic reasons such as job opportunities, commercial activities, ease of recourses etc. Globally, the urban population has tended to increase in rate of 1.84% per year in between 2015-2020 [1].

The urbanization does not only result in increasing the population density but many effects such as increase the number of residencies, constructions to accommodate the population and development of other infrastructural facilities which clearly affects the vegetation cover of the land. In most of the third world countries those infrastructural developments and projects are carried out with proper planning as well as improper planning. Roads, bridges, private automation, single-use zones, low density residential houses and transportation cause drastic changes in land use pattern as well as the vegetation cover. Also, when the vegetation cover is removed and replaced with such infrastructure which are significantly impervious, dark colour, have higher solar radiation absorption, high thermal conductivity and capacity the urban areas are encountering higher temperature than rural areas. The phenomena which occur in urban areas compared to the rural surrounding is called Surface Urban Heat Island effect [1].

Colombo Metropolitan Area (CMA) (Fig 1) [2] is the capital city in Sri Lanka which has been facing to hyper urban development rates and commercial activities with significantly increasing population growth and population density. From late 1990s up to present the increase of population has been causing a drastic stress on environment with the unplanned constructions and improper land use. [1] According to the census details and estimations, the highest rate of households is recorded from Western province and most specifically from CMA [1]. According to the data, residential population of CMA is estimated at 619,001 by 2021 according to the UN World Urbanization Prospects. Also, the data shows an annual increase of population by 1.06% in the area. The proper city is about 14.41 square miles and the population density is over 52,000 per square mile [2]. The level of urbanization within last two decades of the city is massive and number of buildings covering the Colombo skyline is significantly higher in present compared to the two decades back in time. Hence, proper scientific studies are essential in deriving the effect of Surface Urban Heat Island Effect (SUHI) along the past decades in order to address the environmental changes occurred with the unplanned urbanization and mitigate the issues by alternative environmentally friendly methods such as green concepts.

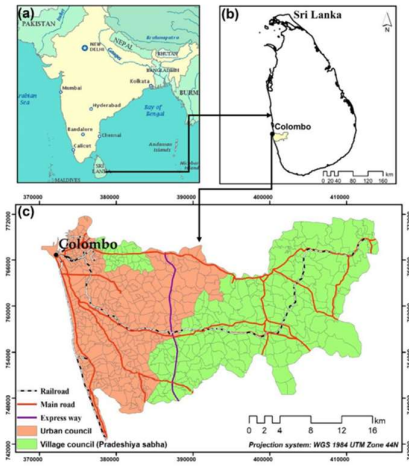


Fig. 1. Study Area, CMA [2]

II. CONCEPTUAL FRAMEWORK

A. Urban Heat Island Effect (UHI)

Structures such as buildings, parking lots, roads, pavements and other infrastructures can be considered as impervious elements as they absorb and re-emit the radial energy compared to the natural landscapes such as grasslands, croplands, forests and water bodies. These kind of structures are common in Urban areas which lacks the natural vegetation cover. Such urban environments are having the risks of becoming “islands” of high temperature compared to its surrounding. These segments of high temperature zones are known as “heat islands. Ways of formation of heat islands can be different including during the day or night, scale of the cities, in rural areas, in different climates, and in any season [14].

B. Normalized Difference Vegetation Index (NDVI)

Normalized Difference Vegetation Index (NDVI) is a parameter of the amount of vegetation in a considered area by measuring the difference between near-infrared (which vegetation strongly reflects) and red light (which vegetation absorbs) [4]. NDVI values are often varies within the range of -1 to +1. Normalized Difference Vegetation Index (NDVI) uses the Near Infra-Red (NIR) and red channels in its formula.

$$NDVI = (NIR - Red) / (NIR + Red) \quad (1)$$

For Landsat 7,

$$NDVI = (Band 4 - Band 3) / (Band 4 + Band 3) \quad (2)$$

For Landsat 8,

$$NDVI = (Band 5 - Band 4) / (Band 5 + Band 4) \quad (9)$$

Healthy vegetation (chlorophyll) reflects more near-infrared (NIR) and green light compared to other wavelengths. But it absorbs more red and blue light. Therefore, healthy vegetation gives higher NDVI values while unhealthy vegetation and vegetation less areas give lesser value. Satellite sensors like Sentinel-2, Landsat and SPOT have the necessary bands with NIR and red [4].

C. Normalized difference built-up index (NDBI)

Normalized difference built-up index (NDBI) is an indicator used to analyse the build-up area. The areas with buildings and artificial impervious surfaces and vegetation-less soil are reflecting more Mid Infra-Red (MIR) than NIR and water bodies are not reflecting on Infrared spectrum. Green surfaces are reflecting more NIR is than Short wave infra-red (SWIR) spectrum [5]. (Fig 3)

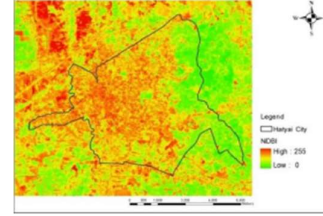


Fig. 3. [16]

NDBI can be calculated by,

$$NDBI = (MIR - NIR) / (MIR + NIR) \quad (4)$$

For Landsat 7,

$$NDVI = (Band 5 - Band 4) / (Band 5 + Band 4) \quad (5)$$

For Landsat 8,

$$NDVI = (Band 6 - Band 5) / (Band 6 + Band 5) \quad (6)$$

D. Built Up Index

Build-up Index used to analyse the urban pattern using NDBI and NDVI. It is the binary image with only higher positive value indicates the areas with buildings and other impervious elements. Build-up Index used to analyse the urban pattern using NDBI and NDVI.

$$BU = NDBI - NDVI \quad (7)$$

E. Land Surface Temperature (LST Retrieval)

The standard method of retrieving LST from raw data (Landsat Images) is conversion of thermal band's digital number (DN) values into radiance values. These radiance values are the ones used to derive at-satellite brightness temperatures. Although in this study itself, pre-processed thermal bands (with at-satellite brightness temperatures values expressed in degrees Kelvin) have been used. The at-satellite brightness temperatures must be to be scaled using land surface emissivity values in order to retrieve LST values After deriving the emissivity values, the emissivity-corrected LST values were extracted as follows: [2]

$$LST = TB 1 + (\lambda \times TB / \rho) \ln(\epsilon) \quad (8)$$

“TB = Landsat TM Band 6 and Landsat TIRS Band 10 at-satellite brightness temperature in degrees Kelvin; λ = wavelength of emitted radiance ($\lambda = 11.5 \mu\text{m}$ for Landsat TM Band 6 [4] and $\lambda = 10.8 \mu\text{m}$ for Landsat TIRS Band 10 [10]; $\rho = h \times c / \sigma$ ($1.438 \times 10^{-2} \text{ m K}$), where σ = Boltzmann constant ($1.38 \times 10^{-23} \text{ J/K}$), h = Planck's constant ($6.626 \times 10^{-34} \text{ Js}$), and c = velocity of light ($2.998 \times 10^8 \text{ m/s}$); and ϵ is the land surface emissivity estimated using the NDVI method [5]. The extracted LST values were subsequently converted from degrees Kelvin to degrees Celsius ($^{\circ}\text{C}$).” [2]

F. Hot and Cold Spots Analysis

The ArcGIS optimized hot spot analysis (Getis-Ord G_i^*) tool can be used to identify hot and cool spots of LST, NDBI, NDVI, ECI etc. in the given division. The G_i^* statistic for each feature class or administrative division represented the z-score. Higher positive z-values were categorized as a hot spot, and smaller negative z-values were classified as a cold spot. The z-value represents the clustering significance for a specified distance based on the confidence level.

G. Environmental Criticality Index (ECI)

The Environmental Criticality Index (ECI) is a parameter used to identify the environmentally critical areas by the ratio between LST and NDVI. The LST and NDVI layers used to derive the ECI Equation are first being normalized using the histogram equalization method, resulting in a 1–255-pixel value range. When the environmental criticality is high ECI indicates a higher value [2].

$$ECI = \frac{LST(\text{Stretched } 1-255)}{NDVI(\text{Stretched } 1-255)} \quad (9)$$

H. Modified normalized difference water index (MNDWI)

Water bodies are analysed using modified normalized difference water index (MNDWI). It can be calculated using manually calibrated thresholds to separate water bodies from non-water areas.

$$MNDWI = \frac{Green - SWIR1}{Green + SWIR2} \quad (10)$$

III. SURFACE URBAN HEAT ISLAND EFFECT THROUGHOUT THE TIMELINE OF 1997-2020

A. Data Sources and satellite images used

Landsat images acquired from the United States Geological Survey (USGS) sources on the dates of 7th February 1997, 2nd January 2007 (Landsat-5 TM) and the 13th January 2017, 31 March 2019 (Landsat 8 OLI/TIRS) are used in the for the study (Table I and Table II). The Colombo District is located on path 141 and row 55 and images are subjected to WGS84/UTM 44 N projection. Radiometric calibration and atmospheric correction are carried out before the processing using the TerrSet software. The Digital Number (DN) values of the multispectral bands are been converted to surface reflectance values during the correction and DN values of the thermal bands are converted into atmosphere brightness temperature in Kelvin. [2]

In the latest study carried out with respect to images taken on 31st March 2019, Landsat 8 Operational Land Imager (OLI) and Thermal Infrared Sensor (TRS) images are taken from USGS in 3 different resolution levels. Band 1-7 and 9 are acquired in 30m resolution where band 8 (Panchromatic) and thermal bands (band 10,11) are acquired in 15m and 100m resolutions respectively. Also, an image having a very thin cloud cover (1.98%) has been used to mitigate the data interpretation difficulties. These images are also subjected to atmospheric correction as well as terrain correction.

Those pre-processed images have been used to derive the corresponding measurements required in the study such as LST, NDVI, and NDBI for the timeline of 1997-2020.

Landsat-5 TM – 120m resolution

Landsat-8 OLI/TIRS – 100m resolution resampled to 30m

TABLE I. DESCRIPTIONS OF LANDSAT IMAGES USED [1,2]

Sensor	Scene ID	Acquisition Date	Time		Seasons
			GMT	Local	
Landsat-5 TM	LT5141055 1997038BK T01	7 February 1997	04:18:38	09:48:38	Dry
Landsat-5 TM	LT5141055 1997038BK T01	2 January 2007	04:48:43	-	Dry
Landsat-8 OLI/TIRS	LC8141055 2017013LG N00	13 January 2017	04:54:05	10:24:05	Dry
Landsat-8 OLI/TIRS	-	31 March 2019	04:59:39	-	Dry

Table II. FACTORS OF SATELLITE IMAGES USED [2]

Electromagnetic Region	Landsat-5 TM		Landsat-8 OLI/TIRS		Resolution
	Bands	Wavelength (Micro meters)	Bands	Wavelength (Micro meters)	
Coastal aerosol	-	-	1	0.43-0.45	30
Blue	1	0.45-0.52	2	0.45-0.51	30
Green	2	0.52-0.62	3	0.53-0.59	30
Red	3	0.63-0.69	4	0.64-0.67	30
NIR	4	0.76-0.90	5	0.85-0.88	30
SWIR 1	5	1.55-1.75	6	1.57-1.65	30
SWIR 2	7	2.08-2.35	7	2.11-2.29	30
Panchromatic	-	-	8	0.50-0.68	30
Cirrus	-	-	9	1.36-1.38	30
TIR 1	6	10.40-12.50	10	10.60-11.19	120' 30
TIR 2	-	-	11	11.50-12.51	100' 30

B. LST variation from 1997 – 2019

The LST images of CMA are shown by Fig 4, 5 and the statistics of the retrieved LST values are shown in the Table III. According to the statistics, on 7th February 1997 the LST values have ranged within 21.06-34.86 degree Celsius with a mean of 26.98 and on 2nd January 2007 the LST values have ranged within 21.10-34.02 degree Celsius with a mean of 26.96. By 13th January the range has changed to 22.31-35.94 degree Celsius and the mean has changed to 28.62. On 31st March 2019 the LST values have ranged from 28.71-40.33 degree Celsius with a mean of 35.26 degrees.

According to the statistics found by the previous researchers, it clearly shows that there is a significant increase of surrounding temperature within the two timelines of 2007-2017 and 2017-2019 compared to 1997-2007 which we can express those timelines as the peaks of the urbanization in CMA[1,2].

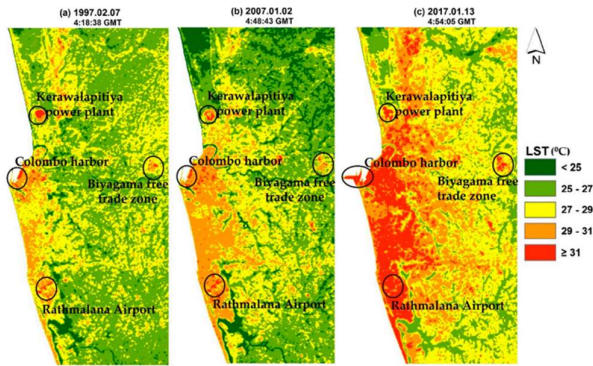


Fig. 4. [2]

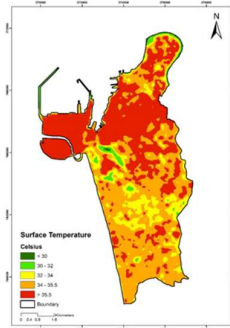


Fig 5 [1]

TABLE III. [1,2]

Date	Time	Min	Max	Mean
1997 Feb 7	04:18:38	21.6	34.86	26.98
2007 Jan 2	04:48:43	21.10	34.02	26.96
2017 Jan 13	04:54:05	22.32	35.94	28.62
2019 March 31	04:59:39	28.71	40.33	35.26

C. NDVI variation

The NDVI values retrieved from the satellite images of the three time points have recorded as -0.74 to 0.84 in 1997, -0.36 to 0.77 in 2007 and -0.25 to 0.81 in 2017 (Table IV) which shows reduction from 1997 to 2007 and slight growth by 2017 (Fig 6). By comparing NDVI maps of 2007 and 2017, 2017 map shows some growth of vegetation near by the built up areas compared to 2007 and has many deeply green spots compared to 2007

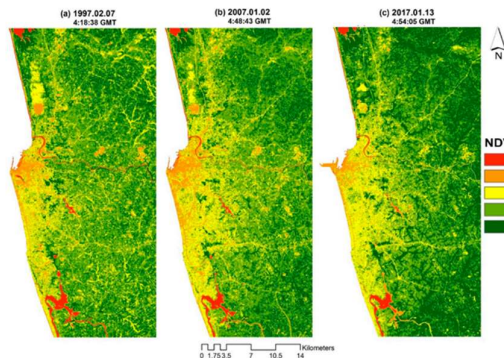


Fig 6 [2]

TABLE IV.

Date	Min	Max	Mean
7 February 1997	-0.75	0.84	0.17
2 January 2007	-0.36	0.77	0.16
13 January 2017	-0.25	0.81	0.16

D. NDBI variation

According to the NDBI maps constructed by the satellite data, the levels of NDBI clearly shows a major difference by 2017 in a higher value. The values of 1997, 2007, 2017 have ranged from -0.1 to 0.46 , -0.1 to 0.05 and -0.67 to 0.66 respectively. According to Ranagalage, it has mentioned that in 1997 and 2007, areas with high NDBI values were concentrated mainly near the city centre and along the coastal belt. However, by 2017 those high NDBI characteristics have spread away from city centre and coastal belt. [2] (Fig 7) (Table V)

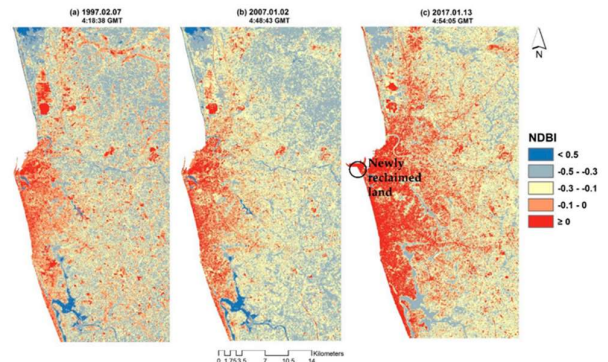


Fig 7 [2]

TABLE V.

Date	Min	Max	Mean
7 February 1997	-1.00	0.46	-0.23
2 January 2007	-1.00	0.51	-0.23
13 January 2017	-0.67	0.66	-0.15

E. Correlation between NDVI and LST and NDBI and LST

The regression analysis of the study has shown that the NDVI is negatively correlated with the LST and slope of the 3 years has been increases from a significant amount which can be explained as a result of higher rate of urbanization. Even though, the research results does not mention the other factors that might effect LST like air pollution and other LST increasing factors the NDVI gives a considerable explanation to increasing of LST. (Figure 8) The NDVI vs LST scatterplots gives a positive correlation between each factors and it also shows the increase of the slope by the time and a clear difference in the intercepts. By 2019, the results obtained by Dissanayake shows a strong negative relationship ($r = -0.6800$) between NDBI and NDVI. Also, it shows a negative relationship ($r = -0.4512$) between NDVI and LST and positive relationship ($r = 0.5935$) between NDBI and LST. The strong negative relationship between NDBI and NDVI implies that the vegetation cover reduction has proceeded to a crucial level and land cover has replaced with impervious elements. (Table VI)

As mentioned in the section 3.4, even though there is a considerably high difference in NDBI from 2007 to 2017 there is a slight increase of NDVI from 2007 to 2017 which can be a result of effects of urban design and geometry on wind flow, including the size, shape and orientation of buildings, and other possible mitigation and adaptation measures including the use of green roofs, cool roofs and cool pavements, the abundance and spatial pattern of green spaces in urban areas.

TABLE VI. [1]

	LST	NDVI	NDBI
LST	1.00	-0.4513	0.5935
NDVI	-0.4513	1.00	-0.6800
NDBI	0.5935	-0.6800	1.00

F. ECI in 1997- 2019

The spatial pattern of the ECI values generally follows the spatial patterns of LST values (Fig 4,5) and NDBI values (Fig 7) and Urban rural gradient of the CMA has showed a higher increase within 2007 to 2017-time period. Since, the mean LST increased in these zones between 2007 and 2017 and also there was an increase in the mean NDVI in these same zones the mean ECI has decreased in said zones during aforesaid period

IV. LIMITATIONS OF SUHI OBSERVATIONS VIA REMOTE SENSING TECHNIQUES

In the definition of SUHIs, the formation of Surface Urban Heat Islands is occurred due to temperature elevations which can be affected by many phenomena. Mainly by using the remote sensing techniques the factors such as the effect of the reduction of vegetation cover, unplanned land use, impervious elements are taken into consideration and correlation between land surface temperature (LST) with respect to other parameters such as NDVI and NDBI is further analysed for a meaningful interpretation. In the practical scenario, the increase of land surface temperature is not only affected by the vegetation cover reduction and higher build up index but affected by many natural and artificial causes such as air pollution due to heavy industrialization, vehicle emissions and other Carbon Dioxide emitting sources around the city. [15]

Other than that, there is a significant difference in readings on a rainy season compared to dry season. The seasons along the year acts in different ways on surface temperature. The temperature differences occurred due to the seasonal variations, alignment of the sun, wind patterns etc. affects much on surface temperature. In a tropical country like Sri Lanka, reliability of weather forecasts cannot be same for all the areas and such dry and wet natures due to rainfall can affect the surface temperature significantly. Also, as a tropical country sudden rainfall on small areas within the considered area can also happen. In such cases, small variations within the area can occur. Most importantly thermal infrared images can be highly affected by weather conditions including cloud cover. [4]

Also, the results are changing with the time of the day and there is a considerable gap when it comes to day and night time. Hence, when the data is gathered it is important to acquire the satellite images of the same time and same dates. The data gathered from Landsat satellites are gathered in day

time. Satellite derived land surface temperature values can be affected by scene view angles, internal errors of sensors other than cloud cover. To improve the accuracy of the LST values the cloud affected pixels are eliminated by cloud screening algorithms. Yet, it limits the application of LST in SUHI observation due to significant temporal and spatial variations that can cause by that. To produce cloud free seamless remote sensing images temporal aggregation is often used. [4]

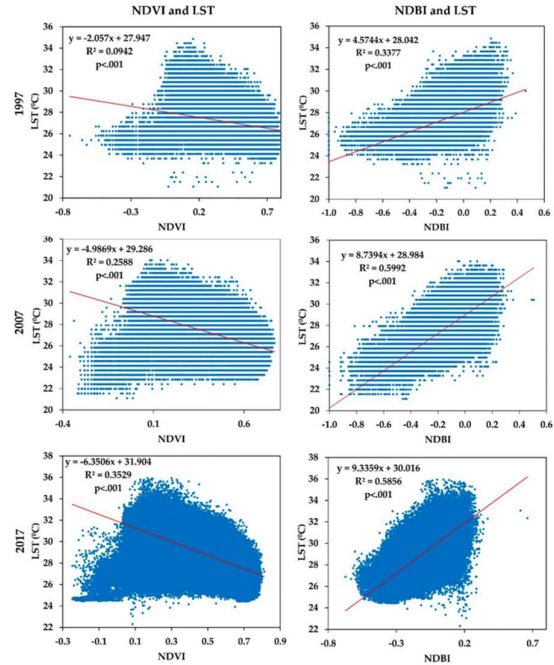


Fig 8 [2]

V. DISCUSSION

This research has examined the SUHI effect along the timeline of 1997-2020 which includes 23 years of Colombo Metropolitan Area. Mainly the 4 different data points are used for the study taken from the resources of previous researches and the parameters of each point are stated including NDVI, NDBI, LST, ECI. With all the data gathered it was intended to emphasize the differences occurred within the time period and crucial situation which is already in CMA.

In general, Colombo city is the economic capital of the country as well as the most prominent city regarding the amount of population, number of occupied housing units and the floating population. Within the years of the research that has taken into consideration, the digits of the amount of population have raised to 561,314 with a floating population around 400,000 according to the census of population and housing 2012(Fig 4) [2].

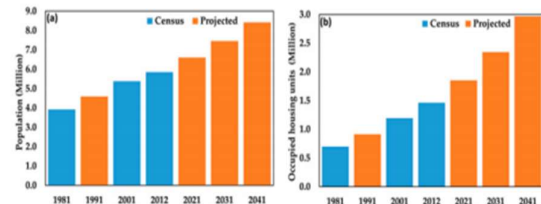


Fig 4 [2]

Within the considered period, Sri Lanka has recorded a significant rate of Gross Domestic Production (GDP) as well. It has recorded the highest rate of GDP per capita by 2008 and it was slightly lagging due to different social and political factors from time to time. When considering the rate of growth of GDP over the years, with the conclusion of the civil war by 2009, many urban development projects have been carried out and major scaling up of industries have been occurred within the 23 years of 1997 to 2020. Those recent developments can be mentioned as strong evidences for the growth of GDP (Fig 5)

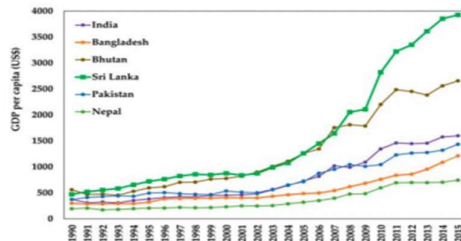


Fig. 5. [2]

Therefore, with the significant amount of urbanization which has happened over the period, the amount of land, water and air pollution is also huge. According to the numbers provided by the world health organization, PM10 Pollution level has recorded as high in Colombo metropolitan area. [7] When it comes to LST and air pollution, there is a significant connection between the two factors and Colombo metropolitan area is subjected to numerous ways of air pollution. Especially the number of vehicles running over the area and the number of factories and other industries operating in the selected region. Department of Motor traffic in Western province has recorded the three are more than 9.5 million total number of issued revenue license over the 9 years of 2008-2016 [8]

Furthermore, Colombo city belongs to the wet zone of Sri Lanka and it is a coastal city which has a major harbor as well. According to the climatic pattern over the year Colombo city has a typical hot humid climate. The country is affected by southwest monsoon from late May to the end of September, and the northeast monsoon blows from the end of November to mid-February. Air temperature and humidity are considerably high during the year. Low wind speeds are present during the inter-monsoon periods (March–April and October–November). The average annual rainfall in CMA is about 2300 mm [2]. Other than that January is considered as the warmest and driest month of the year.

The data has been gathered around the month of the February which is a dry period and in 2019 it has taken in March which can be affected by some rainfall. Other than that, within some decades of time the beginnings of seasonal changes and rainfall patterns might show some differences as well. However, all the data points can be considered as seasonally equal points.

The data points were taken within the dry season of the years 1997, 2007, 2017 and 2019 (7 February 1997, 2 January 2007, 13 January 2017, 31 March 2019) which has a slight difference in amount of vegetation compared to the other seasons of the year and according to the Sri Lankan climatic

pattern there is a slight change in temperature as well. (Fig 6) And also the temperature varies over the daytime. (Fig 7) The amount of vegetation in the dry seasons of the year is quite lesser than the rest of the year due to many reasons. Farmers are not engaging in crop cultivation in the dry period and grass lands and some of the vegetation is drying off due to the strong sunlight and high temperature.

The days and the time of the satellite images used for the study can be considered as the warmest and driest days of the year and warmest hours of the day. Since the considered days are in tough dry season the NDVI values are slightly lesser than the rest of the year. By the study carried out by I.P. Senanayake it has shown 3 satellite image results over a one single year which was showing the NDVI differences over 3 different seasons in the year. [10] Compared to that data set there is a slight difference of NDVI values of the month January from March and September

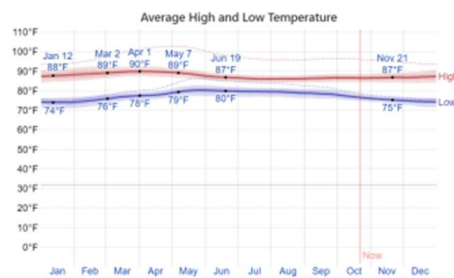


Fig. 6. [9]

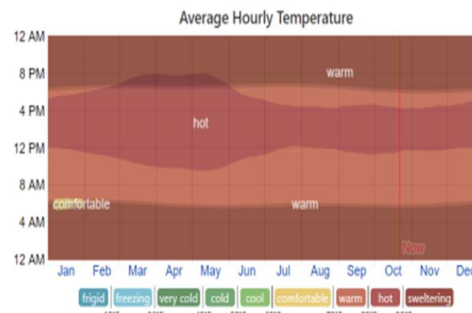


Fig. 7. [9]

In Ranagalage’s data points, the Landsat-5 TM data have 30m spatial resolution, while the thermal band has 120m spatial resolution, which has been resampled to 30m. For, the Landsat-8 OLI/TIRS data, the multispectral bands also have 30m spatial resolution. Its panchromatic band has 15 m spatial resolution, while its thermal bands have 100m spatial resolution, which have also been resampled to 30m. During the selection of image data, cloud-free images (<10%) were considered.[2] Also, in Dissanayake’s data points Landsat 8 Operational Land Imager (OLI) and Thermal Infrared Sensor (TRS) images are taken from USGS in 3 different resolution levels. Band 1-7 and 9 are acquired in 30m resolution where band 8 (Panchromatic) and thermal bands (band 10,11) are acquired in 15m and 100m resolutions respectively. Also, an image having a very thin cloud cover (1.98%) has been used

to mitigate the data interpretation difficulties. [1] Hence, the effect of the clouds can be considered as negligible in all 4 scenarios.

And in the study it was been used some preprocessed datasets taken from earth explorer and all the images were undergone standard terrain and atmospheric correction (level 1T) and also have been geo referenced to the WGS84/UTM 44 N projection system. The digital number (DN) values of the multi spectral bands were being converted in to surface reflectance values whilst thermal bands were being converted in to at satellite brightness temperature. Therefore, the level of accuracy is satisfactorily higher since the number of pixels that were being tested is considerably high. March and September

In order to retrieve LST values by the Landsat dataset, land surface emissivity (ϵ) is derived by the equation, $\epsilon = m PV + n$. Using the $m = (\epsilon - \epsilon) - (1 - \epsilon\sigma) F_{\epsilon v}$ and $n = \epsilon s + (1 - \epsilon s) F_{\epsilon v}$, m and n were calculated ($m = 0.004$, $n = 0.986$). By taking PV as a proportion of vegetation using NDVI equation, $PV = ((NDVI - NDVI_{min}) / (NDVI_{max} - NDVI_{min}))^2$ LST was calculated using, $LST (^{\circ}C) = TB/1 + (\lambda \times TB/\rho) \ln \epsilon$ [2] Indeed, it is a clear deviation from general method of retrieval of LST. From the general method it requires a conversion of the DN values of the thermal bands into radiance values, which are then used to derive at-satellite brightness temperatures which is time taking and also less accurate. Instead, above calculations seems productive and accurate way of deriving LST.

According to the results gathered using the mentioned technique, descriptive statistics of the retrieved LST values summarized in Table 3.3 states that the higher LST values are found along the coastal belt which is the most urbanized part. Also, high LST were mostly concentrated near the Colombo harbor, Ratmalana Airport, and the Kerawalapitiya power plant area and observed that the LST values of the areas where the free trade zones (e.g., Biyagama free trade zone) which are not only high urbanized but the areas which has major scaled industries and factories are operating on. And also the external factors like heat Generated from Human Activities: Vehicles, air conditioning units, buildings, and industrial facilities all emit heat into the urban environment. and also the amount of air pollution is significantly high in these areas and kept increasing in the two decades of 1997 to 2007 and 2007 to 2017. By 2019 it states that the critical areas have emerged to Colombo harbor and port city, central region (including Pettah, central railway station, central bus terminal, main banks, customs, head offices, government departments and other public and private buildings are located), northern (i.e. Colombo 15) and eastern (i.e. Borella) regions of the city while the areas like Thunmulla, Viharamahadevi Park, Thibirigasyaya have low LST values and with higher vegetation cover. According to the analysis of Kithsiri Dissanayake, it has further mentioned that the large hotel complexes such as Shangrila, in the weseyern part of the CMA also shows hot spots with high LST due to use

of dark surfaces and low albedo materials. [1] Therefore, there are many other causes of increasing LST other than the reduction of vegetation and urbanization over the time period. The change of LST from 2007 to 2017 is considerably higher than from 1997 to 2007 and that is even more higher in the 3 years of 2017-2019 considered to the consecutive decade which are the times of huge industrial scaling up was happened. Therefore, amount of pollution, hot gas emmision and heat generated from human activities other than urban developments also can be taken as another cosniderable cause of increasing LST as well as the reduction of vegetation.

The NDVI of the three time points have recorded as -0.74 to 0.84 in 1997, -0.36 to 0.77 in 2007 -0.25 to 0.81 in 2017 (Table 3.4) which shows reduction from 1997 to 2007 and slight growth by 2017. By comparing NDVI maps of 2007 and 2017, 2017 map shows some growth of vegetation near by the built up areas compared to 2007 and has many deeply green spots compared to 2007 which the researcher Manjula Ranagalage has mentioned as “In the CMA, we recognize the efforts of the local government for initiating urban development programs that could also improve the status of urban green spaces in the area” which is mentioning a possible adaptation measures including the use of green roofs, cool roofs and cool pavements, the abundance and spatial pattern of green spaces in urban areas which is a very important aspect of mitigating the issue by sustainable urbanization.

Other than that in the study, water bodies and wetland areas were excluded and that has a significant effect on the results. Since Colombo metropolitan area is in the coastal line there are some mangrove environments and wetlands which consist of a considerable amount of vegetation and natural biodiversity like Muthurajawela, Diyasuru – Thalawathugoda, Bellanwila – Aththidiya and Diyatha. “Despite progressive and degradation, wetlands still cover some 20 km² of the Colombo Metropolitan Region... Due to evaporative cooling, the wetlands can reduce air temperatures, the effect of which can extend into areas up to 100m away from the wetlands’ physical boundaries. This means that over 65 km², or more than 50% of urban Colombo, benefits from this natural air conditioning.” [11]

According to the NDBI maps constructed by the satellite data, the levels of NDBI clearly shows a major difference by 2017 in a higher value. The values have ranged from -0.1 to 0.46 , -0.1 to 0.05 -0.67 to 0.66 in 1997, 2007, 2017 respectively. In the first decade of 1997-2007, areas with high NDBI values were concentrated near the city center and along the coastal belt mostly. But by 2017, those hot spots have greatly expanded outside the city center, towards the other parts of the Colombo city which indicates a higher rate of construction of impervious elements. [2] (Fig 7, Table 3.5)

The regression analysis of the study has shown that the NDVI is negatively correlated with the LST and slope of the 4 years has been increases from a significant amount which can be

explained as a result of higher rate of urbanization. Even though, the researcher has failed to mention the other factors that might effect LST like air pollution and other LST increasing factors the NDVI gives a considerable explanation to increasing of LST. (Fig 8) The NDVI vs LST scatterplots gives a positive correlation between each factors and it also shows the increase of the slope by the time and a clear difference in the intercepts. As mentioned in the section 3.4, even though there is a considerably high difference in NDBI from 2007 to 2017 there is a slight increase of NDVI from 2007 to 2017 which can be a result of effects of urban design and geometry on wind flow, including the size, shape and orientation of buildings, and other possible mitigation and adaptation measures including the use of green roofs, cool roofs and cool pavements, the abundance and spatial pattern of green spaces in urban areas.

The spatial pattern of the ECI values generally follows the spatial patterns of LST values (Fig 8) and NDBI values (Fig 7) and Urban rural gradient of the CMA has showed a higher increase within 2007 to 2019-time period. Since, the mean LST increased in these zones between 2007 and 2019 and also there was an increase in the mean NDVI in these same zones the mean ECI has decreased in aforesaid zones during the period.

According to the results gathered in different years, it shows that heat islands are spreading all over the area. Not just the number of hot spots but the rate of increase of hot spots also increasing with the time. Hence, CMA is in a fast track of facing environmentally critical condition as the unplanned urbanization proceeds further in future. Since it is the capital city and economic hub of Sri Lanka, it is severely important of analyzing the hot spots of the CMA and take remedial measures to mitigate the issue and take further steps to convert the upcoming projects to proceed with green or environmentally healthy (with high albedo materials, less dark surfaces and not building impervious surfaces) approaches.

VI. CONCLUSION

This review was intended to identify Surface Urban Heat Island effect within the area of Colombo Metropolitan Area within the timeline of 1997-2020. The main of objective of the study was to resemble the past data and results of remote sensing studies in order to derive on a conclusion for a more continuous timeline (1997-2020) with general objectives of stating the conceptual background and deriving the possible limitations of remote sensing techniques in identifying surface urban heat island effect in Sri Lanka. By the available data points, it indicates that the level of increasing of SUHIs along the CMA is considerably high and the rate of increasing the SUHI also in a crucial level. The results also show some indication of reduction of SUHI in the green approaches and planned urbanization. Even though the available remote sensing data has built a strong indication of emerging hot spots of heat islands it is not completely considering the other socio-economic variables and the intensity of SUHI (including its

spatial and temporal changes) which can be considered as a limitation. Also, the review has stated more limitations specifically that can affect to Sri Lankan context with the geography and climatic pattern in the island. The study also made a strong argument about the critical situation that CMA has already passed and it is time to move on to the SUHI mitigation techniques and green concepts in future sustainable urbanization strategies.

REFERENCES

- [1] K. K. C. R. Kithsiri Dissanayake, "Ecological Evaluation of Urban Heat Island Effect in Colombo City, Sri Lanka Based on Landsat 8 Satellite Data," Moratuwa Engineering Research Conference (MERCon), pp. 531-536, 2020.
- [2] . Manjula Ranagalage 1, "Spatial Changes of Urban Heat Island Formation in the Colombo District, Sri Lanka: Implications for Sustainability Planning," Sustainability, pp. 1-21, 2018.
- [3] United Nations Department of Economic and Social Affairs, "United Nations Department of Economic and Social Affairs," United Nations, 2018. [Online]. Available: <https://population.un.org/wup/>. [Accessed 05 08 2021].
- [4] Decheng Zhou, Jingfeng Xiao 2, Stefania Bonafoni 3 , Christian Berger 4 , Kaveh Deilami 5 , Yuyu Zhou 6 , Steve Froelking 2, Rui Yao 7, Zhi Qiao 8 and José A. Sobrino. Q. 8, J. A. S. 9. Decheng Zhou 1, "Satellite Remote Sensing of Surface Urban Heat Islands: Progress, Challenges, and Perspectives," Remote Sensing, vol. 11, no. 48, pp. 1-36, 2019.
- [5] Kshetri, T. (., 2018. LinkedIn. [Online] Available at: <https://www.linkedin.com/pulse/ndvi-ndbi-ndwi-calculation-using-landsat-7-8-tek-bahadur-kshetri/> [Accessed 21 10 2020].
- [6] Poonyanuch RUTHIRAKO1, *. R. D. a. W. C., 2014. Intensity and Pattern of Land Surface Temperature in Hat Yai City, Thailand. Walailak Journal, 12(1), pp. 83-94.
- [7] Numbeo, 2020. Numbeo. [Online] Available at: <https://www.numbeo.com/pollution/in/Colombo> [Accessed 21 10 2020].
- [8] Office of the provincial commissioner of motor traffic (Western province), 2017. [Online] Available at: motortraffic.wv.gov.lk/index.php?option=com_content&view=category&layout=blog&id=45&Itemid=41&lang=en [Accessed 21 10 2020].
- [9] Weather Spark, 2016. Weather Spark. [Online] Available at: <https://weatherspark.com/Average-Weather-in-Colombo-Sri-Lanka-Year-Round> [Accessed 21 10 2020].aaaaaaaaaaaaaaaaaaaa
- [10] I.P. Senanayake, W. W. P. N., 2013. Remote sensing based analysis of urban heat. Urban Climate, Volume 5, pp. 19-35.
- [11] Landscape and Urban design office _ FRANCE, 2016. COLOMBO WETLAND MANAGEMENT STRATEGY, Colombo: Metro Colombo Urban Development Project - Consultancy Services for the Preparation of Management Strategy for Wetlands and.
- [13] Manjula Ranagalage, Ronald C. Estoque and Yuji Murayama 1., 2017. An Urban Heat Island Study of the Colombo. International journal of geo information .
- [14] United States Environmental Protection Agency, n.d. EPA. [Online]

Available at: <https://www.epa.gov/heatislands/learn-about-heat-islands#:~:text=These%20heat%20islands%20form%20because%20urban%20surfaces%20such,high%20as%2060%C2%B0F%20warmer%20than%20air%20temperatures.%20%5B2%5D> [Accessed 20 10 2020].

[15] L. M. a. N. Liyanage, "Identifying Surface Temperature Pattern of the City of Colombo," ENGINEER, vol. XXXXI, no. 05, pp. 133-140, 2008.

[16] GISGeography, 2019. GISGeography. [Online]
Available at: <https://gisgeography.com/ndvi-normalized-difference-vegetation-index/> [Accessed 20 10 2021]

Spatial and Temporal Aggregation Analysis of Crash in “A004” Road - Development of Traffic Accident Prediction Model using Traffic & Road Characteristics

Wasala Rajapaksha
Department of Civil Engineering
University of Peradeniya
Sri Lanka
wasala.krajapaksha@gmail.com

Jayalath Edirisinghe
Department of Civil Engineering
University of Peradeniya
Sri Lanka
Jayalath@eng.pdn.ac.lk

Abstract— Road Traffic Crashes (RTC) has become a global problem, causing damage to human lives and properties. According to the estimations by WHO, RTC ranked the fifth leading cause of death of world in 2020. WHO has estimated 3.5 million deaths each year (WHO 2018). RTC is one of the major problems for most developing countries, it is essential to pay serious attention on searching for preventive measures to minimize this problem. The RTC in most times are just merely statistics and do not consider for further analyses and detailed studies. According to the Sri Lanka Police, the second highest RTC are reported on A004 highway. The A004 highway passes through four provinces covering a total length of 425km. Spatial and Temporal analysis are performed using ArcGIS software based on Kernel Density Estimation (KDE) to identify hotspots. Further, the said highway was subdivided into segments of 5 km to find critical segments based on three indices: (i) Accident Rate, (ii) Accident Frequency and (iii) Accident Severity. The main objective of the study was to find relationships among major accident categories(Y), namely [under Fatal only, Grievous only, Fatal + Grievous only] and possible contributory factors such as Number of Intersections Existence (X1), Percentage of Overtaking Prohibited length of the section (X2), Average Daily Traffic Flow in thousands (X3), Average Vehicle Speed of the Section (X4), Commercial Land Use Area of the section (X5). In this study, three (03) relationships were generated to predict possible number of crashes.

Keywords—Road Traffic Crashes (RTC), Kernel Density Estimation (KDE), ArcGIS, Google Earth, RTC Analysis, Accident Prediction Model

I. INTRODUCTION

RTC have become a world class problem which costs human lives and property damages. According to the world health organization the road Crash is one of the leading causes of death for the people between the ages of 5-44 (WHO 2011 A). Road Crash fatalities are projected to become the fifth leading cause of death worldwide by 2020 which could result estimated 2.4 million deaths per each year. (WHO 2011 A). As a developing country, Sri Lanka is experiencing the same issue with rising road traffic crashes in all over the country. At the same time traffic Crash results

in huge loss of inland economy as traffic crashes eventually lead to a wide variety of consequences such as traffic delays, supply chain interruption, undependability of travel time, increased noise pollution and contamination of air.

Sri Lanka has a 12,333 km long road network (Class A and B) and “A” class roads where the total length is about 4217km. annually, around 70,000 RTC s are happening in Sri Lanka. From that, about 40 % of the crashes are occurring in “A” class roads which counts for 2.3 crashes/km. Therefore need to identify the high crash density road segments to mitigate crashes that happen due to regular mistakes or features.

This study is focused on basic patterns and future crash predictions of the crashes happening on A004 highway. Comparing with other “A” class highways A004 road is more vulnerable to crash. It has shown second highest road crashes as an individual road (just behind A002 “CGHW” Highway). This has an accident density - 6.3 acc. /km and 0.3 fatal acc. /km.

A004 (Colombo-Rathnapura-Beragala-Monragala-Pothuwil-Batticaloa) is one of the major highways in Sri Lanka which is about 430 km long. It connects eastern and western parts of country. It is along through urban, sub urban, rural, and agricultural and builds up areas in between the 425 Km length.

Many researchers have introduced various kinds of solutions and recommendations towards preventing vehicular Crashes using road geometric and traffic characteristics [11], [14], [15]. According to the previous studies avg. vehicle speed, existence of intersection, ADT value, terrain type, land use pattern, overtaking manoeuvres, bendiness are some major causative factors for crashes except driver related facts. [1], [2], [3]. This study attempted to use those accident data and develop a model for predicting potential accident prone locations along the highway based on traffic, geometric and

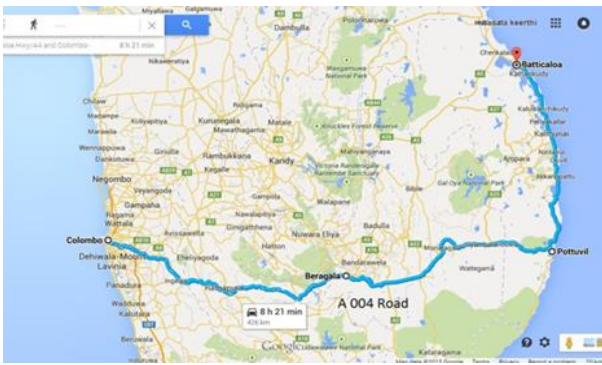


Fig. 1. Study Area A004 Highway, Source: GOOGLE MAP

Land use characteristics. The specific objectives of this research are to (i) identify the existing critical road segments in A004 highway, Sri Lanka using accident related data (2011-2014) (ii) develop a model by relating number of crashes (Y) with the geometric characteristics (X1, X2, X4) and traffic flow (X3), and commercial land use vicinity (X5), (iii). Check the model accuracy with actual RTC data and select the suited model using RTC data (2015-2017).

II. METHODOLOGY

The study area of the research is 425km road segment along A004 highway between Colombo fort to Batticaloa, it runs through four provinces and six districts in Sri Lanka as shown in below figure.

A. Data Collection

1. *Crash Data* which were collected from Sri Lankan traffic police accident database for seven years period (2011-2017) was analysed in this study. That database included all related factors regarding the particular accident. The RTC records acquired from the traffic police division's database were filtered to extract the relevant records for A004 highway. The table shows an aggregated summary of number of accident record over 2011 - 2017 years based on their accident severity types. However non grievous and damage only crashes are not considered for further analysis due to less accuracy and underreporting issues. (According to the Sri Lanka Police Department)

TABLE I. RTC CIRCUMSTANCES; A004 HIGHWAY 2011 - 2017

Year	Road Traffic Crash Type				Total Crashes
	Fatal	Grievous	Non Grievous	Damage only	
2011	167	437	795	1145	2544
2012	139	395	891	1271	2696
2013	129	399	946	1302	2776
2014	120	437	777	1014	2348
2015	164	482	882	1115	2643
2016	147	505	868	973	2493
2017	139	470	809	1015	2433

Source: Sri Lanka POLICE DEPARTMENT

2. *Traffic and Road geometric data* Avg. Daily Traffic Data (ADT) collected from Road Development Authority planning division and road geometric characteristics (No Passing length percentage, existence of

intersection, Avg. Daily Traffic, Terrain Type and etc.) data extracted from Google Earth, Map and Street view.

3. *Land Use Data* Commercial Land use length exacted from Google Earth along the road beside.

B. Data Analysing

1. *Spatial and Temporal Analysis* Statistical spatial mapping is key to understand the spatial and temporal occurrences of Crash, and spatial statistics are methods for describing and formatting spatial data. Statistical spatial analysis of traffic Crash can be done on a spatial database, which includes all the desired information and generates layers of data from sources that can be updated by field verification. All spatial settings were performed using ArcGIS. Hotspot analysis and Kernel density assessment were also performed based on kernel density function. The analyses were carried out using ArcGIS spatial statistical tools [4], [14].

Spatial, temporal analysis was performed using 2011,12,13,14 RTC data for Fatal and (Fatal + Grievous). Temporal hotspots were identified as crashes occurred time and Weekday, Weekend crashes [12].

To identify the hotspots, this study used the KDE which was then supplemented by a Mathematical analysis procedure to find the significant critical sections of RTCs in A004 Highway. These additional steps were developed to overcome the drawback of the KDE [9].

This limitation can be overcome by reflecting additional data –ADT values (or another estimation of traffic flow). The reason comes from the fact that the number of Crash depends on the intensity of the traffic and therefore they have to be weighted by a factor to get comparable results. KDE outputs are given in below figures. Therefore Critical road segments were identified based on Accident rate, Accident frequency and Accident severity [8].

Figure 3, 4 has shown how crash density behavior throughout the A004 highway under fatal crashes, sum of fatal and grievous crashes. The temporal pattern shown in fig 5-8, the analysis based on crashes occurred time, week day crashes and weekend crashes. Crash density variance indicated same as a spatial data analysis. (as per the figures shown). Both spatial and temporal data extracted from 2011-14 crash data

2. *Critical Road Segment Identification* Accident data collected from the Sri Lanka Traffic police divisions were used for formulation of Critical Road Segments identification. The entire road is divided into 5.0 km road segments (83 No's).[7] After that following three indices (Accident Rate, Accident Frequency and Accident Severity) and corresponding critical values, as given by Kent et al (2001), were used to identify the Critical Road Segments. It contains three estimators which estimate the accident hot spots with the places where highest number of Crash likely to be occurred. The used formulas have shown below

a. Accident Rate

Where, $R_j = A_j / m_j$ (1)

A_j : Number of Crash on segment j during a certain time period

m_j : Number of vehicle kilometers in millions on segment j during the same time period (based on ADT data – source Road Development Authority)

$$R_c = \gamma + \frac{k\alpha\sqrt{\gamma}}{m_j} - 0.5/m_j \quad (2)$$

$$\gamma = \frac{\sum_{i=1}^n A_i}{\sum_{i=1}^n m_i} \quad (3)$$

Where,

R_c : critical value for accident rate

γ : estimated average accident rate for segment belonging to same population

(0.5/mj): correction for continuity when approximating with the normal distribution k constant that is chosen for the significance test.

Segment j is considered to be a critical segment, from the accident rate point of view, if: $R_j > R_c$

b. Accident Frequency

$$A_c = F_{avg} + \frac{k\alpha\sqrt{F_{avg}}}{L_j} - 0.5/L_j \quad (4)$$

$$F_{avg} = \frac{\sum_{i=1}^n A_i}{\sum_{i=1}^n L_i} \quad (5)$$

Where,

A_c : critical value for accident frequency, L_j = length of segment j, F_{avg} = average accident frequency for all road segments

Section j is considered to be a critical segment, from the accident frequency point of view, if: $A_j > A_c$

c. Accident Severity

For this case have considered weighted for each accident type, these weighted values are given below,

Fatal-15, Grievous-10, Non-grievous-5, Damage only - 1

$S_j = \text{Fatal} * 15 + \text{Grievous} * 10 + \text{Non-Grievous} * 5 + \text{PDO} * 1$

$$S_c = \frac{\sum_{i=1}^n S_j}{n} \quad (6)$$

S_c : Critical value for crashes severity (average crashes severity for all road sections)

Section j is considered as a Critical Road Section, from the accident Severity point of view if $S_j > S_c$

According to Kent et al. [8], Using this three indices to consider as a Critical Road Segment

Accident Rate $R_j > R_c$

Accident Frequency $A_j > A_c$

Accident Severity $S_j > S_c$ [8]

C. Accident Prediction Model

1. *Multiple Linear Regression Analysis* in previously, black spot study and crash prediction carried out using multiple linear regressions. The study focused to develop an accident prediction model for a selected route and in the model the independent variables were number of access points per one kilometre road section, hourly traffic flow and 85th percentile speed [10]. Another study was developed a multiple linear regression traffic accident prediction model for urban areas using the parameters of traffic volumes, intersections, connecting roads, traffic signals and existence of median barrier [6]. The regression analysis is performed using Microsoft Excel for this study [3]. Another study has been carried to develop the multiple regression models for Homagama- Colombo area using independent variables of ADT, Commercial Land use patterns and Intersection existence in the Area. [14].

$$Y = \beta_0 + \beta_1 X_1 + \beta_2 X_2 + \beta_3 X_3 + \beta_4 X_4 + \beta_5 (D) + \varepsilon \quad \text{Equation}$$

Where in this Equations;

Dependable Y - Number of Crash

Independent X_1 - No. of intersection within particular 5 km Critical Road Segment

Independent X_2 - No passing length (Overtaken Prohibited) percentage within particular 5 km Critical Road Segment

Independent X_3 - Avg. Daily Traffic within particular 5 km Critical Road Segment

Independent X_4 - Avg. Speed (Km/h) in particular 5 km section in between starting point and end point

Independent D - Dummy Value / Commercial Land use (Urban - 1, other - 0)

ε - Error Term

TABLE II. SELECTED 22 CRITICAL ROAD SEGMENTS – BASED ON THREE INDICES

0-5 km	40-45 km	100-105 km	245-250 km
5-10 km	45-50 km	115-120 km	250-255 km
10-15 km	55-60 km	140-145 km	350-355 km
15-20 km	70-75 km	225-230 km	420-425 km
20-25 km	85-90 km	230-235 km	
30-35 km	95-100 km	240-245 km	

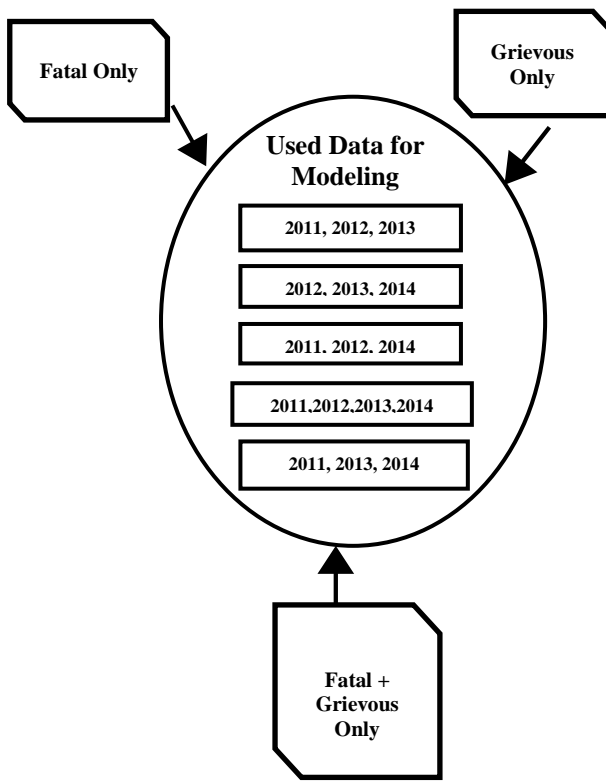


Fig. 2. Data Modelling for Each category

2. *Model Development* The model development carried out for critical road segments using 2011 – 2014 RTC data, using these data built five model from each category. Fifteen models are developed considering Fatal crashes, Grievous Crashes and Fatal + Grievous crashes as five from each type. Accuracy and fitting percentages are surveillance by comparing relevant 2015, 2016 and 2017 RTC data.

Multiple regression models were developed with aid of Microsoft Excel to predict numerical outcomes. As mentioned in the methodology chapter five parameters were selected for the regression analysis. They are Average daily traffic flow, Average travel speed, Intersection Existence, Overtake Prohibited length percentage, and Commercial land pattern. So based on result given by the regression analysis Model Summary shows, an organized observable pattern of growth in road traffic Crash with parameters of average daily traffic, Average travel speed, Intersection Existence, Overtake Prohibited length percentage, whether the section is Commercial land use area or not, proof of statistical relationship between road traffic crashes. Finally a regression model developed for the purposes of estimation and forecasting on the basis of the analysis, specifically based on test of hypotheses and model validation.

If the R squared exceeds 0.6 (60%), those regression were considered for the further analysis in this study. other models were not considered for crash predictions.

3. *Model Prediction Comparison with Actual Cases* After completion of model development for each type, it is compared with actual cases to find out much suited prediction model for each road segment. Avg. accurate summary is shown in this paper (Table 08) for each developed model category with respect to actual crashes

(2015, 2016 and 2017). In the study, more than 60% accuracy considered as a fitting model.

a. *Avg. Accuracy Percentage of Selected Sections with the Prediction Model* Furthermore, after selecting much fitted section for model equation, found the Avg. accurate percentage based on following formula for the particular section.

$$(\text{Avg. Accurate \%}) = \left[\frac{(\text{Model Prediction}_n - \text{No. of Actual Crashes}_n)}{(\text{Model Prediction}_n)} \times 100 \right] / 3$$

Where $n = 2015$ to 2017 , Based on this calculation, has selected above mentioned fitting model for each critical road segments considering 60% avg. accuracy.

b. *Fatal Only Model* Five (05) critical road segments are fitted out of twenty two (22) sections, fitted sections and model details are given in below Table IV.

c. *Grievous Only Model* Seven (07) critical road segments are fitted out of twenty two (22) sections, fitted sections and model details are given below Table V.

d. *Sum of Fatal and Grievous Crashes only Model* Twelve (12) critical road segments are fitted out of twenty two (22) sections, fitted sections and model details are given below Table VI.

III. RESULTS

A. KDE Analysis

Important criteria to estimate the most suitable density level is bandwidth [4]. Selecting bandwidth affects output of hotspots. For instance, larger bandwidth shows hotspots area in larger form. In this analysis, categories were performed based on the standard deviation which considers that, one can prioritize investigations to solve safety problem of hotspots and this classification is shown in Table 3.

Fig. 3-8 show results of kernel density level for crashes leading to death, injury and damages in A004 Highway 2011-2014. Kernel density computations are computed through Arc Map. The default option and the only kernel density option in this software is quadratic density model. Each independent point of mound-shaped kernel density level is like quadratic functions. The results showed that the high crash-prone zones are concentrated in the vicinity of urban areas in A004 highway. This is intuitive as the higher level of traffic interactions generates more safety problems. As the highways are extending outward from the core urban areas, the risk level is decreasing.

TABLE III. CLASSIFICATION OF REGIONS OF A004 HIGHWAY FOR KDE ANALYSIS

Type of Region	Color based on standard deviation in terms of distance between crashes
Very Low Risk	
Low Risk	
Average Risk	
High Risk	
Very High Risk	

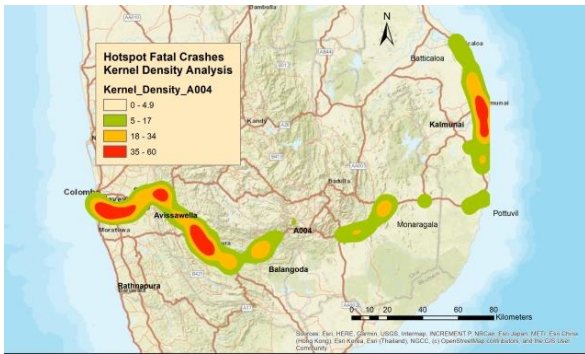


Fig. 3. Hotspots – Fatal crashes in A004 Highway (2011, 12, 13, 14)

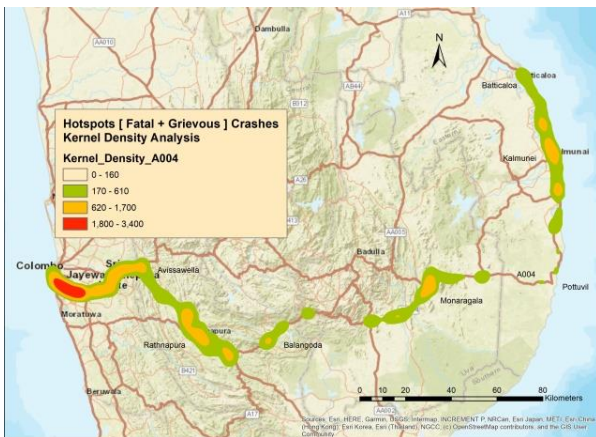


Fig. 4. Hotspots – Fatal + Grievous crashes in A004 Highway (2011, 12, 13, 14)

When the above spatial distributions (figures 3 and 4) are compared, there is a significant difference between fatal only crashes hotspot and sum of fatal and grievous crashes hotspot risk level distribution. Colombo- Kottawa (0-20 km), Awissawella(45-50 km), Eheliyagoda – Kuruwita (70-75 km) and Kalmunei (350-355 km) areas have shown very high risk for fatal crashes. When considering sum of fatal and grievous crashes hotspot distribution, very high risk area is limited to Colombo – Kottawa. However, both crash densities are higher in between urban and suburban area along the highway.

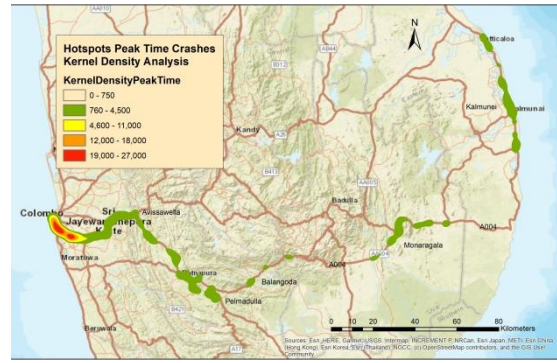


Fig. 5. Hotspots –Crashes occurred during 7.00 – 8.30AM / 12.30 – 2.30PM / 5.00 – 6.30 PM in A004 Highway (2011, 12, 13, 14)

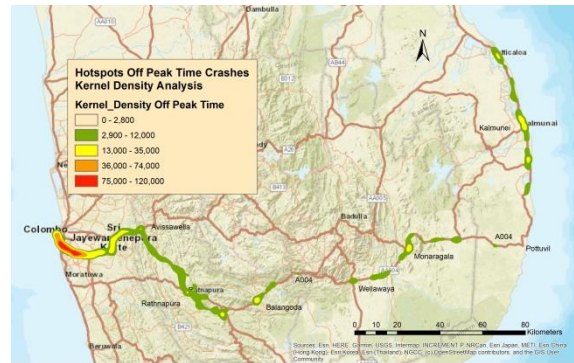


Fig. 6. Hotspots – Crashes occurred during other time in A004 Highway (2011, 12, 13, 14)

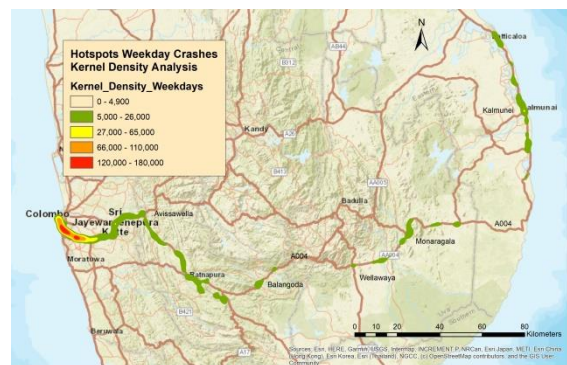


Fig. 7. Hotspots – Week day crashes in A004 Highway (2011, 12, 13, 14)

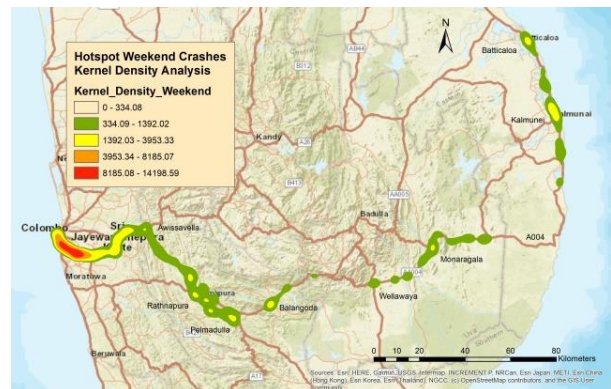


Fig. 8. Hotspots – Week end crashes in A004 Highway (2011, 12, 13, 14)

As per the figure 5, crash density is accumulated in between Colombo-Kottawa (0-20 km) area. Other urban and sub urban areas are shown low risk for selected time intervals occurred crashes. For other time occurred time crashes, very high and high risk area remain as previous. When considering average risk area has shown significant distribution in other urban and sub urban areas.

When compared temporal pattern in week day and weekend days (Figure 7 and 8), almost same as occurred time distributions (Figure 5 and 6). Weekday crash densities are fully accumulated throughout Colombo-Kottawa (0-20 km) area. Average risk is shown that urban and suburban areas along the highway. Very high risk and high risk remain in between Colombo-Kottawa (0-20 km) area according to the KDE analysis.

B. Regression Model Prediction

TABLE IV. APPLICABLE SELECTED CRITICAL ROAD SEGMENTS FOR FATAL CRASHES MODEL

Fitting Section (km)	Avg. Accuracy	R squared value
05-10	60.0	0.63
15-20	72.5	
30-35	69.6	
45-50	82.1	
70-75	70.0	

Multiple Regression Model prediction equation for fatal crashes is given below (7). The summarize detail of fatal crashes is shown in table IV. The observed and estimated fatal crashes show good relationship as high R² value for five critical road segments.

$$Y = -0.227X_1 + 0.022X_2 + 0.112X_3 + 0.036X_4 + 0.0542(D) - 0.189 \quad (7)$$

According to fatal crashes model, as number of intersections increases, fatal crash rate decreases, overtaking prohibited length, ADT value, average vehicle speed and commercial land use have positive relation with fatal crash rate.

TABLE V. APPLICABLE SELECTED CRITICAL ROAD SEGMENTS FOR GRIEVOUS CRASHES MODEL

Fitting Section (km)	Avg. Accuracy	R squared value
05-20	79.9	0.64
40-50	66.9	
240-245	66.3	
420-425	64.4	

The summarized detail of grievous crashes is shown in table V. The observed and estimated grievous crashes show good relationship as high R² value for seven critical road segments

$$Y = 0.426X_1 - 0.210X_2 + 0.399X_3 + 0.246X_4 - 0.850(D) - 5.116 \quad (8)$$

Grievous crashes model equation show that, as number of intersections increases, grievous crash rate increases, overtaking prohibited length, commercial land use have negative relation with crash rate. ADT value and average vehicle speed have positive relation with fatal crash rate.

TABLE VI. APPLICABLE SELECTED CRITICAL ROAD SEGMENTS FOR SUM OF FATAL AND GRIEVOUS CRASHES MODEL

Fitting Section (km)	Avg. Accuracy	R squared value
10 - 25	80.3	0.68
55 - 60	77.3	
70 - 75	74.8	
85 - 90	63.6	
115-120	60.8	
140-145	62.3	
225-230	61.2	
230-235	88.5	
245-250	61.3	
420-425	65.6	

The observed and estimated sums of fatal, grievous crashes show good relationship as high R² value. Twelve critical road segments are fitting with developed regression model. Prediction model equation is given below.

$$Y = 0.193X_1 - 0.201X_2 + 0.513X_3 + 0.267X_4 - 1.685(D) - 4.101 \quad (9)$$

According to developed fitting crashes model, as number of intersections increase, grievous crash rate increases, overtaking prohibited length, commercial land use have negative relation with crash rate. ADT value and average vehicle speed have positive relation with fatal crash rate.

IV. DISCUSSION

This Analysis and prediction is based on only reported details for Sri Lanka Police department. The recorded crashes coordinates are feuded to Google Earth. Somehow, there were few unacceptable positions in crashes. Therefore this analysis considered reporting errors and recording errors.

Spatial and temporal crashes prone areas shown in Figure 3-8. The estimation carried using ArcGIS- Kernel Density Estimation (KDE), red colour areas indicated that hotspots with higher density crashes. It has shown how differentiate behaviour of spatial and temporal pattern under each category. 2011-2014 crashes data were based for the estimation.

The Model shown that, for the fatal crashes five road segments are fitted with developed prediction model from twenty-two critical segments. About 120 – 170 fatal crashes per year were recorded along the highway (Source: Sri Lanka Police Department). For the grievous crashes model seven road segments are fitted with developed prediction model from twenty-two critical segments. Total grievous crashes vary from 375 – 500 per year along the highway (Source: Sri Lanka Police Department). When considering Fatal + Grievous crashes analysis, twelve sections are applicable with developed prediction model out of selected critical sections.

This study developed a crash prediction model by multiple linear regression analysis. In regression analysis, high R^2 value is needed for the model selection. In this study fifteen (15) equations are generated initially, however low R^2 models were rejected at the beginning without checking fitting and accuracy with the actual crashes. Furthermore, some models were not shown higher accuracy with actual crashes (2015-2017). This behaviour shows either some predictor variables are missing or the relation between dependent and independent variable is not linear or does not follow normal distribution. Most suited three (03) relationships found under each crash category at the end of the study. The model developed and calibrated in this study exhibits results in terms of goodness-of-fit measures. The statistic of the model indicate that the variable grievous crashes and fatal crashes relating to classified independent variables are significant at 95 % confidence level in this regression model.

V. CONCLUSION

Spatial and temporal analysis proposed an integrated method to evaluate and analysis the occurrence of traffic Crash through a GIS-based. The purpose of the analysis is to investigate the relationship between time and the location of traffic Crash. The proposed approach is suitable for identifying the cluster pattern of traffic Crash, fig 3-4 shown spatial behavior of crashes in each type of crashes. Higher intensity locations are shown by red color in the maps. Temporal patterns under specific time intervals and weekday/ weekend basis shown in Fig 5-8. According to the KDE estimation, higher crashes intensity taken place in high urbanized Areas. Most crashes were occurred around commercial capital city area (Colombo Metropolitan and sub urban area) in all categories. However, during unspecified time and weekend days it is visible higher intensity areas in urban and semi urban locations which located outside from capital city (Fig 5-8). Fatal crashes hotspots are shown in the same way while other crashes types are highly compacted in capital city area. KDE (Fig - 3) for fatal crashes are shown that some higher intensity locations also in urban/semi urban and rural areas. The highest traffic volume in A004 highway in between Colombo urban area (ADT – RDA), thus the results shown that traffic volume is not only effected on the fatal crashes on highway. It is a considerable factor for the further study.

According to the KDE analysis shown in Fig 3-8 and three indices (Accident rate, Accident frequency, Accident severity) which used for identified critical road segments, are indicated that same areas as higher crashes intensity area. From the analysis, 5 km long twenty-two (22) sections were selected as critical road segment for crashes. That indicated 26% length of the highway is more critical for the crashes. The stats shown about 30% form the total crashes and 25% from fatal crashes are taken place within these critical sections. (Source: Sri Lanka Police Department)

The specialty of this study is after the development of model, checking the fitting and accuracy based on actual crashes. Therefore, selected models efficiency and accuracy already proved in the same study. Three models are finalized under each mentioned crashes category, in somehow some critical sections are almost fitted with in all categories and some sections are not fitted with the single section. The prediction model produced under each crash category type, therefore responsible authorities can make remedial measures to mitigate crashes based on each crash type's circumstances amount and social/ economic impact based on prediction.

As number of intersections increase, grievous crashes rate increases, ADT value, average speed have positive relation with all crashes rate. Overtaking prohibited length and commercial land use shows negative relation with grievous crash rate. All selected model indicated that ADT and average speed shown direct relationship with all crashes type. Therefore, ADT and vehicle speed reduction will work on crash impairment. For grievous crashes and sum of fatal and grievous crashes prediction model shown same positive and negative relation with parameters. In identified higher crashes intensity areas, speed limitation, display warning notice is the possible countermeasures for deduct crashes in A004 Highway.

ACKNOWLEDGEMENT

This study was conducted with the aid of Sri Lanka Police Department (Traffic division – RTC data) and Road Development Authority (RDA – ADT values). Hence it is my duty to thank both organizations and professional staff that extended their helping hand to make this study possible. Further, I express my endless gratitude to Dr. Loshaka Perera and Dr. H.R. Pasindu for their valuable support and help.

REFERENCES

- [1]. Angus Eugene Retallack, Bertram Ostendorf, "Relationship between Traffic Volume and Accident Frequency at Intersections", International Journal of Environmental and Public Health, Feb. 2020.
- [2]. Consolata Wangari Ndung'ua, Ratemo Matayo Bonfaceb, Lydia K. Mwaic, "Analysis of Causes & Response Strategies of Road Traffic Crash in Kenya", Journal of Business and Management (IOSR-JBM) 17, 58 -77. 2015.
- [3]. Crash Factors in Intersection related crashes: An on Scene Perspective, U.S. Department of Transportation, National Highway Traffic Safety Administration (NHTSA- September 2010).

- [4]. Gholam Ali Shafabakhsh, Afshin Famili, Mohammad Sadegh Bahadori, "GIS based Spatial Analysis of Urban Traffic Accidents: Case Study in Mashhad, Iran", *Journal of Traffic and Transportation Engineering* 4, 290-299, 2017.
- [5]. Homayoun Harirforoush*, Lynda Bellalite, Goze Bertin Bénié, "Spatial and Temporal Analysis of Seasonal Traffic Crash", *American Journal of Traffic and Transportation Engineering* 4(1): 7-16, 2019.
- [6]. Hong, D., Lee, Y., "Development of traffic accident prediction models by traffic and road characteristics in urban areas, *Proceedings of the Eastern Asia Society for Transportation Studies*", Vol. 5, 2046-2061, 2005.
- [7]. Isabelle Thomas, "Spatial Data Aggregation: Exploratory Analysis of Road Accidents", *Accident Analysis and Prevention* 28, 251-254. (1996).
- [8]. Kent S., Hans, E., *Black Spot Manual*, General Directorate of Highways, Road Improvement and traffic safety project, Traffic Safety Consultancy Services. SweRoad Ankara, 2001.
- [9]. Michal Bíl, Richard Andrášik, Jiří Sedoník, "A detailed spatiotemporal analysis of traffic crash hotspots", *Applied Geography* 107, 82-90, 2019.
- [10]. Mustakim, F., Yusof, I., Rahman, "Blackspot Study and Accident Prediction Model Using Multiple Linear Regression", *First International Conference on Construction In Developing Countries (ICCIDC-I)*, Karachi, Pakistan, 2008
- [11]. NSSR Murthy, R Srinivasa Rao, "Development of Model for Road Accidents based on Intersection parameters using Regression Models", *International Journal of Scientific and Research Publications*, Volume 5, January 2015.
- [12]. Spencer Logan, Frank Wilmert, "Spatial, Temporal, and Space-time Analysis of Fatal Avalanche Crash in Colorado and the United States", Paper presented at the International Snow Science Workshop, Anchorage, Alaska, 2012.
- [13]. Thillaiampalam Sivakumar, Dinusha Amarathunga, "Development of Traffic Accident Prediction Models Using Traffic and Road Characteristics: A Case Study from Sri Lanka" Downloaded through internet, 2015.
- [14]. V. Prasannakumara*, H. Vijitha, R. Charuthaa, N. Geethaa, "Spatio-Temporal Clustering of Road Crash: GIS Based Analysis and Assessment", *Procedia Social and Behavioral Sciences* 21, 317-32, 2011.
- [15]. Veluru Sailaja, S. Siddi Raju, "Accident Analysis on NH-18 by using Regression Model and its Preventive Measures", *International Journal of Science and Research (IJSR)*, 2013.

GPR and LiDAR Synergy: Honeycomb detection in Concrete Structures

R.Subakaran
Department of Civil Engineering
University of Moratuwa
Moratuwa, Sri Lanka
haranniro@gmail.com

Sumudu Herath
Department of Civil Engineering
University of Moratuwa
Moratuwa, Sri Lanka
sumuduh@uom.lk

Abstract— Honeycombs are formed due to trapped air voids around the coarse aggregates during concreting. These can form inside the concrete structures and on the surface as well. Detecting honeycomb concrete structures is essential to ensure the structural integrity and durability of the structure. However, detecting internal honeycombs are much cumbersome as it is not visible to naked eyes. Ground Penetrating Radar (GPR) is a system that emits and receives Electromagnetic waves which can penetrate through different materials and could detect any disturbances on its travel path. Using the GPR output data, we can identify the defects, honeycombs. Further, Laser imaging Detection and Ranging (LiDAR) emits and receives Laser waves to acquire surface details and reconstruct 2.5D models as Point Clouds. Each of these systems has individual drawbacks. By combining both the systems we can produce data sets that can be used to reconstruct a full 3D understanding of the structure and to conduct further analysis. This paper reviews the pros and cons of GPR and LiDAR and proposes a method on how a full 3D understanding can be obtained using both of these systems and the limitations in the real-world applications of this synergy.

Keywords— Honeycombs in Concrete, GPR, LiDAR, Point Clouds, NDT, Concrete Defects, Photogrammetry

I. INTRODUCTION

Honeycombs are air voids that are trapped inside the concrete due to the effect of segregation [1]. These can be formed on the concrete surface as well and they become visible to naked eyes as the formworks are removed. Improper vibration, presence of larger size aggregates and using stiff concrete can cause Honeycombing in concrete [3]

Surface honeycombs affect the aesthetics and can be easily recovered but internal honeycombs can lead to the reduction of load-carrying capacity and affect the permeability of the elements. Detecting the honeycombs are still challenging since they form in various sizes, shapes and positions. Honeycombs can be formed as a continuous channel causing severe water penetration and they are critical in Water Retaining Structures and Tunnels [1]. Laser imaging Detection and Ranging (LiDAR) and Ground Penetrating Radar (GPR) are two technologies or rather tools that are used independently and abundantly in many Civil Engineering related principles for two distinctly different purposes. Though both of those technologies have added significant benefits to the industry, they have their own drawbacks as well, but the drawbacks of those individual technologies can be eliminated by using both in combination during projects.

GPR works on the basic principle of reflection of Electromagnetic Waves [4]. One of many uses of GPR is

performing various Non-destructive Tests in various materials. Even though GPR has tremendous advantages such as quick data acquisition and detects various elements underneath it, the main drawback is the complexity of the output [5]. The rebars which generally lies near the surface of the majority of the concrete structures, produce stronger reflections, which interrupts weaker reflections from underneath flaws [2]. In the absence of rebars, in structures made up of masonry or mass concrete, they work fine and are able to detect air voids. In Fig. 1, a GPR output obtained during a masonry unit survey is shown and the reflections from a void inside the masonry panel are noticeable at a depth of 20cm and 43cm. Two reflections represent the starting boundary of the void and the finishing boundary of the void respectively.

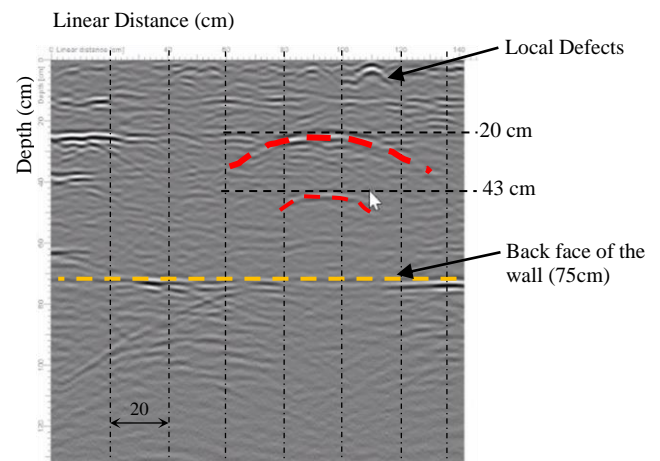


Fig. 1. The result obtained from a GPR survey done on a masonry unit.

Meanwhile, according to [2], using the GPR in transmission mode than reflection mode reduced the attenuation caused by the rebars and have provided promising results to detect voids in structures which has access from opposite sides. Fig. 2 (a) shows the test specimen used by [2] and Fig. 2 (b) represents the output GPR data when it is used in the transmission mode configuration than in the reflection mode configuration and it can be clearly seen that the disturbances caused by the rebars are eliminated to a greater extent and it has shown the size effect of the voids in the output.

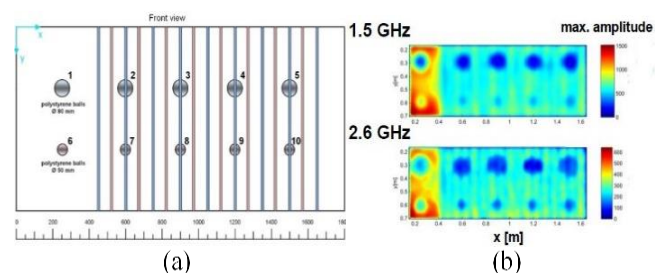


Fig. 2. (a) Test specimen (b) GPR output.

Meanwhile, on the other hand, LiDAR emits and receives laser pulses to reconstruct the surface model. This is widely used in the Civil Engineering industry to produce Digital Twin of structures [6]. The faster scanning time, precision and accuracy of the laser scanning systems are some notable advantages [8, 7], but it cannot penetrate through surfaces and extract features underneath the surface. Therefore, the subsurface conditions would not be detected in LiDAR scan outputs but only in the surface conditions.

Output from LiDAR can be obtained in the form of Point Clouds. A Point Cloud is a set of points in the 3-dimensional space with semantic information embedded in each point in the data set [7, 21]. Photogrammetry is an easy and inexpensive technique from which the point cloud data can be obtained by combining several photos and videos of structures using commercially available software. The reconstructed models using Photogrammetry or LiDAR is called a 2.5D representation [9]. In Fig. 3 the point cloud representation of a retaining wall structure is shown. This is created using 36 images using Agisoft Metashape software.

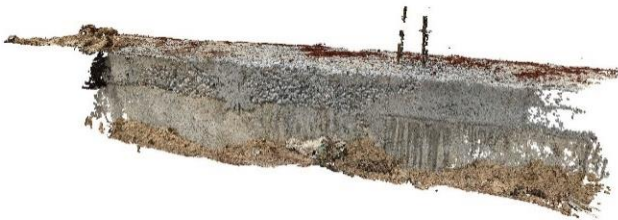


Fig. 3. Point Cloud representation of a retaining wall, reconstructed using Agisoft Metashape.

The drawback of LiDAR technology is the inefficiency to reconstruct features underneath the surface but it is well known to reconstruct surface features and produce point cloud data [21]. This paper is concentrated on how to improve the LiDAR point cloud data to reconstruct a complete 3D point cloud understanding of a structure when combined with GPR data and to detect and identify honeycombs in concrete.

II. REVIEW OF EXISTING TECHNIQUE

A. Data Collection Techniques

GPR data collections are done both manually and automatically. For any scanning, firsts the scan location is analysed and a grid of particular spacing is chosen, such that the GPR scanner is passed over individual grid lines. The selection of grid density depends on the accuracy and density of the data required. Usually, the GPR scanners are scanned in two perpendicular directions, because the scanners that are commonly available in the market can acquire data along a single direction, whereas there are advanced scanners that do not require scanning in two different directions at one pass as well. There is a variety of equipment available in the industry for various purposes, for scanning Highway Road pavements, an automobile mounted with a GPR system [12], as shown in Fig. 4. Meanwhile, there are handheld and compact scanners as well for small-scale tasks or applications.



Fig. 5. A standard vehicle used for mobile surveys, image source [12]

B. Data Processing and Interpretation

After the scanning process has finished, the data require postprocessing, where the data is converted to a more usable and understandable format, often they are converted as the amplitude representation of the reflected waves plotted against distance along with the wave propagation. Fig. 5 shows raw data and the post-processed data of a scanning project.

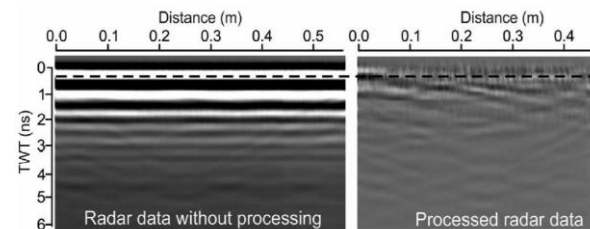


Fig. 6. Raw data (left) and the processed data (right) of a scan done on a test slab, image source [13]

But the post-processed data too require substantial prior knowledge about the data interpretation. While scanning a hypothetical slab element, where there is no other disturbance causing elements in the subsurface region other than the reinforcements, the data interpretation would be straightforward, because the reflections are only due to the presence of reinforcements. Fig. 6 which is obtained as a result of a scan done on a concrete bridge deck indicates the series of reinforcements underneath the top surface [10].

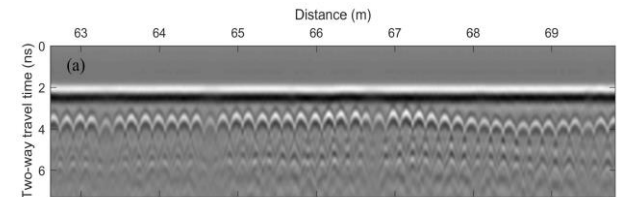


Fig. 4. Processed data showing a series of reinforcements in the subsurface. image source [10]

Usually, this may not be the actual case, there could be many unknown subsurface disturbances in a single element, such as voids, separations, cracks, reinforcements, variation in materials, etc. [11]. With the increase in the number of disturbances causing factors, the reflected waves become more and more complex due to the superimposition. The interpretation of these complex representations requires prior knowledge and experience, or if the tentative subsurface elements are known before the scan, they could be first scanned and analyzed in a control setup in a testing laboratory, and later the site data can be compared and controlled test data and interpreted. A processed data of a scan done on a pavement and the interpretation (which is not

drawn to the same scale as that of the scan) is shown in Fig. 7.

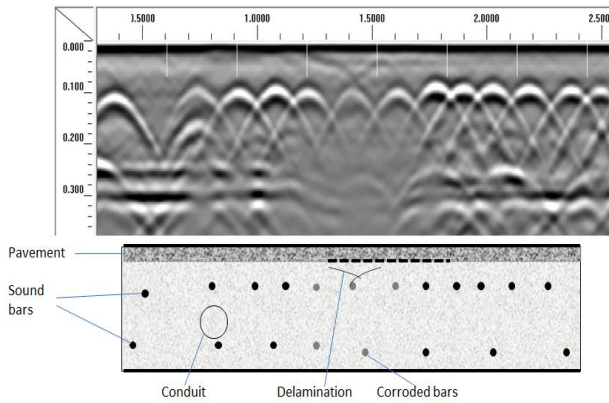


Fig. 7. Processed GPR data (top) and its interpretation (bottom). (The interpretation image is not drawn to scale)

C. Void Detection

GPR systems emit waves, and the antennas detect the reflected waves typically in homogenous media. Waves get reflected whenever there is a change in the medium occurs along the direction of propagation of waves. Any object with a dimension greater than the wavelength of the emitted Electromagnetic waves would reflect. So, not every crack or void would be identified in a single scan, instead, multiple scans of different wavelengths are required to detect all possible cracks. Every recorded data along each of the gridline are then merged to form a complete image, which is known as Radargram. The left of Fig. 8 shows the reflected wave obtained as a result of reflections on multiple layer interfaces and the right image shows the radargram obtained by merging several such series of recorded reflected wave data [13].

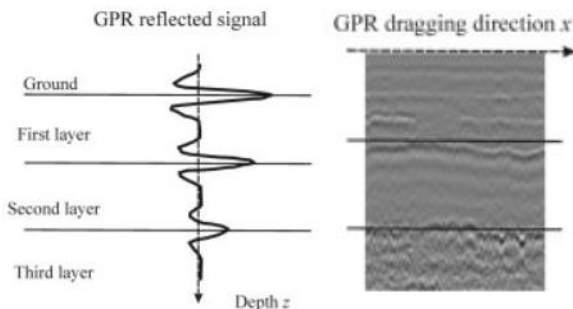


Fig. 8. The reflected wave pattern of a single wave (left) and radargram (right), image source [13]

Consider a concrete element with a void in it. Voids could be either filled with water or air, which is a different medium to that of concrete. So, in the similar fashion, waves would be reflected, and voids can be detected in a spatial coordinate system [13]. Fig. 9 illustrates two different

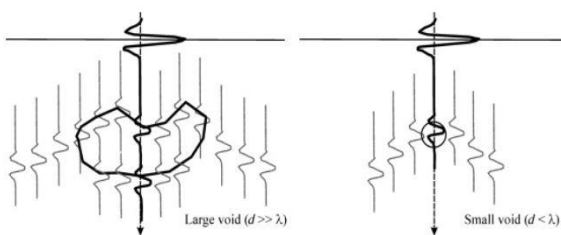


Fig. 9. Reflected wave patterns from voids of two different sizes, image source [13].

reflected wave patterns that could be obtained from two different sizes of voids.

III. PROPOSED METHODOLOGY

A. Reconstruction of representative Point cloud

LiDAR produces point cloud data only as a surface representation, but GPR produces data to represent the subsurface characteristics. There are instances where other sensors and radars are used along with LiDAR to obtain different combinations of results along with the surface details [14,15].

Consider a homogenous concrete beam element of dimensions 0.3 m x 0.5 m x 2 m. Using Matlab as the tool of choice, synthetic point clouds were created as solid 3D Point Cloud data instead of conventional 2.5D. This representation is not valid if LiDAR alone is used in real life but when we combine the GPR data with LiDAR data, this is a realistic geometry representation. Fig. 10 shows the point cloud representation of the aforementioned beam.

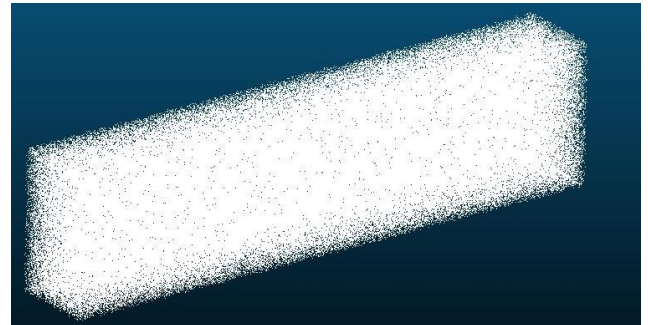


Fig. 10. Point cloud representation of the considered beam element, reproduced using CloudCompare software.

Point density is one of the important parameters in a point cloud. The higher the point density, the better the results are. But having high point cloud density would be computationally expensive and may contain unnecessary data, which needs to be eliminated before making it into a usable form [12,21]. Fig. 11 shows four Point Cloud representations of the same beam but with different Point densities.

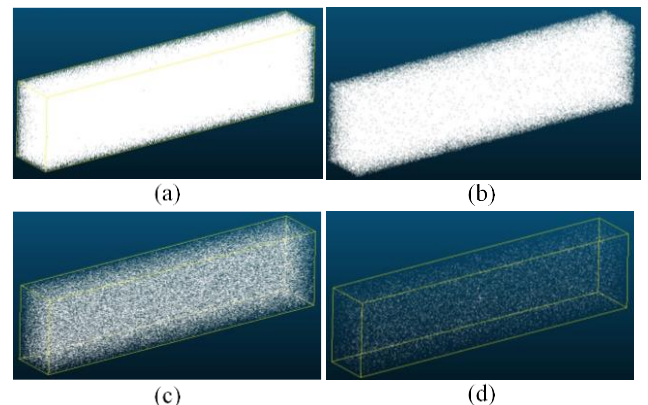


Fig. 11. Point Clouds with different Point densities, (a) 1000000 (b) 500000 (c) 100000 and (d) 10000 points, recreated using CloudCompare.

B. Introducing voids to the beam

Honeycombs in a concrete structure are voids that are created due to improper casting of concrete [1]. The

honeycombs are idealised as voids and for the analysis purpose, hollow spheres are introduced to the beam to represent the honeycombs [2]. This was created by initially defining a random matrix with three columns (representing the spatial coordinates x, y and z of the points) and rows equal to the density of the point cloud (say n), such that the dimension of the random matrix becomes 3xn. Chosen point cloud densities for the analysis were 200,000, 500,000, 1,000,000 and 2,000,000. Later, six centres (x_i, y_i, z_i) were selected at two different levels of the beam (3 centres in each level) at sufficiently enough spacing, so that the created spheres will not overlap on each other. Spheres were later introduced while the centres of the spheres lie on the selected 6 centres and with defined radii. Selected radii for the analysis were 1cm, 2cm, 4cm, 6cm, 8cm and 10cm. This was done using an algorithm developed in MATLAB R2021a. Later the matrices were exported as ASCII files and fed as the input for the CloudCompare software for the cloud-to-cloud comparisons. The positions of the spheres are depicted in Fig. 12 which is a sectional cut created using SOLIDWORKS software (only for demonstration purpose and drawn to the same scale as that of the created synthetic point cloud). All spheres are embedded within the beam, thus in real-life these voids cannot be seen.

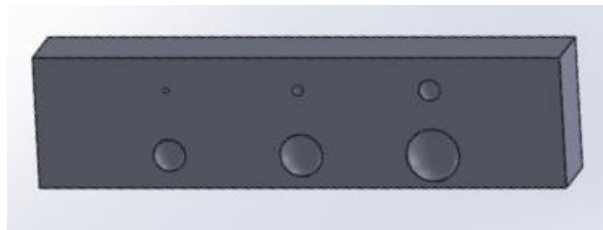


Fig. 12. The beam with voids of diameters 10 cm, 8 cm, 6 cm, 4 cm, 2 cm and 1 cm.

The synthetic point cloud representation of the beam that we created earlier is taken as the reference point cloud for the comparison and this can be created for any geometry comfortably using any 3D modelling software and later can be converted as a point cloud.

Meanwhile, another point cloud with voids embedded in the beam is also created. Fig. 13 shows the point cloud of the beam embedded with the voids. It is clearly understood that the voids that are embedded into the beam would not be visible for naked eyes, which is a similar case when there are honeycombs inside concrete structures.

C. Cloud-to-Cloud Comparison

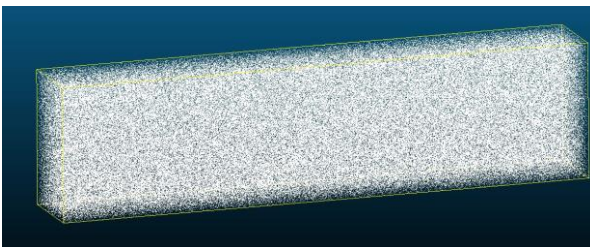


Fig. 13. Point Cloud of the beam with Voids embedded, created using Matlab and visualized in CloudCompare.

Cloud-to-Cloud comparison is a technique in which two selected point clouds can be compared to detect any changes. It works reliably only when the two point clouds can be aligned to each otherwise there could be a significant discrepancy in the results. One point cloud is considered as a *Reference Point cloud*, whereas the other is the *Compared*

point cloud. The principle behind the comparison is, finding the nearest neighbour distance to compute the distance between two points, one from the reference point cloud and another from the compared point cloud [13]. The mathematical principle used to compute the Cloud-to-Cloud distance is a part of the Hausdorff Distance algorithm [20]. The x and y are elements of the subsets X and Y of a metric space. Distances between a point from subset X to all the points from subset Y is calculated and the highest lower bound, the infimum, is determined. Here sets X and Y are the two point clouds selected for the comparison. The generalized equation that is utilized in the CloudCompare software is given as in (1), here 'a' is an element of the set A (reference point cloud), 'b' are the elements of set B (compared point cloud), and A and B are subsets of metric space.

$$d(a,B) = \inf \{d(a,b) \mid b \in B \} \quad (1)$$

The distance calculated using Equation (1) can be interpreted as the distance from any points 'a' from the reference point cloud to another point from the compared point cloud. The point in the reference point cloud would be the nearest of all the points from the other point cloud. To make the calculation process quicker, the maximum distance can be set by the user [20], such that the distance calculation is restricted inside a sphere of radius equivalent to the maximum distance provided by the user and having the point 'a' as the centre of the sphere. A 2-dimensional visual representation of Equation (1) is given in Fig. 14 for better understanding.

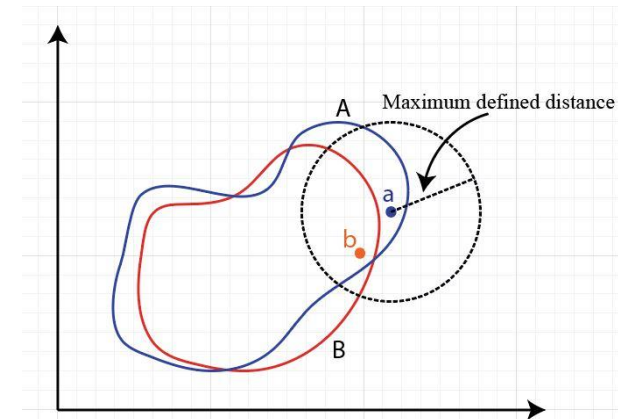


Fig. 14. 2D visual representation of the algorithm used in CloudCompare for Cloud-to-Cloud distance calculation.

All the results that are provided in this paper are the outputs of the Cloud-to-Cloud comparison done using CloudCompare software and a sample of the results along with the distance spectrum is provided in the latter part of the paper.

The results obtained after Cloud-to-Cloud comparison in the CloudCompare software is shown in Fig. 15. Fig. 15 (a) represents the voids introduced at the upper level of the beam section (smaller voids), while Fig. 15 (b), represents the voids introduced at the lower level of the beam section (larger voids) respectively. According to the comparison done using the CloudCompare software for the reference point cloud and point cloud with voids, at the point cloud density of 500,000 points, the voids of diameter less than 2cm are barely visible in Fig. 15 (a).

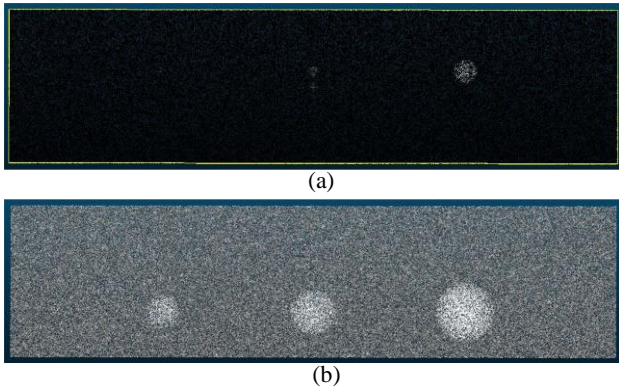


Fig. 15. Results of the Cloud Compare, obtained using

Since the voids of diameter less than 2 cm were undetected in the comparison done at a density of 500,000 points, those three voids were again compared using point cloud densities of 100,000, 1,000,000 and 2,000,000. According to the comparison results obtained using CloudCompare, by increasing or reducing the point cloud density from a density of 500,000 points, the void identification did not show any significant improvement. Also, with the increase and decrease in the point cloud density, the void corresponding to 4 cm diameter tends to diminish. Therefore, finding an optimum point cloud density for the purpose depends on the time and availability of resources to obtain dense point clouds, if required. The Cloud-to-Cloud comparison results obtained using CloudCompare software are shown in Fig. 16.

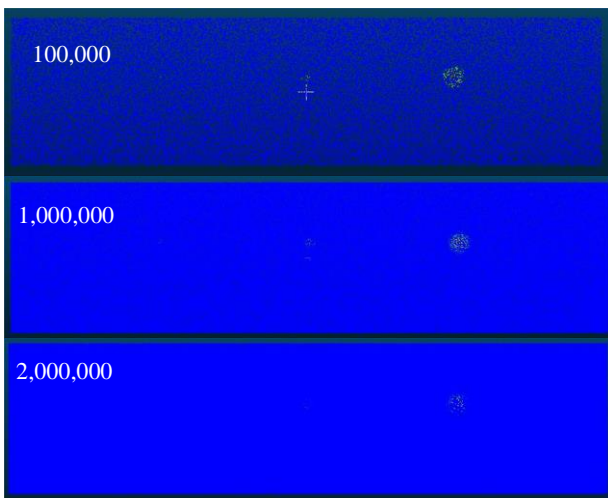


Fig. 16. Cloud-to-Cloud comparison results for different point cloud densities, obtained using CloudCompare.

The comparison was done repeatedly by changing the maximum distance to be detected during the Cloud-to-Cloud comparison at an expense of time taken for the completion of the analysis. The analysis was done using point clouds with 500,000 and 2,000,000 points with a maximum detection distance of 0.005 m and the results are shown in Fig. 17. When the maximum distance is reduced to 0.5 cm, the 2 cm diameter void became visible and it is noticeable in Fig. 17 irrespective of the point cloud density, though the 1 cm diameter void was barely visible.

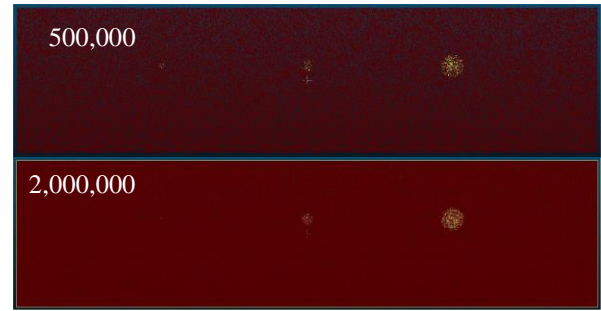


Fig. 17. Cloud-to-Cloud comparison for 500,000 and 2,000,000 point cloud densities at 0.005m maximum distance level, obtained using CloudCompare.

D. Extracting the Voids from the Reference Point Cloud

Even though the results obtained using CloudCompare software after Cloud-to-Cloud comparison are satisfactory to observe voids visually, it may not always be possible to identify voids that are embedded deeper in the concrete element with relatively larger section size, because the points that are at the surface often conceal the points below the dense point cloud.

To overcome this issue, a different approach was formulated. Using Matlab and CloudCompare together, we have developed a simple filtration to extract the voids from the reference point cloud. It is possible since the after-comparison results from CloudCompare software provides the data of the distance between each point in the reference point cloud to that of the nearest point in the compared point cloud, the distance is often represented as a spectrum as shown in Fig. 18.

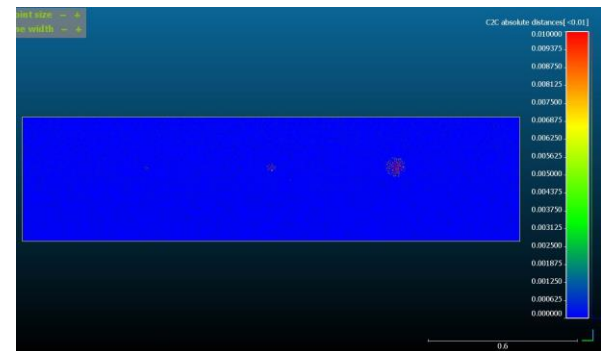


Fig. 18. Cloud-to-Cloud comparison results, obtained using CloudCompare.

First, the output of the Cloud-to-Cloud comparison from CloudCompare is obtained as an image format. An image file can also be represented in terms of pixel data, which contain spatial coordinates of each pixel (x,y,z) and the RGB values of each pixel, in other words, pixel data is a matrix representation of an RGB image, with 6 columns and rows equal to the number of pixels in the image. Then using the pixel data the points are filtered based on the colours using Matlab as a tool. Here the filtration should be done based on the dimension of the voids that the user is required to check. Then the filtered points are exported as a separate Point Cloud, which contains only the points from the reference point cloud, which have higher or equal Cloud-to-Cloud distance as mentioned by the user in the filtration, which interprets the voids in the concrete beam element that we considered in the study. Using this extracted point cloud, identification of voids at any depth is possible. The extracted point cloud is shown in Fig. 19.



Fig. 19. Extracted points corresponding to the voids, obtained using Matlab software

The pixel filtration approach proposed in this paper is given in Fig. 20.

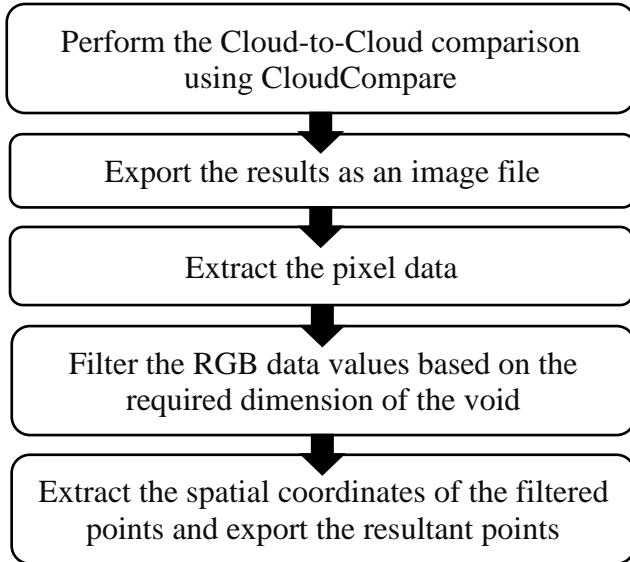


Fig. 20. Flow chart of the performed filtration algorithm

Extracting the points corresponding to the voids as a separate point cloud have tremendous advantages, the continuity of voids can be easily discovered, the severity of the honeycombs can be identified and further inspected. If these combined scans are performed in newly built structures, not only the results can be used to identify the defects, also can be used as a digital twin of the structure and the data can be submitted for the as-built drawing submissions which are often required at the end of the construction and handing over phase [21].

IV. DISCUSSION

GPR and LiDAR are two different technologies/tools that are widely used in several instances and so far, they have been used independently. GPR is generally used to perceive the subsurface conditions, whereas LiDAR is used for the surface reconstruction of objects. GPR could not be used for surface reconstruction, while LiDAR could not be used for subsurface detail extraction are the drawbacks that could be eliminated when both are used in combination. Because LiDAR is a tool that can be utilized to compare the as-built and as-planned structures in the Civil Engineering industry [21], but it only compares the surface alignments. But when paired with GPR and the output of the GPR data is converted to point cloud format and merged with the LiDAR point cloud output, a full 3-dimensional reconstruction of the whole structure is possible, and this would lead to easy identification of subsurface and surface defects in the elements of the structure in terms of quality control. The scope of this research paper was narrowed down to verify the usability of Point cloud in only

honeycomb detection and illustrated using synthetic point cloud of a beam element with and without artificially introduced voids embedded into the beam, which corresponds to the honeycombs in real life [2]. Since the actual geometry of the elements would be known in a real-life scenario, it is possible to create synthetic point clouds using the method proposed in this paper as a reference point cloud and the data for the real elements can be obtained by both LiDAR and GPR scans, which will represent the compared point cloud.

The analysis conducted is made as realistic as possible and since the target criteria are well constrained, the idealization is valid for the selected case. Using CloudCompare as a tool, both the synthetic point clouds (reference and compared point cloud) were visualized and compared. The comparison made it possible to identify voids of diameter 2 cm and greater, and void of diameter 1cm was barely visible in the compared point cloud, but in a real test case, when the locations of the voids are unknown and other disturbances are present, it may be difficult to interpret the 1cm range voids as voids. Using CloudCompare, section slices can be obtained in places where required and a sample of a section slice is shown in Fig. 21.

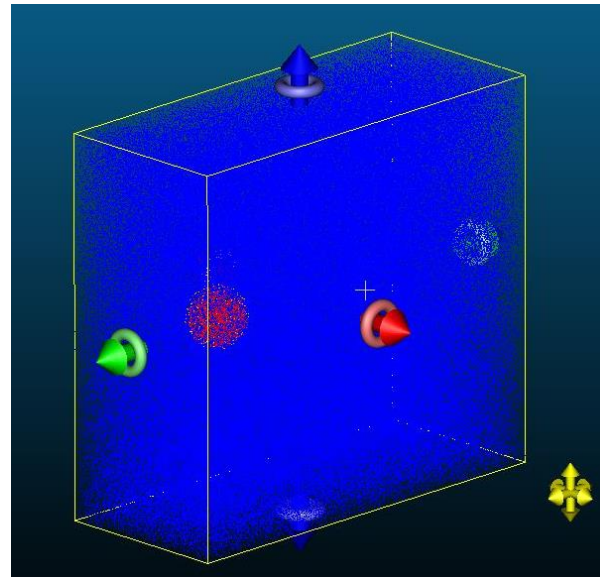


Fig. 21. Section slice of the beam section and the 0.04m void, obtained using CloudCompare.

Even though point cloud can be used to detect honeycombs in concrete while used together with GPR as explained in this paper, the output of the GPR plays a major role. Detection of voids depends on the wavelength of the GPR signal [13] and other abnormalities. With the increase of abnormalities, the reflected wave becomes more complex. When the abnormalities are known to a certain extent, in the case of concrete elements, we can remove unwanted abnormalities in the Point cloud and use the rest for further analysis. In a field and lab test conducted using only GPR, GPR showed promising results in finding voids as small as 3.2 cm in dimension during the early stage of the concrete (before the setting of concrete) [18]. According to a field test experiment conducted as in [19], only the GPR survey was done using two different frequencies, 450 MHz and 900 MHz and the results were compared. The results of 450 MHz showed stronger reflections from the rebars, less or no reflections from the top of the voids and no reflection from the bottom of the concrete slab but 900 MHz results

defined the top of the voids clearly and the bottom of the concrete slab. Therefore, conducting scans at two different frequencies would help identify the location and arrangements of the rebars and the voids underneath the rebars, and most importantly selection of the frequency play a major role in the output of the GPR. By increasing the frequency of the GPR system, even fine cracks can be detected but it requires a detector at the opposite side of the scanner, which is not considered in the scope of this research paper.

To implement this in real-world scenarios, the LiDAR point cloud data and the GPR output data are required in addition to the dimension details of the elements under consideration. With the dimensions and the shape of the elements are known, a synthetic point cloud can be created as the reference point cloud. This will well suit linear elements such as beams, slabs, walls and columns. Meanwhile, the GPR output can also be converted as a point cloud output. By using CloudCompare as a tool, the point cloud of the GPR output and the reference synthetic point cloud can be compared and visualized. Then the output of the CloudCompare could be obtained in image formats and the points corresponding to the honeycombs can be separated using the pixel data filtration approach as mentioned in this paper. To reconstruct a complete 3D representation of the structure or the elements, the extracted point cloud from the filtration process can be aligned with the LiDAR point cloud output, so that now the aligned point cloud consists of both surface details and the subsurface details (honeycombs, rebars, cracks, foreign particles, etc) simultaneously. This would aid during the quality control procedures (easy detection of the location and size of the honeycombs) and the as-built vs as-planned model or drawing preparations.

V. CONCLUSION

This paper clearly shows the possibility for the use of GPR and LiDAR together for better honeycomb detection and produce a full 3-dimensional representation of the whole structure or individual elements using synthetic point clouds and the advantages of using point cloud in honeycomb detection. From the comparison results obtained from CloudCompare, the following conclusions are made.

1. The synergy of GPR and LiDAR allows the digital recognition of voids in concrete and 3D reconstruction of concrete structures or elements rather than 2.5D representations.
2. The density of the point clouds influences the easy detection of the voids; higher point cloud density could conceal the voids underneath, whereas point cloud with lower density could produce inaccurate or unreliable outputs.
3. By adjusting the maximum distance during the cloud-to-cloud comparison in CloudCompare, void detection can be improved, and the computation time can be reduced.

For the considered beam, void of diameter 2 cm is visible for point cloud of the density of 2,000,000 points than point cloud of density 500,000 and the void corresponding to 0.01 m is barely visible for point cloud of density 2,000,000, at a maximum distance of 0.5 cm. Even

though there are restrictions for the GPR signal travel depth in objects, since the study is mainly focused on concrete structures, there are possibilities to access the elements from several directions. Meanwhile, when the GPR output is combined with LiDAR data, a complete Point Cloud representation of concrete elements or a complete structure can be obtained. Using this combined result, the honeycombs, both internal and surface honeycombs, can be easily figured out in terms of their locations and their dimensions. From this, an analyst would be able to determine which voids are at critical locations, which reduces the time of going through every scanned output and locating their relative locations in the structure.

ACKNOWLEDGEMENT

The authors of the paper gratefully acknowledge the support and guidance given by the staff member of Murphy Geospatial and Dr Wayne B Muller.

REFERENCES

- [1] Völker, C., & Shokouhi, P. (2015). Multi sensor data fusion approach for automatic honeycomb detection in concrete. *NDT & E International*, 71, 54-60.
- [2] Trela, C., Kind, T., & Schubert, M. (2015, July). Detection of air voids in concrete by radar in transmission mode. In 2015 8th International Workshop on Advanced Ground Penetrating Radar (IWAGPR) (pp. 1-4). IEEE.
- [3] Mishra, G. (2019, April). Honeycombs in Concrete – Their Causes and Remedies. *The Constructor*. <https://theconstructor.org/practical-guide/honeycombs-in-concrete-and-remedies/6889/>
- [4] Cafiso, S., Di Graziano, A., Goulias, D., Mangiameli, M., & Mussumeci, G. (2020). Implementation of GPR and TLS data for the assessment of the bridge slab geometry and reinforcement. *Archives of Civil Engineering*, 66(1).
- [5] Giannopoulos, A. (2005). Modelling ground penetrating radar by GprMax. *Construction and building materials*, 19(10), 755-762.
- [6] Greif, T., Stein, N., & Flath, C. M. (2020). Peeking into the void: Digital twins for construction site logistics. *Computers in Industry*, 121, 103264
- [7] El-Omari, S., & Moselhi, O. (2008). Integrating 3D laser scanning and photogrammetry for progress measurement of construction work. *Automation in construction*, 18(1), 1-9.
- [8] Walsh, S. B., Borello, D. J., Guldur, B., & Hajjar, J. F. (2013). Data processing of point clouds for object detection for structural engineering applications. *Computer - Aided Civil and Infrastructure Engineering*, 28(7), 495-508.
- [9] Brenner, C. (2005). Building reconstruction from images and laser scanning. *International Journal of Applied*
- [10] Halabe, U. B. (2013). Non-destructive evaluation (NDE) of composites: techniques for civil structures. In *Non-Destructive Evaluation (NDE) of Polymer Matrix Composites* (pp. 483-517e). Woodhead Publishing.
- [11] Penetradar.com. 2021. GPR Inspection Vehicles – Penetradar. [online] Available at: <http://penetradar.com/new/?page_id=525> [Accessed 5 July 2021].
- [12] Rasol, M. A., Pérez-Gracia, V., Fernandes, F. M., Pais, J. C., Santos-Assunção, S., Santos, C., & Sossa, V. (2020). GPR laboratory tests and numerical models to characterize cracks in cement concrete specimens, exemplifying damage in rigid pavement. *Measurement*, 158, 107662.
- [13] Hashmi, S. (2014). *Comprehensive materials processing*. Newnes.
- [14] Narváez, F. J. Y., del Pedregal, J. S., Prieto, P. A., Torres-Torriti, M., & Cheein, F. A. A. (2016). LiDAR and thermal images fusion for ground-based 3D characterisation of fruit trees. *Biosystems Engineering*, 151, 479-494.
- [15] Comstock, J. M., Ackerman, T. P., & Mace, G. G. (2002). Ground - based lidar and radar remote sensing of tropical cirrus clouds at Nauru Island: Cloud statistics and radiative impacts. *Journal of Geophysical Research: Atmospheres*, 107(D23), AAC-16.

- [16] Kim, M. K., Cheng, J. C., Sohn, H., & Chang, C. C. (2015). A framework for dimensional and surface quality assessment of precast concrete elements using BIM and 3D laser scanning. *Automation in Construction*, 49, 225-238.
- [17] Antova, G. (2019). Application of areal change detection methods using point clouds data. In *IOP Conference Series: Earth and Environmental Science* (Vol. 221, No. 1, p. 012082). IOP Publishing
- [18] McCabe, T., Erdogmus, E., Kody, A., & Morcou, G. (2021). Early Detection of Honeycombs in Concrete Pavement Using GPR. *Journal of Performance of Constructed Facilities*, 35(1), 04020138.
- [19] Cassidy, N. J., Eddies, R., & Dods, S. (2011). Void detection beneath reinforced concrete sections: The practical application of ground-penetrating radar and ultrasonic techniques. *Journal of Applied Geophysics*, 74(4), 263-276.
- [20] *Cloud-to-Cloud Distance - CloudCompareWiki*. (n.d.). CloudCompare. Retrieved July 28, 2021, from https://www.cloudcompare.org/doc/wiki/index.php?title=Cloud-to-Cloud_Distance
- [21] Subakaran, R., & Herath, H. M. S. T. (2021). Feasibility of using 3D point cloud technologies in Sri Lankan Civil Engineering Industry. *Modulus*, 31(01), 19–25. <http://dl.lib.uom.lk/handle/123/16510>
- [22] *MATLAB Documentation - MathWorks India*. (n.d.). MathWORK. Retrieved May 10, 2021, from <https://in.mathworks.com/help/matlab/>
- [23] *Cloud Compare V2.6.1-User Manual(huhongjun)*. (n.d.). UserManual.Wiki. Retrieved May 10, 2021, from <https://usermanual.wiki/Document/CloudCompareV261User20manualhuhongjun.1487341153/html>
- [24] *Manual Download - 2019 - SOLIDWORKS Help*. (n.d.). DASSAULT SYSTEMS. Retrieved May 10, 2021, from https://help.solidworks.com/2019/english/SolidWorks/install_guide/HID_STATE_MANUAL_DOWNLOAD.htm
- [25] *User Manuals*. (n.d.). Agisoft. Retrieved May 10, 2021, from <https://www.agisoft.com/downloads/user-manuals/>

Assessing the Applicability of Lean Construction Techniques in Sri Lankan Construction Sector

Hirusheekesan S.
Department of Civil Engineering
University of Sri Jayewardenepura
Rathmalana, Sri Lanka
hirushee12@gmail.com

Satanarachchi N.N.
Department of Civil Engineering
University of Sri Jayewardenepura
Rathmalana, Sri Lanka
niranji@sjp.ac.lk

Abstract—“Lean Construction is a project management method that primarily focuses on minimizing the wastage while maximizing the value of a project. This concept is derived from “Lean Production” or “Toyota Production System” which revolutionized the production sector in the 20th century. Some of the lean tools and concepts are currently being practiced in many countries and have proven to be successful. However, in Sri Lanka, it is still in its initial stages. Sri Lankan Construction Companies are facing many challenges in realizing profits due to many reasons such as COVID-19 pandemic, unstable dollar prices, foreign competition etc. One of the ways in which the local companies could increase their competitive advantage is by reducing the wastage in their projects, in which Lean Construction Techniques will be very useful. Hence this study attempts to identify the barriers and reasons why Lean Construction is still in its initial stages in Sri Lanka and assess its applicability in Sri Lankan Construction Sector by utilizing a literature review and a questionnaire survey. From the study it was found out that some of the lean tools and lean principles are being practiced in Sri Lanka, even though the professionals are not fully aware of it. The local construction industry is optimistic about practicing Lean in their operations despite the several financial, managerial, technical, social and technical barriers of lean identified during this study.

Keywords—*Lean Construction, Lean Tools, Barriers,*

I. INTRODUCTION

In the past decade, up until the surge of current pandemic, the construction industry in Sri Lanka has gone through an unprecedented amount of growth owing to several reasons. The contribution of the construction industry to the GDP had increased from approximately 8000 LKR million to 170000 LKR million from 2010 to 2020 (Department of Census and Statistics, 2020). Also, it contributed 6-7% of the total GDP of the country making the industry to become the 4th largest sector (Central Bank, 2019; Jayalath *et al.*, 2017). Despite this rapid growth, the industry had also started to head towards a recession from 2011 (Hadiwattege, 2014). This can be attributed to the high import taxes, political instability, unstable dollar price, lack of skilled labor and competition from foreign companies etc. (Hadiwattege, 2014; Silva *et al.*, 2008). This condition further deteriorated with the current COVID-19 pandemic situation and the consequent depletion of the business activities. All these call the local construction companies to focus on new strategies and innovations to keep their margins and profits intact, while winning their tenders. One of the ways in which this can be done is minimizing the wastage in the construction processes, as the industry is considered to be highly prone to wastage.

Koskela (1992) defined waste as not only based on material, but “any inefficiency that results in the use of equipment, materials, labor or capital in larger quantities than those considered as necessary in the production of a building”. The above definition is actually based on the Lean Production concept that revolutionized the production sector in the 20th century. However, these concepts are now used in the construction industry as “Lean Construction” (LC). However in Sri Lankan construction sector has not embraced LC as some other places. From the preliminary literature review it was identified that a number of studies were made on identifying the barriers for the successful implementation of LC and the lean tools. But, not much studies are done on how to address those barriers. Also, from the Sri Lankan context, applicability and barriers of implementation of LC tools with respect to different phases of a project are not well explored. Therefore, this paper attempts to find the barriers in implementing the LC techniques in Sri Lanka successfully, and by addressing those barriers to identify the applicability of LC in the Sri Lankan Construction Industry.

II. METHODOLOGY

The study is done in two distinctive steps. The first step is the literature based critical exploration of the barriers of lean tools in Sri Lankan context, where the LC is considered as a form of innovation in the construction industry. The second step is the exploration of the views from the experts in the industry on the possible barriers in implementing LC and the subsequent assessment of the applicability of LC in the local construction industry. For the first step, a comprehensive literature review was employed, while the second step was supported by a questionnaire survey circulated among the industry professionals that included Engineers, Architects, Technical Officers, Managers etc. using which based on the findings from the two steps comparison was made among the conceptual and empirical observations regarding the barriers of LC, and further discussion are made with respect to suitability and acceptance of LC in the local construction sector.

III. OVERVIEW ON LEAN CONSTRUCTION

A. Lean Construction

During the 20th century, a new project management strategy based on the “Toyota Production System Principles” became popular in the production industry which was later came to be known as “Lean Production” (Aziz & Hafez, 2013). This is based on the “Lean Philosophy” which is all about designing and operating the right resources at the right

time with the right systems. The main objectives of lean philosophy is to identify, eliminate waste and achieve the customer needs in all aspects (Ahuja, 2013). Koskela in 1992, reported that this Lean Production Concept can be adapted to the construction industry as well to achieve the same objectives mentioned earlier (Aziz & Hafez, 2013). He put forward its basic principles as reduce variability, reduce cycle times, minimize the number of steps, parts and linkages, simplicity, focus control on the complete process, balance flow improvement with conversion improvement, benchmarking, increase output flexibility and increase transparency (Bashi *et al.*, 2016). This new concept came to be known as “Lean Construction”.

LC can be defined as a project management based, new way that concentrated on the maximization of a construction project’s value while minimizing waste (Marhani *et al.*, 2013). LC also refers to the application and adaptation of the underlying concepts and principles of the Toyota Production System to construction (Nesensohn *et al.*, 2016). Another definition for LC is that it is an integrated socio-technical system whose main objective is to eliminate waste by concurrently reducing or minimizing supplier, customer and internal variability (Solaimani & Sedighi, 2019). LC involves ways of designing production systems to minimize waste in materials, time and human effort, with the aim of generating maximum cost-effective value (Pinch, 2005; Sarhan *et al.*, 2017). It is concerned with a holistic pursuit of concurrent and continuous improvements in the design, construction, activation, maintenance, salvaging and recycling in building projects (Howell, 1999; Sarhan *et al.*, 2017). There are five main principles in LC that helps to achieve the above objectives (Marhani *et al.*, 2013; Sarhan *et al.*, 2017; Thomas, 2018). These principles of LC are namely (i) defining the value i.e. the customer’s need and expectation from the product, (ii) mapping the value stream which use customer’s value as a reference point to identify the activities required to carry out the project and pinpoint the non-value adding activities as wastage, (iii) creating a workflow for the construction processes to flow smoothly without any bottleneck or delays, (iv) establishing pull by which the inventory and in-progress materials are managed efficiently to ensure the flow of the work and (v) pursuing perfection by iteration and regular assessment are these principles of LC. Thus it is clear from the literature that the main objectives of the LC is to minimize the waste while increasing the value of the project to the customer. However, despite this inherent advantage of LC, it is still in its initial stage in Sri Lanka and other developing countries (Senaratne & Wijesiri 2008; Aziz & Hafez, 2013), and there have not been much exploration on the barriers of the implementation of LC in the context of Sri Lankan construction industry or why LC is in the initial stages in the country.

B. Barriers to Innovations in Construction Industry

Construction industry by nature have been slow to embrace new techniques and innovations. There could be several reasons for this inherent disadvantage of the industry. Benmansour & Hogg (2002), stated in their study that high capital requirement, difficulty in shifting the strategic paradigms and prevailing patterns, lack of education, lack of communication and constraints from the organizational structures and cultures as the main barriers in successfully implementing innovations in construction industry. Faleye *et al.* (2019) put forward, lack of understanding of the benefits of innovations, cost of innovations, poor technical knowledge,

culture that is averse to change, temporary and the fragmented nature of the industry as the main barriers for innovating in the construction industry. Alinaitwe *et al.* (2007) stated Lack of capital investment for Research and Development and the insecurity or the uncertain nature of the result of innovation as the barriers for the implementation of innovations in the Ugandan Construction Industry. Ilter *et al.* (2008) poised several barriers for the implementation of innovations in construction industry. Government regulations, lack of confidence and knowledge, fragmented and unique nature of construction projects, high investment costs, psychological and cultural barriers are some of them. Even though not much literature is present in the context of Sri Lankan construction industry for the barriers of innovations, Kariyapperuma S. (2012) did a study on the barriers of innovations for the small and medium sized enterprises of Sri Lanka. According to the study, author cited shortage of capital for research and development, absence of technical and managerial skills, inadequate financial means, lack of technical personnel etc. as the main barriers. A careful insight from above review would show that all the above barriers could be divided into Financial, Managerial, Technical, Social and Educational.

Considering the fact that LC is not used well in the context of Sri Lanka and due to its certain characteristics that goes against the traditional way of the construction industry, it is possible to consider using LC as innovating. Hence, it is acceptable to assume that the barriers in implementing LC could be categorized under the themes of Financial, Managerial, Technical, Social and Educational.

Nevertheless, assessing the barriers of using LC as a whole may provide only a generic set of results which may not be very useful in practical situation as it could only be used in the form of Lean Tools. Hence, in order to get more specific results that can be applied to more practical situations, it is more desirable to identify the set of Lean Tools that can be used in the Sri Lankan Construction Industry and assess the barriers in implementing them, along with gaining a good understanding of their current practice, suitability and the acceptability.

C. Lean Tools

Several lean tools have been developed over the years to manage construction projects. Some of these are procedural, some are conceptual while some are embedded in programming. Besides, while some of these tools are simple, complexities revolve around others (Ansah *et al.*, 2016). In production sector there are many types of lean tools that have been formulated. Standard Work, Value Stream Mapping, 5S, Visual Management, Kanban, Total Product Management, Line Balancing and Total Quality Management (Oliveira & Fernandes, 2017; Bajjou *et al.*, 2017; Sacks *et al.*, 2010). Ansah *et al.*, (2016) tried to find the applicability of lean tools in the production industry to the construction sector. They ranked the lean tools according to how suitable they are to be applied in the construction sector. They concluded that Last Planner System, Concurrent Engineering, Daily Huddle Meetings, 5S, Visual Management, Kanban, Just-In-Time are the most suitable to be used in the construction industry. In addition, there are other tools such as Value Stream Mapping (mapping the flow of resources), Root Cause Analyzing (a problem solving technique that focuses on resolving the real problem instead of a quick, temporary solution), Poka- Yoke (mechanism designed to detect and prevent errors), Bottleneck Analysis (identifying the part of the process that limits the

overall productivity), Visual Management (information communication using visual signals) etc. have been identified which have the potential to be used in the construction industry for the implementation of lean philosophy (Ansah *et al.*, 2016).

Out of these, some tools have been selected to be studied where the basis of selecting these tools is their suitability to be practiced in construction industry, ability to be used in different phases of a construction project and the level of previous studies surrounding them.

1) Concurrent Engineering (CE)

It is a concept that is widely used in manufacturing industry. It is defined as a systematic approach to the integrated, concurrent design of products and their related processes, including manufacture and support (Kamara *et al.*, 2000). Aziz & Hafez (2013) defined CE as a parallel execution of various tasks by multidisciplinary teams with the goal of obtaining most favorable products concerning functionality, quality and productivity. Due to the need of minimizing the fragmentation of construction industry, it is believed that CE can be used to unite the different professionals such as Architects, Engineers, Managers etc. and work parallel.

2) Value Stream Mapping (VSM)

VSM is basically a technique for visually analyzing, documenting and improving the flow of a process in a way that highlights the improvement opportunities (Rahman *et al.*, 2012; Ansah *et al.*, 2016). VSM can be defined as a map to identify waste, improvement opportunities and which lean tools to use. Also a properly applied VSM enables people to see the flow of values i.e. Customer Value-added Vs Business Value-added Vs Non Value-added as well as the percentage of each in the process. Non Value-added components tend to creep into a process over time and by understanding the process, a project team is better able to design a solution that optimizes functionality and eliminates.

3) Kanban Systems (KAN)

This is a Japanese word which literally means “billboard or signboard”. It is an information control process which regulated the movements or flow of resources so that parts and supplies are ordered and released as they are needed (Ansah *et al.*, 2016; Aziz & Hafez, 2013). Kanban is basically a lean approach developed in the automotive industry as a mechanism to pull materials and parts throughout the value stream on a just-in-time basis (Ballard *et al.*, 2014). Arbulu *et al.* (2003), presented a management strategy to use Kanban in construction an site management and has proved that it can be useful.

4) Daily Huddle Meetings (DHM)

This is a technique used for communicating and for everyday meeting process of the project team in order to accomplish workers’ involvement. With project awareness and problem solving contribution alongside some training that is given by different tools, the satisfaction of job (sense of growth , self-esteem) will increase for the workers (Ansah *et al.*, 2016; Salem *et al.*, 2005).

5) First-In-First-Out (FIFO) Line

FIFO Line method of handling storage management is an approach for handling work request in the order of flow from first to the last (Ansah *et al.*, 2016). This basically posits that

whatever the inventory that is loaded first should be unloaded first while the inventory loaded last should be unloaded last, not in the other way around in which the inventory loaded first being unloaded last (Alireza & Sorooshian, 2014).

6) First Run Studies (FRS)

FRS is a trial execution of a process with a specific end goal to decide the best means, strategies, sequencing among others to perform it. FRS are done a couple of weeks ahead of the scheduled execution of the process, in order to secure some time to acquire diverse or extra essentials and resources. In construction, this is used for redesigning critical assignments. This is part of continuous improvement effort and incorporate efficiency studies and review work techniques by redesigning and streamlining the distinctive function involved (Ansah *et al.*, 2016; Salem *et al.*, 2005; Rahman *et al.*, 2012).

7) Prefabrication (PFAB)

Prefabrication is defined as transferring the stages of a construction project from the field to an offsite production facility (Tatum 1986; Tam *et al.*, 2006; Olsen & Ralston, 2013). By utilizing prefabricated assemblies, components which are assembled in a production facility and then integrated into a construction project, industry professionals can lower costs and reduce project time while delivering a product of higher quality (Olsen & Ralston, 2013). The prefabricated elements that can be used in a project include precast façade units, staircases, drywall and semi-precast floor planking etc. (Tam *et al.*, 2006). Coincidentally, one aspect of LC is the utilization of prefabricated materials. The strong increases in productivity offered by using prefabrication and modularization fit squarely into the Lean Building Model (Bernstein, 2011). All these factors encourage that prefabrication can be used as a lean tool.

IV. RESULTS AND DISCUSSION

A. Exploring the Barriers in Implementing LC in Sri Lankan Construction Industry

Through the understanding of the functions and the objectives of these tools, it can be understood that there are certain barriers in implementing these tools which can again be categorized into the above mentioned barrier categories i.e. Financial, Managerial, Technical, Social and Educational. The possible barriers that can be experienced when implementing these tools are tabulated below in Table I.

TABLE I. BARRIERS IN IMPLEMENTING LC IN LOCAL CONSTRUCTION SECTOR

(F: Financial M: Managerial T: Technical
S: Social E: Educational)

Tools	Barriers	References
CE	<ul style="list-style-type: none"> High cost incurred when setting up relevant IT tools and BIM initially (F) Reluctant to change the current method from the top management (M) Lack of technical know-how on properly implementing CE (T) 	Enshassi <i>et al.</i> , 2019; Tan <i>et al.</i> , 2019; Zidane <i>et al.</i> , 2015; Raudberget, 2010; Taurianen <i>et al.</i> , 2016

	<ul style="list-style-type: none"> Goes against the traditional waterfall model of project management (T) When several professionals intend to work together, it would induce more discussions and delay decision making (T) Employees would be less motivated to try and change their current method of working (S) When several professionals intend to work together, there might be clashes of ideas and arguments (S) Lack of trained personnel in implementing CE (E) 	
VSM	<ul style="list-style-type: none"> High cost incurred when setting up the necessary I.T infrastructure to maintain all the flow of values (F) Lack of support from the top management to record and account all the flow of values, that leads to high level of transparency (M) Too complex to maintain all the records (T) Employees would be less motivated to try and adopt these new techniques (S) Lack of trained professionals (E) Lack of knowledge on how to implement the tool properly (E) 	Bajjou & Chafi, 2018; Forno <i>et al.</i> , 2014; Leite & Neto, 2013; Reyes <i>et al.</i> , 2018
KAN	<ul style="list-style-type: none"> Too much tedious to maintain (T) Employees would be less motivated to try and adopt these new techniques (S) Lack of trained professionals (E) Lack of knowledge on how to implement the tool properly (E) 	Bayhan <i>et al.</i> , 2018; Burgos & Costa, 2012; Enshassi <i>et al.</i> , 2019; Jan & Kim, 2007
DHM	<ul style="list-style-type: none"> Decisions taken in the meeting may not be implemented properly and taken just for the name sake (M) Difficult to assemble all the employees of all levels at the given time (M) Might be time consuming to hold meetings every day (T) May lead to clash of ideas or arguments (S) Might induce too much unnecessary discussion and hard to take decisions quickly (S) 	Bayhan <i>et al.</i> , 2018; Babalola <i>et al.</i> , 2019; Enshassi <i>et al.</i> , 2019; Salem <i>et al.</i> , 2006;

FIFO	<ul style="list-style-type: none"> Initial cost to change current orientation of the warehouse maybe high (F) Lack of support and reluctance of the top management to change the existing way of practice. (M) Has not been used much in the construction industry and is risky to implement due to the uncertainty (T) Employees might be less motivated to try new techniques (S) People would be reluctant to change (S) Lack of knowledge on building and maintaining a FIFO line in a construction project (E) Lack of experienced personnel (E) 	Manohar & Aapaiah, 2017; Parlar <i>et al.</i> , 2011; Utami <i>et al.</i> , 2018
FRS	<ul style="list-style-type: none"> Should be done iteratively. Thus, there could be more wastage in the beginning stage (F) Lack of support from the top management to pour the necessary resources for the implementation of this technique. (M) Not all construction processes are repetitive enough to implement FRS (T) Lack of experienced people on how to apply FRS and find the wastage (E) Lack of technical knowhow of FRS (E) 	Babalola <i>et al.</i> , 2019; Bajjou & Chafi, 2018; Enshassi <i>et al.</i> , 2019; Salem <i>et al.</i> , 2006;
PFAB	<ul style="list-style-type: none"> High initial cost involved in the setting up and installation of the yard (F) Reluctance of top management to implement PFAB as it is still under research (M) High manpower required (T) Transport and Logistics issue (T) Reluctance of the employees to change the current method of practice (S) Lack of properly trained personnel (E) Lack of knowledge and research findings (E) 	Abidi & Ghazali, 2015; Rahman, 2014; Tan <i>et al.</i> , 2019; Yuan <i>et al.</i> , 2020

Although the Lean Tools for this analysis were selected based on their potential applicability in Sri Lankan construction industry, the level to which these tools are used in the industry already are not comprehensible by literature alone, hence remains unknown. It is also doubtful that even though these tools may not be used exactly as they are

presented in Lean Concepts, there could at least be a vague version of these tools that may be in use.

Further, for successful adoption of LC, assessing the acceptance of these tools in the industry by the industrial community is important as they are the ones who would be actually practicing the lean tools if they prove suitable for the industry. If the professionals from industry felt reluctant to initiate and practice these tools in their work environment for any reason, such tools will not be successfully planted in practice. Hence, the acceptance of professionals in using LC is also something important to be measured by examining their views and sentiment.

B. Exploring the Barriers of implementing LC from the experts' views

Considering the above necessities and to explore the validity of the conceptualized barriers, a further online questionnaire was circulated among the industry professionals from which 28 responses were collected. The descriptions of the targeted respondents are well diversified such as site engineers, planning engineers, project managers, supervisors, researchers etc. making the responses to give a balanced insights from diverse phases of a construction project. Descriptive type of questions were directed surrounding the barriers of using LC and its applicability in local construction sector in regards to the individual tools of CE, VSM, KAN, DHM, FIFO, FRS and PFAB which were shortlisted earlier. The questions also tried to collect the opinion of the respondents on how suitable these tools are to be used in the Local Construction Industry. From the responses collected, the following results about the barriers were derived.

The respondents were asked to specify the barriers that they face to implement the above mentioned tools in construction sector. The Table II below shows the barriers that were specified by the respondents to implement the lean tools.

TABLE II. BARRIERS IN IMPLEMENTING LC FROM THE QUESTIONNAIRE

Tools	Barriers
CE	<ol style="list-style-type: none"> Lack of knowledge on BIM and other software (T) Lack of financial incentives (F) Lack of support from top management (M) Delays in decision making (T) People working in multiple projects (M) Lack of cooperation (S) Clashing of ideas and arguments (S)
VSM	<ol style="list-style-type: none"> Lack of skilled personnel (E) Lack of financial incentives (F) Reluctance to adapt new changes (S) Too tedious to implement and maintain (T) Unpredictable nature of the construction project (T)
KAN	<ol style="list-style-type: none"> Complex to implement and maintain (T) Lack of financial incentives (F) Lack of experienced personnel (E) Lack of motivation among the employees (S)
DHM	<ol style="list-style-type: none"> Decisions taken in the meetings are not implemented (M) Unnecessary waste of time (T) Unavailability of the employees (M) Lack of space for the meetings (M)

	<ol style="list-style-type: none"> Lack of motivation of the employees (S)
FIFO	<ol style="list-style-type: none"> Lack of experienced personnel (E) Reluctance to change (S) Quality limitations when changing the warehouse (T)
FRS	<ol style="list-style-type: none"> Lack of knowledge (E) Lack of skilled personnel (E) High time and resource consumption (T) Unpredictable nature of the project (T)
PFAB	<ol style="list-style-type: none"> Lack of support from the client (M) High machinery requirement (T) Logistics and storage issue (T) High manpower requirement (T) Lack of experienced personnel (E)

C. Assessing the applicability of LC in Sri Lankan Construction Sector

As it has been discussed earlier, only identifying the barriers of implementing the above tools is not only redundant but also not that much useful for the successful and prolonged implementation of LC. Thus, it was decided to assess the applicability of using the above tools in the local construction industry. Their applicability is gauged by three different aspects namely, a) current usage of those Tools in Sri Lanka b) feasibility/suitability of using them in the industry and c) professionals' acceptance were examined to gain further understanding of successful implementation of LC in Sri Lanka. Accordingly, the following results were further derived from the questionnaire.

1) Usage of Lean Tools in Sri Lanka

Interestingly, it was identified that even though the selected lean tools were not practiced in their respective names, there are at least tools that are somewhat similar to them. In addition, it was observed only some tools are widely used in local construction sector. The tools such as DHM and CE are already widely being used, at least in some phase of a construction project, however is not the case for some other tools like FIFO and PFAB. It should be noted that none of the respondents said that they use FIFO in their activities. Also, relatively smaller number of respondents said that they use KAN in their operations. This clearly portrays that even though some tools are widely used in construction sector, some are not used that much. Table III summarizes how well the tools are being used in each phase of the project.

TABLE III. USAGE OF LEAN TOOLS IN LOCAL CONSTRUCTION SECTOR

Tool	Usage
CE	Used in some projects
VSM	Used in some projects
KAN	Used in some projects
DHM	Used well
FIFO	Not used at all
FRS	Used in the construction phase of some projects
PFAB	Used in some projects

Another interesting factor observed is that the percentage of respondents said that they use lean tools in their operations in the beginning of the questionnaire was lesser than that of

the respondents who said they use those tools after providing a brief explanation. This highlights the fact that, lean tools are already utilized in the industry to some extent, but the industrial professionals are not aware of or consider them explicitly as lean tools and their benefits.

2) Suitability of Using Lean Tools in the Local Construction Industry.

One of the most optimistic results that came from this questionnaire survey is almost all the respondents were positive that all these tools are feasible to be used in their respective phases. However, although it shows only the subjective view of the respondents regarding the feasibility, it also may indicate that the professionals and industry welcomes innovative and new methods of project management that is said to reduce wastage and increase the profit.

3) Professionals' Acceptance in using those tools in the industry.

Almost all of the professionals were optimistic and enthusiastic about the application of lean tools in their site. This fact is further proved when they believed that almost all the tools are feasible to be used in their respective phases.

V. DISCUSSIONS ON THE RESULTS

As it can be seen, the feedback on barriers for each of the lean tools collected from the questionnaire, mirrored some of the assumptions that were made in the initial overview section. Especially the assumed financial, educational and social aspects of the barriers align well with results gathered from the survey, verifying that LC in the Sri Lankan context needs to be considered as an innovation in the construction industry, hence the barriers applicable for innovations can be observed. Nevertheless, it has to be noted that as the results are more qualitative, the results from the survey and the results from conceptual review may have slight deviation with respect to implied meaning. Also, in certain tools such as DHM and PFAB, certain Technical and Managerial barriers too were visible.

Further it was noted in certain tools, only one or two specific categories of barrier seem to be dominant. For example, most of the barriers in PFAB are technical and most in DHM are managerial. Such findings are crucial as focusing more on those specific categories when implementing these tools would be really useful for their successful implementation.

In addition, most of the respondents cited the lack of proper skilled personnel and knowledge on how to implement these tools as a barrier to all the lean tools. This may call for an appropriate governing organization to step up and create awareness among the professionals in lean concepts and train them to practice. Similar practices can be observed from the initiations of organizations such as Urban Development Authorities and Green Building Councils of various countries including Sri Lanka which play a role in promoting green buildings in local contexts. Another set of common barriers emphasized were the lack of motivation, reluctance to adapt new methods, lack of financial incentives and lack of support from top management, suggesting that despite the recent challenges the companies face such as the pandemic, dollar fluctuations, foreign competitions etc. if they invest the required time and effort to incentivize the practice of LC, the employees would get motivated and attempt to practice these

concept. Such attempts in the long term, can reduce the wastage in the construction projects, increasing the profitability.

VI. CONCLUSION

This study explores and illustrates that Lean concepts can be used in construction projects of Sri Lanka even though it has some barriers to be practiced successfully. There are many lean tools that can be used in the construction sector such as CE, KAN, VSM, FRS etc. and many more. In Sri Lankan construction sector, these lean tools are already being practiced in the local construction sector to some extent even though the awareness of the explicit tools is lacking among the professionals. However, the industry welcomes the idea of practicing them in their projects and were highly optimistic that these tools could reduce the wastage in construction processes. It was also found that these tools are indeed feasible to be used in the local industry i.e. the benefit harnessed from them is actually higher than the cost and effort spent to implement them. However, it was also found in the study that there are many barriers in implementing these tools in Sri Lanka as well. Some of them are more general such as lack of experienced personnel, lack of financial incentives etc. while some are more tool-specific such as lack of knowledge in BIM for CE and the logistics issue for PFAB. These barriers should be addressed properly to ensure the successful prolonged practice of LC in Sri Lanka.

There are several limitations in this study. The respondents of this questionnaire are from different projects and different companies. A questionnaire focused on professionals of the same or similar project or company belonging to the different phases of a project, may show better relationship on how lean tools are used throughout the project lifecycle. Further, the feasibility assessments and mitigations for the barriers of implementing lean tools were made conceptually and verified through limited observations from generalized local construction context. More advanced studies should be made on specific construction projects such as buildings, roads, bridges etc. for more insights. Carrying forward the more generic findings from this study, further case-based studies are recommended that are focused on one project throughout its lifecycle or one type of project.

ACKNOWLEDGEMENT

The authors would like to take this opportunity to extend their heartfelt gratitude towards all the respondents of the questionnaire survey whose generous responses and feedback serves as invaluable for the successful completion of this work.

REFERENCES

- [1] Abusalah, M. and Tait, J. (2018) 'Innovation Management in Construction - Practical Approach', *Pipeline Technology*, (March), pp. 1-12.
- [2] Alaghbari, W., Al-Sakkaf, A. A. and Sultan, B. (2019) 'Factors affecting construction labour productivity in Yemen', *International Journal of Construction Management*, 19(1), pp. 79-91. doi: 10.1080/15623599.2017.1382091.
- [3] Alinaitwe, H. M. et al. (2007) 'Innovation barriers and enablers that affect productivity in Uganda building industry', *Journal of Construction in Developing Countries*, 12(1), pp. 59-75.
- [4] Ansah, R. H. et al. (2016) 'Lean construction tools', *Proceedings of the International Conference on Industrial Engineering and Operations Management*, pp. 784-793.

- [5] Arbulu, R., Ballard, G. and Harper, N. (2003) 'Kanban in construction', *International Group for Lean Construction*, (September), pp. 1–12. Available at: http://leanconstruction.dk/media/17574/Kanban_in_Construction.pdf.
- [6] Ballard, G. *et al.* (2002) 'Chapter 15: Lean Construction Tools and Techniques', *Design and Construction: Building in Value*, 15, pp. 227–255.
- [7] Bayhan, H. G., Demirkesen, S. and Jayamanne, E. (2019) 'Enablers and Barriers of Lean Implementation in Construction Projects', *IOP Conference Series: Materials Science and Engineering*, 471(2). doi: 10.1088/1757-899X/471/2/022002.
- [8] Benmansour, C. and Hogg, K. (2002) 'An Investigation Into the Barriers To Innovation and Their Relevance Within the Construction Sector', *18th Annual ARCOM Conference*, 2(September), pp. 677–686. Available at: http://www.arcom.ac.uk/-docs/proceedings/ar2002-677-686_Benmansour_and_Hogg.pdf.
- [9] Chauhan, K. *et al.* (2019) 'Deciding between prefabrication and on-site construction: A choosing-by-advantage approach', *27th Annual Conference of the International Group for Lean Construction, IGLC 2019*, pp. 749–758. doi: 10.24928/2019/0158.
- [10] Dinesh, S., Sethuraman, R. and Shivaprakasam, S. (2017) 'the Review on Lean Construction an Effective Approach in Construction', *International Journal of Engineering Research and Modern Education*, Special is(April), pp. 119–123. doi: 10.5281/zenodo.570523.
- [11] Enshassi, A., Saleh, N. and Mohamed, S. (2019) 'Barriers to the application of lean construction techniques concerning safety improvement in construction projects', *International Journal of Construction Management*, 0(0), pp. 1–17. doi: 10.1080/15623599.2019.1602583.
- [12] Forno, A. J. D. *et al.* (2014) 'Value stream mapping: A study about the problems and challenges found in the literature from the past 15 years about application of Lean tools', *International Journal of Advanced Manufacturing Technology*, 72(5–8), pp. 779–790. doi: 10.1007/s00170-014-5712-z.
- [13] Ghaben, R. and Jaaron, A. A. M. (2015) 'Assessing Innovation Practices in Project Management: The case of Palestinian Construction Projects THE IMPACT OF PROFESSIONAL TRAINING ON COMMERCIAL/FREIGHT DRIVERS IN THE ARAB REGION View project Assessing Innovation Practices in Project Management: The', *International Journal of Innovation and Scientific Research*, 17(2), pp. 451–465. Available at: <http://www.ijisr.issr-journals.org/>.
- [14] Hoegl, M., Gibbert, M. and Mazursky, D. (2008) 'Financial constraints in innovation projects: When is less more?', *Research Policy*, 37(8), pp. 1382–1391. doi: 10.1016/j.respol.2008.04.018.
- [15] Jang, J. W. and Kim, Y.-W. (2007) 'Using the Kanban for Construction', *15th Annual Conference of the International Group for Lean Construction*, (July), pp. 519–528. Available at: <https://iglcstorage.blob.core.windows.net/papers/attachment-4eeb12cb-3736-40f7-b19e-d9cef825e9dd.pdf>.
- [16] Karunanayake, S. G. S. and Ananda, H. S. R. (2020) 'Environmental expansion of a cohesive appliance for a cost effective road construction process using Lean Constructions', *Journal of Earth and Environmental Sciences Research*, 2(2), pp. 1–4.
- [17] Kamara, J. M., Anumba, C. J. and Ebuomwan, N. F. O. (2000) 'Establishing and processing client requirements—a key aspect of concurrent engineering in construction', *Engineering, Construction and Architectural Management*, 7(1), pp. 15–28. doi: 10.1108/eb021129.
- [18] Koskela, L. (1992) 'Application of the new production philosophy to construction', 72.
- [19] Marhani, M. A. *et al.* (2013) 'Sustainability Through Lean Construction Approach: A Literature Review', *Procedia - Social and Behavioral Sciences*, 101, pp. 90–99. doi: 10.1016/j.sbspro.2013.07.182.
- [20] Michael J. Horman, David R. Riley, M. H. P. and C. L. (no date) 'LEAN AND GREEN: INTEGRATING SUSTAINABILITY AND LEAN CONSTRUCTION Michael J. Horman, Ph.D., David R. Riley, Ph.D., Michael H. Pulaski and Chris Leyenberger, AIA', pp. 1–10.
- [21] Nesensohn, C., Bryde, D. and Pasquire, C. (2015) 'A measurement model for lean construction maturity', *Proceedings of IGLC 23 - 23rd Annual Conference of the International Group for Lean Construction: Global Knowledge - Global Solutions*, 09, pp. 652–660.
- [22] Nikakhtar, A. *et al.* (2015) 'Application of lean construction principles to reduce construction process waste using computer simulation: A case study', *International Journal of Services and Operations Management*, 20(4), pp. 461–480. doi: 10.1504/IJSOM.2015.068528.
- [23] Oliveira, J., Sá, J. C. and Fernandes, A. (2017) 'Continuous improvement through "Lean Tools": An application in a mechanical company', *Procedia Manufacturing*, 13, pp. 1082–1089. doi: 10.1016/j.promfg.2017.09.139.
- [24] Owolabi, J. D. *et al.* (2019) 'Barriers and drivers of innovation in the Nigerian construction industry', *International Journal of Mechanical Engineering and Technology*, 10(2), pp. 334–339.
- [25] Prayuda, H. *et al.* (2021) 'Critical Review on Development of Lean Construction in Indonesia', *Proceedings of the 4th International Conference on Sustainable Innovation 2020—Technology, Engineering and Agriculture (ICoSITA 2020)*, 199(ICoSITA 2020), pp. 83–88. doi: 10.2991/aer.k.210204.018.
- [26] Salem, O. *et al.* (2006) 'Lean Construction: From Theory to Implementation', *Journal of Management in Engineering*, 22(4), pp. 168–175. doi: 10.1061/(asce)0742-597x(2006)22:4(168).
- [27] Senaratne, S. and Wijesiri, D. (2008) 'Lean construction as a strategic option: Testing its suitability and acceptability in Sri Lanka', *Lean Construction Journal*, 2008, pp. 34–48.
- [28] Shang, G. and Sui Pheng, L. (2013) 'Understanding the application of Kaizen methods in construction firms in China', *Journal of Technology Management in China*, 8(1), pp. 18–33. doi: 10.1108/jtmc-03-2013-0018.
- [29] Tam, V. W. Y. *et al.* (2006) 'Cutting Construction Wastes by Prefabrication', *International Journal of Construction Management*, 6(1), pp. 15–25. doi: 10.1080/15623599.2006.10773079.
- [30] Tan, T. *et al.* (2019) 'Barriers to Building Information Modeling (BIM) implementation in China's prefabricated construction: An interpretive structural modeling (ISM) approach', *Journal of Cleaner Production*, 219, pp. 949–959. doi: 10.1016/j.jclepro.2019.02.141.
- [31] Tauriainen, M. *et al.* (2016) 'The Effects of BIM and Lean Construction on Design Management Practices', *Procedia Engineering*. The Author(s), 164(June), pp. 567–574. doi: 10.1016/j.proeng.2016.11.659.
- [32] Thilakarathna, N. and Senaratne, S. (2012) 'A preliminary literature review into lean construction implementation', *World Construction Conference 2012 - Global Challenges in Construction Industry*, (June), pp. 345–354. Available at: <https://www.baufachinformation.de/aufsatz/A-Preliminary-Literature-Review-Into-Lean-Construction-Implementation/2013011001150>.
- [33] Zidane, Y. J.-T. *et al.* (2015) 'Barriers and Challenges in Employing of Concurrent Engineering within the Norwegian Construction Projects', *Procedia Economics and Finance*, 21(2212), pp. 494–501. doi: 10.1016/s2212-5671(15)00204-x.

Challenges in implementing LED Lighting in Commercial Buildings in Sri Lanka

P. Madhavi Perera
Department of Building Services Technology
University of Vocational Technology
Rathmalana, Sri Lanka, madhavikdy@gmail.com

Abstract— Conserving energy and being sustainable is of utmost importance for any commercial building in the current context. Therefore it is essential to implement energy efficient lighting systems for any such building. LED lighting is the most energy efficient lighting technology available today. LED lighting has been used in commercial buildings in Sri Lanka for over ten years now however technology is still developing. There can be many challenges faced by the professionals in using LED lighting. This study aims to identify the perception of LED lighting of professional involved in commercial buildings and challenges they have faced. Further it was necessary to identify possible measures that can be taken to overcome the prevailing issues identified. A survey questionnaire was conducted among the different stakeholders involved in commercial building projects. Further a desk study was conducted regarding the standards, regulations prevailing in Sri Lanka and the initiatives taken by other countries to identify the possible strategies that can be used to overcome the identified issues. It was found that stakeholders were enthusiastic in implementing LED lighting but they had several concerns. The main challenge identified was the lack of standards and relevant regulations in Sri Lanka with regards to LED lighting used for commercial buildings. Further the educational gaps among the professionals in this regard was identified. It was discussed to implement several measures to solve these issues and utilize the LED lighting in an optimum manner to reach the sustainability goals of the country.

Keywords— LED lighting; commercial buildings; Sri Lanka; challenges

I. INTRODUCTION

With global phenomena such as climate change, global warming and energy crisis, sustainability in buildings has become a mandatory requirement. Reducing the energy usage of the building is one of the key aspects of a sustainable or green building. There are few building systems that consume the majority of the energy in a building and lighting is one such system.

“Globally, almost one-fifth of the total amount of electricity generated is consumed by the lighting sector. Almost half of the global lighting electricity is consumed by the commercial/tertiary sector, estimated at 1133 TWh, representing 43% of lighting consumption” [1]

Out of all the lighting technologies available today, LED (Light Emitting Diode) technology have become the most preferred choice. “The European Commission further expects that LED lighting can “make our cities ‘greener’ by saving up to 70% of lighting energy and reducing costs compared to existing lighting infrastructure” [2]

In Sri Lanka also, LED lighting has been used in households, commercial, and other types of large buildings

for about 10 years now. Since Sri Lanka as a country, is facing an energy crisis and the consumers are also very concerned about the energy cost, using LED for lighting has become a common practice in the recent past.

This study specifically targets commercial buildings in Sri Lanka. During the last decade, Sri Lanka has observed very rapid development in the commercial building sector with many investors starting high rise building construction projects. As per [3], GP category (under which the commercial buildings are categorized) consumed 21.1% of total annual energy generation. Hence, it is important to implement suitable strategies to improve the energy efficiency of these commercial buildings. In commercial buildings where the main functions will be office and retail, air conditioning and lighting will be the main energy consuming systems.

II. RESEARCH PROBLEM

As discussed number of commercial buildings is growing in Sri Lanka and LED lighting is the most commonly used strategy for energy management of these buildings. LED lighting has been used in this type of buildings in Sri Lanka for over ten years now. Although several studies have been done in other countries in implementation of LED [1], the research work done in this area to identify driving factors and the problems in implementing LED lighting in commercial building in Sri Lanka is very limited. Since LED is still an evolving technology and it is continuously growing, there can be many challenges faced by the professionals, in using LED lighting in these buildings. If there are such issues they have to be identified and addressed by relevant policy makers, hence a study to identify the challenges is required..

III. OBJECTIVES

The objectives of this study are to identify the perception of different stakeholders of a construction project towards implementing LED lighting in commercial buildings and the reasons for the said perceptions. Another objective is to identify the challenges in implementing LED lighting for commercial buildings in Sri Lanka. Further, it also aims to recommend strategies to overcome the challenges identified.

IV. METHODOLOGY

A survey questionnaire was conducted among the different stakeholders of commercial buildings such as Electrical Consultant, Architect, Lighting Designer, Lighting Consultant, Electrical Contractor, Maintenance Engineer, Facility Manger and Client (Building Owner) who are involved in a commercial building projects during different phases of the building life cycle. The survey questionnaire

was conducted as an online survey due to the pandemic situation. The questionnaire was sent to 70 professionals and out of them 63 had responded. This sample of 70 was selected randomly using random sampling. A desk study was conducted regarding the standards, regulations and import duty in relation to energy efficient lighting and LED lighting in particular in Sri Lanka. Another desk study was conducted regarding regulations and standards implemented by other countries in order to maintain the performance, safety and energy efficiency of LED lamps and luminaires.

V. RESULTS

A. Study on the regulatory status of LED lighting in Sri Lanka

As mentioned in the research methodology several sources were referred to understand the regulatory factors that drive the decision makers to implement LED lighting and ensure the quality of LED lighting products used in the country.

1) *Standards:* There are only two standards available in the country for LED lighting, that is SLS 1530 & SLS 1458. Both these standards apply to self-ballasted LED lamps which are usually used in residential applications. But SLS 1530 and SLS 1458 are still voluntary standards hence many LED lamps that do not comply to this standards are available in the country. Further this standard do not cover luminaires used in commercial applications such as ceiling mounted LED luminaires, LED tubular lamps, LED downlights. Therefore there are no standards in Sri Lanka that applies to LED luminaires used in the commercial buildings.

2) *Energy efficient building codes & green building rating tools in the country:* At the time the research was conducted (2020) the building code that was active was the Code of practice for energy efficient buildings in Sri Lanka 2008 [4] which was published in 2009 and a new version of the building code [5] had been drafted and published for public comments. This draft version was used for this study. Further the two green building codes practiced in the country, [6] and [7] is also referred for the study. The observations on how influential the codes are for implementation of LED lighting is tabulated in table I.

TABLE I. OBSERVATIONS ON BUILDING CODES

Building Code	Observations
Energy efficient building codes - 2020 draft	It will be necessary for the building projects to use LED lighting in their buildings to achieve the adhere to this code by lighting power densities specified in the code
GreenSL Rating system	Energy & Environment section is directly related with LED lighting. In the prerequisite 2 the building must comply with the requirement given minimum lighting power densities that can be achieved only by LED lighting.
UDA- Blue-Green Sri Lanka Green Building Guideline	It was observed that the requirement given is too lenient and the building does not necessarily have to implement LED lighting to achieve these points. Further only two points are allocated for fulfilling the.

The new draft building code [5] was further analysed with a calculation. A sample lighting calculation was done using Dialux Evo software for a sample office area with LED and T5 fluorescent lighting. T5 fluorescent is the most energy efficient lamp technology available for office lighting after LED. As per the [5] recommended illuminance level for an office area is 500 lux. The design outputs are indicated below in figure I and II.

As per the results indicated in figure I and III in both cases the average illuminance level in work plane is approximately 500 and lighting power density for T5 fluorescent case is 11.35 W/m² and for LED lighting power density is 7.03 W/m². As per Table 9.5-1 in [5] by space by space method the allowable maximum lighting power density of an enclosed office is 8.0. According to the sample calculation this can be only achieved by LED. Hence it is clear that when the 2020 version of building code [5] is activated it will be necessary for the building projects that follow this code to implement LED lighting.

3) *The import taxes imposed on the LED lighting products:* In commercial buildings usually LED luminaires with inbuilt LEDs are widely used. It was observed the custom duty and other taxes imposed in these category is almost same as the other types of non LED luminaires. Therefore this duty structure does not encourage the customers or electrical contractors to install LED luminaires in their buildings because there are no duty concessions and hence LED products do not have any price advantages.

B. Study regarding regulations and standards implemented by other countries

From the desktop study carried out the data on initiatives and the regulations practiced by different countries to promote usage of LED lighting was collected. The identified key strategies in several countries/regions are listed in table II. In addition to this many countries have either phased out or in the process of phasing out incandescent lamps [8] which will indirectly promote usage of LED lighting.

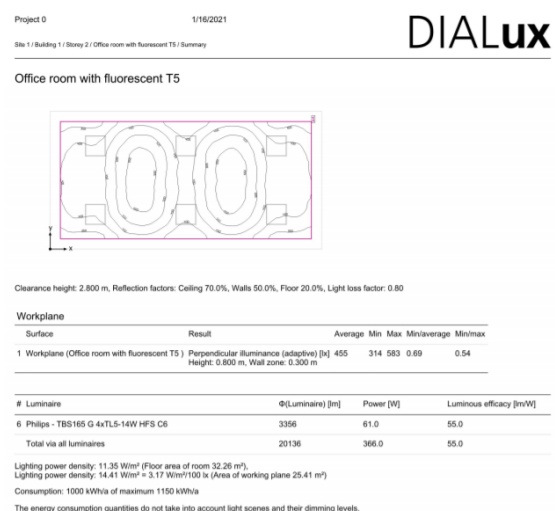
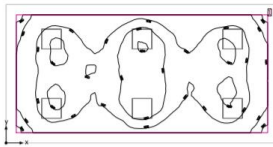


Fig.1. Lighting Calculation with T5 fluorescent

Office room with LED



Clearance height: 2.800 m. Reflection factors: Ceiling 70.0%, Walls 50.0%, Floor 20.0%. Light loss factor: 0.80

Workplane

Surface	Result	Average	Min	Max	Min/Average	Min/Max
1 Workplane (Office room with LED)	Perpendicular (illuminance (adaptive)) [lx]	502	335	603	0.67	0.56
Height: 0.800 m. Wall zone: 0.300 m						

# Luminaire	Φ(Luminaire) [m]	Power [W]	Luminous efficacy [lm/W]
6 Philips - RC380B LED42S-6500 G4 L60 W60	4210	37.8	111.5
Total via all luminaires	25260	226.8	111.4

Lighting power density: 7.03 W/m² (Floor area of room 32.26 m²).
Lighting power density: 8.93 W/m² = 1.78 W/m²100 lx (Area of working plane 25.41 m²)

Consumption: 620 kWh/a of maximum 1150 kWh/a

The energy consumption quantities do not take into account light scenes and their dimming levels.

Fig. 2. Lighting Calculation with LED

Further many international standards institutes such as ANSI, IESNA, IEC, CIE, FCC, IESNA, NEMA, NFPA and UL have established measurement, performance, electromagnetic compatibility and safety standards which promote the quality and efficiency of LED lighting. [1]

TABLE II. STRATEGIES IMPLEMENTED FOR PROMOTING LED LIGHTING

Country /Region	Strategies Implemented For Promoting LED Lighting
China	<ul style="list-style-type: none"> Energy Certifications are implemented for LED luminaires and LED lamps [8]
USA	<ul style="list-style-type: none"> Government procurement policies are giving priority for energy efficient lighting and LED lighting has been included to energy efficient product list for government procurement [8] Energy star ratings are awarded for LED lamps and some indoor LED luminaires [9] DLC Certification has been implemented for LED luminaires which are not covered from Energy Star rating. [9]
EU	<ul style="list-style-type: none"> Implemented energy efficient and performance standard for residential LED lamps [1] EU energy label is mandatory for all lamps. The label will indicate energy efficiency category, lumen output, average lifetime and energy consumption [1]
Malaysia	<ul style="list-style-type: none"> Government implemented a program to develop at least five local LED manufacturers by 2020 [10] State governments and municipal councils have implemented rules compelling the commercial buildings to use LED lighting [10] Training public and private sectors on LED renovations and LED lighting in general [10] Implementing tax concessions for companies implementing green technologies including LED lighting [10] Implementing LED standards for Malaysia, Energy labeling schemes and MEPS (Minimum Energy Performance Standards) for LED lighting Products [10]
India	<ul style="list-style-type: none"> A comprehensive set of LED standards has been implemented. [11] Formalized, acknowledged and subsidized local LED manufacturers [12] Implemented local R&D programs for solid state lighting [12]

Sri Lanka too can adopt the suitable strategies that have been implemented by other countries such as energy labeling (for commercial lighting products), subsidizing green products and establishing comprehensive standards etc.

VI. ANALYSIS OF QUESTIONNAIRE SURVEY

A. The composition of the respondents

The majority of the respondents are electrical consultants (36.5%), electrical contractors (19%) and architects (14.3%). This can be justified since most of the decisions regarding the lighting of the a building will be done by these three parties.

B. Perception of the stake holders towards implementing LED lighting

It was found that in 84.1% cases the percentage of LED lighting points is more than 80% of the total lighting points in the building projects in which the respondents were involved. This means that the LED lighting is commonly used in these commercial buildings.

It was also looked at the whether the stakeholders (respondents) are aware of the technical advantages of LED lighting.

Majority of respondents have selected the most popular advantages of LED, energy efficiency (96.8%) and longer life time (73%). However it is important to note that important advantages in the context of environment and human health such as not containing mercury and non-emission of UV radiation seems to be lesser known factors among the respondents. This indicates the need of a structured awareness building among the stakeholders regarding the technical aspects of LED lighting.

The respondents were asked the reasons for implementing LED lighting in commercial buildings and they were asked to rank the applicability of each reason. It was found that most respondents strongly agreed on energy saving. Further compact nature and wide range of LED luminaires, longer lifetime and reduction of maintenance, LEDs not containing mercury were identified as the other significant reasons for implementing LED in commercial buildings.

Then the respondents were asked to rate the weight allocated for different factors in selection of the best LED product out of few LED luminaires or lamps. It was found that the more weightage is given for factors such as luminous efficacy, brand, claimed lifetime and physical appearance. It was also noticed that the cost is given the least weightage which is a good trend that indicates the quality of the product is given more attention than the cost.

C. The challenges in implementing LED lighting for commercial buildings in Sri Lanka

Respondents were presented with several challenges that they may face during implementation of LED in their projects and they were asked to rank their response. It was found that the most significant challenge the respondents have faced is lack of standards in the country (hence low quality products being available in the market) and the inability to verify the parameters claimed by the manufacturers in the technical literature. The respondents also identified power quality issues and LED lighting being

expensive than other technologies as significant challenges as well.

Since this analysis is very crucial, another analysis was carried out stakeholder category wise as well. All categories identified lack of standards as a main challenge. Electrical contractors and clients particularly identified cost of LED, non-availability of spare parts for LED luminaires and technical difficulties in verifying the performance parameters as significant challenges as well.

It was also found that 58.7% of the respondents were aware of the lighting testing laboratories in Sri Lanka where photometric and electrical parameters of LED luminaires (light fittings) and LED lamps can be tested but only 38.7% of the total respondents have used these reports for the technical evaluations in selection of LED luminaires for their projects.

Overall, out of the respondents, 52.4% claimed that although there are issues in implementing LED, they will be using LED lighting in projects due to the benefits of LED lighting. 47.6% respondents said they do not have any issues regarding LED lighting and they will continue to use LED lighting in future as well.

VII. DISCUSSION

From the above mentioned results it was evident that most of the decision makers and stakeholders of commercial buildings are willingly implementing LED lighting in the commercial buildings they are involved in. They seem to have a general idea regarding the advantages of LED lighting. However, it must be noted that the detailed deeper understanding regarding the technical aspects and selection of LED lighting is lacking in most of these professionals.

The lack of standards and lack of regulatory measures have resulted the country's market being flooded with low quality LED luminaires and lamps. Hence, the professionals can not easily differentiate good quality LED products. Also it was observed that the professionals are not much familiar with testing facilities available in the country to verify the performance of LED lighting.

From the desk studies done it was identified that the regulatory and policy drivers in the country towards energy efficient lighting should be further improved and also Sri Lankan performance, safety and energy efficiency standards should be developed for commercial LED luminaires and lamps. And they should be made mandatory. It was also observed that the other countries have implemented many policy decisions that encourage implementation of energy efficient lighting and they have developed their own standards and energy efficient rating systems. Also financial concessions should be given by the government for the parties who are implementing green initiative such as LED lighting since they will make a positive impact to overall economy of the country.

VIII. CONCLUSION

The main challenge identified in this study and the survey is the lack of standards and regulations in the country with regards to LED lighting specially in the commercial applications. In conclusion Sri Lankan regulatory bodies need to implement the necessary standards and other policy decisions required to encourage Energy efficient lighting technologies and also educate the professionals further on LED lighting. Since this is the major challenge faced by the construction sector with regards to LED lighting if it can be addressed correctly then the country will be able to maximize the benefits of the LED lighting in the construction sector by improving the energy efficiency of commercial buildings who consume about one fifth of country's energy consumption, This will immensely help Sri Lanka to achieve its demand side management and sustainability goals.

ACKNOWLEDGMENT

Author would like to thank all the professionals who took part in the survey and shared their valuable opinions which immensely contributed for the research findings.

REFERENCES

- [1] A. de Almeida, G. Zisis, M. Quicheron and P. Bertoldi, P. "Accelerating the deployment of Solid State Lighting (SSL) in Europe", Publications Office of the European Union., Luxembourg, 2013
- [2] N. Schulte-Römer, J. Meier, M. Söding and E. Dannemann, "The LED paradox: how light pollution challenges experts to reconsider sustainable lighting." Sustainability, 2019
- [3] Ceylon Electricity Board, "Statistical digest 2019", 2019
- [4] Sustainable Energy Authority, "Code of practice for energy efficient buildings in Sri Lanka 2008", 2009
- [5] Sri Lanka Sustainable Energy Authority, "Energy efficiency building code of Sri Lanka", 2020.
- [6] Green Building Council of Sri Lanka, "GREENSL® Rating system for built environment version 2.0", 2018
- [7] Urban Development Authority, "Blue Green Sri Lanka green building Guidelines for Sri Lanka", 2017
- [8] P. Waide, "Phase out of incandescent lamps: implications for international supply and demand for regulatory compliant lamps". IEA Energy Papers, 2010
- [9] Q. Ding, X. Liang, Y. Zhao and R. Liu, "Study on Chinese and U.S. energy efficiency regulations and standards for efficient lighting products", ICAEER 2018 E3S Web of Conferences 53, 2018
- [10] Q. Ding, L. Pengcheng, L. Meng, L. Xiuying, C. Haihong and W. Zhonghang, "Study on policy and measures, standards and certification system of LED lighting industry in Malaysia, ICAEER 2020 E3S Web of Conferences 194, 2020
- [11] Indian standards on LED published. [Online] Available at: <https://bis.gov.in/other/LEDSeries.pdf>
- [12] A.S. Kamata, R. Khosla and V. Narayanamurti, "Illuminating homes with LEDs in India: Rapid market creation towards low-carbon technology transition in a developing country". Energy Research & Social Science vol 66, 2020

Low cost, Compact Webcam-based System for Biomedical Microscopic Image Analysis

D. G. Isuri Madhubhashinee
*Department of Electrical and
Electronic Engineering
Faculty of Engineering, University of
Sri Jayewardenepura
Sri Lanka
en86185@sjp.ac.lk*

Hirusajini Jeyatharan
*Department of Electrical and
Electronic Engineering
Faculty of Engineering, University of
Sri Jayewardenepura
Sri Lanka
en86173@sjp.ac.lk*

M. H. Rifadh Ahamed
*Department of Electrical and
Electronic Engineering
Faculty of Engineering, University of
Sri Jayewardenepura
Sri Lanka
en86122@sjp.ac.lk*

Dr. Akila Subasinghe
*Department of Electrical and
Electronic Engineering
Faculty of Engineering, University of
Sri Jayewardenepura
Sri Lanka
akila@sjp.ac.lk*

Dr. Vidura Jayasooriya
*Department of Electrical and
Electronic Engineering
Faculty of Engineering, University of
Sri Jayewardenepura
Sri Lanka
vidura@sjp.ac.lk*

Abstract— A light microscope is an essential tool in medicine and biology, which is being used in monitoring and diagnosing communicable and non-communicable diseases. However, same as other contemporary emerging medical technologies, modern microscopes too are not affordable and not in line with the requirements of the low- and middle-income countries like Sri Lanka. Therefore, we require low-cost, robust, and portable diagnostic devices that can be adapted to meet diverse medical needs. Addressing the issue, here we present a novel concept of a webcam-based automated system to acquire and analyze the microscopic images, which is intended to be an alternative for existing bulky microscopes. The system comprises an inverted webcam lens that works as a microscope lens, a motorized stage, a light source, and a computer interface to control the microscope stage/magnification. The compact design of the proposed system enables it to be used inside conventional incubators. Thus, it possesses capabilities that cannot be achieved by conventional microscopes like monitoring real-time behavior/growth of cells, microorganisms (viruses, bacteria), and monitoring the drug efficacy of cancer treatments under microscopes. In this paper, two algorithms with basic image processing techniques were tested in morphological operations for cell segmentation and counting objects in the input image. Based on the accuracy of counting the number of cells in acquired test images, the nuclei detecting watershed algorithm was selected as the better algorithm after comparing results from two proposed algorithms. Results obtained from the proposed watershed transform algorithm showed promising accuracy levels > 96% and low computational time with an average time of 1.83575 seconds. Further, the proposed development can be easily adopted in other applications beyond the biomedical field with alterations in machine learning algorithms and training the data sets.

Keywords— *Disease diagnosis, Image analysis tools, Automated applications, MATLAB, Nuclei detecting watershed transform algorithm*

I. INTRODUCTION

Optical Microscopy has demonstrated an important role in biology and medicine since the 16th century. Optical microscope is a type of microscope which uses optical lenses to generate magnified images of small objects by diverting the light beams by means of refraction. Since its discovery, microscope technology has developed over time to cater different demands in optical imaging. It has been an essential

tool in medicine and biology in monitoring, diagnosing, and sometimes in therapeutic needs. Different types of optical microscopes are utilized in biomedical applications based on different applications. Bright field microscopes, the most basic and common type of microscope, are generally used in biological sample monitoring applications like in situ cell monitoring, blood sample testing, tissue analyzing, and surgical operation monitoring. Since brightfield microscopy is unable to give information in 3D and its contrast is low, phase contrast microscopy was introduced. In phase-contrast microscopy, special phase contrast objectives and condensers are introduced to the conventional bright field microscopes. It allowed visualizing the living cells and other microorganisms in their natural state with better contrast. Then the fluorescence microscopy came into play with the development of optical filters which opened the pathway to view selectively stained structures, cells, and anomalies in studying histochemistry, tissue analysis, microorganism analysis etc. Recently, with the advances in image sensors, automation, and computer technology, other types of optical microscopes like confocal microscopy were introduced which require advanced technology. Likewise, optical microscopy was developed in terms of resolution, contrast and to satisfy special optical imaging needs, but only few efforts have been focused on miniaturizing the microscopes. Conventional microscopes are designed in such a way that they must be mounted on a table, and supposedly not intended to be used as a mobile device. Therefore, it refrains them from being used in situ monitoring of cells inside incubators for applications like embryonic development, wound healing, and disease progression [4]. Furthermore, With the novel technologies like lab on a chip, a miniaturized microscope will be an invaluable tool to monitor microscopic processes. Another main concern with microscopes is that it's always a compromise between the cost and the quality of images. In general, medical grade microscopes are expensive and thus the availability of these microscopes is limited to major medical centers and laboratories in low- and middle-income countries. Thus, even during times like Covid 19 pandemic people in rural areas must travel to reach facilities in major cities where the tests are being conducted. Considering the requirements of miniaturized and affordable microscopy, here we propose a solution with recent developments of

digital image sensors to replace conventional microscopy. There are reports of such systems which have been developed using Image sensors like Complementary Metal Oxide Semiconductors (CMOS) and Charge coupled devices (CCD) [4]. R. K. D. Ephraim et al has reported a similar type of portable microscopic system which can be used in field settings for diagnosis of Malaria, schistosomiasis and soil-transmitted which are needed for diagnosis in rural areas with limited access for sanitary facilities. This is not a completed system for the image analysis process [13]. Inspired by those reports, here we have developed a system where a wide-angle web camera lens is inverted to work as a magnifying lens and its image sensor is used to feed the captured magnified image to the computer. The role of the lens in a conventional webcam is demagnification but in this proposed microscopic setup lens is reversed for the purpose of magnification. The magnification is determined by the distance between the lens and the image sensor.

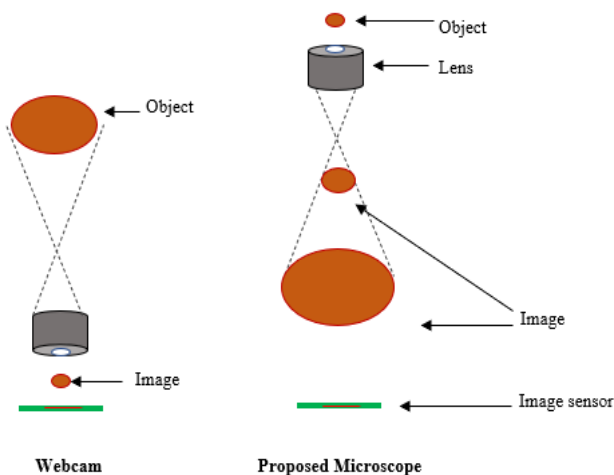


Fig. 1. Schematic diagram of comparison of the image capturing on webcam and reversed lens-webcam

Comparatively, the resolution of an image which is captured by such a device is lower than an image captured using a medical grade light microscope. Therefore, it is required to conduct post processing of the captured images to extract useful information from such a device. Therefore, in order to utilize this design alone at rural clinical settings it is required to have trained people to capture and process the images. Therefore, it will be convenient to have a full system composed of an automated microscope and image analysis tool setup with plug and play compatibility to acquire images, process and give analysis results. Here we demonstrate an implementation of such a system which is tested for cell counting application. The presented system can be easily modified and be utilized in other applications with few modifications. Briefly, the presented work here demonstrates a hardware system based on a webcam to capture blood sample images and software system which can automate the manual method of detecting and counting cells based on thresholding segmentation, morphological functions and counting of cells using watershed algorithm. The proposed algorithm achieves considerable accuracy and low computational time. Hence, this system can be classified as a real time application.

II. DESIGN AND METHODS

The system comprises a miniaturized microscope setup which can be controlled electronically, a software platform to control the focus of the microscope and image acquisition along with image analysis.

A. Hardware Design

Hardware design consists of a microscope system which is designed by modifying a commercial webcam. A webcam with a compact CMOS (Complementary Metal Oxide Semiconductors) imaging sensor and a simple wide-angle lens from a CCTV was utilized in the design [12]. We have proposed the configuration of the webcam-based microscope as shown in figure 2. All the components used in this setup are cost less and arrangements are done in order to ensure the portability of the microscope.

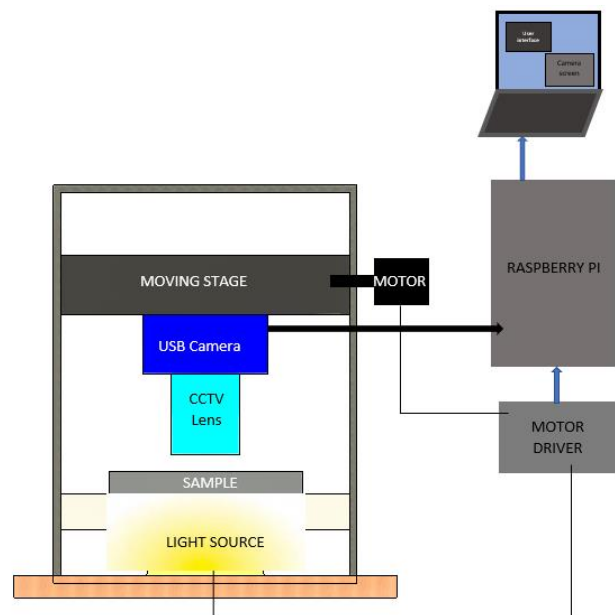


Fig. 2. Configuration of proposed low-cost, compact webcam-based system

Microscope design consists of 5 major parts as shown in figure 2.

- Light source - A white LED light source was utilized as the light source which provides a broader spectrum. The brightness of LED light can be controlled by the Raspberry pi.
- Lens system of Webcam - The lens of the webcam was replaced with a wide-angle CCTV lens with 6mm diameter, which had a wider angle as it provides a better magnification once its inverted (Fig. 1) [12]
- Stage – A fixed stage made out of glass was used to mount the samples.
- CMOS image sensor of Webcam – A color CMOS image sensor was used with the features of the frame rate of 320*240 up to 30 frame/sec, dynamic range of 72 dB and focus range of 3cm to infinity.

- The moving stage - The inverted lens system along with the image sensor was mounted on a moving stage which runs on a rail obtained from a used CD-ROM. A stepper motor along with an L293d motor driver was used to move the webcam up and down in order to focus the target. The stepper motor with motor driver is controlled using a raspberry pi module.

The main processor which was used in this design is a Raspberry pi 3B+. The webcam was connected to the USB port of raspberry pi. The motor and the light source were connected to the GPIO pin of the raspberry pi and the live feed from the camera was fed to the computer. The signal from the raspberry pi to the motor driver controls the motor which moves the webcam up and down along from the vertical axis of the stage. According to the command of the raspberry pi the motor driver controls the motor operation. Also, from the command of the raspberry pi the LED brightness will also be controlled to the required level using the similar method where we used in controlling the motor speed. The system was powered by a 12V DC supply. Further, a GUI Interface was developed to control the image focusing, capturing as well as intensity control deployed using a newly created Application.

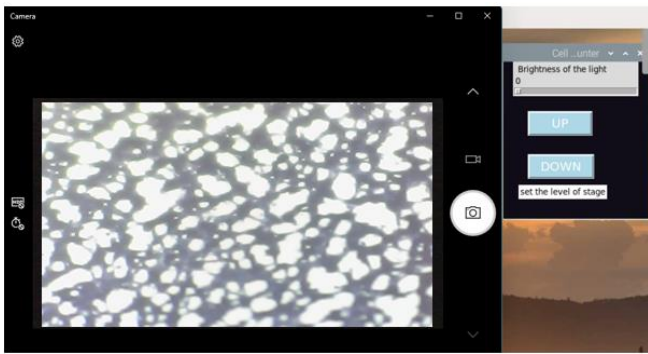


Fig. 3. User Interface of the microscope system for capturing images.

The distance for the cell sample to the lens is approximately 3mm and distance from lens to the image sensor is approximately 8mm. Figure 3 shows the computer interface which enables the user to control the light source and adjust the stage upside and downside in order to capture a clear image of the blood sample and Figure 4 shows the actual setup of the proposed microscope system.

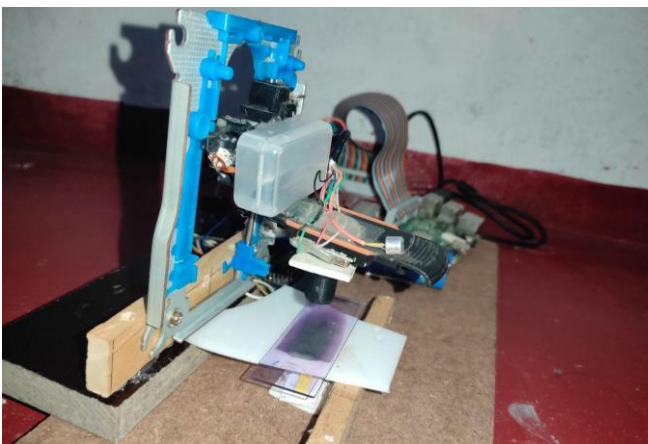


Fig. 4. Real image of the experimental setup of the microscope.

B. Software Design

In general, there are several approaches and in many research of automated methods for the analysis and counting of the cells in the blood. In this paper, we focus on a custom-coded MATLAB script by concerning the resolution, intensity levels and shape of the cells captured images by using our webcam-base microscope. In this section, we mainly focus on two approaches because these are the most straightforward algorithms which are based on image processing techniques. First, we discuss the algorithm for blood analyzing and cell counting application based on image segmentation by using morphological operations and watershed transform.

Although there are many advanced techniques for cell segmentation, we used the method of nuclei detecting watershed algorithm (Fig. 5) to test on our images in order to its simplicity and ease of implementation.

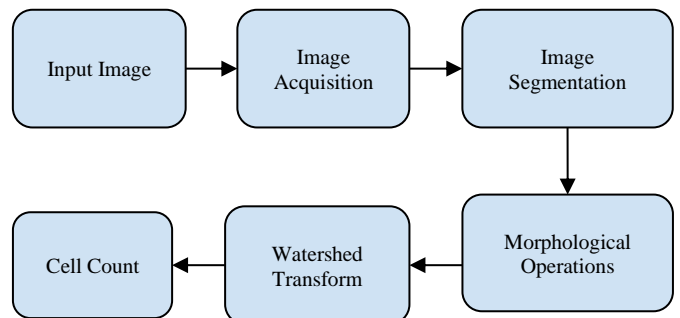


Fig. 5. Flowchart of Nuclei detecting Watershed Transform Algorithm

- **Image Acquisition:** This is the fundamental step of proposed approach in which images are segmented and labelled to analyze the image further. These images have been captured with our webcam-based microscope. All the blood sample images in the dataset are in JPG format.
- **Image Segmentation:** Image segmentation is a technique used to separate an image into its constituent regions or objects [8]. There are several methods for image segmentation. In this segmentation process, a method based on thresholding of grayscale image is used to directly generate regions of uniformity within the given image based on some threshold criteria or intensity values. Cells are extracted from the background by replacing each pixel in the image with black and white pixels by comparing the intensity value of the image with the threshold value. This is the method of converting grayscale images into binary images based on thresholding.
- **Image morphology for noise reduction:** Image morphology is used to remove unwanted elements from an image in order to prepare the image for further analysis. In this proposed algorithm, Median filtering which is a non-linear smoothing spatial filter is used for noise reduction and enhancing the quality of edges in an image. Although this is not visible to the naked eye, it will greatly reduce the number of incorrect cells found. Image regions and holes are filled because cells are having different contrast within itself. Also, morphological opening is performed, and all connected cells less than 5 pixels are removed from the binary image.

- Detecting perimeter and nuclei of cells: Perimeters of cell or connected cell groups are extracted by using a binarization technique because counting the number of groups of cells is not giving the accurate counts of cells. Many of the cells are grouped in these blood sample images. Therefore, these grouped cells are visualized by overlaying the detected perimeters over the grayscale image using the “imoverlay function” [10]. Watershed algorithm is applied on the image which is able to partially divide the group of cells into distinct cells. The watershed algorithm comprehends the gray level of pixels as the altitude of a relief. Therefore, the image should be modified as the cell borders are having the highest intensity values and the background is clearly marked as negative infinity. This can be achieved by detecting the maxima which approximately coincides with the cell nuclei and then transforming these extended maxima and background pixels in the image as the only local minima in the image because the watershed algorithm identifies only low points.
- Counting cells: The image is labeled by applying the watershed transform and then counting of the cells is given [10].

In the process of cell counting in an image, we have analyzed another method called object counting using labelling method with morphological operations. For this operation, a Python with OpenCV was used to feed the codes to hardware design to obtain results. Image Acquisition, Segmentation, and Morphology [8] were followed similarly in the above Nuclei cell detecting algorithm. In addition to these techniques there are several techniques that have been included in this labelling method Morphological Operations (Fig. 6) which consists of Filtering, Smoothing and Edge Detection.

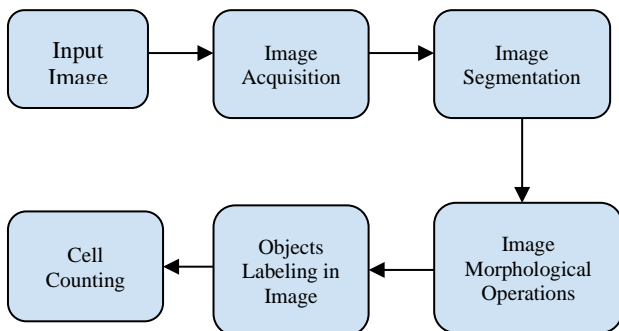


Fig. 6. Flowchart of Labelling method of Morphological Algorithm.

- Filtering: Median filtering is applied to the segmented image as median filtering is a non-linear smoothing technique often used in noise reduction [8].
- Edge Detection: Edge of the objects in the image is detected using the Kernel method. In this method, Erosion and Dilation techniques are applied for smoothing the image before cell counting. These techniques help to connect nearest regions in order to have one region per object by improving the quality of the edges in the image. Dilation adds pixels to the boundaries of objects in the image. Region boundaries are obtained by erosion [11].

- Labelling: Labelling technique is applied by using connected Components, ones like, merge and cvtColor functions. Labelling is end up with coloring the objects in the image [11].
- Counting cells: The cells are counted using labelling connected regions as one colored object per connected region.

III. PRELIMINARY RESULTS

In this section, outcomes of the two proposed algorithms are demonstrated. These proposed algorithms consist of basic MATLAB Image processing techniques, morphological operations and watershed algorithms. The entire process is initiated by acquiring a blood sample image which is then transferred to further processing levels in order to count the total number of cells in the captured blood sample. The output results of the original blood sample test images from labelling method of morphological algorithm and nuclei detecting watershed transform algorithm are represented in the fig. 7.

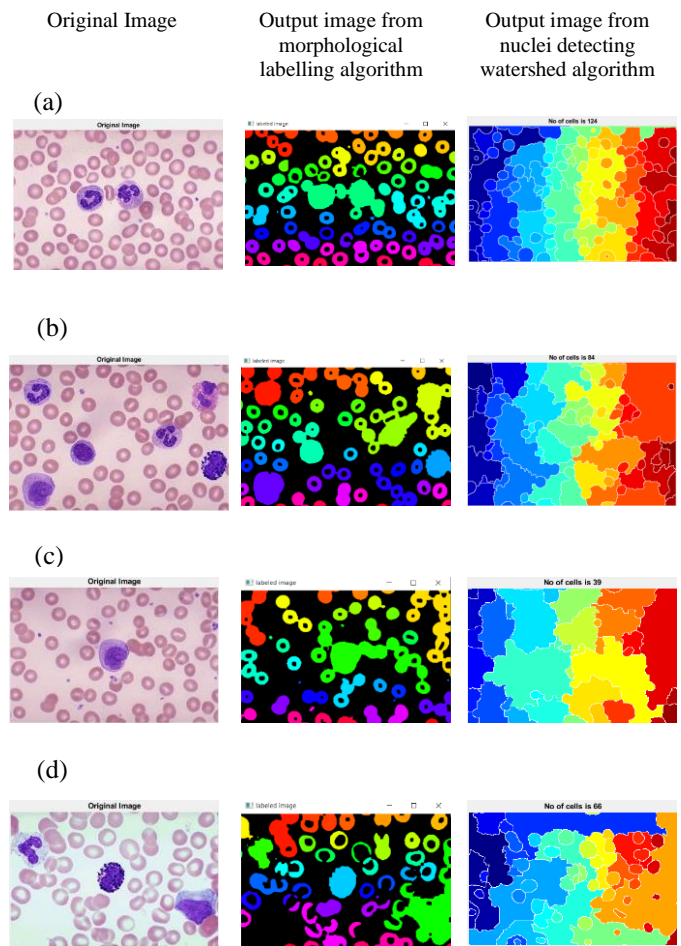


Fig. 7. Original blood sample test Image [14, 15] (Left) Output image with cell count from the Labelling method of Morphological Algorithm (Middle) Output image with cell count from the Nuclei detecting Watershed Transform Algorithm. (Right)

TABLE I. COMPARISON OF MANUAL COUNTING AND ALGORITHMIC COUNTING FOR WATERSHED ALGORITHM AND LABELING ALGORITHM

Test Images	Manual Counting	Algorithmic Counting for Nuclei Detecting Watershed transform Algorithm	Algorithmic counting for Labeling method using Morphological Operations Algorithm
Image (a)	115	124	76
Image (b)	85	84	46
Image (c)	40	39	34
Image (d)	63	66	48

TABLE I represents the comparison of the results between the blood cell count in the sample test images using the proposed algorithms and the manual blood cell count. It clearly shows that the proposed approach is able to count cells with better accuracy in Nuclei detecting Watershed Algorithms. According to the obtained results for the labeling algorithm when the objects in the images are overlapped then it might count as one single object and it provides the count of cells always less than the manual count. According to GRAPH I (Fig 8), the Watershed Algorithm gives exact cell counting values compared to labelling morphological operations algorithm to manual counting values. Watershed algorithm is aiming to perform the detection and counting of nuclei and verify the applicability of the methodology when compared to others. Therefore, even with both algorithms performing detection of cells, this algorithm gives better results due to detecting both perimeter and nuclei of cells.

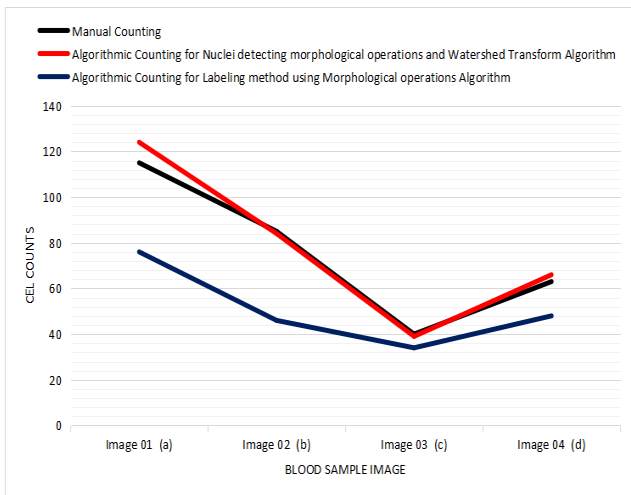


Fig. 8. The compared results of cell counting of both algorithms with the manual counting numbers.

TABLE II. ERROR PERCENTAGE COMPARISON BETWEEN NUCLEI DETECTING WATERSHED ALGORITHM AND MORPHOLOGICAL LABELLING ALGORITHM.

Test Images	Manual Counting	Error percentage for Nuclei detecting morphological operations and Watershed Transform Algorithm (%)	Error percentage for Labeling method using Morphological operations Algorithm (%)
Image (a)	115	7.826086957	38.70967742
Image (b)	85	1.176470588	45.23809524
Image (c)	40	2.5	12.82051282
Image (d)	63	4.761904762	27.27272727

According to TABLE II, a comparison of Error percentage for both proposed algorithms provide a better understanding for selecting the most suitable algorithm. The Nuclei detecting watershed algorithm has less error percentage than another algorithm. Therefore, the experiential results are obtained only for Nuclei detecting Watershed Transform Algorithm.

TABLE III. COMPUTATIONAL TIME FOR NUCLEI DETECTING WATERSHED TRANSFORM ALGORITHM.

Test Images	Computational Time
Image (a)	1.887 s
Image (b)	1.839 s
Image (c)	1.626 s
Image (d)	1.991 s

TABLE III shows the computational time taken to analyze the blood cell count in each test blood sample image. This verifies that the proposed algorithm is efficient in terms of computation as it takes an average time of 1.83575 seconds for the entire process of counting blood cells in a blood sample.

IV. EXPERIMENTAL RESULTS

In this section, the proposed algorithm is tested by using the blood sample images which are taken from the proposed webcam-based microscope. Fig. 9 presents the original blood sample image captured from the proposed webcam-based microscope and it is processed through the nuclei detecting watershed algorithm in order to give the cell count of the blood sample.

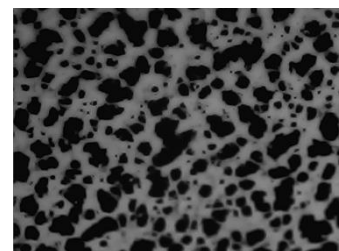


Fig.9. Blood sample image captured by using a proposed webcam-based microscope.

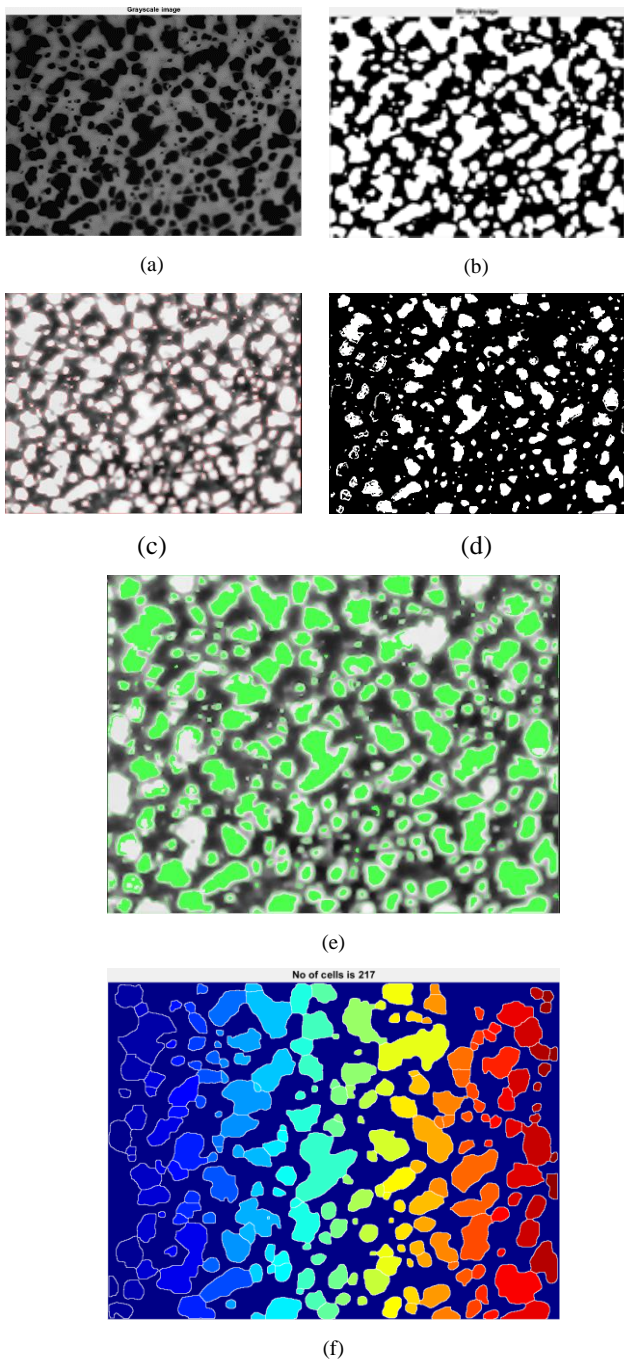


Fig. 10. (a) Converted grayscale image (b) Segmented binary inverted image based on thresholding (c) Detecting perimeters of cells (d) Detecting nuclei of cells (e) Overlaying the detected cell perimeters and nuclei over the grayscale image. (f) Counting the total number of cells using watershed transform (no of cells detected is 217)

Fig. 10 presents the stepwise outcomes of the proposed algorithm. The algorithmic cell count output is 217 and the manual cell count of that blood sample image is 208.

Following we present a pair of blood sample images we captured from our microscope along with respective output images with blood cell counting displayed on the top of the output image. It can be observed that the proposed algorithm works on the images captured from our proposed microscope. The figure 11 represents the few blood sample images from the proposed microscope and the corresponding results obtained from the proposed nuclei detecting watershed transform algorithm.

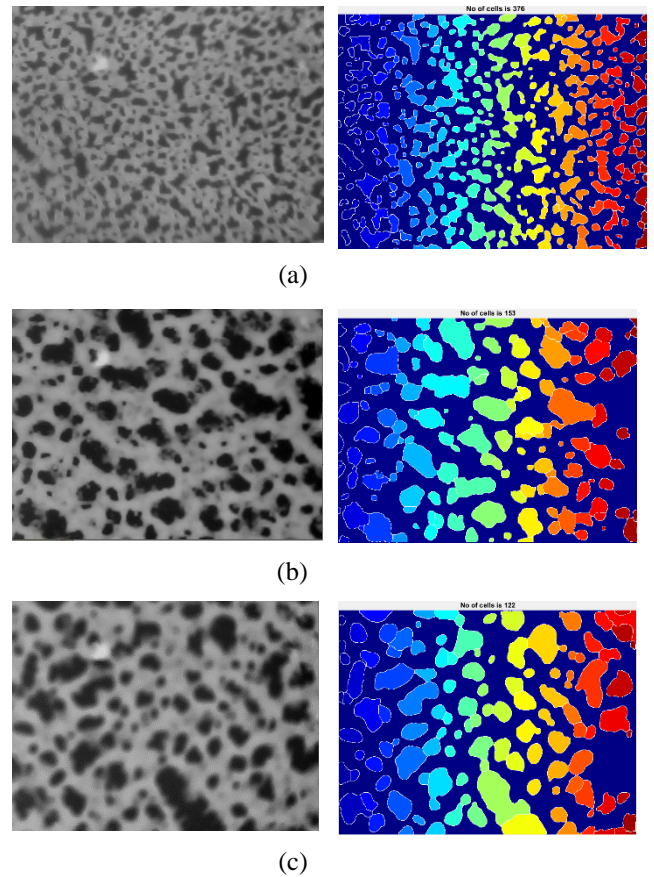


Fig. 11. (a) blood sample image from proposed microscope (Left) respective output images with cell count of 376 (Right) (b) blood sample image from proposed microscope (Left) respective output images with cell count of 153 (Right) (c) blood sample image from proposed microscope (Left) respective output images with cell count of 122 (Right)

TABLE IV. COMPARISON OF MANUAL COUNTING AND ALGORITHMIC COUNTING

Test Images	Manual Counting	Algorithmic Counting for Nuclei Detecting Watershed Transform Algorithm
Image (a)	376	357
Image (b)	153	144
Image (c)	122	116

The comparison table (Table IV) ensures that the proposed system gives the output with a considerable accuracy level which is more than 96% with low computational time.

During the development of the selected algorithm many improvements and changes have been made according to the quality and resolution of acquired images from our microscope and also the shape and size of the cells. Based on the comparison of manual counting of cells we carried out and algorithmic count of each acquired image, we can say that the system has achieved the goal of detecting and counting the number of cells in a sample to a considerable extent. But it is not achieved 100% of accuracy when comparing the acquired image with the image after watershed transformation because of not segmenting the grouped cells correctly and the acquired images are not much clear with high resolution.

V. DISCUSSION AND CONCLUSION

A low-cost, compact webcam-based microscope image analysis tool is presented. The initial phase of the proposed tool was tested successfully for an automated cell counting application, which is a time-consuming, tedious manual process to be performed at laboratories. The tool consists of a microscope system, a computer interface, and an image analysis tool. The microscope system was built with a webcam CMOS imager, a plastic lens from a CCTV camera, an LED light source, and a movable stage made from a used CD-ROM. The assembly cost of the unit was only about Rs.3000.00. Then an in-house application was deployed in order to capture the microscopic images and to control the designed webcam by interfacing through a commercially available raspberry pi model. Furthermore, two algorithms with basic image processing techniques were tested in morphological operations for cell segmentation and counting objects in the input image. The decision of choosing the best algorithm between the watershed algorithm and labelling algorithm depends on the accuracy of counting the number of cells in acquired test images. Considering the outcomes of both algorithms presented under the results section, the watershed algorithm was chosen as the best one to proceed with. Watershed algorithm is detecting and estimating the number of cells in a sample by finding the cell perimeter and cell nuclei. Results obtained from the proposed algorithm showed promising accuracy levels $> 96\%$ and low computational time with an average time of 1.83575 seconds. The computational time for the proposed algorithm was significantly less because this technique does not engage with many looping processes in the MATLAB source code program. Comparing with the same algorithm run on high-resolution images, it can be concluded that the low-resolution images captured from our design caused the imperfection in the segmentation of cell clusters and reduced accuracy levels. These values can be improved with a better image sensor, better optical lenses, and finer focusing methodologies with smoother motor movements. Investigations on these hardware improvements should be done without compromising the cost in future work. For the future extension for this research work, we propose machine learning, Neural Network and deep learning processes to classify blood sample images using different blood cell image data sets to segment and identify the symptoms in the blood samples to diagnose diseases. This can significantly improve the accuracy level of the proposed tool.

VI. REFERENCES

- [1] A. Majeed, "Blood Cell Segmentation Using Matlab Nuclei , Cell Counting , Splitting Cell , SBF , Blood Cell Segmentation Using Matlab Nuclei , Cell Counting , Splitting Cell , SBF , LCF cell image processing," no. August, 2019.
- [2] N. A. Arofathullah, U. G. Mada, D. Widiyanto, U. G. Mada, I. D. Prijambada, and U. G. Mada, "Open Hardware Webcam Microscope and its Impact on Citizen Science Jogja River Project Open Hardware Webcam Microscope and its Impact on Citizen Science Jogja River Project," no. June, 2014.
- [3] N. H. Mahmood, "Red Blood Cells Estimation Using Hough Transform Technique," *Signal Image Process. An Int. J.*, vol. 3, no. 2, pp. 53–64, 2012, doi: 10.5121/sipij.2012.3204.
- [4] Y. S. Zhang et al., "A cost-effective fluorescence mini-microscope for biomedical applications," *Lab Chip*, vol. 15, no. 18, pp. 3661–3669, 2015, doi: 10.1039/c5lc00666j.
- [5] G. O. F. Parikesit, "Quantitative low-cost webcam-based microscopy," *Opt. Eng.*, vol. 49, no. 11, p. 113205, 2010, doi: 10.1117/1.3517747.
- [6] M. Yeldhos and K. P. Peeyush, "Red Blood Cell Counter Using Embedded Image Processing Techniques," *Res. Reports*, vol. 2, no. 2018, pp. 1–5, 2018, doi: 10.9777/tr.2018.10325.www.companyofscientists.com/index.php/chd .
- [7] S. Chourasiya and G. U. Rani, "Automatic Red Blood Cell Counting using Watershed Segmentation," *Int. J. Comput. Sci. Inf. Technol.*, vol. 5, no. 4, pp. 4834–4838, 2014.
- [8] G. K. Chadha, A. Srivastava, A. Singh, R. Gupta, and D. Singla, "An Automated Method for Counting Red Blood Cells using Image Processing," *Procedia Comput. Sci.*, vol. 167, no. 2019, pp. 769–778, 2020, doi: 10.1016/j.procs.2020.03.408.
- [9] A. Carolina, B. Monteiro, Y. Iano, and R. P. Franca, "Proceedings of the 3rd Brazilian Technology Symposium," *Proc. 3rd Brazilian Technol. Symp.*, no. January, 2019, doi: 10.1007/978-3-319-93112-8.
- [10] E. Steve, "blogs.mathworks," 2 June 2006. [Online]. Available at: <https://blogs.mathworks.com/steve/2006/06/02/cell-segmentation/>.
- [11] Medium. 2021. Image Processing: Segmentation and Objects Counting with Python and Opencv. [online] Available at: <https://medium.com/analytics-vidhya/images-processing-segmentation-and-objects-counting-in-an-image-with-python-and-opencv-216cd38aca8e>
- [12] Kim, Sang and Koo, Kyo-in and Bae, Hojae and Dokmeci, Mehmet and Hamilton, Geraldine and Bahinski, Anthony and Kim, S. Min and Ingber, Donald and Khademhosseini, Ali, "A mini-microscope for in situ monitoring of cells," *Lab on a chip*, vol. XII, pp. 3976-3982, 2012.
- [13] R. K. D. Ephraim et al., "Diagnosis of Schistosoma haematobium infection with a mobile phone-mounted Foldscope and a reversed-lens CellScope in Ghana," *Am. J. Trop. Med. Hyg.*, vol. 92, no. 6, pp. 1253–1256, 2015, doi: 10.4269/ajtmh.14-0741.
- [14] "Northern Kentucky University," [Online]. Available: <https://www.nku.edu/~dempseyd/agranular-leukocytes.html>
- [15] P. Mooney, "Kaggle," [Online]. Available: <https://www.kaggle.com/paultimothymooney/blood-cells>.

AI Based Integrated Autonomous and Mind Controlled UAV

Kasun Karunanyake
Department of Electrical and Electronic
Engineering
University of Sri Jayewardenepura
Rathmalana, Sri Lanka.
en82667@sjp.ac.lk

Lahiru Randika
Department of Electrical and Electronic
Engineering
University of Sri Jayewardenepura
Rathmalana, Sri Lanka.
en82703@sjp.ac.lk

Lasitha Gajanayake
Department of Electrical and Electronic
Engineering
University of Sri Jayewardenepura
Rathmalana, Sri Lanka.
en82653@sjp.ac.lk

Ravindu Fernando
Department of Electrical and Electronic
Engineering
University of Sri Jayewardenepura
Rathmalana, Sri Lanka.
en82673@sjp.ac.lk

Manushi de Silva
Department of Electrical and Electronic
Engineering
University of Sri Jayewardenepura
Rathmalana, Sri Lanka.
en83102@sjp.ac.lk

Nimesha Weerasinghe
Department of Electrical and Electronic
Engineering
University of Sri Jayewardenepura
Rathmalana, Sri Lanka.
en82738@sjp.ac.lk

Dr. Vidura Jayasooriya
Department of Electrical and Electronic
Engineering
University of Sri Jayewardenepura
Rathmalana, Sri Lanka.
vidura@sjp.ac.lk

Dr. Akila Subasinghe
Department of Electrical and Electronic
Engineering
University of Sri Jayewardenepura
Rathmalana, Sri Lanka.
akila@sjp.ac.lk

Abstract — Unmanned Aerial Vehicles (UAVs) have revolutionized many industrial, commercial, and recreational applications such as aerial photography and videography, security surveillance, agriculture, mapping and surveying etc. as it inherits economic opportunities and multitude of advantages to the consumers. On the contrary drone control using dedicated point to point communication through unlicensed spectrum results in limited data rate, unreliable connections, and insecure communication. Thus, an Unmanned Aerial Vehicle (UAV) driven by Artificial Intelligence (AI) based autonomous navigation integrated with mind controlling through wireless mobile communication network will be a smart solution to overcome the drawbacks in conventional drone control. Here UAVs will be guided by the Global Positioning System (GPS) to reach the set point, finding the most secured and the energy efficient path optimizing the battery life. Moreover, an Artificial Neural Network (ANN) model is developed for the purpose of stability control and obstacle avoidance. Furthermore, the user is able to access real time telemetry data via mobile communication system in Beyond Visual Line of Sight (BVLOS) operations. In instances where autonomous navigation is not feasible such as an indoor environment the user can take over the control of the drone with his/her mind. To facilitate mind controlling, obstacles will be detected through the sensors and cameras mounted on UAVs and the user will see the degree of freedom in the physical space to escape the obstacles. Then the relevant control signals to the UAV are given through Steady-State Visual Evoked Potential (SSVEP)-based Brain Computer Interface (BCI). The use of SSVEP evoked Electroencephalogram (EEG) signals in drone control can make people with neurodegenerative disabilities to interact with the environment as it creates a new way of communication. Therefore, this proposed autonomous and mind-controlled drone can be operated in BVLOS commercial and industrial applications with reliable and secure connectivity.

Keywords— Mobile Communication Network, Unmanned Aerial Vehicle (UAV), Steady State Visual Evoked Potential (SSVEP), Path planning, Artificial Intelligence (AI), Brain Computer Interface (BCI), Artificial Neural Network (ANN).

I. INTRODUCTION

Unmanned Aerial Vehicles (UAVs) inherit multitude of advantages such as higher mobility, flexible control, easy deployment, Flexibility for quick inspection, Survey of inaccessible locations and minimizing the exposure of people to potentially hazardous scenarios. In recent years UAVs have been used in the fields including aerial photography and videography, security surveillance, precision agriculture, search and rescue, package delivery, telecommunication, traffic control etc. However existing drone technologies contain several drawbacks. Drone control through traditional controller devices such as Radio Frequency (RF) control, smart phone, tablets confined operation within the operator's Visual Line of Sight (VLOS) limit. The dedicated point to point communication over the unlicensed spectrum results in limited data rate, unreliable connections, and insecure communications. The emerging use cases of UAVs require Beyond Visual Line of Sight communication that are reliable and secure. Since mobile network offers wide area coverage, high speed and reliable wireless connectivity, operation of UAVs in BVLOS use cases is possible with mobile communication network. Integrating the UAV with the mobile network has to overcome number of challenges including technical as well as law enforcements. Communication of UAVs can be Control and Non payload communication (CNPC) and Payload communication. When integrating to mobile communication, BS-UAV link (downlink) is important for the CPNC whereas UAV-BS link (uplink) is important for the payload communication. Flying

UAVs are served by the side lobes of the antennas and therefore, 3D coverage analysis is required to support the mobility of the drones in air. Channel modeling, Interference detection and mitigation techniques should also be taken into consideration.

Brain Computer interfaces (BCI) provides an innovative solution for developing an easy and user-friendly assistive system for mind controlling a drone. Electrical waves generated by human brain for different emotional states can be sensed using brain wave sensors and measured through Electroencephalography (EEG). BCIs that consist of evoking sources such as SSVEP or ERP to generate the brain signals for signal acquisition, data analysis and control of the objects have recently become an emerging area. In autonomous navigation, path planning and obstacle detection are vital in order to find the collision free and shortest safe path for a UAV. Stability and control of a UAV is done by PID controlling which is a method of achieving the optimum status of stability through taking feedback from the output and considering its proportionality, integration, and derivation.

This paper focuses on an automated integrated mind-controlled UAV that navigates between a starting point and destination through wireless mobile communication network by finding the shortest safe path while avoiding obstacles and maintaining the stability and control. The next part of this paper presents a detailed description of literature survey. After that the methodology of implementing the UAV is presented followed by the results gained. Then the discussion and conclusion are presented and finally the recommendations and future work are suggested.

II. LITERATURE REVIEW

Electroencephalogram (EEG) is an electrophysiological method that is used to monitor the electrical activity of brain placing electrodes on the external surface of the scalp. Based on brain activity patterns, EEG based BCI systems are categorized into four different types [1] – [4]; Steady State Visual Evoked Potential (SSVEP), Event Related Desynchronization/ Synchronization (ERD/ERS), Event Related Potential (ERP) and Slow Cortical Potential (SCP). Among them, the SSVEP, ERPs, ERD/ERS, and their hybrids attract the interests of researchers. SSVEP mainly includes Oz, O1, O2, Pz, P3, P4 and some electrodes located at the occipital. These SSVEP based brain signal models [6] are easy to analyze but requires an external LED source. ERP brain signal model includes positive & negative waves (P1, N1, P2, N2, P3 (P300)) where it is possible to observe P300 component in 300ms after the target stimuli appears although there is a high interference impact.

Brain signal decoding methods [1]-[9] focuses on signal processing components of a BCI, preprocessing, feature extraction and feature classification. In these research two types of preprocessing techniques; Frequency domain filtering using bandpass or notch filters [8] and spatial filtering where Minimum Energy Combination (MEC), Conical Correlation Analysis (CCA), Common Average Reference (CAR), Principal Component Analysis (PCA), Independent Component Analysis (ICA), Auto Correlation methods to extract features. Feature extraction plays an important role in to whole BCI system. A variety of methods such as Fast Fourier Transform (FFT) [11], Discrete Fourier Transform (DFT), Wavelet Transform (WT), Hilbert-Huang Transform (HHT), Independent Component Analysis (ICA), Common

Spatial Pattern (CSP) were used in the existing BCI to extract features. Linear Discriminant Analysis (LDA), Support Vector Machines (SVM), neural networks [8], nonlinear Bayesian classifiers, nearest neighbor classifiers were the classifiers that were used in signal decoding. By using the potential of a noninvasive SSVEP BCI system, a mind-controlled drone had been implemented [11] to control in 3D physical space. The system is based on a 4-class SSVEP model able to move the drone where an average Information Transfer Rate (ITR) of 10 bits/min and a Positive Predictive Value (PPV) of 92.5%. has been achieved. Thus, mind-controlled drones appear to be a new research insight.

Basic considerations in Mobile-Network Connected Drones include technologies, basic requirements, potential, and challenges. [13],[14],[16],[17],[22]. Wireless connectivity is required for payload and non-payload communication [16]. Payload communication includes telemetry report such as the flight altitude and the velocity, real time remote command and control (C and C) and regular flight command updates [17]. Two main aspects that make the utilization of LTE networks for UAVs communication challenging are the coverage and the interference. Mobile networks are optimized for terrestrial communication by tilting down the base station (BS) antennas to enhance the terrestrial coverage. The design considerations for UAV BVLOS communication includes 3D coverage, unique channel characteristics, aerial ground interference, asymmetric uplink downlink traffic requirement as it needs to support much higher data rates in the uplink transmission from the UAV to BSs and inter-cell interference mitigation techniques including Coordinated multipoint (CoMP) transmission and uplink power control mechanisms [13],[14]. Mobile network connected drones field trials, simulations, and design insights and performance analysis [12],[15],[13],[22] positive aspects include joint trajectory and communication design, 3D coverage analysis, spectrum sharing, and the drawbacks include the less work which has been done to explore mobility, latency, and cell association aspects, not exploring the mobile network connectivity for higher-altitude drones. a UAV having frequent up and down motions along its trajectory is susceptible to lower rates of handover [13]. When considering the LTE connectivity for low altitude drones [16],[21],[19]. UAV mounted wireless connectivity consists of two perspectives: aerial users and aerial base stations. Moreover, when considering the 3GPP requirements on command and control and data communication [16],[20] some of the important points were highlighted such as high likelihood of line-of-sight (LOS) propagation conditions to multiple neighboring eNodeBs, if the interference to multiple enodeBs is not mitigated, may impact the uplink performance of existing terrestrial users. Existing mobility mechanism of LTE networks is sufficient or whether it needs enhancements to support cellular connectivity of aerial vehicles is discussed in [20]. Following should be enhanced and the less research work has been done in the following areas namely interference detection, uplink interference mitigation, mobility performance and Aerial UE identification. UAV trajectory design problem subject to practical communication connectivity constraints [18] such as a flexible tradeoff between complexity and performance and yielding a performance close to the optimal solution, trajectory optimization with other QoS requirements in cellular-enabled UAV communication.

Stability control is a most important aspect when it comes to operation of the UAV. Designing and manufacturing UAVs and Autonomous flight control systems are presented in [23],[24]. Stability and control of UAV [25] is critical when it is in air. In [25] dynamic stability and control of UAV has been done using 3DoF models, but it was not capable to analyze the stability of complex systems. A Neural Network based control system [26] has been proposed to obtain less transient time and error compared to PID based control where there is a considerable overshoot in robust movements. Stability of a quadcopter depends on the speed of propellers where a fuzzy system (function) [27] has been used to find the speed of the propellers but the estimating here is not accurate. Maintaining the stability of drone during the loss or failure of propellers [28] where a solution for the loss of diagonal propellers has been presented and have considered about the failure of two adjacent propellers.

Obstacle detection and avoidance is important in deploying the UAV in a dynamic environment. Basic obstacle detection method is the pixel-based detection such as color and shape-based detection. But this method is affected by lighting condition of the environment, require manual tuning before each run and the accuracy of the results is reduced by the overlapping of objects in the image. Vision-based image processing techniques [29], [30] have been used to detect obstacles. Optical flow techniques provide high computational abilities and detect frontal obstacles and guide the UAV with a proper direction but in stereo vision, multiple cameras are required. It is difficult to approach the real time constraints with optical flow techniques Therefore, research have focused on Convolution Neural Network (CNN) based object detection [32],[35] methods such as YOLO (You Only Look Once) can be used in real time obstacle detection applications [34]. Single shot detectors use only one shot to detect multiple objects in an image using multiple boundary boxes [31]. Adaptive background subtraction technique [22] detects and tracks unusual events in a video sequence faster and robustly. When avoiding the once detected obstacle LoS guidance algorithm shows an excellent performance in indoor environments [36]. The Part based multitask deep network is also used in obstacle detection & avoidance [37] where improved reliability and higher processing speed is achieved. But there is an over-prediction of the results.

There are a number of 2D path planning algorithms used to plan the path for an environment with obstacles [38] Node based optimal algorithms such as Dijkstra, A*, Lifelong Planning A*(LPA), Theta*, Lazy Theta*, Dynamic A* (D*), D*-Lite are some of them. A* algorithm which is used in google maps like 2D environments achieves high efficiency using a heuristic function which requires pre information sensing & processing. Dijkstra algorithm, which is a greedy algorithm, provides the shortest distance between any two nodes with a value above a certain metric value. Path planning in 3D environment shows great prospect, but unlike 2D path planning, the difficulties increase exponentially with kinematic constraints [39]. 3D path planning algorithms tend to integrate with other algorithms or combine one by one, aim to plan an optimal path (distance, time, energy, and mobile coverage). Combining several algorithms together to achieve global optimal path like multi-fusion-based algorithms. Sampling based algorithms use Monte Carlo sampling classifies, Active means algorithm like Rapidly exploring Random Trees (RRT) procedure. Passive means algorithms like Probabilistic Roadmaps (PRM) generates a road net map

from start node to the goal. Bio-inspired algorithms [39] which applies biological behavior to deal with problems leaves out the process of constructing complex environment models and proposes a strong searching method to converge to the goal stably. This method is not used for real time applications as the iteration time is higher. Multi-fusion-based algorithms which combines several algorithms together to achieve global optimal path, manage the problems that a single algorithm proposed cannot achieve an optimal result individually. Several algorithms' advantages together; these algorithms work in simultaneous model, thus ensuring a tightly coupled approach to achieve better performance. Multi-fusion algorithm represents 3D grid as environment & 3D PRM (Probabilistic Road Map) to form road map of free space then A* achieves the optimal path. 3D propagation is approximated by Euclidean distance transformation using 3D Propagating Approximate Euclidean Distance Transformation algorithm (3D- PAEDT) [40] and this 3D- PAEDT algorithm applies only for indoor environments. Deep reinforced learning for UAV navigation [41] consists of Virtual environment by simulation to implement UAV navigation in large-scale complex environments.

To summarize what is presented above as a whole, it can be noted that even though mind controlling, and autonomous drone navigation is thoroughly studied as individual research, less amount of research work have been done integrating these two concepts together i.e., related to the fully autonomous drones in BVLOS operations to facilitate a wide range of commercial and industrial applications. The previous line of sight trials have limited the flight distances of the drones hence hindering the full potential of them and the sharing of telemetry images and videos with the user was not possible with the non-cellular communication technologies used. Moreover, the integration of mind controlling into the drone controlling is a new research direction where the people with neurodegenerative disabilities could also participate in exploring and interacting with the society and the environment.

III. METHODOLOGY

Non-invasive Steady State Visual Evoked Potential (SSVEP) based BCI (Brain Computer Interface) was developed to control the drone. As the major component of the signal acquisition process Graphical User Interface (GUI) was developed as shown below as the visual stimulus in evoking the SSVEP based EEG signals. The GUI was developed using JavaScript and HTML. The arrows depict the commands Up, Down, Forward, Backward, Turn Left, Turn Right. EEG signals that are used for signal processing were collected by looking at the arrows that blink at six distinct frequencies. Once the controller wants to move the drone to a particular direction, it is required to focus on the arrow relevant to that direction. Then the corresponding EEG signal can be recorded and stored for processing. Even though it is required to have 06 distinct command signals we were only able to capture 04 types of signals related to the operations up, down, forward, and backward using the Biopac. The designated frequencies are as follows.

TABLE I. DIRECTIONS OF DRONE CONTROL AND THE CORRESPONDING FREQUENCIES

Direction	Frequency (Hz)
Up	8.57
Down	10
Forward	12
Backward	15

In capturing the EEG signals 03 electrodes were used and the wet electrode method was followed. First of all, the subject was seated in a suitable position and during calibration the subject remains seated, relaxed and still with eyes closed. For the skin preparation for the set-up hair was cut shorter and a special highly conductive water-soluble gel suitable for short- and long-term EEG recording was applied before on the electrodes placing the electrodes on the O2, Pz, and P4 positions and BIOPAC data acquisition system was used in recording EEG signals.

Preprocessing of the captured EEG signals - The raw data values obtained through the sensors are not always accurate and there can be missing data bits so that the length of the data samples can be different, biasness of the data, duplicates of the data samples and also some data can be missing. Therefore, the analysis of missing values and preparation of the data in a suitable format is necessary to ensure the availability of a high-quality data set to train and test the algorithm. For classifying each SSVEP, a threshold technique was used, and specific threshold levels were applied on both frequency and magnitude axis. Here the length of the data samples was fixed by replacing the missing values by the mean value of that sample. Further class imbalance was eliminated by resampling and to increase the size of the dataset data augmentation was used. Now all the 04 classes have dataset of equal size and from all the datasets 80% was allocated as training data 20% as test data. In deep neural network 80% was allocated for training data and 10% was allocated for both validation and testing.

Feature extraction - Discrete Wavelet transforms, Fast Fourier Transforms (FFT) and multi decomposition Stationary Wavelet Transforms (SWT) were used in feature extraction to identify the discriminative features. Several options were tried in feature extraction and the output was fed into the machine learning model as the inputs. The options are listed as follows. When FFT was used the length of the sequence was indefinite and changes from time to time. Multi decomposition SWT was used as the feature extraction method after trying the above-mentioned possibilities.

Design of a model for the classifier - Different machine learning models were used in the design of a classifier. The amount of data that we could collect was limited by the number of days we had laboratory access. So, depending on the collection of data the best accuracy was given by the random forest algorithm as the classifier.

After classification four distinct signals were obtained for controlling the drone. After processing the EEG signals, the relevant commands were planned to be transmitted to the drone via mobile communication network.



Fig 1: (a) Nonprogrammable Mavic drone (b) the set up used to demonstrate the proof of the concept of controlling a drone using EEG signals

For the demonstration of the proof of concept of this project a non-programmable Mavic drone was utilized as shown in fig.1(a). As the alternative approach the classified signal was uploaded into cloud named Firebase which is cloud storage platform developed by Google which facilitates robust uploads and downloads using a Python script. The database keeps on updating in real time. This database can be accessed using a Node MCU and the relevant signal was transmitted to the drone controller. Therefore, an electromechanical system was developed as shown in fig.1(b) to control the remote controller of the drone with the classified EEG signal which can be accessed using node MCU. The node MCU was programmed in such a way that according to the received signal through the wireless connection with the Firebase cloud to actuate the relevant remote controller joystick using servo motors.

When it comes to the actual implementation of this project continuous connectivity between the mobile communication system is required and if it is not available the drone will lose its control. Therefore, the operator should have a clear and a better understanding of the routes that it can take without causing a drop in connection. A customized coverage map was designed for this purpose based on the coverage details provided by Mobitel as the service provider. This map with the best possible path determined by an algorithm will be displayed at the Graphical User Interface (GUI) for the UAV. The provided coverage details were the results of a drive test performed by Mobitel at the ground level and it was assumed to be the results remain same for a low altitude of 10m. The Google map for the development purposes was obtained by using the Google API. When designing the algorithm to select the best possible path two constraints were considered namely the distance to optimize the power consumption of the UAV and the coverage and capacity of the mobile communication network to facilitate reliable communication. The weights assigned to the constraints are 0.3 and 0.7 respectively to the distance and the mobile connectivity where the reliable mobile connectivity was focused more over the power consumption as the whole operation of the drone can get interrupted in the absence of a reliable connectivity with the mobile communication network while causing a total damage. Subsequently, the direction which drone is moving, is updated on the GUI. The view of the camera mounted on the drone was proposed to depict on the GUI to control the drone so that the observer can take decisions by looking at the camera view.

The autonomous navigation of the drone was demonstrated completely using simulations in three specific sub areas namely path planning, stability and control and obstacle detection and avoidance. In order to select an optimal algorithm for navigation and path planning of UAV, several 3D path planning algorithms were subjected to compare and contrast. Multi fusion based algorithms were decided to use in 3D path planning while constructing the feasible road map by applying PRM and adapting to A* and D* to execute the best

optimum route. A MATLAB based hybrid of mathematical model-based algorithms with EA is used to solve UAV navigation which is NP-hard problem. For a photorealistic simulation, MATLAB Simulink UAV toolbox with unreal engine by Epic games can be used but due to its constraints like requiring more computational power, with the available limited resources that was impossible. Therefore, virtual reality platform was chosen. So that, simple virtual environment was designed in order to demonstrate the scenario. The 2D coverage map of the ground level that was received by the service provider was assumed as the coverage map in a fixed altitude approximately in 5m height. The service provider's map was converted into a binary occupancy map and thereby areas with coverage were represented by white areas and coverage-less areas were represented by black areas in the binary occupancy map. The performances were compared using A* and PRM algorithms.

Maintaining stability during the travel time is very important to have a safe flight between given two coordinates. Therefore, the roll, pitch, yaw, and altitude of the UAV should have to adjust accordingly to handle different kinds of situations. PID tuning needs manual fine tuning of the gains K_P , K_I , and K_D parameters to obtain a better control. In order to have a better performance we used an ANN for real-time tuning of PID parameters. When considering the developed ANN, it consists with an input layer, one hidden layer, and an output layer. When the quadcopter starts to fly, initially it used PID parameters to stabilize the quadcopter. After that the ANN starts real-time tuning process of K_P , K_I and K_D parameters according to the training data.

An algorithm was designed for obstacle detection but due to its low accuracy, pre-trained tiny YOLO algorithm was used. After that the algorithm was extended to divide the image into rectangular spaces followed by a rectangular overlapping detection algorithm for finding the free space. For the simulation-based solution, coverage-less areas were assumed as objects because in real time obstacles like buildings normally have poor coverage compared to free spaces. In order to avoid collisions, the poor coverage areas were expanded considering the dimensions of UAV.

IV. RESULTS

Shown in the fig. 2 below is the captured SSVEP evoked EEG signals corresponding to the directions and the frequencies provided in table 1. The x and y axes of fig.3 represents the sequence number and amplitude in mV respectively. Here the signal sampling frequency was 256 Hz and signals were acquired for a period of 4s. The GUI developed in order to facilitate the mind controlling mechanism is shown below in fig.3 which shows the flickering arrows corresponding to the frequencies provided in table 1, the coverage map depicting the best possible path between the starting point and the destination and the coverage details of the immediate vicinity and the current flight direction of the drone.

As mentioned above autonomous navigation of the drone was demonstrated with the aid of simulations, for that the coverage map provided by the service provider was converted into binary occupancy map as shown in fig.4. The following figures show the converted coverage maps; first a simpler environment followed by a more complex environment.

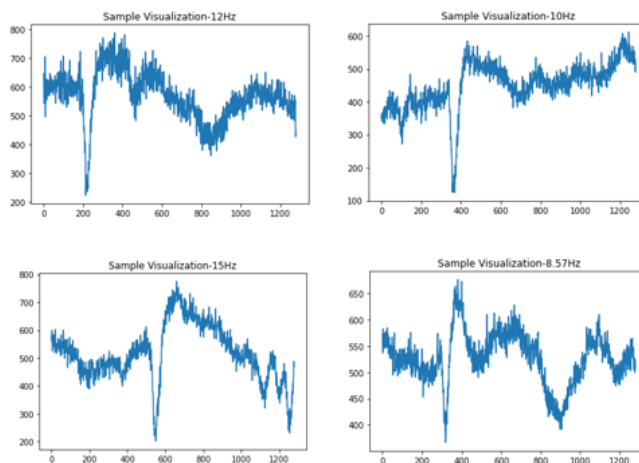


Fig 2: SSVEP evoked signals with the corresponding frequencies

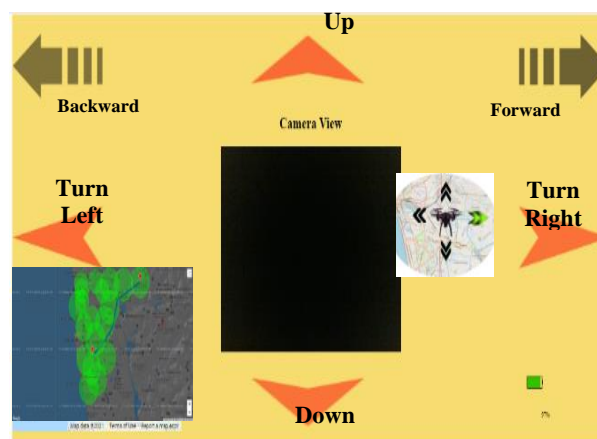


Fig 3: GUI developed to facilitate the mind controlling mechanism of the drone

Then for the obstacle detection and avoidance, the binary occupancy map was inflected corresponding to the UAV dimensions using the PRM algorithm. The following figures fig.5 and fig.6 show the inflected maps related to the binary occupancy maps presented above. The simulations of the three path planning algorithms; A*, Hybrid A* and Probabilistic Road Maps (PRM) are presented below in fig.7, fig.8 and fig.9 respectively. Moreover, some instances of UAV simulation in the virtual environment is shown below in fig.10 where the UAV was able to traverse through successfully while avoiding the obstacles.

V. DISCUSSION

The results from the project presented above have clearly demonstrated that people are able to control a drone in 3D space with the state-of-the-art technology, known as the BCI. In the signal acquisition process the number of subjects was limited to one. By presenting visual stimuli of flickering arrows in front of user's retina, evoked brain signals (SSVEP) were recorded using the BIOPAC data acquisition system from the occipital region of the brain using EEG techniques. If a more sophisticated EEG set other than the BIOPAC was used signals with better accuracy could have obtained. As we are dealing with sequences of data in EEG based signals and depending on the sampling rate, we use in feature extraction

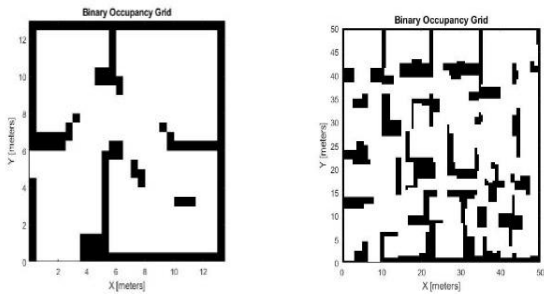


Fig 4: Binary occupation map of a simple and a complex environment

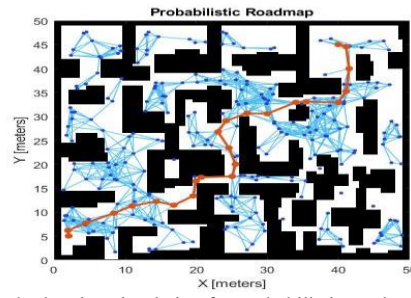


Fig 9: Path planning simulation for probabilistic road maps

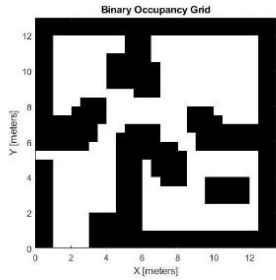


Fig 5: Inflated binary occupational map for simple environment

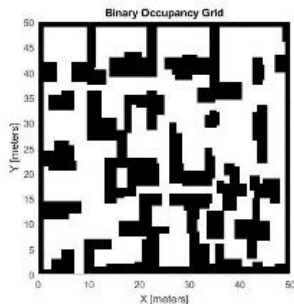


Fig 6: Inflated binary occupational map for complex environment

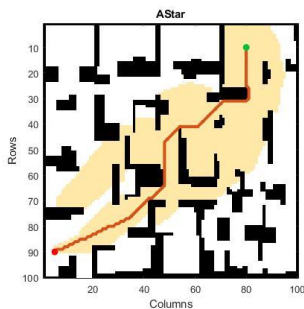


Fig 7: Path planning simulation using A* algorithm

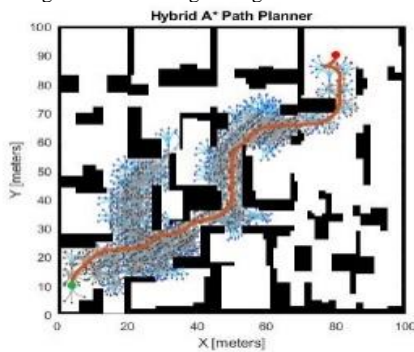


Fig 8: Path planning simulation for Hybrid A* algorithm

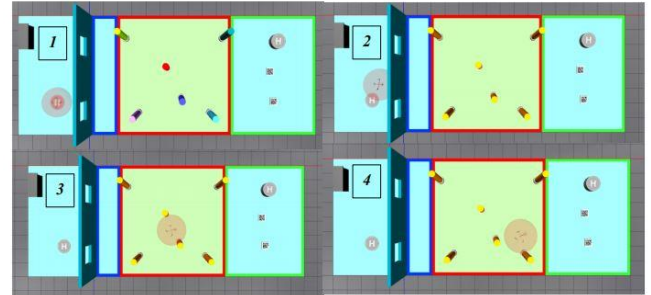


Fig 10: UAV simulation in virtual environment to demonstrate autonomous navigation

the number of sequences we will be getting will vary. Therefore, Random Forest, Random Tree and support vector machine architectures are better suited for this EEG signal classification rather than neural networks as their accuracy is comparatively high. Most importantly when feature extraction is not used the classifier accuracies are quite low as shown in the results comparison provided in table II. The amount of data we could collect was limited because of the limited access to the laboratory facilities was limited. If we had data collected from a wide range of subjects such as subjects from different genders and age groups neural networks could have outperformed the sequential classifiers that we have used. Even from one particular subject if we could have obtained a large number of samples better accuracies could have been obtained. Firebase is comparatively an easy cloud platform that could be accessed and, in the future, when the 5G connections are available in Sri Lanka this would be a better and a practical solution. The coverage map was built considering only the Received Signal Received Power (RSRP) as a performance matrix but if we could have a combination of performance matrices then the accuracy of the results would be higher. Moreover, here we have considered the signal strengths to be static, but the dynamically varying nature of the capacity dynamically nature of the capacity and coverage characteristics must be considered for a better result. Furthermore, this is limited to one specific service provider and if this can be extended to multiple service providers sometimes better results of more optimized paths could have been obtained. The performance of three path planning algorithms; A*, Hybrid A* and PRM are compared as illustrated in the result section and the PRM algorithm was selected. There the white colour areas in fig.4 and fig.5 represent the better coverage areas while the black areas represent coverage-less areas. It can be seen that the algorithms navigate the UAV through coverage available path.

TABLE II. ACCURACIES OF DIFFERENT CLASSIFIERS WITH DIFFERENT FEATURE EXTRACTION METHODS USED IN EEG SIGNAL CLASSIFICATION

	Sampling sequence	Statistical indices	Discrete Wavelet Transform features	Statistical Wavelet Transform	Multi decomposition SWT features (with level one sequential dataset)	Multi decomposition SWT features (with level one eight sequential data set)
Support Vector Machines	15%	20%	18%	40%	27%	65%
Random forest	11%	22%	21%	58%	65%	81%
Gradient Boost Tree Model	8%	20%	29%	46%	68%	79%
Sequential Neural Network	3%	6%	11%	13%	15%	25%
Convolutional Neural Network	5%	31%	13%	15%	15%	18%
VGG based branching	9%	4%	18%	-	-	-
Multi Output Architecture	4%	2%	21%	-	-	-

However, the mobile communication network coverage is not a constant over time. But in this it is considered as constant, and it is expected to address the dynamic coverage as a future improvement.

When it comes to the obstacle avoidance the coverage-less areas are considered as obstacles because in most of the cases, buildings and other similar obstacles interrupt the signal propagation and thereby having low coverage areas. Further, the binary occupancy maps are inflected to broaden the obstacle areas in order to avoid the collision of drone. Then the other figures show designed virtual environment in MATLAB simulation tool. As indicated in the fig.10, the UAV navigates with close proximity to base stations in order to keep the connectivity over mobile communication network while keeping the stability and control.

The performance of three path planning algorithms; A*, Hybrid A* and PRM are compared as illustrated in the result section and the PRM algorithm was selected. There the white colour areas in fig.4 and fig.5 represent the better coverage areas while the black areas represent coverage-less areas. It can be seen that the algorithms navigate the UAV through coverage available path. However the mobile communication network coverage is not a constant over time. But in this it is considered as constant and it is expected to address the dynamic coverage as a future improvement. When it comes to the obstacle avoidance the coverage-less areas are considered as obstacles because in most of the cases buildings and other obstacles interrupt the signal propagation and thereby having low coverage areas. Further, the binary occupancy maps are inflected to broaden the obstacle areas in order to avoid the collision of drone. Then the other figures show designed virtual environment in MATLAB. As indicated in the fig.10, the UAV navigates with close proximity to base stations in order to keep the connectivity over mobile communication network while keeping the stability and control.

VI. CONCLUSION

The goal of this project was to develop an autonomous mind-controlled drone which navigates through the mobile communication network. Here a proof of the concept of is presented using a non-programmable drone as the initial stage. A non-invasive Steady State Visual Evoked Potential (SSVEP) based Brain Computer Interface (BCI) was developed to generate the EEG signals that are required to control the drone. In order to generate SSVEP evoked EEG

signals that are required to control the drone, a graphical user interface with arrows blinking at frequencies 8.57Hz, 10Hz, 12Hz, 15Hz was used. These blinking arrows depicts the moving directions of the drone; up, down, forward, and backward. The EEG signals captured by the sensor employed head band are preprocessed, extracted, and classified in order to identify the command that is required to control the drone. Then we identified the possible extensions of UAV applications enabled by the mobile communication network like secured, reliable and scalable uses in BVLOS applications. The mind controlling allows the drone operator to control the drone in 3D space when the autonomous navigation of the drone is not possible. The relevant control commands are transmitted to the drone using the mobile communication network. This project intends to enhance the quality of life allowing users with neurodegenerative disorders to interact with the environment around them. Most importantly this work highlights the fact that the mind controlling of a drone can be done by capturing and classifying the relevant EEG signals. The results show the applicability of communication networks in low altitude drone communication which is more or less the same as the terrestrial communication. A customized map was developed to depict the best possible path to reach the destination. Two constraints, mobile network connectivity and the distance to optimize the power were considered in designing the algorithm. So, by concluding these several points together AI

based integrated autonomous and mind-controlled UAV using wireless mobile communication network mind controlled modular UAV using wireless mobile communication network is an emerging field in biomedical

engineering as well as in wireless communication while opening some fruitful research directions for future.

VII. RECOMMENDATIONS AND FUTURE WORK

In future continuation of the project hardware development as well as the complete demonstration of the project is to be done with a fully programmable drone along with a programmable 4G LTE/5G communication module to obtain the experimental results. Moreover, the UAV should be designed to perform more accurate stability and control in order to withstand complex terrain. When it comes to the dynamic path planning, the coverage is varying time to time. Here we assumed a constant coverage. So, in the future work this variation of coverage needs to be addressed. And also, the UAV should be capable of responding the dynamic faults as well. Therefore, it is needed to design the UAV to be survival despite of its propeller failures. In case of power outage or any other cases, emergency landing should be taken into consideration. The UAV should be stable throughout the entire flight time, starting, flying, and landing. Energy is one of the most crucial constraints related to UAVs therefore we need take the energy related responses of UAV into consideration. For an example if the UAV is running out of energy while navigating, we need to plan something like emergency landing.

Mobile Edge Computing (MEC) is an emerging field that can be applied to this mind control UAV where ultra-low-latency communication, offboard computation and control among large number UAVs is possible. Accurate channel models must be developed after performing drive tests at varying altitudes to see the behavior of air to ground channel characteristics variation in the time domain as well as the spatial domain. Measurement based research have to be conducted on mobile network coverage and capacity analysis, interference mitigation and detection, performance estimation. UAVs are served by the side lobes of the base station antennas which results in frequent handovers depending on the mobility, altitude of the UAV. Improved handover mechanisms for high mobility is a future outlook of this project. Handovers can be done considering more handover decision parameters such as location information of the drone, airborne status, flight paths other than RSRP values of the neighboring cells and time to trigger (TTT). Extension of the mobile network connectivity to operate this mind-controlled UAV in the higher altitude using beamforming will be a good research direction. Trajectory optimization was done considering two constraints; distance to optimize the power consumption and the mobile network connectivity. As a future work, interference aware trajectory optimization which minimizes the interference on the ground network can be done. BVLOS drone operation would be a potential use case of 5G technology so this can be tested with 5G connectivity in near future.

As a future extension EEG signal can be captured without using visual stimuli. Novel EEG evoking pattern could be used for developing the BCI. Further hybrid methods of SSVEP, ERP, ERD / ERS could be used to develop the BCI. As a future extension EEG recording device with dry electrodes can be used capture the EEG signals instead of

using wet electrodes. This would offer efficient long-term EEG signal recording within a shorter set up time consistency due to the interface medium air. Due to the limitations in accessing resources EEG signals was recorded from only one healthy subject but as a future extension several subjects can be selected from different genders and age groups. Further to verify the applicability of this mind controlling to assist the people with neurogenerative disabilities could be tested with subjects having various types of neural disorders.

ACKNOWLEDGEMENT

We, the team of 'AI based integrated autonomous and mind-controlled UAV' would like to extend our gratitude to several parties for supporting in the success of the project. First, we are highly indebted to the Department of Electrical and Electronic engineering, University of Sri Jayewardenepura for giving the opportunity and being a valuable asset of acquiring resources. The special thank should also be given to Mr. W.H.M. Daksith Mevan Dias and Mr. Thilanka Weerasekara from SLT-Mobitel (pvt) ltd for giving valuable advice and information. Last but not least, we remember all the other parties who willingly helped to successfully finish the project with their knowledge and effort.

REFERENCES

- [1] S. Amiri, A. Rabbi, L. Azinfar et al., "A review of P300, SSVEP, and hybrid P300/SSVEP brain-computer interface systems," in *Brain-Computer Interface Systems—Recent Progress and Future Prospects*, InTech, 2013.
- [2] B. Wodlinger, J. E. Downey, E. C. Tyler-Kabara, A. B. Schwartz, M. L. Boninger, and J. L. Collinger, "Ten-dimensional anthropomorphic arm control in a human brain-machine interface: difficulties, solutions, and limitations," *Journal of Neural Engineering*, vol. 12, no. 1, Article ID 016011, 2015.
- [3] C.-Y. Chen, C.-W. Wu, C.-T. Lin, and S.-A. Chen, "A novel classification method for motor imagery based on Brain-Computer Interface," in *Proceedings of the International Joint Conference on Neural Networks (IJCNN '14)*, pp. 4099–4102, July 2014.
- [4] M.L.W.L.L.N.B.X.M.Z.a.G.C. Xiaoqian Mao, "Progress in EEG-Based Brain Robot Interaction Systems," p. 25, 2017.
- [5] C. Escolano, J. M. Antelis, and J. Minguez, "A telepresence mobile robot controlled with a noninvasive brain-computer interface," *IEEE Transactions on Systems, Man, and Cybernetics, Part B: Cybernetics*, vol. 42, no. 3, pp. 793–804, 2012.
- [6] F. Gemblér, P. Stawicki, and I. Volosyak, "Autonomous parameter adjustment for SSVEP-based BCIs with a novel BCI wizard," *Frontiers in Neuroscience*, vol. 9, article 474, pp. 1–12, 2015.
- [7] Piotr Stawicki, Felix Gemblér, and Ivan Volosyak, "Driving a Semiautonomous Mobile Robotic Car Controlled by an SSVEP-Based BCI," *Computational Intelligence and Neuroscience*, June 2016,
- [8] D.K.,G.K.a.A.A. Nikolaos Korovesis, "Robot Motion Control via an EEG-Based Brain-Computer Interface by Using Neural Networks and Alpha Brainwaves," p. 16, 2019.
- [9] Hareendar S, Jeya raghul R, Aashish kumaravelan, "Brain Computer Interface for controlling mobile Robot", *International Journal of Recent Technology and Engineering*, July 2019
- [10] Gaetano Gargiulo, Paolo Bifulco, Rafael A. Calvo, Mario Cesarelli, Craig Jin1 and André van Schaik, "A mobile EEG system with dry electrodes"
- [11] Andrei Chiuzbaian, Jakob Jakobsen, Sadasivan Puthusserypady, "Mind Controlled Drone: An Innovative Multiclass SSVEP based Brain Computer Interface"
- [12] R. W. S. E. A. S. H.-L. M. S. D. M. S. G. Y.-P. E. W. J. K. Z. Z. a. V. Y. Xingqin Lin, *Mobile-Network Connected Drones: Field Trials, Simulations, and Design Insights*, Ericsson.
- [13] J. W. J. C. Y. G. a. G. D. Haichao Wang, "Network-Connected UAV Communications: Potential and Challenges," 2018.
- [14] R. Z. a. T. J. L. Yong Zeng, "Wireless Communications with Unmanned Aerial Vehicles: Opportunities and Challenges," 2016.

- [15] H. N. P. M. I. Z. K. J. W. a. T. B. S. Raphael Amorim, "Radio Channel Modeling for UAV Communication Over Cellular Networks," 2017.
- [16] [V. Y. S. D. M. S. G. H. A. H.-L. M. M. B. Xingqin Lin, "The Sky Is Not the Limit: LTE for Unmanned Aerial Vehicles," IEEE Communications Magazine, 2018 April.
- [17] J. L. a. R. Z. Yong Zeng, "Cellular-Connected UAV: Potential, Challenges, and Promising Technologies," IEEE Wireless Communications, 2019 February.
- [18] M. I. Y. Z., M. I. a. R. Z., F. I. Shuowen Zhang, "Cellular-Enabled UAV Communication: A Connectivity-Constrained Trajectory Optimization Perspective," IEEE TRANSACTIONS ON COMMUNICATIONS, vol. 67, 2019 March.
- [19] M. A. . M. I. . A. W. . T. Y. . F. O. . H. Iida3, "UAV communication system integrated into network traversal with mobility," Springer nature journal, 2020 April.
- [20] X. L. H.-L. M. J. S. Z. Z. W. A. H. S. Y. Siva D. Muruganathan†, "An Overview of 3GPP Release-15 Study on Enhanced LTE Support for Connected Drones," Ericsson.
- [21] H. S. S. D. B. M. M. A. S. Evgenii Vinogradov*, "Tutorial on UAVs: A Blue-Sky View on Wireless Communication," 2019 January.
- [22] H S. M. I. W. S. F. I. M. S. M. I. Ramy Amer, "Mobility in the Sky: Performance and Mobility Analysis for Cellular-Connected UAVs," 2019 August.
- [23] H International Journal of Scientific and Research Publications, Volume 4, Issue 9, September 2014 1 ISSN 2250-3153.
- [24] H Osama Jamal Al-zogphy, Osama Ibrahim Khalil, Abanoub Monir reda, "Design and Manufacturing of Quadcopter", The 4th International under-Graduate Research Conference, IUGRC, August 2019.
- [25] H X. H. Y. Z. a. Y. Z. Yunping Liu, "Dynamic Stability and Control of a Manipulating Unmanned," p. 14, 2018.
- [26] H J. M. a. B. Kusumoputro, "Neural Network Control System of UAV Altitude Dynamics and Its Comparison with the PID Control System," p. 19, 2018.
- [27] H E. A. Seidabad, S. Vandaki and A. V. Kamyad, "Designing Fuzzy PID Con`troller for Quadrotor," International Journal of Advanced Research in Computer Science Technology, vol. 2, no. 4, pp. 221-227, 2014.
- [28] H M. W. M. a. R. D'Andrea, "Stability and control of a quadcopter despite the complete loss of one,," p. 8, 2014.
- [29] H D. Magree, J. Mooney, and E. Johnson, —Monocular visual mapping for obstacle avoidance on uavs, | Journal of Intelligent Robotic Systems, vol. 74, no. 1-2, pp. 17–26, 2014. [Online]. Available: <http://dx.doi.org/10.1007/s10846-013-9967-7>
- [30] H Xin-Zhong Peng, Hwei-Yung Lin, and Jyun-Min Dai, "Path Planning and Obstacle Avoidance for Vision Guided Quadrotor UAV Navigation", 12th IEEE International Conference on Control Automation (ICCA), Kathmandu, Nepal, June 1-3, 2016.
- [31] H W. Liu, D. Anguelov, D. Erhan, C. Szegedy, S. Reed, C.-Y. Fu, and A. C. Berg, Ssd: Single shot multibox detector, In European conference on computer vision. Springer, 2016, pp. 2017.
- [32] H S. Jung, H. Lee, S. Hwang, and D. H. Shim, Real time embedded system framework for autonomous drone racing using deep learning techniques, In 2018
- [33] S. Kamate and N. Yilmazer, Application of object detection and tracking techniques for unmanned aerial vehicles, Procedia Computer Science, vol. 61, pp. 436441, 2015.
- [34] J. Redmon, S. Divvala, R. Girshick, and A. Farhadi, You only look once: Unified, real-time object detection, In Proceedings of the IEEE Conference on Computer Vision and Pattern Recognition, 2016, pp. 779788.
- [35] K. Simonyan and A. Zisserman, Very deep convolutional networks for large-scale image recognition, arXiv preprint arXiv:1409.1556, 2014.
- [36] Sunggoo Jung, Sunyou Hwang, Heemin Shin and David Hyunchul Shim, Perception, "Guidance and Navigation for Indoor Autonomous Drone Racing using Deep Learning", IEEE ROBOTICS AND AUTOMATION LETTERS. PREPRINT VERSION. ACCEPTED JANUARY 2018.
- [37] Xiangzhu Zhang, Lijia Zhang, Hailong Pei and Frank L. Lewis, "Part-based multi-task deep network for autonomous indoor drone navigation", Transactions of the Institute of Measurement and Control 1–11 The Author(s) 2020 Article reuse guidelines: [sagepub.com/journals-permissions](https://www.sagepub.com/journals-permissions) DOI: 10.1177/0142331220947507 journals.sagepub.com/home/tim.
- [38] Elaf Jirjees Dhulkefl, Akif Durdu , "Path Planning Algorithms for Unmanned Aerial Vehicles", International Journal of Trend in Scientific Research and Development (IJTSRD) Volume: 3 ,Issue: 4 ,May-Jun 2019 Available Online: www.ijtsrd.com e-ISSN: 2456 - 6470.
- [39] Liang Yang, Juntong Qi, Jizhong Xiao, Xia Yong, "A Literature Review of UAV 3D Path Planning", Proceeding of the 11th World Congress on Intelligent Control and Automation, 29 June-4 July 2014.
- [40] Fangyu Li, Sisi Zlatanovac, Martijn Koopmand, Xueying Baie, Abdoulaye Diakité, "Universal path planning for an indoor drone", Automation in Construction, 2018.
- [41] Chao Wang, Student Member, IEEE, Jian Wang, Senior Member, IEEE, Jingjing Wang, Member, IEEE, and Xudong Zhang, Member, IEEE, "Deep Reinforcement Learning-based Autonomous UAV Navigation with Sparse Rewards", IEEE Internet of Things Journal, DOI 10.1109/JIOT.2020.2973193

Identification of Dengue Mosquito Sound Using Spectral Based Features

Gayani Rajapaksha
Department of Electrical and Electronic Engineering
University of Jaffna
Sri Lanka
gayanirajapaksharm@gmail.com

Yuvaraj Manchukan
Department of Electrical and Electronic Engineering
University of Jaffna
Sri Lanka
yuvaraj@eng.jfn.ac.lk

Miyushani Sachinthanee
Department of Electrical and Electronic Engineering
University of Jaffna
Sri Lanka
miyushani@gmail.com

Thiruvaran Tharmarajah
Department of Electrical and Electronic Engineering
University of Jaffna
Sri Lanka
thiruvaran@eng.jfn.ac.lk

Abstract— Dengue disease is one of the fatal diseases in Sri Lanka that is transmitted by mosquitos. The type of mosquitos called *Aedes* species is the prime cause for Dengue disease in Sri Lanka. Identifying the *Aedes* species is very important to prevent or reduce the spread of that virus. So for mostly image based visual methods are used to classify mosquito species but very few works were done using acoustical wing beat frequency data. This project targets to develop an automatic system to classify the mosquitos as Dengue and non-Dengue. A possible application is a mobile app that could make a warning sound whenever there is a Dengue mosquito in the acoustic vicinity of the phone. Initially MFCC (Mel Frequency Cepstral Coefficients) feature which is a popular feature in speech based automatic systems is used. As the back-end classifier, (DNN) deep neural network is used. This system produced a result of more than 75% of accuracy. Targeting to derive a more specific feature for this classification the spectral contents of the mosquito sounds are analyzed. For this analysis filtered normalized energy of different frequency bands are investigated to located the most discriminative spectral space in order to develop a feature specific for Dengue mosquito classification. It is observed that the spectral region of approximately 0- 3150 Hz and 3200- 8250 Hz shows discrimination between dengue and non-dengue wing beat sound.

Keywords— *Aedes*, MFCC, DNN

I. INTRODUCTION

Dengue is one of the fatal disease that the world is facing. There are 505,430 dengue cases reported in 2000, also over 2.4 million, and 5.2 million reported in 2010 and 2019 respectively. As per WHO, Dengue cases are increased over 8 fold over the last two decades. The reported deaths between the year 2000 and 2015 have increased from 960 to 4032 [1]. Dengue is widespread in the tropics and risk levels depend on weather conditions such as rainfall, temperature, and relative humidity. Unplanned rapid urbanization also indirectly contributes to the increment of the spread. The principal Dengue virus carrying mosquito species is *Aedes aegypti*. Mosquito species in genus *Aedes* such as *Aedes albopictus*, *Aedes polynesiensis*, *Aedes scutellaris* and Asian tiger mosquito species also have less ability to carry dengue virus [2]. *Aedes aegypti* mosquitoes are responsible for transmitting dengue, Zika, yellow fever, and chikungunya viruses. Controlling *Aedes aegypti* has extremely challenging because of complications like endophilic behavior of mosquitoes, their propensity to oviposit within containers transported long distances, and increasing insecticide

resistance [3]. In order to minimize the spread of the diseases by mosquitoes worldwide, new techniques based on behavioral studies of mosquitoes are required. Many monitoring techniques rely on mosquito trapping and, so far, the majority of mosquito traps utilize attractant and catch cues[4], [5].

In recent years, the process of identifying disease-carrying mosquitoes by their flight tones has been researched [6], [7], [4], [8]. The male flight tone frequencies were similar in both *A. Aegypti* and *A. Albopictus* species. and higher than their females. The female *Aedes aegypti* flight tone ranges ranging from 250 to 620 Hz [7] . The fundamental frequency of wing beat, which varies between 300 and 600 Hz depending on species, is usually the most behaviorally important frequency component of flight tone[9]. The male *Aedes albopictus*, female *Aedes albopictus*, male *Culex quinquefasciatus* and female *Culex quinquefasciatus* wing-beat shows fundamental frequencies at 550 Hz, 460 Hz,750 Hz and 440 Hz respectively [5].

Though most of the researchers have studied about the behavior of *Aedes Aegypti* mosquitos, the automatic classification of Dengue and Non-Dengue vectors has not been researched. This study considers only the *Aedes* genus mosquitoes, since dengue viruses are transmitted by *Aedes* species mosquitoes[2]. We classified *Aedes* genus mosquitoes as one class and other mosquito species into another class.

Manual monitoring of mosquitoes is time consuming, cost-intensive, needs an expert to accurately identify the mosquitoes and labor effort which can raise safety issues for humans. Nowadays, low-cost mobile phones with very basic functionality are capable of sensitively acquiring acoustic data on species-specific mosquito wingbeat sounds, while simultaneously recording the time and location of the human mosquito encounter. When performing free-flight recordings of wing beat sound in the field the sound can be detectable up to about 50 mm from a mosquito when using old basic phone such as SGH T-209. In the case of smartphones like the Xperia, this distance can increase up to about 100 mm, making it even easier for consumers to record mosquito sound. The mosquito sound becomes undetectable beyond these distances due to background noise. Possible environment to record are calm to moderately noisy

workplaces with background noise levels less than 50 dB, but they decrease dramatically in louder noisy area [6]. The main objective of this project is to make a mobile app which can automatically identify mosquitos by their sounds when dengue mosquitos are nearby. As an initial step, we focused on studying the acoustic features of dengue and non-dengue mosquitos and evaluated the ways to incorporate signal processing techniques into mosquito detection. Here we used MFCC for feature extraction and neural network based algorithm for classification. MFCCs are the most successful feature in speech based application and used in few mosquito detection applications such as classifications of male female mosquitos, classifications of mosquito species and etc. [8], [10], [11], [12], [13], [14], [15].

The rest of paper is structured as follows. First we present the details about dataset and methodology we used for the mosquito identification. After that we show the classification performance and discuss about the results. Finally, we conclude the paper and discuss future developments.

II. METHODOLOGY

A. Data Acquisition

Dataset collection plays an important role in this research. Because the selection of the dataset will influence the results that would be produced. We concentrated on field data sets to do a Real-time application. There were only few openly available datasets that fulfil all the requirements. For this research a publicly available dataset in Dryad Digital Repository collected by Mukundarajan et al [6] was used. It consists of wing-beat frequency data (WBF) of twenty mosquito species that are recorded using different kinds of mobile phones. For this dataset live mosquito species was captured from the field and recorded in different labs and facilities to create those recordings of different mosquito species. Further, field acoustic data also have been collected from different locations using mobile phone recorders during mosquito's free flight or after trapped in Ziploc bag. From that dataset all Aedes species are taken as one class named as 'Dengue' and the rest of the mosquito species are taken as the other class names as 'Non-Dengue' since the aim of this research is to automatically classify a wingbeat sound as either 'Dengue' or 'non-Dengue'. Table 1 shows the two classes, the species and the corresponding number of available recordings that are used in this research.

B. Data Pre-processing

In above dataset have recordings recorded in two different sampling frequencies that are 44100 Hz and 8000 Hz. In order to have consistency 8000 Hz recordings were up sampled to 44100 Hz. This sampling frequency is chosen in order not to lose any information.

Some parts of the recordings contain only unwanted noise without the wingbeat sound. So those noisy parts are removed manually and then the rest of the recordings are trimmed into equal sized recordings with a duration of 1 second samples. Any recordings less than 1 second are removed from the dataset. After this pre-processing the number of 1-second recordings are as below.

- Aedes genus recordings-120

- Other species recordings- 182

The spectral subtraction approach was employed to reduce noise that was part of the wingbeat sound. This is achieved by subtracting the noise only spectrum from the noisy wingbeat spectrum similar to how noise is removed in speech signal in [5].

TABLE 1: THE DETAILS OF THE DATASET USED IN THIS RESEARCH

	Species	Number of Recordings
Dengue	Aedes aegypti	21
	Aedes albopictus	7
	Aedes mediiovittatus	3
	Aedes sierrensis	156
Non Dengue	Anopheles albimanus	30
	Anopheles arabiensis	13
	Anopheles atroparvus	7
	Anopheles dirus	39
	Anopheles farauti	36
	Anopheles freeborni	49
	Anopheles gambiae	54
	Anopheles merus	5
	Anopheles minimus	50
	Anopheles quadriannulatus	7
	Anopheles quadrimaculatus	6
	Anopheles stephensi	58
	Culex pipiens	9
	Culex quinquefasciatus	13
	Culex tarsalis	12
	Culiseta incidens	37

C. Data Analysis

To obtain the difference between dengue and non- dengue recordings we have done the frequency spectrum analyzing and energy band analyzing for each recordings. Since it is difficult to locate the difference by visualizing each spectrum of dengue and non-dengue recordings the average energy in different bands are analyzed. A filter bank is used to extract the energy and that is normalized to total energy. Then this filtered normalized energy is averaged over all the recordings separately for each class. The normalized energy vs frequency bands according to the bandwidth of the filter bank are shown in Fig. 1.

From this figure a significant variation on normalized energy can be observed in the frequency range approximately in 0- 3150 Hz and 3200 - 8250 Hz for dengue and non-dengue mosquitos.

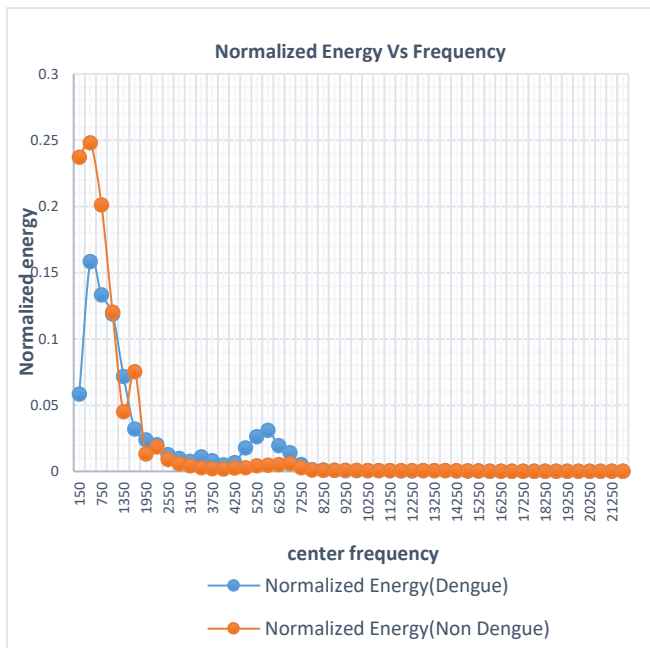


Fig. 1: Normalized Energy Vs Frequency

D. Feature extraction

Most researchers have used Mel frequency cepstral coefficients (MFCC) as the feature extracting method. MFCCs are computationally efficient while compare with just getting STFT or fundamental frequencies and harmonics. Here we used python librosa library inbuilt function to get the MFCCs. The process of extracting MFCC is as below:

- i. Frame blocking - due to characteristics of mosquito sound signal being relatively stable for a short time period. So we have used 512 frame length for each frame.
- ii. Windowing - To remove discontinuities of the overlay frames here hanning windows are applied.
- iii. Get the Fourier transform.
- iv. Applying Mel filter bank- Mel filters are sharper triangular overlapping windows in Mel scale.
- v. Applying the discrete cosine transformation give the MFCC feature.

E. Classification

After feature extraction, classification process was done using Deep Neural Network (DNN). DNN is good for non-linearly separable classifications and can learn mosquito classes [12]. Here we used Flatten layers, Dense layers and Dropout layers as hidden layers. Flatten layer was used to convert 2D features into 1D. Dense layer was used to provide learning features from all combination of features of the previous layer. Dropout layer was used to drop the unnecessary features in the model. To decide whether the particular neuron should be activated or not we have used 'relu' activation layer in hidden layers and to reduce the overfitting, regularizer L2 is used. Since this is a two class separation, sigmoid activation function is used for output layer. [16]

Architecture is checked with,

- Flatten layer
- Dense layer with 512 neurons
- Dropout layer with 30% dropout rate
- Dense layer with 256 neurons
- Dropout layer with 30% dropout rate
- Dense layer with 64 neurons
- Dropout layer with 30% dropout rate
- Dense layer with 1 neuron

Initial learning rate 0.0001

Optimizer- Adam

Loss- binary cross entropy

Performance is measured using accuracy and the cross validation provides information about how well a classifier generalizes, specifically the range of expected errors of the classifier. Here we used 10- fold cross validation to evaluate our model.

III. RESULTS AND DISCUSSION

Here we used sequential 2 model with DNN and 10-fold cross validation to obtain the accuracy with 0.0001 learning rate. Because the too large learning rate may result in learning an unstable training process and small learning rate may result in a long training process [17]. The experimental results are shown in Table 2 for different number of MFCC coefficients.

TABLE 2: FOR 100 EPOCHS, THE 10 FOLD CROSS VALIDATION ACCURACY WITH VARIOUS NUMBER OF MFCC COEFFICIENTS

Number of MFCCs	Accuracy Rate
11	79.40%
12	79.21%
13	79.54%
14	79.21%

Table 2 shows that the highest accuracy is achieved when the number of MFCC coefficients are 13 which is 79.54%. It also shows that the number of MFCCs will affect its accuracy.

IV. CONCLUSION AND FUTURE WORKS

Dengue and non-dengue classification using MFCC feature and deep neural network was performed. Up to now accuracy of 79.54% was achieved with 13 MFCCs. The discriminative frequency areas for dengue and non-dengue mosquitos have been identified using filtered band energy. This work can be further improved in future by a hyper parameter tuning and modification in Mel- filter bank according to the most discriminative spectral region identified. Modification of Mel- filter bank can be done by allocating more filers in discriminative regions and having less filters in other areas, according to normalized energy vs frequency graph. In future stage of the research, it is planned to demonstrate the system using mobile phone by deploying a mobile app.

REFERENCES

- [1] World Health Organization, "Dengue and severe dengue," *World Health Organization*, 2021. <https://www.who.int/news-room/fact-sheets/detail/dengue-and-severe-dengue/> (accessed Jul. 29, 2021).
- [2] Nature Education, "Dengue Transmission," *Scitable*, 2014. <https://www.nature.com/scitable/topicpage/dengue-transmission-22399758/>.
- [3] K. M. Staunton, L. Usher, T. Prachar, S. A. Ritchie, N. Snoch, and B. J. Johnson, "A novel methodology for recording wing beat frequencies of untethered male and female aedes aegypti," *J. Am. Mosq. Control Assoc.*, vol. 35, no. 3, pp. 169–177, 2020, doi: 10.2987/18-6799.1.
- [4] L. J. Cator, B. J. Arthur, L. C. Harrington, and R. R. Hoy, "Harmonic Convergence in the Love Songs of the Dengue Vector Mosquito," vol. 35, no. February, pp. 1077–1079, 2009.
- [5] C. R. Bellini, "A sound trap for Aedes albopictus (Skuse) male surveillance. Response analysis to acoustic and visual stimuli.," *Acta Trop.*, 2016, doi: 10.1016/j.actatropica.2016.09.002.
- [6] H. Mukundarajan, F. J. H. Hol, E. A. Castillo, C. Newby, and M. Prakash, "Using mobile phones as acoustic sensors for high-throughput mosquito surveillance," *Elife*, vol. 6, pp. 1–26, 2017, doi: 10.7554/eLife.27854.
- [7] W. G. Brogdon, "Measurement of flight tone differences between female Aedes aegypti and A.albopictus (Diptera: Culicidae)," *J. Med. Entomol.*, vol. 31, no. 5, pp. 700–703, 1994, doi: 10.1093/jmedent/31.5.700.
- [8] A. Lukman, A. Harjoko, and C. K. Yang, "Classification MFCC feature from culex and aedes aegypti mosquitoes noise using support vector machine," *Proc. - 2017 Int. Conf. Soft Comput. Intell. Syst. Inf. Technol. Build. Intell. Through IOT Big Data, ICSIT 2017*, vol. 2018-Janua, pp. 17–20, 2017, doi: 10.1109/ICSIT.2017.28.
- [9] S. M. Villarreal, O. Winokur, and L. Harrington, "Behavior, Chemical Ecology The Impact of Temperature and Body Size on Fundamental Flight Tone Variation in the Mosquito Vector Aedes aegypti (Diptera : Culicidae) : Implications for Acoustic Lures," vol. 54, no. April, pp. 1116–1121, 2017, doi: 10.1093/jme/tjx079.
- [10] Y. Li *et al.*, "Mosquito detection with low-cost smartphones: data acquisition for malaria research," 2017, [Online]. Available: <http://arxiv.org/abs/1711.06346>.
- [11] D. Vasconcelos, N. Nunes, M. Ribeiro, C. Prandi, and A. Rogers, "LOCOMOBIS: A low-cost acoustic-based sensing system to monitor and classify mosquitoes," *2019 16th IEEE Annu. Consum. Commun. Netw. Conf. CCNC 2019*, no. January, pp. 1–6, 2019, doi: 10.1109/CCNC.2019.8651767.
- [12] Y. Li *et al.*, "Fast mosquito acoustic detection with field cup recordings: an initial investigation," *Proc. Detect. Classif. Acoust. Scenes Events 2018 Work.*, no. November, pp. 153–157, 2018.
- [13] I. Kiskin *et al.*, "Mosquito Detection with Neural Networks: The Buzz of Deep Learning," pp. 1–16, 2017, [Online]. Available: <http://arxiv.org/abs/1705.05180>.
- [14] I. Kiskin, D. Zilli, Y. Li, M. Sinka, K. Willis, and S. Roberts, "Bioacoustic detection with wavelet-conditioned convolutional neural networks," *Neural Comput. Appl.*, vol. 32, no. 4, pp. 915–927, 2020, doi: 10.1007/s00521-018-3626-7.
- [15] G. Siva, "Related Papers," *Over Rim*, pp. 191–199, 2017, doi: 10.2307/j.ctt46nrzt.12.
- [16] musikalkemist, "Deep Learning For Audio With Python," *GitHub*, 2021. <https://github.com/musikalkemist/DeepLearningForAudioWithPython/>.
- [17] J. Brownlee, "Understand the Impact of Learning Rate on Neural Network Performance," *Machine Learning Mastery*, 2021. <https://machinelearningmastery.com/understand-the-dynamics-of-learning-rate-on-deep-learning-neural-networks/>.

Comparison of Constitutive Models for Nonlinear Response of Cracked Reinforced Concrete

Kopitha Kirushnapillai
Department of Civil Engineering
University of Peradeniya
Kandy, SriLanka
kopikiru18@gmail.com

Rifnaz Rafeek
Department of Civil Engineering
University of Peradeniya
Kandy, SriLanka
rifnazrz@gmail.com

Kushan Kalmith Wijesundara
Department of Civil Engineering
University of Peradeniya
Kandy, SriLanka
kalmithkush@yahoo.com

Abstract— Over the past few decades, many constitutive models have been proposed to analyze the behavior of cracked reinforced concrete members taking into account the axial-shear-moment interaction. Basically, they can be classified into discrete crack models and smeared crack models. Out of these models, Modified Compression Field Theory, Disturbed Stress Field Model and Total Strain Smeared Crack Model are widely used as smeared crack models in commercial finite element codes. However, many researchers have highlighted the limitations of these models specially when predicting the shear-critical response of the cracked reinforced concrete elements. Therefore, the objective of this research is to review the selected three constitutive models and to compare their capabilities in predicting load-deformation response of wide range of concrete elements depending on different shear span to depth ratio, percentage of longitudinal and transverse reinforcement and concrete grade and hence identify best model based on coefficient of variation and mean of test results. A database including some reinforced concrete specimens was developed by collecting past experimental data. Numerical analyses were performed for all the specimens using commercial finite element software and their results were compared with the experimental data in order to validate the capability of the constitutive models to predict the overall response of shear-critical reinforced concrete elements. In addition, coefficient of variation of the predicted strength of the elements by the three constitutive models are presented. Finally, some guidelines are proposed on how to select the parameters in the constitutive models for better prediction of load-deformation response of reinforced concrete elements. It was concluded that by comparing experimental and numerical results, Modified Compression Field Theory and Disturbed Stress Field Model have some drawbacks in capacity prediction in specific situations while Total strain model give better prediction with the suitable selection of material models.

Keywords— axial-shear-moment interaction, constitutive models, force-deformation response.

I. INTRODUCTION

Cracking of reinforced concrete members is a major issue in the structures for their service life. Basically, there are two types of cracks observed in reinforced concrete members. They are called flexural and shear cracks. As a structural engineer, we have to predict those types of failures. Prediction of shear failure is quite complex. Some constitutive models have developed to predict these type of failure modes in reinforced concrete elements. Cracked reinforced concrete constitutive models can be divided into discrete and smeared crack models. Smeared crack models can be further divided into fixed, rotating, and multi-direction crack models. In rotating crack models, it is assumed that the orientation of the crack direction and principal stress and principal strain

directions in the concrete change with externally applied loading. To address the rotating crack concept Vecchio and Collins (1982), Barzegar-Jamshidi and Schnobrich (1986), Ayoub and Filippou (1998), and Vecchio (2000) have formulated rotating crack models. Contrarily, in the fixed crack model, crack direction and principal stress and principal strain directions remain fixed in the direction of the first crack. Okamura and Maekawa (1998), and Kaufmann and Marti (1998) have proposed fixed crack models.

II. LITERATURE REVIEW

Flexural failure and shear failure are the failure modes of reinforced concrete elements. To analyse shear failure there are many constitutive crack models. The concrete crack model can be divided into two categories: discrete crack model and the smeared crack model. The smeared crack model can be further divided into fixed, rotating and multi-directional crack model. In the fixed crack model, orientation of the crack is kept constant and in the rotating crack model, orientation of the crack is varying with externally applied loading.

A. Modified Compression Field Theory

Modified compression field theory (MCFT) proposed by Vecchio and Collins (1986) tested 30 reinforced concrete panels under a variety of well-defined uniform biaxial stresses including pure shear. And from compatibility condition, equilibrium condition and the constitutive relationship they developed a constitutive model to predict the response of reinforced concrete elements when in-plane shear and axial stresses are active.

B. Disturbed Stress Field Model

Disturbed stress field model (DSFM) proposed by Vecchio (2000) to mainly readdress the two main weaknesses in MCFT: the assumption of principal average strain and principal average stress directions are same, and shear check at the crack. For calculation of DSFM total strain was considered instead of net strain. Total strain includes net strain, elastic strain, plastic strain offset, and average shear slip strain. Therefore, principal average strain and principal average stress directions are no longer aligned. Compatibility, equilibrium, and constitutive response are formulated in terms of average stresses and average strains. To calculate principal average tensile stress, in DSFM two constitutive models used one is tension stiffening and another one is tension softening.

C. A Constitutive Model for Analysis of Reinforced Concrete Solids

Vecchio and Selby used MCFT to develop this 3D model. Because of that in this model also they assumed the direction

of principal stress and directions of principal strain were coinciding. Cracked concrete was considered as an orthotropic material. And for the calculation, they considered average stress and average strain terms. Local stress conditions at crack were also considered for calculation. This constitutive model subject to short-term monotonic loading.

III. DATA COLLECTION

To analyse the limitation and compare above three theorems when the material properties, shear span and amount of longitudinal and transverse reinforcement vary on reinforced concrete beams, needed experimental results. Therefore, many research papers were reviewed, and database was created with different material properties, shear span to depth ratio and amount of longitudinal and transverse reinforcement.

To assemble a database, we could collect only 18 research papers because of availability. We couldn't include some of them due to unavailability of load-deformation curves and not enough data to proceed. Non-prestressed concrete members and not subjected to axial load members were selected. In this research, only point load at middle or known shear span members were selected. Only one fixed support beam and others are simply supported. Extracted data from experimental results are under conditions as shown in Table I.

TABLE I. EXPECTED DATA EXTRACTED FROM EXPERIMENTAL RESULTS

Specimen Properties	Range
Shear span depth ratio	2.8-6
Amount of longitudinal reinforcement	0.5%-4.9%
Amount of transverse reinforcement	0%-0.2%
Concrete grade	23MPa-80MPa

IV. PERFORM SENSITIVE STUDY

We have selected commercial software, which are based on the constitutive models. Response2000 based on the MCFT, VecTor5 based on the DSFM and Midas based on the total strain model have been selected to perform the numerical analysis. We must play with the parameters which are available to change in the commercial software to get the accurate result. Therefore, before performing numerical analysis we went with parametric study for each commercial software.

Parametric study was carried out for each constitutive model. There is no option to play with selection of parameters in response2000. Therefore sensitive study was carried out for VecTor5(DSFM) and Midas (TSM).

Parametric analysis was carried out to determine the influence of the key parameters, which govern performance. The key parameters in TSM are element size, crack model(Rotating,Fixed), tension function(exponential,hordijk), compression function(Parabola, Thorenfeldt), shear function, displacement increment, lateral crack effect and confinement effect.

V. RESULTS AND DISCUSSION

Experimental results were compared with numerical results. All the graphs illustrating comparison of results are attached in Annex II.

A. Specimen Without Transverse Reinforcement

- Specimen with low shear span to depth ratio

Fig. 1 shows the comparison of force-displacement response of different constitutive models with experimental result of specimen having shear span to depth ratio of 3.3 and crack pattern on the corresponding beam is shown in Fig. 2.

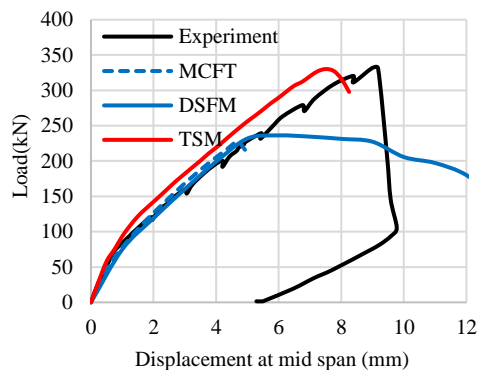


Fig. 1. Comparison of force-displacement response of different constitutive models with experimental result of specimen having shear span to depth ratio of 3.3.

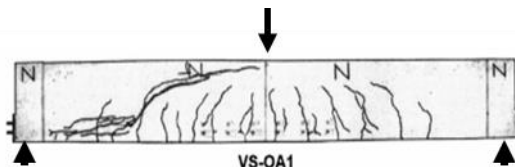


Fig. 2. Crack pattern on beam with no shear reinforcement and Shear span to depth ratio of 3.3.

- Specimen with high shear span to depth ratio

Fig. 3 shows the comparison of force-displacement response of different constitutive models with experimental result of specimen having shear span to depth ratio of 5.8 and crack pattern on the corresponding beam is shown in Fig. 4.

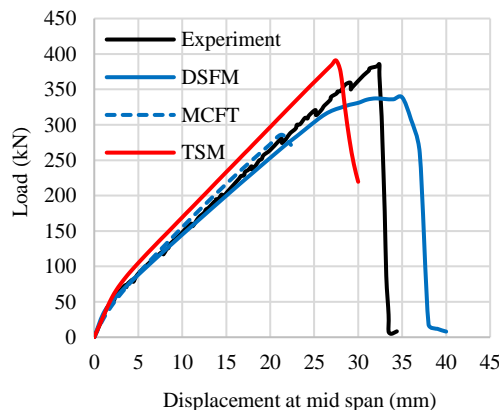


Fig. 3. Comparison of force-displacement response of different constitutive models with experimental result of specimen having shear span to depth ratio of 5.8.

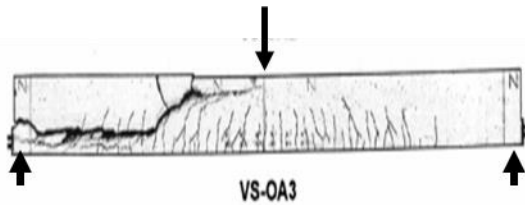


Fig. 4. Crack pattern on beam with no shear reinforcement and Shear span to depth ratio of 5.8.

B. Specimen With Transverse Reinforcement

- Specimen with low shear span to depth ratio.

Fig. 5 shows the comparison of force-displacement response of different constitutive models with experimental result of specimen having shear span to depth ratio of 3.3 and crack pattern on the corresponding beam is shown in Fig. 6.

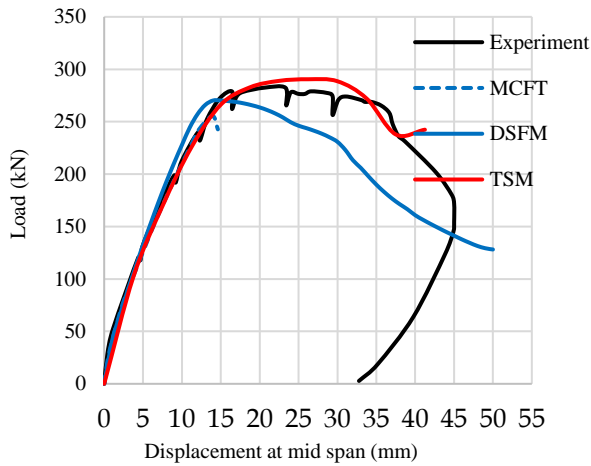


Fig. 5. Comparison of force-displacement response of different constitutive models with experimental result of specimen having shear span to depth ratio of 3.3.

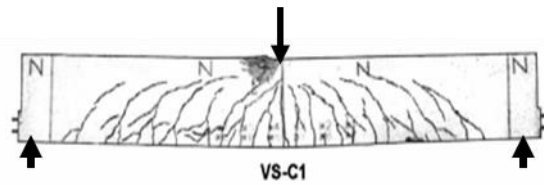


Fig. 6. Crack pattern on beam with shear reinforcement and Shear span to depth ratio of 3.3.

- Specimen with high shear span to depth ratio.

Fig. 7 shows the comparison of force-displacement response of different constitutive models with experimental result of specimen having shear span to depth ratio of 5.8 and crack pattern on the corresponding beam is shown in Fig. 8.

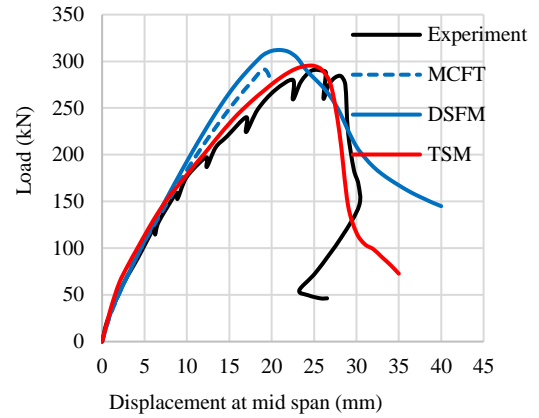


Fig. 7. Comparison of force-displacement response of different constitutive models with experimental result of specimen having shear span to depth ratio of 5.8

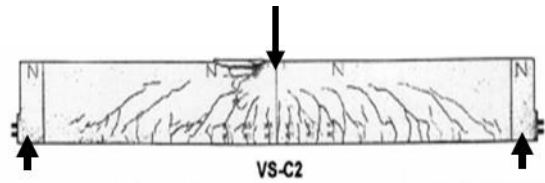


Fig. 8. Crack pattern on beam with shear reinforcement and Shear span to depth ratio of 5.8.

C. Comparison of Constitutive Models

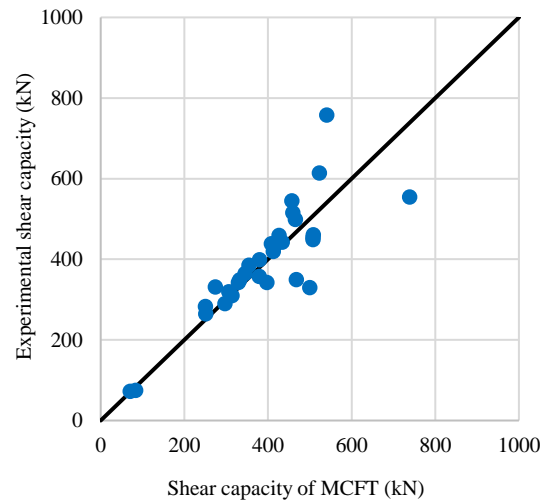


Fig. 9. Comparison of numerical result and experimental result of MCFT

Mean of MCFT is 1.01. Coefficient of variation of MCFT is 15%. Mean is nearest to one. Mean capacity prediction of MCFT is good. But it is 15% of variability.

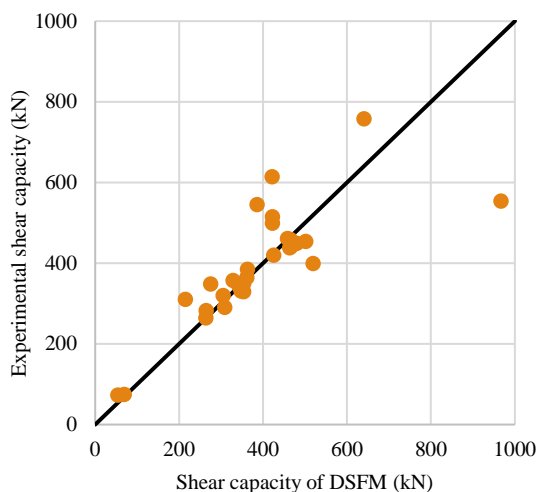


Fig. 10. Comparison of numerical result and experimental result of DSFM

Mean of DSFM is 1.06. Coefficient of variation of MCFT is 19%. Even though improvements have been made for DSFM, coefficient of variation become much higher than MCFT. But mean capacity prediction is good as mean is nearest to one.

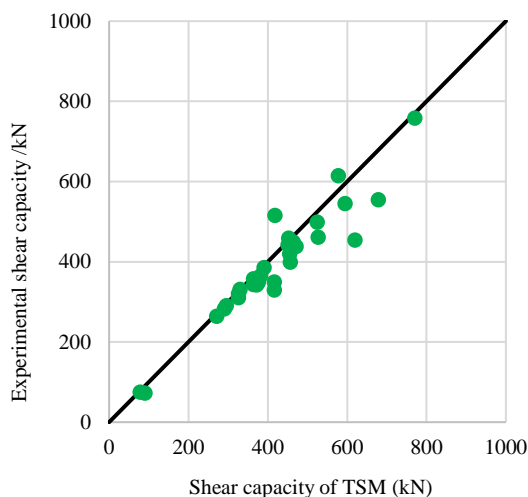


Fig. 11. Comparison of numerical result and experimental result of TSM

Mean of TSM is 0.94. Coefficient of variation of TSM is 9%. Shear capacity prediction of TSM is good compared to DSFM and MCFT. Mean is nearest to one and coefficient of variation is less than DSFM and MCFT.

TABLE II. COMPARISON OF MEAN AND COEFFICIENT OF VARIATION OF EACH CONSTITUTIVE MODEL

Constitutive Model	Mean	Coefficient of Deviation %
MCFT	1.01	15
DSFM	1.06	19
TSM	0.94	09

VI. CONCLUSIONS

When specimen having no shear reinforcement, it is proposed to use the following combination of parameters for the accurate prediction of shear capacity.

TABLE III. TSM PARAMETERS USED FOR SPECIMENS HAVING NO SHEAR REINFORCEMENT

No	Parameter	Suitable parameter
1	Fixed cracked model Rotational cracked model	Fixed crack model
2	Secant stiffness Tangent stiffness	Secant stiffness
3	Confinement effect	Not significant
4	Lateral crack effect	Not significant
5	Tension function	Exponential (decay)
6	Compression function	Thorenfeldt
7	Shear function	Constant (sensitive for β)

When specimen having shear reinforcement, it is proposed to use the following combination of parameters for the accurate prediction of shear capacity.

TABLE IV. TSM PARAMETERS USED FOR SPECIMENS HAVING SHEAR REINFORCEMENT

No	Parameter	Suitable parameter
1	Fixed cracked model Rotational cracked model	Rotating crack model
2	Secant stiffness Tangent stiffness	Secant stiffness
3	Confinement effect	Not significant
4	Lateral crack effect	Not significant
5	Tension function	Hordijk
6	Compression function	Parabolic
7	Shear function	None

By comparing coefficient of variation and mean of numerical result, it can be concluded that TSM predict the shear capacity accurately compared to the MCFT and DSFM. However, it should be noted that accuracy of shear capacity prediction by TSM based on the selection of parameters.

ACKNOWLEDGMENT

The authors would like to thank postgraduate student Mr.H.M.S.S.Hippola, lab assistants and the individuals who helped for this project.

REFERENCES

- [1] A.Ayoub, and F.C.Filippou, "Nonlinear finite element analysis of reinforced concrete shear panels and walls", Journal of Structural Engineering, American Society of Civil Engineers, 124(3), 1998, pp. 298-308.
- [2] Dino Angelakos, "The influence of concrete strength and longitudinal reinforcement ratio on the shear strength of large-size reinforced concrete beams with and without transverse reinforcement", M.Sc. Thesis, University of Toronto, 1999.

- [3] H.Okamura, and K.Maekawa, "Nonlinear analysis and constitutive methods of reinforced concrete", International Standard Book Number 7655-1506-0, University of Tokyo, Tokyo, 1991.
- [4] R.G.Selby, and F.J.Vechio, "A constitutive model for analysis of reinforced concrete solids", Canada Journal of Civil Engineering, 24(2), 1997, pp. 460-470.
- [5] ShenCao, "Size effect and the influence of longitudinal reinforcement on the shear response of large reinforced concrete members. M.sc Thesis, University of Toronto, 2001
- [6] F.J.Vecchio, and M.P.Collins, "Predicting the response of reinforced concrete beams subjected to shear using modified compression field theory", American Concrete Institute Structural Journal, 85(5),1982, pp. 258-268.
- [7] F.J.Vecchio, and M.P.Collins, "Modified compression field theory for reinforced concrete elements subjected to shear", American Concrete Institute Structural Journal, 83(2), 1986, pp. 219-231
- [8] F.J.Vecchio, and W.Shim, "Experimental and analytical reexamination of classic concrete beam tests" Journal of Structural Engineering, American Society of Civil Engineers, 130(3), 2004, pp.460-469.
- [9] F.J.Vecchio, "Disturbed stress field model for reinforced concrete: formulation", Journal of Structural Engineering, American Society of Civil Engineers, 124(3), 2000, pp. 298-308.
- [10] E.G.Sherwood, E.C.Bentz, and M.P.Collins, "Evaluation of shear design methods for large, lightly-reinforced concrete beams, Advances in Engineering Structures, Mechanics & Construction,2006, pp.153-164.

Determination of Transverse Thermal Conductivity of Coir Fibres by Analytical Methods

L.G. Chamath^{1,3}

*Division of Mechachanical Engineering
Technology
Institute of Technology, University of
Moratuwa
Diyagama, Homagama, Sri Lanka
chamathl@itum.mrt.ac.lk*

L.K.T. Srimal²

*Department of Mechanical and
Manufacturing Engineering, Faculty of
Engineering
University of Ruhuna
Galle, Sri Lanka
srimal@mme.ruh.ac.lk*

Galhenage A. Sewvandi³

*Department of Materials Science
and Engineering, Faculty of
Engineering
University of Moratuwa
Katubedda, Sri Lanka
galhenagea@uom.lk*

Abstract— Sustainable insulation materials can be produced by lignocellulose fibres (natural plant fibres). These are biodegradable, having low embodied energy required for production and low-cost materials for insulation. The environmental impact of sustainable insulation materials is minimal; hence a good candidate for replacing conventional insulation materials. In addition to fibres, a binder material should be introduced to adhere fibres, and then the whole material can be formulated as a composite. The volume fraction of each phase determines the insulation properties of the composite material (fibre and binder). However, high cost for experiments limit the experimental determination of the effect of volume fraction with thermal properties. Hence, numerical methods and empirical methods are alternative solutions to determine the thermal properties with the variation of physical parameters due to faster and more cost-effective when compared to the experimental methods. The thermal conductivity of each phase is required to determine the insulation properties of the composite using numerical and analytical methods. Determination of the transverse thermal conductivity of a single fibre is challenging. In this research work, a method is suggested to find the transverse thermal conductivity of a single fibre. Here, the two-phase composite was fabricated by coir fibres and epoxy with different volume fractions. Then the thermal conductivity was measured for the fabricated composite, and epoxy using the hot disk method. Next, the transverse thermal conductivity of the fibre was calculated using available analytical models, and the value was determined as 0.3084 W/mK. Finally, it can be concluded that the values calculated by analytical methods correlate with the experimental results.

Keywords— *Lignocellulose, Coir, Composites, Insulations, Thermal conductivity, Analytical methods*

I. INTRODUCTION

The Air Condition (AC) load of a building heavily depends on the heat transfer through the building envelope, and the nature of the envelope affects the amount of heat transfer through the building. Hence, the thermal insulation of principal components in the building envelope increases the energy efficiency of air conditioning while maintaining the indoor temperature at a desired value [1]. The commonly available building insulation materials are conventional materials such as expanded polystyrene, polyethylene, extruded polystyrene, and fiberglass [1,2]. However, the demand for sustainable insulation materials produced from lignocellulose fibres (natural plant fibres) has drastically increased over the recent two decades [3]. The reason is that these materials are a good alternative solution to mitigate the environmental issues during the material supply, production

process, installation, and disposal of the conventional materials [4].

Further, the sustainable insulation materials have properties such as low embodied energy required for production, biodegradable than conventional materials, and cost effectiveness [1,2,5]. Moreover, lignocellulose fibres exhibit low density, low thermal conductivity, and better mechanical properties to produce sustainable insulation materials [3,6,7]. Sugarcane fibre, palm oil fibre, coir fibre, cotton, jute fibre, and other natural fibres can be used to fabricate sustainable insulation materials for building applications [6,8].

However, binder material (matrix material) should be incorporated to adhere to the fibres, and then the insulation material can be identified as a composite material. The insulation properties of these composite materials change with the volume fraction of each phase (fibre and matrix). Here, the effective thermal conductivity (K_{eff}) of the composite material is the critical factor that decides the insulation properties of the whole material. Experimental, numerical, and analytical methods can be used to analyse the effect of insulation properties with respect to the volume fraction of each phase. Apart from the experimental and numerical methods, analytical models have been proposed to find the K_{eff} of the composite in the past. The reason is that the analytical models are more effective than numerical and experimental methods. The finding of K_{eff} using analytical methods is faster and cheaper than numerical and experimental methods. However, different types of basic models, empirical models, and semi-empirical models have been introduced previously according to fibre size, distribution throughout the matrix, shape, and the bonding between fibre and matrix to evaluate the K_{eff} of composites [9,10].

Devireddy [11] analytically evaluated the transverse thermal conductivity of banana – jute hybrid mixture using Rule of the mixture, Halpin-Tsai, and Lewis Nielsen models [11]. Here Halpin – Tsai and Lewis Nielsen models show better agreement with the experimental results [11]. However, the Lewis Nielsen model is the modification of the Halpin-Tsai model [12]. Also, the Lewis Nielsen model shows better agreement with the experimental results in Devireddy's works to determine the K_{eff} in hybrid composite with longitudinally oriented fibres [13]. Further, Sahu [14] evaluated the thermal conductivity of glass fibre-epoxy composite and banana fibre-epoxy composite using analytical, numerical, and experimental methods. In this work, the K_{eff} of composite with longitudinally oriented fibres was determined using the Rule

of the mixture, Maxwell model, and Bruggeman model [14]. The Maxwell model shows a better-closed agreement with the experimental results than other models [14]. Also, values obtained from the analytical models are well agreed with the experimental values within the fibre to the matrix volume fraction of 0 to 0.1 [11,13,14]. Moreover, Rayleigh's model is essential to find K_{eff} in the composite containing cylindrical fibres in a continuous matrix [9].

The above empirical models [9,11,13,14] can use to determine the thermal conductivity of a composite material. However, the thermal conductivity of each phase is required to find the K_{eff} of the composite using numerical and analytical models. Nevertheless, the above discussed research works used the literature values for the thermal conductivity of fibres [11,13,14]. The reason is that the finding of the transverse thermal conductivity of a single fibre is a challenging work. Also, the thermal properties of the fibre can be changed from, region to region, at fibre maturity, while extraction process, etc [15]. Therefore, this work mainly suggests a method to find the transverse thermal conductivity of a fibre. Here, coir fibres were selected as the fibre material. Because coir fibre exhibits properties such as high moisture resistance, high thermal stability, and low thermal conductivity [5]. Then, two-phase composite materials were fabricated by coir fibres and epoxy resin with different volume fractions. Then the thermal conductivity was measured for pure cured epoxy and fabricated composite using the hot disk method. Then the transverse thermal conductivity of the fibre was calculated using Maxwell's model, Lewis Nielsen model, and Rayleigh's model.

II. MATERIALS AND METHODS

A. Density Measurement of Coir Fibres

Coir fibres were pre-treated using 4% concentrated NaOH [16]. Then the density of fibres was measured using the Archimedes method using a 25 ml volume density bottle. The market available canola oil was used as the submerged fluid [17,18], and the fibre density (P_{fibre}) was calculated as in (1).

$$P_{fibre} = \frac{(W_2 - w_1)}{(W_4 - W_1) - (W_3 - W_2)} \times \frac{W_4 - w_1}{25} \quad (1)$$

W_1 is the weight of the density bottle, W_2 is the weight of the density bottle with fibres, W_3 is the density bottle with canola oil and fibres, and W_4 is the weight of the density bottle with canola oil. All weighted values are given here in grams (g).

B. Fabrication of the Composite

The fibre length should be uniaxial to get uniform distribution [19]. However, if the aspect ratio is higher than 15 then it can be taken uniaxial oriented fibres according to the Lewis Nielsen model [12,13]. But practically, too long fibre gives a curliness and it reduces the uniformity. Therefore, Coir fibres were cut into 5 mm length by considering the above parameters. The hand layup method was used to fabricate the composite [3]. Therefore, fibres were mixed with epoxy resin [3] to produce different volume ratios of fibre to epoxy resin, as shown in Table 1. Then the mixture was poured into the wooden mould with 50 mm × 100 mm × 1 mm dimensions. Here, the hardener and epoxy were mixed as the 2:1 weight ratio as per manufacturer recommendations.

TABLE I. THE VOLUME FRACTION OF FIBRE TO EPOXY RESIN

Sample no.	Weight of fibres (g)	Volume of epoxy (ml)	Volume fraction of fibres (v_f) and epoxy (v_m)
1	1.150	49.0	$V_f = 0.02, V_m = 0.98$
2	2.300	48.0	$V_f = 0.04, V_m = 0.96$
3	2.875	47.5	$V_f = 0.05, V_m = 0.95$
4	3.450	47.0	$V_f = 0.06, V_m = 0.94$
5	4.600	46.0	$V_f = 0.08, V_m = 0.92$
6	5.750	45.0	$V_f = 0.10, V_m = 0.90$

Here, the K_{eff} of the fabricated composites was measured using the hot wire disk method [20,21], as shown in Fig. 1. Therefore, each sample was cut into two similar parts as per the requirement of the instrument setup. Then, the sensor of the hot wire disk was placed between the separated sample and the K_{eff} of the composites was measured.

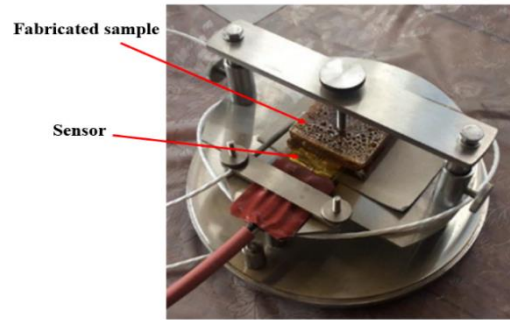


Fig. 1. Measuring the K_{eff} of the fabricated composite

III. CALCULATION

A. Analytical Methods to Find the Transverse Thermal Conductivity of Coir Fibres

The thermal conductivity of coir fibres was calculated after measuring the K_{eff} of the composite by using existing analytical models for a solid-solid system. Here, the Maxwell model, Rayleigh's model, and Lewis Nielsen model were used to determine the transverse thermal conductivity of coir fibres.

The first analytical model to find the K_{eff} of heterogeneous composite is the Maxwell model [9,10,12]. It gives better results below the volume fraction less than 0.1 [11,13]. Equation 2 provides the Maxwell equation.

$$K_{eff} = k_m \frac{2k_m + k_f - V_f(k_m - k_f)}{2k_m + k_f + V_f(k_m - k_f)} \quad (2)$$

Where k_m is the thermal conductivity of matrix and k_f is the thermal conductivity of fibre.

Rayleigh's model predicts the effective thermal conductivity in the composite, which contains cylindrical fibres in a continuous matrix [9]. Equation 3 gives the transverse thermal conductivity of Rayleigh's model.

$$\frac{K_{eff}}{k_m} = 1 + \frac{2V_f}{C_1 - V_f + C_2(0.30584V_f^4 + 0.013363V_f^8 + \dots)} \quad (3)$$

$$\text{Where } C_1 = \frac{k_f + k_m}{k_f - k_m} \quad \text{and} \quad C_2 = \frac{k_f - k_m}{k_f + k_m}$$

Lewis Nielsen model gives accurate results up to a 0.4 volume fraction without considering the interfacial thermal

resistance [9]. Therefore, it is commonly used to predict K_{eff} in composites. Further, this model considers the shape and orientation of the fillers. Equation 4 presents the model.

$$k_{eff} = k_m \left[\frac{1 + ABV_f}{1 - BV_f\Psi} \right] \quad (4)$$

$$\text{Where } B = \frac{\frac{k_f}{k_m} - 1}{\frac{k_f}{k_m} + A} \text{ and } \Psi = 1 + \left(\frac{1 - \phi_m}{\phi_m^2} \right) V_f$$

The values for the constant 'A' in various systems is given in Table 2. Here, the aspect ratio of the fibres is greater than 15. Then the dispersed phase can be taken as uniaxial oriented fibres according to the Lewis Nielsen model. Also, the direction of heat flow is perpendicular to the fibre direction and the 'A' value can be selected as 0.5.

TABLE II. VALUES FOR 'A' FOR VARIOUS SYSTEMS

Type of dispersed phase	Direction of heat flow	A
Cubes	Any	2.00
Spheres	Any	1.50
Aggregate of spheres	Any	$\frac{2.50}{\phi_0} - 1$
Randomly oriented rods aspect ratio = 2	Any	1.58
Randomly oriented rods aspect ratio = 4	Any	2.08
Randomly oriented rods aspect ratio = 6	Any	2.80
Randomly oriented rods aspect ratio = 10	Any	4.93
Randomly oriented rods aspect ratio = 15	Any	8.38
Uniaxial oriented fibres	Parallel to fibres	$2l/D$
Uniaxial oriented fibres	Perpendicular to fibres	0.50

The values for the constant ' ϕ_m ' in various systems is given in Table 3. Also, the packing type can be taken as uniaxial random. Therefore the value of ' ϕ_m ' is equal to 0.82.

TABLE III. VALUES FOR ϕ_m FOR VARIOUS SYSTEM

Shape of Particle	Type of Packing	ϕ_m
Spheres	Hexagonal close	0.7405
Spheres	Face centered cubic	0.7405
Spheres	Body centered cubic	0.60
Spheres	Simple cubic	0.524
Spheres	Random close	0.637
Spheres	Random close	0.601
Rods of fibres	Uniaxial hexagonal close	0.907
Rods of fibres	Uniaxial simple cubic	0.785
Rods of fibres	Uniaxial random	0.82
Rods of fibres	Three dimensional random	0.52

IV. RESULTS AND DISCUSSION

In this study, the K_{eff} of the fabricated composite was experimentally measured by a hot-wire disk. Here, the temperature of the sensor was maintained at 30 °C. Fig. 2 shows the K_{eff} values of fabricated composite with different volume fractions.

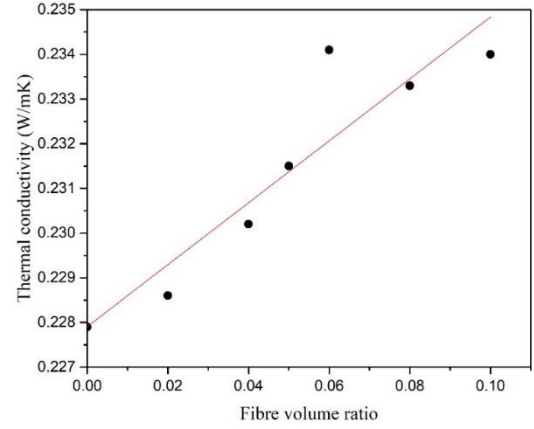


Fig. 2. Thermal conductivity of the composite

The effective thermal conductivity of the composite was increased with the fibre loading. It shows that the thermal conductivity of fibres is higher than the thermal conductivity of epoxy. However, there is a slight reduction in the K_{eff} after the 0.6 volume ratio. It may be due to the formation of voids inside the composite [11,13]. Then the thermal conductivity of coir fibres can be calculated by available analytical methods such as the Maxwell model, Rayleigh's model, and Lewis Nielsen model. Table 4 summarizes the thermal conductivity value obtained from each model for the respective fibre loading.

TABLE IV. CONDUCTIVITY VALUE OBTAINED FROM EACH MODEL FOR THE RESPECTIVE FIBER LOADING

Fibre loading	Thermal conductivity of composite (W/mK)	k_f from Maxwell model (W/mK)	k_f from Rayleigh's model (W/mK)	k_f from Lewis Nielsen model (W/mK)
0.02	0.2286	0.2620	0.2629	0.2637
0.04	0.2302	0.2890	0.2918	0.2944
0.05	0.2315	0.3067	0.3113	0.3157
0.06	0.2341	0.3473	0.3579	0.3692
0.08	0.2333	0.3014	0.3053	0.3085
0.1	0.2340	0.2937	0.2967	0.2989
Average K_f value		0.3000	0.3043	0.3084

Then the calculated average k_f values (0.3000 W/mK, 0.3043 W/mK, and 0.3084 W/mK) obtained from each model were re-substituted to Maxwell, Rayleigh's, and Lewis Nielsen models for validation of the results and identification of the value closer to the experimental values. Then the re-substituted k_f values to Maxwell, Rayleigh's, and Lewis Nielsen models could be graphically represented as per Fig. 3, Fig. 4, and Fig. 5.

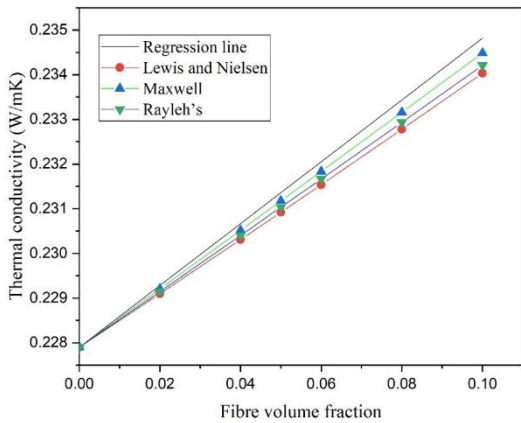


Fig. 3. Behavior of Maxwell, Rayleigh's, and Lewis Nielsen models at thermal conductivity of 0.3000 W/mK.

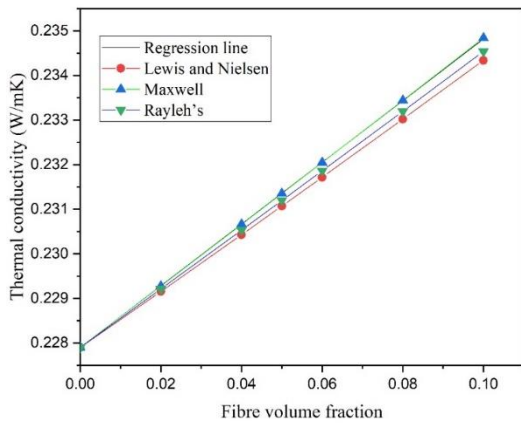


Fig. 4. Behavior of Maxwell, Rayleigh's and Lewis Nielsen models at thermal conductivity of 0.3043 W/mK.

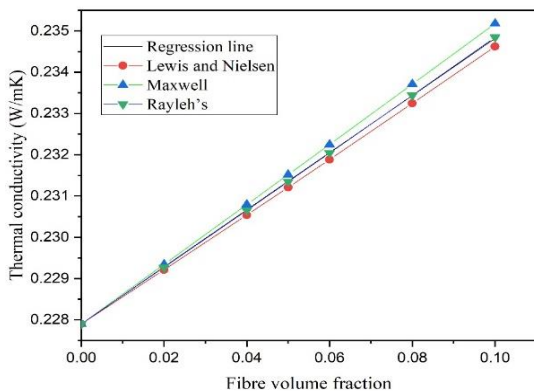


Fig. 5. Behavior of Maxwell, Rayleigh's and Lewis Nielsen models at thermal conductivity of 0.3084 W/mK.

According to Fig. 3, the value of 0.3000 W/mK shows the highest deviation with the regression line than other average values obtained from Rayleigh's and Lewis Nielsen's models. However, the substitution of 0.3043 W/mK into Rayleigh's model overlapped with the regression line in Fig. 4, and the

substitution of 0.3084 W/mK into Maxwell model overlapped with the regression line. Therefore, it is better to consider percentage errors with the regression line, shown in Fig. 4 and Fig. 5, to select the average k_f . Thus, the percentage errors with the regression line in Fig. 4 are shown in Table 5.

TABLE V. THE PERCENTAGE ERRORS WITH THE REGRESSION LINE IN FIG. 4

Fibre loading	Experimental value (Values on regression line)	Percentage error		
		Maxwell	Rayleigh's	Lewis Nielsen
0.02	0.2286	0.0021	0.0303	0.0547
0.04	0.2302	0.0018	0.0570	0.1022
0.05	0.2315	0.0010	0.0690	0.1231
0.06	0.2341	0.0009	0.0801	0.1423
0.08	0.2333	0.0061	0.0996	0.1750
0.1	0.2340	0.0136	0.1156	0.2005
Average percentage error (X)		0.0042	0.0753	0.1330
Mean value of average percentage error (\bar{X})		0.0708		

According to the Table 5, the mean value of average percentage error for Maxwell, Rayleigh's, and Lewis Nielsen is 0.0708. The same procedure was followed to find the percentage error in Figure 5. Here, the \bar{X} value is 0.0462. Therefore, the minimum percentage error is given by the average K_f value of 0.3084 W/mK. Thus, the value of 0.3084 W/mK can be taken as the transverse thermal conductivity of coir fibres. The percentage error can happen to some assumptions considered during the development of analytical models, such as fibres are distributed in the matrix as a regular periodical array. However, fibres are randomly distributed throughout the matrix, and these random fibres can touch each other. Some fibres can also be oriented in the longitudinal direction due to randomness and void content in the fabricated composite cause to error percentage in the thermal conductivity in experimental and analytical models.

V. CONCLUSION

The K_{eff} of the composite increased with the volume fraction of the fibre content. Hence, the thermal conductivity of coir fibre is higher than the thermal conductivity of epoxy. Further, the analytical modeling is a valuable approach to find the thermal conductivity in each phase, and the results are very close to the experimental values. Also, the transverse thermal conductivity of fiber could be considered as 0.3084 W/mK. Additionally, validating the results using numerical methods will add a value for this research work.

ACKNOWLEDGMENT

The authors wish to thank the Department of Physics, The Open University of Sri Lanka, for providing lab facilities for this study.

REFERENCES

- [1] D. Kumar, M. Alam, P. X. W. Zou, J. G. Sanjayan, and R. A. Memon, "Comparative analysis of building insulation material properties and performance," *Renewable and Sustainable Energy Reviews*, vol. 131, no. March, p. 110038, 2020. doi: 10.1016/j.rser.2020.110038.

- [2] L. Aditya, T.M.I.Mahlia, B.Rishmanchi, H.M.Ng, and H.B.Aditya., "A review on insulation materials for energy conservation in buildings," *Renewable and Sustainable Energy Reviews*, vol. 73, no. June, pp. 1352–1365, 2017. doi: 10.1016/j.rser.2017.02.034.
- [3] S. K. Santhosh and S. S. Hiremath, "Natural fiber reinforced composites in the context of biodegradability: a review," *Encyclopedia of Renewable and Sustainable Materials*, vol. 322, no. 1567. Elsevier Ltd., 2020. https://doi.org/10.1016/b978-0-12-803581-8.11418-3.
- [4] M. Casini, "Insulation Materials for the Building Sector: A Review and Comparative Analysis," *Encyclopedia of Renewable and Sustainable Materials*, Elsevier Ltd., 2019. https://doi.org/10.1016/B978-0-12-803581-8.10682-4.
- [5] L. C. Hao, S. M. Sapuan, M. R. Hassan, and R. M. Sheltami, "Natural fiber reinforced vinyl polymer composites," *Natural Fibre Reinforced Vinyl Ester and Vinyl Polymer Composites*, Elsevier Ltd, 2018. https://doi.org/10.1016/b978-0-08-102160-6.00002-0.
- [6] R. Gellert, "Natural fibre and fibre composite materials for insulation in buildings," *Materials for Energy Efficiency and Thermal Comfort in Buildings*, pp. 229–256, 2010, doi: 10.1533/9781845699277.2.229.
- [7] M. Volf, J. Diviš, and F. Havlík, "Thermal, moisture and biological behaviour of natural insulating materials," *Energy Procedia*, vol. 78, pp. 1599–1604, 2015, doi: 10.1016/j.egypro.2015.11.219.
- [8] K. Manohar, "Experimental investigation of building thermal insulation from agricultural by-products," *British Journal of Applied Science & Technology*, vol. 2, no. 3, pp. 227–239, 2012. https://doi.org/10.9734/bjast/2012/1528.
- [9] K. Pietrak and T. Wiśniewski, "A review of models for effective thermal conductivity of composite materials," *Journal of Power of Technologies*, vol. 95, no. 1, pp. 14–24, 2015.
- [10] P. Kosbe, and P. A. Patil, "Effective thermal conductivity of polymer composites: a review of analytical methods," *International Journal of Ambient Energy*, pp. 1–12, 2018. https://doi.org/10.1080/01430750.2018.1557544.
- [11] S. B. R. Devireddy, and S. Biswas, "Physical and thermal properties of unidirectional banana-jute hybrid fiber-reinforced epoxy composites," *Journal of Reinforced plastics and composites*, vol. 35, no. 15, pp. 1157–1172, August 2016. https://doi.org/10.1177/0731684416642877.
- [12] R. C. Progelhof, J. L. Throne, and R. R. Ruetsch, "Methods for predicting the thermal conductivity of composite systems: A review," *Polymer Engineering & Science*, vol. 16, no. 9, pp. 615–625, 1976. https://doi.org/10.1002/pen.760160905.
- [13] S. B. R. Devireddy, and S. Biswas, "Thermo-physical properties of short banana-jute fiber-reinforced epoxy-based hybrid composites," *Journal of Materials Design and Application*, vol. 232, no. 11, pp. 939–951, Nov. 2018, doi: 10.1177/1464420716656883.
- [14] Y. K. Sahu, A. Agrawal, and A. Satapathy, "Heat conduction behavior of short fiber reinforced polymer composites," *International Journal of Advanced Technology in Engineering science*, vol. 04, no. 1, Feb. 2016.
- [15] L. Mishra, and G. Basu, "Coconut Fibre: Its structure, properties and applications," *ICAR-National Institute of Research on Jute and Allied Fibre Technology*, Kolkata, West Bengal, India no. February, 2020.
- [16] L.G. Chamath, L.K.T. Srimal, and G.A. Sewvandi, "Effect of alkaline concentration on the surface properties of coir fibers," *National Engineering Research symposium 2020, NERD, Ekala, Ja- Ela , Sri Lanka, December 2020.* ISBN: 978- 624- 5505- 00-5
- [17] M. Truong, W. Zhong, S. Boyko, and M. Alcock, "A comparative study on natural fibre density measurement," *The Journal of The Textile Institute*, vol. 100, no. 6, pp. 525–529, 2009. https://doi.org/10.1080/00405000801997595.
- [18] A. Amiri, Z. Triplett, A. Moreira, N. Brezinka, M. Alcock, and C.A. Ulven, "Standard density measurement method development for flax fiber," *Industrial Crops and Products*, pp. 196-202, 2017. https://doi.org/10.1016/j.indcrop.2016.11.060.
- [19] T. G.Y. Gowda, M. R. Sanjay, K. Subrahmanya Bhat, P. Madhu, P. Senthamarikannan, and B. Yogesha, "Polymer matrix-natural fiber composites: An overview," *Cogent Engineering*, vol. 5, no. 1, 2018, doi:10.1080/23311916.2018.1446667.
- [20] N. Yuksel, "The Review of Some Commonly Used Methods and Techniques to Measure the Thermal Conductivity of Insulation Materials," *Intech*, pp. 13, 2016, [Online]. Available:https://www.intechopen.com/books/advanced-biometric-technologies/liveness-detection-in-biometrics.
- [21] D. Zhao, X. Qian, X. Gu, S. A. Jajja, and R. Yang, "Measurement for thermal conductivity and interfacial thermal conductance film materials," *Journal of Electronic Packaging*, *Transactions* vol. 138, no. 4, pp. 1–64, 2016, doi: 10.1115/1.4034605.

Experimental Investigation On Compressive Strength And Porosity In Pervious Concrete With The Effect Of Aggregate Size

Nilakshan Balasubramaniam
Department of Civil Engineering
University of Jaffna
Sri Lanka
nilakshan@eng.jfn.ac.lk

Tharshikka Vicgneswaran
Department of Civil Engineering
University of Jaffna
Sri Lanka
tharshikkasakthy@gmail.com

Daniel N.Subramaniam
Department of Civil Engineering
University of Jaffna
Sri Lanka
daniel@eng.jfn.ac.lk

Abstract— With rapid urbanization, surfaces are being covered by impermeable surfaces, which results in increased surface run off and consequently floods. Pervious or porous concrete, which allows water through it is said to be one of the answer for this problem. As less or no fine aggregates are used in pervious concrete, its strength is always in focus. At the same time, when fine aggregates percentage is increased, it will result in reduced porosity. This study focusses on finding out the aggregate combination that results in optimum compressive strength and porosity of pervious concrete. The aggregate size and the combination of pervious concrete are not well established. The aggregates passing 12.5 mm and retaining in 9.5 mm sieve sizes, passing 9.5 mm and retaining in 4.75 mm and passing 4.75 mm and retaining in 2.36 mm were used throughout the study for analyzing the aggregate combination. The water cement ratio that yields maximum compressive strength was found out by preparing samples using all three aggregates size. The water cement ratio was found to be 0.31 and was used throughout the study. For the analysis of aggregate combination, larger aggregate was replaced by the smaller aggregate. Test cubes were prepared by combining any two of the selected aggregate size. 7 day and 21-day compressive strength of the test cubes were tested. Concurrently, the porosity of the test cubes were measured. A relationship between the aggregate combination, porosity and compressive strength was formulated. From the formulated relationship, the optimum aggregate combination from each category was selected.

Keywords—Pervious concrete, Porosity, Compressive strength, aggregate size

I. INTRODUCTION

Pervious concrete dominates the world by being unique to environmental issues and to sustainable development. Constituents of pervious concrete are coarse aggregates, cementitious materials, water and with low or no fine aggregates. Compressive strength of pervious concrete is comparatively lower than the conventional concrete which is a drawback to pervious concrete [19]. The special feature of pervious concrete over conventional concrete is the Porosity. There should always be a balance between the compressive strength and porosity of pervious concrete to get the optimum output. The compressive strength and porosity of pervious concrete depends on the aggregate size, aggregate cement ratio and water cement ratio. In laboratories the compressive strength of pervious concrete found out to be in the range of 3.5 MPa to 28 MPa [3]. Although the addition of fine aggregates to pervious concrete can increase the compressive strength, it comes at the expense of permeability of pervious concrete. Therefore it is crucial to find a balance

between the amount of coarse aggregate added and compressive strength so as to get optimum output.

Selection of Aggregates, clogging and the environment to which it is exposed has major influence in the durability of porous concrete. Thus the research question of the study will be “How does the durability of porous pavements can be enhanced through the selection of aggregates composition with optimum compressive strength and porosity?”

Although there are studies on the properties of porous concrete with the change of aggregates, limited studies were done on the relationship of aggregate ratio with compressive strength and porosity. Further, aggregate composition in mixtures is only defined up to 3 ratios. Clogging Analysis had been done only to certain soil sizes, not for a combination.

Thus, this study aims at finding the optimum aggregate selection for optimizing the compressive strength and hydraulic conductivity of pervious concrete to increase the durability of pavements.

II. LITERATURE REVIEW

Pervious concrete is made with coarse aggregate, cement and water by excluding fine aggregate or with low fine aggregate. The coarse aggregates used in the pervious concrete are commonly gap graded or single sized aggregates. Angular aggregates result in higher voids with less density and less compressive strength compared with rounded aggregate [3]. Normally the coarse aggregates within the range of 9.5 mm and 19 mm is used and usage of aggregate more than this size could lead to high porosity and low strength [18]. Different size of aggregates have been used, for example aggregate with 9.5 mm [18] and mix of 9.5 mm and 12.7 mm aggregate [1]. Institute for Safe Quiet and Durable Highways in Purdue University recommends to use a mix of 9.5 mm or 12.5 mm of aggregate to achieve optimum noise lessening, has less segregation and better void distribution which avoid clogging of particles. The gradation that include the aggregates passing 4.75 mm sieve and retaining in 2.36 mm sieve, passing 9.5 mm and retaining in 4.75 mm and passing 12.5 mm and retaining in 9.5 mm results in the porosity ranging from 15 – 30 % [12].

When using aggregate ranging from 20 mm to 10 mm and 10 mm to 6 mm separately and by mixing them equally, the highest compressive strength was obtained for the mixture made by mixing both aggregates equally [16]. When coarse aggregate ,4.75 mm to 9 mm, 9 mm to 12.5 mm, 12.5 mm to 16 mm and 16 mm to 20 mm is used, maximum compressive

strength is obtained for the aggregate 12.5 mm to 16 mm and the lowest strength was obtained for 4.75 mm to 9 mm [6]. Water conductivity and connected porosity increase with increasing aggregate size [5]. On the other hand increasing aggregate size decreases the mechanical strength of pervious concrete. Therefore there is no specified aggregate selection and the selection of aggregate depends on the requirements. Among the aggregate to cement ratio 3:1, 4:1, 5:1, 6:1 and 7:1, maximum compressive strength of 15.87 N/mm² was obtained for 3:1. It was found that there was 70% increase in cube strength and 45 % increase in the cube strength for the Cement to aggregate ratio 1:4 than the cement to aggregate ratio 1:5 in 7 days and 21 days respectively [7]. Increase in aggregate cement ratio increases the permeability of pervious concrete. More cement in the mixture would fill void spaces once occupied by air, thereby reducing the permeability of the concrete [20]. Therefore an appropriate Aggregate cement ratio should be selected to have a balance in the aggregate and cement inclusion in cube casting. Further important consideration of pervious concrete is water cement ratio. W/C ratio dominates various properties of pervious concrete like compressive strength, porosity, permeability and density [4]. There are no clear evidence for the relationship between the compressive strength and water cement ratio for pervious concrete as for conventional concrete. 0.27 to 0.36 water cement ratio is commonly used in pervious concrete. Water cement ratio for pervious concrete should be less than the conventional concrete[11].

Maximum compressive strength was obtained for water cement ratio 0.38 than 0.41 and 0.45 [10], [13]. In some studies Water cement ratio was maintain a constant throughout the experiments as 0.33 [8] and in some other studies ranging from 0.28- 0.40. The increase in the W/C led to the increase in density and compressive strength but it reduces the void ratio and infiltration rate. If low W/C ratio is used then the porous concrete will have low workability that is <30 %. Maximum compressive strength is obtained for the water cement ratio for 0.43 [13]. Increasing the water cement ratio pave way for the increase of paste which can clog the pores in the concrete and it reduces the porosity. It is recommended not to use high water cement ratio which can cause flow of the cement paste [15]. It is obvious that when the water cement ratio is increased the paste content decrease. Permeability is increased with decrease in compressive strength of pervious concrete by the variation of water to cement ratio from 0.28, 0.32 and 0.36 [2]. Using 0.3 W/C ratio gives better result for pervious concrete [9]. Therefore W/C ratio of 0.35 to 0.31 will be appropriate to get maximum strength and permeability.

III. METHODOLOGY

A. Materials

Coarse aggregates: Aggregates used in the study are divided into three main category. Passing 12.5 mm and retained on 9.5 mm is named as category A01, while aggregates passing 9.5 mm and retained on 4.75 mm is named as category A02 and passing 4.75 mm and retained on 2.36 mm is named as category A03.

Fine aggregates: No fine aggregates are used.

Cement: Ordinary Portland cement as specified in Sri Lankan standard 855: 1989.

Water: Colourless, odourless and tasteless potable water as specified in Sri Lankan standard 855: 1989 is used.

The Table 1 and Table 2, shows the water absorption and specific gravity and aggregate impact value of the aggregates used for the project respectively.

B. Specimen Preparation

The water cement ratio 0.31 was selected from the water cement ratios 0.31, 0.33 and 0.35 as it yielded maximum compressive strength as shown in the Table 3. The aggregate cement ratio was maintained as 2.5:1 throughout the study. 1543 kg of aggregates and 309 kg of cement were used for the test cube preparation. The test cubes were prepared by mixing any two aggregates groups by replacing the larger aggregate group by smaller one in the percentage of 10%, 20%, 30%, 40% and 50%.

Thus, the aggregates group A01 & A02, A02 & A03 and A01 & A03 were mixed for test cubes preparation. Test cubes were prepared according to BS1881-113 1983. Moulds of 150 mm × 150 mm × 150 mm were used. Oil was applied in the interior layer of the moulds before cube casting. Cubes were casted by filling the whole cube at a time and finally five blows were given on the final layer using the 1.77 kg rammer. After twenty four hours of casting, the cubes were demoulded and placed in the curing tank for 7 days and 21 days at room temperature. The compressive strength of the test cubes were tested using the digital compression machine according to BS 1881: Part 116: 1983.

Archimedean principle was employed to determine the total void ratio of porous concrete cube. Three specimens for each type of porous concrete were tested to calculate the mean value. The total void ratio was obtained by dividing the difference between the initial mass (M1) of the specimen in the water and the final mass (M2) measured following air drying for 24 h with the specimen volume (V), where ρ is the density of water.

$$A(\%) = 1 - \frac{M2 - M1}{\rho V} \quad (1)$$

IV. RESULTS AND DISCUSSIONS

I. Water absorption and specific gravity

Water absorption of coarse aggregates gives clear idea about the strength of the aggregate. The water absorption is related to the porosity of the aggregates. If the water absorption is high, then the porosity will be high and the strength will be low. High value of absorption indicates that the aggregate is non- durable. Also absorption can specify the amount of binder the aggregate will absorb.

The upper limit of the water absorption is 3, in accordance with BS 5337:1976 for natural aggregates. Test results listed in Table 1 show that absorption values are higher for group A03. There exists an inverse relationship between the aggregate size and water absorption. From the specific gravity, the amount of aggregates required for a given volume of concrete can be found.

TABLE I. WATER ABSORPTION AND SPECIFIC GRAVITY OF AGGREGATES

Sample	Oven Dried Bulk Specific Gravity	Saturated Surface Dry Bulk Specific Gravity	Apparent Specific Gravity	Water absorption (%)
Passing 12.5 mm and retaining in 9.5 mm	2.831	2.853	2.895	0.780
Passing 9.5 mm and retaining in 4.75 mm	2.774	2.802	2.856	1.040
Passing 4.75 mm and retaining in 2.36 mm	2.520	2.551	2.602	1.257

If the aggregates absorb more water, when the water freezes and enlarges the concrete cannot tolerate the build-up of internal pressure. The larger the particle the need of water is also larger. Group A01 require more water than the other categories of aggregates. Therefore, it yields higher strength when compared with other aggregates.

II. Aggregate Impact Value

Commonly, aggregates of AIV less than 30% are used for pavement utilities. If Aggregate Impact Value is less than <20% then the aggregates are extremely strong and if the value is from 20 % to 30 %, then the aggregate is satisfactory for road construction [3]. AIV values listed in Table 2 shows that the aggregates used are in satisfactory range.

III. Void ratio

Aggregate gradation exhibited significant effect on the total void ratio. The total void ratio decreased with decreasing aggregate size. It was observed that most of the porous concretes had total void ratio ranging from 22 to 35% regardless of aggregate size. This is acceptable as a good ratio ranges between 15 and 30%.

TABLE II. AGGREGATE IMPACT VALUE

Sample	Aggregate Impact Value (%)
Passing 12.5 mm and retaining in 9.5 mm -A01	29.4
Passing 9.5 mm and retaining in 4.75 mm- A02	27.9
Passing 4.75 mm and retaining in 2.36 mm- A03	27.7

TABLE III. 7-DAY AND 21-DAY COMPRESSIVE STRENGTH

W/C ratio	Test cube		Control cube	
	7-Compressive strength MPa	21-Compressive strength MPa	7-Compressive strength MPa	21-Compressive strength MPa
0.31	4.7	7.8	3.5	7.1
0.33	3.8	6.3	3.5	7.1
0.35	3.4	5.8	3.5	7.1

IV. Compressive strength

The compressive strength was tested at 7 day and 21 day. The porosity of the pervious concrete was measured along with compressive strength using Archimedean principle. Fig. 1, shows the variation of average compressive strength of cubes casted with aggregates of A02 that was replaced by A01 aggregates, against the percentage of substitution. The Fig. 1 also shows the average values of the control cubes that were casted with only A01 aggregates (no substitution) and with all aggregates in equal amounts (33% of each aggregate group). Although the control cubes did not have substitution, the values of the control cubes shown which were cast on the same day as the respective test cubes were cast. There is no much variation observed between the compressive strength. The compressive strength increases with the increase in the substitution of the smaller aggregates (A02). The trend curves of linear and second order polynomial were fitted for compressive strength of test cubes for both 7 days and 21 days of curing. From that second order polynomial showed best fit for both cases (7 days and 21 days of curing) with an R² of 0.97. Same phenomenon were observed for other substitution shown in Fig. 2 and Fig. 3.

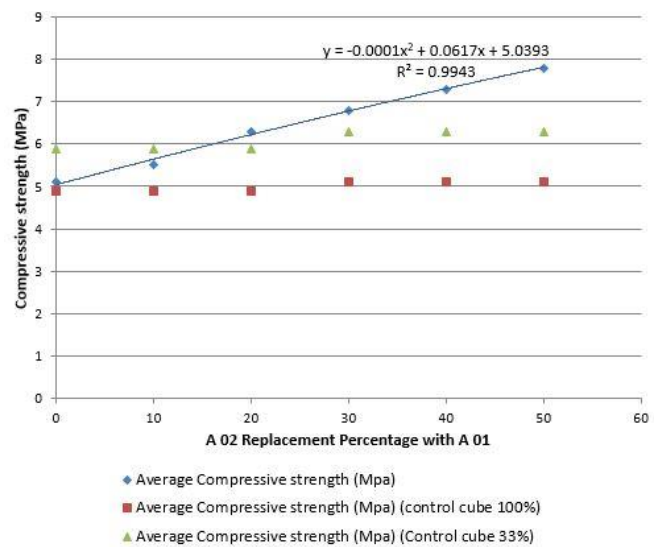


Fig. 1. 7-day compressive strength of A01 cubes replaced with A02

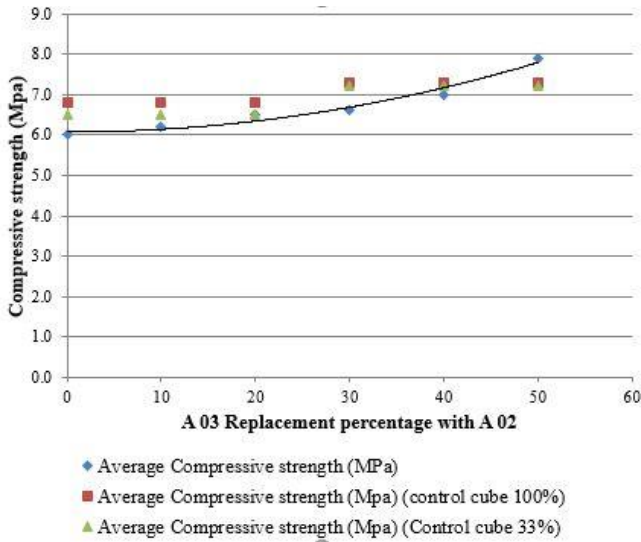


Fig. 2. 7-day compressive strength of A02 cubes replaced with A03

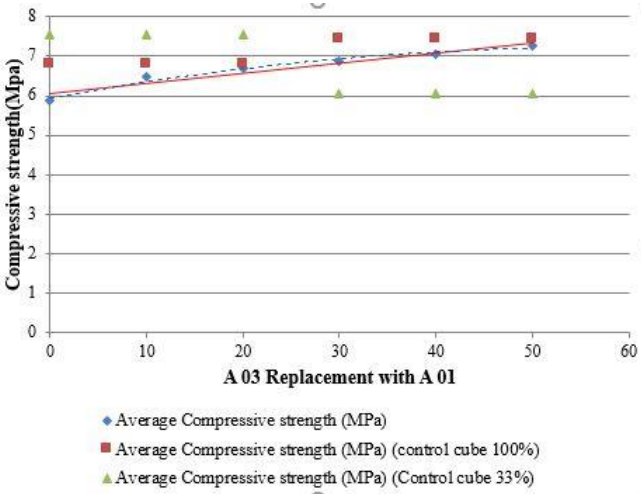


Fig. 3. 7-day compressive strength of A01 cubes replaced with A03

Fig. 4 shows the development of compressive strength with time for porous concrete for 7 and 21 days. It can be observed that the values of compressive strength for 7 and 21 days are increasing with the increasing mixing percentage.

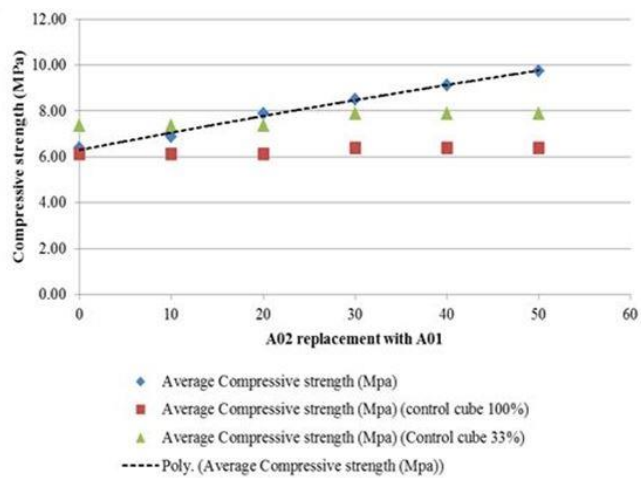


Fig. 4. 21-day compressive strength of A01 cubes replaced with A02

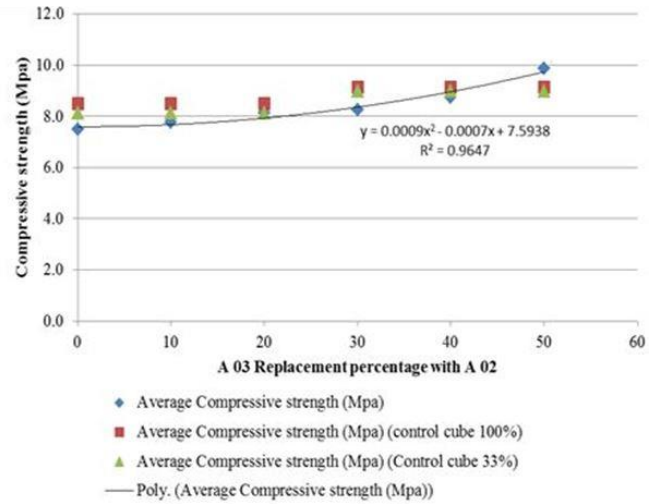


Fig. 5. 21-day compressive strength of A02 cubes replaced by A03

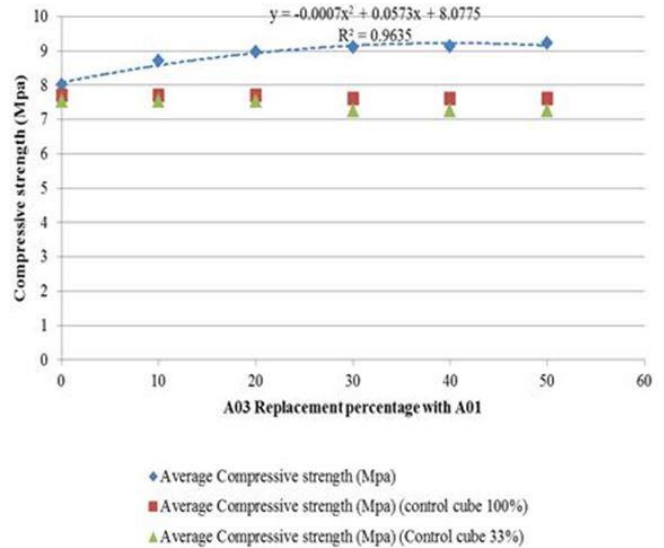


Fig. 6. 21-day compressive strength of A01 cubes replaced with A03

It was also observed in Fig. 1, Fig.2, Fig.3, Fig.4, Fig.5 and Fig.6 that, for the age of 7 days all concrete mixtures achieved the slight strength, i.e. 15% out of 21 day compressive strength.

The similar pattern was observed for the A03, shown in figure 8, replacement with A02 and A03 replacement with A01. The compressive strength is higher for the combination of A01 and A03 than A02 and A03 and A01 and A02 (Fig.7).

The selection of aggregates composition from each category was selected based on the aggregate combination that gives optimum compressive strength and void ratio. The aggregate replacement was mentioned in the x- axis and the compressive strength and void ratio were drawn in the y-axis. The compressive strength was drawn in the primary Y-axis and Void ratio in the X-axis. Therefore, the aggregate combination that is selected finally should satisfy the compressive strength and void ratio.

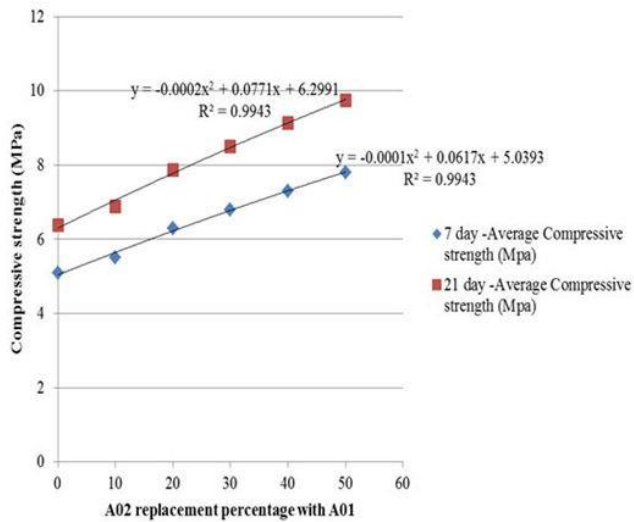


Fig. 7. 7-day and 21-day compressive strength of A01 cubes replaced with A02

The Fig. 8 shows the replacement of A01 (Passing 12.5mm and retaining in 9.5 mm) with A02 (Passing 9.5mm and retaining in 4.75mm aggregates). The both graphs intersect at the 20% of A02 group of aggregates and 80 % of A01 aggregate group. Similarly the aggregate selection was selected by drawing similar graph as shown in the Figure 3. The combinations of 90% of 9.5 -4.75 mm and 10% of 4.75 -2.36 mm and 80 % of 12.5 -9.5 mm and 20 % of 4.75 -2.36 mm yielded optimum compressive strength and porosity.

V. CONCLUSIONS

Increase in the compressive strength can be observed by the substitution of smaller aggregates. The compressive strength with no substitution is very much lower than the other substitution. It was also noted that the porosity decreases with the addition of smaller aggregates. There is no much different in the compressive strength of control cube comparing with the test cubes. Therefore, the compressive strength is influenced more by the addition of two aggregates than using single aggregate. The combinations of 80% of 12.5 -9.5 mm and 20% of 9.5 - 4.75 mm , 90% of 9.5 -4.75 mm and 10% of 4.75 -2.36 mm and 80 % of 12.5 -9.5 mm and 20 % of 4.75 -2.36 mm yielded optimum compressive strength and porosity.

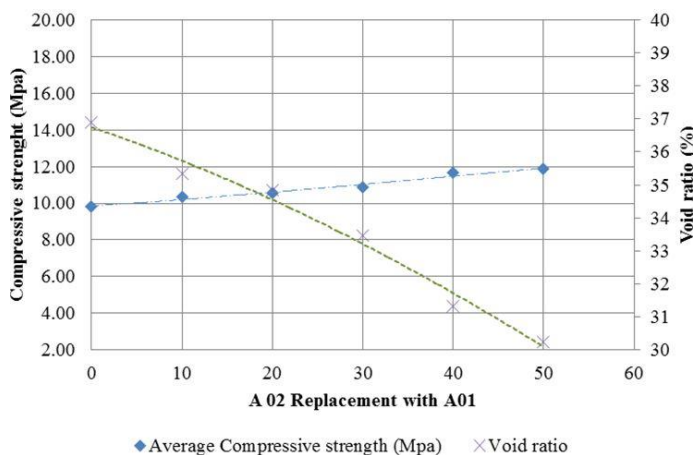


Fig. 8. A02 replacement with A01 vs compressive strength and void ratio

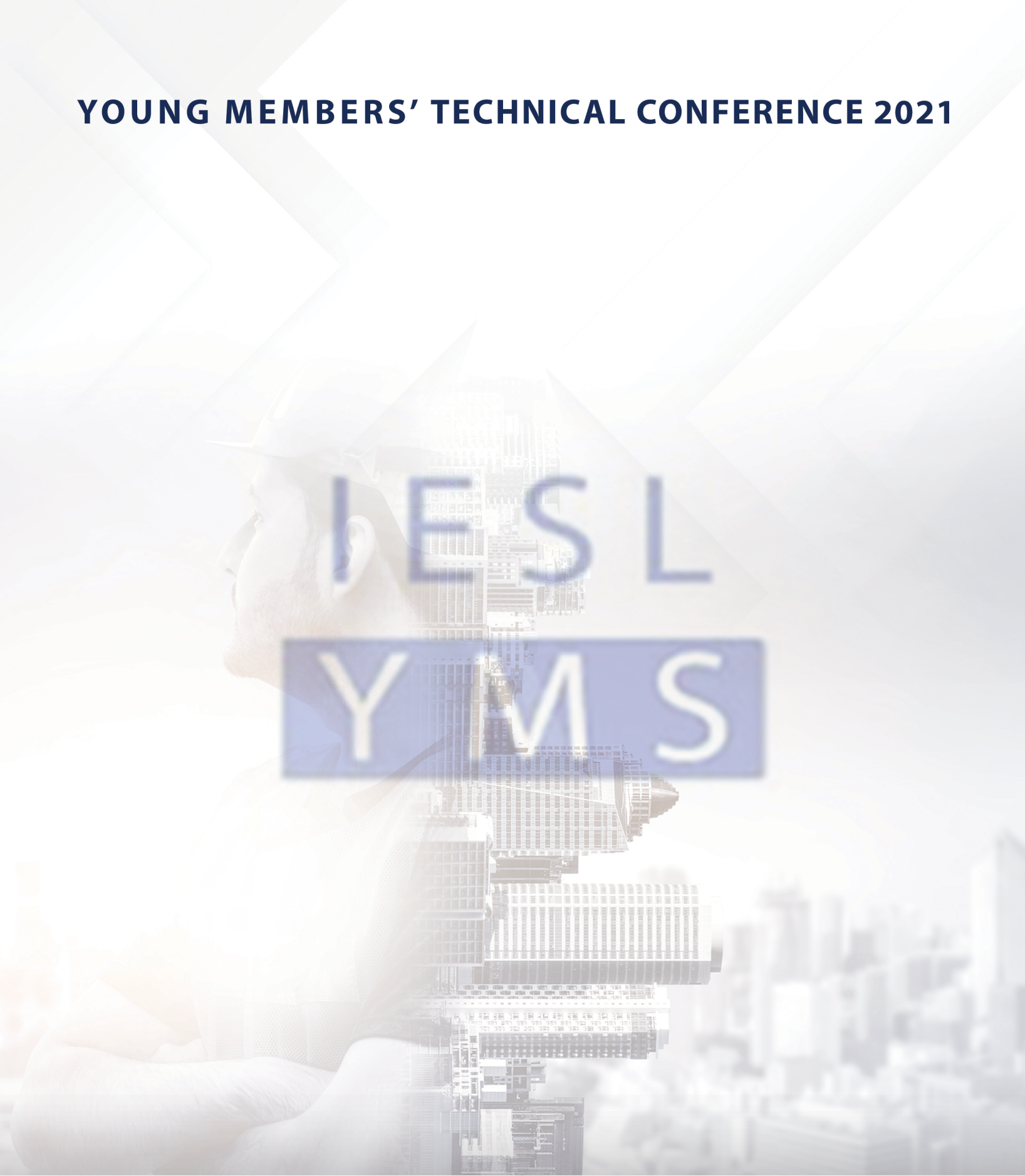
Porous concretes are usually preferred in pavement application where loads are quite low. Parking lots, walk paths are examples of such places where porous concrete is preferred. Ability of porous concrete allow water through it is the key factor for selecting that in pavement application though it's compressive strength is low. This helps in reducing the runoff and subsequently flooding. Porous concrete with the above mentioned combination exhibited good porosity values which is enough for storm water to infiltrate the concrete layer. Thus, through the findings of this study, it is recommended that the concrete in the above mentioned combination can be used for non-load bearing pavement applications.

REFERENCES

- [1] Dang Hanh Nguyen, Nassim Sebaibi, Mohamed Boutouil, Lydia Leleyter and Fabienne Baraud (2014) A modified method for design of Pervious concrete mix. Available at: (Accessed: 22 September 2014).
- [2] Journal of Hydrology, Issue 350, pp. 100-113. Shetty, M.S., 2010. Concrete technology, theory and practice. India: S. Chand and Company Limited. 73 Scholz, M. & Grabowiecki, P., 2007.
- [3] Kevern, J. T., 2006. Mix design development for Portland cement pervious concrete in cold climates, s.l.:WorldCat.
- [4] Kosmatka, S., Kerkhoff, B. & Panarese, W.C., 2002. Design and control of concrete mixtures. 14th ed. Skokie.
- [5] Lian, C., Zhuge, Y. and Beecham, S. (2011) „The relationship between porosity and strength for porous concrete“, Construction and Building Materials, 25(11), pp. 4294–4298. doi: 10.1016/j.conbuildmat.2011.05.005.
- [6] Manan, A., Ahmad, M., Ahmad, F., Basit, A. and Ayaz Khan, M., 2018. Experimental Investigation of Compressive Strength and Infiltration Rate of Pervious Concrete by Fully Reduction of Sand. Civil Engineering Journal, 4(4), p.724.
- [7] Meddah, M., Al-Jabri, K., Hago, A. and Al-Hinai, A., 2017. Effect of granular fraction combinations on pervious concrete performance. Materials Today: Proceedings, 4(9), pp.9700-9704.
- [8] McMillan, T, 2007. Comparison Traditional Concrete to Permeable Concrete for a Community College Pavement Application.
- [9] Montes, F. and Haselbach, L. (2006) „Measuring hydraulic conductivity in Pervious concrete“, Environmental Engineering Science, 23(6), pp. 960–969. doi: 10.1089/ees.2006.23.960. 32
- [10] Naik, R.T & Kraus, N.R., 2002. Development and demonstration of high carbon CCPs and FDG by products impermeable roadway base construction.
- [11] Nakahara, D., Nota, E. & Endo, K., 2004. Utilization of pavement quality porous concrete and its performance. In Symposium on Concrete pavement.
- [12] Neithalath, N., Sumanasooriya, M. and Deo, O., 2010. Characterizing pore volume, sizes, and connectivity in pervious concretes for permeability prediction. Materials Characterization, 61(8), pp.802-813.
- [13] Neithalath, N, Weiss, J & Olek, J, 2006. Characerizing enhanced porosity concrete using electrical impedance to predict acoustic and hydraulic performanve. In Cement and Concrete. pp.74-85. Obla, K., 2007.
- [14] Review of permeable pavement systems. Building and Environment, 5(42), pp. 3830-3836. Semadeni, D., Hernebring, A., Svensson, C. & Gustafsson, G., 2008.
- [15] Siregar, A., Rafiq, M. and Mulheron, M., 2017. Experimental investigation of the effects of aggregate size distribution on the fracture behaviour of high strength concrete. Construction and Building Materials, 150, pp.252-259.
- [16] Su, J., Cheng, Y. and Wu, N., 2019. Mixture Proportioning Design of Pervious Concrete Using the Paste Content Ratio Method (Aggregate Gradation 19mm~9.5mm and 9.5mm~4.75mm). Materials Science Forum, 947, pp.207-211.

- [17] The impacts of climate change and urbanisation on drainage in Helsingborg, Sweden: Combined sewer system. *Journal of Hydrology*, Issue 350, pp. 100-113. Suleiman, M., 2006. Development of Mix Proportion for Functional and Durable Porous Concrete.
- [18] Wanielista, M. and Chopra, M., 2007. Performance assesment of portland cement pervious concrete. Construction and maintentanance assesment of pervious concrete pavements. Florida: Storm water management academy.
- [19] Yang, J. and Jiang, G. (2003) "Experimental study on properties of pervious concrete pavement materials", *Cement and Concrete Research*, 33(3), pp. 381–386. doi: 10.1016/s0008-8846(02)00966-3.
- [20] Yu, F., Sun, D., Wang, J. and Hu, M., 2019. Influence of aggregate size on compressive strength of pervious concrete. *Construction and Building Materials*, 209, pp.463-475.

YOUNG MEMBERS' TECHNICAL CONFERENCE 2021



For Further Details

📍 Manager Publicity
The Institute of Engineers, Sri Lanka,
120/15, Wijerama Mawatha, Colombo 07

☎ +94 112 698 426/232

✉ ymstechconf2021@gmail.com/mgr.pub@iesl.lk